



**GEOCHEMICAL AND GEOCHRONOLOGICAL
CONSTRAINTS ON TERRANE DEFINITION IN MEXICO**

HENRY EIRIAN COOMBS

Submitted in partial fulfilment of the requirements for
the degree of PhD

February 2016

Declaration

This work has not previously been accepted in substance for any degree and is not concurrently submitted in candidature for any degree.

Signed (candidate)

Date

Statement 1

This thesis is being submitted in partial fulfilment of the requirements for the degree of PhD.

Signed (candidate)

Date

Statement 2

This thesis is the result of my own independent work/investigation, except where otherwise stated. Other sources are acknowledged by explicit references.

Signed (candidate)

Date

Statement 3

I hereby give consent for my thesis, if accepted, to be available for photocopying and for inter-library loan, and for the title and summary to be made available to outside organisations.

Signed (candidate)

Date

Statement 4

I hereby give consent of my thesis, if accepted, to be available for photocopying and for inter-library loans after expiry of a bar on access previously approved by the Graduate Development Committee.

Signed (candidate)

Date

ABSTRACT

Mexico has played host to a variety of igneous events since the Paleozoic, relating to the formation and subsequent breakup of the supercontinent Pangaea, as well as to intermittent subduction along its western coast. Through analysis of the crystalline basement of the Western Gulf of Mexico this project has introduced the first detailed tectonomagmatic model relating to the pre- and post- amalgamation of Pangaea in Mexico. Additionally, post-Pangaea rifting has been investigated in the extensional basin of the northern Cuicateco terrane.

This study has identified three igneous events in the crystalline basement of the Western Gulf of Mexico: 1) An Early Permian (294 Ma) continental arc that formed on Gondwana during the final amalgamation of Pangaea. These rocks appear to be related to Late Carboniferous-Early Permian plutons found in the Oaxaca area of Southern Mexico (Ortega-Obregon et al., 2014). 2) Late Permian-Early Triassic (274-243 Ma) anatectic magmatism that formed in a post-collisional environment after the final amalgamation of Pangaea. These rocks appear to be related to plutons of comparable age found in the Oaxaca area and Chiapas Massif of Southern Mexico (Weber et al., 2005; Ortega-Obregon et al., 2014). 3) Early Jurassic (189-164 Ma) continental arc rocks that likely relate to the Nazas arc system that existed across Mexico at the time (Dickinson & Lawton, 2001).

Major element and trace element geochemistry, used in conjunction with Hf and Nd isotopic analysis have revealed that the Early Cretaceous units of the northern Cuicateco terrane formed in a subduction related environment, likely associated with the closure of the Arperos oceanic basin. Extrusive and intrusive arc rocks have been dated between 140-133 Ma (Xonamanca Formation and Teotitlán Migmatitic Complex); with subduction of the Arperos ridge later causing extension (Chivillas Formation). Spreading in the Chivillas Formation stopped in the Earliest Aptian, likely due to the collision of the Guerrero terrane with Mexico.

ACKNOWLEDGEMENTS

I firstly must thank my supervisors, Andrew Kerr, Jim Pindell and David Buchs for all of their help and assistance over the last four years. Andrew and David have been superb supervisors in Cardiff, both demonstrating an eagerness to help out in all aspects of the PhD, from explaining geochemical principles to providing invaluable feedback to chapters. I owe a tremendous debt of gratitude to Jim for creating the PhD project. His knowledge on all things tectonics is awe inspiring, and helped significantly in forming the models. I must also give a special thank you to Uwe Martens for all he has done for me throughout this process. I owe him a lifetimes worth of gratitude for his unwavering willingness to help and guide.

It is important that I also thank Roberto Molina, Maria Isabel Sierra Rojas, Juan Pablo Zapata, Isidro Loza, Tomás Pena Alonso and Juliana Estrada for their assistance during fieldwork and Iain McDonald, Tony Oldroyd, Pete Fisher, Bodo Weber, Luigi Solari, Jose Duque, Ricardo Milián for their help during sample processing and analysis.

I would like to also thank all of my PhD colleagues at Cardiff University and UNAM University, as well as friends from outside of the PhD. They are what made doing the PhD an enjoyable and unforgettable experience.

Finally I must thank my family for all of their support, patience and financial aid during the slow process of writing up. Completing the PhD would have been an impossible task without it.

CONTENTS

1	INTRODUCTION.....	1
1.1	Project rationale.....	1
1.2	Aims.....	2
1.3	Thesis structure.....	3
2	GEOLOGICAL OVERVIEW OF THE CRYSTALLINE BASEMENT OF MEXICO.....	5
2.1	Introduction.....	5
2.2	Rodinia	5
2.2.1	Formation.....	5
2.2.2	Grenville Orogeny and Oaxaquia.....	7
2.2.3	Breakup.....	11
2.3	Gondwana.....	14
2.4	Laurasia.....	15
2.5	The formation of Pangaea.....	16
2.6	The breakup of Pangaea.....	24
2.7	Paleozoic-Mesozoic Subduction.....	27
2.8	Review of Mexico’s basement.....	28
3	PETROGRAPHY & GEOCHRONOLOGY OF THE WESTERN GOM.....	29
3.1	Introduction.....	29
3.2	Early Permian granitoids.....	32
3.2.1	Pinonal N2F3C1.....	32
3.2.2	Arenque N15F3+4C2.....	34
3.2.3	Paso de Oro N8F4C2.....	37
3.3	Late Permian.....	40
3.3.1	Benemerito-1 N2F7bC5.....	40
3.3.2	Trincheras N3F5aC1.....	45

3.3.3	Linares N7F1C1.....	48
3.3.4	Chaneque N6F1C4.....	51
3.3.5	Nayade N13F2C1.....	54
3.3.6	Tamaulipas N1F2C1.....	58
3.3.7	Erizo N19F19C1.....	62
3.3.8	Pinonal N2F11C2.....	64
3.3.9	Cupelado N9F1C1.....	68
3.3.10	Plan de Las Hayas N14F1C1.....	72
3.3.11	Plan de las Hayas N14F6C2.....	75
3.3.12	Paso de Ovejas N6F9C2.....	78
3.3.13	Orizaba N6F1C1.....	82
3.4	Jurassic granitoids.....	86
3.4.1	Muro-2 N12F2C1.....	86
3.4.2	Tlapacoyan N10F18C5.....	89
3.5	Sediments and meta-sediments.....	93
3.5.1	Salto N8F1C1.....	93
3.5.2	Gonzales N9F1C1.....	97
3.5.3	Gonzales N9F2C1.....	101
3.6	Summary.....	104
4	WESTERN GOM: MAJOR, TRACE AND HF ISOTOPE RESULTS AND DISCUSSION.....	105
4.1	Introduction.....	105
4.2	Analytical techniques.....	105
4.3	Alteration and element mobility.....	106
4.4	Classification.....	110
4.5	Major elements.....	116
4.6	Trace Elements.....	118

4.7	Petrogenesis of the crystalline basement of the Western GOM.....	122
4.7.1	Fractional Crystallisation.....	124
4.7.2	Tectonic setting of the granitoids.....	127
4.7.3	I vs S type granites.....	131
4.7.4	Age of magma extraction from the mantle.....	133
4.7.5	Refined LA-ICP-MS results.....	140
4.8	Summary.....	143
5	PETROGENESIS OF THE WESTERN GOM.....	144
5.1	Introduction.....	144
5.2	Petrogenesis of the Western Gulf of Mexico.....	144
5.2.1	Relation to the formation of Pangaea.....	144
5.2.2	Episodes of magmatism.....	145
5.2.3	Terrane migration.....	150
5.2.4	Gondwanan arc.....	152
5.2.5	Post-collisional magmatism.....	155
5.3	Summary.....	157
6	GEOLOGICAL OVERVIEW OF THE CUICATECO TERRANE.....	158
6.1	Introduction.....	158
6.2	Northern Cuicateco Terrane.....	158
6.2.1	Chivillas Formation.....	160
6.2.2	Teotitlán Migmatitic Complex.....	162
6.2.3	Pochotepec Formation.....	163
6.2.4	Mazateco Metamorphic Complex.	164
6.2.5	Xonamanca Formation.....	165
6.2.6	Existing models for the origin of the northern Cuicateco terrane.....	166
6.2.7	Deformation and Metamorphism.....	171

6.2.8	Basement.....	173
6.3	Southern Cuicateco Terrane.....	173
6.3.1	Geology.....	173
6.3.2	Age.....	174
6.4	Other Cretaceous terranes of Mexico.....	174
6.4.1	Guerrero Terrane.....	174
6.4.2	Xolapa Terrane.....	180
6.4.3	Chortis Block.....	181
6.5	Adjacent Terranes.....	184
6.5.1	Zapoteco Terrane.....	184
6.5.2	Maya Terrane.....	187
6.6	Gulf of Mexico.....	189
6.7	Summary.....	191
7	FIELDWORK AND PETROGRAPHY.....	192
7.1	Introduction.....	192
7.2	The Chivillas Formation.....	194
7.2.1	Fieldwork.....	194
7.2.2	Petrography.....	198
7.3	Teotitlán Migmatitic Complex.....	202
7.3.1	Fieldwork.....	202
7.3.2	Petrography.....	204
7.4	Pochotepec Formation.....	207
7.4.1	Fieldwork.....	207
7.4.2	Petrography.....	209
7.5	Xonamanca Formation.....	211
7.5.1	Fieldwork.....	211

7.5.2	Petrography.....	213
7.6	Summary.....	215
8	GEOCHRONOLOGY RESULTS OF THE CUICATECO TERRANE.....	216
8.1	Introduction.....	216
8.2	Pochotepec Formation.....	219
8.2.1	Sample 10-17-11-15c.....	219
8.2.2	Sample 10-17-11-8a.....	221
8.3	Xonamanca Formation.....	225
8.3.1	Sample 12-12-10 7B.....	225
8.3.2	Sample 12-12-10 7C.....	228
8.4	Teotitlán Migmatitic Complex.....	231
8.4.1	Sample 5-11-11-01.....	231
8.4.2	Sample 5-11-11-03.....	233
8.4.3	Sample 10-18-11-7A.....	235
8.4.4	Sample 10-18-11-9d.....	238
8.4.5	Sample 10-18-11-9E.....	240
8.4.6	Sample 10-18-11-9F.....	243
8.5	Chivillas Formation.....	247
8.5.1	Sample 10-18-11-1B.....	247
8.5.2	Sample 10-18-11-2A.....	251
8.5.3	Sample 10-18-11-5B.....	255
8.5.4	Sample 5-10-11-02.....	258
8.6	Summary.....	260
9	CUICATECO: MAJOR, TRACE ELEMENT AND HF-ND GEOCHEMISTRY.....	262
9.1	Introduction.....	262
9.2	Analytical techniques.....	262

9.3	Alteration and element mobility.....	265
9.4	Xonamanca Formation.....	266
9.4.1	Element Mobility & Alteration.....	266
9.4.2	Classification.....	267
9.4.3	Trace element variation.....	269
9.5	Granites from the Teotitlán Migmatitic Complex.....	271
9.5.1	Element Mobility & Alteration.....	271
9.5.2	Classification.....	272
9.5.3	Trace element variation.....	275
9.6	Chivillas Formation.....	278
9.6.1	Element Mobility & Alteration.....	278
9.6.2	Classification.....	282
9.6.3	Major element variation.....	284
9.6.4	Trace element variation.....	288
9.6.5	Nd & Hf isotopes.....	295
9.7	Tectonomagmatic Setting of the Xonamanca Formation & Teotitlán Migmatitic Complex..	298
9.8	Tectonomagmatic setting of the Chivillas Formation.....	303
9.8.1	Degree of partial melting.....	303
9.8.2	Fractional Crystallization trends.....	305
9.8.3	Composition of source: Subduction fluid vs. continental contamination.....	306
9.8.4	Composition of source: OIB.....	312
9.8.5	Composition of source: Lower crust ultramafic source.....	316
9.8.6	Composition of source: slab & sediment melt metasomatism.....	317
9.8.7	Basin Maturity.....	326
9.9	Summary.....	327
10	PETROGENESIS AND PALEOGEOGRAPHY OF THE CUICATECO TERRANE.....	329

10.1 Introduction.....	329
10.2 Early Cretaceous subduction in Mexico.....	329
10.3 Petrogenesis of the Cuicateco terrane.....	332
10.3.1 Mechanism for back arc extension.....	334
10.3.2 Back-arc Model: 150-140 Ma.....	337
10.3.3 Back-arc Model: 133 Ma.....	339
10.3.4 Back-arc Model 130 Ma.....	341
10.3.5 Back-arc Model 126 Ma.....	343
10.4 Summary.....	346
11 CONCLUSIONS.....	347

1 Introduction

1.1 Project rationale

The continental crust which comprises Mexico has been involved in numerous episodes of major collisional and rifting events since the Proterozoic (Pindell & Dewey, 1982; Pindell, 1985; Dickinson & Lawton, 2001; Pindell & Kennan, 2001; Solari et al., 2003; Keppie et al., 2004; Talavera-Mendoza et al., 2005; Pindell & Kennan, 2009; Vega-Granillo et al., 2009; Nance et al., 2010; Weber et al., 2010; Schulze, 2011; Weber & Schulze, 2014; Ortega-Gutiérrez et al., 2014). These are associated with the formation and breakup of supercontinents, most recently Pangaea (Dickinson & Lawton, 2001). In addition, Mexico has had an intermittently active continental margin along its western flank since the Early Paleozoic, which has formed several arc systems, including the Trans Mexican Volcanic Belt that exists today (Ferrari et al., 2012). As a result of this complex tectonomagmatic history the continental crust of Mexico is very heterogeneous and composed of a series accreted blocks with varying ages and origins, known as terranes. Many areas in this vast and often remote country have yet to be studied in detail.

Such areas of Mexico where the geological evolution is poorly understood include the unexposed crystalline basement along the Western Gulf of Mexico, which covers an area $\sim 130,000 \text{ km}^2$ from the border of the USA down to Southern Mexico (Figure 1.1). Another is the extensional basin of the northern Cuicateco terrane in Southern Mexico which covers an area of $\sim 20,000 \text{ km}^2$ (Figure 1.1).

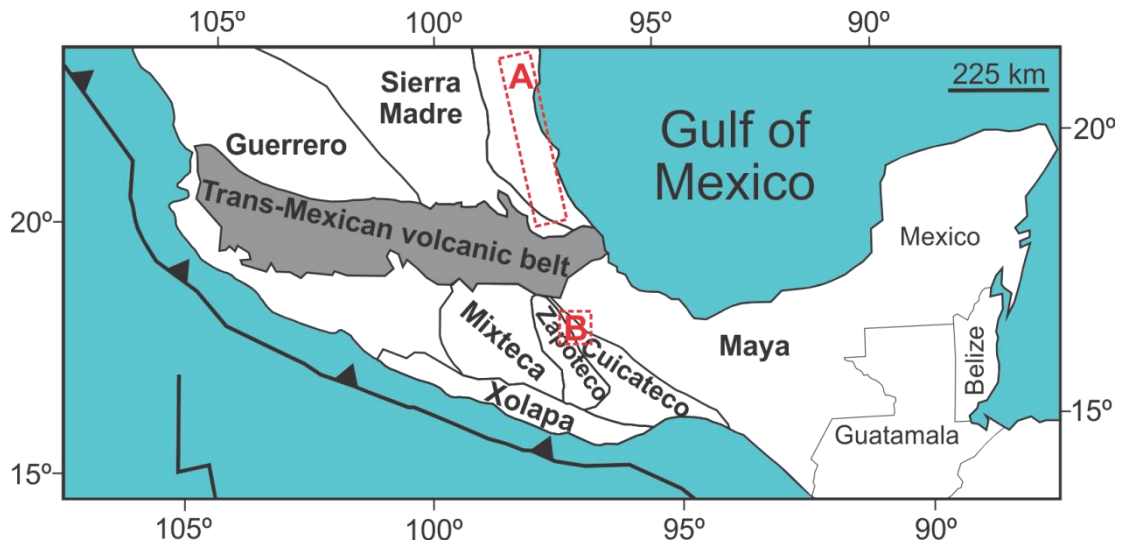


Figure 1.1. Schematic map of the terranes of Southern Mexico. The dashed box marked A shows the study area for Chapters 2-5 which concentrates on the crystalline basement of the Western Gulf of Mexico. The dashed box marked B shows the study area for Chapters 6-10 which concentrates on the northern Cuicateco terrane.

The crystalline basement of the Western Gulf of Mexico has only been reported in studies conducted by PEMEX, the national oil company (Ramos-Lopez, 1972). Previous studies on the northern Cuicateco terrane have provided detailed structural (Angeles-Moreno, 2006) and stratigraphic interpretations (Mendoza-Rosales et al., 2010), as well as geochronological data, from which tectonic models have been proposed. However, the geochemical dataset for this terrane is somewhat limited and restricted to a small portion of the terrane (Mendoza et al., 2010).

1.2 Aims

This thesis presents the first comprehensive geochemical and geochronological study on the basement of the Western Gulf of Mexico and the extensional basin of the northern Cuicateco terrane, Southern Mexico. The major and trace element data obtained from Cardiff University, U/Pb zircon geochronology analysed at Universidad Nacional Autónoma de México (Juriquilla, Mexico) and

isotopic data analysed at the Centro de Investigación Científica y de Educación Superior de Ensenada (Mexico) have been used to:

- Produce a comprehensive geochemical and geochronological dataset for the crystalline basement of the Western Gulf of Mexico and each of the units in the northern Cuicateco terrane.
- Constrain the age of granitoids that form the crystalline basement of the Western Gulf of Mexico.
- Investigate whether a mantle source was involved during this igneous event.
- Determine the tectonic setting for the igneous event that formed the basement of the Western Gulf of Mexico.
- Constrain the age for the units of the northern Cuicateco terrane, Southern Mexico.
- Investigate the likely tectonic setting that the igneous rocks of the northern Cuicateco terrane were formed in.
- Synthesise the geochronological and geochemical interpretations to produce tectonomagmatic models for both the crystalline basement of the Western Gulf of Mexico and northern Cuicateco terrane, Southern Mexico.

1.3 Thesis structure

Due to the apparent separate tectonic histories of the basement of the Western Gulf of Mexico and the northern Cuicateco terrane the two areas have not been directly compared. The thesis has therefore been split into 11 chapters, with the first half covering the Western Gulf of Mexico and the second half focussing on the northern Cuicateco terrane. Chapter 2 reviews our current understanding of the

crystalline basement of Mexico and briefly discusses its tectonic evolution since the Proterozoic. Chapter 3 presents the U/Pb zircon geochronology results for the crystalline basement of the Western Gulf of Mexico while Chapter 4 details the results and discussion on the major element, trace element and Hf isotope analysis. A tectonomagmatic model for the basement of the Western Gulf of Mexico is presented in Chapter 5.

The second half of the thesis concentrates on the northern Cuicateco terrane, with Chapter 6 reviewing the tectonic history of Mexico during the Mesozoic. Chapter 7 summarises the field observations from the northern Cuicateco terrane from this study, as well as describing the main petrographic features of each of the units. Chapter 8 introduces the geochronology results for the units of the northern Cuicateco terrane, while Chapter 9 presents the results and discussion for the major, trace element and isotopic analysis. Chapter 10 presents the tectonomagmatic model for the evolution of the northern Cuicateco terrane. Finally, Chapter 11 synthesises and makes some concluding remarks on what has been discovered about the crystalline basement of the Western Gulf of Mexico and northern Cuicateco terrane and proposes recommendations for future research in these areas.

2 Geological overview of the crystalline basement of Mexico.

2.1 Introduction

Mexico has had an active continental margin through at least two supercontinent cycles since the Proterozoic and as a result is composed of continental crust of varying age and composition. This chapter will review the existing models for the formation and breakup of supercontinents since the Proterozoic, and relate these events to the crystalline basement of Mexico up until the Jurassic. Tectonic and basement forming events in Mexico relating to the Cretaceous will be discussed further in Chapter 6.

2.2 Rodinia

2.2.1 Formation

The supercontinent originally known as Pangaea I (Valentine and Moores, 1970) and later renamed Rodinia (McMenamin and McMenamin, 1990) is believed to have formed between 1300 and 900 Ma through orogenic events that included most of the continental blocks that existed at the time (Li et al., 2008). The continental block of Laurentia is commonly positioned in the centre of Rodinia models (Hoffman, 1991; Li et al., 2008) due to Neoproterozoic passive margins that run along its perimeter. The location of the remainder of the continental blocks has been a contentious topic of over the last 30 years.

Chapter 2: Geological overview of Mexico's basement

One of the first models to be proposed for the north eastern flank of Rodinia was the southwest U.S.-East Antarctic connection or SWEAT hypothesis (Eisbacher, 1985; Bell and Jefferson, 1987; Dalziel, 1991; Hoffman, 1991; Moores, 1991); others include “the missing link” model by Li et al. (1995), Australia-Southwest U.S. connection (AUSWUS; Brookfield, 1993) and the Australia-Mexico connection (AUSMEX; Wingate et al., 2002).



Figure 2.1. One possible arrangement of the continental blocks during Rodinia from the review paper by Li et al. (2008).

Chapter 2: Geological overview of Mexico's basement

There is general agreement that during the existence of Rodinia the continental blocks of Amazonia, Baltica and West Africa were positioned to the south east of Laurentia (Figure 2.1; Hoffman, 1991; Bogdanova et al., 2008; Pease et al., 2008; Li et al., 2008). Other large continental blocks such as the Congo-São Francisco, Rio de la Plata and Kalahari cratons are believed to have been stitched to the south west of Laurentia during the formation of Rodinia (Figure 2.1; Hoffman, 1991; Weil et al., 1998; D'Agrella-Filho et al., 2004; Li et al., 2008).

A detailed description of all of the Rodinia formation models is beyond the scope of this study but can be found in the review paper by Li et al. (2008). The one aspect of Rodinia's formation that is of interest to this study is the Grenville Orogeny, which constitutes a large proportion of modern-day Mexico's basement.

2.2.2 Grenville Orogeny and Oaxaquia

The Grenville Orogeny affected many continental blocks, such as Laurentia, Amazonia and Baltica during the amalgamation of Rodinia in the Mesoproterozoic (Figure 2.1). Basement rocks belonging to this orogeny stretch from Mexico, through the US and into Canada; with remnants also found in Scotland. The Mexican extent of the Grenville Orogeny is known as Oaxaquia or the Oaxaquia microcontinent and has been described as the backbone of Mexico (Ortega-Guiterrez et al., 1995) due to the way it stretches the length of the country. Outcrops of Oaxaquia type crust in Mexico can be found in the Oaxacan Complex, Novillo Gneiss, Huiznopala Gneiss and Guichicovi Complex (Figure 2.2).

The oldest reported ages for Oaxaquia range between 1.5 and 1.4 Ga (orthogneiss and migmatites; Solari et al., 2003; Schulze, 2011; Weber & Schulze,

Chapter 2: Geological overview of Mexico's basement

2014) from U/Pb dates on zircons (LA-ICP-MS and ID-TIMS). They have been interpreted to represent an early island arc system called Proto-Oaxaquia (Weber and Schulze, 2014). A later and more prevalent pulse of island arc magmatism occurred between 1.3 and 1.2 Ga, with possible associated back arc magmatism (Figure 2.3A; Lawlor et al., 1999; Keppie et al., 2001; Dostal et al., 2004; Keppie, 2004; Weber et al., 2010; Weber and Schulze, 2014).

The Olmecan event records localised migmatization in Oaxaquia that has been dated to ca. 1.1 Ga (Solari et al., 2003). It has been suggested that this migmatization is associated with ~1.16-1.13 Ga extensional back arc granites (Keppie et al., 2001, 2003; Keppie, 2004). However, others argue (Weber et al., 2010; Weber and Schulze, 2014) it is related to a compressional event during island arc (Oaxaquia) accretion to Amazonia (Figure 2.3C). Following migmatization, an anorthosite-mangerite-charnockite-granite (AMCG) suite was emplaced (dated to ~1012 Ma; Solari et al., 2003). This suite, has been again either linked to back arc extension (Solari et al., 2003; Keppie et al., 2004) or island arc (Oaxaquia)-continent (Amazonia) collision (Figure 2.3C; Weber et al., 2010).

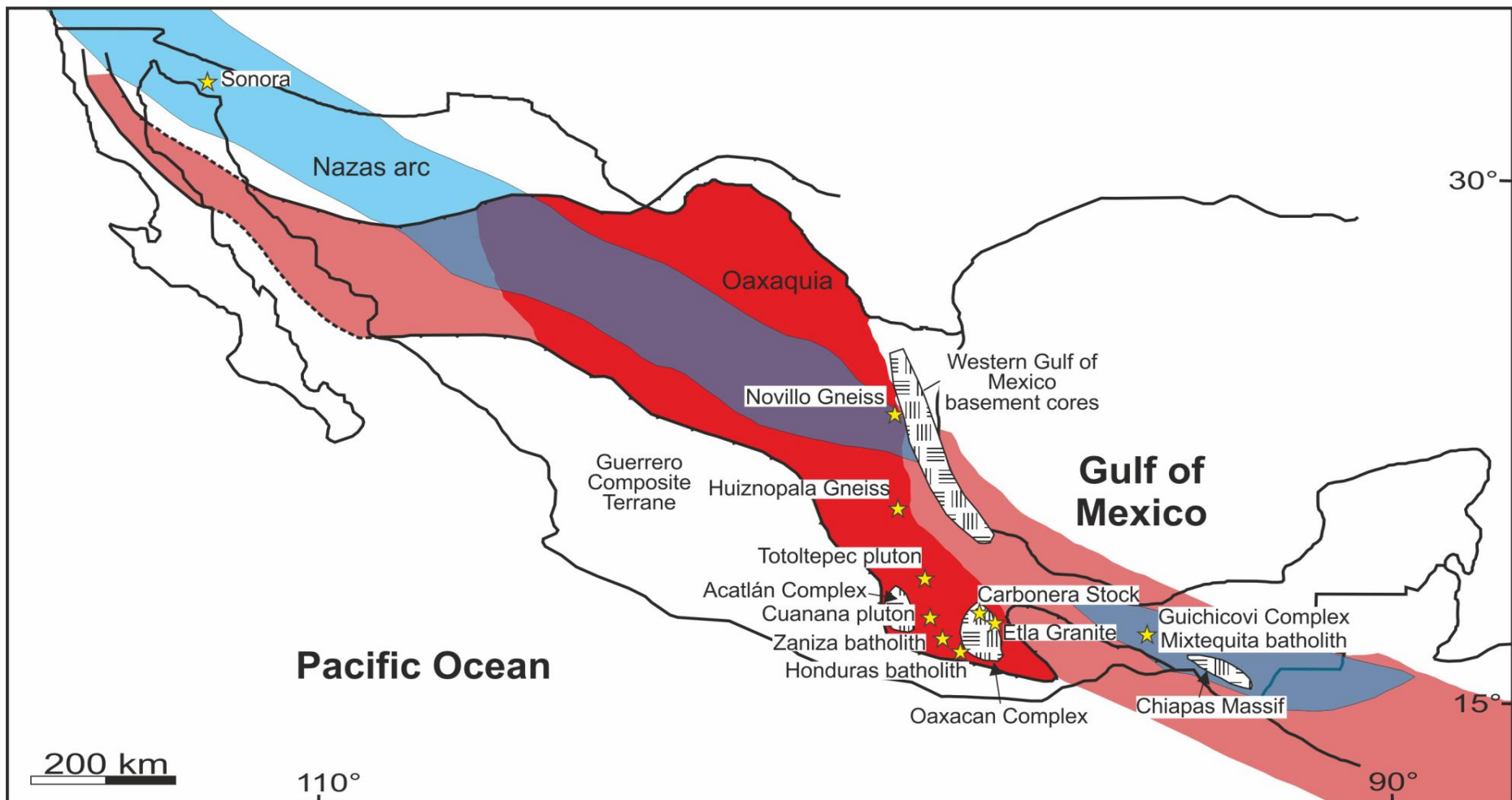


Figure 2.2. Schematic map of basement outcrops in Mexico. Dark red shading marks the boundaries of Oaxaquia as set by Ortega-Gutierrez et al. (1995) and the light red shading marks possible extensions proposed by Keppie et al. (2003). The blue shaded area represents the locality of the Jurassic Nazas arc from Lawton & Molina Garza (2014).

Chapter 2: Geological overview of Mexico's basement

The final stage of Oaxaquia's evolution is recorded in the Zapotecan event, which has been dated to ~1004-978 Ma (Solari et al., 2003). This period of Oaxaquia's history preserves evidence of granulite facies metamorphism, (to a depth of ~30 km ;Solari et al., 2003, Keppie et al., 2004; Weber et al., 2010; Weber et al., 2014). The process of burial is contentious but one possible scenario is Oaxaquia was thrust beneath Baltica-Sveconorwegia as the continental craton collided with Amazonia, during the formation of Rodinia (Figure 2.3D; Weber et al 2010; Weber and Schulze, 2014).

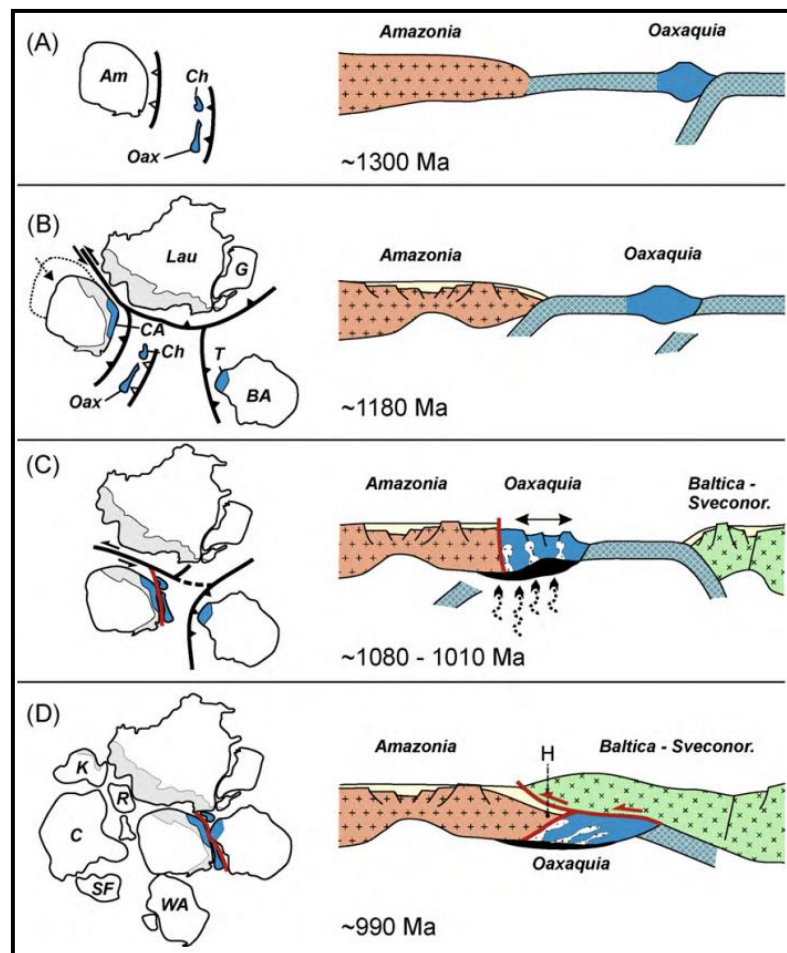
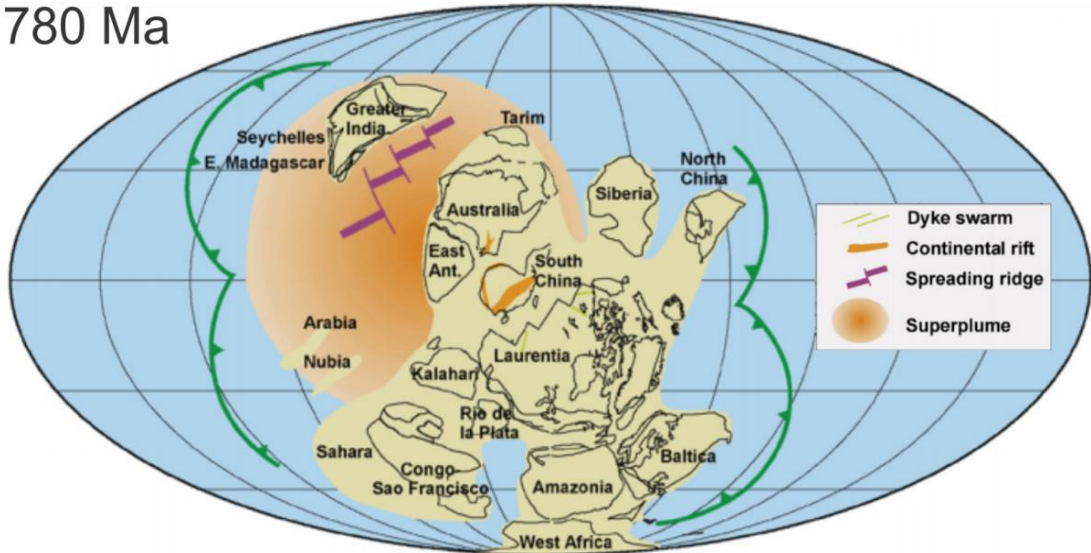


Figure 2.3. Paleogeographic and tectonic model for the formation of Oaxaquia, from Weber et al. (2010). Abbreviations: Am= Amazonia, BA- Baltica-Sveconorwegia, C= Congo, CA= Colombian Andes, Ch= Chortis, G= Greenland, K= Kalahari, Lau= Laurentia, Oax= Oaxaquia, R= Rio de la Plata, SF= São Francisco, T= Telemarkia, WA= West Africa. Grey shaded areas represent other areas of the Grenville Orogeny.

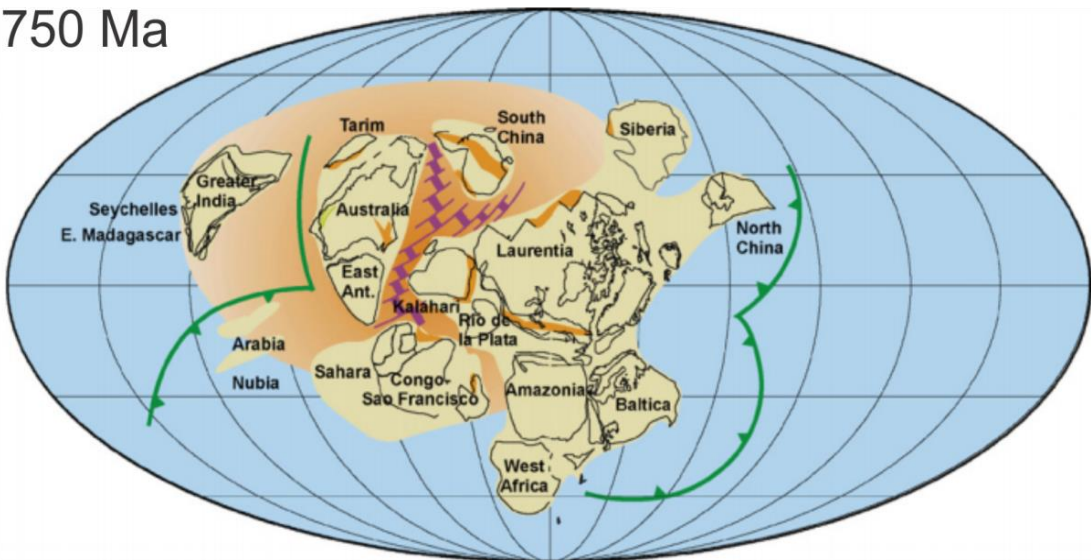
2.2.3 Breakup

Rodinia completed its assembly ~900 Ma and is thought to have remained stable for 150 Ma before rifting initiated ~750 Ma. The cause of rifting may well have been due to a mantle plume forming beneath Rodinia (Li et al., 2008 & references therein). The initiation of plume magmatism in Rodinia is recorded in anatectic melts that have been dated to 870-845 Ma in Southern China (X.H. Li et al., 2003), Africa (Johnson et al., 2005), the Scandinavian Caledonides (Paulsson and Andreasson, 2002) and Scotland (Dalziel and Soper, 2001). More widespread, mafic plume magmatism dated to ca. 825 Ma is recorded in Australia (Zhao et al., 1994; Wingate et al., 1998), South China (Li et al., 1999; X.H. Li et al., 2003a; Z.X. Li et al., 2003c), Tarim (Zhang et al., 2006), India (Radhakrishna and Mathew, 1996), Kalahari (Frimmel et al., 2001), and the Arabian-Nubian terranes (Stein and Goldstein, 1996; Teklay et al., 2002). As plume activity persisted, continental rifting became widespread between 780 and 720 Ma (Figure 2.4). This rifting eventually led to the separation (ca. 630-550 Ma) of the continental blocks that were attached to Laurentia, marking the end of the supercontinent of Rodinia (Figure 2.5; Zhang et al., 2006; Cawood and Pisarevsky, 2006; Li et al., 2008; Pisarevsky et al., 2008).

780 Ma



750 Ma



720 Ma

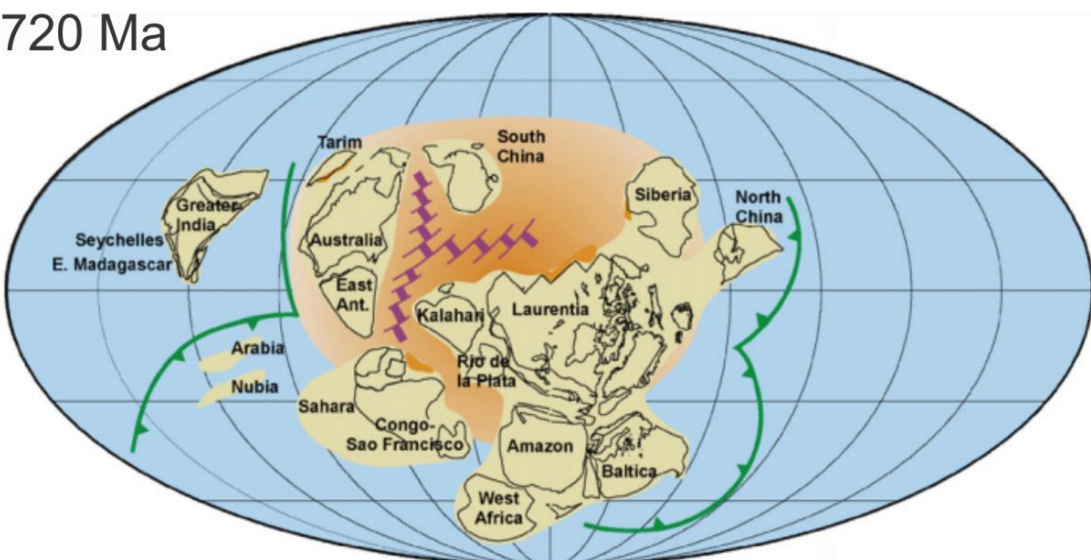
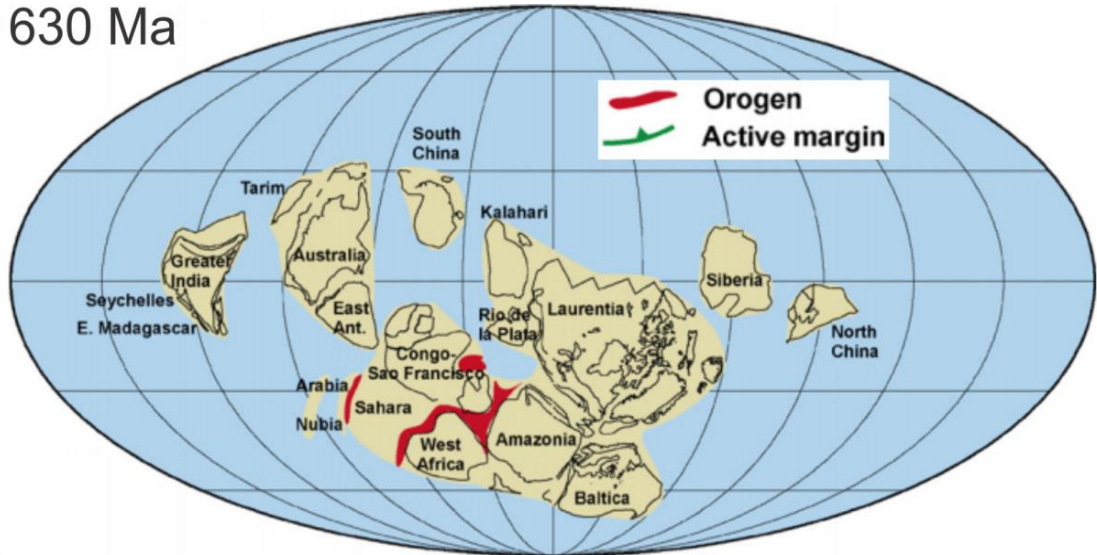


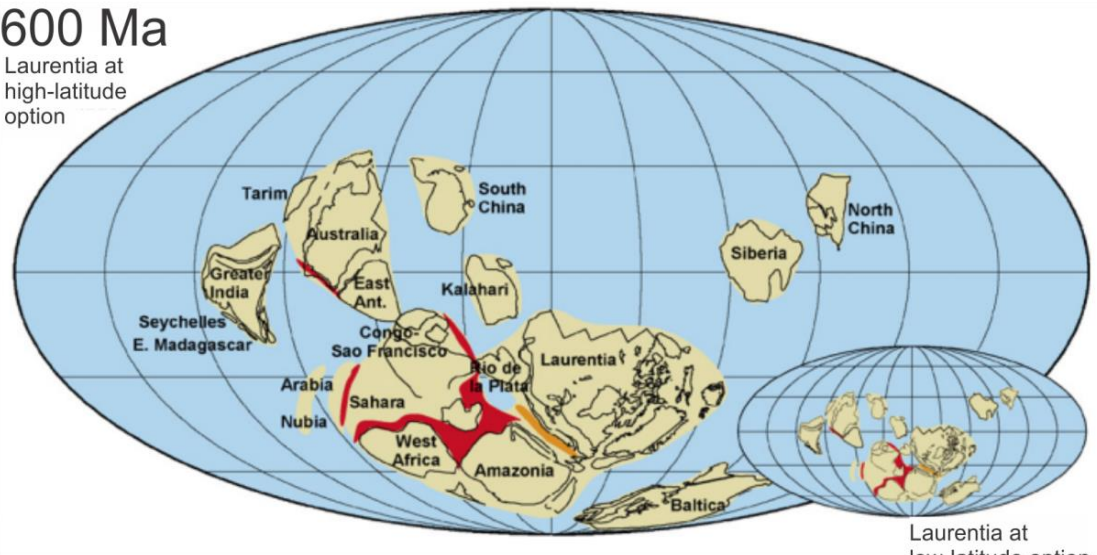
Figure 2.4. Schematic maps for the initiation of rifting in Rodinia as a result of mantle plume activity, adapted from Li et al.(2008)

630 Ma



600 Ma

Laurentia at high-latitude option



Laurentia at low-latitude option

550 Ma

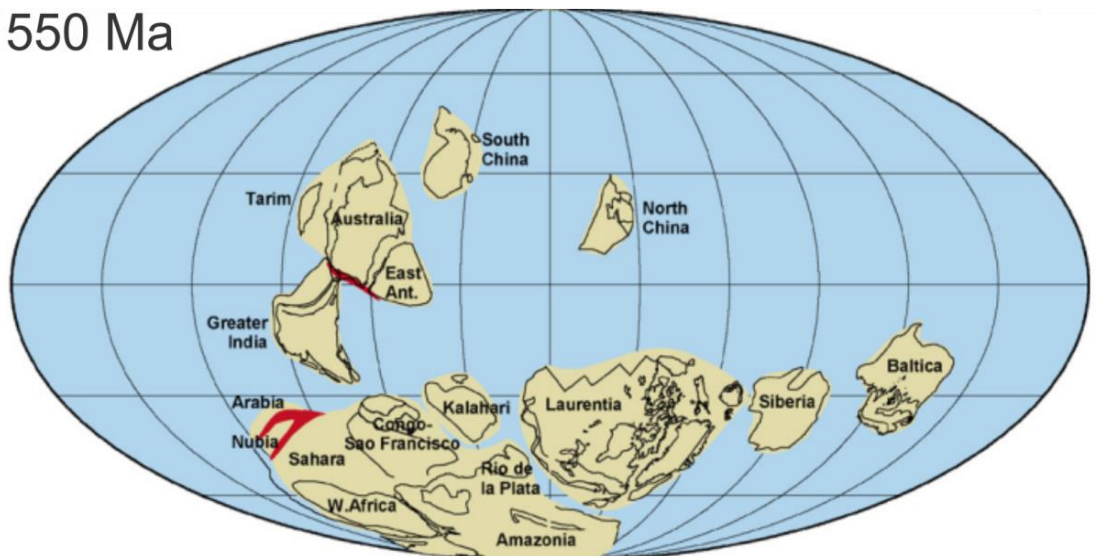


Figure 2.5. Schematic maps for the separation of the continental blocks that made up Rodinia, adapted from Li et al. (2008).

2.3 Gondwana

The breakup of Rodinia led to the formation of Gondwana or Gondwanaland (Hoffman, 1991); a supercontinent that spanned the Palaeozoic. It consisted of the continental cratons of Tarim, Australia, East Antarctica, Greater India, Arabia, Nubia, Sahara, W. Africa, Congo-São-Francisco, Kalahari, Rio de la Plata and Amazonia (Li et al., 2008).

The first cratons to collide during the formation of Gondwana were Amazonia, W. Africa and Congo-São-Francisco, forming the Brasiliano Orogeny (Trompette, 1997) ~600 Ma (Figure 2.5). By ~550 Ma the cratons that would make up Gondwana had separated from Laurentia via extension in the Amazonia and Rio de la Plata plates (Figure 2.5). Also in this period the minor cratons of Nubia and Arabia collided with the Sahara craton and the Kalahari collided with the Congo and Rio de la Plata through the closure of the Adamastor Ocean (Prave, 1996).

The final phase of Gondwana's formation saw the closure of the Mozambique Ocean, causing the collision of Tarim, Australia, East Antarctica and Greater India with the remainder of the already amalgamated continental cratons (Li et al., 2008). Palaeomagnetic analyses suggest final amalgamation had occurred by 540-530 Ma (Meert and Van der Voo, 1996). Gondwana would eventually collide with Laurasia, forming the southern portion of the Permo-Triassic supercontinent of Pangaea (see following sections).

2.4 Laurasia

After the fragmentation of Rodinia, Laurentia was separated from surrounding continental cratons by the Iapetus Ocean (to the east) and Rheic Ocean (to the south). The closure of the Iapetus Ocean throughout the Paleozoic led to the formation of Laurasia, a supercontinent that consisted of Laurentia, Baltica and Avalonia (Figure 2.6).

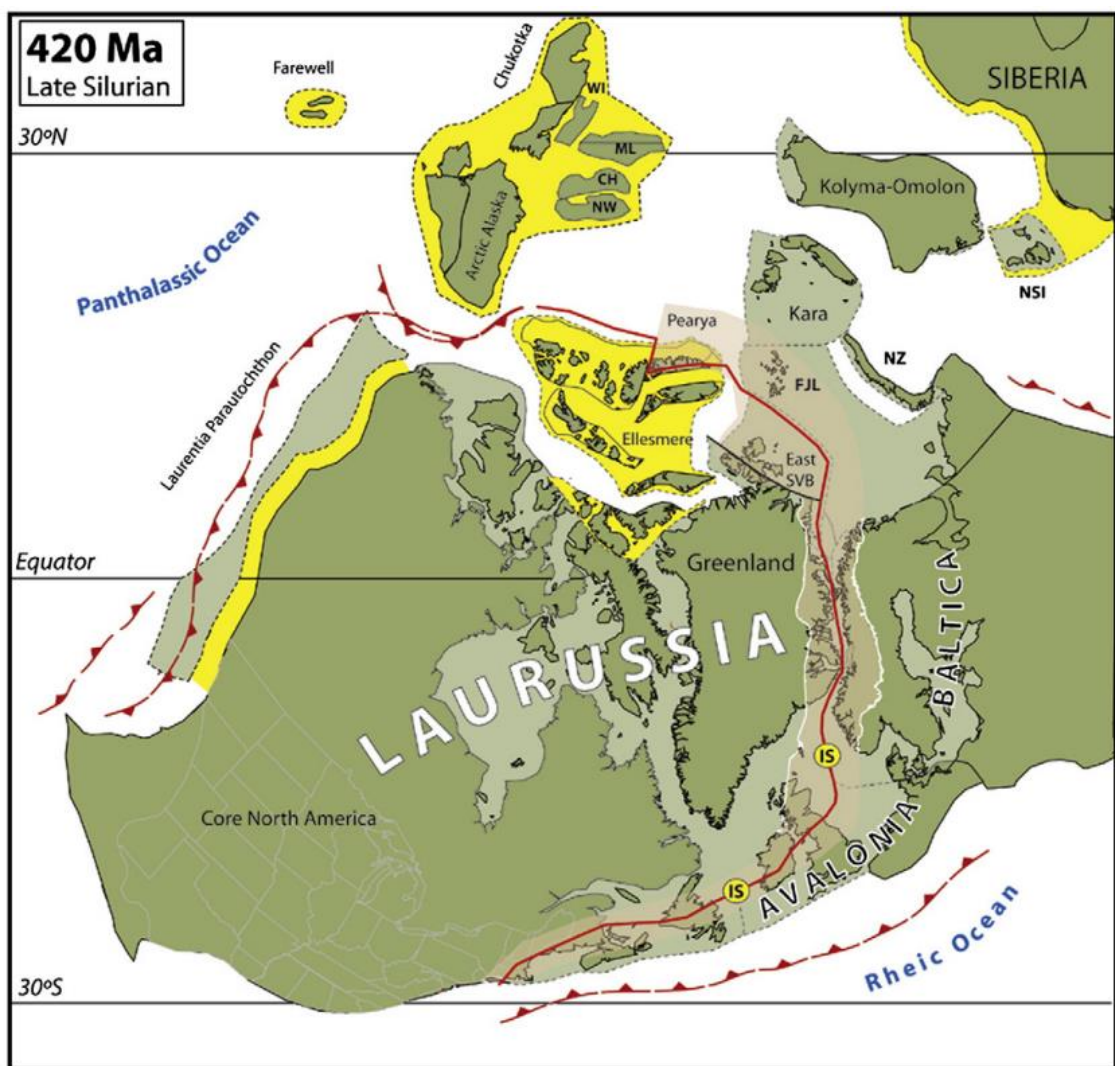


Figure 2.6. Map showing the formation of Laurasia from Cocks and Torsvik (2011). Light brown represents Caledonian orogenic deformation and yellow shading represents probable continental areas and terrane extension. Abbreviations: CH= Chukchi, FJL= Franz Josef Land, IS= Iapetus Suture, ML= Mendeleev, NSI= New Siberian Islands, NW= Northwind, NZ= Novaya Zemlya, SVB= Svalbard, WI= Wrangel Island.

Chapter 2: Geological overview of Mexico's basement

Extension in the Iapetus Ocean started in the Neoproterozoic, during the fragmentation of Rodinia. It reached its peak extension by the Early Ordovician and subduction was initiated by the Floian (478-470 Ma; Cocks and Torsvik, 2011), producing island arcs along the eastern flank of Laurentia. These island arcs were accreted to Laurentia throughout the Late Cambrian-Ordovician (Mac Niocaill et al., 1997), forming the Taconic Orogeny of the Appalachian mountain belt (Dewey et al., 2015). Island arc accretion to Laurentia is also recorded in the Paleozoic Acatlán Complex of Southern Mexico (see Section 2.5). These collisional events along the flanks of Laurentia marked the beginning of the Caledonian Orogeny, which would result in the formation of Laurasia.

The Caledonian Orogeny has been broadly defined as any tectonic or orogenic event (related to arc-arc, arc-continent or continent-continent collisions) occurring as a result of the closure of the Iapetus Ocean, between Laurentia, Baltica and Avalonia (McKerrow et al., 2000). The first continent-continent collision occurred between Avalonia and Baltica during the Late Ordovician, forming the Polish Caledonides (Dewey et al., 2015). The docking of Baltica and Avalonia to Laurentia occurred throughout the Silurian, forming the British Caledonides and Greenland/Scandinavian Caledonides (Torsvik et al., 1996; Cocks and Torsvik, 2011; Dewey et al., 2015). This marked the final stage of the assembly of Laurasia (Figure 2.6).

2.5 The formation of Pangaea

The supercontinent of Pangaea is the last time the continental cratons were amalgamated as one. It formed from the diachronic collision of Gondwana and

Chapter 2: Geological overview of Mexico's basement

Laurasia that initiated in the Carboniferous (~350-320 Ma), and finished in the Early Permian (~280-250 Ma). This collision occurred through the closing of the Rheic Ocean and is recorded in the Ouachita-Marathon-Alleghanian Orogenies of Northern Mexico and the USA, and the Variscan Orogeny of Europe and Western Africa (Figure 2.7).

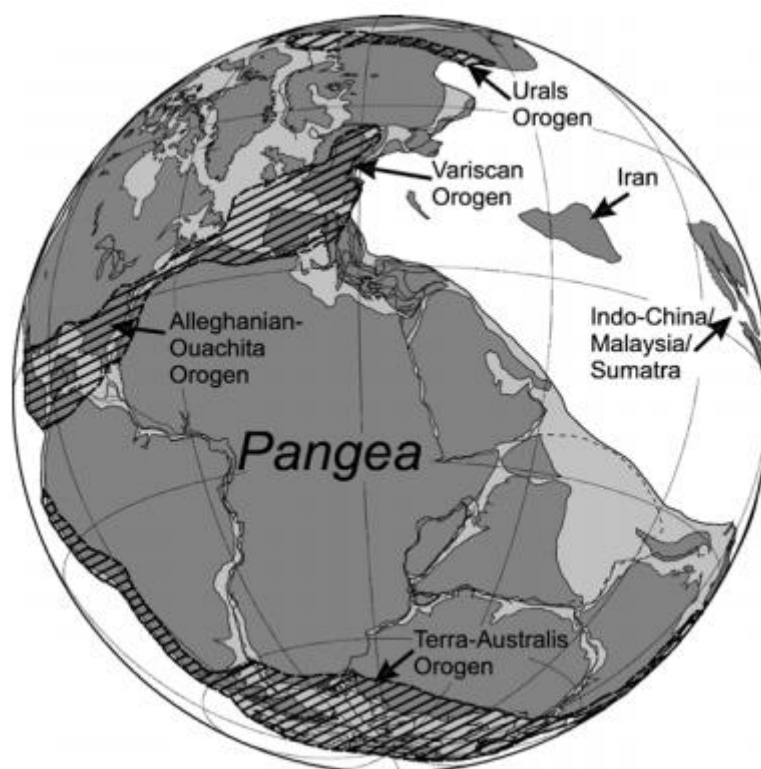


Figure 2.7. Reconstruction of Pangaea ca. 250 Ma from Cawood and Buchan (2007).

The Alleghanian Orogeny refers to the collision between Gondwana and Laurasia in the Appalachian region of North America (Figure 2.7). The initiation of thrusting is recorded in orthogneisses, granitic gneisses and syn-kinematic granites of the South Appalachians. The oldest of these rocks have been dated to 335 Ma (U/Pb zircon; Wortman et al., 1998). Anatectic melts due to crustal thickening are recorded in the orogeny in two phases, the first in the Late Carboniferous (ca. 325-

Chapter 2: Geological overview of Mexico's basement

305 Ma), and the second in the Late Permian (ca. 275 Ma; Samson, 2001; Hatcher, 2002; Nance et al., 2010).

The Variscan Orogeny is the eastern extension of the collisional zone between Gondwana and Laurasia (Figure 2.7) that has subsequently been separated from the North American Alleghanian Orogeny through the opening of the Atlantic Ocean (see section 2.6). The orogeny covers an area 1000 km in width and 8000 km in length (Matte, 2001), stretching across Central and Western Europe as well as West Africa (also referred to as the Mauritanide Orogen; Piqué and Skehan, 1992; Nance et al., 2010).

The Ouachita-Marathon Orogeny is the western most point of the collision between Gondwana and Laurasia, covering Arkansas, Texas and Mexico (Figure 2.7). It differs from the Alleghanian Orogeny in that there is no associated magmatism and only low grade metamorphism is present (Nance et al., 2010). The collision between Laurentia and Gondwana along the Ouachita-Marathon segment is believed to have occurred between the Late Carboniferous-Early Permian (Pindell and Dewey, 1982; Pindell, 1985; Ross, 1986; Viele and Thomas, 1989; Sedlock et al., 1993; Dickinson and Lawton, 2001). It is thought that the Ouachita-Marathon Orogeny lay to the north of the Rheic suture zone (Nance, et al., 2010). The location of the boundary between Laurentia and Gondwana in Mexico is poorly constrained.

Some authors (Ross, 1986; Handschy et al., 1987; Dickinson and Lawton, 2001) trace the Gondwana-Laurentia suture from the Ouachita-Marathon segment to the south through Mexico (Figure 2.8). These interpretations were made from gravity anomalies and similarities in Pennsylvanian-Middle Permian sheared

Chapter 2: Geological overview of Mexico's basement

metasediments found in the Coahuila block and Texas (Figure 2.8), which are inferred to represent the interior metamorphic core of the of the suture (Handschy et al., 1987).

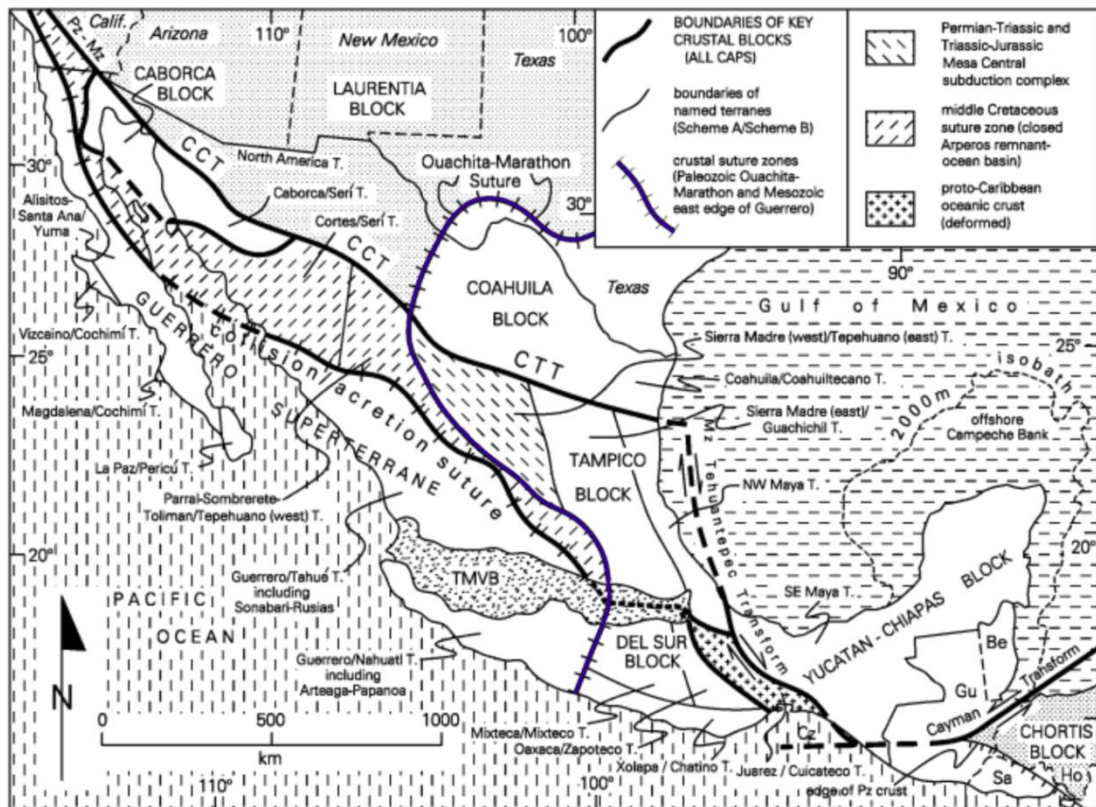


Figure 2.8. Distributions of key crustal blocks and formally named Mexican terranes, from Dickinson and Lawton (2001). Gondwana-Laurentia suture highlighted in blue, running through the south of Mexico. Abbreviations: Be—Belize, CCT—California-Coahuila transform (Permian–Triassic slip), CTT—Coahuila-Tamaulipas transform (infra-Jurassic slip), Cz—Cenozoic, Gu—Guatemala, Ho—Honduras, Mz—Mesozoic, Pz—Paleozoic, Sa—El Salvador, TMVB (dot pattern)—Neogene Trans-Mexico volcanic belt.

However, later studies (Poole et al., 2003 and 2005) dispute this interpretation, instead proposing that the suture extends across Northern Mexico, into Sonora (Figure 2.9). This interpretation was based on stratigraphic and structural data that indicate a continuous 3000 km Paleozoic carbonate continental shelf from Sonora to Southern USA, marking a Sonora-Marathon-Ouachita segment to the suture (Poole et al., 2005; Figure 2.9).

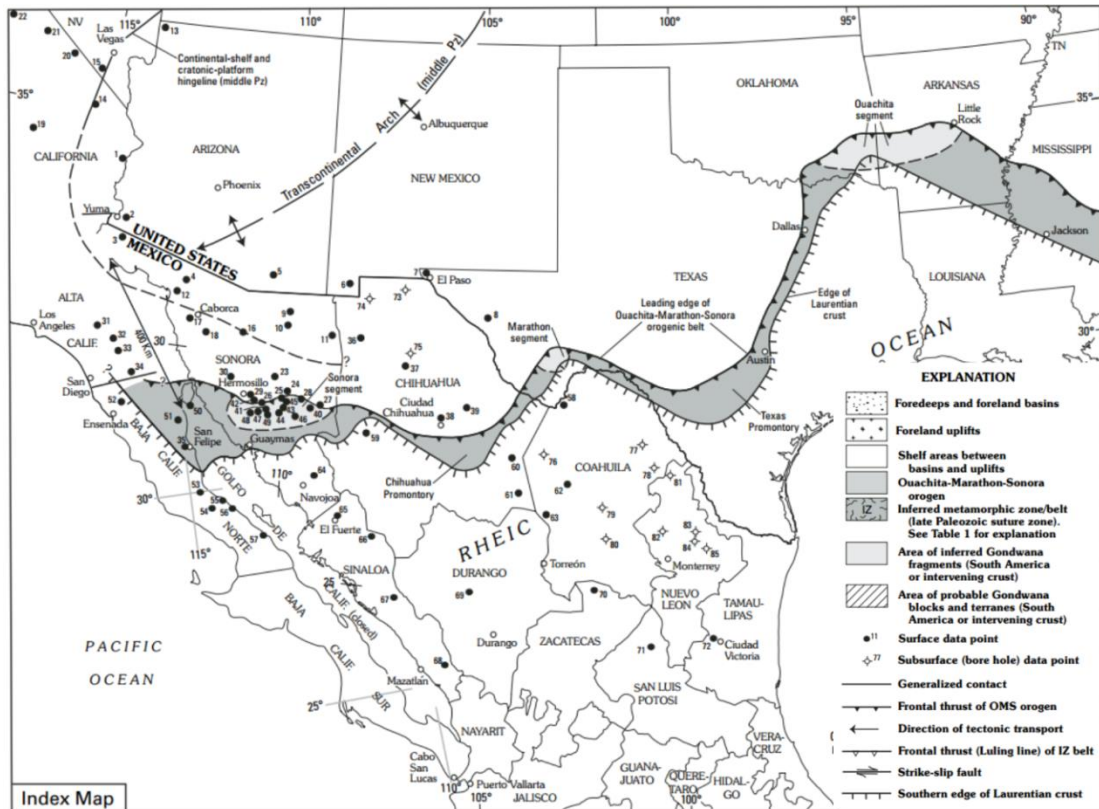


Figure 2.9. Poole et al. (2005) map of southern North America (present-day position) and palinspastically restored Baja California and adjacent Alta California (400 km to pre-Tertiary position). Numbers refer to localities of data. Consult Poole et al. (2005) for explanation of data sources. Also shown, are the middle Paleozoic Transcontinental arch, shelf-platform hingeline, edge of Laurentian crust, and leading edge of the late Paleozoic Ouachita-Marathon-Sonora orogenic belt.

One of the few areas exposed in Mexico that preserves Paleozoic rocks is the Acatlán Complex of the Mixteca terrane in Southern Mexico. It is composed of a complex succession of deformed high pressure (HP) metamorphic rocks, including eclogites and blueschists, deformed granitoids and sediments. The origin of these Paleozoic rocks has been a topic of debate over the past decade, with some authors indicating an affinity with Laurentia (Figure 2.10; Talavera-Mendoza et al., 2005; Vega-Granillo et al., 2007 and 2009), and others interpreting the rocks as having formed in a peri-Gondwanan terrane (Figure 2.11; Keppie et al., 2008, Ortega-Obregon et al., 2009 and 2014).

Chapter 2: Geological overview of Mexico's basement

Authors that associate the Acatlán Complex with Laurentia (Talavera-Mendoza et al., 2005; Vega-Granillo et al., 2007 and 2009) interpret U/Pb zircon ages of granitoids and metasediments as showing an affinity with the North American craton rather than Gondwana (Figure 2.10). Within this suite, three phases of HP metamorphism have been identified: Early Ordovician, Late Ordovician-Early Silurian and Devonian. These metamorphic events have been associated with a series of arc systems accreting to the southern boundary of Laurentia during the closing of the Iapetus and Rheic Oceans (Talavera-Mendoza et al., 2005; Vega-Granillo et al., 2007 and 2009; Figure 2.10). By the Carboniferous uplift of the Acatlán Complex had occurred in response to the approach of Gondwana (Gondwana), during the initial phase of the formation of Pangaea.

This interpretation of the Acatlán Complex therefore marks the suture between Laurentia and Gondwana during Pangaea. This would suggest the Pangaea suture extends into Southern Mexico as suggested by Ross (1986), Handschy et al. (1987) and Dickinson and Lawton (2001). However, in many models of Pangaea, overlap is observed between central and Southern Mexico and Northwest South America (Pindell and Dewey, 1982; Pindell, 1985; Handschy et al., 1987; Pindell and Kennan, 2001), indicating that the terranes of Southern Mexico are likely to be allochthonous. Therefore the current location of the Acatlán Complex may not represent the position in which it formed.

Chapter 2: Geological overview of Mexico's basement

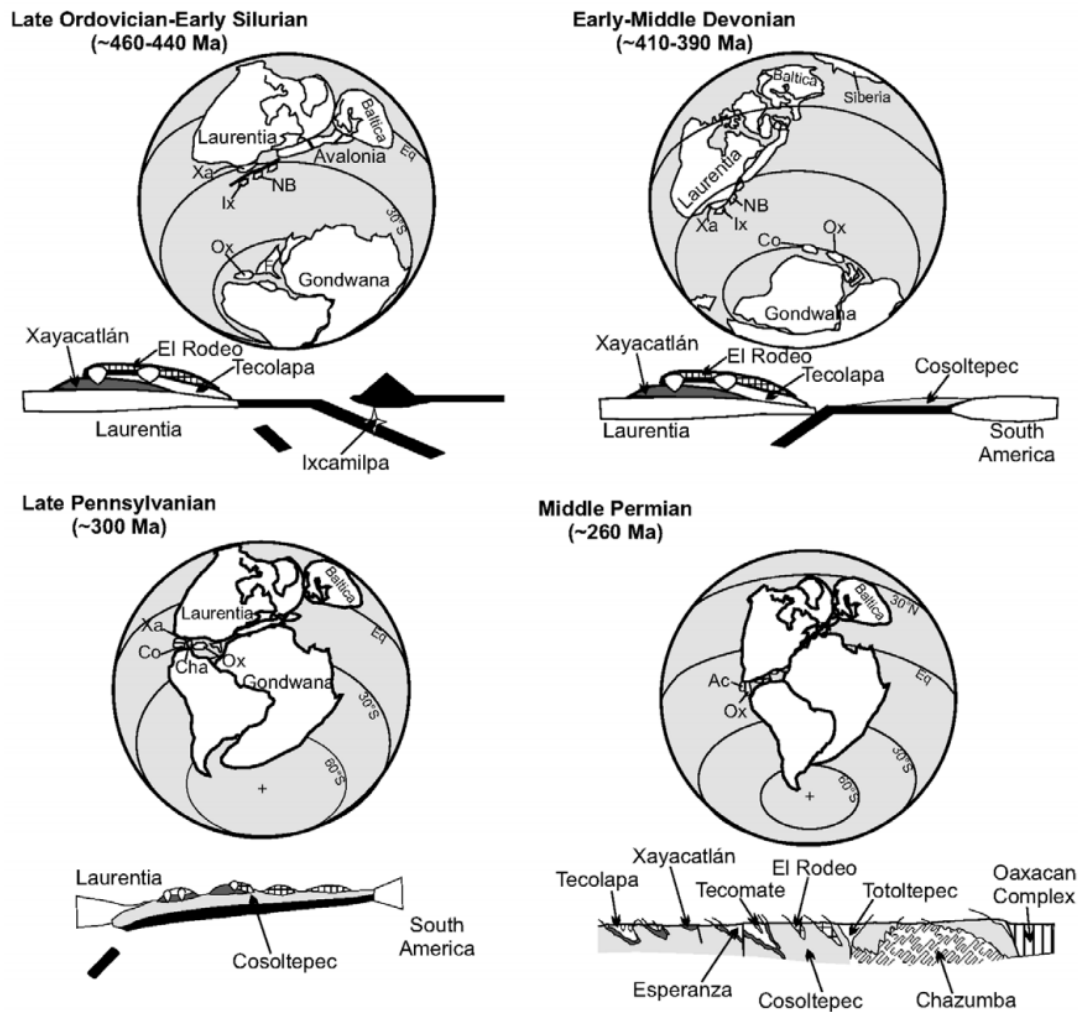


Figure 2.10. Simplified paleogeographic reconstructions showing probable locations of Acatlán units and their tectonic setting (Talavera et al., 2005). Mesoproterozoic, Early–Middle Devonian, Late Pennsylvanian and Middle Permian reconstructions adapted after Keppie and Ramos (1999). Early Ordovician and Late Ordovician–Early Silurian reconstructions adapted after Mac Niocaill et al. (1997). Oaxacan Complex position after Keppie and Ramos (1999). Te=Teocolapa; Co=Cosoltepec; Xa=Xayacatlán; Ix=Ixcamilpa; Cha=Chazumba; Ac=Acatlán Complex (Xayacatlán, Cosoltepec and Chazumba Formations already amalgamed); Ox=Oaxacan Complex. A=Avalonian blocks; F=Florida; NB=New Brunswick.

Other authors (e.g., Keppie et al., 2008; Ortega-Obregon et al., 2009 and 2014; Galaz et al., 2013) suggest the Acatlán Complex formed in a terrane proximal to the northwest flank of Gondwana; interpreting Grenville aged zircons found in the complex as being derived from Oaxaquia continental crust (Figure 2.11). This interpretation also runs counter to the idea of multiple HP systems in association with arc accretion. Instead, it identifies one HP event in the Carboniferous, forming

Chapter 2: Geological overview of Mexico's basement

in response to the extrusion into the upper plate of a Middle Devonian arc that had undergone subduction erosion. This interpretation does not therefore recognise the Acatlán Complex as forming the suture between Gondwana and Laurentia in Pangaea.

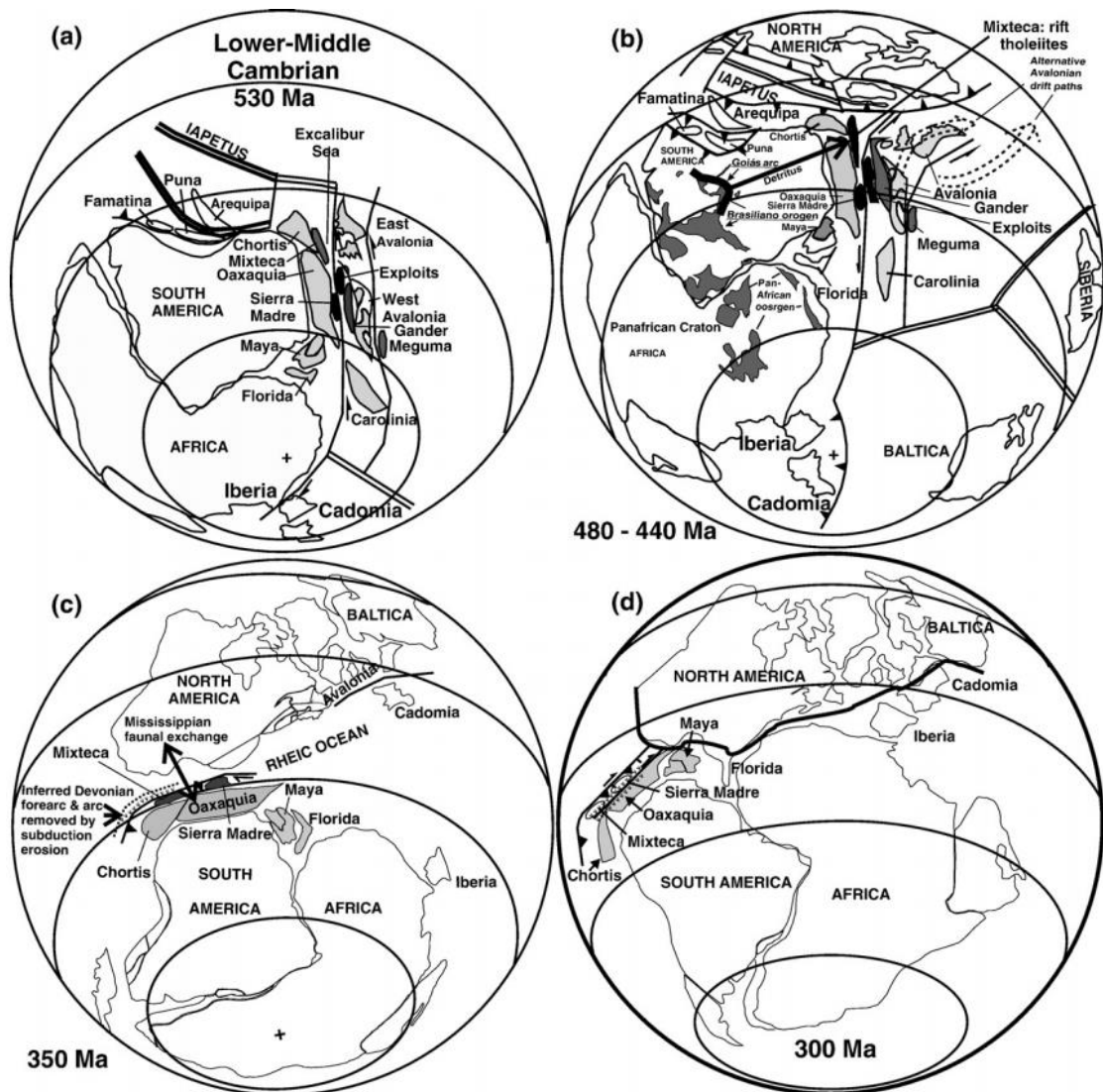


Figure 2.11. Paleogeographic reconstructions showing the location of southern Mexico through time, from Keppie et al. (2008): (a) separation of Avalonia from Oaxaquia in the Cambrian; (b) further rifting and separation of Avalonia, Ganderia and Carolina from Oaxaquia during the Ordovician; (c) Carboniferous reconstruction showing southern Mexico on the active Pacific margin with subduction beneath the Acatlán and Oaxaquia terranes, which underwent Devonian–Mississippian subduction erosion and extrusion; (d) Permian arc magmatism during oblique dextral subduction.

2.6 The breakup of Pangaea

Pangaea remained stable as a supercontinent after final amalgamation in the Late Carboniferous-Early Permian for ~120 Ma. During this period, however, rifting events did occur, most notably forming the Tethys Ocean. This rifting had no significant effect on the structure of Pangaea as it mostly involved closing of the Paleo-Tethys Ocean. However, a slice of continental crust known as the Cimmerian Domain became separated from Gondwana in the Late Permian and accreted to Laurasia by the Late Triassic (Figure 2.12; de Lamotte et al., 2015). Other minor rifting events occurred in Pangaea as a result of orogenic collapse (e.g. Variscan and Caledonian Belts; Burg et al., 1994; Oftedal et al., 2005; Faleide et al., 2008; Stolfova and Shannon, 2009) or extension in back arc regions (e.g. Cordilleran orogeny of South America; Sempere, 2002; Limarino and Spaletti, 2006; Javadi et al., 2011).

The main fragmentation of Pangaea started around the Triassic-Jurassic boundary (ca. 200 Ma), and appears to have been associated with the formation of the Central Atlantic Magmatic Province (CAMP) large igneous province (LIP; e.g. Marzoli et al., 1999; de Lamotte et al., 2015). Extension first caused Laurasia and Gondwana to separate along the Palaeozoic collision zones of the Alleghanian and Variscan Orogenies (Figure 2.12; de Lamotte et al., 2015), leading to sea floor spreading in the earliest Jurassic (Sahabi et al., 2004; Labails et al., 2010; Kneller et al., 2012). By the Middle Jurassic, further extension facilitated by the emplacement of the CAMP resulted in the separation of the Eurasian Plate from the North America plate in Laurasia. A separate LIP known as Karoo-Ferrar initiated the Karoo II rift system in Gondwana ca 183 Ma (Riley et al., 2004), leading to the separation of first

Chapter 2: Geological overview of Mexico's basement

the Antarctic, Australian and Indian plates and later the African plate from South America (Malod et al., 1991; de Lamotte et al., 2015).

As North and South America split apart during the breakup of Pangaea, part of Gondwana remained attached to the Laurentian craton. As a result modern Mexico displays affinities with both Gondwana and Laurentia. As previously noted the location of the suture between the two continental blocks remains uncertain.

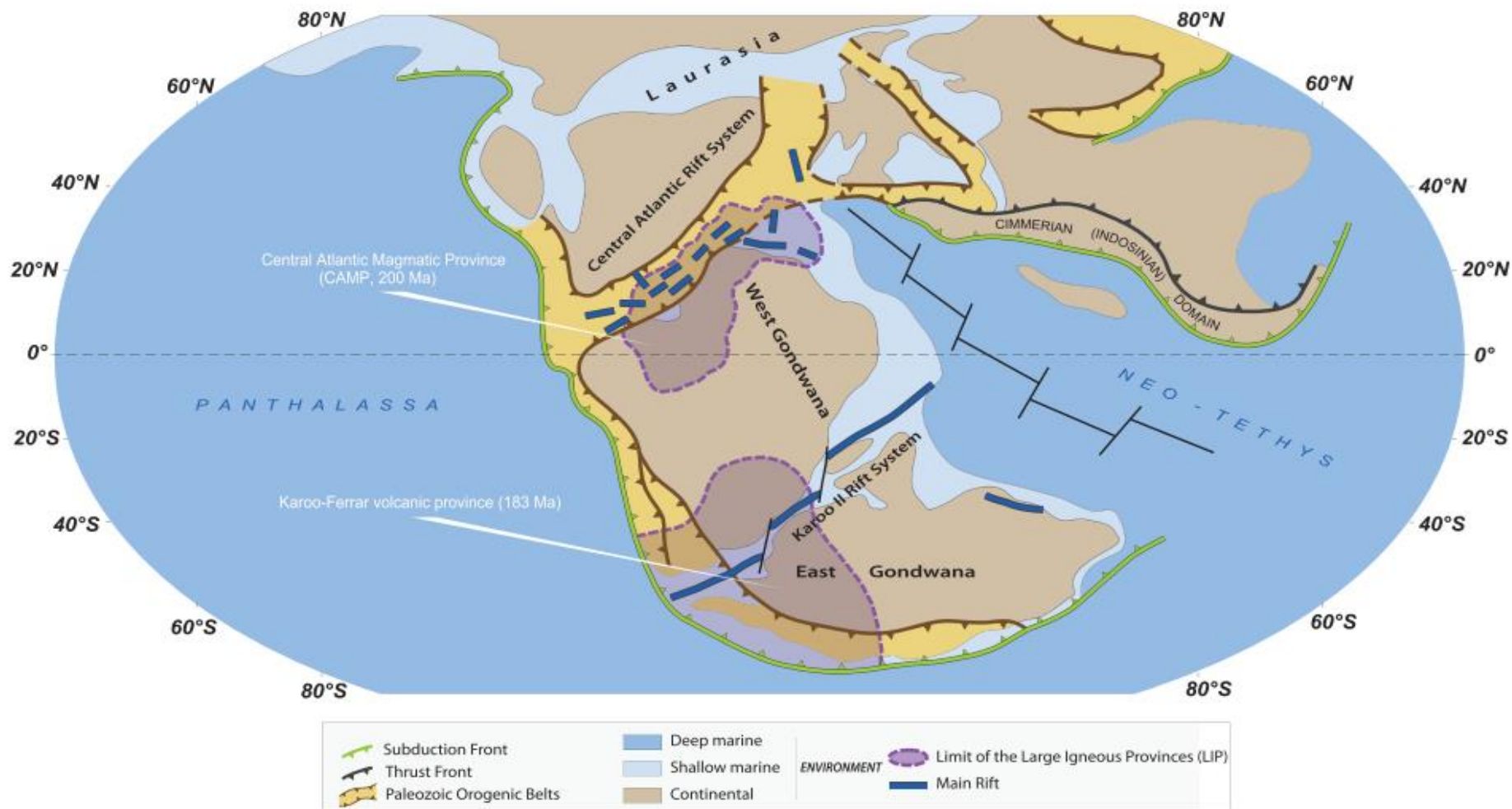


Figure 2.12. Schematic map for the initiation of breakup in Pangaea (ca. 190 Ma) from de Lamotte et al, (2015)

2.7 Paleozoic-Mesozoic Subduction

It has been proposed that continental arc systems existed in Mexico simultaneously with the collisional and rifting tectonics associated with the formation and break up of Pangaea. Igneous rocks dating from the Late Carboniferous-Early Triassic can be found across Mexico (Figure 2.2; Table 2.1).

Location	Age (U/Pb zircon)	Reference
Chiapas Massif	272 Ma igneous event. 254 Ma metamorphism.	<i>Weber et al., 2005</i>
Honduras Pluton	290 Ma	<i>Ortega-Obregon et al., 2014</i>
Cuanana Pluton	311 Ma	<i>Ortega-Obregon et al., 2014</i>
La Mixtequita batholith	254 Ma	<i>Weber and Kohler, 1999</i>
Zaniza Pluton	287 Ma	<i>Ortega-Obregon et al., 2014</i>
Totaltepec Pluton	306-283 Ma	<i>Kirsch et al., 2013</i>
La Carbonera stock	272 Ma	<i>Solari et al., 2001; Ortega-Obregon et al., 2014</i>
Etla Pluton	255 Ma	<i>Ortega-Obregon et al., 2014</i>
Sonora	275-258 Ma	<i>Arvizu & Iriando, 2011</i>

Table 2.1. Late Carboniferous-Early Permian plutons of Mexico.

These igneous rocks have been interpreted to have formed in a continental arc environment during eastward dipping subduction along the western flank of Pangaea (Ortega-Obregon et al., 2014). This proposed arc magmatism in Mexico may form part of the same belt of Permo-Triassic igneous rocks found in Ecuador and Colombia that are also reported to have formed in a continental arc environment during eastward dipping subduction of the Panthalassa Ocean beneath Pangaea (Vinasco et al., 2006; Cochrane et al., 2014; Spikings et al., 2015).

Chapter 2: Geological overview of Mexico's basement

A later phase of Late Triassic-Early Jurassic magmatism formed the Nazas arc in Mexico (Figure 2.2; Dickinson and Lawton, 2001). Volcanic exposures outcrop in northern Central Mexico (Barboza-Gudiño et al., 2008) and possibly extend as far down as Chiapas (Figure 2.2; Godínez-Urbán et al., 2011). Plutonic equivalents to these Jurassic arc rocks can be found in the northern Sonora area of Mexico (Figure 2.2; Ortega-Gutiérrez et al., 2014).

2.8 Review of Mexico's basement

As highlighted in the above sections the crystalline basement of Mexico is defined by a complex assembly of continental blocks of differing provenance and age.

- The oldest and most prevalent basement type is the Mesoproterozoic Oaxaquia crust (1400-970 Ma). Outcrops of which can be found in the Oaxacan Complex, Novillo Gneiss, Huiznopala Gneiss and Guichicovi Complex (Figure 2.2).
- During the Early Paleozoic, island arcs systems were accreted to Laurentia which now form part of Acatlán Complex of Southern Mexico (Figure 2.2).
- Late Carboniferous-Early Triassic (310-250 Ma) plutons (Totoltepec pluton, Cuanana pluton, Sonora plutons, Zaniza pluton, Etna granite, Honduras batholith, Carbonera Stock, Mixtequita batholith and Chiapas Massif; Figure 2.2) outcrop across Mexico, and may relate to arc magmatism.
- Alternatively, the Late Carboniferous-Early Triassic plutons found in Mexico may be related to the formation of Pangaea, which occurred synchronously

Chapter 2: Geological overview of Mexico's basement

(Pindell and Dewey, 1982; Pindell, 1985; Ross, 1986; Viele and Thomas, 1989; Sedlock et al., 1993; Dickinson and Lawton, 2001).

- The Late-Triassic-Middle Jurassic Nazas arc is proposed to extend from Sonora in the north of Mexico, to Chiapas in south. However, the arc rocks are mostly buried so constraining its extent is difficult.

3 Petrography & geochronology of the Western Gulf of Mexico basement

3.1 Introduction

This chapter presents petrographic and geochronological results for the 21 basement core samples of the Western Gulf of Mexico that zircons were successfully extracted from (Figure 3.1; Appendix B). Extraction as well as analysis (via LA-ICP-MS) was done in the facilities at National Autonomous University of Mexico (UNAM) in Juriquilla, Mexico. For further information concerning the method of extracting the zircons, analysis procedure and corrections of initial results please consult Appendix A and C.

Ages have been determined using the radiometric method of uranium-lead (U-Pb) dating on zircons. Unless otherwise stated the depth at which the cores are taken is unknown and there has been no previous radiometric dating done for the basement in each of the well localities. Results of the analysis have been graphically presented in either a Tera-Wasserburg in association with a $^{206}\text{Pb}/^{238}\text{U}$ weighted-mean age calculation or Wetherill Concordia diagram in association with a $^{207}\text{Pb}/^{206}\text{Pb}$ weighted-mean age calculation, depending on the age of the zircons present. The Tera-Wasserburg and $^{206}\text{Pb}/^{238}\text{U}$ weighted-mean age calculation are more reliable with Phanerozoic zircons whereas the Wetherill Concordia and $^{207}\text{Pb}/^{206}\text{Pb}$ weighted-mean age calculations are more reliable with Precambrian zircons (Jackson et al., 2004; Ludwig, 2012). Most of the age calculations have been made using weighted mean plots but in samples where there is a large range in the population age then the TuffZirc plot

has been used which uses the median age of a population. All figures presented in this section have been constructed using the excel macro “isoplot 4.15” created by Dr. Ken Ludwig at the Berkeley Geochronology Center (Ludwig, 2012).

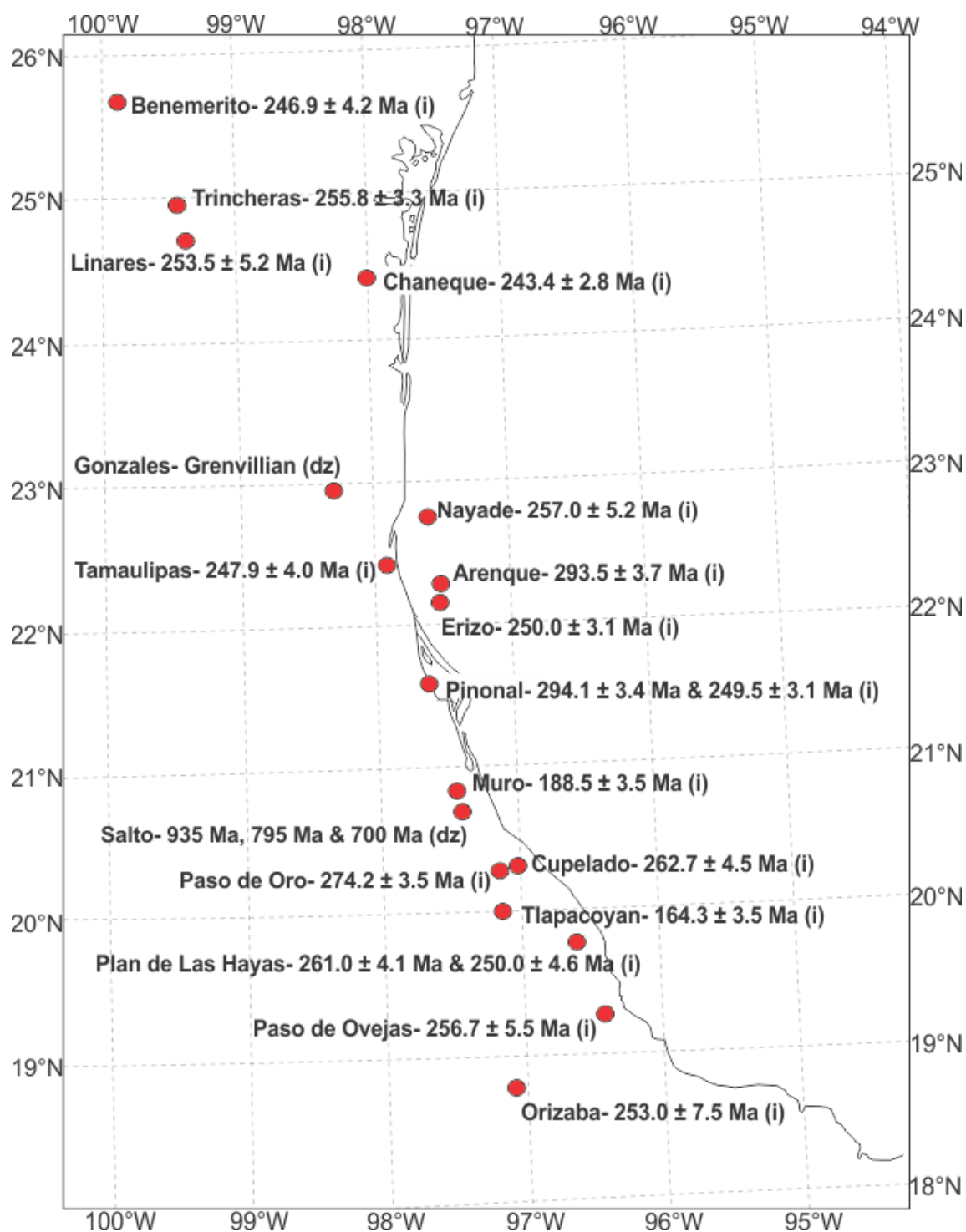


Figure 3.1. Map showing the localities and ages of the PEMEX wells used to obtain basement samples of the Western Gulf of Mexico. Igneous crystallization ages are indicated by (i) and detrital zircon ages from meta-sediments and sediments indicated by (dz).

Chapter 3: Petrography & Geochronology Results

The data presented will constrain the ages of the basement of the Western Gulf of Mexico. Cathodoluminescence (CL) images used in conjunction with Th/U ratios and rare earth element (REE) patterns have been used to distinguish between metamorphic and igneous zircon growth. Zircons forming in metamorphic environments usually, but not exclusively, yield Th/U ratios of <0.1 , whereas igneous zircons generally have ratios >0.2 . The REE patterns in magmatic zircons have pronounced Eu negative anomalies and steep/enriched heavy rare earth elements (HREE) (Rubatto & Hermann, 2007). The REE patterns in metamorphic zircons on the other hand have less pronounced/absent negative Eu anomalies and HREE patterns that are suppressed (Rubatto and Hermann, 2007). The U concentration of the zircons will be used to identify any grains that are likely to have undergone metamictization (Nasdala et al., 2001). On samples that have a sedimentary protolith the detrital zircons will be used to identify the provenance of the grains as well as constrain the maximum age of deposition, using the youngest population of zircons.

3.2 Early Permian granitoids

3.2.1 *Pinonal N2F3C1*

The first analysed sample from the Pinonal well (Figure 3.1) is a phaneritic biotite granitoid that has undergone severe subsequent alteration. Petrographic interpretations (Figure 3.2 a-b) reveal crystals that range in size from 4000 to 250 μm , principally composed of quartz that has been recrystallized in some instances (20%), chloritized biotite (35%) and feldspars that have been severely altered to clay minerals and sericite (40%). The remaining 5% is made up of the accessory minerals zircon and apatite, as well as a skeletal opaque mineral (possibly ilmenite) that appears to be

Chapter 3: Petrography & Geochronology Results

forming from the breakdown of biotite. Due to the degree of feldspar alteration it is difficult to distinguish between the plagioclase and alkali feldspars and therefore an accurate classification of the sample is not possible from the thin section alone.

The sample contains large subhedral zircon grains and fragments that are 200-800 μm along their longest axis, with aspect ratios of 2:1-5:1. The CL textures are characterised by oscillatory and sector zoning, typical of zircons that form in igneous environments (Figure 3.2 i). Common lead contamination may be an issue during interpretation of the results as fractures are present in some of the zircon grains.

The sample has fairly uniform Th/U ratios and U concentrations (0.3-1, 55-400 ppm respectively; Figure 3.2 e-f). These results are typical of the values you would expect to find in zircons that crystallize in igneous environments.

Tera-Wasserburg plots (Figure 3.2 c) for the sample show that there is one dominant Permian population of zircons. There also appears to be an inherited xenocryst in one of the analyses which yields a Carboniferous age of 351 ± 13 Ma.

Of the 43 analysis 36 were deemed suitable to be used in age calculations (<20% discordance, <5% error and <5% inverse discordance). Weighted-mean plots (Figure 3.2 d) yield an age of 294.1 ± 3.4 Ma, with a mean square weighted deviation (MSWD) of 1.15 (one age was rejected by the algorithm). This can be interpreted as the age of crystallization for the zircons associated with an igneous event. The sample may contain inheritance from a previous igneous event in the Carboniferous. However, this is not clear as it is difficult to relate this older age to CL images (Figure 3.2 i). Alternatively, the older age obtained may be the result of common lead contamination.

Pinonal-1 N2F3C1

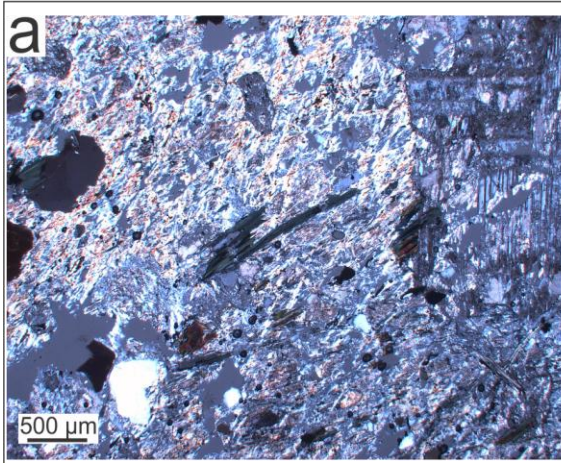


Figure 3a: Cross polarized light (XPL) thin section image for the analysed sample showing severely sericitized plagioclase, quartz and chlorite.

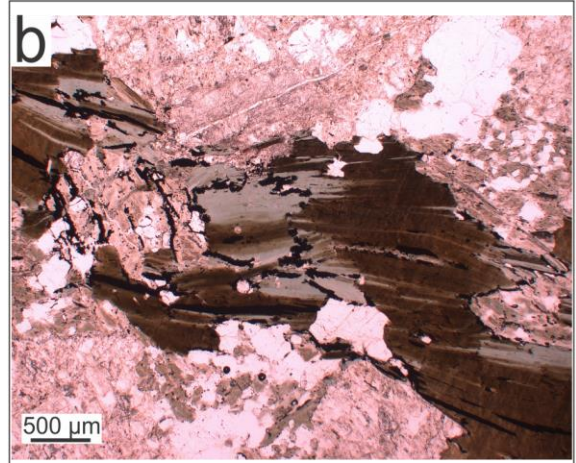


Figure 3b: Plane polarized light (PPL) thin section image for the analysed sample showing chloritized biotite.

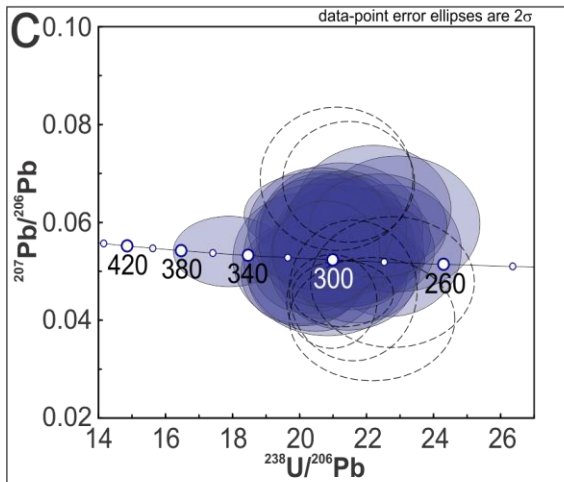


Figure 3c: Tera Wasserburg plot of the analysed grains (n=43). The blue ellipses represent zircons that were taken further to age calculations (n=36) and the dotted ellipses show those that were disregarded (> 20% discordance, > 5% inverse discordance, > 5% error).

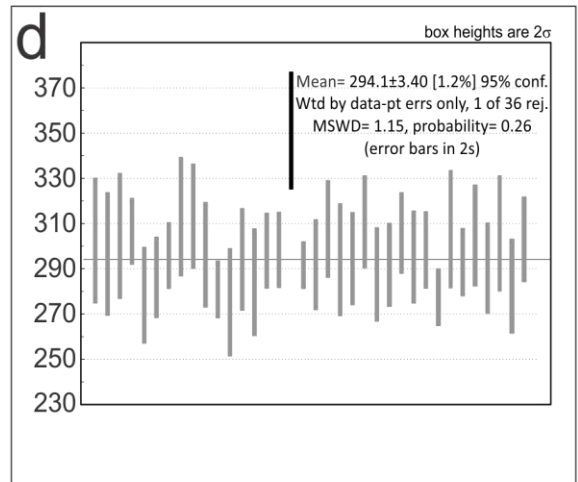


Figure 3d: Weighted mean plot for the zircons considered for age calculations (n=36).

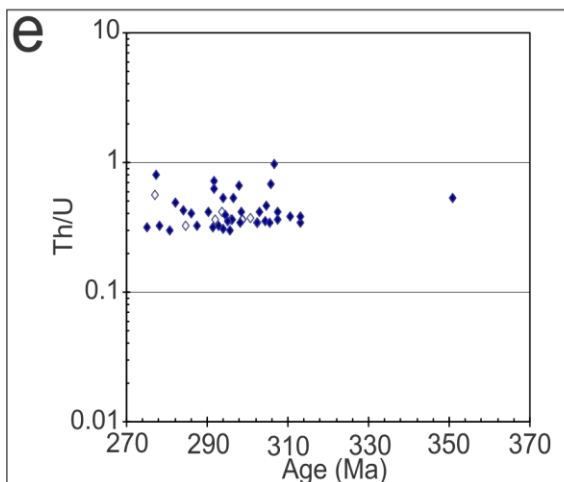


Figure 3e: Th/U vs. Age (Ma) plot for all of the analysed zircons (n=43). The blue points represent the grains that were used in age calculations and the clear points show those that were disregarded.

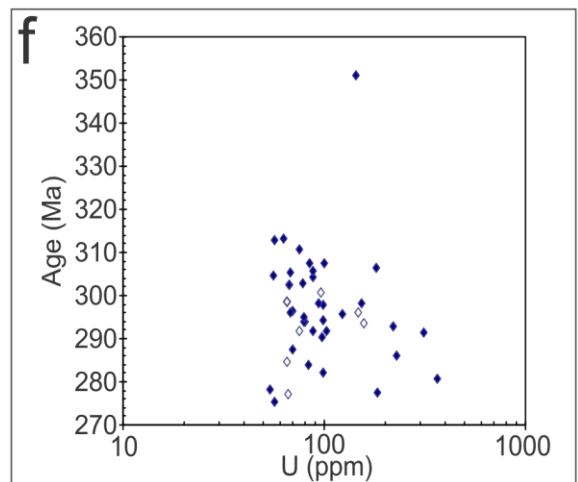


Figure 3f: Age (Ma) vs. U (ppm) diagram for all of the analysed grains (n=43). Blue points represent grains that were used in age calculations and clear points show those that were disregarded.

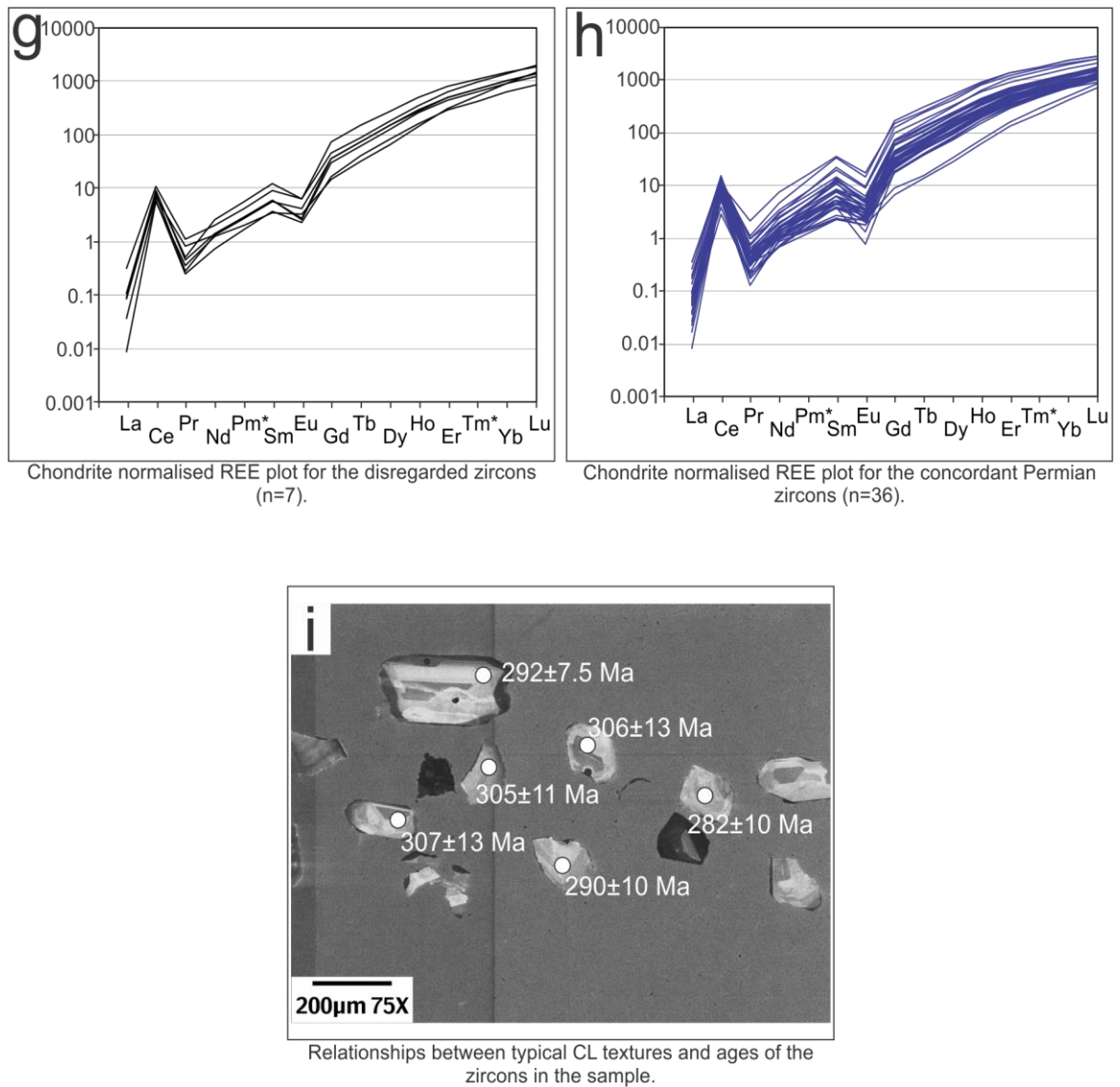


Figure 3.2. Geochronology results for the Pinonal N2F3C1 basement core from the Western Gulf of Mexico.

3.2.2 *Arenque N15F3+4C2*

The analysed sample from the Arenque well (Figure 3.1) is a biotite granite (phaneritic in texture) that has undergone subsequent alteration. Petrographic interpretations (Figure 3.3 a-b) reveal crystals that range in size from 4000 to 200 µm, principally composed of quartz (20%), partially sericitized feldspars (65%) and partially chloritized biotite (10%). The remaining 5% is made up of the accessory minerals zircon and apatite, opaque minerals that form in association with the breakdown of biotite and

Chapter 3: Petrography & Geochronology Results

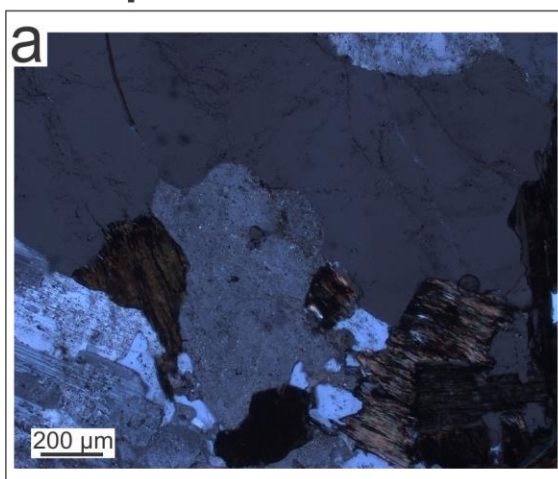
minor calcite veining. Alteration of the feldspars makes defining them difficult but they appear to be mainly composed of alkali feldspar (60%) rather than plagioclase (40%).

Zircons in this sample are euhedral-subhedral and 100-300 μm along their longest dimension, with aspect ratios of 2:1-5:1. The CL images display oscillatory and sector zoning (Figure 3.3 i), suggesting that the zircons formed in an igneous environment. In some of the analysed grains there appears to be core and rim relationships.

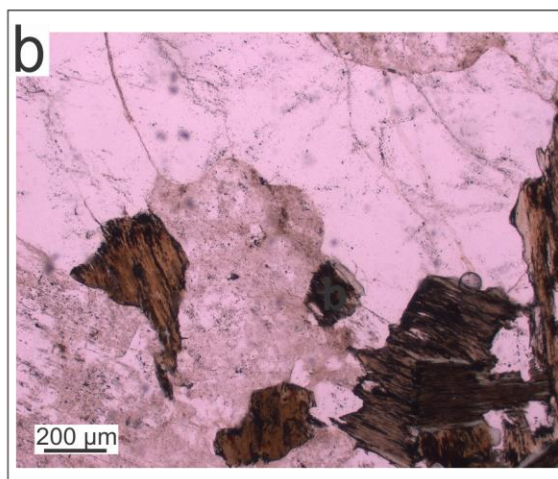
U concentrations in the sample range from 60-300 ppm (Figure 3.3 f) and the Th/U ratios fall between 0.3-1.1 (Figure 3.3 e). These results support the interpretations based on the CL images suggesting that zircons in this sample formed in an igneous environment.

The Tera-Wasserburg plot for the analysed grains (Figure 3.3 c) displays one population of zircons that formed in the Late-Carboniferous to Early-Permian. Of the 40 zircons that were analysed 36 were deemed reliable enough to be used for age calculations (< 25 % discordant and < 5% error). Weighted-mean plots for the accepted zircons (Figure 3.3 d) yield an age of 293.5 ± 3.7 Ma with an MSWD of 1.4 (two ages were rejected by the algorithm). The older of the rejected zircons yields an age of 322 ± 10.6 Ma and may represent the cores that were highlighted in the CL images (A numbering error for the analysed zircons during analysis means this theory cannot be tested). The age obtained can therefore be interpreted as an Early Permian igneous event which may have inherited cores from a previous igneous episode in the Carboniferous (possibly related to the inherited grains found in Pinonal N2F3C1 sample).

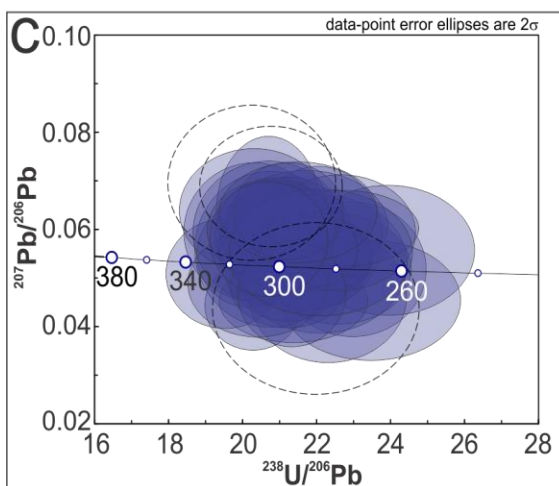
Arenque-22 N15F3C2



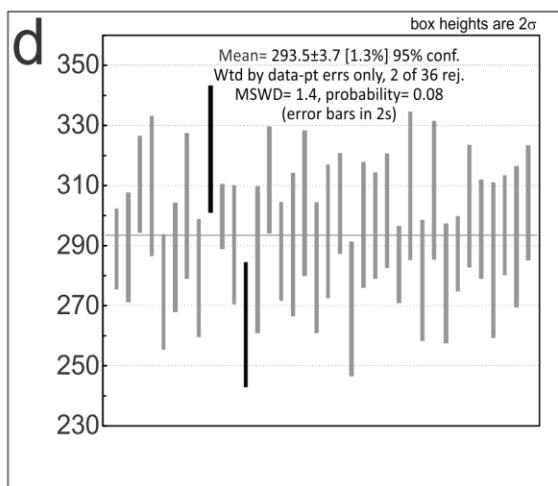
a Cross polarized light (XPL) thin section image for the analysed sample showing sericitized plagioclase, perthite, quartz and chloritised biotite.



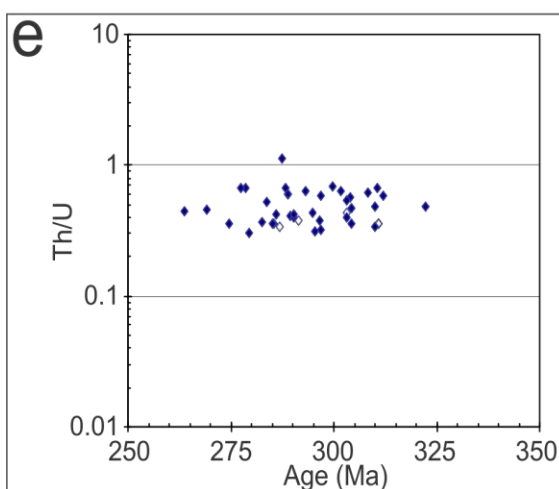
b Plane polarized light (PPL) thin section image for the analysed sample showing how the biotite has been partially chloritised.



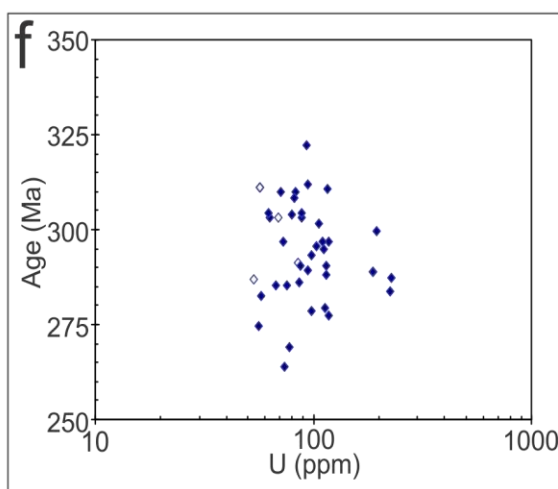
c Tera Wasserburg plot of the analysed grains (n=40). The blue ellipses represent zircons that were taken further to age calculations (n=36) and the dotted ellipses show those that were disregarded (> 25% discordance and > 5% error).



d Weighted mean plots for the zircons used in age calculations (< 25% discordant, < 5% error; n=36).



e Th/U vs. Age (Ma) plot for all of the analysed zircons (n=40). The blue points represent the grains that were used in age calculations and the clear points show those that were disregarded.



f Age (Ma) vs. U (ppm) diagram for all of the analysed grains (n=40). Blue points represent grains that were used in age calculations and clear points show those that were disregarded.

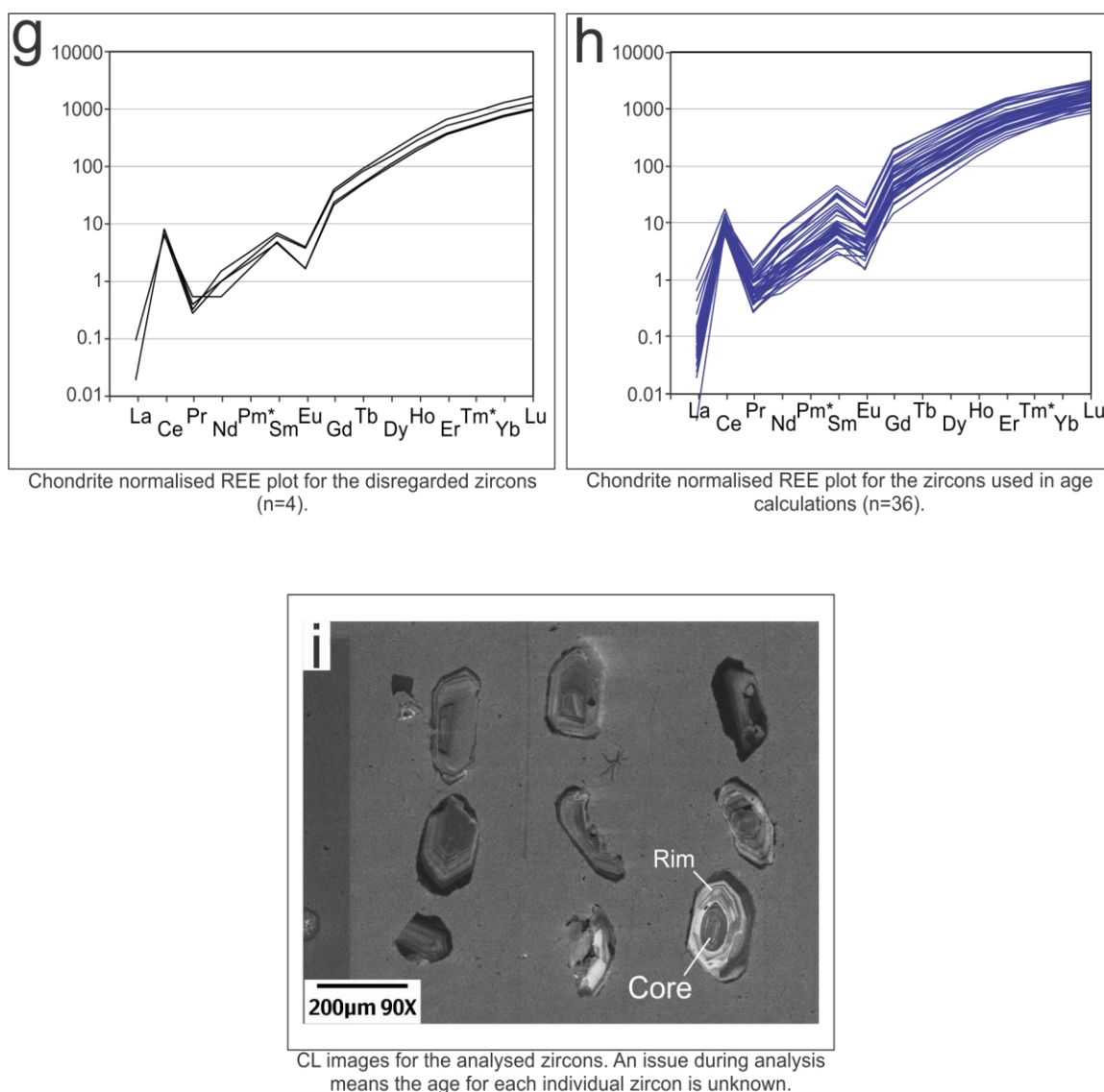


Figure 3.3. Geochronology results for the Arenque N15F3+4C2 basement core from the Western Gulf of Mexico

3.2.3 Paso de Oro N8F4C2

The analysed sample from the Paso de Oro well (Figure 3.1) was taken from a depth of 3367-3372 m and has a composition of a granodiorite (phaneritic in texture). Previous dating of the basement in this core produced an age of 258 ± 11 Ma via K-Ar dating methods on biotite (Lopez-Ramos, 1979). Petrographic interpretations (Figure 3.4 a-b) reveal crystals that range in size between 4000 to 200 μm , which are principally composed of quartz (15%), feldspars (60%), severely altered amphiboles (10%) and

Chapter 3: Petrography & Geochronology Results

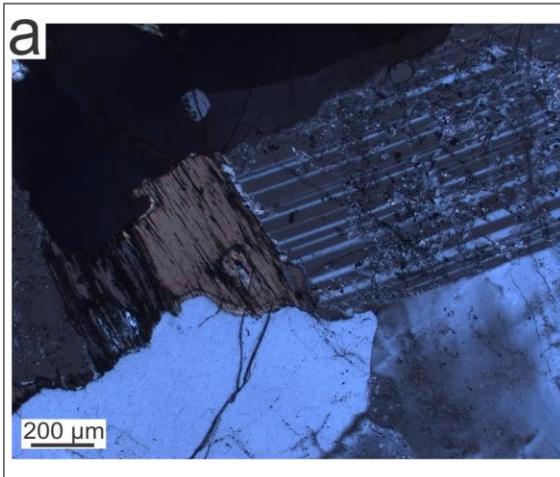
biotite (10%). The feldspars are primarily plagioclase in composition (70%), with only minor alkali feldspar (30%). The primary amphibole that was once present has subsequently been broken down into opaque, epidote, biotite (chloritized), muscovite and serpentine. The accessory minerals of zircon and apatite also exist as a minor phase.

Analysed crystals and fragments display prismatic, euhedral grains that are 100-600 μm along their longest dimension and with aspect ratios of 2:1-8-1. CL textures are characterised by oscillatory and sector zoning in the majority of the grains, with no core-rim relationship evident (Figure 3.4 i). The grains with higher aspect ratios appear to have been affected by common lead contamination in fractures along the c-axis (bright CL in fractures), which may cause age calculations for these examples to be discordant. The form and consistency of the textures in the CL images suggest that that the zircons within the Paso de Oro basement core all formed within the same igneous event, with no evidence of any inheritance from older xenocrysts.

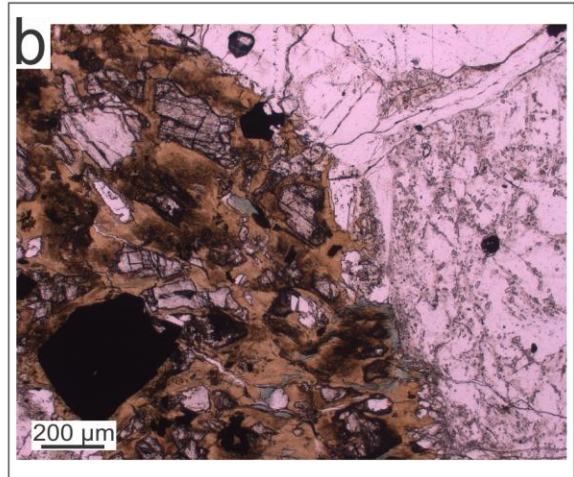
U concentrations range from 70-300 ppm (Figure 3.4 f) and Th/U ratios are broadly uniform (0.4-0.8; Figure 3.4 e) between each of the analysed grains. These observations support the interpretations from the CL images that suggest all the zircons all formed in a single igneous event.

Of the 26 grains analysed, 19 were deemed suitable for further consideration in age calculations (< 20% discordant and < 5% inversely discordant; Figure 3.4 c). The discordance observed in some of the samples is probably due to common Pb contamination highlighted in the CL observations. Weighted-mean plots (Figure 3.4 d) yield an age of 274.2 ± 3.5 Ma ($n = 19$, MSWD = 0.77; one age was rejected by the algorithm) that can be interpreted as the igneous crystallization age.

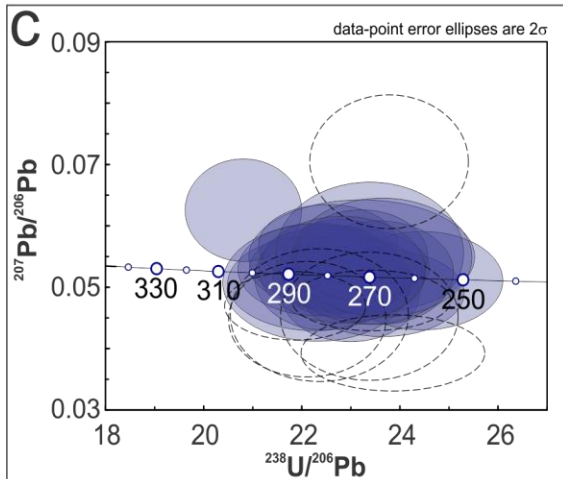
Paso de Oro N8F4C2



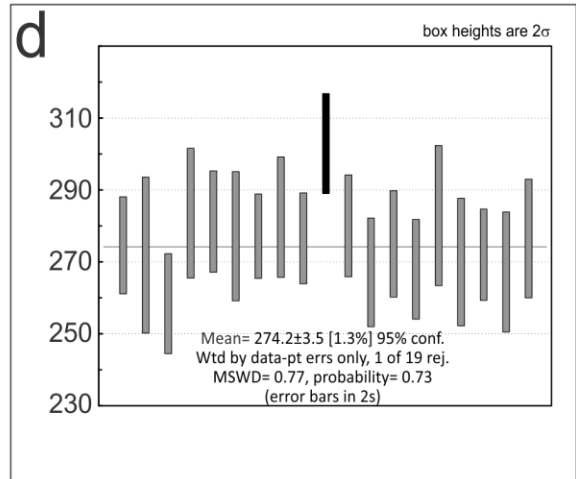
a Cross polarized light (XPL) thin section image for the analysed sample showing partly sericitized plagioclase, quartz, and biotite.



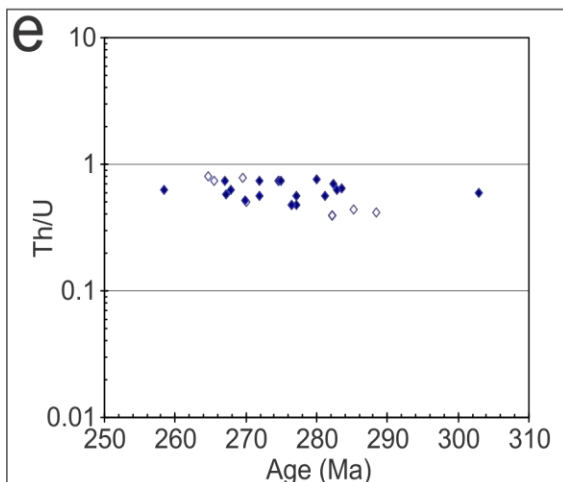
b Plane polarized light (PPL) thin section image for the analysed sample showing low relief plagioclase, opaques and altered hornblende and biotite.



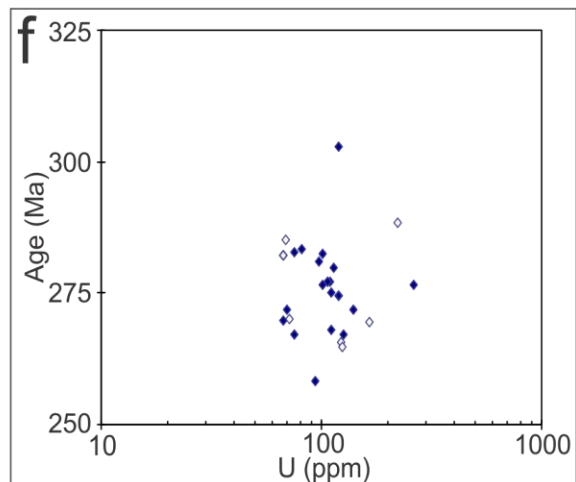
c Tera Wasserburg plot of the analysed grains (n=26). The blue ellipses represent zircons that were taken further to age calculations (n=19) and the dotted ellipses show those that were disregarded (> 20% discordance, > 5% inverse discordance).



d Weighted mean plot for the zircons considered for age calculations (n=19).



e Th/U vs. Age (Ma) plot for all of the analysed zircons (n=26). The blue points represent the grains that were used in age calculations and the clear points show those that were disregarded.



f Age (Ma) vs. U (ppm) diagram for all of the analysed grains (n=26). Blue points represent grains that were used in age calculations and clear points show those that were disregarded.

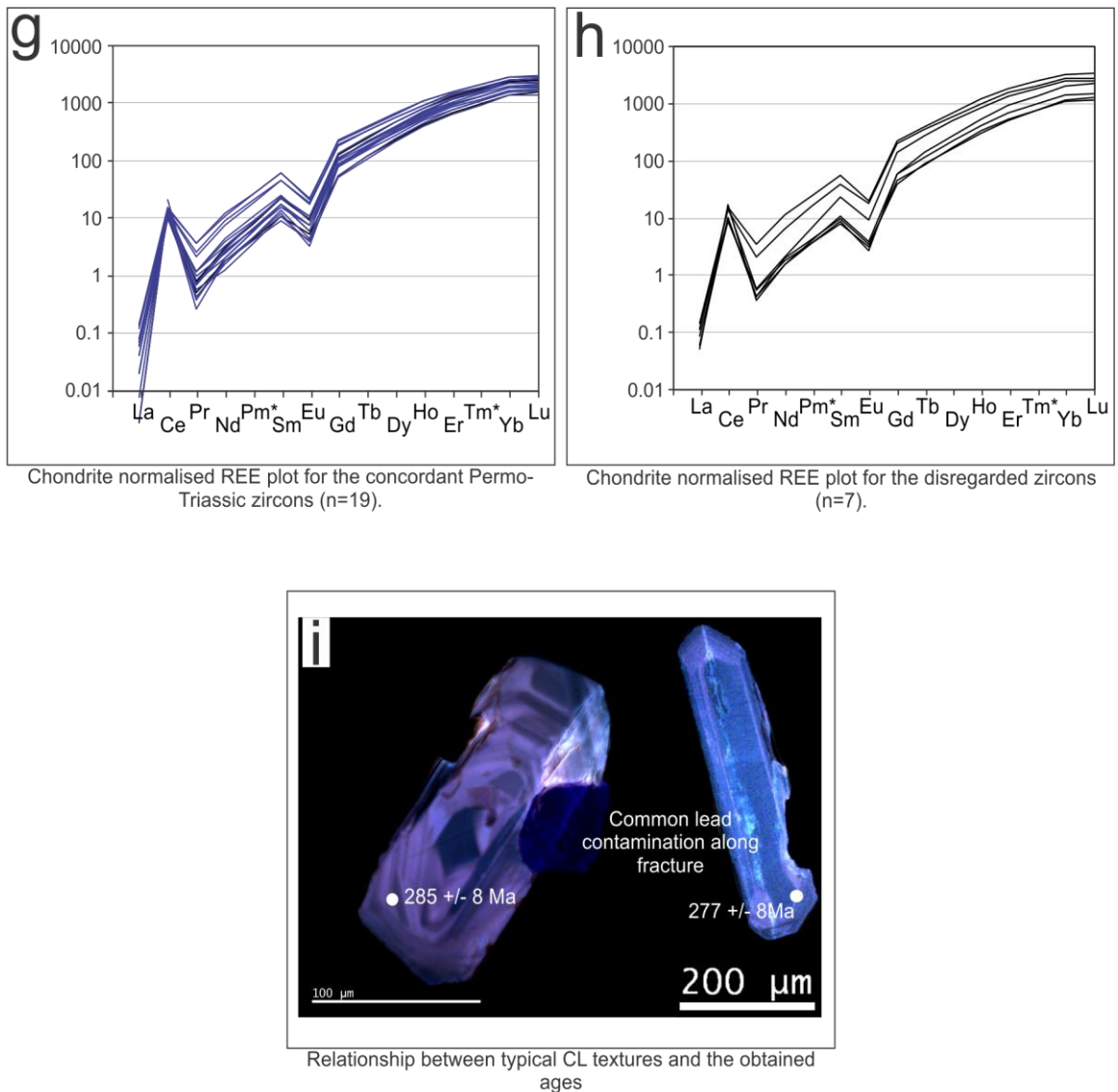


Figure 3.4. Geochronology results for the Paso de Oro N8F4C2 basement core from the Western Gulf of Mexico.

3.3 Late Permian

3.3.1 Benemerito-1 N2F7bC5

The analysed sample from the Benemerito well (Figure 3.1) was taken from a depth of 2580-2588 m and has the composition of a granite (phaneritic in texture). The basement in this well has been previously dated to 916 ± 35 Ma and 203 ± 10 Ma (Lopez-Ramos, 1979). Unfortunately, the method of dating is not mentioned but it is likely to have been dated by K-Ar on biotite.

Chapter 3: Petrography & Geochronology Results

Petrographic interpretations (Figure 3.5 a-b) reveal crystals that range in size from 150-10000 μm , which are primarily composed of quartz (25%), partially sericitized feldspars (70%) and chloritized biotite (5%). The feldspars that are present are made up of perthite (40%), plagioclase (30%), and alkali feldspars (30%). Zircon and apatite are also present in the sample as minor phases.

The sample contains euhedral, prismatic zircon grains and fragments that range in size from 80-250 μm along their longest dimension and with aspect ratios of 2:1-6:1. The CL textures for the sample display oscillatory and sector zoning typical of zircons found in igneous environments (Figure 3.5 k). There is also evidence for a minor influence from inherited xenocrysts, highlighted by truncation in areas of zoning in some of the grains.

Another feature of note in the CL results is how dark the grains appear in many of the zircons, indicating high U concentrations. This may cause metamictization in the grains, resulting in lead-loss and inaccurate age determinations (Nasdala et al., 2001).

There is a strong correlation between discordant analysis and high U levels in the sample (Figure 3.5 f). This confirms the suspicions of metamictization and as a result any analyses (even concordant ones) with uranium concentrations over 900 ppm have been disregarded. Of the 35 analysed grains 13 were considered reliable enough to be considered for age calculations (< 20% discordant, < 5% inversely discordant and <1000 ppm U).

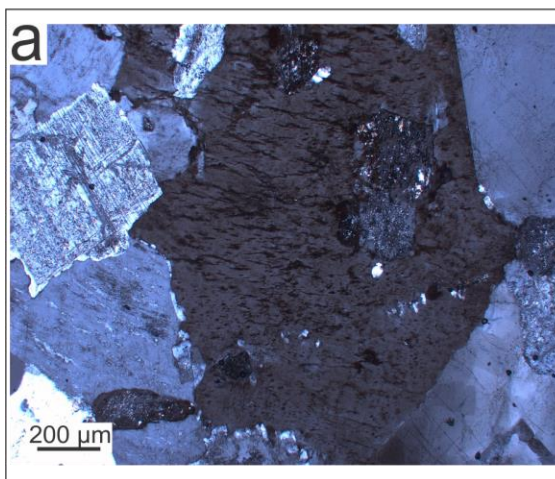
Weighted-mean plots have been constructed for the 13 concordant zircons considered for analysis (Figure 3.5 d) and these yield an age of 246.9 ± 4.2 Ma with a

Chapter 3: Petrography & Geochronology Results

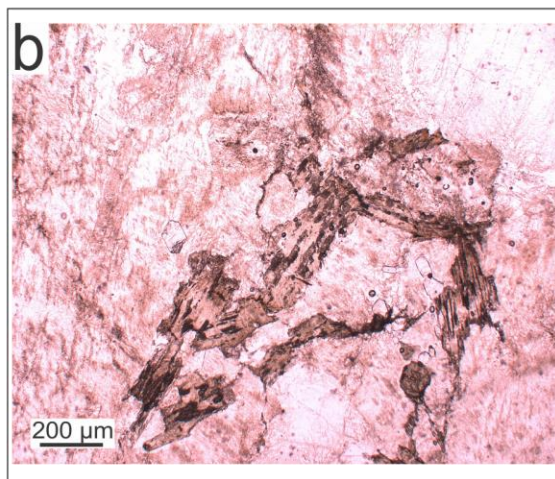
MSWD of 1.4 (one age was rejected by the algorithm). One concordant inherited zircon core yields a Proterozoic age of 1266 ± 93 Ma (Figure 3.5 c), which probably relates to the Oaxaquia microcontinent that makes up the basement of much of continental Mexico (Ortega-Gutiérrez et al., 1995). Other ages that fall between the Proterozoic and Triassic are likely to represent a mixing of both core and rim during laser ablation.

U concentrations for the considered zircons range from 100-1000 ppm (Figure 3.5 f) and have a Th/U ratio of 0.03-1 (Figure 3.5 e). The Triassic age of these zircons is interpreted as the age of igneous crystallization, with minor influence from xenocrysts of (poorly constrained) Proterozoic age.

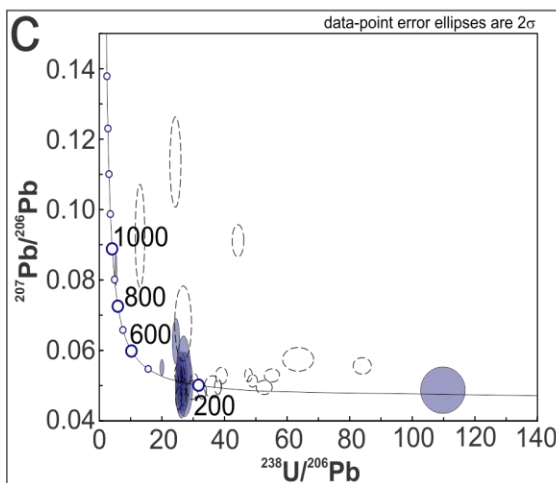
Benemerito-1 N2F7BC5



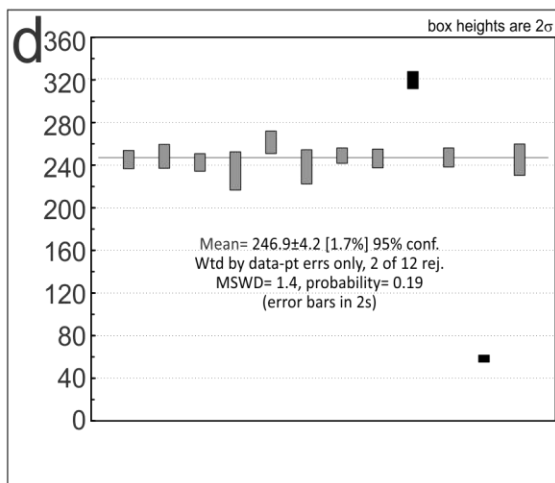
a Cross polarized light (XPL) thin section image for the analysed sample showing sericitized plagioclase, perthite and strained quartz



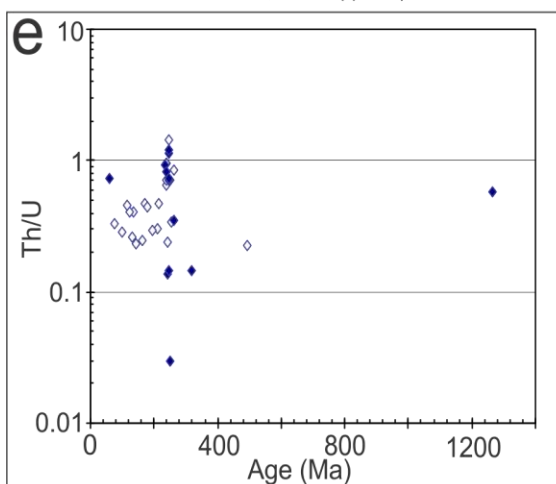
b Plane polarized light (PPL) thin section image for the analysed sample showing low relief feldspars and quartz, chloritised biotite and high relief apatite.



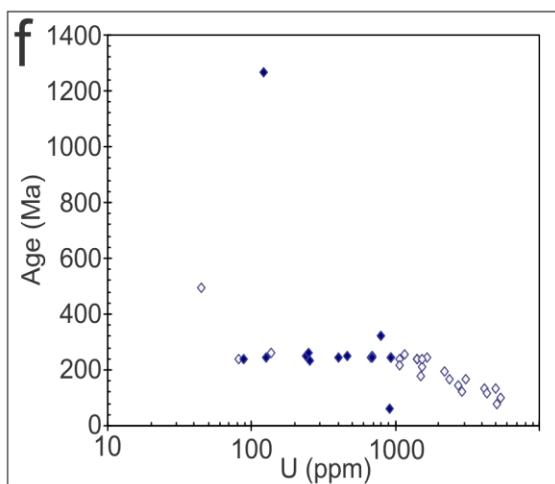
c Tera Wasserburg plot of the analysed grains (n=35). The blue ellipses represent zircons that were taken further to age calculations (n=13) and the dotted ellipses show those that were disregarded (> 20% discordance, > 5% inverse discordance, > 1000ppm U).



d Weighted mean plots for the zircons used in age calculations (> 20% discordance, > 5% inverse discordance, > 1000ppm U).



e Th/U vs. Age (Ma) plot for all of the analysed zircons (n=35). The blue points represent the grains that were used in age calculations and the clear points show those that were disregarded.



f Age (Ma) vs. U (ppm) diagram for all of the analysed grains (n=35). Blue points represent grains that were used in age calculations and clear points show those that were disregarded.

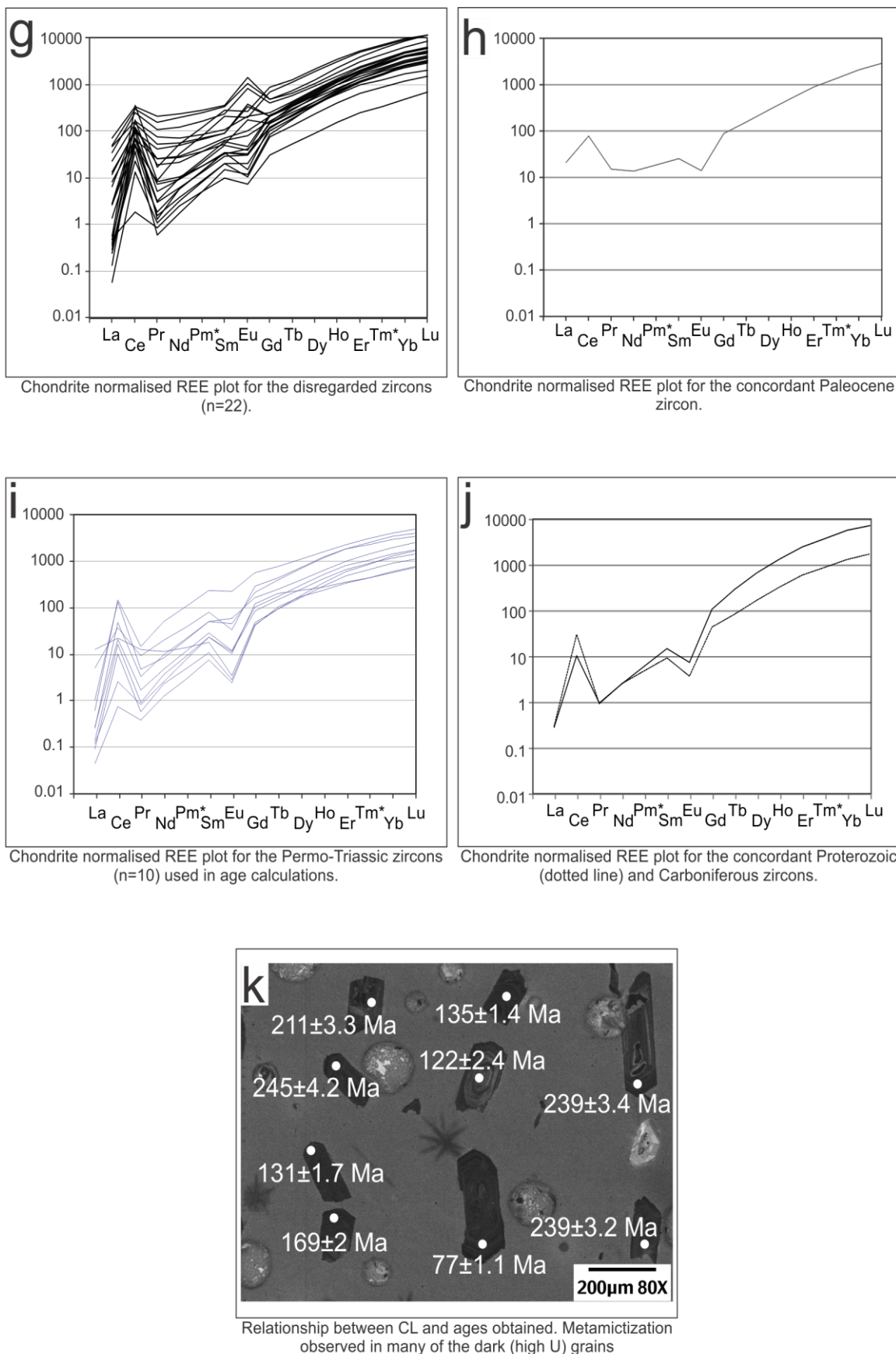


Figure 3.5. Geochronology results for the Benemerito N2F7bC5 basement core from the Western Gulf of Mexico.

3.3.2 *Trincheras N3F5aC1*

The analysed sample from the Trincheras well (Figure 3.1) has the composition of a biotite granite (phaneritic texture) that has subsequently been hydrothermally altered. The basement from this core has been previously dated via K-Ar whole rocks methods at 147 ± 5 Ma (Lopez-Ramos, 1979).

Petrographic interpretations (Figure 3.6 a-b) reveal crystals that range in size from 100 to 4000 μm , which are primarily composed of quartz (25%), partially sericitized feldspars (50%), biotite (15%), muscovite (5%). The feldspars that are found in the sample are made up of plagioclase (30%), alkali feldspars (50%) and perthite (20%). The remaining 5% of the sample is made up of calcite that is present in veins and the accessory minerals of zircon and apatite.

The sample contains euhedral to subhedral zircon grains and fragments that range in size from 100-300 μm along their longest axis, with aspect ratios of 2:1-5:1. The CL textures are characterised by igneous features such as oscillatory and sector zoning (Figure 3.6 j). There appear to be fractures in some of the grains which may have resulted in contamination from common lead. Additionally, some of the analysed grains are very dark, indicating high U concentrations and possible metamictization.

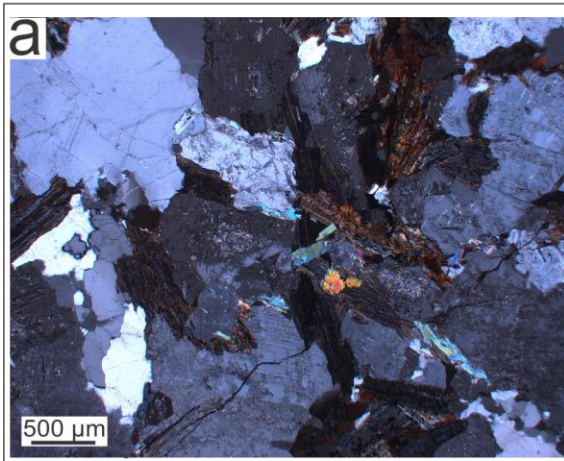
Tera-Wasserburg plots for the sample (Figure 3.6 c) display a population of zircons that are Permian in age as well as 2 concordant grains from the Proterozoic (1018 ± 82 Ma & 755 ± 8 Ma) which indicates inheritance from xenocryst cores, although they are not obvious in the CL images. The older of the cores is likely to derive from the Oaxaquia microcontinent; the younger core's source is unclear.

Chapter 3: Petrography & Geochronology Results

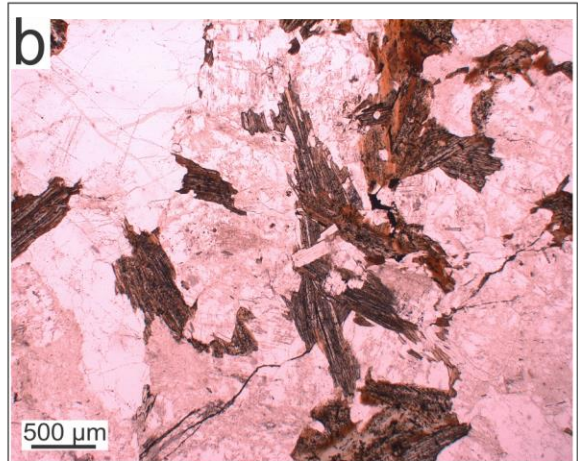
U concentrations between the Proterozoic xenocrysts and Permian zircons are comparable, with values of 100-1200 ppm (Figure 3.6 f). There appears to be a relationship between high U concentrations and the younger ages which reveals that metamictization is indeed an issue in this sample. For this reason all analyses that yield a U concentration above 1050 ppm have been discarded. The REE patterns (Figure 3.6 g) suggest that small inclusions within the zircons may also partially explain the discordant grains, with enrichment of the LREEs and no pronounced Ce negative anomaly indicating contamination from monazite.

Of the 40 analysed grains 25 were used in the age calculations (<10% discordant, <4.8% error and <1000 ppm U). Weighted-mean plots (Figure 3.6 d) have been constructed for the accepted Permian zircons that yield an age of 255.8 ± 3.3 Ma, with an MSWD of 2.7 (three ages were rejected by the algorithm). The two older rejected ages correlate well with the zircons in the Pinonal and Arenque wells (288 ± 5 Ma & 289 ± 4 Ma) which suggests they could be inherited cores. However, this is not clear in the CL images. The zircons in this rock can therefore be interpreted to represent the igneous crystallisation age with some inheritance from Proterozoic and potentially Early Permian xenocrysts. High U concentrations of the zircons from the Mid-Permian igneous event have subsequently resulted in metamictization of some of the grains.

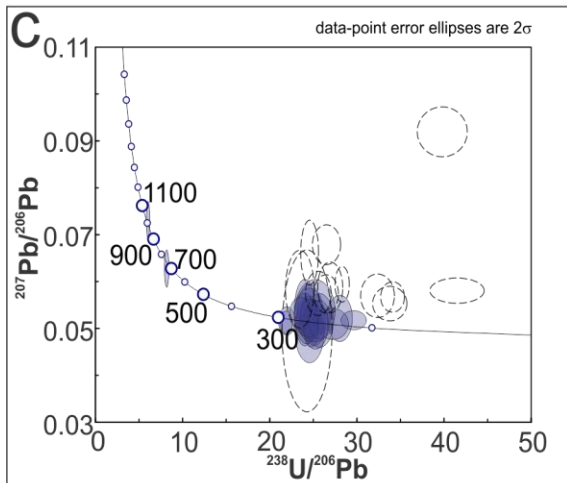
Trincheras-1 N3F5AC1



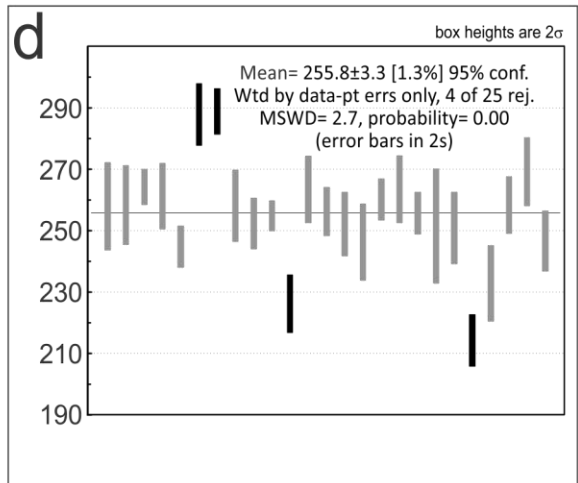
a Cross polarized light (XPL) thin section image for the analysed sample showing perthite, sericitized plagioclase, biotite, muscovite and quartz.



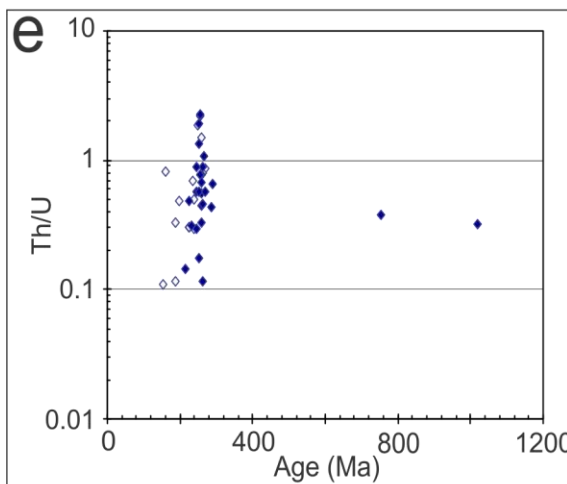
b Plane polarized light (PPL) thin section image for the analysed sample showing low relief perthite, sericitized plagioclase, muscovite, quartz and brown biotite.



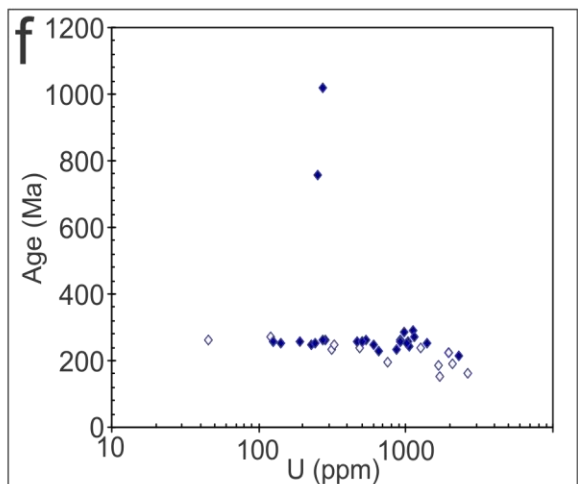
c Tera Wasserburg plot of the analysed grains (n=40). The blue ellipses represent zircons that were taken further to age calculations (n=27) and the dotted ellipses show those that were disregarded (> 10% discordance, > 5% error).



d Weighted mean plot for the zircons used for age calculations. The two rejected older zircons represent inherited cores.



e Th/U vs. Age (Ma) plot for all of the analysed zircons (n=40). The blue points represent the grains that were used in age calculations and the clear points show those that were disregarded.



f Age (Ma) vs. U (ppm) diagram for all of the analysed grains (n=40). Blue points represent grains that were used in age calculations and clear points show those that were disregarded.

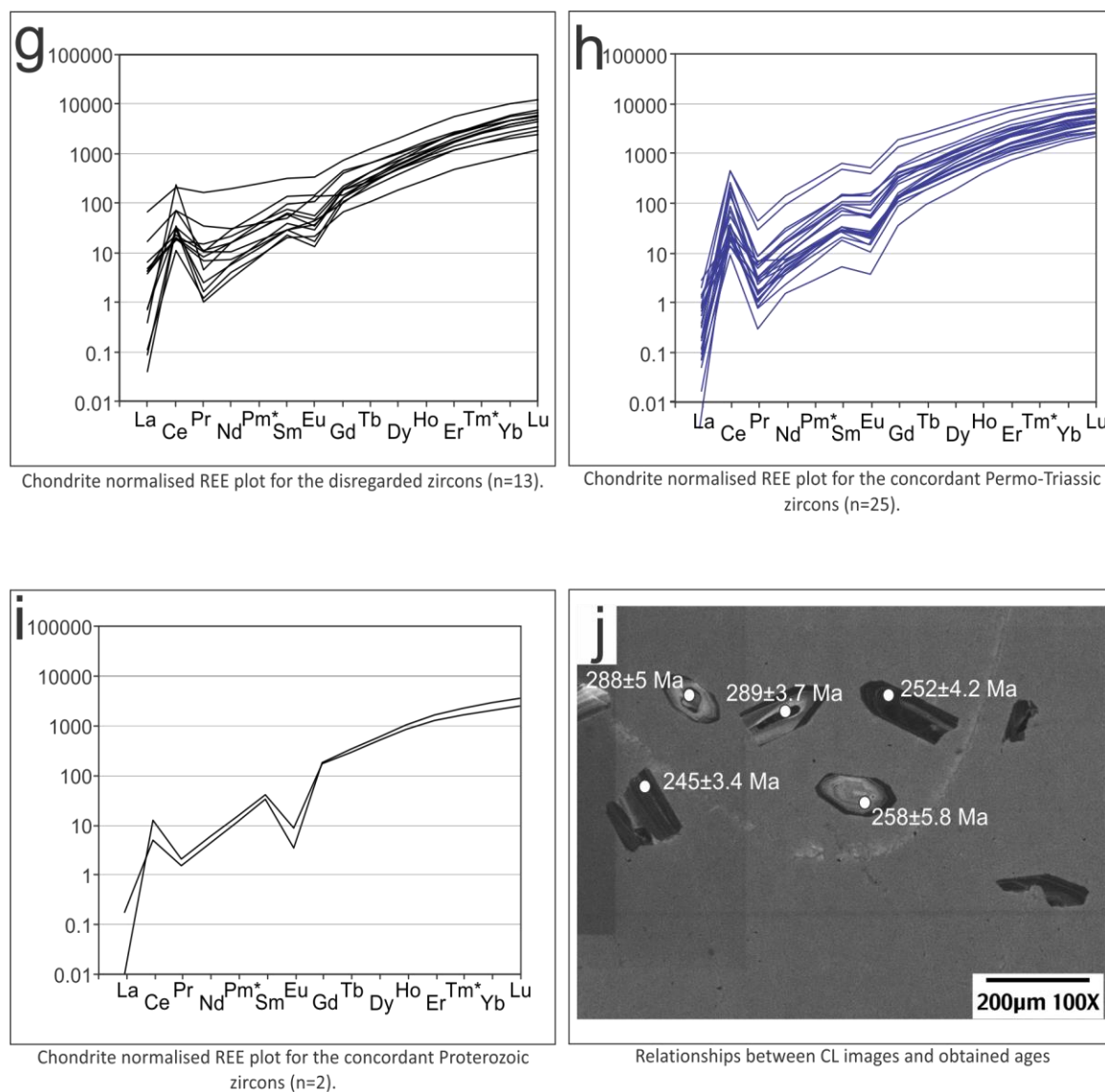


Figure 3.6. Geochronology results for the Trincheras N3F5aC1 basement core from the Western Gulf of Mexico.

3.3.3 Linares N7F1C1

The analysed sample from the Linares well (Figure 3.1) was taken from a depth of 2628-2629.5 m and has the composition of a hydrothermally altered granodiorite (phaneritic texture). Previous dating of a basement sample from this core yielded an age of 112 ± 5 Ma by K-Ar dating of biotite (Lopez-Ramos, 1979).

Petrographic interpretations (Figure 3.7 a-b) reveal crystals that range in size from 100 to 4000 μm , which are principally composed of quartz (10%), sericitized

Chapter 3: Petrography & Geochronology Results

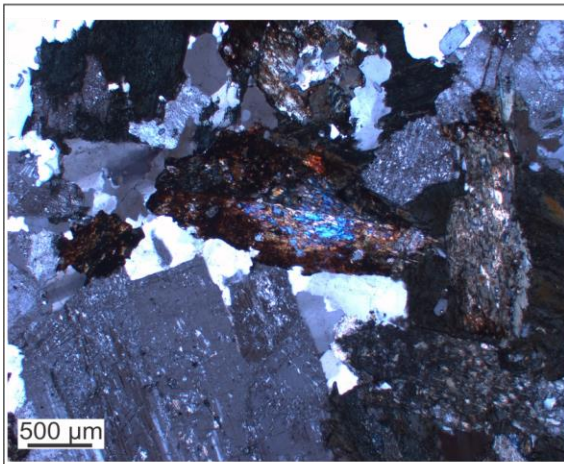
feldspars (55%; mainly plagioclase), chloritized biotite (20%) and amphiboles that display twinning in some instances (10%). The remaining 5% of the sample is composed of the alteration mineral epidote and the accessory minerals of zircon and apatite.

The sample contains euhedral to subhedral zircons that are 150-250 μm along their longest axis and have aspect ratios of 2:1-7:1. The CL images for the zircons are characterised by oscillatory and sector zoning typical of igneous zircons (Figure 3.7). There is also evidence for core and rim relationships within the sample which record two separate zircon forming events.

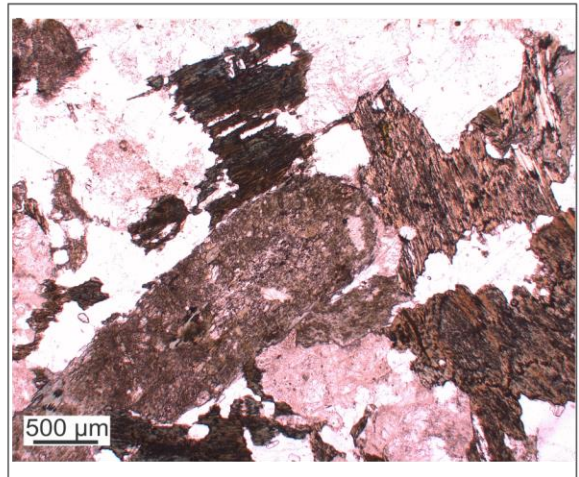
U concentrations for the zircons range from 150-700 ppm (Figure 3.7 f) and Th/U ratios fall between 0.4-1 (Figure 3.7 e). These values are consistent with zircons that crystallise in magmatic environments. There are also anomalous analysed grains that show enrichment in the LREEs as well as a less pronounced Ce positive anomaly (Figure 3.7 g-i) which would suggest contamination from monazite inclusions within the zircons and could potentially affect the age calculations.

Of the 40 zircon analysed grains 33 were used in the age calculations (< 20% discordance and < 10% inversely discordant). Weighted-mean plots were constructed (Figure 3.7 d) for the concordant grains that yielded an age of 253.5 ± 5.2 Ma with an MSWD of 5.4 (two analysis were rejected by the algorithm). The high MSWD and two analyses that were rejected by the algorithm may be a reflection of mixing between core and rim ages. This interpretation, although likely, is speculative as no clear correlations are observed between the age differences and core and rim relationships in the CL images (Figure 3.7 j). The age obtained, although somewhat imprecise, can be interpreted as the best estimate of the igneous crystallization age of the zircons.

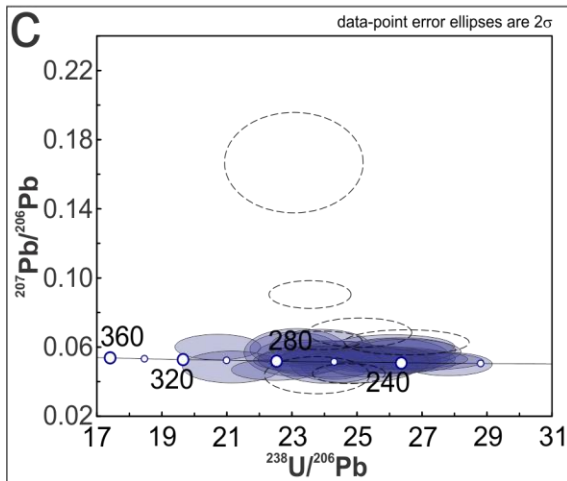
Linares-1 N7C1F1



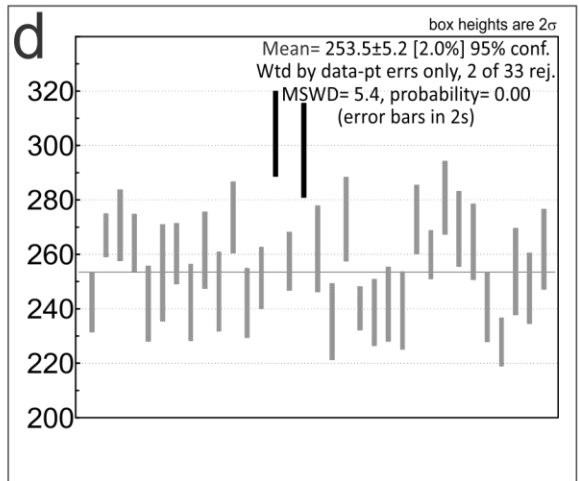
Cross polarized light (XPL) thin section image for the analysed sample showing sericitized plagioclase, quartz and twinned clinopyroxene (altered to iron oxides).



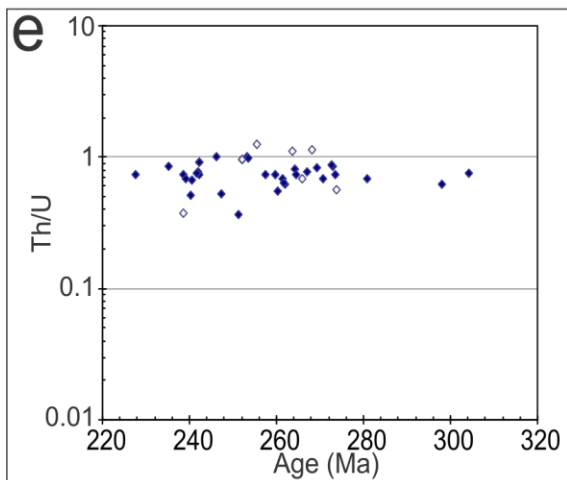
Plane polarized light (PPL) thin section image for the analysed sample showing high relief clinopyroxene, chloritised biotite and low relief quartz and feldspars.



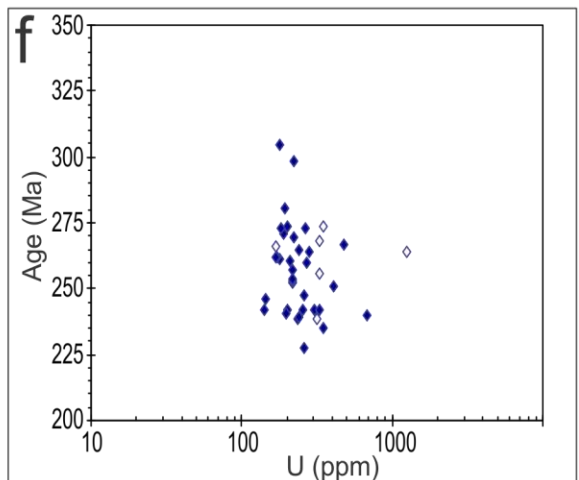
Tera Wasserburg plot of the analysed grains (n=40). The blue ellipses represent zircons that were taken further to age calculations (n=33) and the dotted ellipses show those that were disregarded (> 20% discordance, > 10% inverse discordance).



Weighted mean plot for the zircons considered for age calculations (n=33).



Th/U vs. Age (Ma) plot for all of the analysed zircons (n=40). The blue points represent the grains that were used in age calculations and the clear points show those that were disregarded.



Age (Ma) vs. U (ppm) diagram for all of the analysed grains (n=40). Blue points represent grains that were used in age calculations and clear points show that were disregarded.

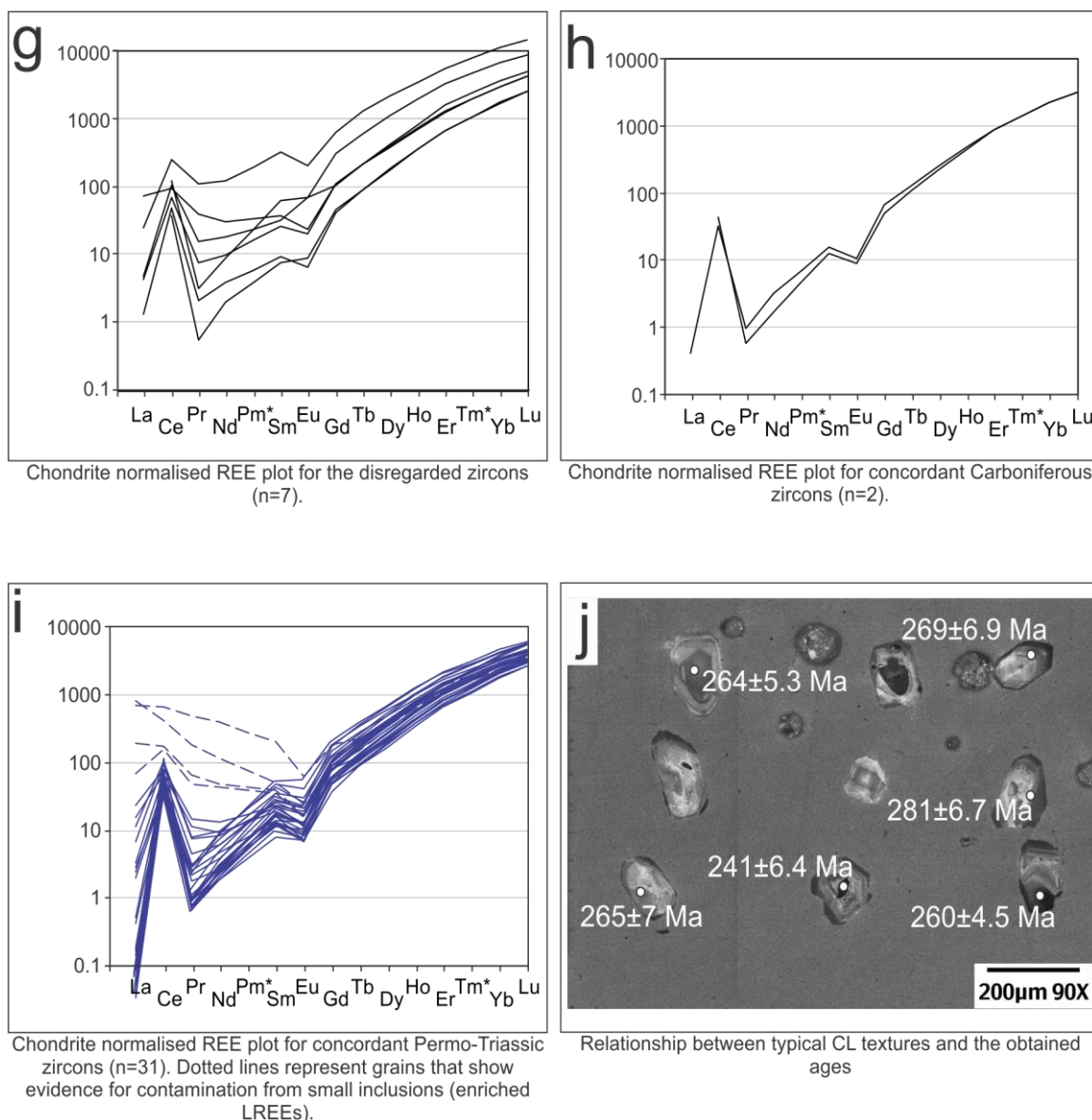


Figure 3.7. Geochronology results for the Linares N7F1C1 basement core from the Western Gulf of Mexico.

3.3.4 *Chaneque N6F1C4*

The analysed sample from the Chaneque well is (Figure 3.1) has the composition of a hydrothermally altered granitoid (phaneritic texture). Previous dating of the basement core on potassium feldspars (K-Ar) yielded an age of 133 ± 5 Ma (Lopez-Ramos, 1979). Petrographic interpretations (Figure 3.8 a-b) reveal crystals that range in size from 150 to 2500 μm , which are principally composed of quartz (10%; present as monocrystalline grains and in veins), feldspars (65%; too altered to differentiate),

Chapter 3: Petrography & Geochronology Results

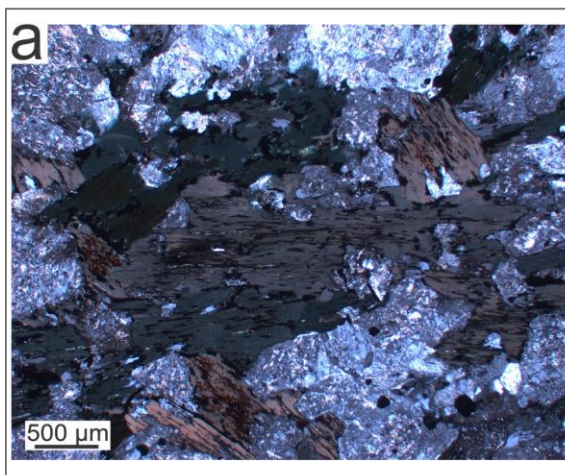
chloritized biotite (15%) and unusually large apatite (up to $\sim 1000 \mu\text{m}$; 5%). The remaining 5% of the sample is made up of opaque minerals and the accessory mineral zircon. The severity of the alteration seen in the feldspars of the sample suggests the K-Ar age obtained by Lopez-Ramos (1979) may not have any geological significance.

This sample contains euhedral, prismatic zircons that are 150-300 μm along their longest axis, with aspect ratios of 3:1-7:1. The CL textures of the zircons are defined by marked oscillatory and sector zoning (Figure 3.8 i). There is no evidence for core and rim relationships but resorption features on inner zoned fractions may suggest that zircon growth was intermittent, occurring in several phases in the same event. The observed CL textures are typical of those found within igneous zircons.

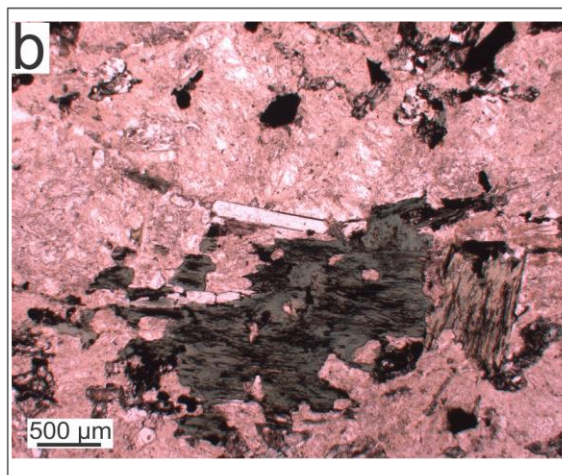
U concentrations of the analysed zircons used in the age calculations range between 50-900 ppm (Figure 3.8 f) and Th/U ratios fall between 0.4-2.4 (Figure 3.8 e). These results are consistent with the igneous source interpretation from the CL images, they are however quite varied which suggests that the source was quite compositionally heterogeneous.

Of the 38 analysed zircons 28 were used for age calculations ($< 20\%$ discordant, $< 5\%$ inversely discordant and $< 5\%$ error). Weighted-mean plots have been constructed for the accepted analysed grains (Figure 3.8 d), yielding an age of $243.4 \pm 2.8 \text{ Ma}$, with an MSWD of 1.9 (two ages have been rejected by the algorithm). This can be interpreted as the igneous crystallization age of the zircons within a geochemically evolving magma chamber.

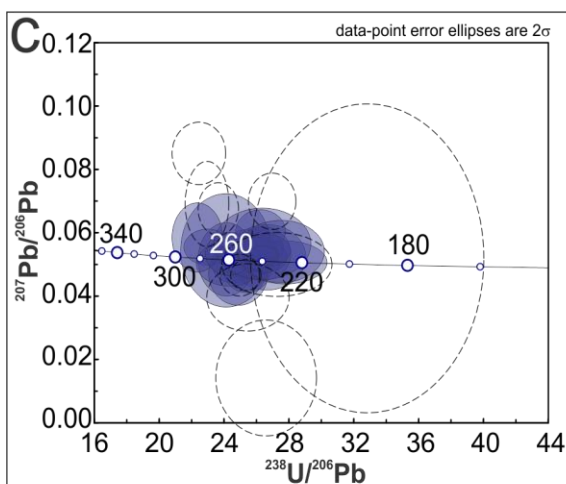
Chaneque-1 N6F1C4



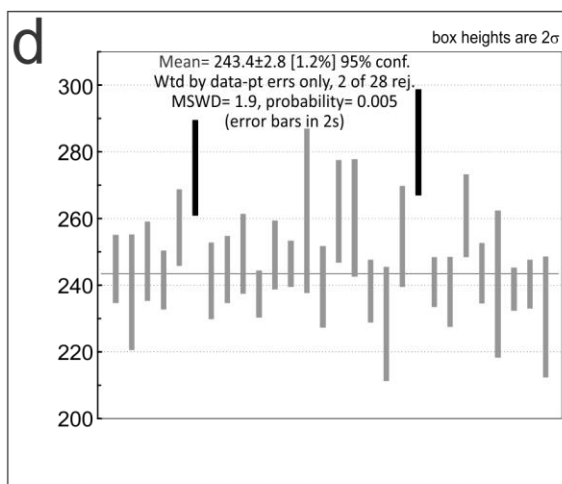
a Cross polarized light (XPL) thin section image for the analysed sample showing sericised plagioclase, chloritised biotite, opaques and apatite.



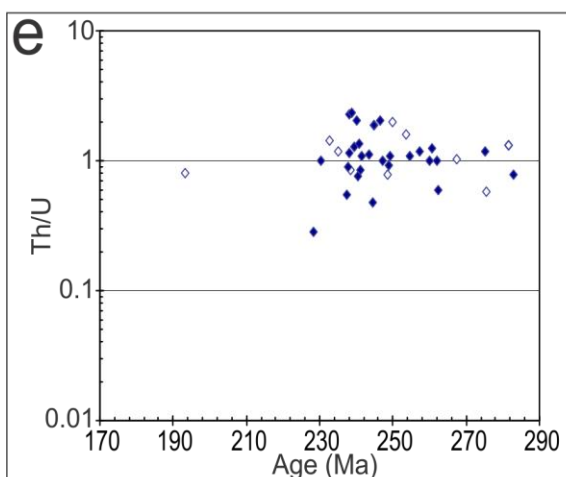
b Plane polarized light (PPL) thin section image for the analysed sample showing low relief sericite, chloritised biotite, apatite and opaque minerals.



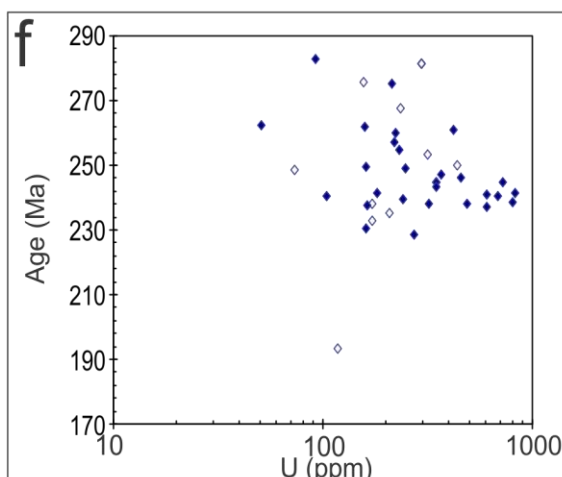
c Tera Wasserburg plot of the analysed grains (n=38). The blue ellipses represent zircons that were taken further to age calculations (n=28) and the dotted ellipses show those that were disregarded (> 20% discordance, > 5% inverse discordance, > 5% error).



d Weighted mean plot for the zircons considered for age calculations (n=28)



e Th/U vs. Age (Ma) plot for all of the analysed zircons (n=38). The blue points represent the grains that were used in age calculations and the clear points show those that were disregarded.



f Age (Ma) vs. U (ppm) diagram for all of the analysed grains (n=38). Blue points represent grains that were used in age calculations and clear points show that were disregarded.

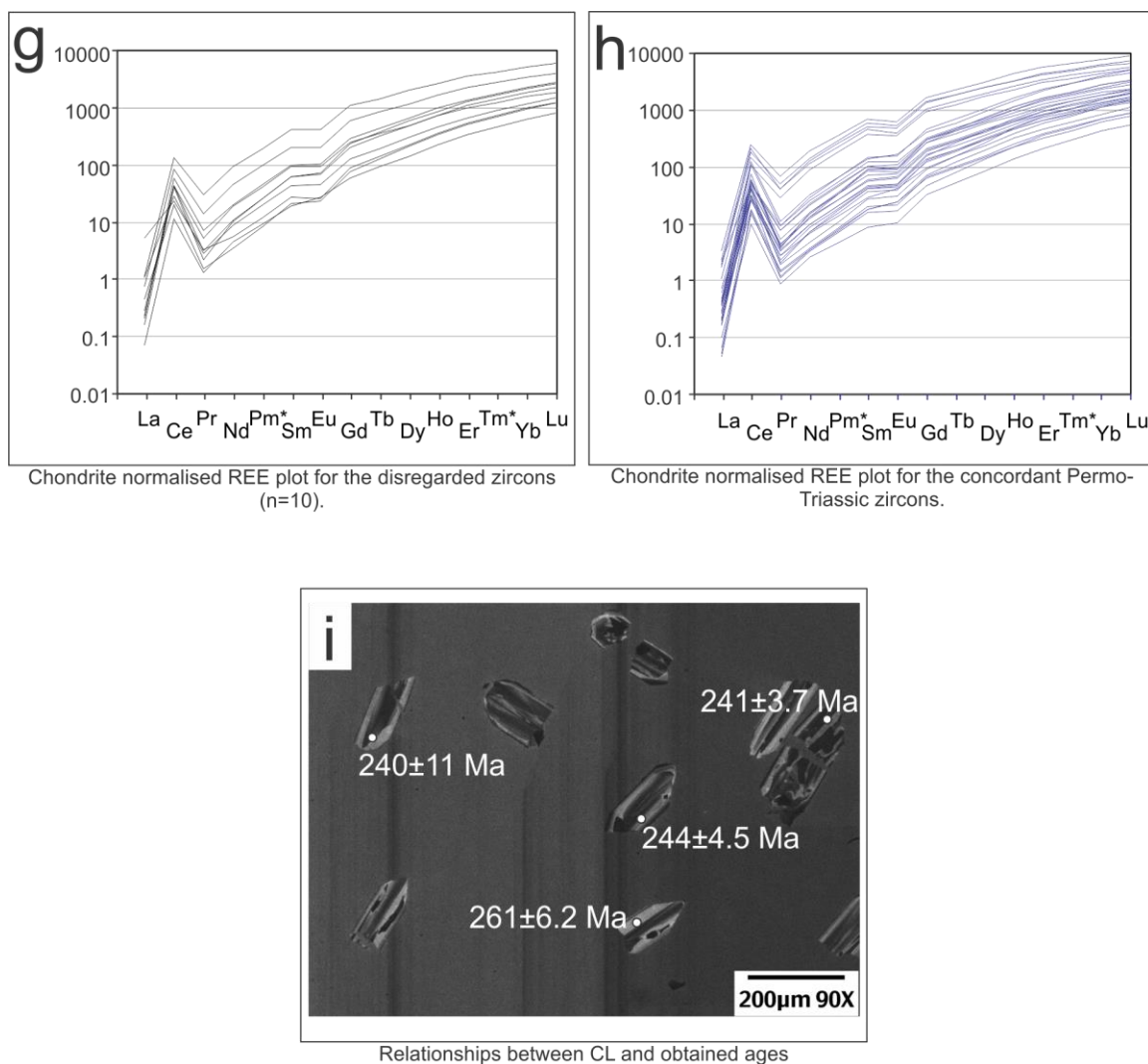


Figure 3.8. Geochronology results for the Chaneque N6F1C4 basement core from the Western Gulf of Mexico.

3.3.5 *Nayade N13F2C1*

The analysed sample from the Nayade well (Figure 3.1) has the composition of hydrothermally altered biotite granite (phaneritic texture). Petrographic interpretations (Figure 3.9 a-b) reveal crystals that range in size from 150 to 7000 μm , which are primarily composed of quartz (35%; monocrystalline and recrystallized polycrystalline grains), altered feldspars (50%; predominantly alkali feldspars) and partially chloritized biotite (10%). The remaining 5% is composed of opaque minerals that form in association with the breakdown of biotite and the accessory minerals zircon and apatite.

Chapter 3: Petrography & Geochronology Results

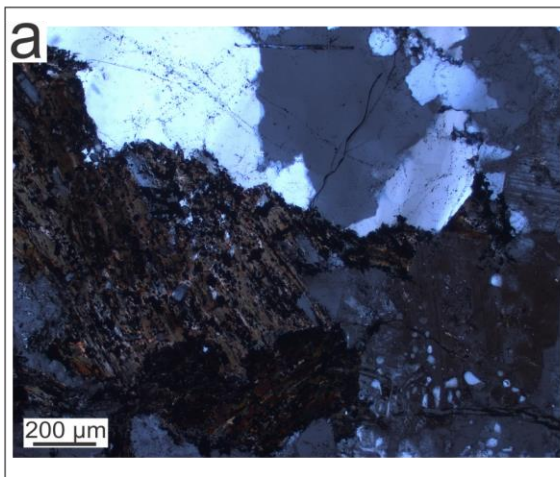
Minor intergrowths of quartz and feldspars are also observed in the sample, producing myrmekitic textures (Figure 3.9 a).

Zircons are subhedral grains and fragments that range in size from 100-400 μm along their longest axis, with aspect ratios of 1:1 to 5:1. The CL textures are characterised by oscillatory zoning and core-rim relationships that are difficult to detect due to the dark nature of the grains (Figure 3.9 k). These relationships suggest that the zircons likely formed in an igneous environment, with inherited xenocrysts. The dark colour of the zircons in the CL images indicates high U concentrations which in turn may affect age calculations due to metamictization.

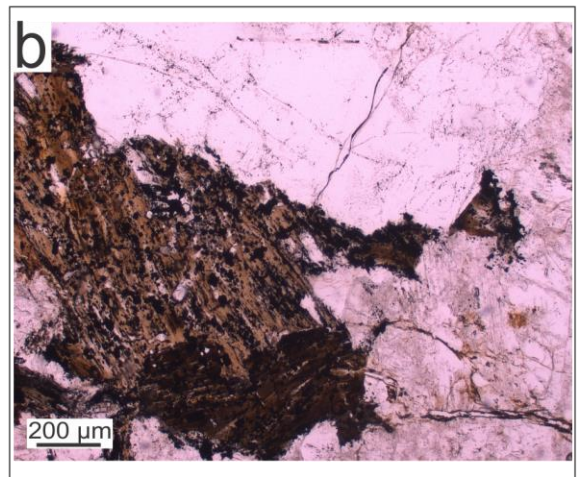
Th/U ratios (Figure 3.9 g) support the CL observations and yield a range typical of igneous zircons (0.2-1.2) throughout core and rim. Suspicions of metamictization are confirmed in the Age (Ma) vs U (ppm) plot (Figure 3.9 f) which clearly shows correlations between the younger ages and high U concentrations. To reduce the effect of metamictization only zircons with < 1000ppm U were used in the age calculations.

Out of the 35 analysed grains 13 were deemed suitable to use in age calculations (< 9% discordant, < 1000ppm U). Weighted-mean plots (Figure 3.9 e) yield an age of 257 ± 5.2 Ma with an MSWD of 3.7 which can be interpreted as the age of the youngest igneous event which created the zircon rims. The concordant inherited cores (Figure 3.9 c) yielded ages of 397 ± 6 Ma, 538 ± 6 Ma and 558 ± 4 Ma.

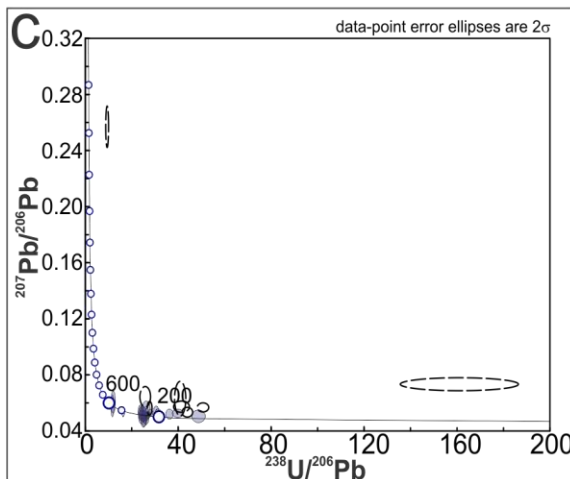
Nayade-1 N13F2C1



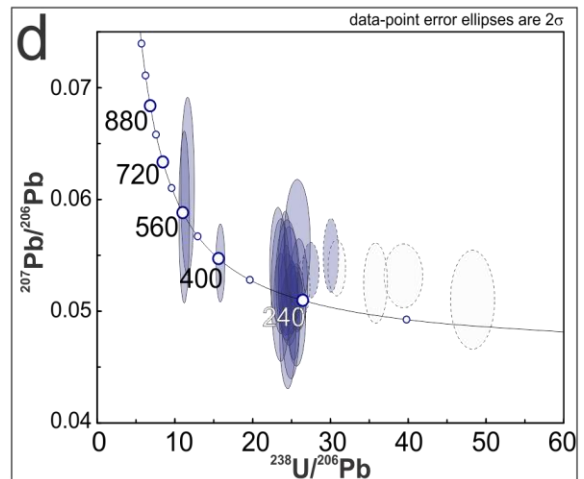
a Cross polarized light (XPL) thin section image for the analysed sample showing plagioclase, quartz (myrmekitic texture present) and biotite filled with inclusions of opaques, apatite and zircon.



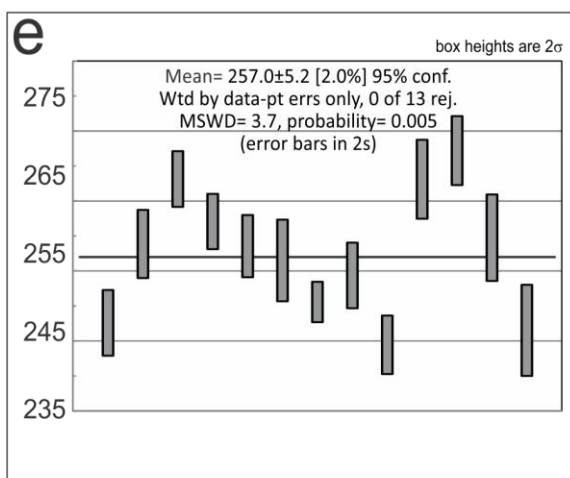
b Plane polarized light (PPL) thin section image for the analysed sample showing plagioclase, quartz and biotite filled with inclusions of opaques, apatite and zircon.



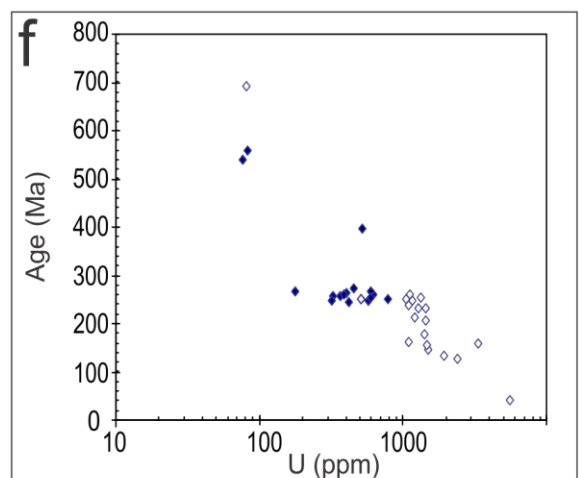
c Tera Wasserburg plot of the analysed grains (n=35). The blue ellipses represent concordant zircons (n=27) and the dotted ellipses show those that were disregarded (> 9% discordance) during initial filtering.



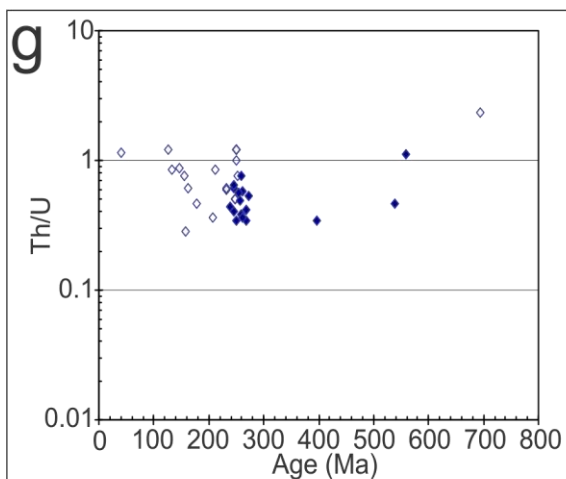
d Tera Wasserburg after initial filtering (n=27). Blue ellipses represent grains used in age calculations (n=16) and dotted ellipses represent those disregarded after final filtering (> 9% discordance, >1000 ppm U).



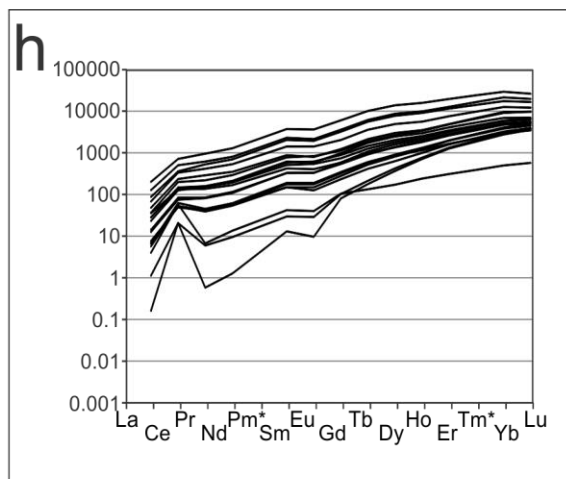
e Weighted mean plot for the youngest population of zircons considered for age calculations (n=13)



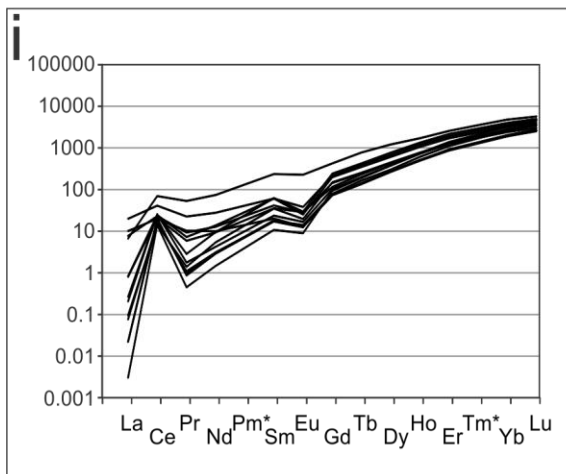
f Age (Ma) vs. U (ppm) diagram for all of the analysed grains (n=35). Blue points represent grains that were used in age calculations and clear points show that were disregarded.



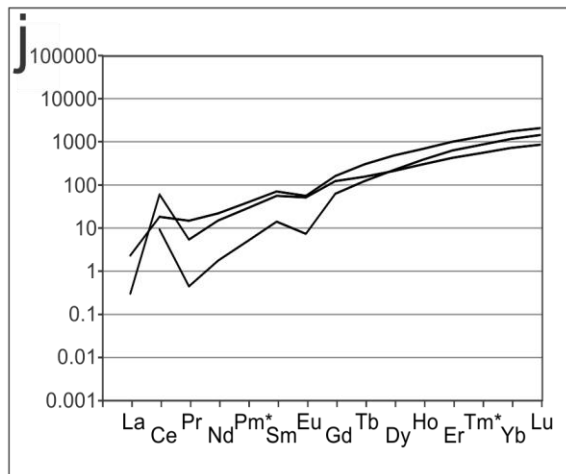
Th/U vs. Age (Ma) plot for all of the analysed zircons (n=35). The blue points represent the grains that were used in age calculations and the clear points show those that were disregarded.



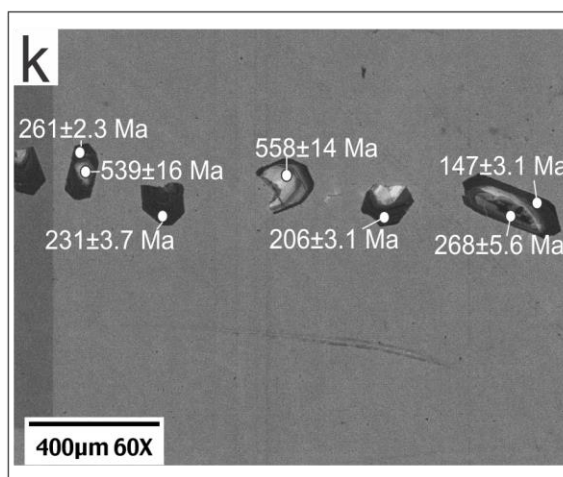
Chondrite normalised REE plot for the disregarded zircons (n=19)



Chondrite normalised REE plot for the youngest population of zircons considered for age calculations (n=13)



Chondrite normalised REE plot for the inherited cores (n=3)



Relationship between CL and obtained ages

Figure 3.9. Geochronology results for the Nayade N13F2C1 basement core from the Western Gulf of Mexico.

3.3.6 *Tamaulipas N1F2C1*

The analysed sample from the Tamaulipas well (Figure 3.1) has a granodiorite composition (phaneritic texture). Petrographic interpretations (Figure 3.10 a-b) reveal relatively unaltered crystals that range in size from 200-7000 μm , primarily composed of quartz (10%), feldspars (60%; predominantly plagioclase), amphibole (15%) and biotite (10%). The remaining 5% is made up of, opaque minerals and the accessory minerals of titanite, zircon and apatite.

Zircons that were separated from the sample are 150-400 μm in size along their longest axis, with aspect ratios of 2:1-6:1. The CL textures are characterised by oscillatory and sector zoning (Figure 3.10 i), indicating that the zircons are igneous in origin. There appears to be a core and rim relationship in a lot of the grains, as well as inclusion of other minerals, which may affect the reliability of the results.

Of the 37 zircon grains analysed 28 were deemed reliable enough to use in age calculations (< 20% discordant, <5% inversely discordant and < 5% error; Figure 3.10 c). The discarded zircons possibly have been affected by contamination from small inclusions within the grains as highlighted in the CL observations (Figure 3.10 i). Interpretation of the zircon REE concentrations (Figure 3.10 g-h) confirms these suspicions, in that they show enrichment in the LREEs and no Ce negative anomaly which is indicative of contamination from monazite.

Weighted-mean plots (Figure 3.10 d) have been constructed for the zircon grains considered for age calculations and yield an age of 247.9 ± 4.0 Ma with a MSWD of 1.8 (two ages were rejected by the algorithm). It may be the case that the rejected ages represent the age of the inner cores (282 ± 10 Ma & 278 ± 7 Ma) observed in some of the

Chapter 3: Petrography & Geochronology Results

zircons. This interpretation is rather speculative however as there is not enough evidence in the geochemistry or CL images to be certain. The age obtained for the zircons can therefore be simply interpreted as the time of igneous crystallization.

Tamaulipas N1F2C1

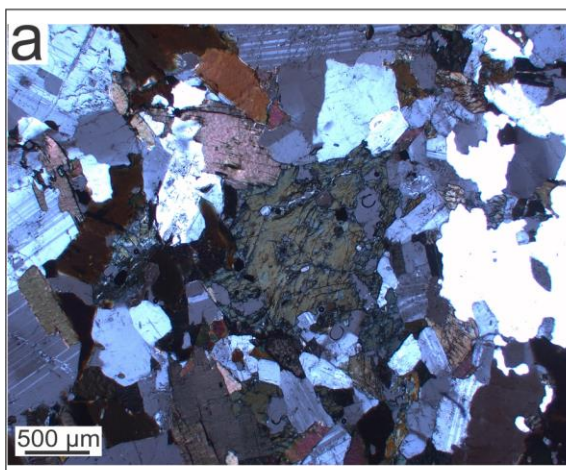


Figure 3.1a: Cross polarized light (XPL) thin section image for the analysed sample showing plagioclase, quartz, hornblende, biotite and minor titanite.

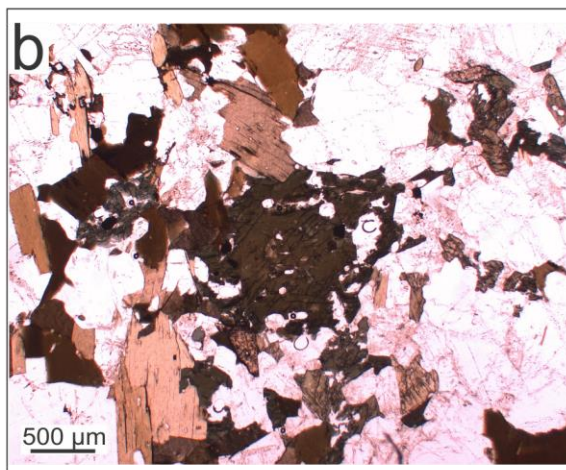


Figure 3.1b: Plane polarized light (PPL) thin section image for the analysed sample showing plagioclase, quartz, hornblende, biotite and minor titanite.

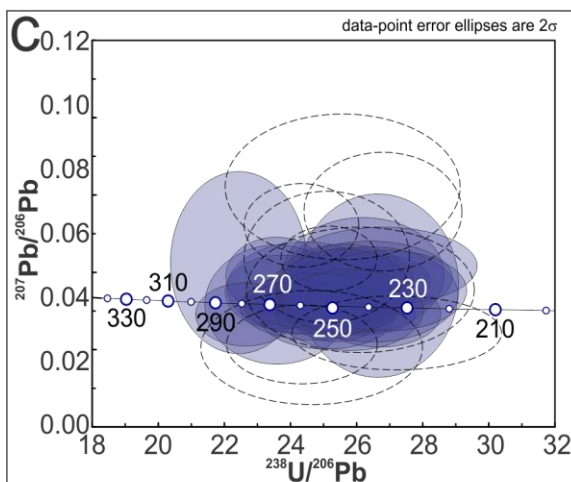


Figure 3.2c: Tera Wasserburg plot of the analysed grains (n=37). The blue ellipses represent zircons that were taken further to age calculations (n=28) and the dotted ellipses show those that were disregarded (> 20% discordance, > 5% inverse discordance, > 5% error).

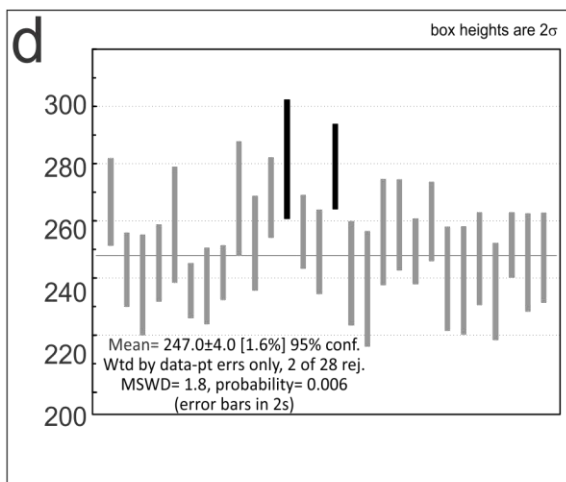


Figure 3.2d: Weighted mean plot for the zircons considered for age calculations (n=28)

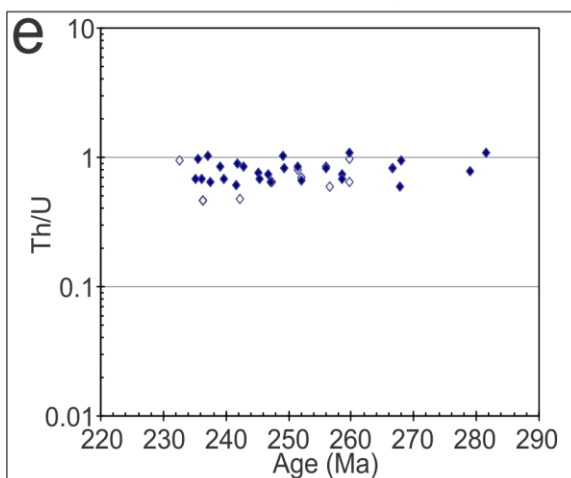


Figure 3.2e: Th/U vs. Age (Ma) plot for all of the analysed zircons (n=37). The blue points represent the grains that were used in age calculations and the clear points show those that were disregarded.

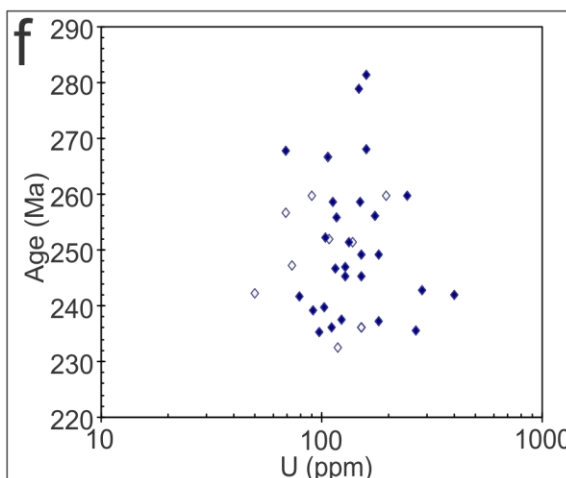


Figure 3.2f: Age (Ma) vs. U (ppm) diagram for all of the analysed grains (n=37). Blue points represent grains that were used in age calculations and clear points show those that were disregarded.

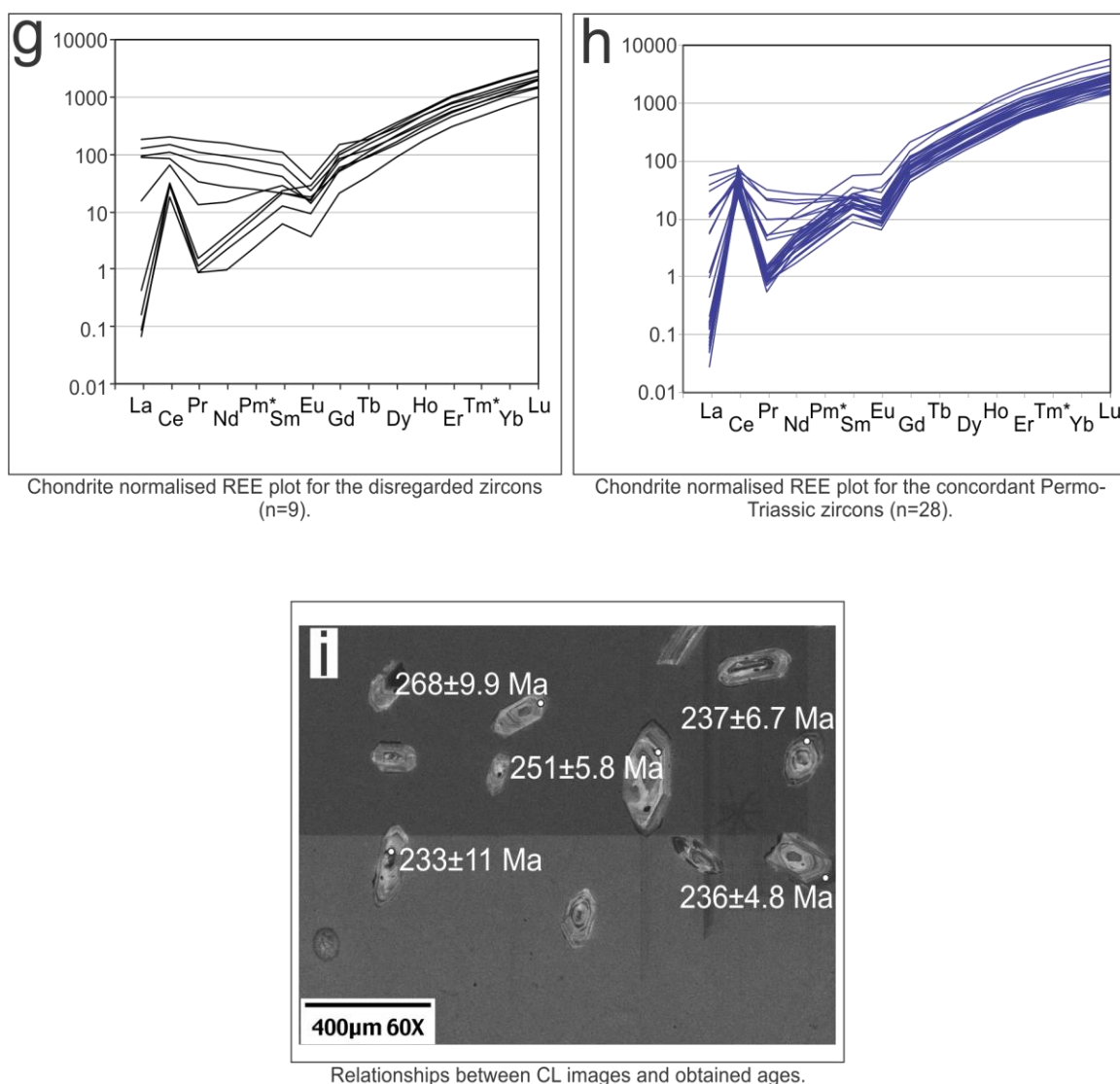


Figure 3.10. Geochronology results for the Tamaulipas N1F2C1 basement core from the Western Gulf of Mexico.

3.3.7 Erizo N19F19C1

The analysed sample from the Erizo well (Figure 3.1) has the composition of hydrothermally altered granite (phaneritic texture). Petrographic interpretations (Figure 3.11 a-b) reveal crystals that range in size from 100-9000 μm , which are primarily composed of quartz (30%), sericitized feldspars (60%; alteration makes it difficult to distinguish between members). The remaining 10% is made up of the alteration mineral calcite and accessory minerals of zircon and apatite.

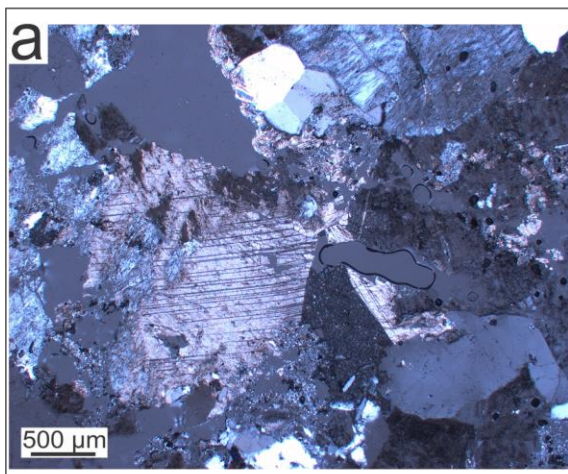
Chapter 3: Petrography & Geochronology Results

The sample contains euhedral to subhedral zircon grains and fragments that are 100-300 μm along their longest dimension, with an aspect ratio of 2:1-5:1. The CL images (Figure 3.11 i) show typical igneous textures such as oscillatory and sector zoning with no apparent inherited cores. Age calculations for the zircons from this sample have been undertaken with care as there are a few aspects of the CL results that may affect the ages. Firstly, there appear to be fractures along the c-axis of the more elongated grains which may be an inlet for common lead. Secondly, the dark colouration of the zircons in the CL images indicates high U concentrations, and possible metamictization.

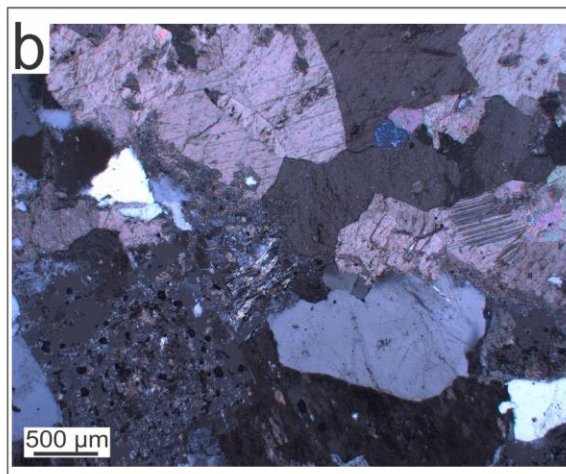
The age (Ma) vs U (ppm) plot (Figure 3.11 f) confirms metamictization, with zircons over 800 ppm uranium displaying an inverse correlation between age and U concentration. To minimise this effect all zircons with >800 ppm uranium were not used in the age calculations. The Th/U ratios (Figure 3.11 e) are very consistent throughout the zircon grains (0.7-1.2), which suggests they all formed from the same magma.

Of the 49 analysed grains 30 were suitable for use in the age calculations (< 25% discordance, < 3% error, < 7% reverse discordance, < 800 ppm U; Figure 3.11 c). Weighted-mean plots (Figure 3.11 d) yield an age of 250 ± 3.1 Ma with an MSWD of 2.2 which can be interpreted as the igneous crystallization age.

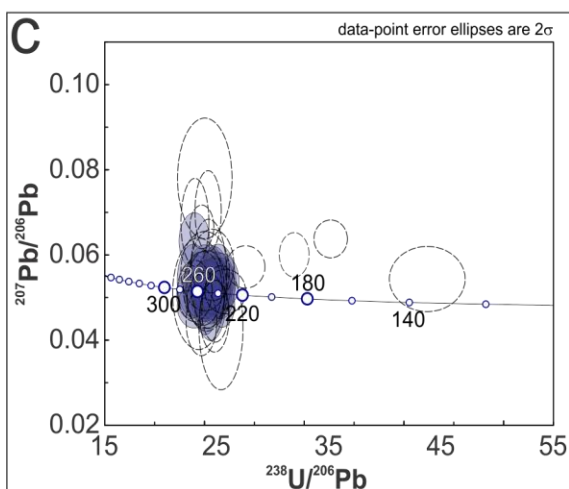
Erizo N19F19C4



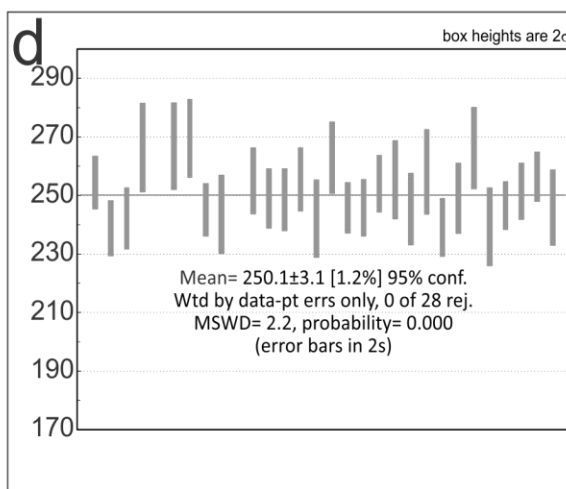
Cross polarized light (XPL) thin section image for the analysed sample showing sericitized plagioclase, perthite, quartz and calcite.



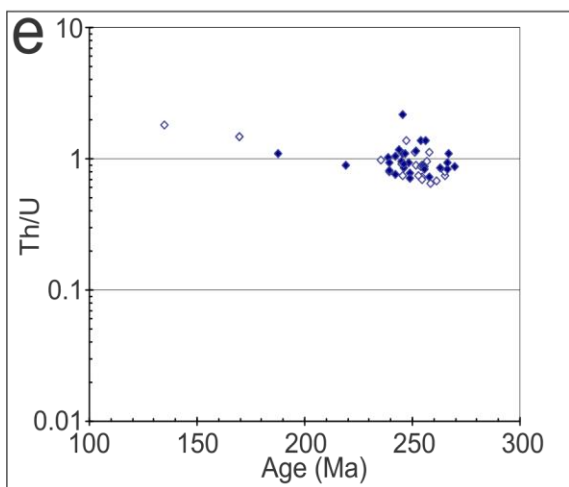
Cross polarized light (XPL) thin section image for the analysed sample showing sericitized plagioclase, perthite, quartz and calcite.



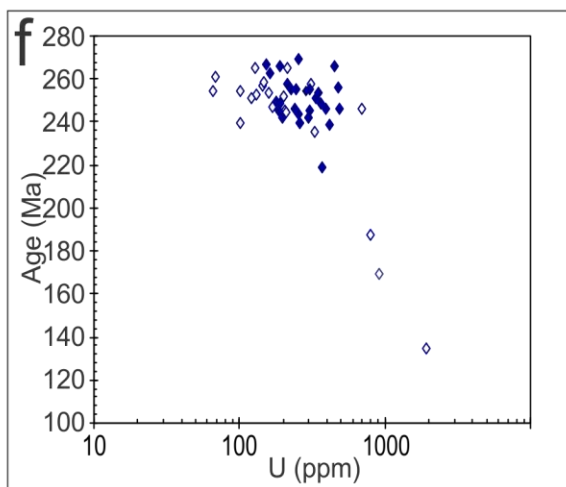
Tera Wasserburg plot of the analysed grains (n=49). The blue ellipses represent zircons that were taken further to age calculations (n=28) and the dotted ellipses show those that were disregarded (> 25% discordance, > 7% inverse discordance, > 3% error).



Weighted mean plot for the zircons considered for age calculations (n=28).



Th/U vs. Age (Ma) plot for all of the analysed zircons (n=49). The blue points represent the grains that were used in age calculations and the clear points show those that were disregarded.



Age (Ma) vs. U (ppm) diagram for all of the analysed grains (n=49). Blue points represent grains that were used in age calculations and clear points show those that were disregarded.

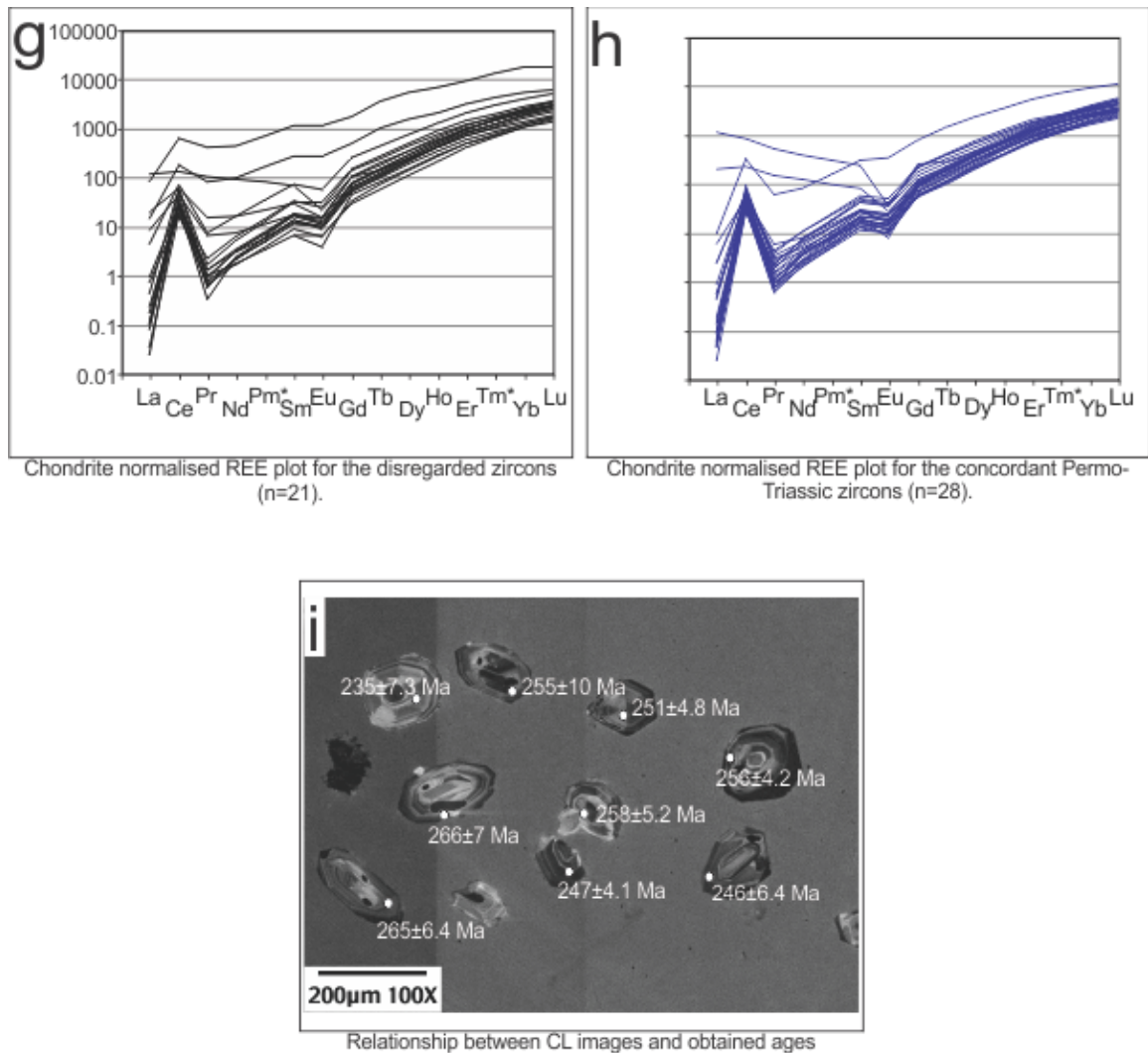


Figure 3.11. Geochronology results for the Erizo N19F19C4 basement core from the Western Gulf of Mexico.

3.3.8 *Pinonal N2F11C2*

The second analysed sample from the Pinonal well (Figure 3.1) has the composition of a hydrothermally altered granodiorite (phaneritic texture). Petrographic interpretations (Figure 3.12 a-b) reveal crystals that range in size from 200-7000 μm , which are primarily composed of quartz (10%; monocrystalline and in veins), feldspars (50%), amphibole (20%; hornblende) and biotite (10%). Minor phases in the sample include calcite veining (1%), opaque minerals (2%), apatite (2%) and zircon (1%). Epidote and titanite also forms (4%) in association with the partial breakdown of hornblende.

Chapter 3: Petrography & Geochronology Results

The sample contains euhedral to subhedral zircon grains and fragments that are 200-400 μm in size along their longest axis, with aspect ratios of 2:1-10:1. The CL images (Figure 3.12 k) are characterised by oscillatory and sector zoning indicating a magmatic origin for the zircons. Some of the more elongated grains have fractures along their c-axis in which common lead appears to be a contaminant (bright CL colours in the fractures) which may affect the reliability of the age calculations.

Of the 31 zircons that were analysed 27 were deemed reliable enough to be used in age calculations ($< 30\%$ discordance and $< 5\%$ error; Figure 3.12 c). Discordant grains correlate with enrichment in the LREEs (Figure 3.12 g-j) and a lack of Ce anomaly which suggests contamination from inclusions (probably monazite). It is apparent from the Tera-Wasserburg plot (Figure 3.12 c) that there are some xenocrystic cores in the sample. These yield a range of concordant ages: Proterozoic ($1235 \pm 153 \text{ Ma}$); Cambrian ($509 \pm 7.8 \text{ Ma}$) and Ordovician ($478 \pm 6.8 \text{ Ma}$). U concentrations in the cores range from 80-300 ppm (Figure 3.12 f) with Th/U ratios of 0.4-0.8 (Figure 3.12 e). These results are consistent with zircons that formed in igneous environments.

Weighted-mean plots (Figure 3.12 d) have been constructed for the Permo-Triassic zircons in the sample and these yield an age of $249.5 \pm 3.1 \text{ Ma}$, with an MSWD of 1.6. U concentrations and Th/U ratios range from 80-1000 ppm & 0.1-1 respectively (Figure 3.12 e-f), which although quite variable are typical of igneous zircons. This Permo-Triassic age can therefore be interpreted as the time of crystallization of the zircons in an igneous event. This event failed to completely resorb pre-existing zircons that are preserved as Proterozoic, Cambrian and Ordovician cores in some of the grains.

Pinonal1 N2F11C2

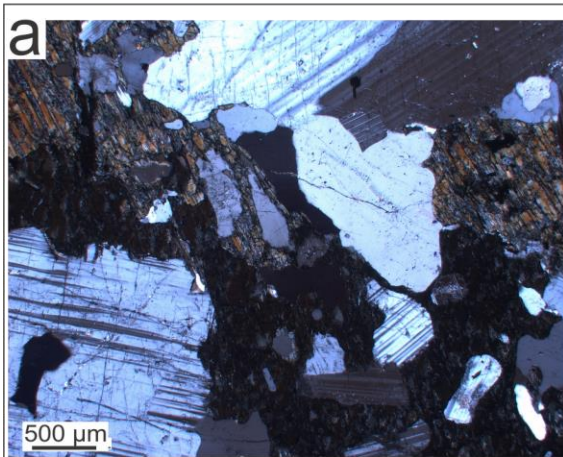


Figure 3a: Cross polarized light (XPL) thin section image for the analysed sample showing plagioclase, quartz, and altered orthopyroxene.

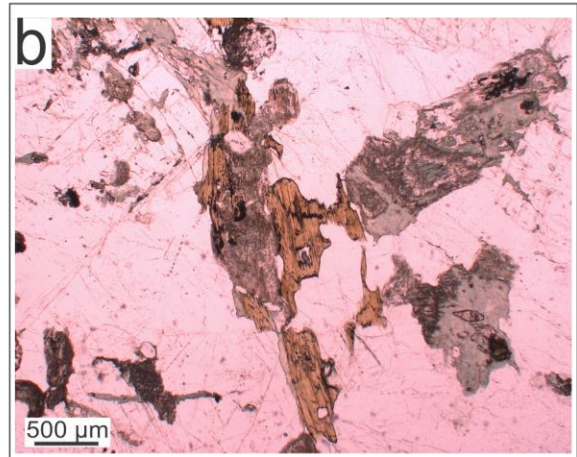


Figure 3b: Plane polarized light (PPL) thin section image for the analysed sample showing low relief plagioclase and quartz and brown biotite, partially chloritised.

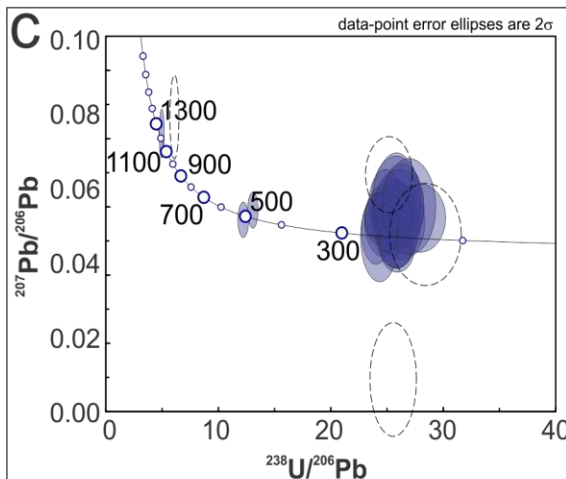


Figure 3c: Tera Wasserburg plot of the analysed grains (n=31). The blue ellipses represent zircons that were taken further to age calculations (n=27) and the dotted ellipses show those that were disregarded (> 30% discordance, > 4% error).

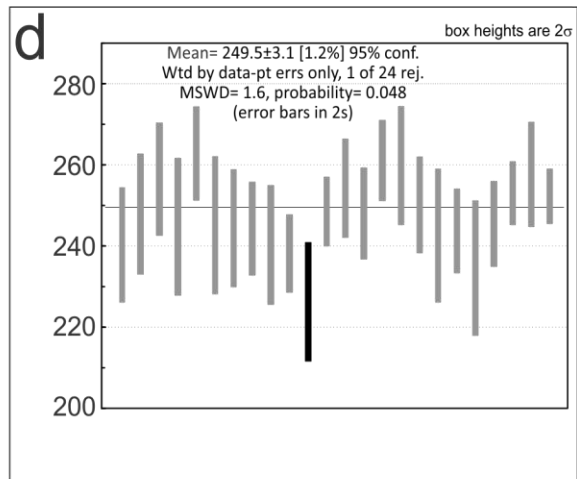


Figure 3d: Weighted mean plot for the youngest group of zircons considered for age calculations (n=24).

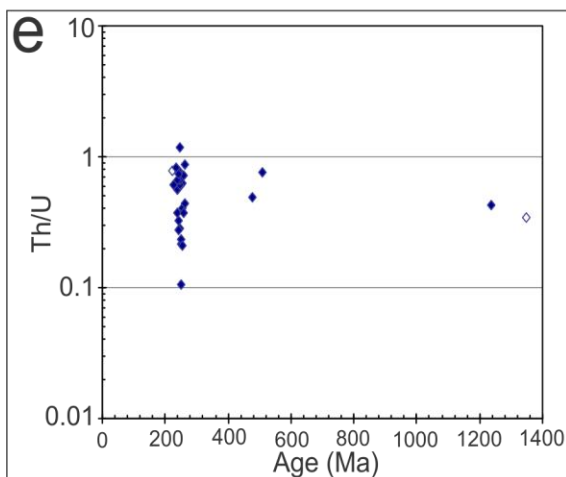


Figure 3e: Th/U vs. Age (Ma) plot for all of the analysed zircons (n=31). The blue points represent the grains that were used in age calculations and the clear points show those that were disregarded.

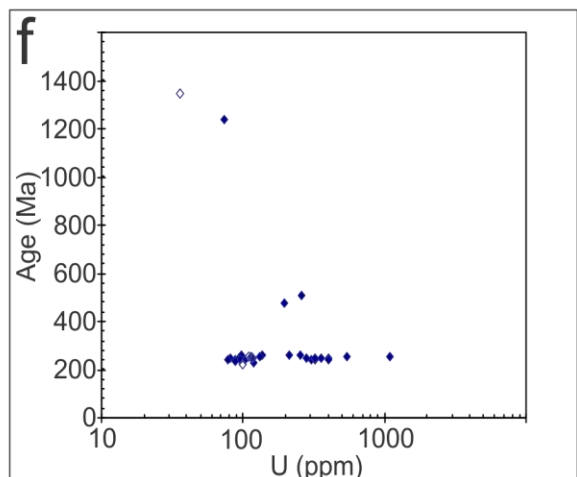


Figure 3f: Age (Ma) vs. U (ppm) diagram for all of the analysed grains (n=31). Blue points represent grains that were used in age calculations and clear points show those that were disregarded.

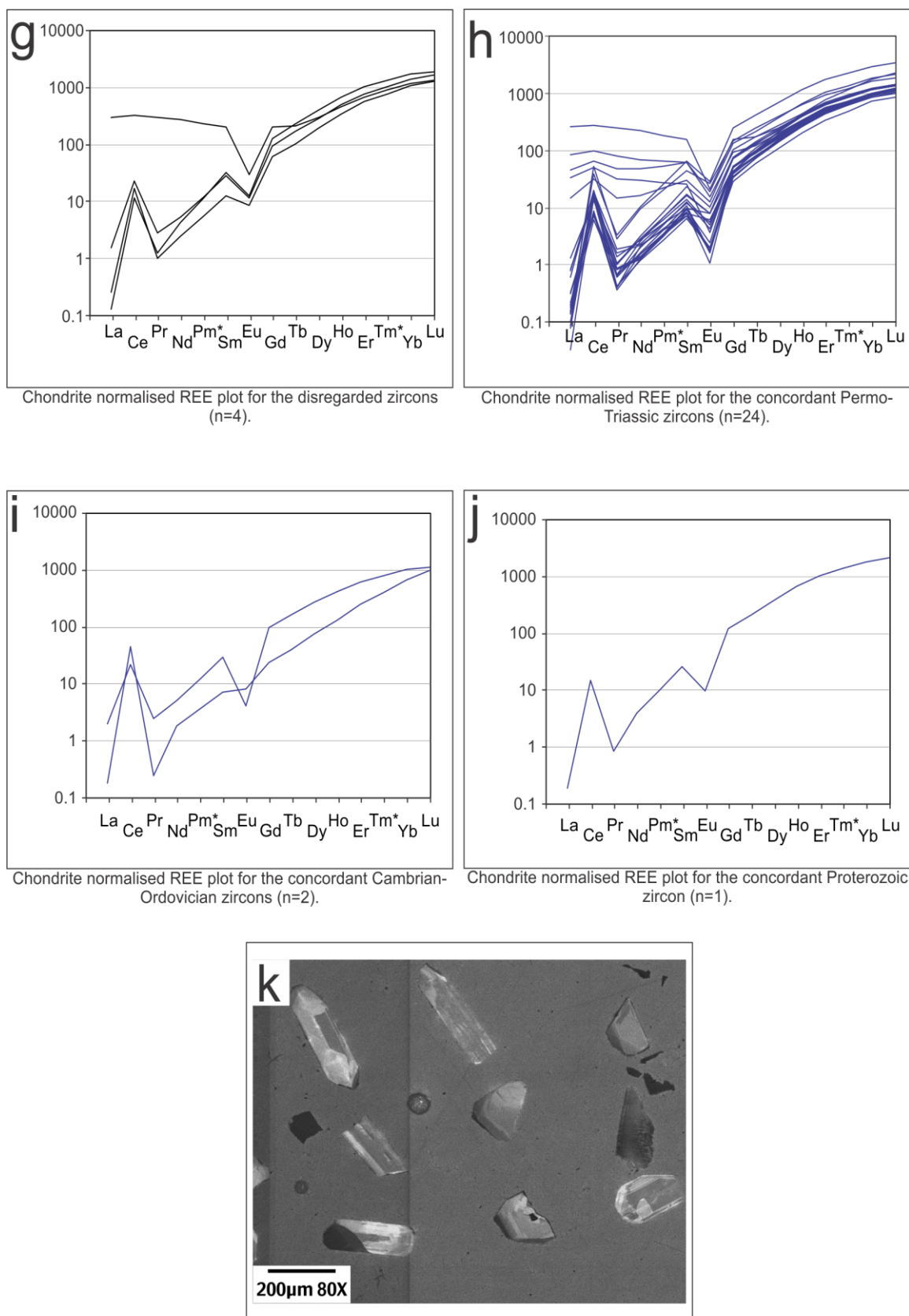


Figure 3.12. Geochronology results for the Pinonal N2F11C2 basement core from the Western Gulf of Mexico.

3.3.9 *Cupelado N9F1C1*

The analysed sample is taken from the Cupelado well (Figure 3.1) at a depth of 3818-3824 m and is composed of biotite granite. The rock was too altered to make a thin section. Many of the zircons analysed are fragmented but some display elongated, euhedral to subhedral shapes that are 100-300 μm along their longest axis. CL textures are characterised by oscillatory and sector zoning (Figure 3.13 i), typical of igneous zircons. There are very distinct populations of zircons in the CL images (high-U dark zircons, strongly zoned zircons and more homogeneous grains) indicating that the crystals did not all grow in the same event. Enriched trends in the LREEs (Figure 3.13 j-k) of some of the grains are likely to be caused by contamination from small inclusions. A lack of Eu negative anomaly is also present in these anomalous zircons which suggest the inclusions might be plagioclase feldspar.

Of the 19 grains analysed 14 were deemed suitable for age calculations (< 16% discordant and <4.7% error; Figure 3.13 c-d). Discordance in some instances appears to correlate with contamination by inclusions in the grains. Alternatively it may represent mixing of isotopic compositions between core and rim.

Weighted-mean plots (Figure 3.13 g) for the strongly oscillatory zoned grains yield an age of 1428 ± 48 Ma (MSWD= 0.21; one of the ages was rejected by the algorithm). U concentrations for the cores fall between 200-500 ppm (Figure 3.13 i) and they possess a Th/U ratio ranging between 0.2-0.8 (Figure 3.13 h). These geochemical results show consistency with the zoning in the CL observations, indicating that they formed in a magmatic event. The Proterozoic age can therefore be interpreted as the igneous crystallization age.

Chapter 3: Petrography & Geochronology Results

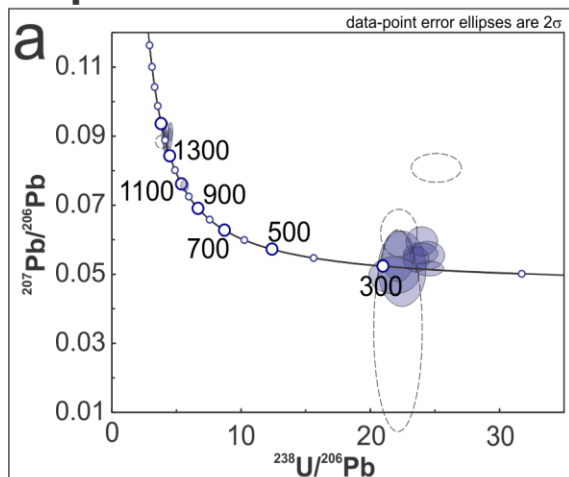
Weighted-mean plots (Figure 3.13 f) for a second population of zircons yield an age of 284.8 ± 9.1 Ma (MSWD= 0.16). U concentrations are low (90-120 ppm; Figure 3.13 i), and Th/U ratios are typically igneous (0.4-0.6; Figure 3.13 h). This population of zircons has similar ages to the igneous zircon forming event in the Early-Permian observed in other wells such as Pinonal and Arenque.

Weighted-mean for the youngest population of zircons (Figure 3.13 e) yield an age of 262.7 ± 4.5 Ma (MSWD= 0.86). U concentrations in this population yield the highest results (400-850 ppm; Figure 3.13 i) but are comparable with the other populations in the Th/U ratios (0.2-0.35; Figure 3.13 h). These zircons can be interpreted to have formed in a Late-Permian igneous event.

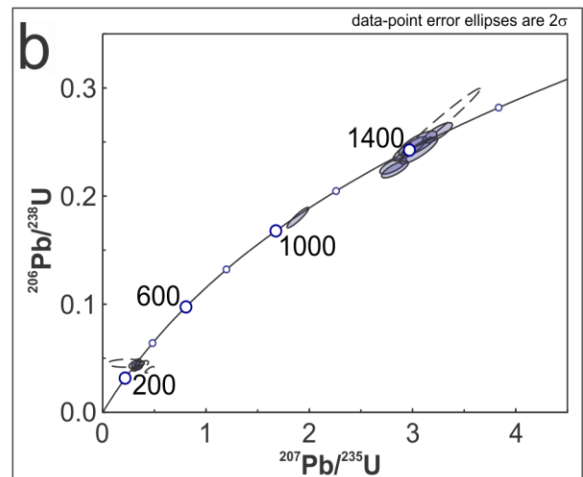
Interestingly, there is no core and rim relationship (Figure 3.13 i) observed between the Proterozoic and Permian zircons which may suggest that this rock formed from the partial melting of a pre-existing sedimentary rock (containing detrital zircons from different areas to form an S-type granite). The age of the S-type granite is not recorded in the zircon populations (no core and rim relationships), we can only conclude that it is younger than 262 Ma. A more effective way of obtaining an age for the youngest igneous event would be to date the rock by ^{40}Ar - ^{39}Ar methods.

Alternatively, the lack of core-rim relationships may simply be due to the low number of zircon grains analysed. In this scenario the youngest population of 262.7 ± 4.5 Ma would represent the age of rock formation, with inheritance from Proterozoic and Mid-Permian cores.

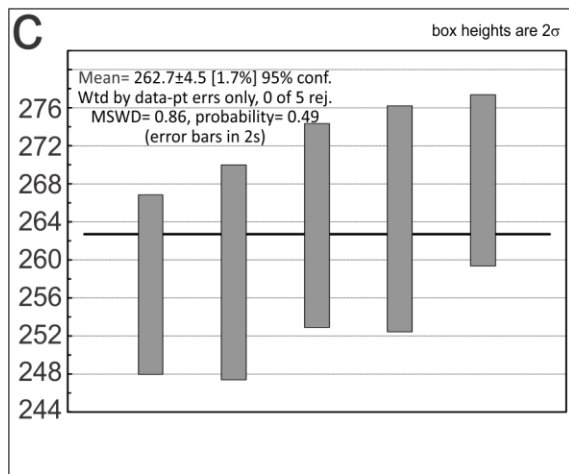
Cupelado N9F1C1



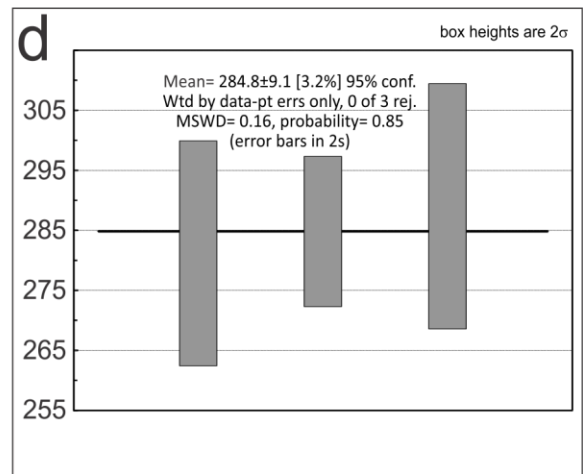
Tera Wasserburg plot of the analysed grains (n=19). The blue ellipses represent zircons that were taken further to age calculations (n=15) and the dotted ellipses show those that were disregarded (> 16% discordance, > 5% error).



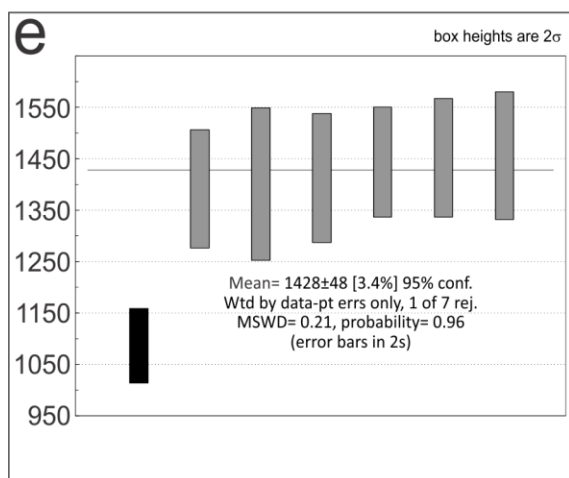
Wetherill plot of the analysed grains (n=19). The blue ellipses represent zircons that were taken further to age calculations (n=15) and the dotted ellipses show those that were disregarded (> 16% discordance, > 5% error).



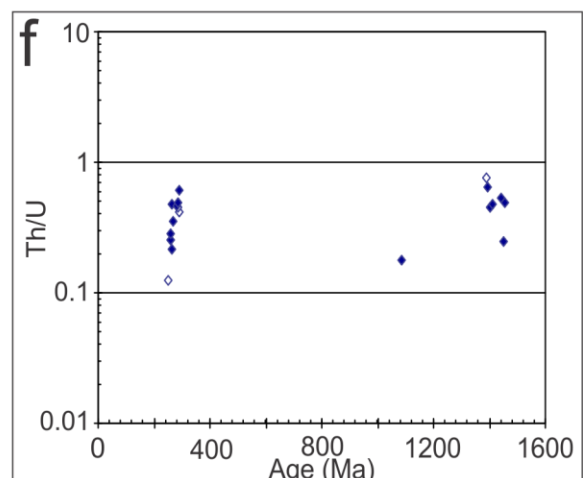
Weighted mean plot for the youngest population of zircons considered for age calculations (n=5)



Weighted mean plot for the Mid-Permian population of zircons considered for age calculations (n=3)



Weighted mean plot for the Proterozoic zircons considered for age calculations (n=7)



Th/U vs. Age (Ma) plot for all of the analysed zircons (n=19). The blue points represent the grains that were used in age calculations and the clear points show those that were disregarded.

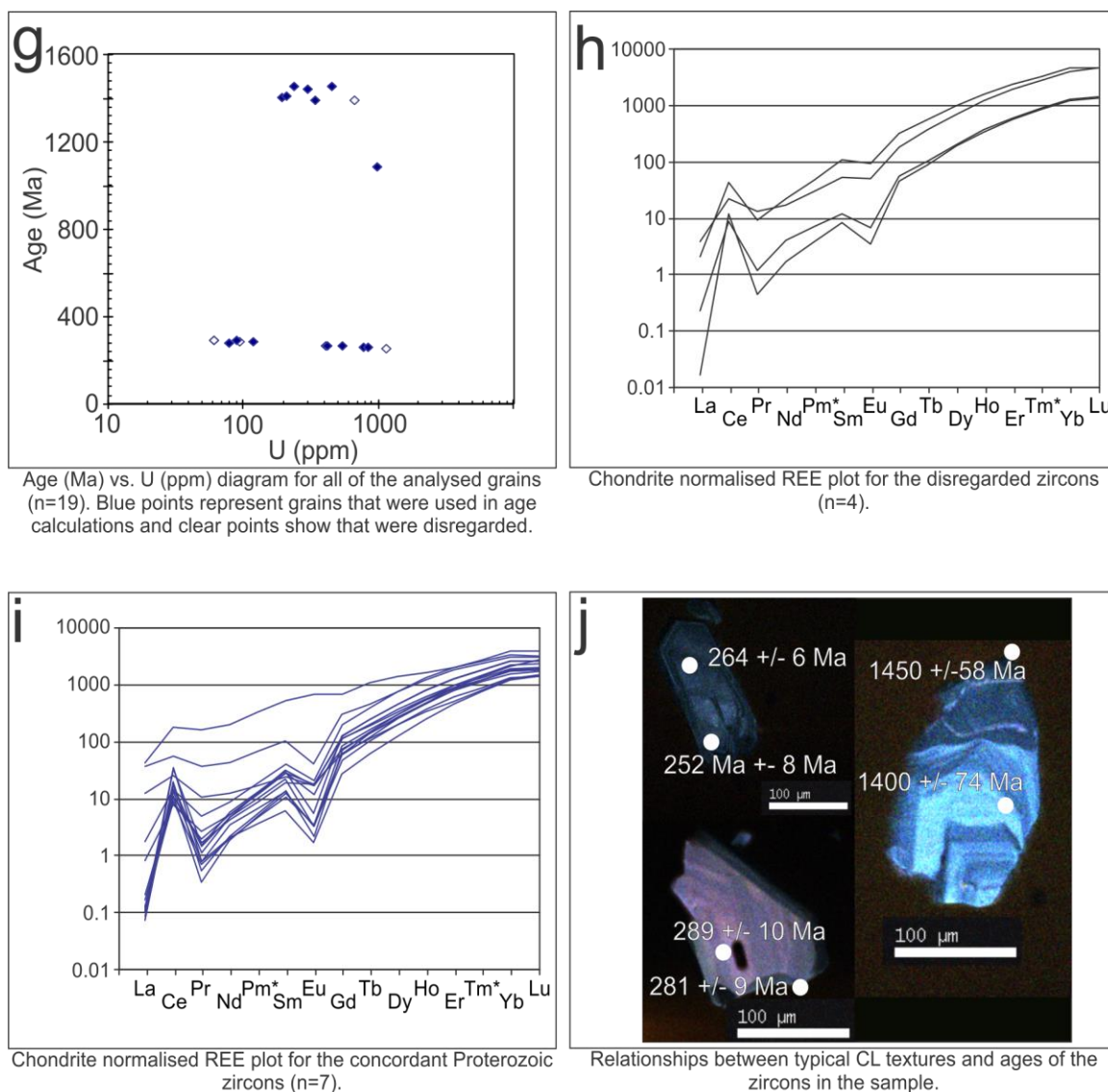


Figure 3.13. Geochronology results for the Cupelado N9F1C1 basement core from the Western Gulf of Mexico.

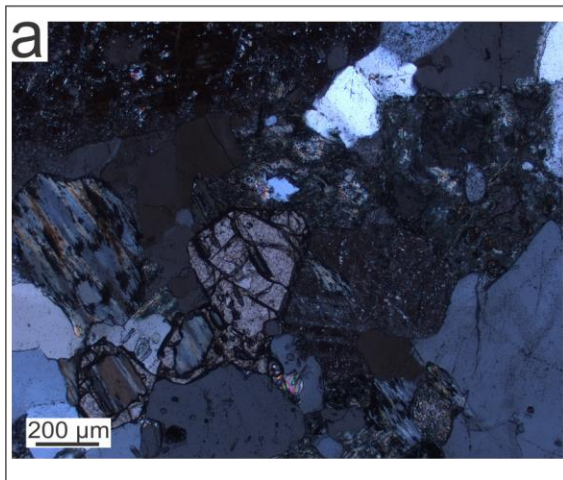
3.3.10 *Plan de Las Hayas N14F1C1*

The analysed sample from the Plan de las Hayas well (Figure 3.1) was taken at a depth of 3316-3321 m and has the composition of an altered granodiorite (phaneritic texture). Previous dating on a sample from the well by PEMEX yielded an age of 312 ± 25 Ma by K/Ar dating methods on potassium feldspars (Lopez-Ramos, 1979). However, the alteration observed in the sample suggests this age may not have any geological significance. Petrographic interpretations (Figure 3.14 a-b) reveal crystals 150-5000 μm in size, which are primarily composed of quartz (10%), sericitized feldspars (60%; 80:20 plagioclase and alkali feldspar respectively) and chloritized biotite (20%). Minor phases in the sample include titanite (5%), calcite (3%), apatite (1%) and zircon (1%).

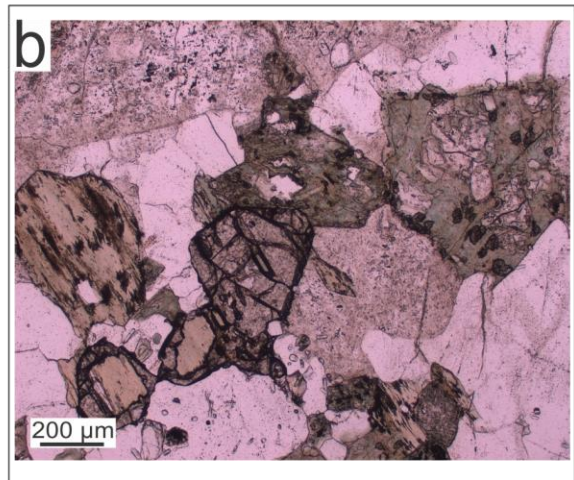
The dated zircons are subhedral, prismatic grains 80-200 μm in size, with aspect ratios of 1:1-4:1. CL textures are characterised by oscillatory and sector zoning (Figure 3.14 i). Some of the zircons contain small inclusions which may have an effect on the ages obtained. U concentrations range between 100-1000 ppm (Figure 3.14 f), and Th/U ratios between 0.1- 1.1 (Figure 3.14 e). In some of the REE trends (Figure 3.14 g-h) the Ce anomaly is less pronounced which suggests that the small inclusions (potentially monazite) observed in the CL images have contaminated some of the analyses. The CL and geochemical observations suggest an igneous origin for the zircons.

Of the 29 analysed grains 23 were considered for age calculations (< 10% discordant and <5% inversely discordant; Figure 3.14 c). The discordance probably relate to contamination from inclusions as mentioned above. Weighted-mean plots (Figure 3.14 d) for the concordant grains yield a Permian age of 261 ± 4.1 Ma with an MSWD of 2.8 which can be interpreted as the igneous crystallization age for the zircons.

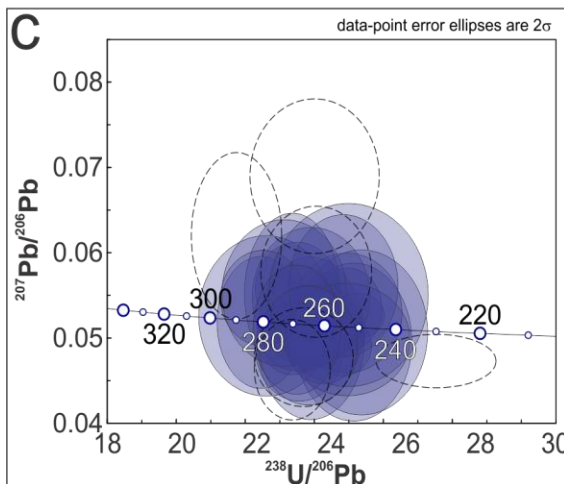
Plan de las Hayas N14F1C1



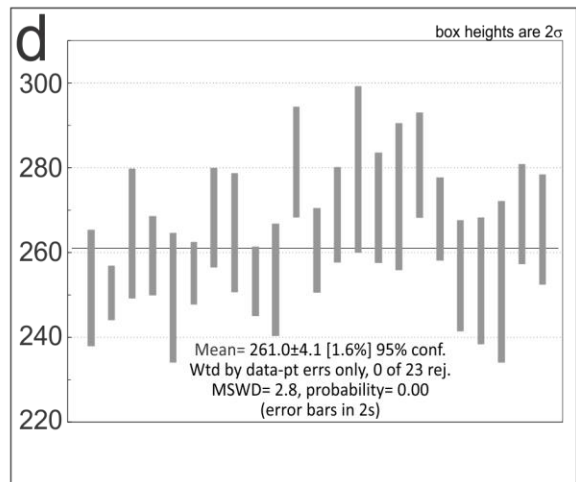
a Cross polarized light (XPL) thin section image for the analysed sample showing sericitized plagioclase, quartz, chloritised biotite and titanite.



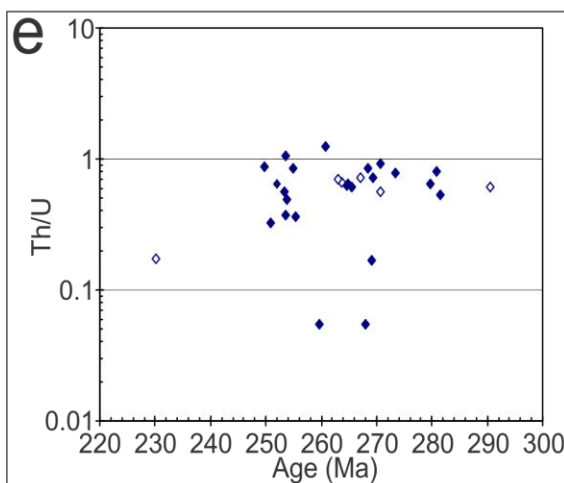
b Plane polarized light (PPL) thin section image for the analysed sample showing sericitized plagioclase, quartz, chloritised biotite and titanite.



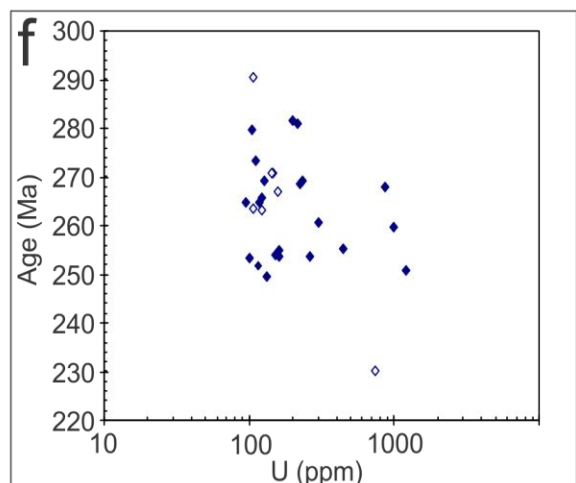
c Tera Wasserburg plot of the analysed grains (n=29). The blue ellipses represent zircons that were taken further to age calculations (n=23) and the dotted ellipses show those that were disregarded (> 10% discordance, > 5% inverse discordance).



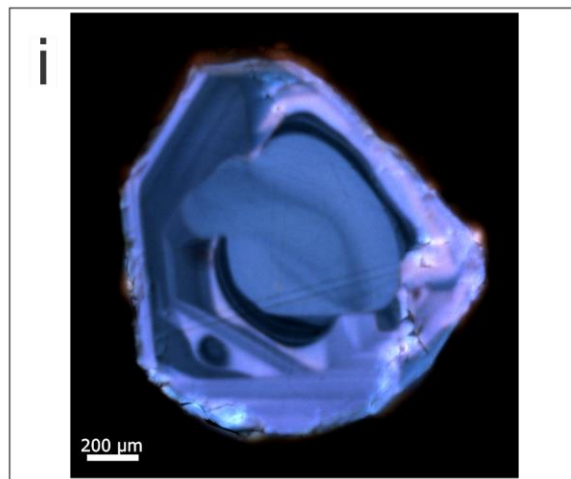
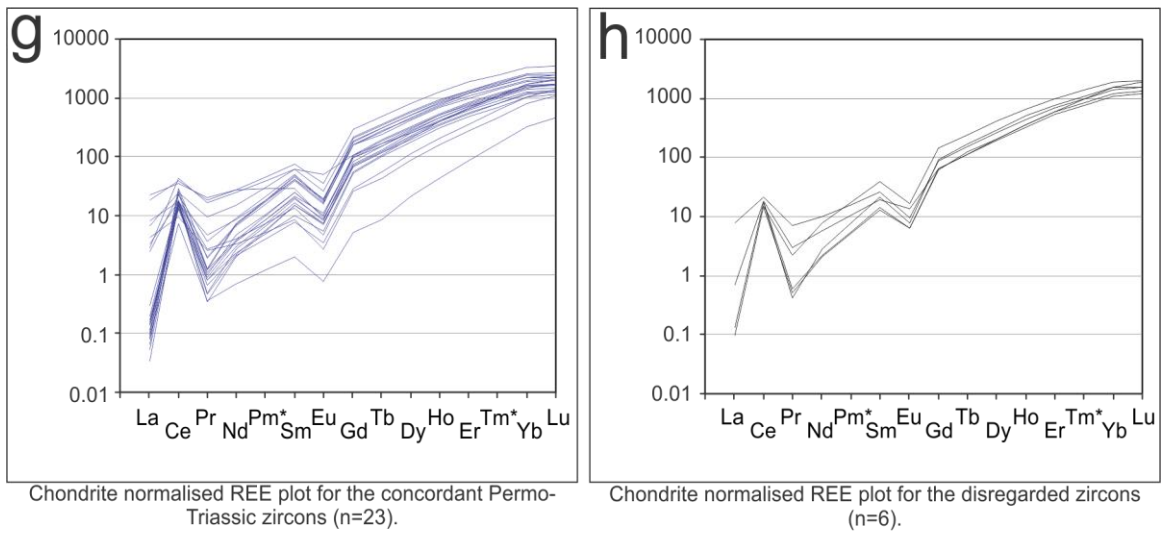
d Weighted mean plot for the zircons considered for age calculations (n=23)



e Th/U vs. Age (Ma) plot for all of the analysed zircons (n=29). The blue points represent the grains that were used in age calculations and the clear points show those that were disregarded.



f Age (Ma) vs. U (ppm) diagram for all of the analysed grains (n=29). Blue points represent grains that were used in age calculations and clear points show those that were disregarded.



Typical CL texture of the zircons in the sample.

Figure 3.14. Geochronology results for the Plan de las Hayas N14F1C1 basement core from the Western Gulf of Mexico.

3.3.11 *Plan de las Hayas N14F6C2*

The second analysed sample from the Plan de las Hayas well (Figure 3.1) is taken from a depth of 3316-3321 m and has the composition of a hydrothermally altered quartz diorite (phaneritic texture). The basement associated with this core has previously been dated to 312 ± 25 Ma using K-Ar methods on potassium feldspar (Lopez-Ramos, 1979). However, the alteration observed in the sample suggests this age may not have any geological significance.

Petrographic interpretations (Figure 3.15 a-b) reveal crystals that range in size from 150-9000 μm , which are primarily composed of quartz (15%), sericitized feldspars (55%; alteration makes distinguishing between members difficult) and chloritized biotite (15%). Minor phases in the sample include titanite (5%; forms in close association with the chloritized biotite), calcite veining (5%; product of hydrothermal alteration), serpentine (3%; product of hydrothermal alteration), opaque minerals (2%), apatite (<1%) and zircon (<1%).

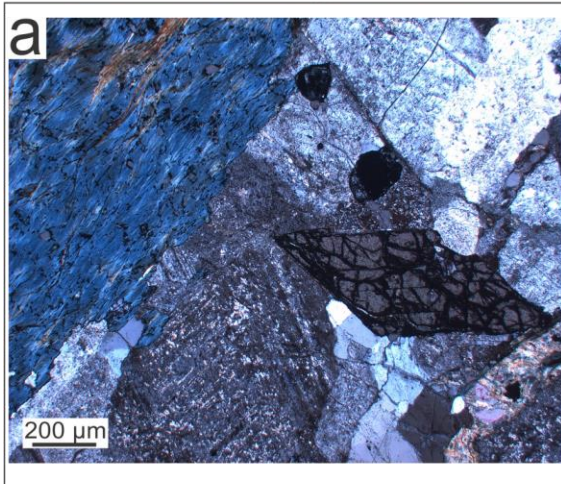
The sample contains euhedral and prismatic zircons that are 150-250 μm along their longest axis and have aspect ratios of 2:1-10:1. CL images are characterised by marked oscillatory zoning inherent throughout the analysed grains, as well as some instances of sector zoning (Figure 3.15 h). There is no evidence to suggest this sample has any inheritance from xenocrystic cores and therefore it is likely that all of the observed zircons formed in one magmatic event due to the homogeneity between grains and types of textures seen in the CL images. It is also apparent that some of the analysed grains contain small inclusions of other minerals which may affect the results of the analysis.

Chapter 3: Petrography & Geochronology Results

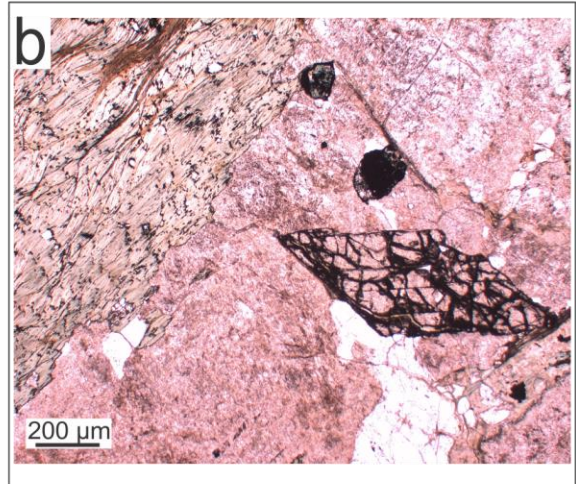
U concentrations and Th/U ratios are fairly uniform between the analysed zircons, with results ranging from 80-400 ppm and 0.3-0.9 respectively (Figure 3.15 e-f). These results are consistent with the interpretations from the CL images, which suggest that the zircons are igneous in origin and all relate to the same event.

Of the 30 grains analysed, 27 were considered reliable enough to use in age calculations (< 20% discordant and yielded < 6% uncertainty in their $^{206}\text{Pb}/^{238}\text{U}$ ratio; Figure 3.15 c). The three grains that were not considered further in the age calculations due to either discordance or high degrees of error are likely to have been affected by contamination from small inclusions (probably monazite), as is indicated by more enriched LREE patterns and lack of Ce positive anomaly (Figure 3.15 g). Alternatively low U concentrations (observed in two of three discarded zircons) could cause the high errors observed (Figure 3.15.f). Weighted-mean plots for the concordant zircons (Figure 3.15 d) yield an age of 250 ± 4.6 Ma with an MSWD of 2.5 (two ages were rejected by the algorithm). This can be interpreted as the igneous crystallization age of the zircons.

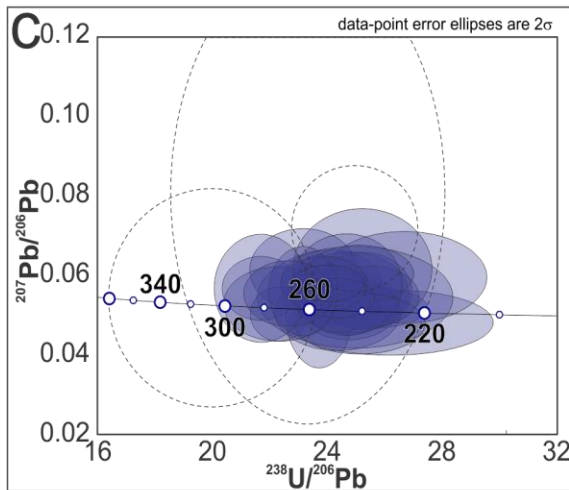
Plan de las Hayas N14F6C2



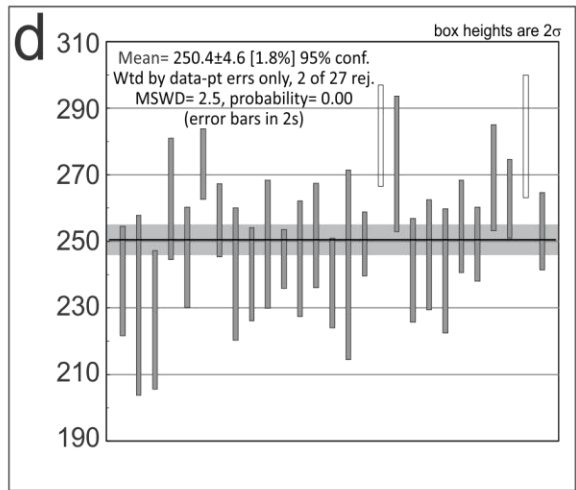
Cross polarized light (XPL) thin section image for the analysed sample showing sericitized plagioclase, chloritised biotite and titanite.



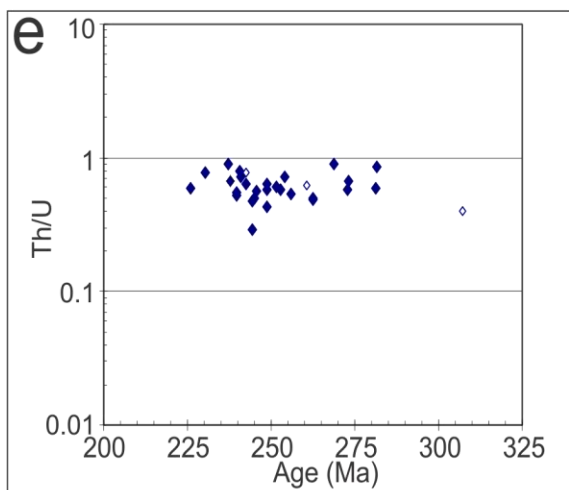
Plane polarized light (PPL) thin section image for the analysed sample showing low relief sericitized plagioclase, chloritised biotite and high relief titanite.



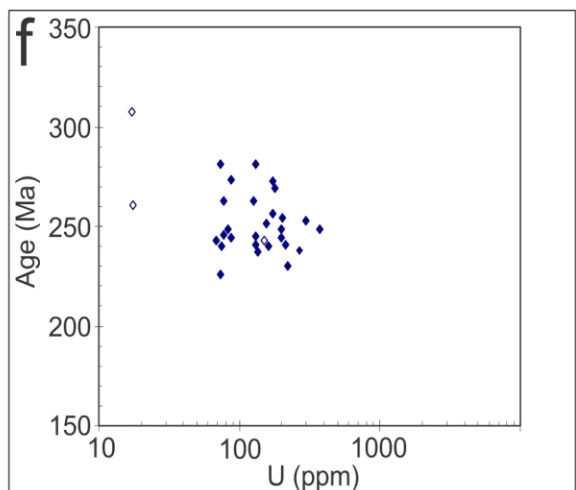
Tera-Wasserburg diagram of all analyses (n=30). Blue ellipses have been used in age calculations and dotted ellipses correspond to analyses disregarded due to high (>20%) discordance or >6% uncertainty in the $^{206}\text{Pb}/^{238}\text{U}$ ratio.



Weighted average plot for the 27 concordant grains. Two ages were rejected by the algorithm.



Th/U vs age (Ma) plot for all of the analysed grains (n=30). White points represent analysis that were disregarded and blue those that were used for age calculations.



Age (Ma) vs U (ppm) plot for all of the analysed grains (n=30). White points represent analysis that were disregarded and blue that were considered for age calculations.

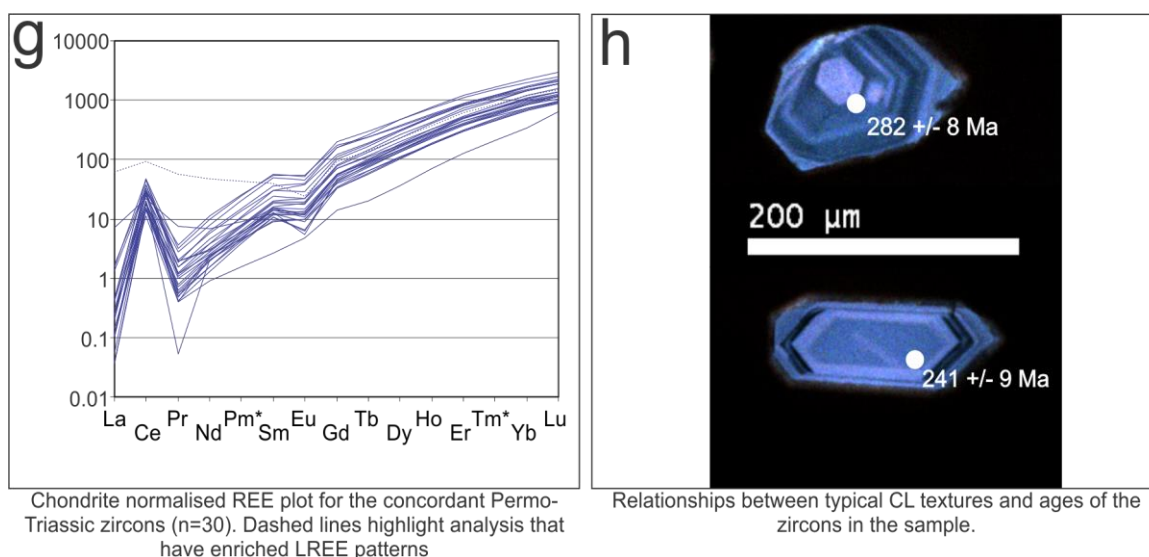


Figure 3.15. Geochronology results for the Plan de las Hayas N14F6C2 basement core from the Western Gulf of Mexico.

3.3.12 Paso de Ovejas N6F9C2

The analysed sample from the Paso de Ovejas well (Figure 3.1) has been taken from a depth of 6114-6117 m and has a composition of a slightly altered quartz monzodiorite (phaneritic texture). Petrographic interpretations (Figure 3.16 a-b) reveal crystals that range in size from 100-5000 μm , which are primarily composed of quartz (10%), partially sericitized feldspars that display zoning (70%; 70:30 plagioclase to alkali feldspars respectively) and partially chloritized biotite (15%). Intergrowths between quartz and feldspars are observed in the sample, producing myrmekitic textures. Minor phases found in the sample include titanite (4%), zircon (< 1%) and apatite (< 1%).

The analysed zircons are elongated, euhedral to subhedral, prismatic grains with aspect ratios of 2:1-10:1 and between 100-300 μm in size along the longest axis. The CL textures are characterised by oscillatory and sector zoning, as well as core and rim relationships in a small number of grains (Figure 3.16 i). More enriched patterns are observed in the LREEs of some of the analysed zircons (Figure 3.16 g-h), possibly caused

Chapter 3: Petrography & Geochronology Results

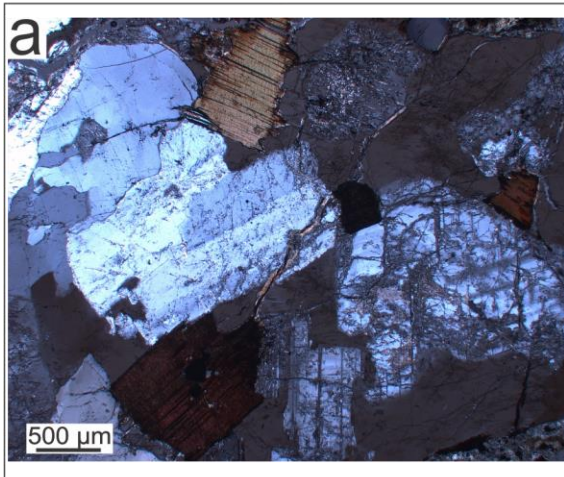
by inclusion contamination (monazite), which may be reflected in higher degrees of discordance when constructing plots.

Of the 30 rims that were analysed 23 were deemed suitable to be used in age calculations (<22% discordance and <5% error). Discordance in some of the analysis is probably related to contamination from small inclusions as previously noted in the REE results.

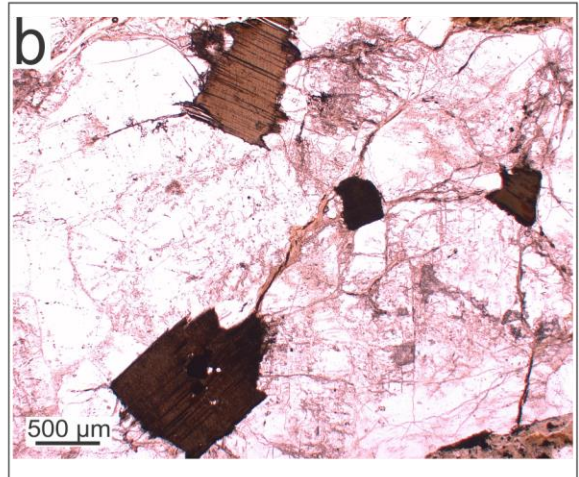
Weighted-mean plots of the concordant grains (Figure 3.16 d) yield an age of 256.7 ± 5.5 Ma with an MSWD of 2.3 (two ages were rejected by the algorithm) with U concentrations of between 40-200 ppm and Th/U ratios of 0.3-0.8 (Figure 3.16 e-f). These results are consistent with zircons that form in a magmatic event, and the age can therefore be interpreted as the timing of crystallization within a magma chamber.

Cores are not a common feature within the sample; however there are two present, yielding ages of 297 ± 9 Ma and 298 ± 7 Ma (Figure 3.16 c). They display comparable results in the REE geochemistry and Th/U ratios to the rims but differ slightly in that they are characterised by slightly higher U concentrations (200-300 ppm; Figure 3.16 f). They are likely to represent xenocrysts from a previous zircon-forming magmatic event, occurring in the Early Permian. This event may well relate to the early Permian zircons found in the Pinonal and Arenque wells.

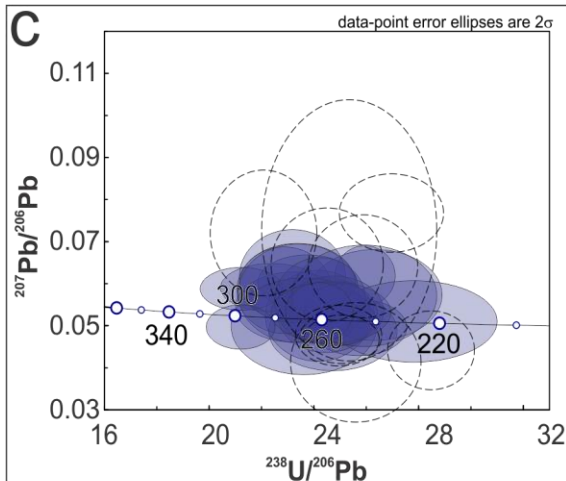
Paso de Ovejas N6F8C4



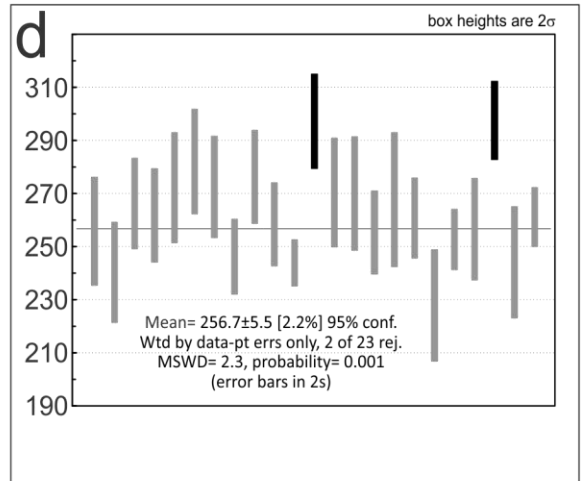
a Cross polarized light (XPL) thin section image for the analysed sample showing sericitized plagioclase, k-spar, quartz, biotite and minor opaques.



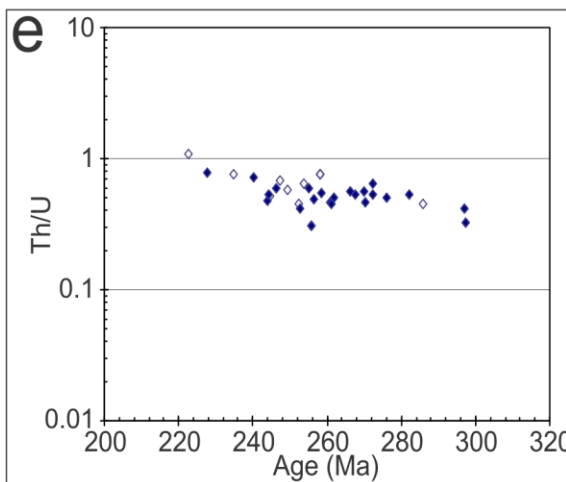
b Plane polarized light (PPL) thin section image for the analysed sample showing low relief plagioclase, k-spar and quartz, biotite and minor opaques.



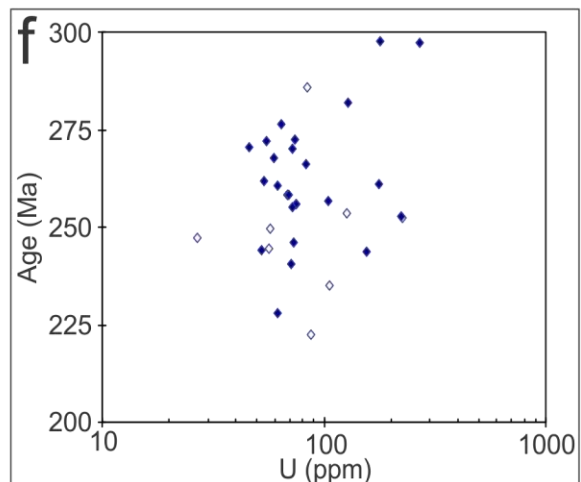
c Tera Wasserburg plot of the analysed grains (n=32). The blue ellipses represent zircons that were taken further to age calculations (n=23) and the dotted ellipses show those that were disregarded (> 22% discordance, > 5% inverse discordance).



d Weighted mean plot for the zircons considered for age calculations (n=23)



e Th/U vs. Age (Ma) plot for all of the analysed zircons (n=32). The blue points represent the grains that were used in age calculations and the clear points show those that were disregarded.



f Age (Ma) vs. U (ppm) diagram for all of the analysed grains (n=32). Blue points represent grains that were used in age calculations and clear points show that were disregarded.

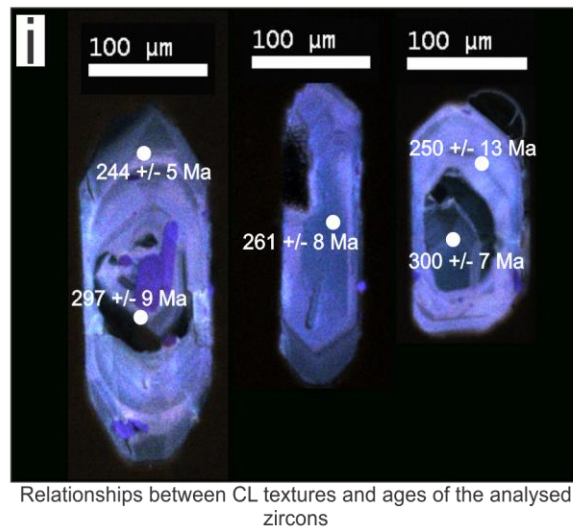
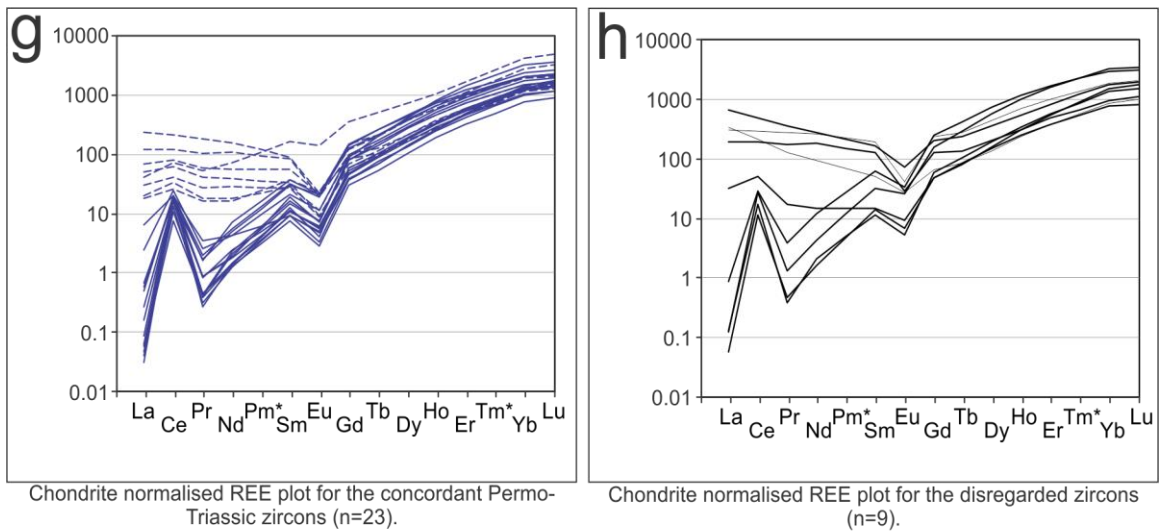


Figure 3.16. Geochronology results for the Paso de Ovejas N6F8C4 basement core from the Western Gulf of Mexico.

3.3.13 *Orizaba N6F1C1*

The analysed sample from the Orizaba well (Figure 3.1) has been taken from a depth of 5042-5044 m and has a composition of monzo-granite (phaneritic texture). Petrographic interpretations (Figure 3.17 a-b) reveal crystals that range in size from 100 to 8000 μm , which are primarily composed of quartz (20%), partially sericitized feldspars (70%; 50:40:10 plagioclase, microcline and perthite respectively). Minor phases include chloritized biotite (5%), muscovite (2%), calcite (2%), apatite (< 1%) and zircon < 1%). The sample also includes small amounts of a relic mineral (<1%) that has $56^\circ/124^\circ$ cleavage characteristic of amphibole.

Zircons from this sample display euhedral to subhedral, prismatic shapes with clear core and rim relationships. Some of the grains contain small inclusions of other minerals which may act as a source of contamination. Oscillatory zoning is inherent throughout a good number of the cores and rims suggesting the zircons record at least two igneous events (Figure 3.17 m). Some cores also show more homogeneity and are rounded in shape which is more characteristic of a high grade metamorphic event. This indicates that not all of the inherited cores were formed in the same tectonic environment.

Of 52 grains analysed 34 were concordant, with a low degree of error (< 14% discordant and < 4% error; Figure 3.17 c). Additional filtering had to be done however to account for an apparent mixing line between cores and rims, leaving 25 grains suitable for age calculations. The isotopic mixing between the cores and rims accounts for a large proportion of the unreliable ages. Discordant grains may also be due to contamination

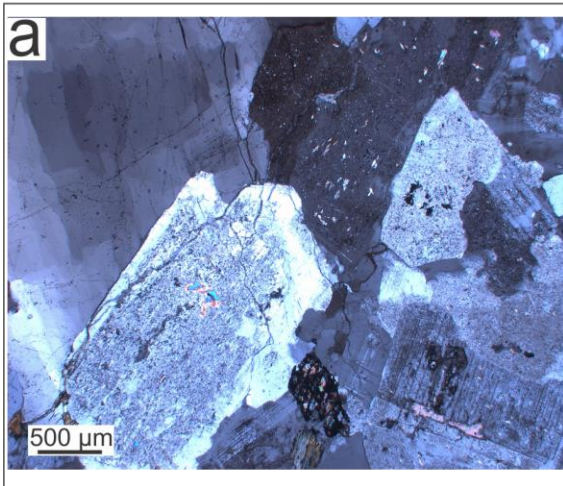
Chapter 3: Petrography & Geochronology Results

from monazite inclusions, as indicated by the REE patterns (enriched LREEs and lack of Ce positive anomaly; Figure 3.17 j-l).

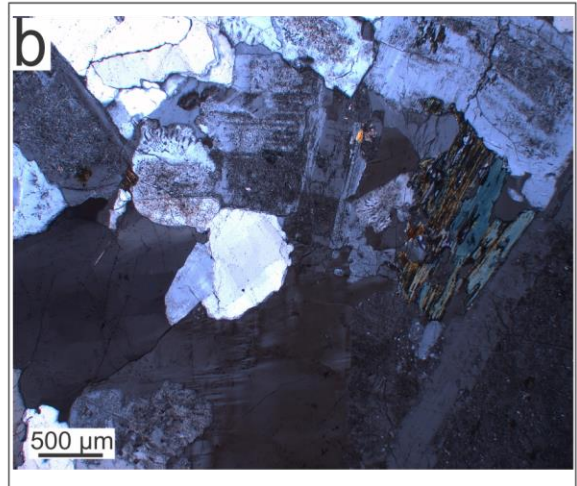
Weighted-mean plots for the cores (Figure 3.17 e-f) yield an age of 1162 ± 38 Ma ($n= 8$; MSWD= 0.78) for the oldest population and 959 ± 59 Ma ($n= 8$; MSWD= 1.2) for the younger ones. U concentrations and Th/U ratios for the cores range from 50-900 and 0.1-0.7, respectively (Figure 3.17 h-i). The chemistry and CL images for the cores suggest a mix of both igneous and metamorphic origins, typical of the type of zircons found in continental Oaxaquia.

Weighted-mean plots for 9 concordant rims (Figure 3.17 g) yield an age of 253 ± 7.5 Ma with an MSWD of 0.23. U concentrations and Th/U ratios range from 200-900 ppm and 0.08-0.3, respectively. This can be interpreted as the best approximation to the timing of an igneous event that occurred in the Permian. This igneous event occurred as a partial melt of the Oaxaquia continental crust, inheriting Precambrian zircon cores that did not completely resorb in the magma.

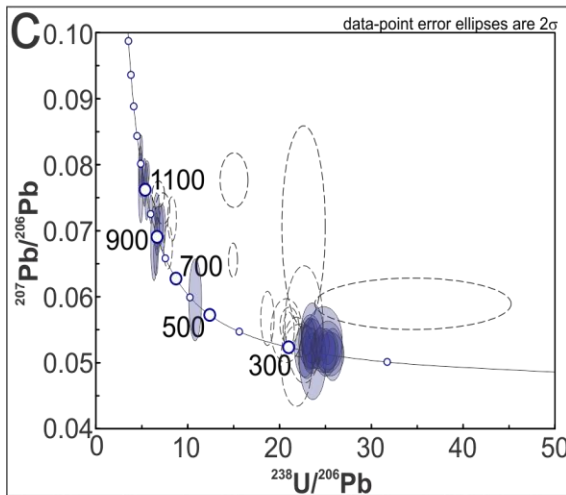
Orizaba N6F1C1



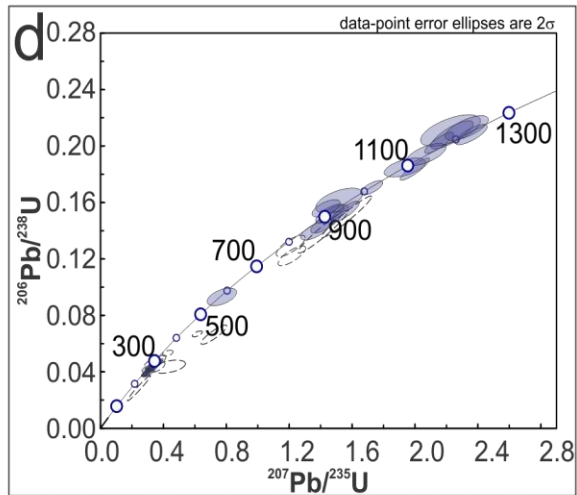
Cross polarized light (XPL) thin section image for the analysed sample showing sericitized plagioclase, strained quartz, altered hornblende and chloritised biotite.



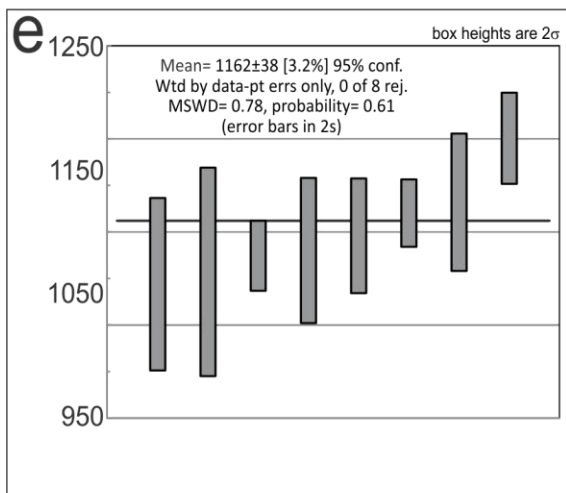
Cross polarized light (XPL) thin section image for the analysed sample showing myrmekitic textures.



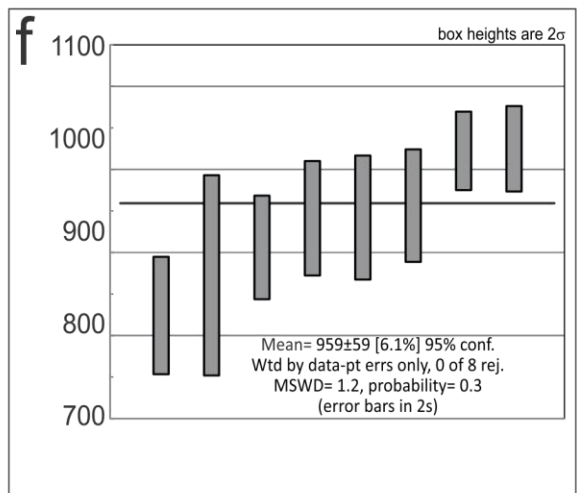
Tera Wasserburg plot of the analysed grains (n=52). The blue ellipses represent zircons that were taken further to age calculations (n=34) and the dotted ellipses show those that were disregarded (> 14% discordance, > 4% error).



Wetherill plot of the analysed grains (n=52). The blue ellipses represent zircons that were taken further to age calculations (n=34) and the dotted ellipses show those that were disregarded (> 14% discordance, > 4% error).

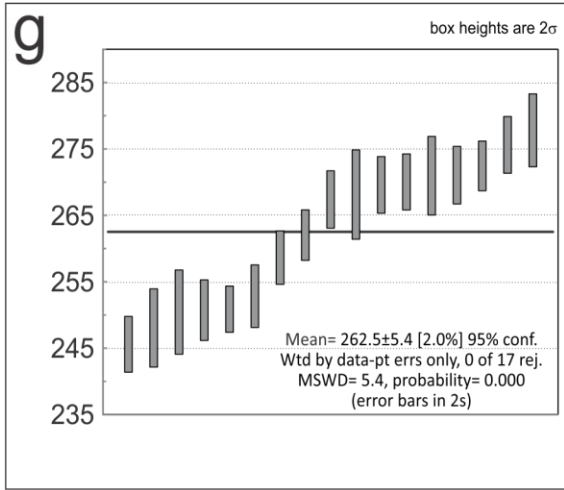


Weighted mean plot for the oldest population of inherited cores (n=8).

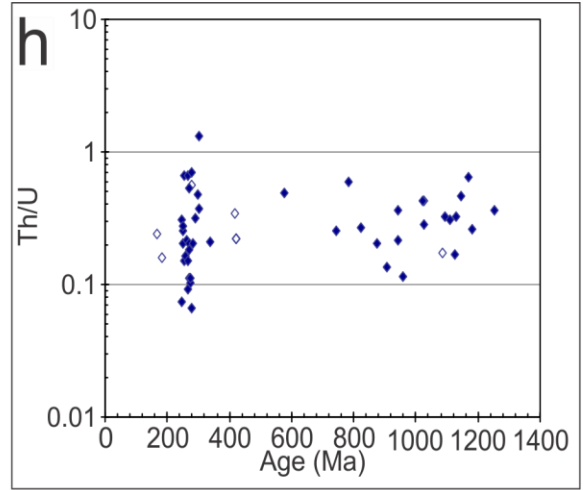


Weighted mean plot for the second population of inherited cores (n=8).

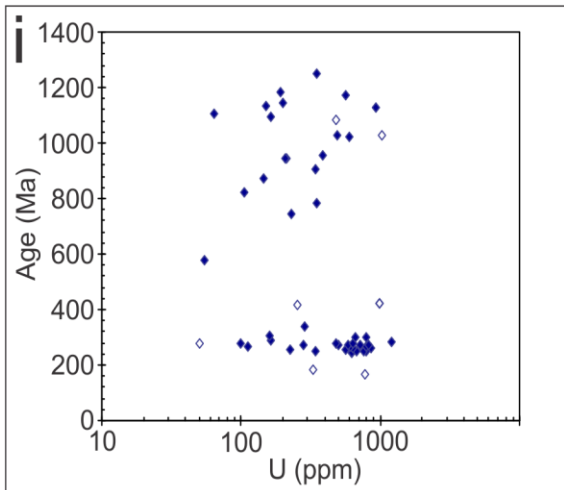
Chapter 3: Petrography & Geochronology Results



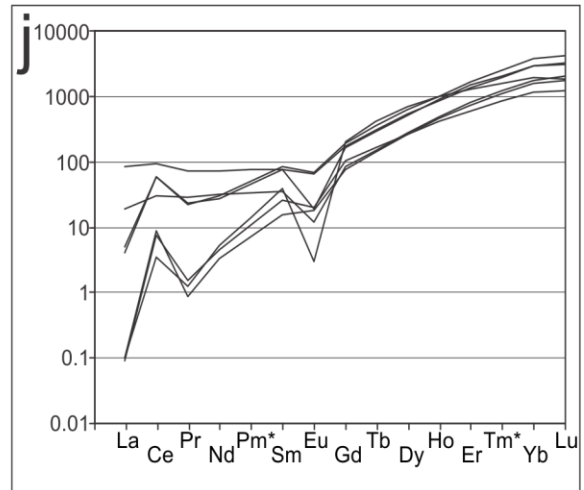
Weighted mean plot for the youngest population of zircons (n=17).



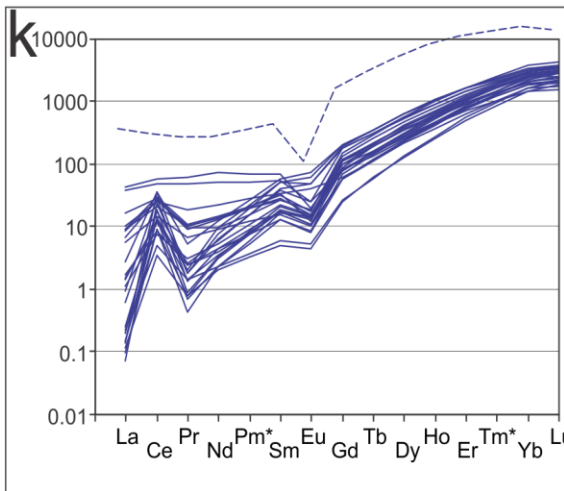
Th/U vs. Age (Ma) plot for all of the analysed zircons (n=52). The blue points represent the grains that were used in age calculations and the clear points show those that were disregarded.



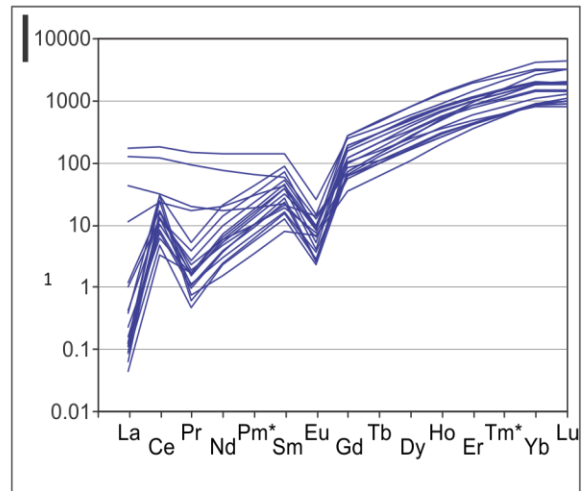
Age (Ma) vs. U (ppm) diagram for all of the analysed grains (n=52). Blue points represent grains that were used in age calculations and clear points show that were disregarded.



Chondrite normalised REE plot for the disregarded zircons (n=7).



Chondrite normalised REE plot for the concordant Paleozoic zircons (n=26). The dotted line highlights analysis enriched in the REE.



Chondrite normalised REE plot for the concordant Proterozoic zircons (n=19).

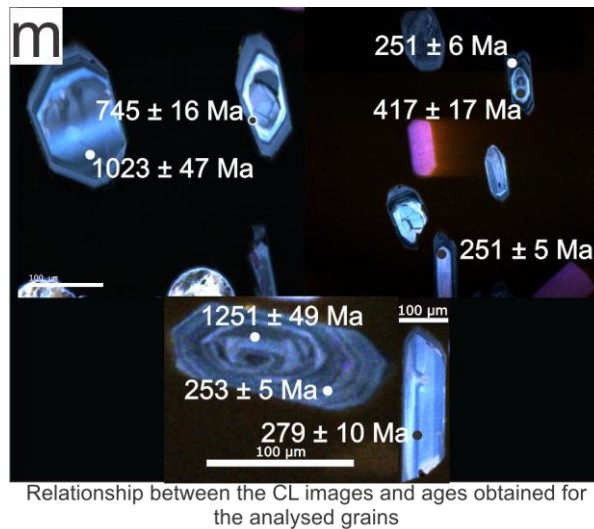


Figure 3.17. Geochronology results for the Orizaba N6F1C1 basement core from the Western Gulf of Mexico.

3.4 Jurassic granitoids

3.4.1 *Muro-2 N12F2C1*

The analysed sample from the Muro well (Figure 3.1) has the composition of a micro diorite (phaneritic texture). The basement for the well has been previously dated at 153 ± 11 Ma and 178 ± 11 Ma via K-Ar on biotite (Lopez-Ramos, 1979). Petrographic interpretations (Figure 3.18 a-b) reveal crystals that range in size from 100 to 2000 μm , which are primarily composed of feldspars that display zoning (80%; 95:5 plagioclase and alkali feldspar respectively). Minor phases include quartz that has an unusual, almost interstitial, like texture (5%), partially chloritized biotite (5%), amphibole (5%) and opaque minerals (5%).

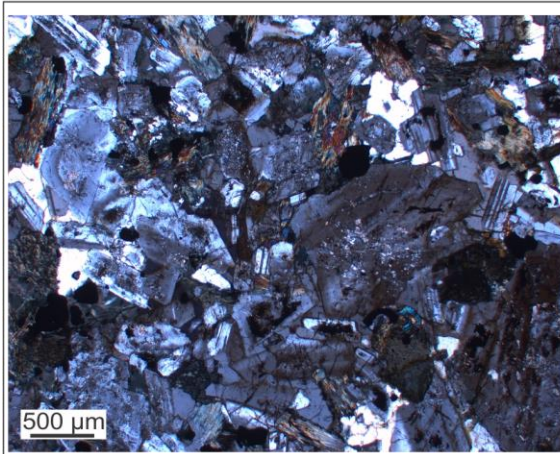
Zircons in this sample are euhedral-subhedral in habit and are 50-120 μm along their longest axis, with aspect ratios of 2:1-7:1. The CL images are characterised by sector and oscillatory zoning, typical of igneous zircons (Figure 3.18 g). There are also fractures along the c-axis of some of the grains which have been an inlet for common

Chapter 3: Petrography & Geochronology Results

lead and so may contribute to discordance in the concordia plots. Th/U ratios and U concentrations yield typical igneous zircon results (0.5-1 and 60-1000 ppm respectively; Figure 3.18 e-f).

Of the 21 grains analysed 15 were deemed suitable for age calculations (<100% discordant, <3% error; Figure 3.18 c). The weighted-mean plot (Figure 3.18 d) yields an age of 188.5 ± 3.5 Ma with an MSWD of 5.6. There are also some inherited cores which yield ages of 1430 ± 24 Ma and 398 ± 3.2 Ma (core and rim mix). The Jurassic zircons can be interpreted as the age of crystallization in an igneous event which inherited Proterozoic zircons.

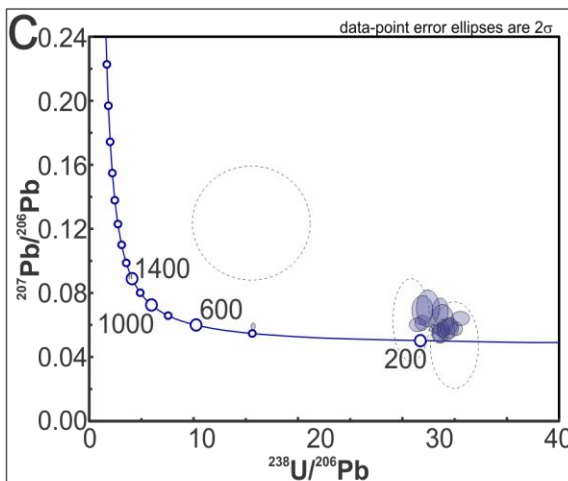
Muro-2 N12F2C1



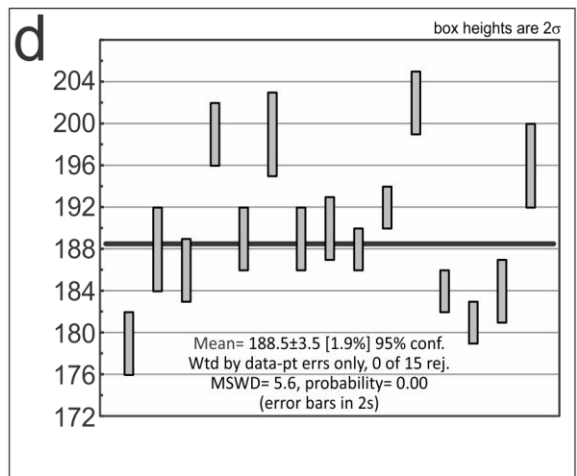
Cross polarized light (XPL) thin section image for the analysed sample showing plagioclase, partially chloritised biotite, opaques and minor quartz.



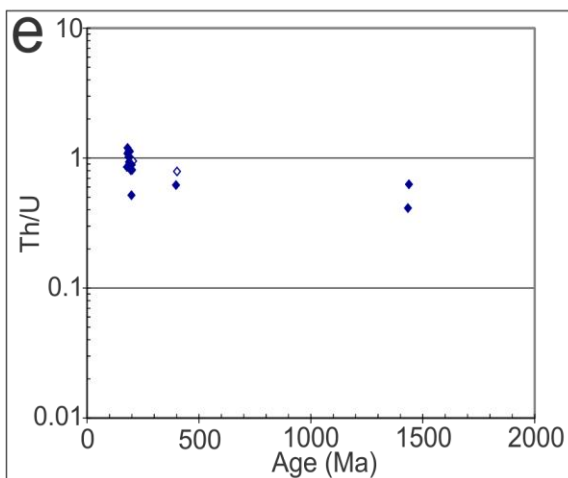
Plane polarized light (PPL) thin section image for the analysed sample showing plagioclase, partially chloritised biotite, opaques and minor quartz.



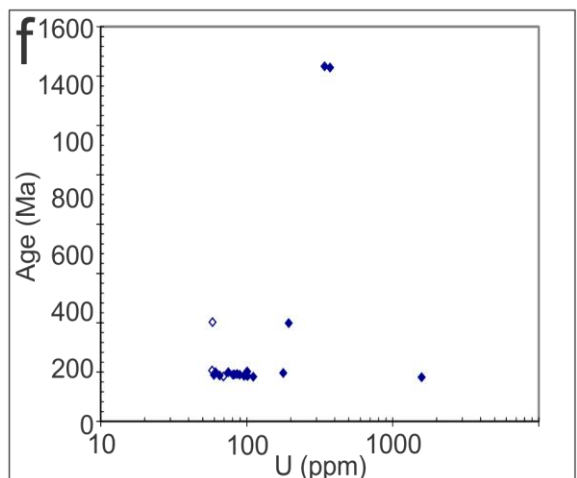
Tera Wasserburg plot of the analysed grains (n=21). The blue ellipses represent zircons that were taken further to age calculations (n=18) and the dotted ellipses show those that were disregarded (> 100% discordance, > 3% error).



Weighted mean plot for the zircons used for age calculations (n=15).



Th/U vs. Age (Ma) plot for all of the analysed zircons (n=21). The blue points represent the grains that were used in age calculations and the clear points show those that were disregarded.



Age (Ma) vs. U (ppm) diagram for all of the analysed grains (n=21). Blue points represent grains that were used in age calculations and clear points show that were disregarded.

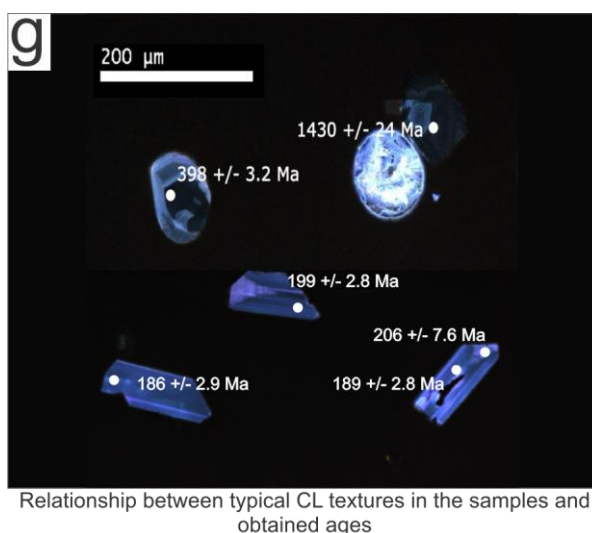


Figure 3.18. Geochronology results for the Muro N12F2C1 basement core from the Western Gulf of Mexico.

3.4.2 *Tlapacoyan N10F18C5*

The analysed sample from the Tlapacoyan well (Figure 3.1) has the composition of a trachyte (porphyritic texture). Previous studies performed by PEMEX on this core yielded ages of 179 ± 14 Ma by K-Ar dating methods on biotite (Lopez-Ramos, 1979). This age may have geological significance as the biotite appears fresh. Petrographic interpretations (Figure 3.19 a-b) reveal phenocrysts that range in size from 250 to 3000 μm that lie in a fine grained matrix. The phenocrysts make up $\sim 10\%$ of the sample and are composed of alkali feldspar (50%), biotite (40%) and calcite (10%). The matrix constitutes the remaining 90% of the sample and is almost entirely made up of alkali feldspars.

The sample contains euhedral to subhedral grains that range in size from 80-200 μm , with aspect ratios of 2:1-7:1. The CL textures are characterised by oscillatory zoning inherent throughout all the grains (Figure 3.19 i). Two grains are anomalous in that they appear to contain inherited xenocrystic cores. The shape of the grains as well as the homogeneity and nature of the CL textures are indicative of zircons that formed in a

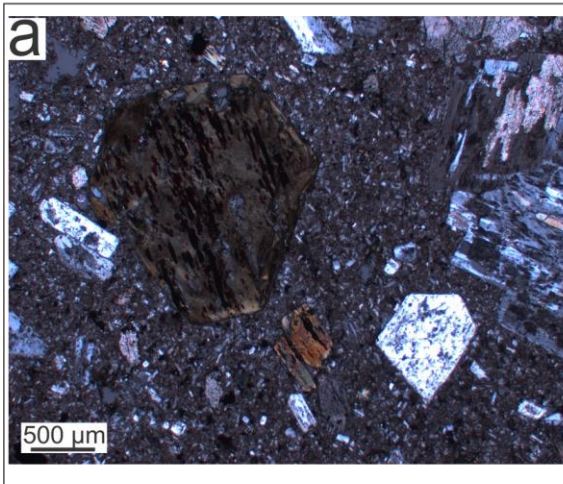
Chapter 3: Petrography & Geochronology Results

single igneous event. The existence of two xenocrystic cores tells us that this igneous event failed to completely resorb zircons during melting of a pre-existing rock.

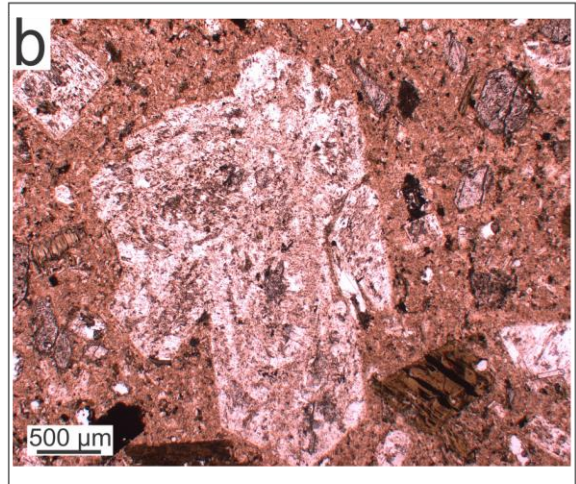
30 grains were analysed, four of which were discarded due to discordance or unacceptable errors (> 4% error in the $^{206}\text{Pb}/^{238}\text{U}$ ratio, >30% discordance, or >10% reverse discordance; Figure 3.19 c). The cores that were observed in the CL images are apparent in Tera-Wasserburg diagrams, plotting as concordant points with Proterozoic and Permian ages (838 ± 60 Ma and 263 ± 7 Ma respectively). The Permian age may relate to the igneous event recorded in the majority of the analysed wells.

Weighted-mean plots have been constructed for 20 analysed grains that were dated to the Jurassic period (Figure 3.19 d). They yield an age of 164.3 ± 3.5 Ma with a MSWD of 2.8 (one age was rejected by the algorithm). U concentrations and Th/U ratios in the grains are consistent throughout, yielding results of 150-500 ppm and 0.6-1.5 respectively (Figure 3.19 e-f). These results can be interpreted as the crystallization age of the rock in an igneous environment, with minor inheritance from zircon xenocrysts of Permian and Proterozoic age.

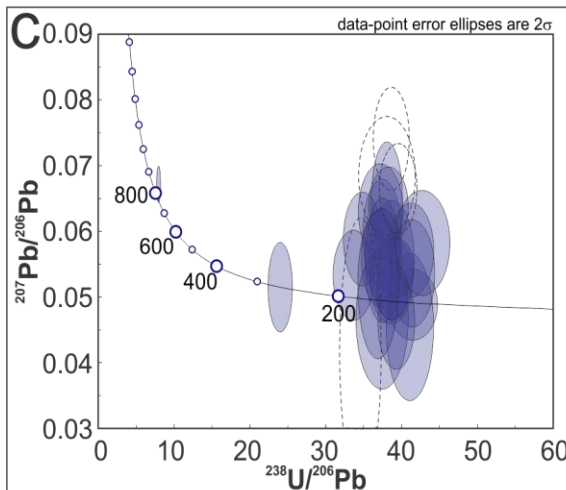
Tlapacoyan-1 N10F18C5



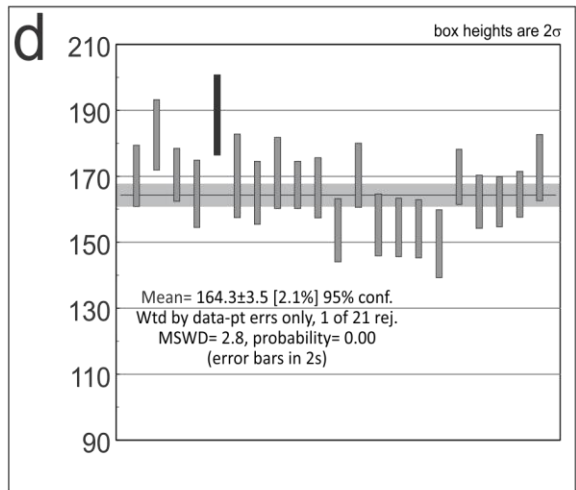
a Cross polarized light (XPL) thin section image for the analysed sample showing phenocrysts of biotite and k-spar and hornblende with a k-spar matrix.



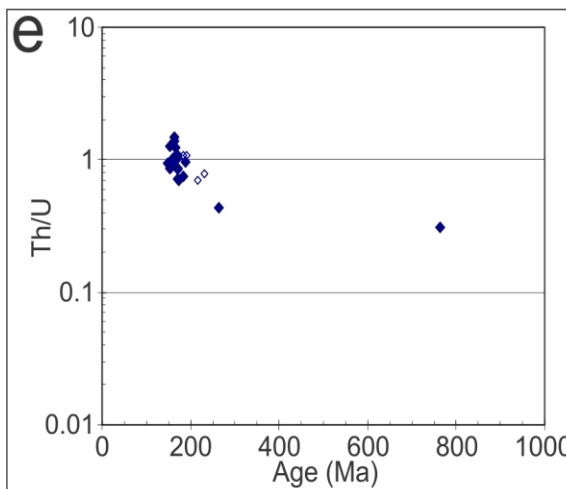
b Plane polarized light (PPL) thin section image for the analysed sample showing phenocrysts of biotite and k-spar and hornblende with a k-spar matrix.



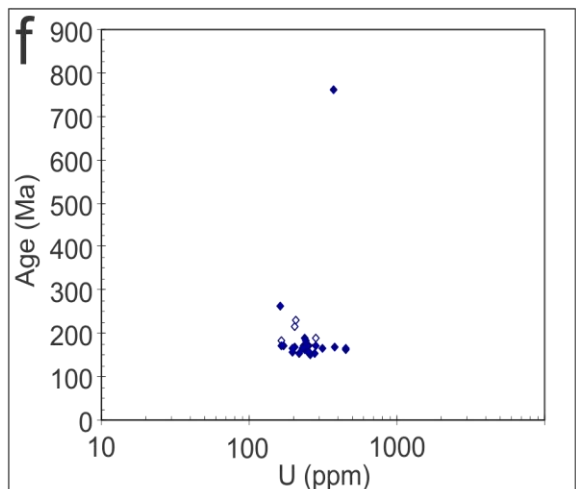
c Tera Wasserburg plot of the analysed grains (n=19). The blue ellipses represent zircons that were taken further to age calculations (n=21) and the dotted ellipses show those that were disregarded (> 4% uncertainty in the $^{206}\text{Pb}/^{238}\text{U}$ ratio, > 30% discordance, or > 10% reverse discordance)



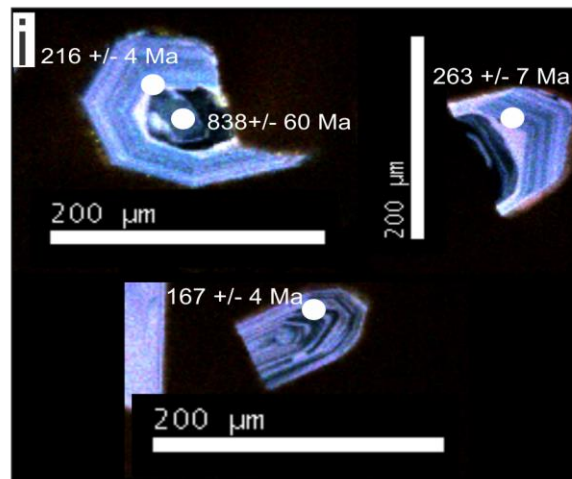
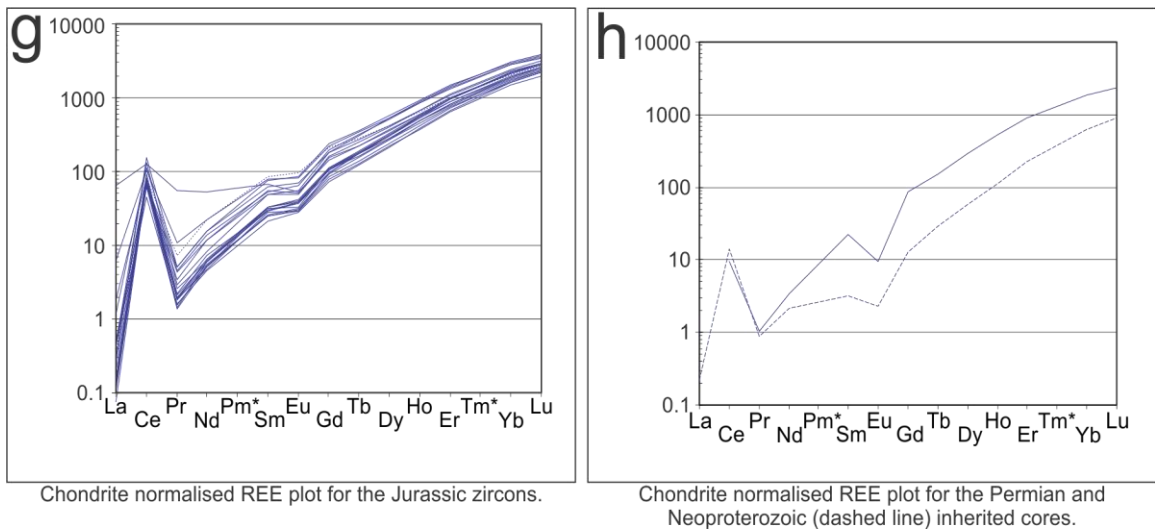
d Weighted-mean plots for the analysed Jurassic zircons (n=21). The algorithm rejected one analysis.



e Th/U vs age (Ma) plot for all of the analysed grains (n=30). White points represent analysis that were disregarded and blue those that were used for age calculations.



f Age (Ma) vs U (ppm) plot for all of the analysed grains (n=30). White points represent analysis that were disregarded and blue those that were considered for age calculations.



Typical CL textures of the analysed grains compared with the recorded ages.

Figure 3.19. Geochronology results for the Tlapacoyan N10F18C5 basement core from the Western Gulf of Mexico.

3.5 Sediments and meta-sediments

3.5.1 *Salto N8F1C1*

The analysed sample from the Salto well (Figure 3.1) is taken from a depth of 2846-2850m and has the composition of a quartz-biotite schist. Petrographic interpretations (Figure 3.20 a-b) reveal foliated crystals that range in size from 1000 to 6000 μm . The sample is composed of felsic bands of quartz (20%; polycrystalline) and feldspars (50%; completely altered to fine micas and clay minerals) that are separated by bands rich in micas (25%; 90:10 biotite and muscovite respectively) and opaque minerals (5%).

Zircons within the sample are well rounded either through mechanical processes or metamorphic zircon growth. The CL for the most part displays homogeneous textures indicating a metamorphic event, as well as many instances of core-rim relationships (cores characterised by zoning typical of igneous zircons; Figure 3.20 l). U concentrations and Th/U ratios are highly variable, ranging from 200-1100 ppm and 0.01-1.1 respectively (Figure 3.20 g-h). The REE geochemistry shows heterogeneous results (Figure 3.20 i-k) with varying degrees of enrichment between the analysed grains. The HREEs range from flat (typical of metamorphic zircons) to steeply inclined trends (typical of igneous zircons); there are also erratic Eu anomalies. These observations on the CL textures and geochemistry of the zircons suggest that this sample records several phases of zircon growth, in both igneous and metamorphic environments.

Of the 100 grains analysed 84 were deemed suitable for age calculations (< 6% discordant; Figure 3.20 c); it is important to note that the observed discordance may well represent a poorly constrained mixing line between two phases of zircon growth.

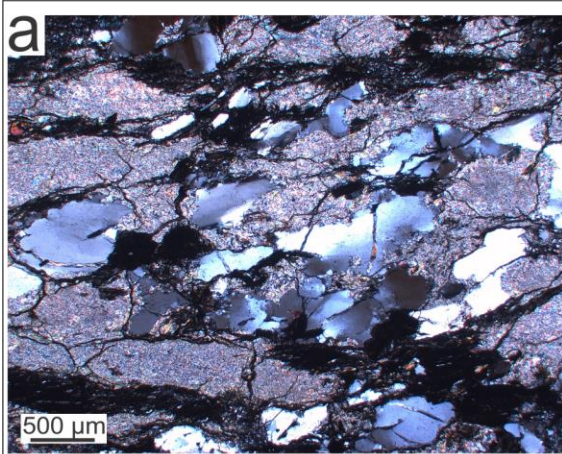
Chapter 3: Petrography & Geochronology Results

Relative probability plots for the concordant grains (Figure 3.20 e) yield a range of populations which include 935 Ma, 795 Ma, 700 Ma. There is also a single concordant grain at 410 Ma, this is unlikely however to hold any geological significance but instead is probably part of a poorly constrained mixing line between a core and rim. The different populations of zircons found within the sample indicate the rock has a sedimentary protolith prior to metamorphism.

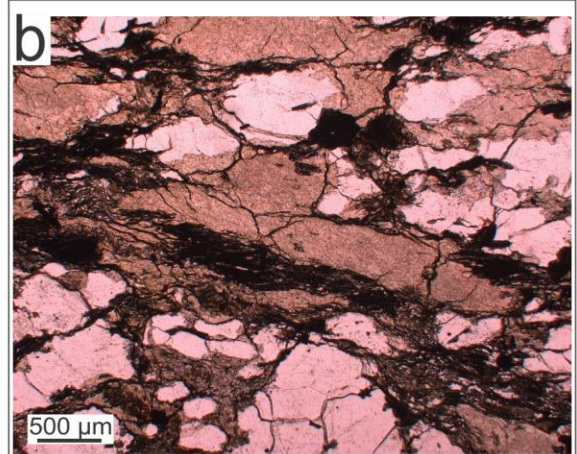
Interpreting the age of metamorphism is challenging as it is difficult to distinguish between detrital zircons populations and what might be the metamorphic age from the chemistry and CL textures. Although poorly constrained the age of metamorphism may be represented in the mixing trend as the lower intercept with the concordia line (ca. 400 Ma; Figure 3.20 d).

Alternatively the main metamorphic event could be recorded in the youngest population of concordant zircons found (700 Ma). In this instance the poorly constrained mixing line that intercepts the concordia line in the Permo-Triassic would be a second and less significant zircon forming metamorphic event.

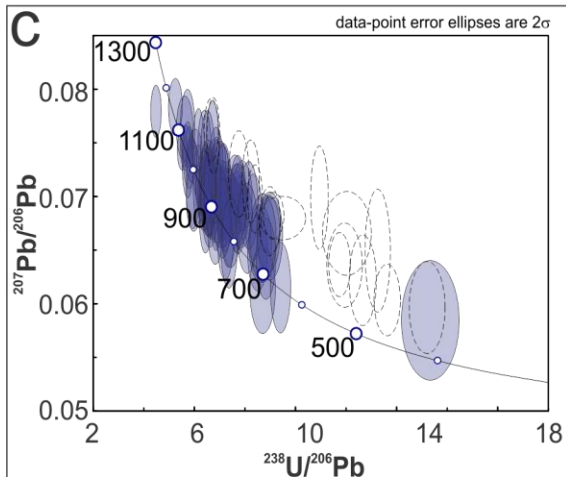
Salto N8F1C1



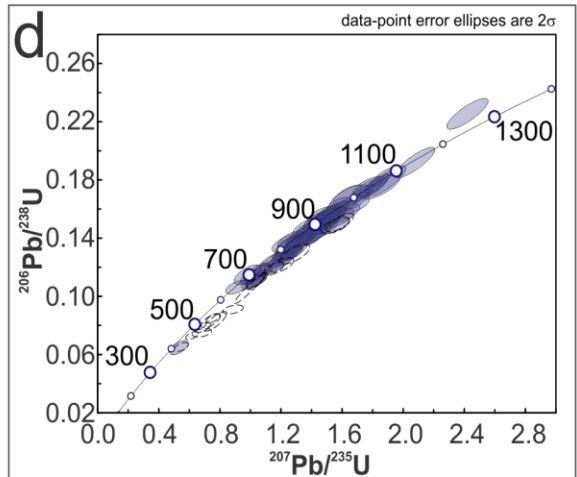
a Cross polarized light (XPL) thin section image for the analysed sample showing schistosity, with bands of quartz and micas (muscovite and biotite).



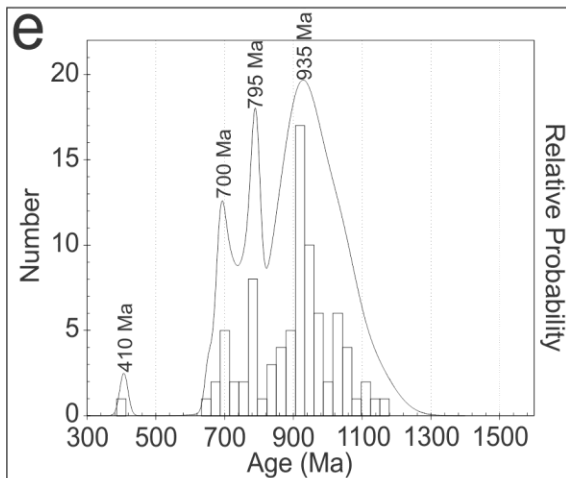
b Plane polarized light (PPL) thin section image for the analysed sample showing schistosity, with bands of quartz and micas (muscovite and biotite).



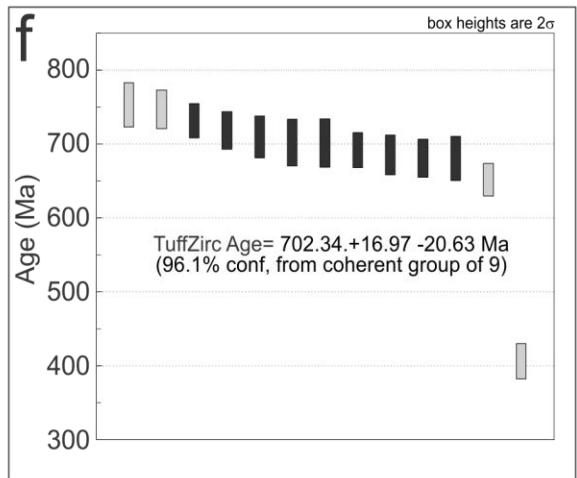
c Tera Wasserburg plot of the analysed grains (n=100). The blue ellipses represent zircons that were taken further to age calculations (n=84) and the dotted ellipses show those that were disregarded (> 6% discordance).



d Wetherill plot of the analysed grains (n=100). The blue ellipses represent zircons that were taken further to age calculations (n=84) and the dotted ellipses show those that were disregarded (> 6% discordance).



e Relative probability plot for the zircons considered in age calculations (n=84).



f TuffZirc Age calculations for the youngest population of zircons in the sample (n=9).

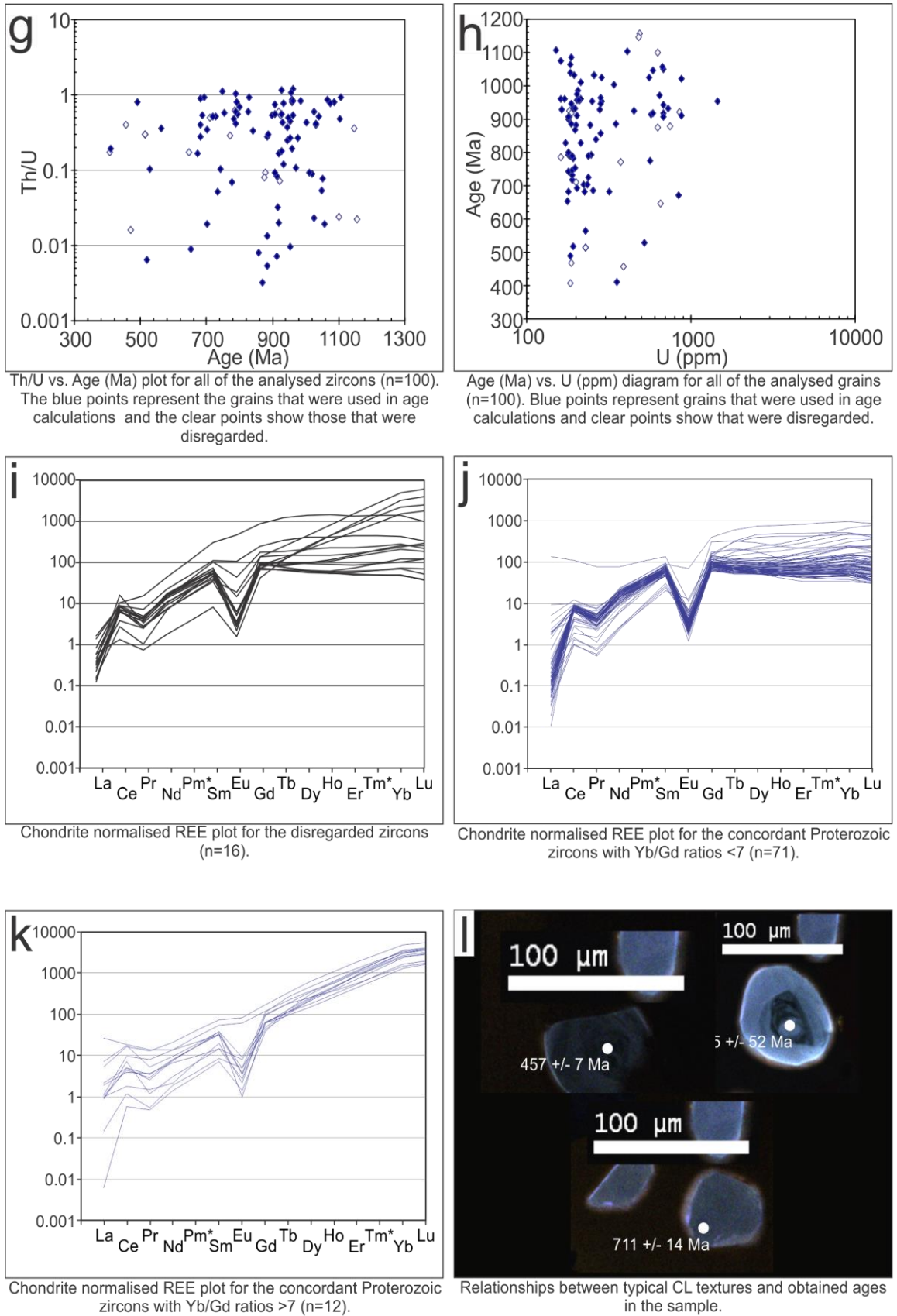


Figure 3.20. Geochronology results for the Salto N8F1C1 basement core from the Western Gulf of Mexico.

3.5.2 *Gonzales N9F1C1*

The first analysed sample from the Gonzales well (Figure 3.1) is composed of a medium grained, moderately sorted arkosic sandstone. Petrographic interpretations (Figure 3.21 a-b) reveal grains that range in size from 100-4000 μm that are sub-angular to sub-rounded in shape. The sample is grained supported (95% grains and 5% cement), with a mineral composition of quartz (20%; monocrystalline and polycrystalline), feldspars (60%; 60:40 microcline and plagioclase respectively), lithic fragments (15%; composed of fragments of limestone and chert). Minor phases include biotite (2%), muscovite (2%), apatite (< 1%) and zircon (< 1%). The initial porosity of the sandstone appears to be around 5% but has subsequently been filled by a calcite cement. The arkosic composition of the sandstone indicates a predominantly granitic source region for the sediment.

The sample contains sub-rounded zircon grains and fragments that are 100-200 μm along their longest axis, with aspect ratios of 2:1-3:1. The CL textures display clear populations of zircons (dark in colour, oscillatory and sector zoning, homogenous textures, core-rim relationships; Figure 3.21 k). The geochemistry shows highly variable Th/U and U concentrations (0.02-1 and 70-1200 ppm respectively; Figure 3.21 e-f). This sedimentary rock contains detrital zircons, with a mix of igneous and metamorphic grains.

Of the 47 grains that were analysed 32 were deemed reliable enough to be used for population age calculations (< 5% error and < 5% discordant; Figure 3.21 c). Discordant ages are again likely to be caused by ablation of cores and rims during the analysis. Probability density models (Figure 3.21 d) display three established ages, with

Chapter 3: Petrography & Geochronology Results

peaks at 976 ± 57 Ma, 1148 ± 32 Ma, 1300 ± 50 Ma which correlate with Oaxaquia continental crustal ages, indicating a likely source area for the majority of the zircons. There are no concordant Permian zircons in this sample but there is a poorly constrained mixing line which may suggest there are Permian rims on some of the grains. If this is indeed the case a maximum age of deposition for the sandstone can be attributed to the Permian.

This interpretation however is highly speculative as the youngest zircon age (366 ± 13 Ma) relates to a grain with a very high U concentration (2537 ppm) which may have probably undergone metamictization. In this scenario the mixing line would be too poorly constrained to say there are Permian zircons in the sample. The interpretation would therefore be that the sandstone contains Precambrian zircons that likely derive from Oaxaquia continental crust, with a maximum age of deposition of 976 ± 57 Ma (relating to the youngest population of concordant zircons in the rock).

Gonzales-1 N9F1C1

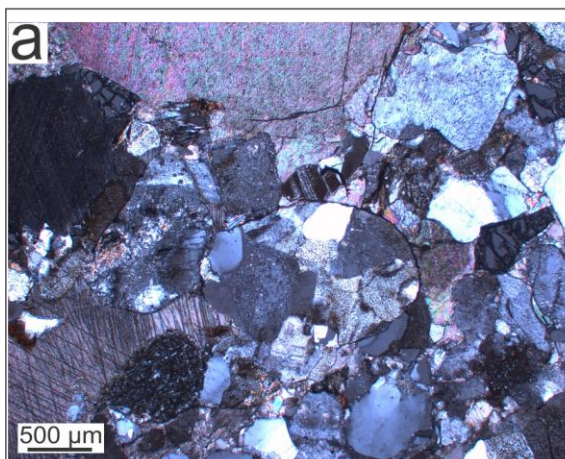


Figure 3a: Cross polarized light (XPL) thin section image for the analysed sample showing fragments that contain calcite, feldspars and quartz.

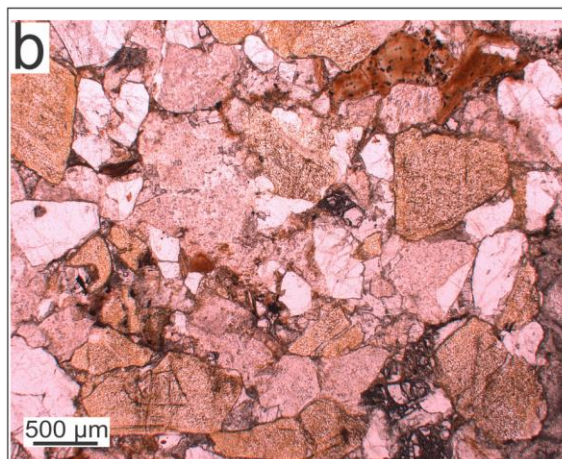


Figure 3b: Plane polarized light (PPL) thin section image for the analysed sample showing fragments that contain calcite, feldspars and quartz.

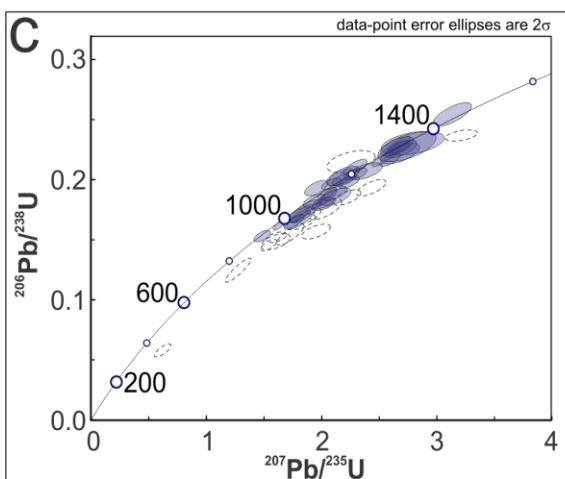


Figure 3c: Wetherill plot of the analysed grains (n=47). The blue ellipses represent zircons that were taken further to age calculations (n=25) and the dotted ellipses show those that were disregarded (> 5% discordance, > 5% error).

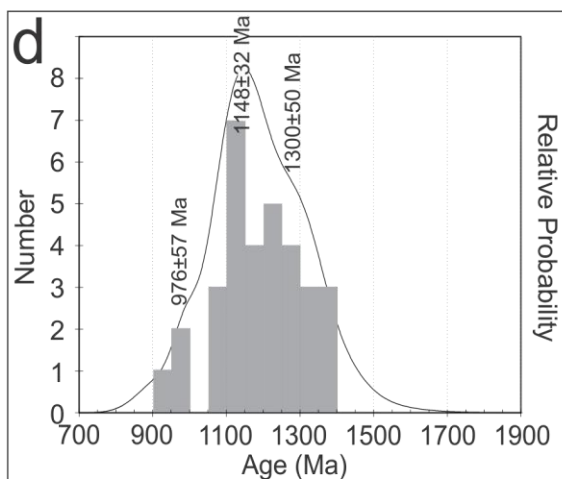


Figure 3d: Probability density model for the concordant zircons (n=25).

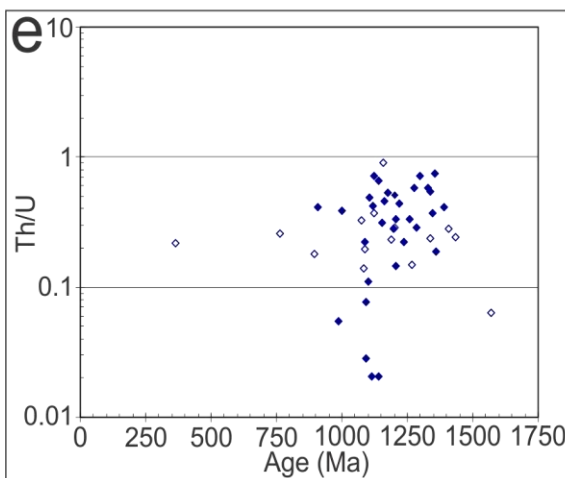


Figure 3e: Th/U vs. Age (Ma) plot for all of the analysed zircons (n=47). The blue points represent the grains that were used in age calculations and the clear points show those that were disregarded.

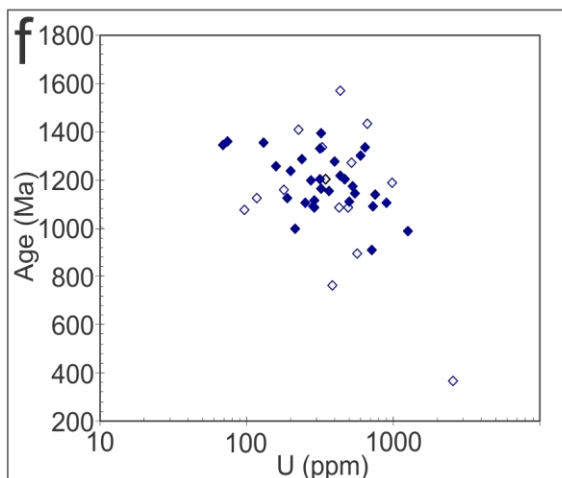


Figure 3f: Age (Ma) vs. U (ppm) diagram for all of the analysed grains (n=47). Blue points represent grains that were used in age calculations and clear points show that were disregarded.

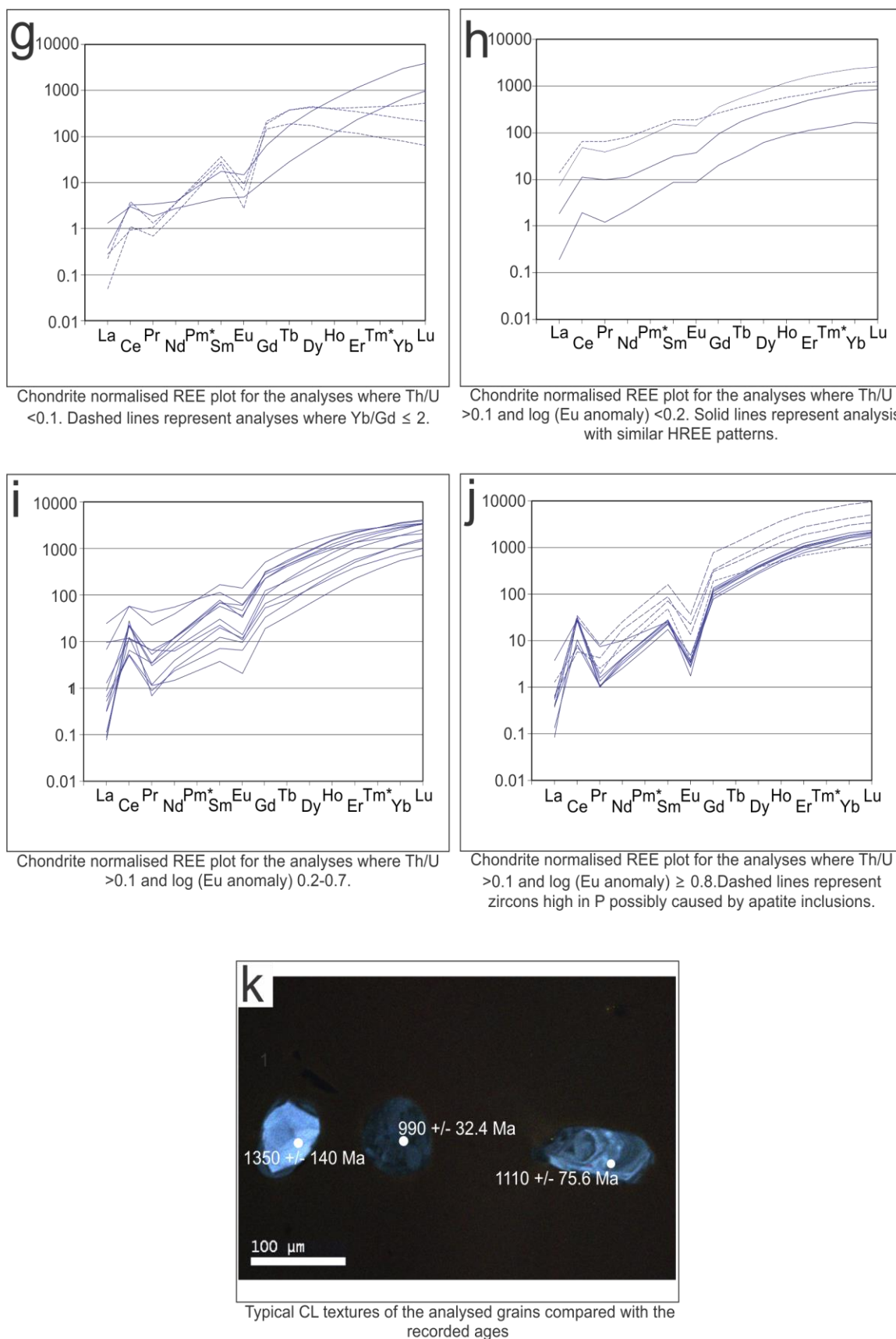


Figure 3.21. Geochronology results for the Gonzales N9F1C1 basement core from the Western Gulf of Mexico.

3.5.3 *Gonzales N9F2C1*

The second analysed sample from the Gonzales well (Figure 3.1) is again composed of a medium grained, moderately sorted arkosic sandstone. Petrographic interpretations (Figure 3.22 a-b) reveal grains that range in size from 100-4000 μm that are sub-angular to sub-rounded in shape. The sample is grained supported (95% grains and 5% cement), with a mineral composition of quartz (15%; monocrystalline and polycrystalline), feldspars (65%; 50:50 microcline and plagioclase respectively), calcite (10%) lithic fragments (5%; composed of fragments of limestone and chert). Minor phases include biotite (2%), muscovite (2%), garnet (< 1%) apatite (< 1%) and zircon (< 1%). The initial porosity of the sandstone appears to be around 5% but has subsequently been filled by a calcite cement. The arkosic composition of the sandstone indicates a predominantly granitic source region for the sediment.

This sample contains zircon grains and fragments that range between 80-200 μm along their longest axis that are sub-rounded with aspect ratios of 2:1- 4:1. The CL textures are quite varied throughout the grains, with some displaying oscillatory and sector zoning whereas others are more homogeneous in texture (Figure 3.22 j). There is also some evidence of core and rim relationships in some of the grains. This variability is also reflected in the geochemistry of the zircons with Th/U ratios and U concentrations ranging between 0.04-1.1 and 50-1000 ppm respectively (Figure 3.22 e-f) and highly variable REE patterns (Figure 3.22 g-i).

Of the 38 analysed grains 31 were deemed reliable enough (< 20% discordant, <5% uncertainty in the $^{206}\text{Pb}/^{238}\text{U}$ ratio; Figure 3.22 c) to be used for age calculations. Those that yield discordant ages are likely to be caused by ablation of core and rims

Chapter 3: Petrography & Geochronology Results

during analysis. Relative probability plots of the 31 concordant grains (Figure 3.22 d) yield three well established populations at 1201 ± 27 Ma, 996 ± 60 Ma and 1751 ± 73 Ma (typical of Oaxaquia continental crust) as well as one concordant Permian grain (285 ± 9 Ma); the significance of which is difficult to determine. There does appear to be a poorly constrained mixing line between this Permian grain and the rest of the analysis which would suggest, although speculatively, the younger age has geological significance. This sandstone can therefore be interpreted as having a strong influence from Precambrian Oaxaquia crust, with a minor influence from a Permian zircon forming event (likely to relate to the igneous crystallization ages in the other basement cores e.g. Pinonal & Arenque). We can therefore assign a maximum age of deposition at 285 ± 9 Ma.

Gonzales-1 N9F2C1

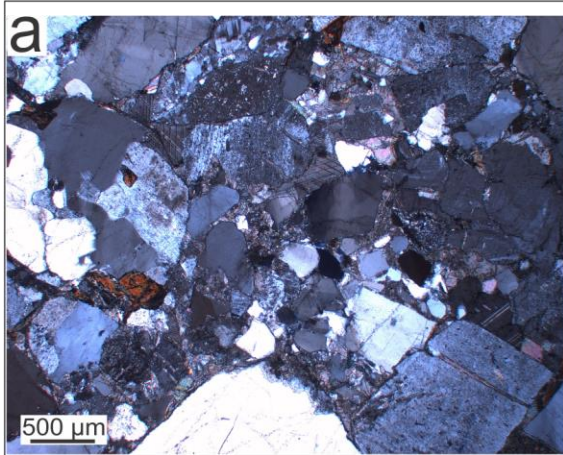


Figure 3.1a: Cross polarized light (XPL) thin section image for the analysed sample showing fragments that contain calcite, feldspars and quartz.

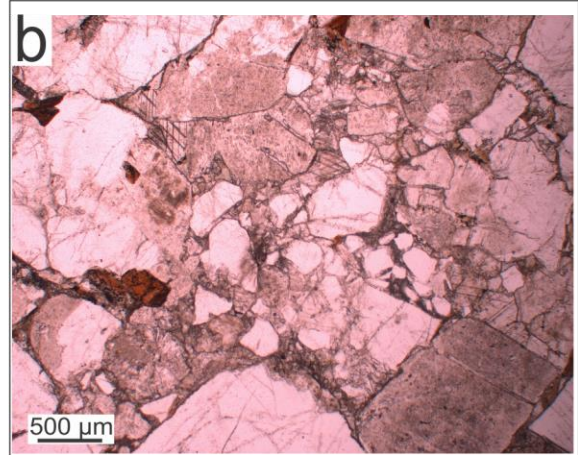


Figure 3.1b: Plane polarized light (PPL) thin section image for the analysed sample showing fragments that contain calcite, feldspars and quartz.

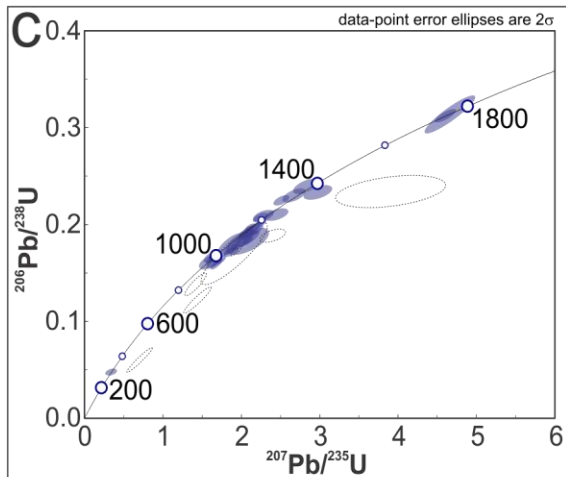


Figure 3.2c: Tera Wasserburg plot of the analysed grains (n=26). The blue ellipses represent zircons that were taken further to age calculations (n=22) and the dotted ellipses show those that were disregarded (> 20% discordance, > 10% error).

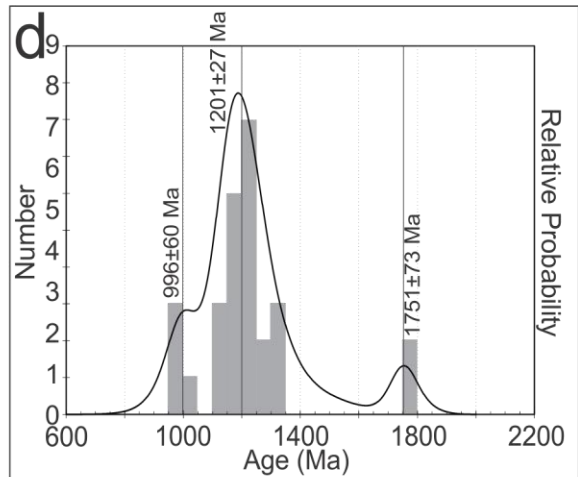


Figure 3.2d: Probability density model for zircons used in age calculations (n=22).

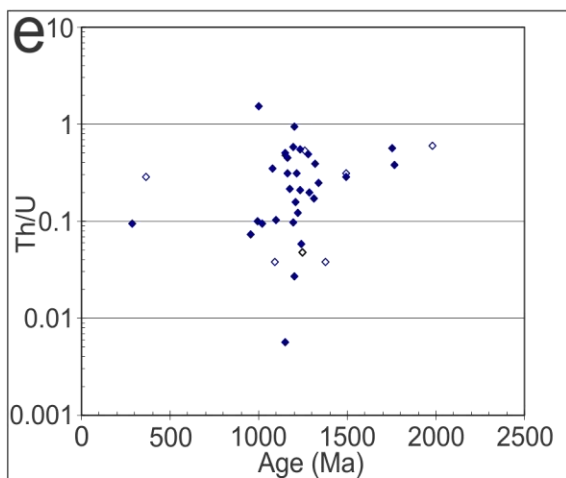


Figure 3.2e: Th/U vs age (Ma) plot for all of the analysed grains. White points represent analysis that were disregarded and blue those that were used for age calculations.

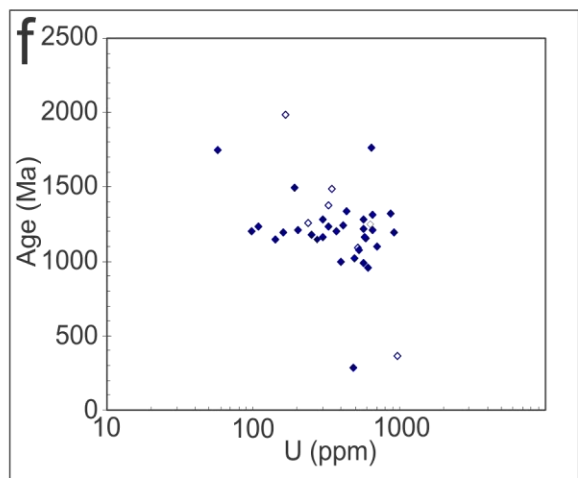


Figure 3.2f: Age (Ma) vs U (ppm) plot for all of the analysed grains. White points represent analysis that were disregarded and blue that were considered for age calculations.

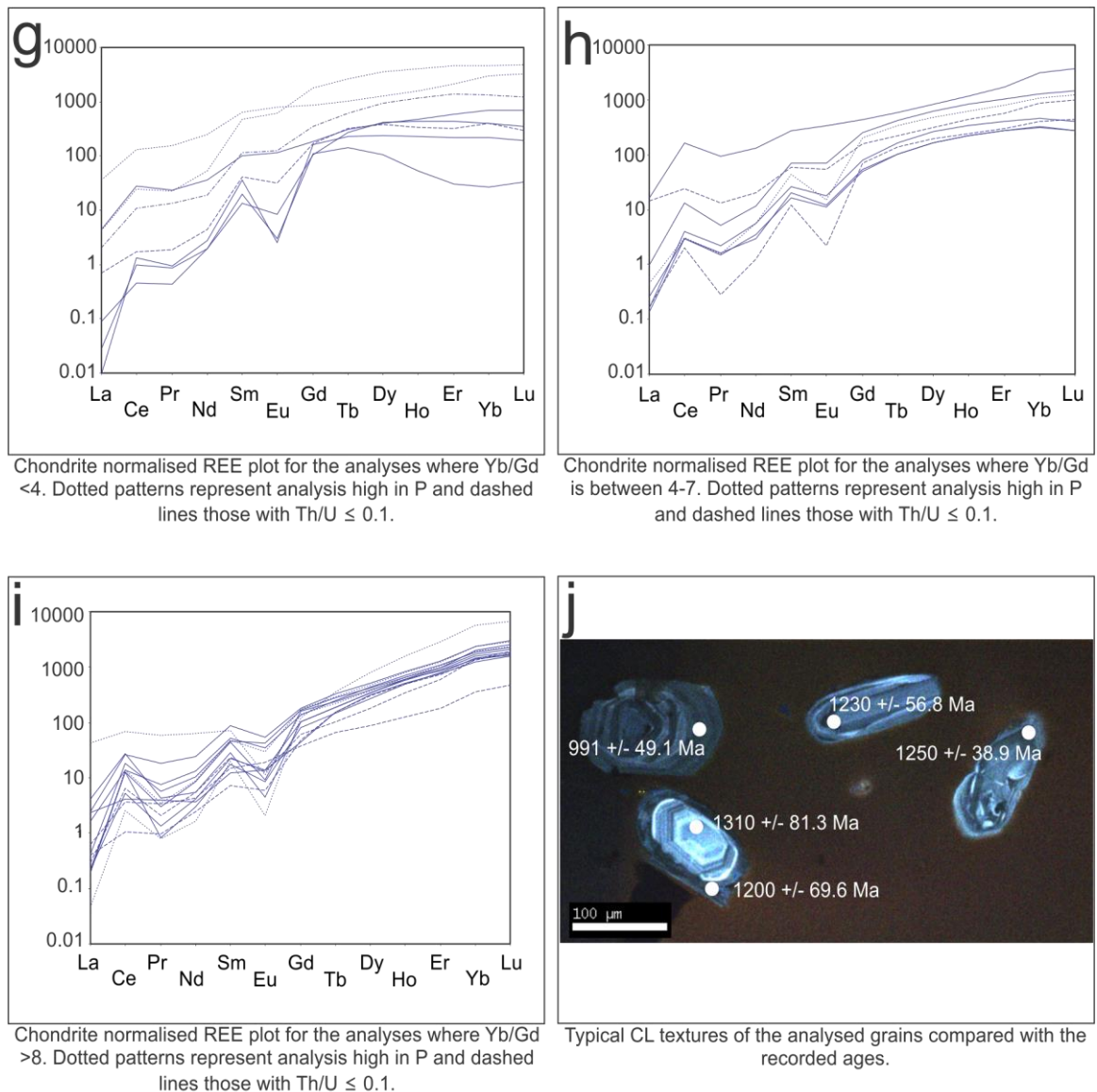


Figure 3.22. Geochronology results for the Gonzales N9F2C1 basement core from the Western Gulf of Mexico.

3.6 Summary

- The crystalline basement of the Western Gulf of Mexico is more homogeneous in age than previously reported by Lopez-Ramos, (1979).
- The igneous rocks can be split into Early Permian (294 Ma), Late Permian-Early Triassic (274-244 Ma) and Jurassic (189-164 Ma) suites (Table 3.1). There is little evidence for inherited zircon cores in the Early Permian igneous rocks however

Chapter 3: Petrography & Geochronology Results

the Late Permian and Jurassic igneous rocks show inheritance from the Grenville aged Oaxaquia continental crust as well as the Early Permian igneous event (Table 3.1).

- There are minor contributions from basement of metamorphic origin along the Western Gulf of Mexico. The age of metamorphism is poorly constrained and could either relate to a Late Paleozoic mixing line or the youngest population of zircons found (700 Ma; Table 3.1).
- Drilling of the Gonzales well did not reach the crystalline basement but instead yield sediments that contain Grenville aged detrital zircons derived from Oaxaquia continental crust (Table 3.1).

Sample	Age	Inheritance
Early Permian		
Pinonal N2F3C1	294.1 ± 3.4 Ma	
Arenque N15F3+4C2	293.5 ± 3.7 Ma	
Late Permian-Early Triassic		
Paso de Oro N8F4C2	274.2 ± 3.5 Ma	
Benemerito N2F7bC5	246.9 ± 4.2 Ma	1266 ± 93 Ma*
Trincheras N3F5aC1	255.8 ± 3.3 Ma	288 ± 5 Ma*; 289 ± 4 Ma*
Linares N7F1C1	253.5 ± 5.2 Ma	
Chaneque N6F1C4	243.0 ± 2.8 Ma	
Nayade N13F2C1	257.0 ± 5.2 Ma	397 ± 6 Ma*; 538 ± 6 Ma*; 558 ± 4 Ma*
Tamaulipas N1F2C1	247.9 ± 4.0 Ma	
Erizo N19F19C1	250.0 ± 3.1 Ma	
Pinonal N2F11C2	249.4 ± 3.1 Ma	478 ± 6.8 Ma*; 509 ± 7.8 Ma*; 1235 ± 153 Ma*
Cupelado N9F1C1	262.7 ± 4.5 Ma	284.8 ± 9.1Ma; 1428 ± 48 Ma
Plan de Las Hayas N14F1C1	261.0 ± 4.1 Ma	
Plan de Las Hayas N14F6C2	250.4 ± 4.6 Ma	
Paso de Ovejas N6F9C2	256.7 ± 5.5 Ma	297 ± 9 Ma*; 298 ± 7 Ma*
Orizaba N6F1C1	253.0 ± 7.5 Ma	959 ± 59 Ma; 1162 ± 38 Ma
Jurassic		
Muro N12F2C1	188.5 ± 3.5 Ma	398 ± 3.2 Ma*; 1430 ± 24 Ma*
Tlapacoyan N10F18C5	164.3 ± 3.5 Ma	263 ± 7 Ma; 838 ± 60 Ma
Meta-sediments and sediments		
Salto N8F1C1	700 +17 -21 Ma	795 Ma; 935 Ma
Gonzales N9F1C1	976 ± 57 Ma	1148 ± 32 Ma; 1300 ± 50 Ma
Gonzales N9F2C1	285 ± 9 Ma	996 ± 60 Ma; 1201 ± 27 Ma; 1751 ± 73 Ma

Table 3.1. shows all of the obtained ages for the analysed samples from the Western Gulf of Mexico. The * symbol represents inherited ages from just one zircon grain.

4 Western Gulf of Mexico Basement Granitoids: Major, Trace and Hf Isotope Results and Discussion.

4.1 Introduction

This Chapter presents major, trace and Hf isotopic geochemical results and interpretations for the Permo-Triassic basement granitoids of the Western Gulf of Mexico to determine their tectonic setting and petrogenesis. This information will be used along with the geochronology presented in Chapter 3 to test the validity of existing/provide new constraints on tectonic models for the amalgamation of western Pangaea.

Samples have been grouped according to their crystallization age as reported in Chapter 3 (Early Permian, Late Permian-Early Triassic and undated). Complete tables of major and trace element geochemical results can be found in Appendix D.

4.2 Analytical techniques

In total 33 basement core samples were provided by Petróleos Mexicanos (PEMEX) for geochemical and geochronological analyses. Of the samples provided, 19 yielded Permo-Triassic igneous crystallisation ages (Chapter 3) and were deemed suitable for geochemical analysis. Unsuitable basement cores were either highly altered, Jurassic in age or not of an igneous origin. Major elements were analysed by inductively coupled plasma optical emission spectrometry (ICP-OES) and trace elements by inductively coupled plasma mass spectrometry (ICP-MS) at Cardiff University, UK. In addition, the zircons in three samples were analysed for Hf

Chapter 4: Geochemical results for Western GoM basement

isotopes (five grains analysed in total) under the direction of Dr. Bodo Weber at *Centro de Investigación Científica y de Educación Superior de Ensenada* (CICESE) research institute (Ensenada, Mexico). Detailed descriptions of analytical techniques are given in Appendix A.

4.3 Alteration and element mobility

When interpreting geochemical data care must first be taken to consider subsequent alteration events that may affect a rock, causing element mobility and masking the original magmatic signatures. Factors that can cause such element mobility include surface weathering, interactions with hydrothermal fluids, diagenesis and metamorphism.

The wt.% loss of ignition (%LOI) for each of the samples can be used to help assess how much sub-solidus alteration a sample has undergone. Low %LOI values in this study are considered to be <5 wt.%, moderate between 5-10 wt.%, and high >10 wt.%. The LOI for the basement samples from the Western Gulf of Mexico ranges from 0.6-6.8 wt.% which suggests that at least some of the samples have been affected by alteration (as also suggested by petrography, Chapter 3).

Another method of determining the degree of element mobility in the samples is to plot each element against Zr (Cann, 1970). Zr is widely accepted to be one of the most immobile elements from early diagenesis to medium-high grade metamorphic conditions (Pearce, 1996b). Assuming that all the rocks lie on a single liquid line of descent and there is no source variation then other immobile elements will show good correlations when plotted against Zr; in contrast, mobile elements

Chapter 4: Geochemical results for Western GoM basement

affected by alteration will display more scatter. However, if scatter or multiple trend lines are observed in elements that are usually immobile during alteration e.g. the light rare earth elements (LREEs) and high field strength elements (HFSEs), then petrological processes, rather than alteration processes, are likely to have controlled the geochemical variability. To quantify the correlation observed between the element in question and Zr, linear trends were constructed along with calculations of the R^2 correlation value. For the purposes of this study if R^2 values >0.65 the correlation will be considered to be good, while values between 0.65 and 0.5 represent moderate correlations, and <0.5 poor correlations.

The petrography of basement core samples (Chapter 3) reveals that they have undergone varying degrees of alteration. The feldspars are most commonly replaced by white micas and, in some instances, epidote. The most severely altered samples are Pinonal N2F3C2, Pinonal N2F11C2, Chaneque N6F1C4, Erizo N19F19C4 and Nayade N13F2C1. These samples have been grouped together in an “altered” group on the Zr mobility plots (Figures 4.1-4.2) to assess how alteration has affected their major and trace element mobility.

Chapter 4: Geochemical results for Western GoM basement

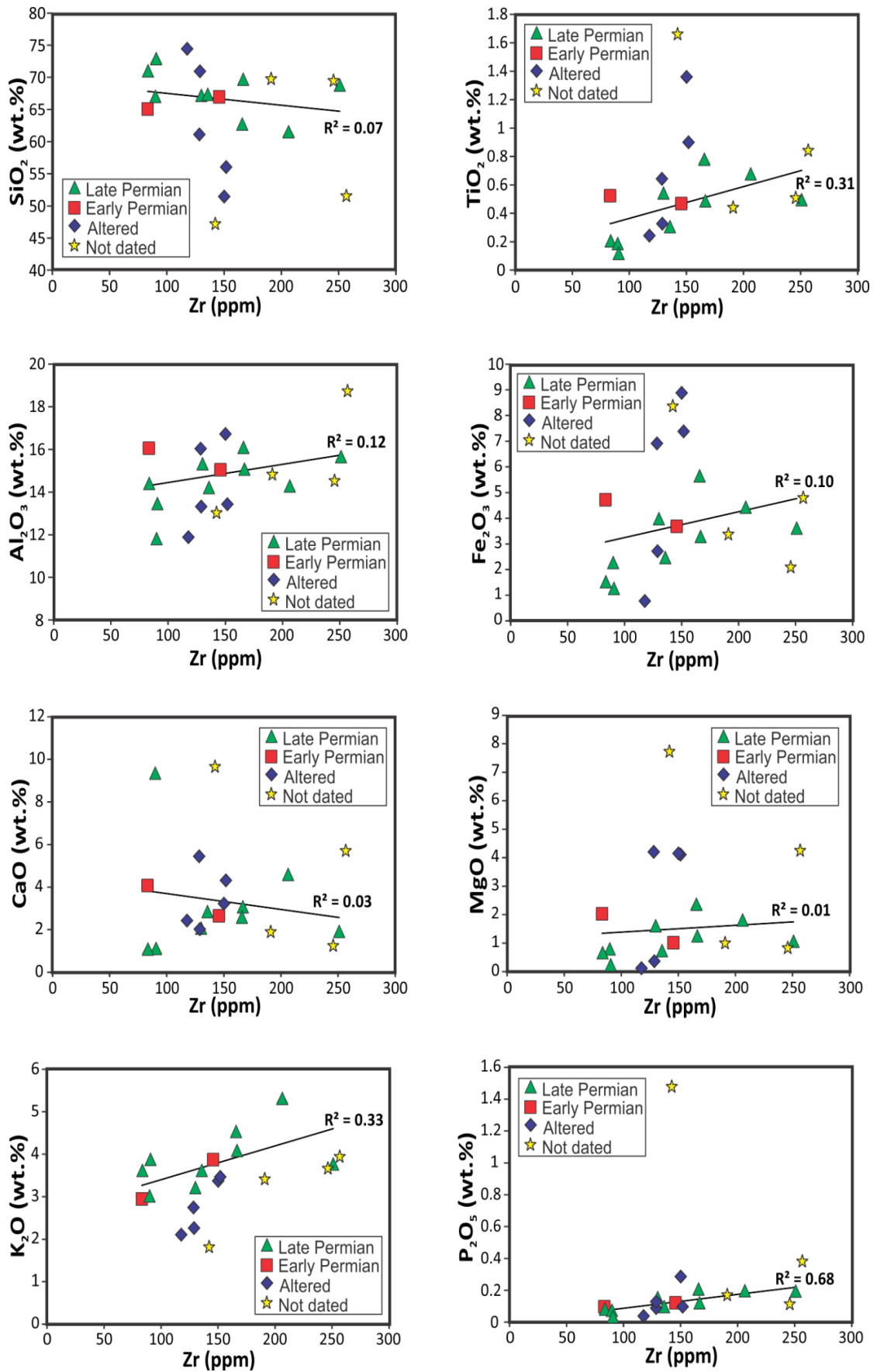


Figure 4.1. Plot showing major elements vs. Zirconium for the basement granitoids of the Western Gulf of Mexico.

Chapter 4: Geochemical results for Western GoM basement

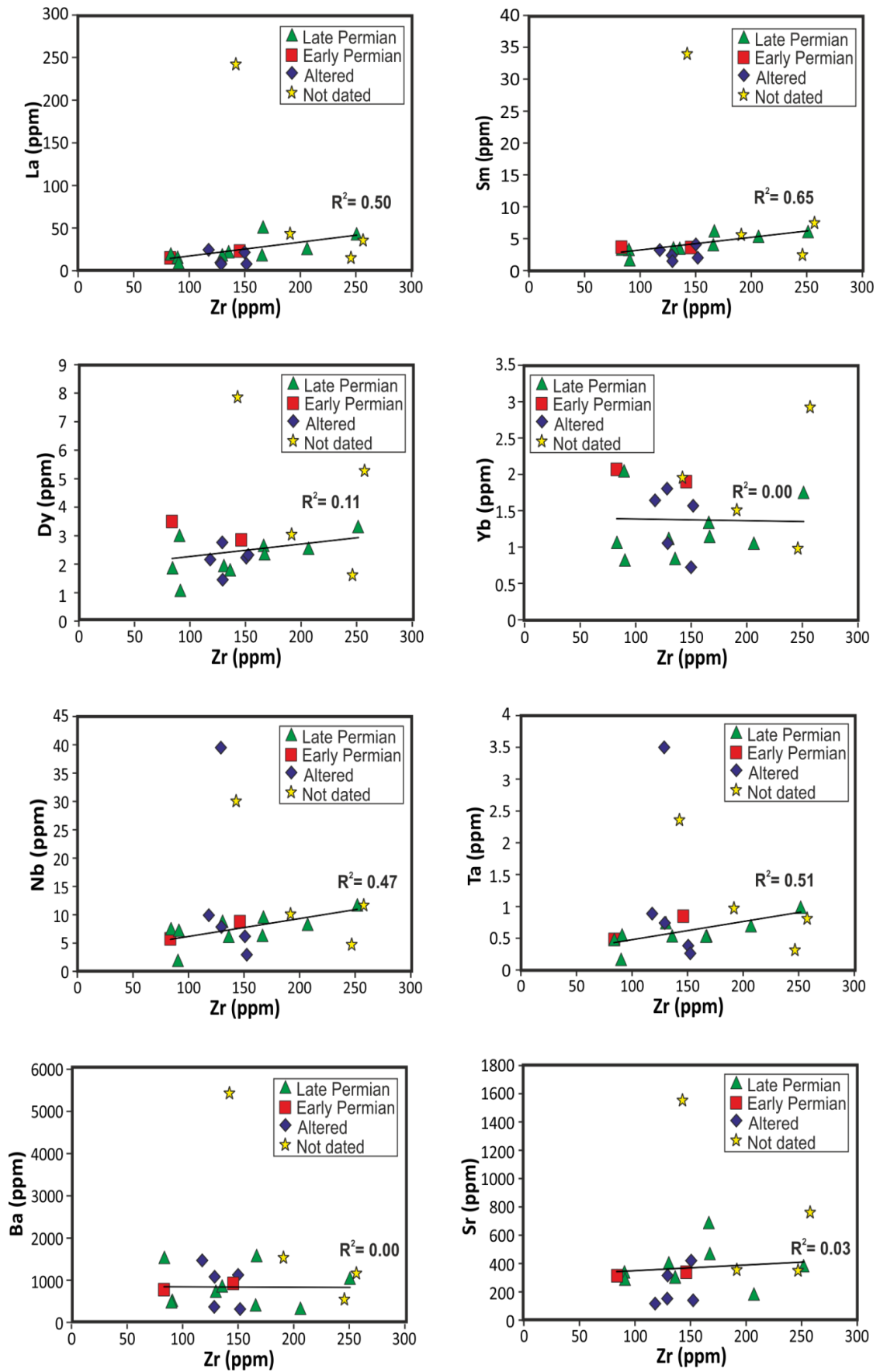


Figure 4.2. Plot showing a representative group of trace elements vs. Zirconium for the basement granitoids of the Western Gulf of Mexico.

Chapter 4: Geochemical results for Western GoM basement

R^2 values have only been calculated using basement cores that were successfully dated and did not show significant petrographic alteration (Figures 4.1-4.2). Good correlations (>0.65) are observed for Sm, Gd and P_2O_5 . Moderate correlations (0.65-0.5) are observed for the remainder of the LREE and middle (M)REEs and Ta. The elements that display poor correlations with Zr are the HREEs, Nb, large ion lithophile elements (LILEs) and the remainder of the major elements. The apparent mobility of the majority of the rare earth elements (REEs) and high field strength elements (HFSEs) is surprising as these are considered immobile during weathering and metamorphism. The scatter in the mobility plots instead may relate to source heterogeneities.

4.4 Classification

Classification of plutonic rocks can be based on petrographic characteristics (see Chapter 3) but they can also be classified using their geochemical characteristics, provided analysed sample are large enough to be truly representative of coarse-grained igneous rocks. In the total-alkali-silica (TAS) diagram (Figure 4.3) the relatively unaltered, dated basement cores plot in the granite (n=5), alkali granite (n=2), tonalite/granodiorite (n=3) and syeno-diorite (n=1) fields. The Early and Late Permian basement samples appear to be compositionally similar. The dated samples that show significant alteration display widespread data (2 granites, 1 diorite, and 2 syeno-diorite) which may relate to element mobility. Two undated samples are mafic, plotting in the gabbro and syeno-diorite fields (Magdalena N6F8C4 and Jurel N6F7C1/5). This may represent a more juvenile subset of the igneous suite or alternatively they may be unrelated to the Permian suite. The

Chapter 4: Geochemical results for Western GoM basement

other 2 undated samples (Benemerito N1F9C8/10 and Trincheras N3F2C2/3) plot in the granite and alkali granite fields and are similar to the early and late Permian igneous suites.

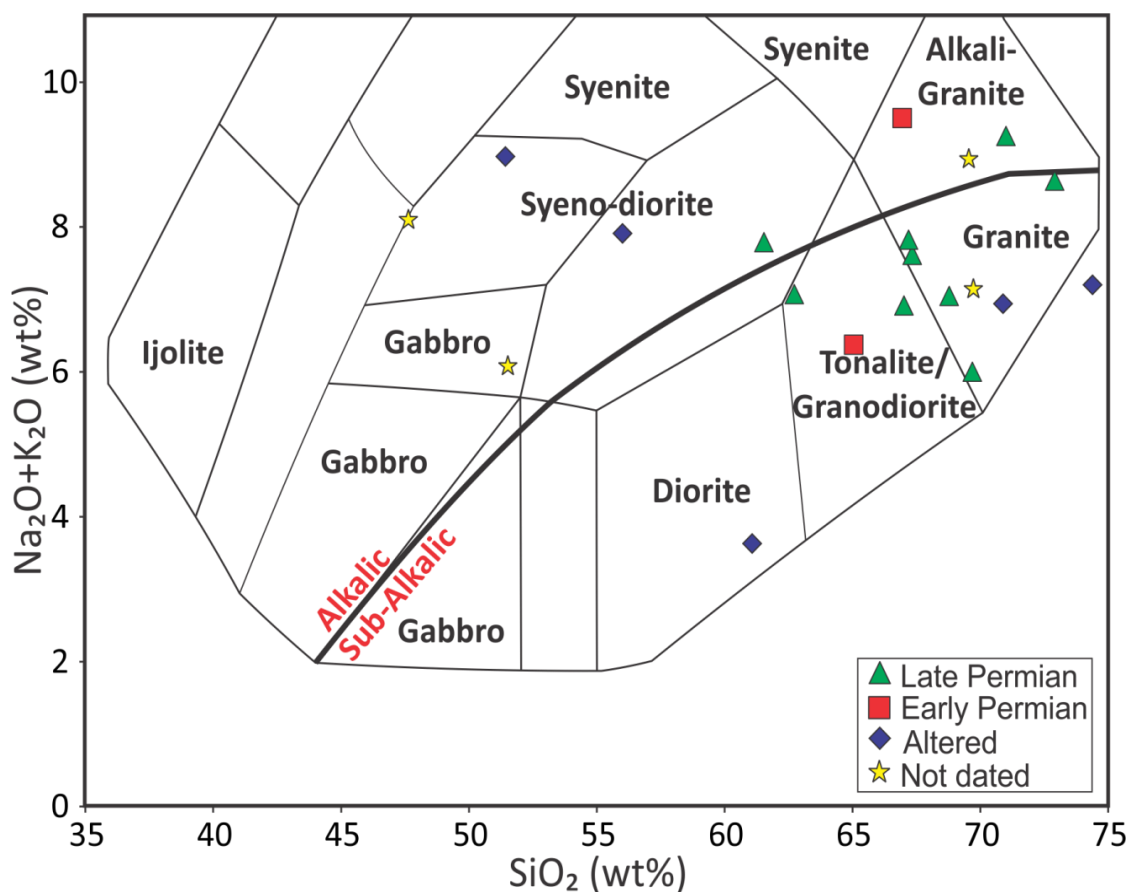


Figure 4.3. Total alkali-silica (TAS) of Le Maitre et al., (1989) showing the composition of the basement samples. Field boundaries taken from Wilson (1989).

The Cross, Iddings, Pirsson, Washington (CIPW) norm has been calculated for the basement samples of the Western Gulf of Mexico, producing a predicted mineralogy from the anhydrous major element concentrations (wt.%). These norms have been plotted on the quartz-alkali feldspar-plagioclase-feldspathoid (QAPF) diagram in Figure 4.4. The Early Permian samples plot in the granodiorite and the quartz monzonite fields. The Late Permian samples give similar results, plotting in the monzo-granite (n= 5), granodiorite (n =3) and quartz monzodiorite/quartz

Chapter 4: Geochemical results for Western GoM basement

monzogabbro (n=1) fields. The altered samples show a large spread in results likely due to element mobility. They plot in the monzo-granite (n= 2), tonalite (n= 1), quartz monzonite (n= 1) and monzonite (n= 1) fields. Two of the undated samples (Benemerito N1F9C8/10 and Trincheras N3F2C2/3) display similar results to the Early and Late Permian samples, plotting in the monzo-granite fields. The remaining undated samples plot in the monzodiorite/monzogabbro (Jurel N6F7C1/5) and foid monzosyenite fields (Magdalena N6F8C4), again suggesting they are unrelated to the Permian basement samples.

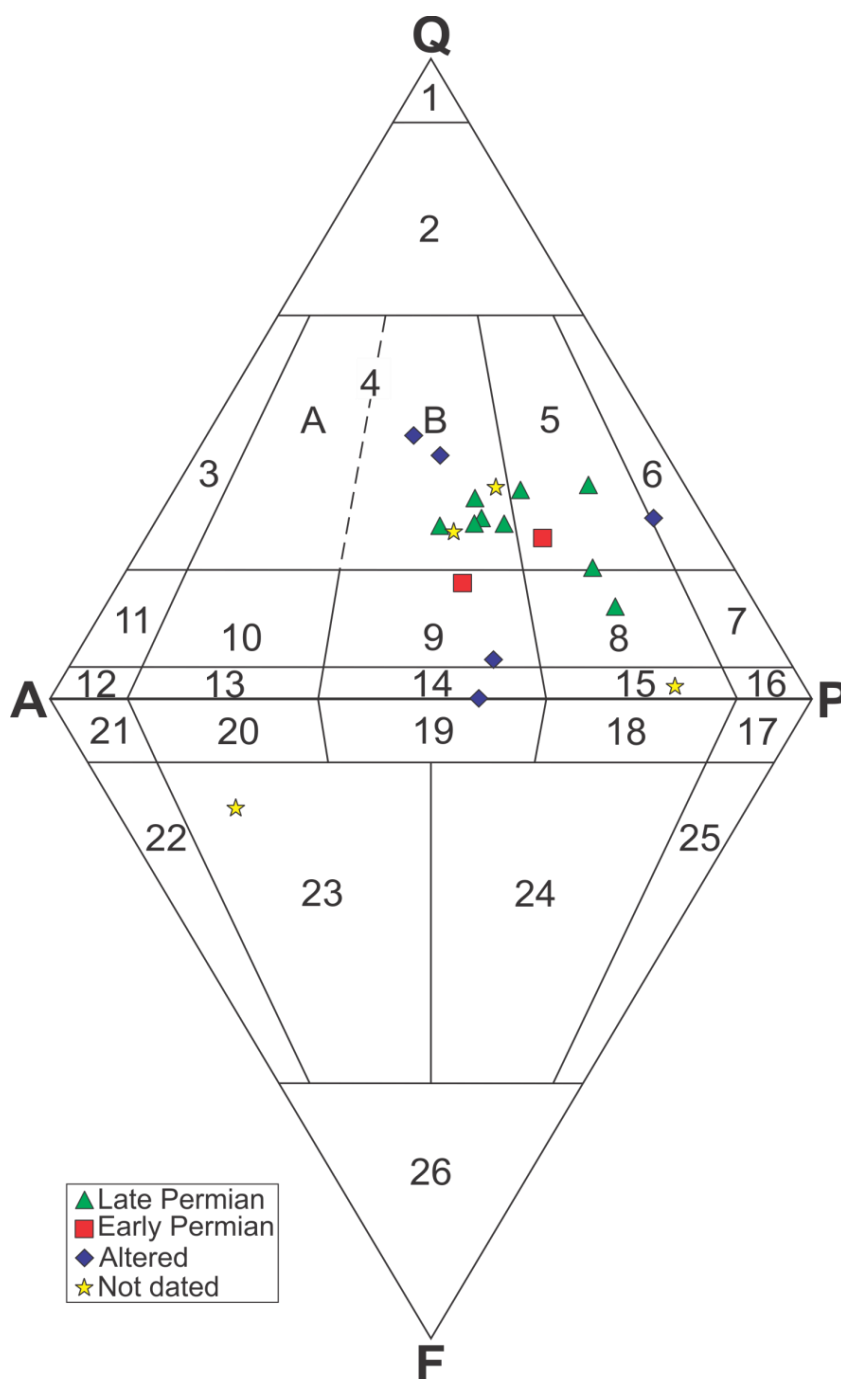


Figure 4.4. Quartz-plagioclase-Alkali feldspar-Feldspathoid (QAPF) diagram for the basement core samples of the Western Gulf of Mexico. CIPW norms first calculated from anhydrous major element concentrations then Q,A,P,F percentages recalculated to 100%. 1= quartzolite, 2= quartz-rich granitoids, 3= alkali feldspar granite, 4= granite (A-syeno-granite, B- monzo-granite), 5= granodiorite, 6= tonalite, 7= quartz diorite/ quartz gabbro/ quartz anorthosite, 8= quartz monzodiorite/ quartz monzogabbro, 9= quartz monzonite, 10= quartz syenite, 11= quartz alkali feldspar syenite, 12= alkali feldspar syenite, 13= syenite, 14= monzonite, 15= monzodiorite/ monzogabbro, 16= diorite/ gabbro/ anorthosite, 17= foid-bearing diorite/ foid-bearing gabbro/ foid-bearing anorthosite, 18= foid-bearing monzodiorite/ foid-bearing monzogabbro, 19= foid-bearing monzonite, 20= foid-bearing syenite, 21= foid-bearing alkali feldspar syenite, 22= foid syenite, 23= foid monzosyenite, 24= foid monzodiorite/ foid monzogabbro, 25= foid diorite/ foid gabbro, 26= foidolite.

4.5 Major elements

The SiO₂ concentrations for the basement cores that yield Early Permian ages range from 65.0-66.9 wt.% with Mg# of 23-32. TiO₂, Fe₂O₃, Al₂O₃ and MgO ranges from 0.47-0.52, 3.7-4.7, 15.0-16.1 and 1.0-2.0 wt.% respectively (Figure 4.5 and Appendix D). In the Late Permian basement cores SiO₂ ranges between 61.5-72.9 wt.% with Mg# of 17-33. TiO₂, Fe₂O₃, Al₂O₃ and MgO range from 0.12-0.78, 1.3-5.6, 11.8-16.1, 0.2-2.4 wt.% respectively (Figures 4.5 and Appendix D). Major elements in the significantly altered samples generally display greater compositional variability than that of the less-altered samples (Figures 4.5). The total alkalis range from 3.6-9.0 wt.% (Na₂O= 2.1-3.5 wt.%; K₂O= 0.9-5.6 wt.%). The 2 undated samples that were comparable to the Early and Late Permian samples in the classification plots (Benemerito N1F9C8/10 and Trincheras N3F2C2/3) again fall within their major element compositional range. Other undated samples (Magdalena N6F8C4 and Jurel N6F7C1/5) have distinct major element contents that outline a more mafic composition.

R² values in the bivariate plots for the major elements (Figure 4.5) surprisingly display strong negative correlations between SiO₂ and MgO, TiO₂ and Fe₂O₃ despite the poor correlations in the Zr mobility plots (Figure 4.1). This suggests that the major elements have not been mobilised but instead might show a liquid line of descent. If this is the case then Zr in the mobility plots of Figures 4.1 & 4.2 is not likely to be behaving incompatibly (fractionating out of the melt in zircon), which has resulted in the poor R² values.

Chapter 4: Geochemical results for Western GoM basement

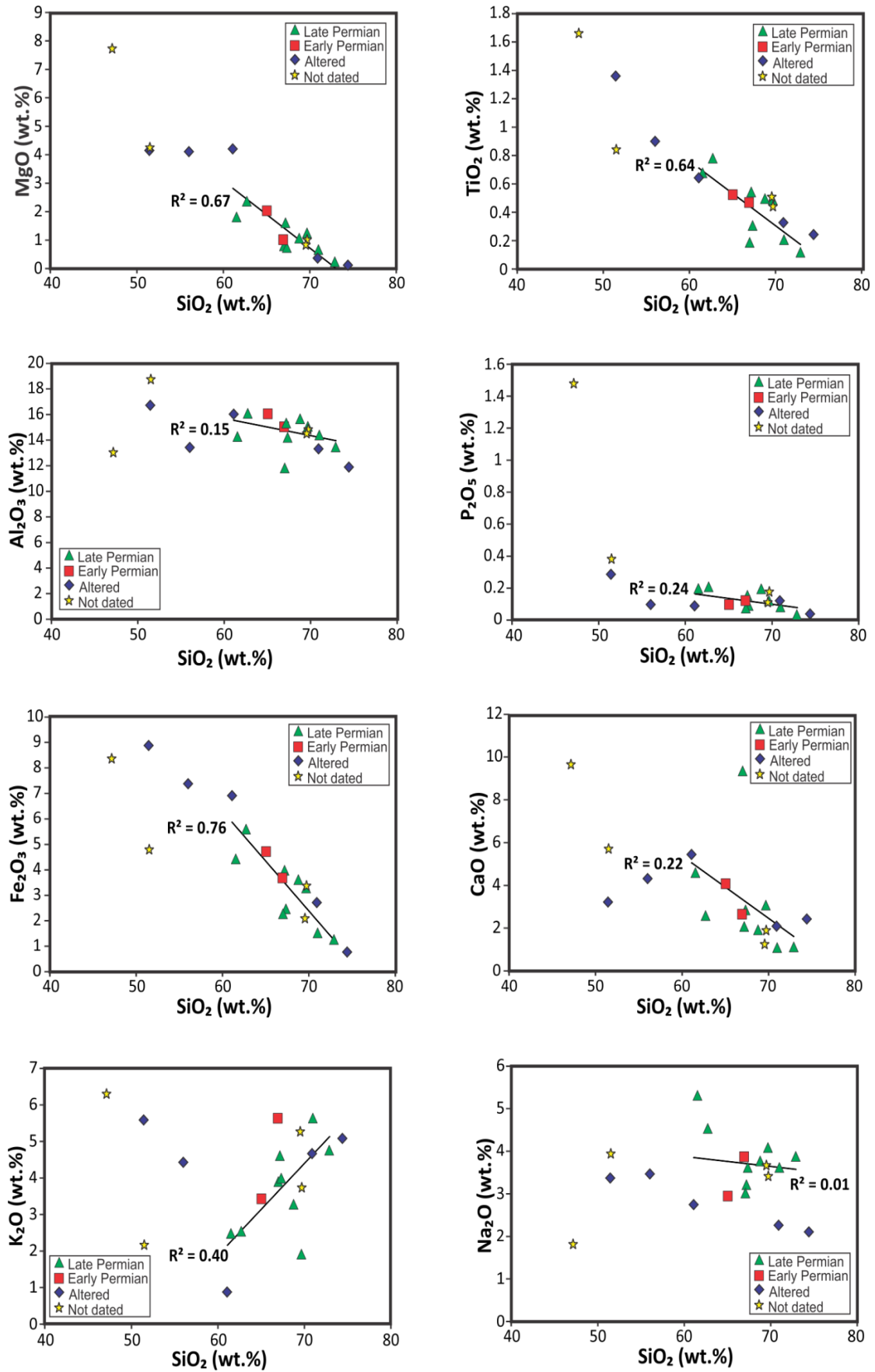


Figure 4.5. Plot showing major elements vs. SiO₂ for the basement granitoids of the Western Gulf of Mexico.

4.6 Trace Elements

The rare earth elements (REEs) display very poor correlations (Figure 4.6) with SiO_2 ($R^2 = 0.00-0.27$). The high field strength elements (HFSEs) display better correlations ($R^2 = 0.19-0.25$) but are still poor. The mobility-susceptible large ion lithophile elements (LILEs) surprisingly display 2 of the best correlations with SiO_2 in Ba ($R^2 = 0.39$) and Rb ($R^2 = 0.49$). The poor correlations observed in the trace elements of the bivariate plots are likely due to a multi-genetic source for the basement of the Western Gulf of Mexico. The trace elements tend to be more sensitive to a multi-genetic nature than the major elements which explains why the R^2 values in the major element bivariate plots are higher than in the trace element ones.

The Early and Late Permian rocks (Figure 4.7 A&B), are enriched in the REE and other trace elements (Early Permian average= x27 chondrite; Late Permian average= x31 chondrite). There is also marked enrichment in the LREE relative to the HREE, with $\text{La}/\text{Sm}_{\text{Ch}}$ (chondrite normalised) for the Early and Late Permian rocks ranging between 2.6-5.1. The MREEs are defined by concave trends across many of the Early and Late Permian granitoids. The HREEs are defined by flat to slightly positively sloping trends, with $\text{Ho}/\text{Lu}_{\text{Ch}}$ for the Early and Late Permian rocks ranging between 0.54-1.15. Two undated samples of the basement cores (Trincheras and Benemerito) have similar REE patterns to the Permian rocks (Figure 4.7 C) which suggests they may be part of the same suite. The incompatible trace element content in the Magdalena sample is very enriched, with a steep LREE pattern ($\text{La}/\text{Sm}_{\text{Ch}} = 7.1$; Figure 4.7 C). This sample also shows significant depletion in HREEs ($\text{Gd}/\text{Yb}_{\text{Ch}} = 12$) and extreme enrichment in Th (Figures 4.7 C&4.10 C).

Chapter 4: Geochemical results for Western GoM basement

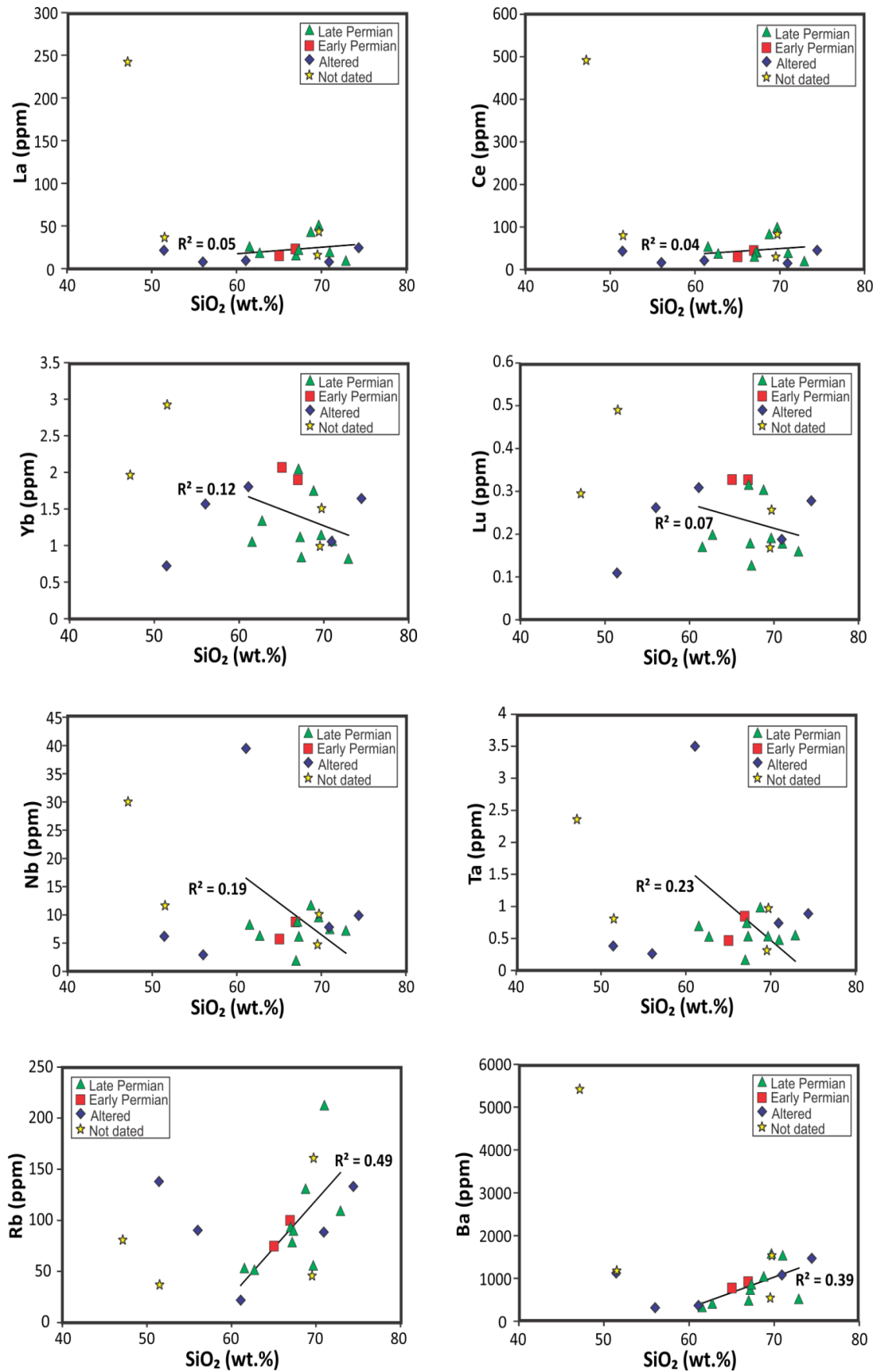


Figure 4.6. Plot showing a representative group of trace elements vs. SiO₂ for the basement granitoids of the Western Gulf of Mexico.

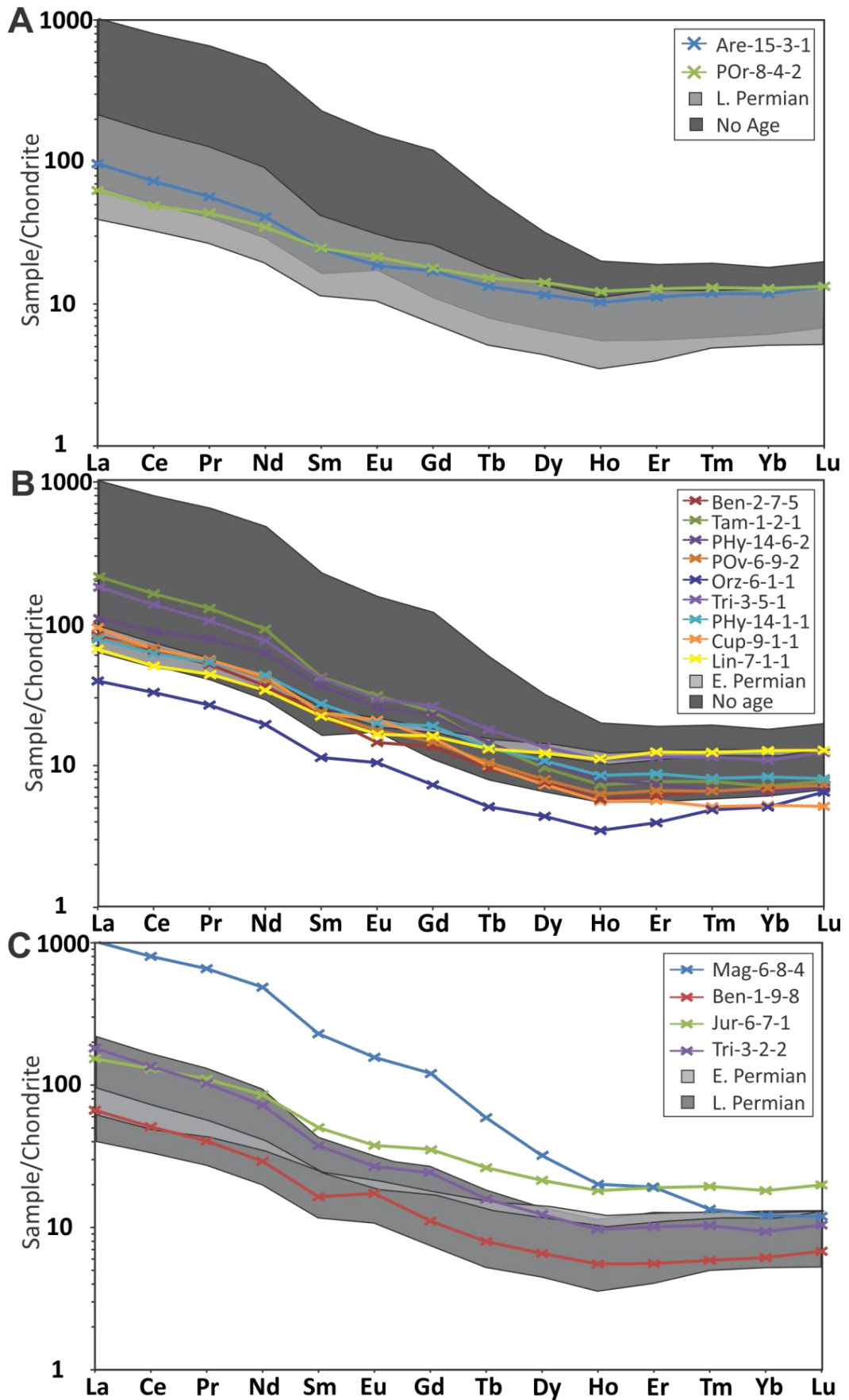


Figure 4.7. Chondrite normalised rare earth element plots for the basement cores. A= Early Permian samples, B= Late Permian samples, C= Not dated samples

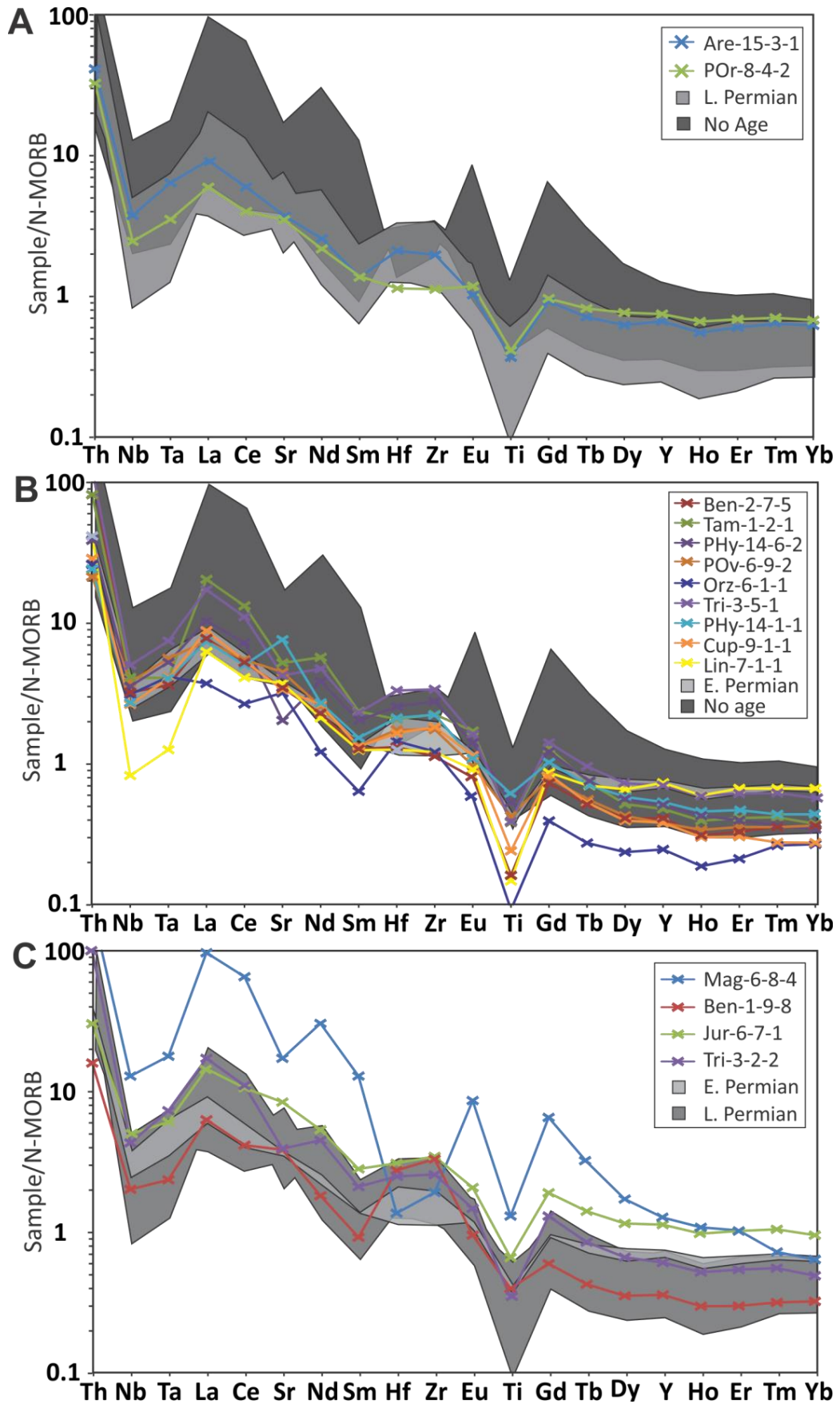


Figure 4.8. N-MORB normalised multi-element plots for the basement cores. A= Early Permian Samples, B= Late Permian samples, C= Not dated samples

Chapter 4: Geochemical results for Western GoM basement

In multi-element plots the basement cores have negative Nb, Ta and Ti anomalies along with variable degrees of enrichment in Th. As in the REE plots the Early and Late Permian samples have very similar incompatible trace element signatures e.g., average $^{1}\text{Nb}/\text{Nb}^*$ and Ta/Ta^* for Early Permian basement= 0.14 and 0.34 respectively; average Nb/Nb^* and Ta/Ta^* for Late Permian basement= 0.13 and 0.26 respectively (Figures 4.8 A&B). The undated samples of Benemerito N1F9C8/10, and Trincheras N3F2C2/3 again yield similar results to the Early and Late Permian magmatism results, with high Th values and negative Nb, Ta and Ti anomalies (Figure 4.8 C).

4.7 Petrogenesis and tectonomagmatic setting for the crystalline basement of the Western Gulf of Mexico

The major element results of the Western Gulf of Mexico basement samples indicate emplacement of differentiated magmas (high SiO_2 and low MgO) in the crystalline basement. The trace element contents are typical of subduction zone magmatism, where the LREE and Th are enriched in subduction related fluids and Nb, Ta and Ti are preferentially retained in a rutile bearing source (e.g. the subducting oceanic crust). Alternatively, similar trends are observed in rocks of the continental crust, which suggest that melting or assimilation of a continental source may have generated the geochemical signatures of the studied igneous rocks. In addition, compositional scattering of nearly all incompatible elements in the mobility

$$\frac{\text{Nb}}{\text{Nb}^*} = \frac{\text{Nb}}{0.5 \times (\text{Th} + \text{La})}$$

(Nb/Nb* used here for an example), the same equation is used to calculate Ta/Ta*

Chapter 4: Geochemical results for Western GoM basement

plots (Figure 4.2) suggests that several sources contributed to the formation of the studied igneous rocks.

The major and trace element results of the undated samples Benemerito N1F9C8 and Trincheras N3F2C2 are comparable to both the Early and Late Permian basement samples. The remaining undated samples (Magdalena N6F8C4 and Jurel N6F7C2) however display major and trace element results that are distinct from the other samples. Their major element contents are characterised by low SiO₂ and high MgO which indicate a composition that is a lot more mafic than the Early and Late Permian granitoids. The Magdalena N6F8C4 sample displays distinct trace element signatures, with significant enrichment of the LREEs as well steep HREE patterns. Petrographic characteristics of this sample (Chapter 3) suggest that it is a lamprophyre. Lamprophyres have been recorded in the modern Trans Mexican Volcanic Belt as small dykes. It is therefore likely that these distinct samples do not belong to the pre-Mesozoic basement of the Western Gulf of Mexico. Because the Magdalena N6F8C4 and Jurel N6F7C2 samples are unlikely to be related to the Permian story of the Western Gulf of Mexico basement they have not been considered further in this chapter. In contrast, the undated Benemerito N1F9C8 and Trincheras N3F2C2 samples have been included in the discussion below due to their chemical similarities with the Early and Late Permian samples.

It is thought that during the Permian, Northwest Colombia was attached to Southern Mexico as part of the super-continent Pangaea (Pindell & Kennan, 2009). It is therefore possible that any Permian magmatic event in Colombia might be related to the Mexican granitoids of this study. Permo-Triassic igneous activity has been

Chapter 4: Geochemical results for Western GoM basement

reported in the Central Cordillera of Colombia by a number of authors (Vinasco et al., 2006; Cardona et al., 2010; Villagomez et al., 2011; Cochrane et al., 2014). The earliest identified Permian phase occurred between 275-240 Ma which correlates with the basement of the Western Gulf of Mexico (294-243 Ma; Chapter 3). Additional exposed Permian plutons have been identified in the Chiapas Massif in Southern Mexico (Weber et al., 2005; Estrada-Carmona et al., 2012), and other locations in Mexico (Arvizu & Iriondo, 2011; Ortega-Obregon et al., 2014), as shown in Figure 2.2. In the following sections the compositions of the crystalline basement from the Western Gulf of Mexico (this study) will be compared with the Permian granitoids of Colombia and elsewhere in Mexico in order to assess if they form part of the same magmatic province.

4.7.1 Fractional Crystallisation

Before interpreting the tectonic setting of the basement cores it is important to assess if fractional crystallisation has had an effect on the chemistry of the rocks. As highlighted in Section 4.6 the REEs in the samples display a concave trend throughout the MREEs. This may be caused by the preferential retention of the MREEs in amphibole during fractional crystallisation or if it is present as a residual phase during partial melting. The concavity of the REE slope can be calculated using the Dy/Dy* ratio from the following equation in Davidson et al. (2013):

$$\frac{Dy}{Dy^*} = \frac{Dy_N}{La_N^{13} Yb_N^{13}}$$

Where values for Dy, La and Yb are normalised to chondrite.

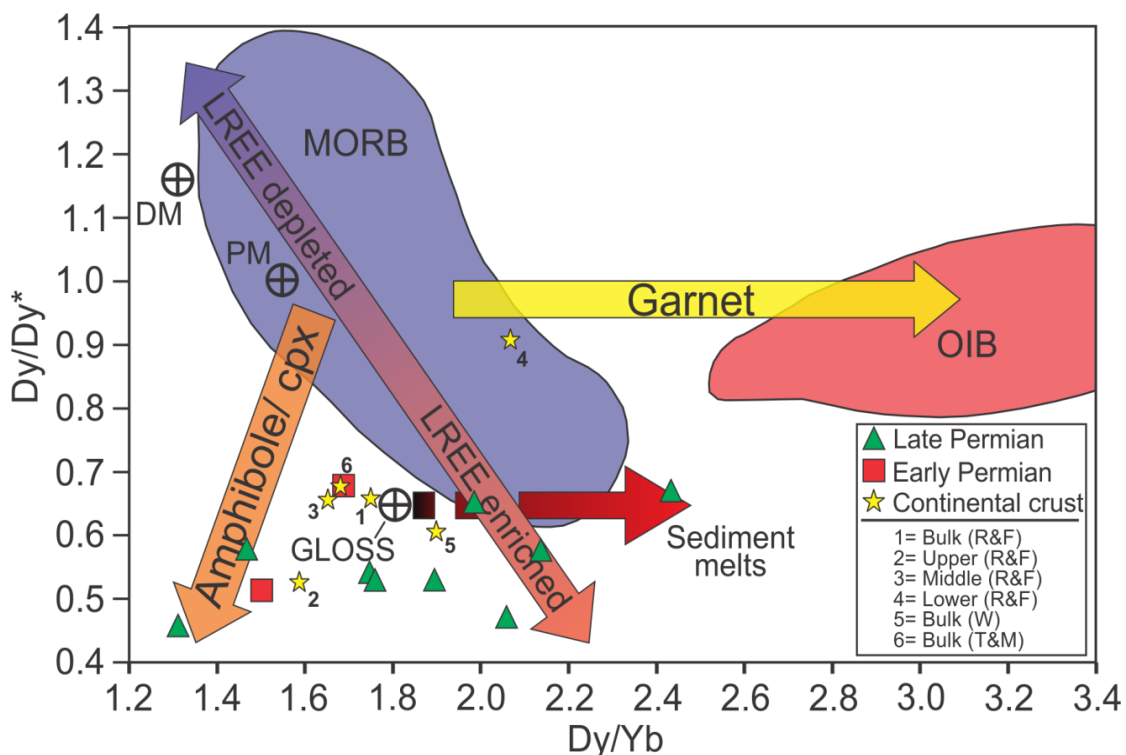


Figure 4.9. Dy/Dy^* vs. Dy/Yb diagram of Davidson et al. (2013) for the Western Gulf of Mexico basement samples. The MORB field has been compiled from N-MORB and E-MORB data from the East Pacific Rise (Nui et al., 1999; Regelous et al., 1999; Turner et al., 2011). The OIB field includes data from Hawaii (Sims et al., 1995, 1999) and the Azores (Beier et al., 2010). Continental crustal estimates are from Rudnick & Fountain (1995); Wedepohl (1995); Taylor & McLennan (1985). PM= primitive mantle (Sun & McDonough, 1989); DM= depleted mantle (Salters & Stracke, 2004); GLOSS= average global subducting sediment (Plank & Langmuir, 1998). Vectors for mineral control are from Davidson et al., (2013).

The samples from the Western Gulf of Mexico have been plotted in the Dy/Dy^* vs. Dy/Yb diagram (Figure 4.9) of Davidson et al. (2013). They display a close affinity with markers for the continental crust (Taylor & McLennan, 1985; Rudnick & Fountain, 1995; Wedepohl, 1995) and average global subducting sediments (Plank & Langmuir, 1998). Samples from the Western Gulf of Mexico basement also display an affiliation with melts that have undergone amphibole or clinopyroxene fractional crystallisation. Garnet does not appear to have had an influence on the samples (Figure 4.9); this is also supported by the flat HREE trends seen in Figure 4.7.

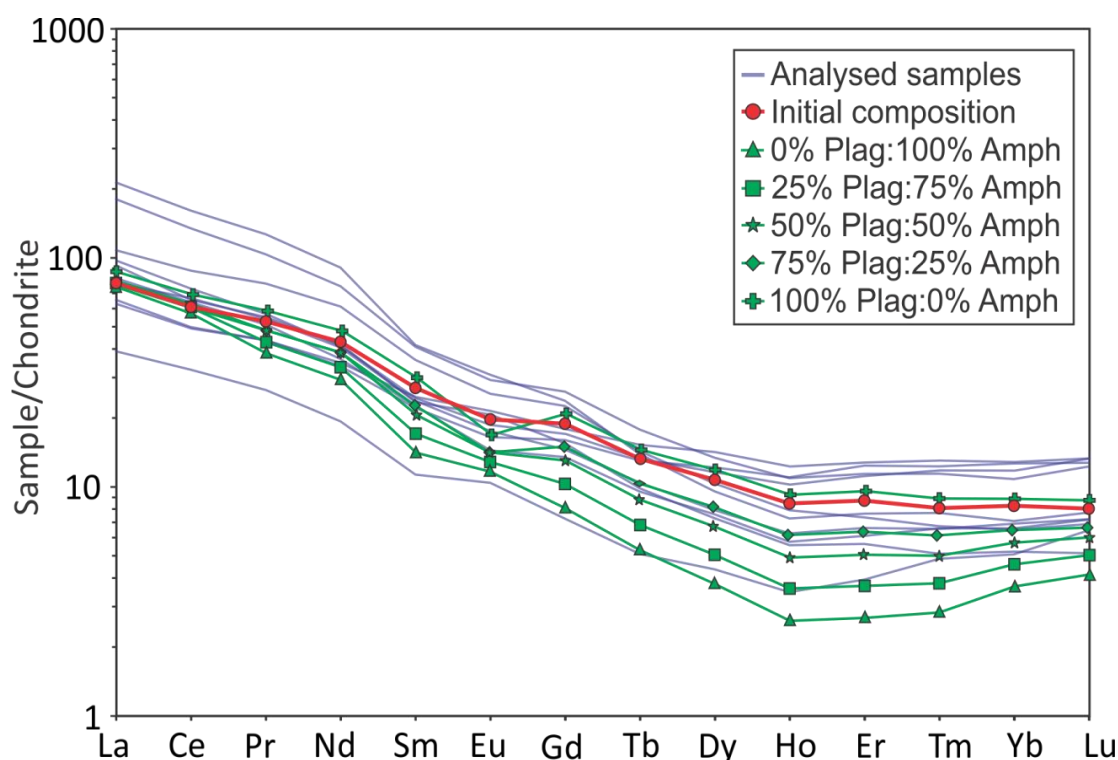


Figure 4.10. Plot showing modelled rare earth element patterns with varying degrees of amphibole and plagioclase fractionation from a magma against the rare earth element patterns for the Western Gulf of Mexico basement samples. Blue lines represent the Western Gulf of Mexico samples, green lines are the modelled patterns and the red line is the starting composition of the magma for the models, chosen from the most mafic analysed sample (Plan de las Hayas N14F6C2).

The REE element trends for the Early and Late Permian samples of the Western Gulf of Mexico have been plotted with model REE trends during varying degrees of amphibole \pm plagioclase fractionation (Figure 4.10) using the Microsoft Excel spreadsheet of Ersoy & Helvaci, (2010). The initial composition of the melt used in the models was selected from the most mafic (lowest SiO₂ and highest MgO) sample of the Western Gulf of Mexico (Plan de las Hayas N14F6C2). From altering the ratio of fractionating plagioclase and amphibole the trends observed in the MREEs of the samples can be replicated. The MREE trends in the samples are most comparable with the 100% plagioclase: 0% amphibole, 75% plagioclase: 25% amphibole, 50% plagioclase: 50% amphibole and 25% plagioclase: 75% amphibole

Chapter 4: Geochemical results for Western GoM basement

models (Figure 4.10). This indicates that the trends observed in the MREEs can be explained by varying degrees of plagioclase and amphibole fractionation. Alternatively the same trends would form if amphibole and plagioclase existed as residual phases of crustal melts. However, the models (Figure 4.10) of amphibole \pm plagioclase fractionation cannot account for the variability of the LREEs, which suggests that this variability reflects partial melting of distinct sources (or a single heterogeneous source) and/or variable assimilation of a crustal component.

4.7.2 Tectonic setting of the granitoids

Granite discrimination diagrams can be used to distinguish volcanic arc signatures from more continental signatures. In the Nb-Y diagram (Figure 4.11) the Early and Late Permian granitoids as well as the undated samples plot within the volcanic arc granites and syn-collisional granites field. Significant overlap is observed between the basement of the Western Gulf of Mexico and Permo-Triassic granitoids from in the Chiapas Massif (Weber et al., 2005; Estrada-Carmona et al., 2012) and the Colombian Cordillera (Vinasco et al., 2006; Cochrane et al., 2014) indicating that they may represent part of the same event. This plot is unable to distinguish between granites that formed in association with a volcanic arc from those formed during a syn-collisional event however.

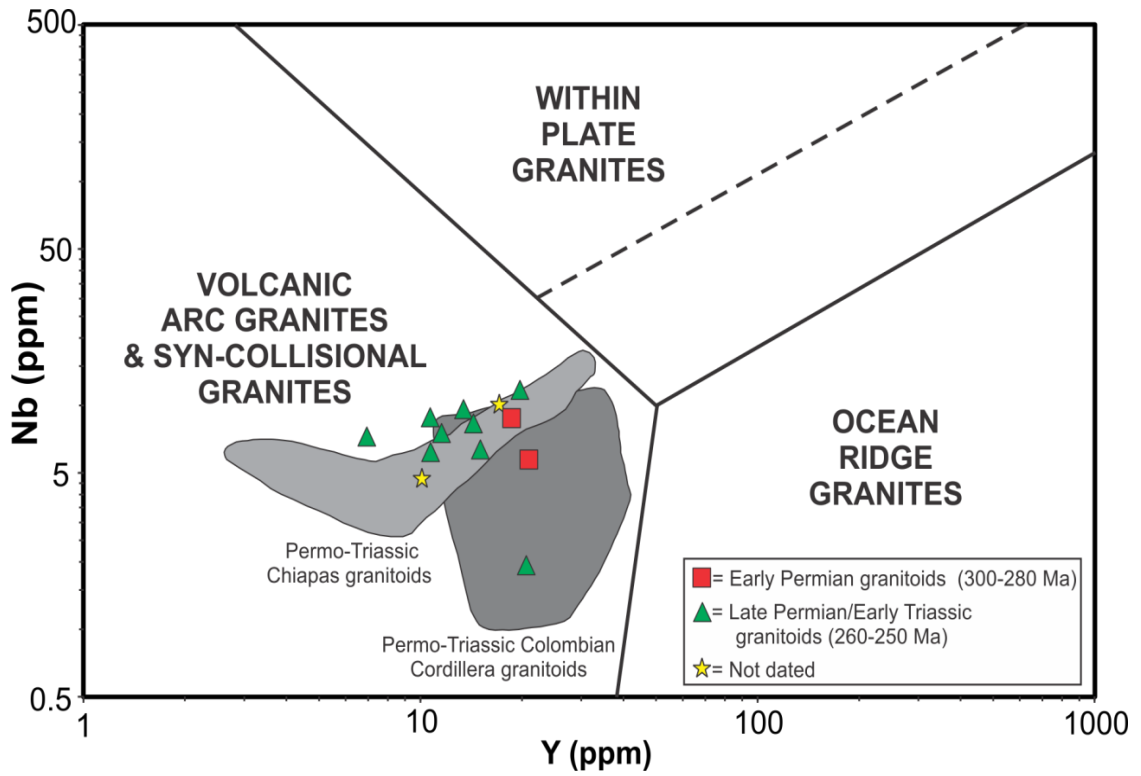


Figure 4.11. Nb vs. Y diagram of Pearce et al., (1984) for the basement granitoids of the Western Gulf of Mexico.

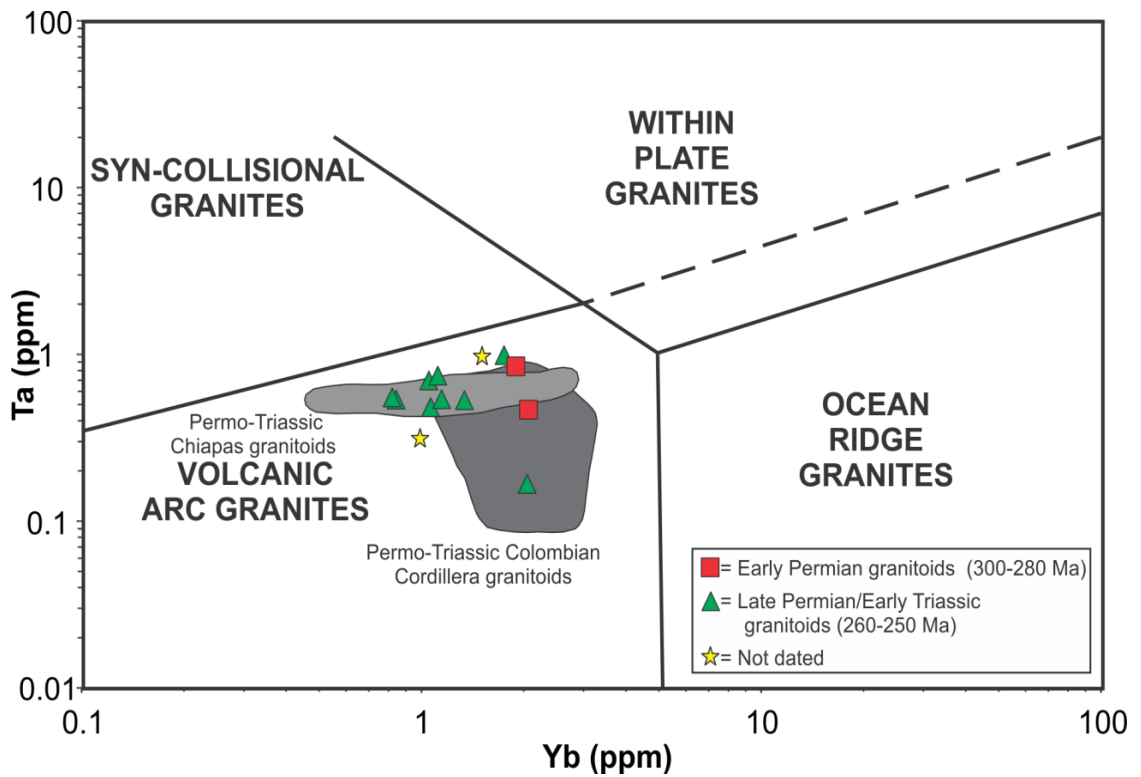


Figure 4.12. Ta vs. Yb diagram of Pearce et al., (1984) for the basement granitoids of the Western Gulf of Mexico.

Chapter 4: Geochemical results for Western GoM basement

A Ta-Yb diagram (Figure 4.12) is better able to distinguish syn-collisional granites and volcanic arc granites. The Early and Late Permian granitoids as well as the two undated samples of the Western Gulf of Mexico basement all plot within the volcanic arc granite field. The Western Gulf of Mexico basement samples overlap with the Permo-Triassic granitoids from the Colombian Cordillera and the Permo-Triassic granitoids from the Chiapas Massif.

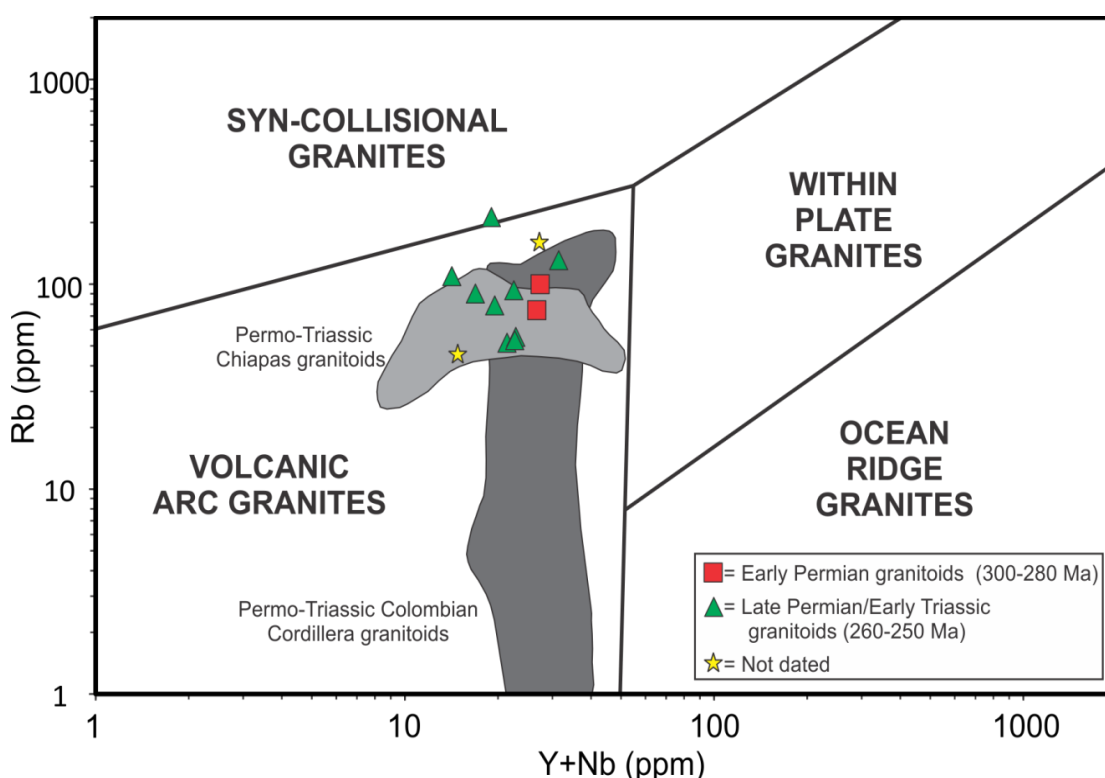


Figure 4.13. Rb vs. Y+Nb diagram of Pearce et al., (1984) for the basement granitoids of the Western Gulf of Mexico.

In the Rb vs. Y+Nb and Rb vs. Yb+Ta diagrams (Figures 4.13-4.14) the Early and Late Permian granitoids of the Western Gulf of Mexico both plot towards the upper limit of the volcanic arc field, with slight overlap into the syn-collisional granite field. There is again overlap between the Western Gulf of Mexico basement samples and the Permo-Triassic Colombian Cordillera and Chiapas Massif samples. The larger

Chapter 4: Geochemical results for Western GoM basement

spread in the results of these plots may be due to the mobility of Rb, or variable subduction/crustal inputs.

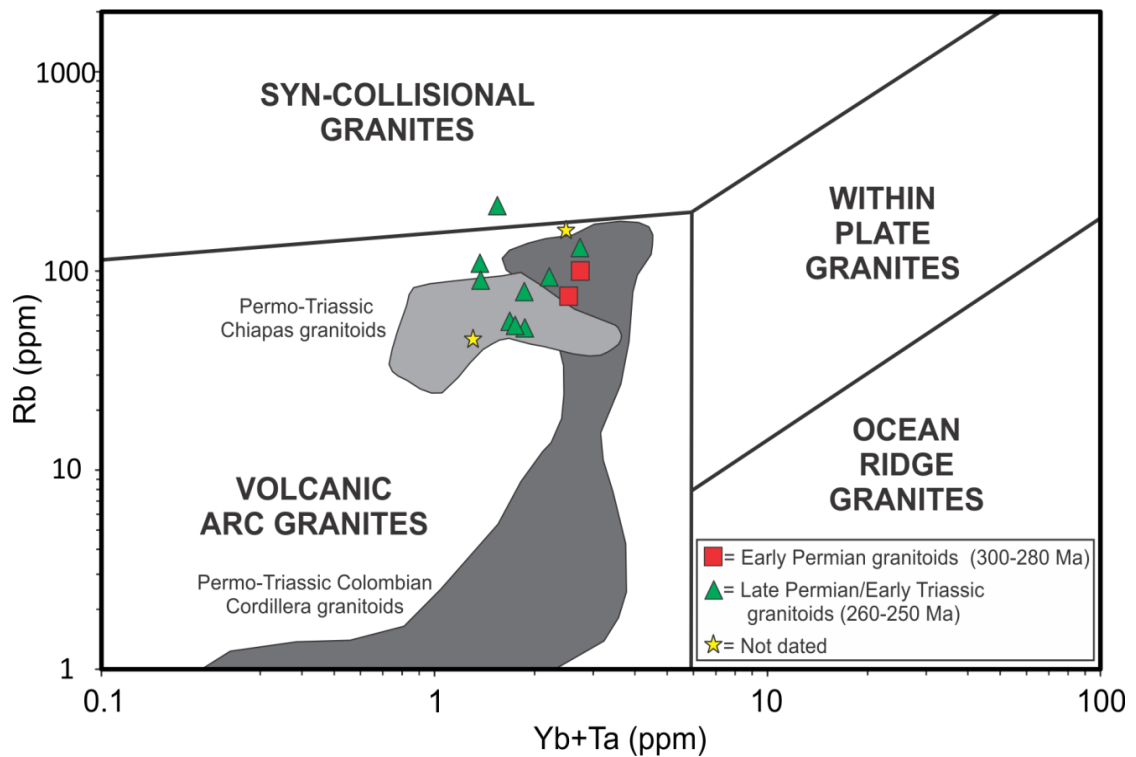


Figure 4.14. Rb vs. Yb+Ta diagram of Pearce et al., (1984) for the basement granitoids of the Western Gulf of Mexico.

The geochemical similarities observed between the Early and Late Permian basement samples from the Western Gulf of Mexico, as well as with the Permo-Triassic granitoids of the Colombian Cordillera and Chiapas Massif support the idea that these granitoids all formed as part of the same event. The trace element geochemical evidence suggest that the grantoids formed in association with a volcanic arc. Larger spread is observed in the plots that use Rb which is likely due to element mobility.

4.7.3 I vs S type granites

The alumina saturation index (ASI) can be used to distinguish between S-type and I-type granitoids (Chappell & White, 1974), and can be calculated from:

$$ASI = \frac{Al_2O_3}{Na_2O + K_2O + CaO}$$

Samples that have high ASI values (>1.1) are classified as S-type granites and those that have low ASI values (<1.1) are I-type granites.

The ASI values for the basement cores have been plotted against their U/Pb age (Figure 4.15; Chapter 3) so that the evolution of magmatism can be traced through time. The samples have been grouped according to their age and to whether inherited cores are present or not (Chapter 3). The Late Permian basement cores that do not display inheritance all have an ASI of <1.1 (mean= 0.86) which suggests that they are I-type granites (metaluminous²), either from mantle derived melts from fusion of a igneous protolith. The Early Permian basement samples that show no inheritance also have similar, typical I-type values (mean= 0.8).

The Late Permian basement samples where inherited cores are present plot more towards the S-type granite field (peraluminous³) in Figure 4.15, however the majority still have ASI values <1.1 (mean= 1.04). This may be because the samples with inherited cores have an influence from a sedimentary protolith, however this cannot be known for sure because they still predominately fall in the I-type (metaluminous) field.

² Metaluminous= [Na+K+2Ca] > [Al] > [Na+K]

³ Peraluminous= [Al] > [Na+K+2Ca]

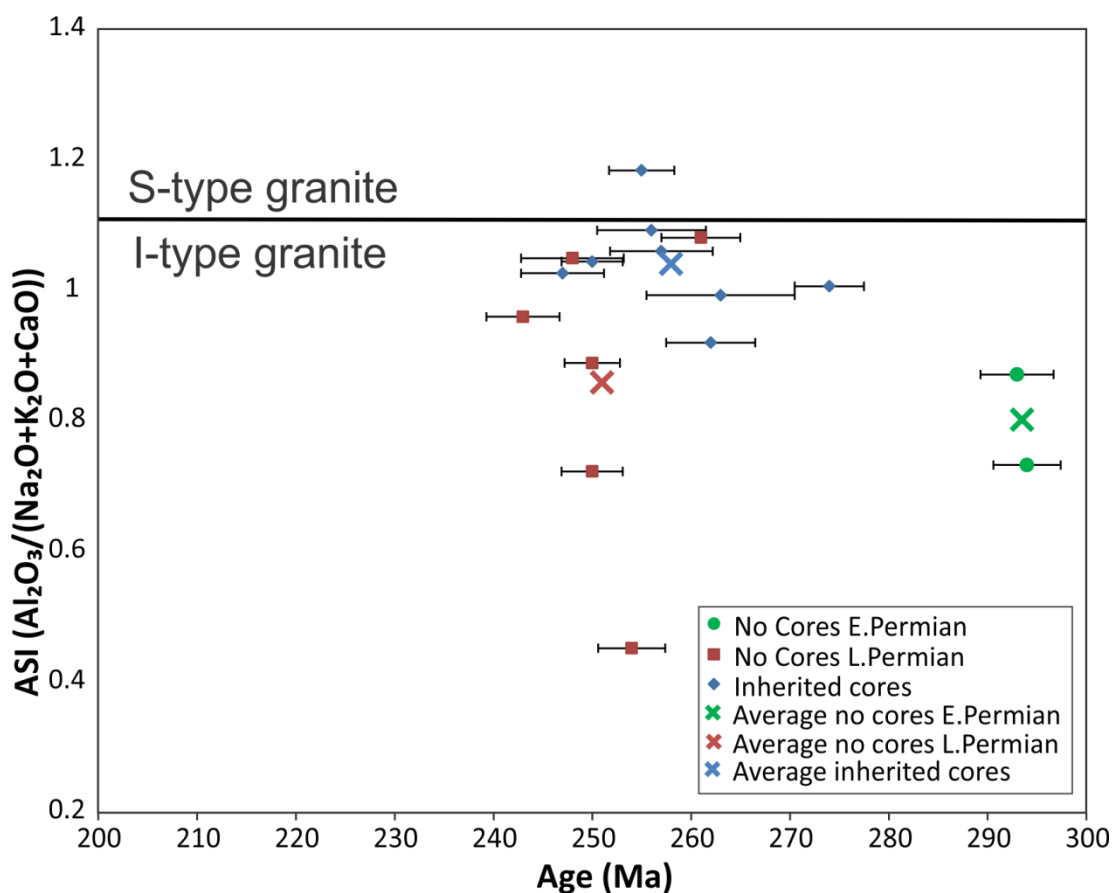


Figure 4.15. Plot showing a ASI values vs. age for the basement cores of the Western Gulf of Mexico.

The difference in magma composition (peraluminous and metaluminous), as well as temperatures that are required to form I and S type granites explain why inherited zircon cores are observed in some of the granites and not others. S-type granites form at relatively cool temperatures ($\leq 700^{\circ}\text{C}$) and are usually peraluminous in composition meaning Zr saturation is reached very quickly, therefore it is common that existing zircons are only partially dissolved (Watson & Harrison, 1983). The increased temperatures needed to form I-type granites ($800\text{-}900^{\circ}\text{C}$) as well as its metaluminous composition (Zr saturation is harder to achieve) means pre-existing zircons often are completely dissolved. The link between temperature and magma

Chapter 4: Geochemical results for Western GoM basement

composition in zircon solubility is defined in (Watson & Harrison, 1983) by the equation:

$$D \frac{\text{Zircon}}{\text{melt Zr}} = \{-3.80 - [0.85(M - 1)]\} + 12900/T$$

Where $D \frac{\text{Zircon}}{\text{melt Zr}}$ is the concentration ratio of Zr in the stoichiometric zircon, T is the temperature and M is the cation ratio $(\text{Na}+\text{K}+2\text{Ca})/(\text{Al}*\text{Si})$.

The ASI results indicate that the granitoids of the Western Gulf of Mexico basement are predominantly metaluminous (I-type) in composition, with a minor peraluminous (S-type) influence. The more peraluminous examples have preserved pre-existing zircons whereas in the metaluminous samples no inheritance is observed. It is unclear if the I-type granites are primary melts from juvenile mantle or if they derive from pre-existing igneous rocks in the crust and the zircon that was contained within them was completely dissolved in the Permian magmatism.

4.7.4 Age of magma extraction from the mantle

Determining the age at which the magmas that formed the basement of the Western Gulf of Mexico were extracted from the mantle into the crust gives a useful insight into the tectonic setting of an igneous rock. To determine the model age of mantle extraction Hf isotopes in zircons can be used. The model age of an environment that involves solely juvenile mantle derived melts should be comparable to the U/Pb zircon crystallization age (mantle extraction and zircon crystallisation occurred at similar times), whereas in an environment where crustal contamination or anatexis has occurred the Hf model age may be a lot older than the U/Pb zircon crystallisation age (Hf model age records the crustal rock that is melted

Chapter 4: Geochemical results for Western GoM basement

and the U/Pb zircon records the age of the new magma). Subduction related magmatism tends to involve mantle derived melts whereas in continental collision environments crustal anatexis is dominant. The Hf model age curves have been calculated from the following equation:

$$\frac{^{176}\text{Hf}}{^{177}\text{Hf}}(i) = \frac{^{176}\text{Hf}}{^{177}\text{Hf}}(m) - \frac{^{176}\text{Lu}}{^{177}\text{Hf}}(m) \times (e^{\lambda t} - 1)$$

i= initial concentration, *m*= measured concentration, *λ*= decay constant and *t*= time

The age of mantle extraction for a magma can be inferred from the intersection between the depleted mantle model age curve (assuming that it was extracted from a depleted mantle reservoir) and the calculated model age curve for an analysed zircon. Model age lines for the CHUR and depleted mantle were calculated using time intervals every 100 Ma and for the analysed samples every 10 Ma (Appendix E). Epsilon values have also been calculated, normalising everything to CHUR values (Bouvier et al., 2008) using the equation:

$$\epsilon_{\text{Hf}}^t = \left(\frac{^{176}\text{Hf}/^{177}\text{Hf}(\text{rock}, t)}{^{176}\text{Hf}/^{177}\text{Hf}(\text{CHUR}, t)} - 1 \right) \times 10^4$$

From the basement cores five zircons were analysed from three wells (Orizaba, Linares and Paso de Ovejas) at the Centro de Investigación Científica y de Educación Superior de Ensenada (CICESE), Mexico under the supervision of Dr. Bodo Weber. More information on the method can be found in Appendix A.

Of the three wells two yielded inherited cores of Proterozoic age (Orizaba and Paso de Ovejas) and one yielded zircons of homogeneous Permian age (Linares). It is interesting to see that all of the analysed zircons yield model ages that fall in the Proterozoic (1.47-1.9 Ga; Figures 4.16-4.17). This indicates that the magmas from

Chapter 4: Geochemical results for Western GoM basement

which the zircons crystallised did not first separate from the mantle during the Permian. Instead the magmas likely formed by fusion of pre-existing continental crustal rocks that were separated from the mantle during the Paleoproterozoic-Mesoproterozoic.

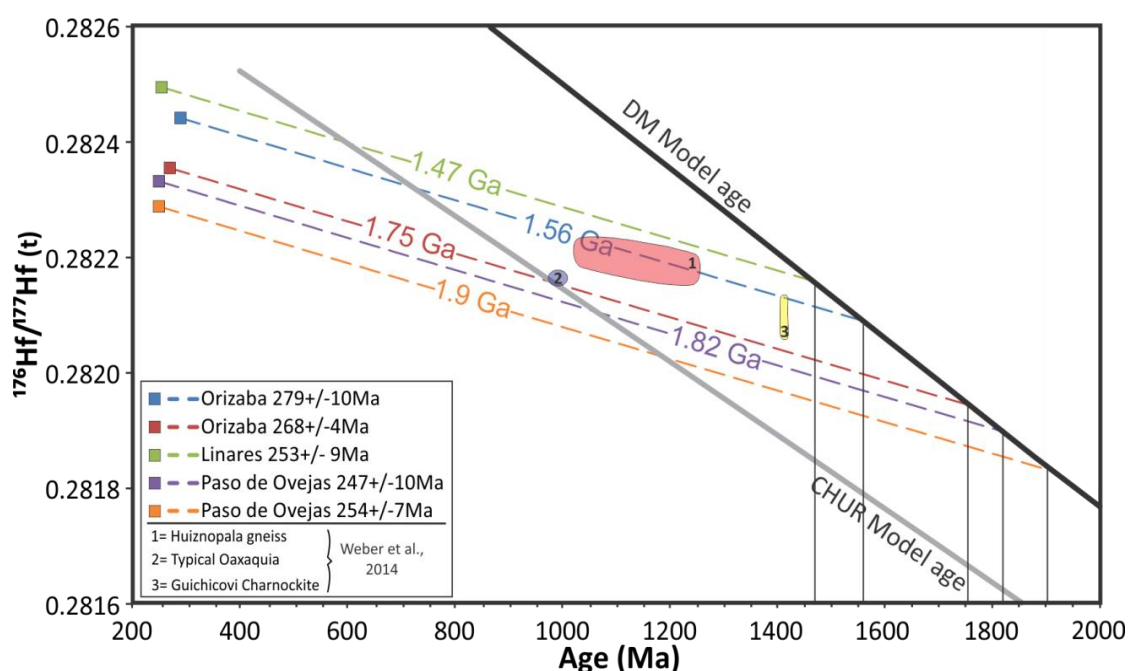


Figure 4.16. $^{176}\text{Hf}/^{177}\text{Hf}$ (t) vs age plot for the samples selected for Hf isotope analysis on zircons. Evolution lines for CHUR from Bouvier et al., (2008) and depleted model mantle from Vervoort et al., (2000). The fields represent Hf model ages for the Proterozoic continental crust in Mexico.

The youngest model age comes from a sample that displayed no evidence of inherited cores (Linares) which yields an age of 1.47 Ga. One grain from the Orizaba well yields similar results with a model age of 1.56 Ga. The likely crustal protolith is the Oaxaquia type basement which forms the backbone of continental Mexico. Although, the Hf model ages appear to be slightly older than the U/Pb igneous zircon ages of Oaxaquia continental crust (1.25-1.2 Ga; Weber et al., 2010). However, Weber et al. (2014) have proposed that the Oaxaquia crust initially formed as an ocean island arc system between 1.5-1.4 Ga from model ages obtained from the

Chapter 4: Geochemical results for Western GoM basement

Huiznopala gneiss, Guichicovi charnockite and typical Oaxaquia type crust (Figures 4.18). They suggest that zircon did not become a common mineral phase in this arc system until it began to form more differentiated magmas (1.25-1.2 Ga). This therefore indicates that the Permian basement from the Orizaba and Linares wells formed from the partial melting of Oaxaquia continental crust which separated from the mantle during the Calymmian (1.6-1.4 Ga). The second zircon analysed from the Orizaba well yields an older Hf model age (1.75 Ga; Figure 4.16-4.17). This could indicate that the source of these rocks is heterogeneous. This is supported by the large spread in the U/Pb ages of the Permian population of zircon (~300-250Ma; Chapter 3), indicating magmatism occurred over a prolonged period of time, giving opportunity for a range of different contaminants to affect the Hf isotope compositions.

The oldest zircon Hf model age from the Western Gulf of Mexico is found in the Paso de Ovejas well, yielding an age of 1.9 Ga (Figure 4.16-4.17). This is comparable to results of Late Permian granitoids reported from Southern Mexico (Figure 4.17; Ortega-Obregon et al., 2014). In the study of Ortega-Obregon et al. (2014) the older model ages are attributed to either Laurentia-derived Paleoproterozoic detritus (Arvizu & Iriondo, 2011) found in the Sonora area of Mexico or alternatively Gondwana-derived Paleoproterozoic belts e.g., Rio Negro-Juruena, Rodinia-San Ignacio Provinces (Bettencourt et al., 2010; D'Agrella-Filho et al., 2012). The 1.9 Ga model age from the Paso de Ovejas well is however also at the upper limit of values for Oaxaquia continental crust from Weber et al. (2010), which seems more likely to be the likely protolith (Figure 4.17).

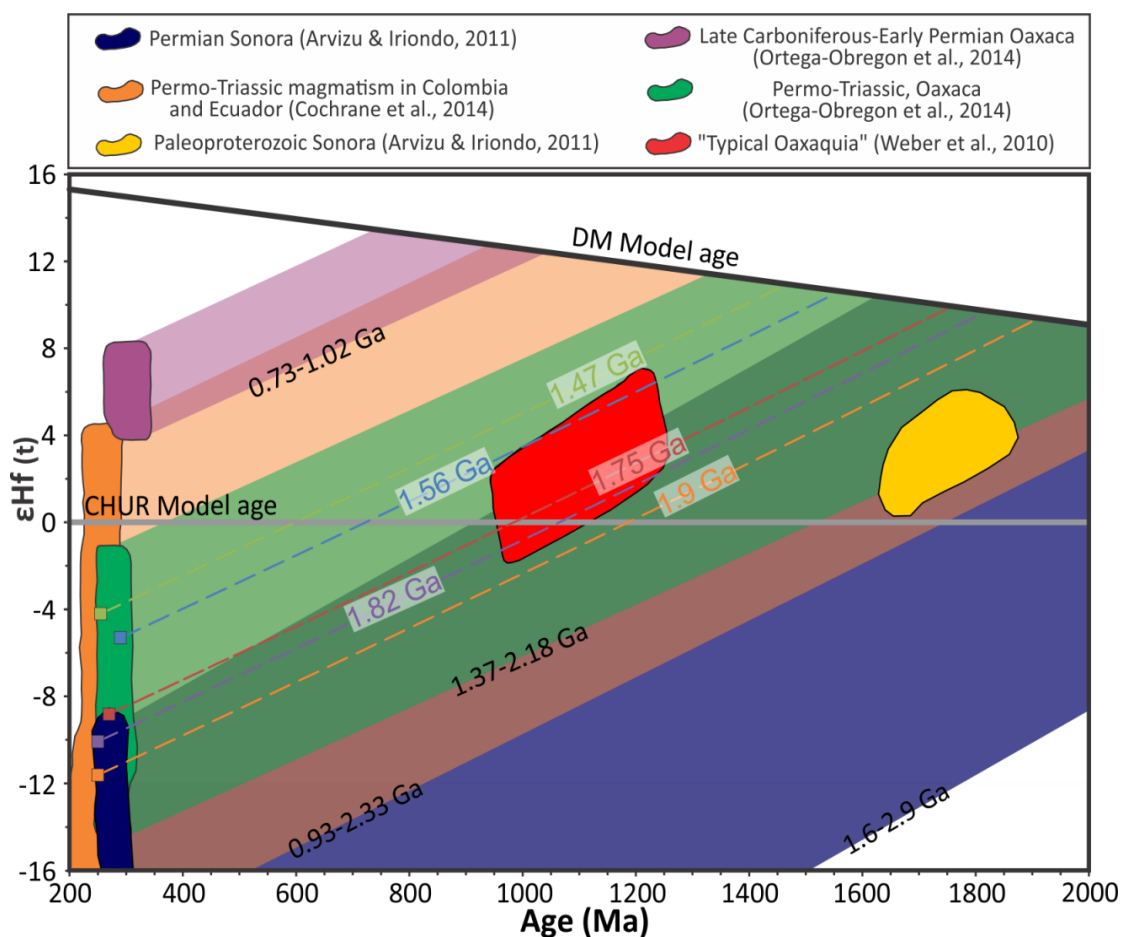


Figure 4.17. $\epsilon_{\text{Hf}}(t)$ vs age plot for Western Gulf of Mexico samples selected for Hf isotope analysis on zircons (TIMS). Our results have been compared to other LA-ICP-MS data from around Mexico, Colombia and Ecuador. Intercept between $\epsilon_{\text{Hf}}(t)$ and the depleted mantle curve based on a $^{176}\text{Lu}/^{177}\text{Hf}$ average crustal ratio of 0.015 (Griffin et al., 2002). Values for CHUR are from Bouvier et al., (2008). The fields represent zircon Hf model ages from Permo-Triassic granitoids in Mexico, Ecuador and Colombia as well as for older igneous events such as the Paleoproterozoic Sonora and Oaxaquia continental crust.

Overall it is apparent that the basement cores from the Western Gulf of Mexico are largely influenced by a crustal component. This crustal component appears to relate to Oaxaquia type continental crust. The lack of mantle derived melts in the Permian igneous event suggests that the rocks formed from crustal anatexis rather than mantle derived magmatism.

In Late Carboniferous-Early Permian granitoids of the Oaxaca area, Southern Mexico (Ortega-Obregon et al., 2014) the Hf model ages (0.78-1.04 Ga) are younger

Chapter 4: Geochemical results for Western GoM basement

than the Oaxaquia continental crust that they are intruding, but older than the obtained U/Pb zircon crystallisation age (Figure 4.17). This has been interpreted to represent mixing between a mantle derived melt and the Oaxaquia continental crust that it is intruding (Ortega-Obregon et al., 2014). Geochronological similarities suggest these granitoids are related to the Early Permian examples found in the Western Gulf of Mexico but unfortunately Hf model ages for the Early Permian granitoids of the Western Gulf of Mexico were unable to be obtained to test this hypothesis.

Later, Permo-Triassic granitoids of the Oaxaca area yield results that are comparable to the Permo-Triassic samples from the Western Gulf of Mexico (this study), with Hf model ages that overlap the Oaxaquia continental crust that they are intruding, as well as an unknown apparently older crustal source (Figure 4.17; 1.37-2.18 Ga). However, there is also a slight indication of mantle-crustal mixing with some results yielding Hf model ages younger than Oaxaquia.

Results from Cochrane et al., (2014) on Hf isotopes in zircons from Permo-Triassic granitoids of the Ecuadorian and Colombian Cordilleras (Figure 4.17) yield model ages between 0.93-2.33 Ga. A large proportion of the model ages coincide with the Proto-Oaxaquia and Oaxaquia type crust. The younger model ages could represent a mixing of Permian juvenile magma and older crust, as is proposed for the Late Carboniferous-Early Permian granitoids of Oaxaca, Southern Mexico (Ortega-Obregon et al., 2014). The older, Palaeoproterozoic model ages could derive from a Gondwanan source other than Oaxaquia, such as the Rio Negro-Juruena, Rodinia and San Ignacio Provinces (Bettencourt et al., 2010; D'Agrella-Filho et al., 2012).

Chapter 4: Geochemical results for Western GoM basement

Permo-Triassic granitoids of the Sonora area of Northeast Mexico yield Hf model ages of 1.6-2.9 Ga (Figure 4.17; Arvizu and Iriondo, 2011). There is overlap between the Permo-Triassic Hf model ages and the Palaeoproterozoic crust that they intrude, indicating strong crustal signatures. There also appears to be influence from an unknown Archaean crustal signature. Hf model ages that are younger than the Palaeoproterozoic crust can be interpreted as representing mantle-crustal mixing.

In summary, the Late Carboniferous-Early Permian granitoids of the Oaxaca area (Ortega-Obregon et al., 2014) display evidence for mantle-crustal mixing and appear unrelated to the Late Permian-Early Triassic granitoids of the Western Gulf of Mexico. Conversely, overlap is observed in the Hf model ages of the Permo-Triassic granitoids of the Western Gulf of Mexico (this study) and Permo-Triassic granitoids from the Sonora, Northeast Mexico (Arvizu and Iriondo, 2011), Oaxaca area of Southern Mexico (Ortega-Obregon et al., 2014) and Colombia and Ecuador (Cochrane et al., 2014), which all indicate strong crustal signatures. However, the Permo-Triassic granitoids of Sonora, Oaxaca, Colombia and Ecuador also display evidence for mantle-crustal mixing which is not seen in the Permo-Triassic granitoids of the Western Gulf of Mexico.

However, a concerning aspect of the LA-ICP-MS data of Cochrane et al. (2014), Ortega-Obregon et al. (2014) and Arvizu and Iriondo (2011) is the large amount of spread that is found in the results. These data were collected by analysing numerous zircons per granitoid, with Hf model ages being calculated from each datum point. The problem with this method is that any erroneous analysis can have

a major impact on the calculated model age and therefore the interpretation of tectonic setting.

4.7.5 Refined LA-ICP-MS results

In order to filter out anomalous LA-ICP-MS results, from Mexico and Colombia, the median value has been calculated from individual datum points in an analysed rock sample (Appendix E). The median averaging value was chosen due to its effectivity at disregarding outlying results. Once this filtering process had been done on the LA-ICP-MS data from Arvizu & Iriondo (2011), Ortega-Obregon et al. (2014) and Cochrane et al. (2014) the spread in the results was greatly reduced (Figure 4.18). The samples taken from Sonora, Northeast Mexico no longer display Hf model ages older than the Palaeoproterozoic crust that they intrude but instead show evidence for magmatism that formed from/strongly assimilated the continental crust, as well as from mixing of mantle derived melt and continental crust (Figure 4.18). The same mantle-crustal mixing signatures are observed in the Permo-Triassic granitoids from Colombia and Ecuador (Figure 4.18; Cochrane et al., 2014), as well as the Late Carboniferous-Early Permian graintoids from Southern Mexico (Figure 4.18; Oretaga-Obregon et al., 2014). The Permo-Triassic granitoids of Southern Mexico (Ortega-Obregon et al., 2014) now display strong correlations to the Permo-Triassic granitoids of the Western Gulf of Mexico (this study). These yield Hf model ages that are inherited from the Oaxaquia continental crust that they intrude, with very little evidence for any influence from a mantle derived melt (Figure 4.18). It is therefore apparent that the Permo-Triassic magmatism from the Western Gulf of Mexico and Southern Mexico formed solely from crustal anatexis,

Chapter 4: Geochemical results for Western GoM basement

whereas the Late Carboniferous-Early Permian granitoids of Southern Mexico and the Permo-Triassic granitoids of Sonora, Colombia and Ecuador display evidence for a mantle derived melt that assimilated continental crust.

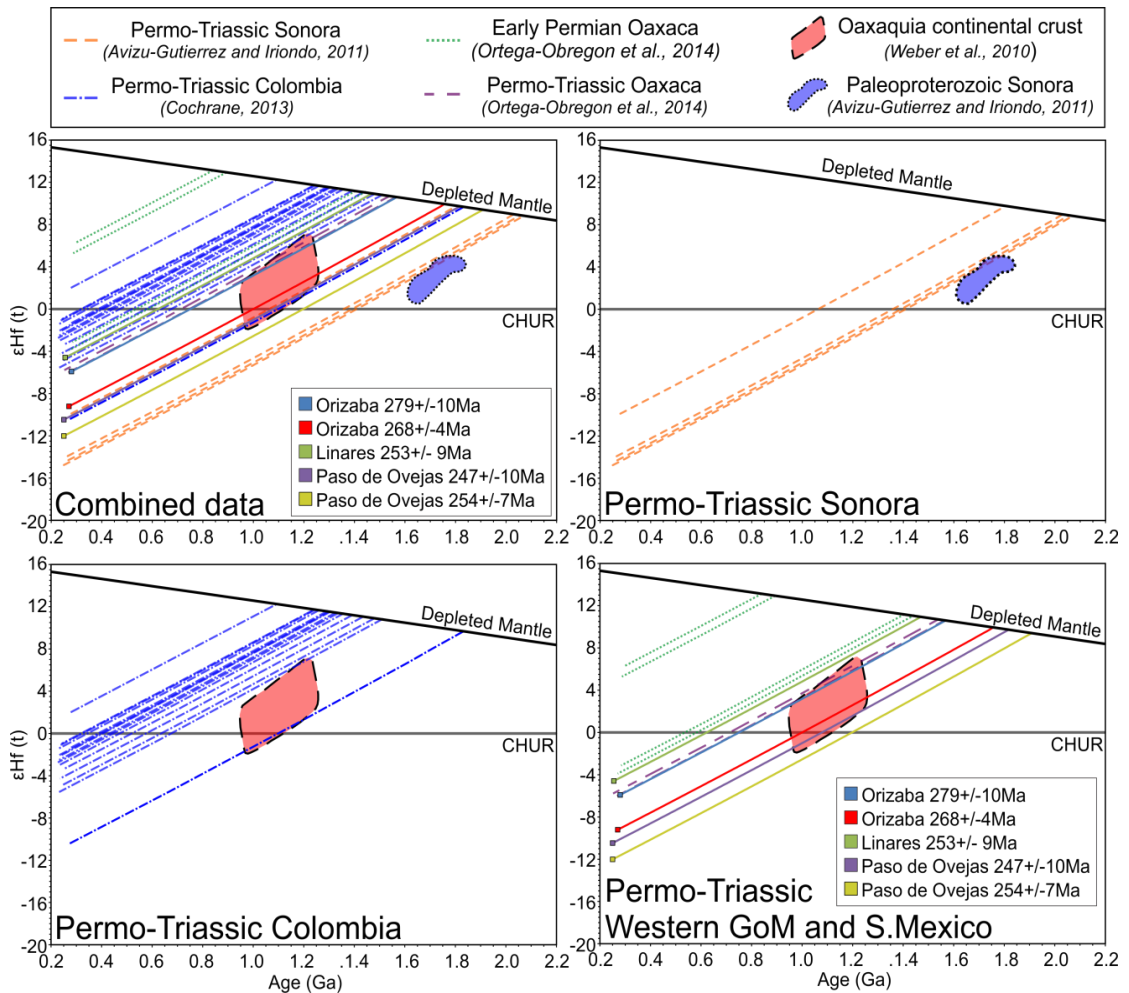


Figure 4.18. $\epsilon_{\text{Hf}}(t)$ vs age plot for the Western Gulf of Mexico samples selected for Hf isotope analysis on zircons. Median values for the LA-ICP-MS data have been taken to reduce the effects of anomalous data points.

The trace element signatures and Hf model ages for the Late Carboniferous-Early Permian granitoids of the Oaxaca area, Southern Mexico (Ortega-Obregon et al., 2014) and Permo-Triassic granitoids of Sonora (Arvizu & Iriondo, 2011), Ecuador and Colombia (Cochrane et al., 2014) are consistent with rocks that formed in

Chapter 4: Geochemical results for Western GoM basement

association with a continental arc, whereby mantle derived melts interact with and assimilate continental crust.

However, the Permo-Triassic granitoids of the Western Gulf of Mexico (this study) and the Oaxaca area (Ortega-Obregon et al., 2014), although displaying arc like trace element signatures, yield Hf model ages that solely indicate crustal anatexis. This type of magmatism is not consistent with a continental arc environment, but instead is more typical of collisional magmatism. However, they do not appear to be related to syn-collisional magmatism, as we would expect to be able to distinguish them from volcanic arc granitoids in the tectonic discrimination diagrams (Figure 4.11-4.14) and to see evidence for deformation, which we do not (petrography in Chapter 3). Post-collisional magmatism on the other hand cannot be identified using the discrimination diagrams of Pearce et al. (1984) as their trace element concentrations are controlled by the tectonic setting that was active prior to the collision (Pearce et al., 1984 and 1996a). Meaning if an arc existed prior to the post-collisional magmatism then the trace element concentrations would inherit arc like signatures from the continental crust. Therefore, the Permo-Triassic granitoids of the Western Gulf of Mexico (this study) and Oaxaca (Ortega-Obregon et al., 2014) can be interpreted to have formed in a post-collisional tectonic setting that has inherited arc like trace element signatures from fusion of the Oaxaquia continental crust that they also intrude and possibly also from the Late Carboniferous-Early Permian arc mentioned above.

4.8 Summary

- The Late Carboniferous-Early Permian granitoids of the Oaxaca area (Ortega-Obregon et al., 2014), and also likely the Early Permian granitoids of the Western Gulf of Mexico (this study) can be linked to a continental arc system that involved the extraction of mantle derived melts that assimilated Gondwanan derived Oaxaquia continental crust.
- A later episode of Permo-Triassic arc magmatism can be found in Sonora, Northeast Mexico (Arvizu and Iriondo, 2011) which assimilates Palaeoproterozoic Laurentian crust and also in Colombia and Ecuador (Cochrane et al., 2014) which assimilates Gondwanan derived Oaxaquia crust.
- Permo-Triassic granitoids of the Western Gulf of Mexico (this study), Oaxaca (Ortega-Obregon et al., 2014) and Chiapas (Weber et al., 2005) appear to have formed as a result of crustal anatexis in association with post-collisional magmatism. This event inherited arc like trace element signatures from Oaxaquia continental crust and possibly the Late Carboniferous-Early Permian arc mentioned above.

5 Petrogenesis of the Permo-Triassic Basement

5.1 Introduction

The geochemical results of Chapter 4 indicate that the basement of the Western Gulf of Mexico is associated with both arc magmatism, as well as post-collisional anatectic magmatism. The U/Pb geochronology results of Chapter 3 suggest the arc magmatism represents an older igneous phase (Early Permian), with the more prevalent post-collisional anatectic magmatism following in the Late Permian-Early Triassic. Geochemical data from Late Carboniferous-Early Triassic granitoids from Southern Mexico (Oaxaca area and Chiapas Massif) are compositionally similar to the Western Gulf of Mexico, indicating a comparable evolutionary history. Permo-Triassic granitoids from Northeast Mexico (Sonora) and Colombia on the other hand appear to have formed in a tectonic environment separate from granitoids of the same age in the Western Gulf of Mexico and Southern Mexico. This chapter will explore possible links between the Carboniferous-Triassic granitoids of the Western Gulf of Mexico and Southern Mexico with the formation of Pangaea, in order to define a viable tectonomagmatic model.

5.2 Petrogenesis of the Western Gulf of Mexico

5.2.1 Relation to the formation of Pangaea

As reviewed in detail in Chapter 2, the formation of Pangaea occurred diachronously from east to west during the Late Paleozoic. In Southern USA and Mexico it is thought that deformation initiated during the Late Carboniferous-Early

Chapter 5: Petrogenesis of the Western Gulf of Mexico

Permian, with the Laurentia-Gondwana collision occurring ca. 290-280 Ma (Pindell and Dewey, 1982; Pindell, 1985; Ross, 1986; Sedlock et al., 1993; Dickinson and Lawton, 2001; Talavera-Mendoza et al., 2005; Vega-Granillo et al., 2007 and 2009). The high pressure metamorphic suite of the Acatlán Complex (Mixteca terrane, Southern Mexico) is believed to represent the suture between Laurentia and Gondwana (Chapter 2; Talavera-Mendoza et al., 2005; Vega-Granillo et al., 2007 and 2009), which would mean the adjacent Gondwanan derived magmatism of the Oaxaca area and the Western Gulf of Mexico formed very close to the Pangaea suture.

The apparent proximity the granitoids of the Western Gulf of Mexico and Southern Mexico have to the Laurentia-Gondwana suture and also the geochronological correlations they have with the amalgamation of Pangaea indicates the magmatism may be related to the final stage of supercontinent formation.

5.2.2 Episodes of magmatism

The U/Pb zircon geochronology presented in Chapter 3 indicates that the Permo-Triassic magmatic basement of the Western Gulf of Mexico likely formed in discrete phases. The geochemistry of Chapter 4 suggests that these phases of magmatism are linked to plutonic rocks of comparable age in the Oaxaca area (Ortega-Obregon et al., 2014) and the Chiapas Massif (Weber et al., 2005). The probability density diagram (Figure 5.1) shows that the first phase of magmatism occurred between ~311-286 Ma, although inherited cores found in the Western Gulf of Mexico granitoids (Chapter 3) indicate that it may stretch back to ~326 Ma. Trace element signatures suggest this phase of magmatism formed in a continental arc

environment (Chapter 4). This interpretation is consistent with the Hf model ages for the Late Carboniferous-Early Permian granitoids of the Oaxaca area (Ortega-Obregon et al., 2014), that indicate the granitoids formed from mantle derived melts mixing with continental crust (Chapter 4). This arc system intrudes into Oaxaquia continental crust, indicating an affinity with the supercontinent Gondwana.

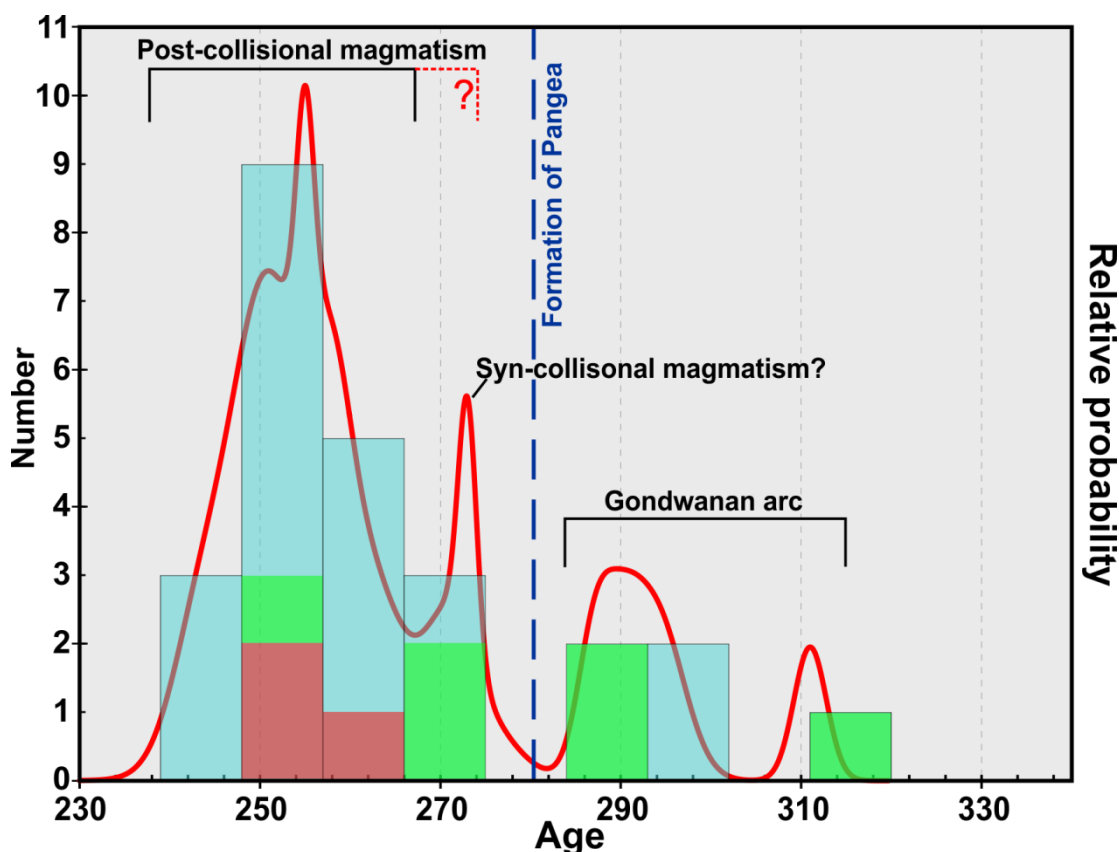


Figure 5.1. Age probability density plot for the granitoids of the Western Gulf of Mexico (blue; this study), the Oaxaca area (green; Ortega-Obregon et al, 2014) and Chiapas Massif (red; Weber et al., 2005).

Ortega-Obregon et al. (2014) have associated this Late Carboniferous-Early Permian arc with the eastward subduction of the Palaeo-Pacific Ocean. However, as highlighted in Section 5.2.1, this area of Mexico likely represents the Northwest edge of Gondwana prior to the final amalgamation of Pangaea ca. 290-280 Ma (Ross, 1986). Therefore the Late Carboniferous-Early Permian arc is perhaps better

Chapter 5: Petrogenesis of the Western Gulf of Mexico

explained by the subduction of the Rheic Ocean beneath Gondwana, prior to the formation of Pangea (Figure 5.2 A and Figure 5.4). The arc system shut down as the Gondwana-Laurentia continental collision took place ca. 286 Ma (this study). This supports observations from the Marathon segment of the Laurentia-Gondwana orogenic belt that places the collision in the Early Permian ca. 290-280.Ma (Ross, 1986).

A later Permo-Triassic phase of magmatism is also recorded in the basement of the Western Gulf of Mexico (Figure 5.1). The trace element signatures for this magmatism again suggest forming in with a continental arc environment. However, Hf model ages do not support this hypothesis, suggesting instead the magmatism is due to crustal anatexis, with no evidence of mantle derived melts (Chapter 4). This type of magmatism is more commonly associated with continental collisions. The same geochemical signatures can be seen in Late Permian-Early Triassic granitoids of the Oaxaca area (Ortega-Obregon et al., 2014) , as well as the Chiapas Massif (Weber et al., 2005; Estrada-Carmona et al., 2012), suggesting they formed in the same tectonic setting.

Post-collisional granitoids often inherit arc like trace element signatures from previous subduction events (e.g. Pearce et al., 1984; Grimes et al., 2015). It is therefore possible that the arc trace element signatures observed in the Permo-Triassic basement of the Western Gulf of Mexico were inherited from the Late Carboniferous-Early Permian arc and Oaxaquia continental crust. This hypothesis is strengthened by the widespread Oaxaquia and Late Carboniferous-Early Permian zircon inheritance observed in the Late Permian-Early Triassic igneous event

Chapter 5: Petrogenesis of the Western Gulf of Mexico

(Chapter 3). This period of post-collisional magmatism occurred between 274 and 248 Ma (Figure 5.1). It is possible that the earliest pulse of the Late Permian-Early Triassic magmatism represents a separate phase of magmatism (Figure 5.1), possibly relating to a syn-collisional phase. However, there is no geochemical evidence or deformation observed in the granitoids to support this hypothesis. The Late Permian-Early Triassic granitoids of the Western Gulf of Mexico and Southern Mexico can therefore be interpreted as having formed during a post-collision magmatic event close to the collision zone between Gondwana and Laurentia, after the final amalgamation of Pangaea (Figure 5.2 A and Figure 5.5). Post-collisional magmatism is thought to occur through a combination of delamination of the lithospheric mantle and melting of the lower continental crust during a period of thermal relaxation following collision e.g. Western Anatolia for an alternative example (Dilek & Altunkaynak, 2007).

Permo-Triassic granitoids found in the Sonora area of Northeast Mexico (Arvizu & Iriondo, 2009) and in Colombia (Cochrane et al., 2014) appear distinct from the Permo-Triassic granitoids of the Western Gulf of Mexico and Southern Mexico, with Hf model ages more typical of continental arcs. This magmatism can therefore be interpreted as forming in an arc environment, likely associated with the subduction of the Palaeo-Pacific beneath Pangaea (Figure 5.2 A).

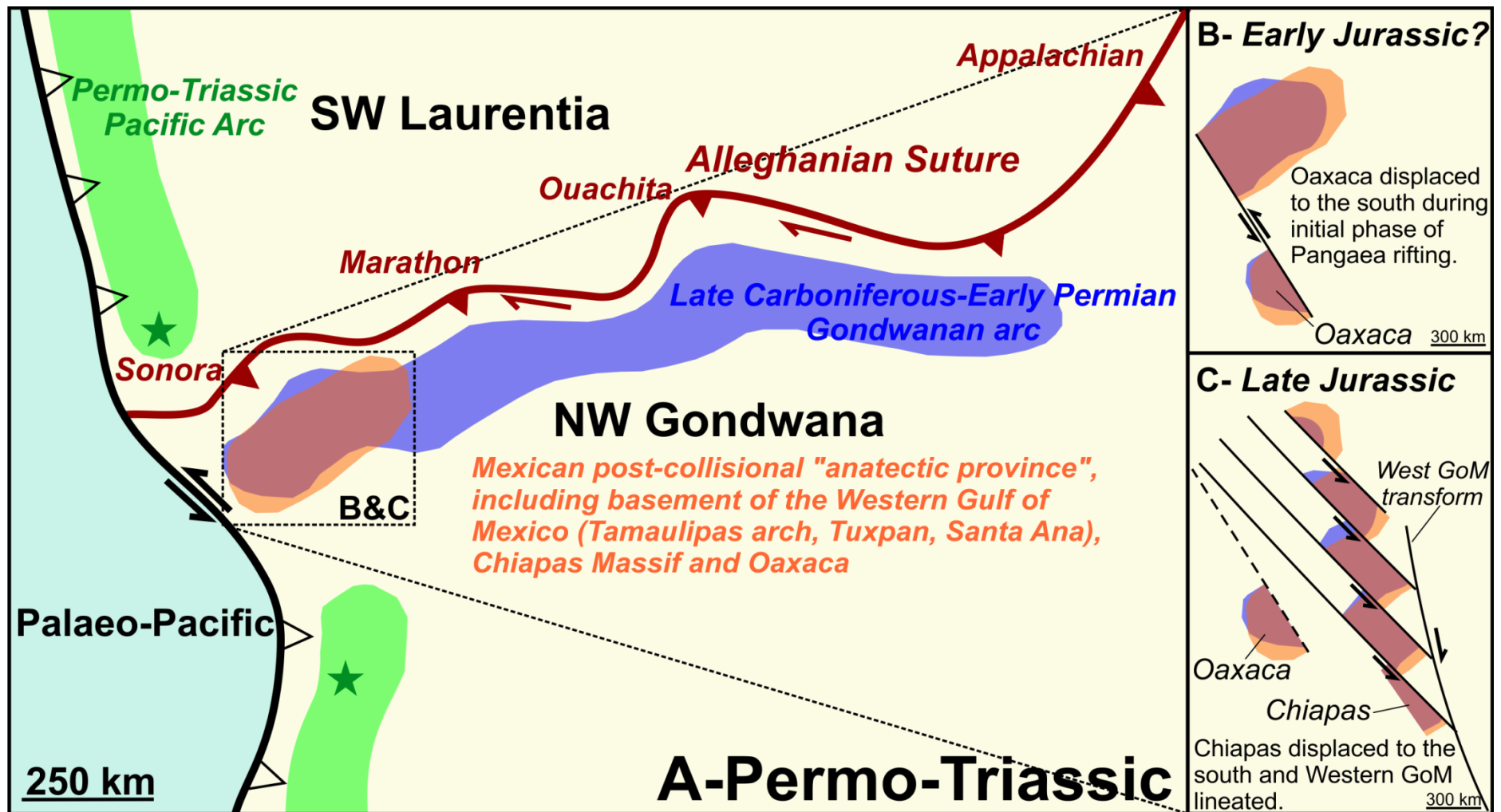


Figure 5.2. A) Schematic palaeogeographic reconstruction of the western flank of the Pangaea collision zone. The green stars represent magmatism related to a continental arc in Sonora (Laurentian side) and Colombia (Gondwanan side). B and C represent phases of shearing in the Permo-Triassic anatectic province.

5.2.3 Terrane migration

In many models of Pangaea, overlap is observed between central and southern Mexico and Northwest South America (Pindell and Dewey, 1982; Pindell, 1985; Handschy et al., 1987; Pindell and Kennan, 2001), indicating the terranes of central and southern Mexico are allochthonous in origin. This implies that the Carboniferous-Triassic plutons of the Oaxaca area (Ortega-Obregon et al., 2014), as well as the suture related HP metamorphic rocks of the Acatlán Complex (Talavera-Mendoza et al., 2005; Vega-Granillo et al., 2007; Vega-Granillo et al., 2009), may have migrated from elsewhere.

One possible mechanism for terrane migration occurred during the Early Jurassic in association with the early stages of the opening of the Gulf of Mexico, along the Mojave-Sonora Megashear (Anderson and Schmidt, 1983; Böhnel, 1999; Pindell and Kennan, 2001). This shear zone is proposed to have accommodated 700 km of left lateral motion along the southwestern flank of the North American Plate (Anderson and Schmidt, 1983; Pindell and Kennan, 2001; Pindell and Kennan, 2009). In this scenario the terranes of central and southern Mexico (including the Mixteca and Oaxaca terranes) originate in Northeast Mexico. Other studies place the timing of shearing during the Permo-Triassic (California-Coahuila transform of Dickinson and Lawton, 2001), arguing that the amount of Jurassic shear proposed by Anderson and Schmidt, (1983) has been overestimated (based on palaeomagnetic data on Lower-Middle Jurassic strata; Molina Garza & Geissman, 1999).

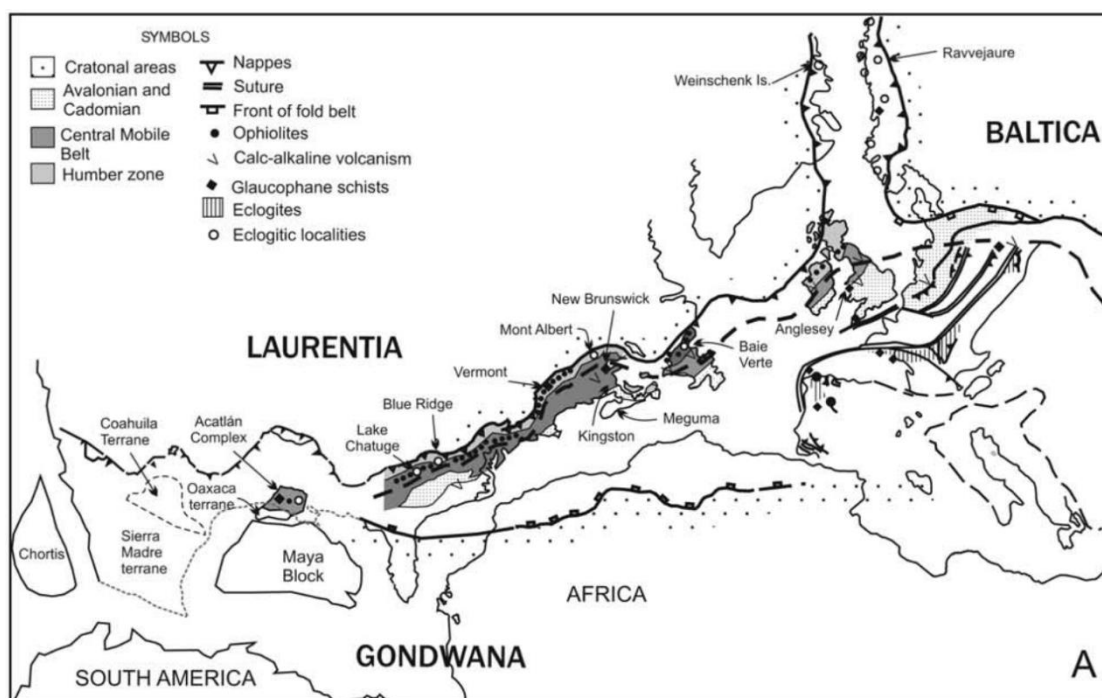


Figure 5.3. Palaeogeographic model for Pangea from Vega-Granillo et al. (2009), with the Acatlán Complex lying above the Maya block and location of main belts of the Appalachian-Caledonian orogen (Appalachian region modified from Neugebauer [1989])

An alternative allochthonous model for the southern terranes associates the migration with the rotational extension during the main phase of the opening of the Gulf of Mexico (Vega-Granillo et al., 2007 & 2009). In this model the Oaxaca and Mixteca terranes of Southern Mexico were initially positioned above the Maya block, supported by correlations in lithological suites, metamorphic-magmatic events, deformational phases and geochemical signatures with the Appalachian chain of eastern North America (Figure 5.3; Vega-Granillo et al., 2007 & 2009). However, the viability of such a model was questioned by Keppie et al., (2009), who disputed the age correlations between events of the Acatlán Complex and the Appalachians. They also argue that palaeomagnetic data from Southern Mexico (Fang et al., 1989; Molina-Garza et al., 1992; Alva-Valdivia et al., 2002) is inconsistent with such a

hypothesis. However, the reliability of this palaeomagnetic data has since been questioned (Vega-Granillo et al., 2009).

The evidence for a NE-SW migration of the Southern Mexican Mixteca and Oaxaca terranes in association with either the Permo-Triassic California-Coahuila transform (Dickinson and Lawton, 2001) or Jurassic Mojave-Sonora Megashear (Anderson and Schmidt, 1983; Böhnel, 1999; Pindell and Kennan, 2001) appears to outweigh that of a rotational translation during the opening of the Gulf of Mexico (Vega-Granillo et al., 2007; Vega-Granillo et al., 2009). For this reason, a model where the HP metamorphic rocks of the Acatlán Complex (Mixteca terrane) and the Carboniferous-Triassic plutons of the Oaxaca terrane have migrated from Northeast Mexico is favoured (Figure 5.2 B).

However, the opening of the Gulf of Mexico does appear to have displaced the Chiapas Massif portion of the Permo-Triassic anatectic province. As the Maya block rotated to the south along the Western Gulf of Mexico transform fault it is likely to have pulled the Chiapas Massif down with it (Figure 5.2 C). This migration of the Maya block may have also fragmented the Permo-Triassic anatectic province, causing the lineated trend that is now seen in the Permo-Triassic basement of the Western Gulf of Mexico today (Figure 5.2 C).

5.2.4 Gondwanan arc (Figure 5.4)

- During the Late Carboniferous-Early Permian (ca. 326-286 Ma) a continental arc formed on the Oaxaquia continental crust, on the Northwest flank of Gondwana.

Chapter 5: Petrogenesis of the Western Gulf of Mexico

- This continental arc formed in association with the subduction of the Rheic Ocean beneath Gondwana, prior to the formation of Pangaea.
- The arc system shut down when the Rheic Ocean was consumed and continental collision between Laurentia and Gondwana followed ca. 286 Ma, marking the formation of Pangaea.
- These arc rocks can be found in the basement of the Western Gulf of Mexico and the Oaxaca area of Southern Mexico (Cuanana pluton, Honduras batholith and Zaniza batholith; Figure 2.2).

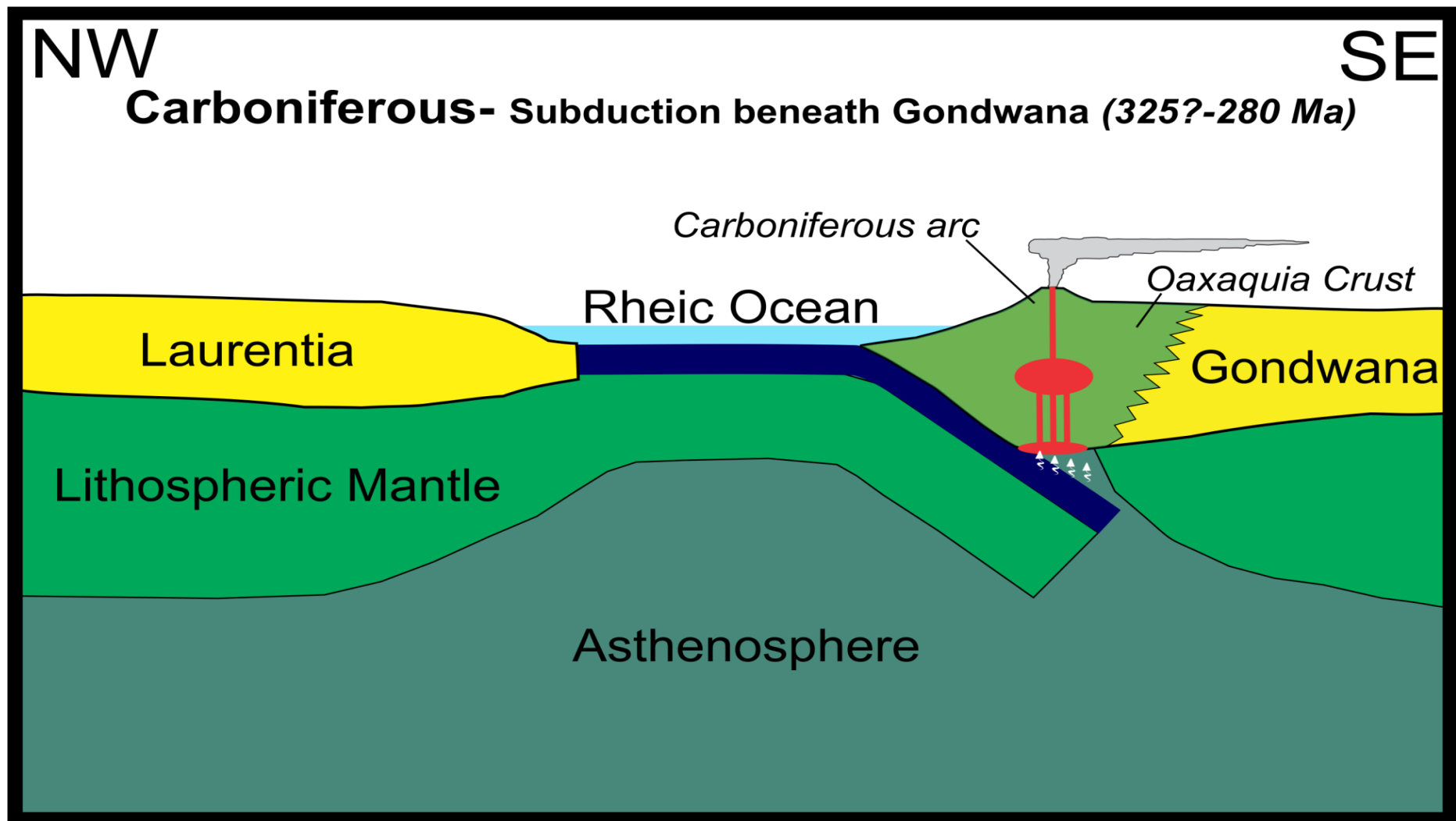


Figure 5.4. Schematic evolutionary model for the basement of the Western Gulf of Mexico prior to the formation of Pangaea.

5.2.5 Post-collisional magmatism (Figure 5.5)

- After the final amalgamation of Pangaea, a post-collision phase of magmatism occurred on the Gondwana side of the collision zone ca. 274-248 Ma.
- This post-collisional magmatism involved the Grenvillian-age Oaxaquia continental crust, as well as the Late Carboniferous-Early Permian continental arc.
- The post-collisional magmatism is the most voluminous event recorded in the basement of the Western Gulf of Mexico (this study) and can also be found in the Oaxaca area (Ortega-Obregon et al., 2014) and Chiapas Massif (Weber et al., 2005).
- Portions of the granitoids generated from this period of post-collisional magmatism appear to have been subsequently displaced. The southern terranes of Mexico (including the Mixteca and Oaxaca terranes) likely migrated from the northeast either during the Permian along the California-Coahuila transform fault or later in the Jurassic along the Mojave-Sonora Megashear.
- Later tectonic activity during the main phase of rifting in the Gulf of Mexico sheared the basement of the Western Gulf of Mexico, and displaced the Chiapas Massif to the south with the Maya block (Figure 2.2).
- Permo-Triassic granitoids from Sonora and Colombia appear unrelated to the Western Gulf of Mexico and Southern Mexico, instead likely forming in a continental arc environment in association with the subduction of the Palaeo-Pacific beneath Pangaea.

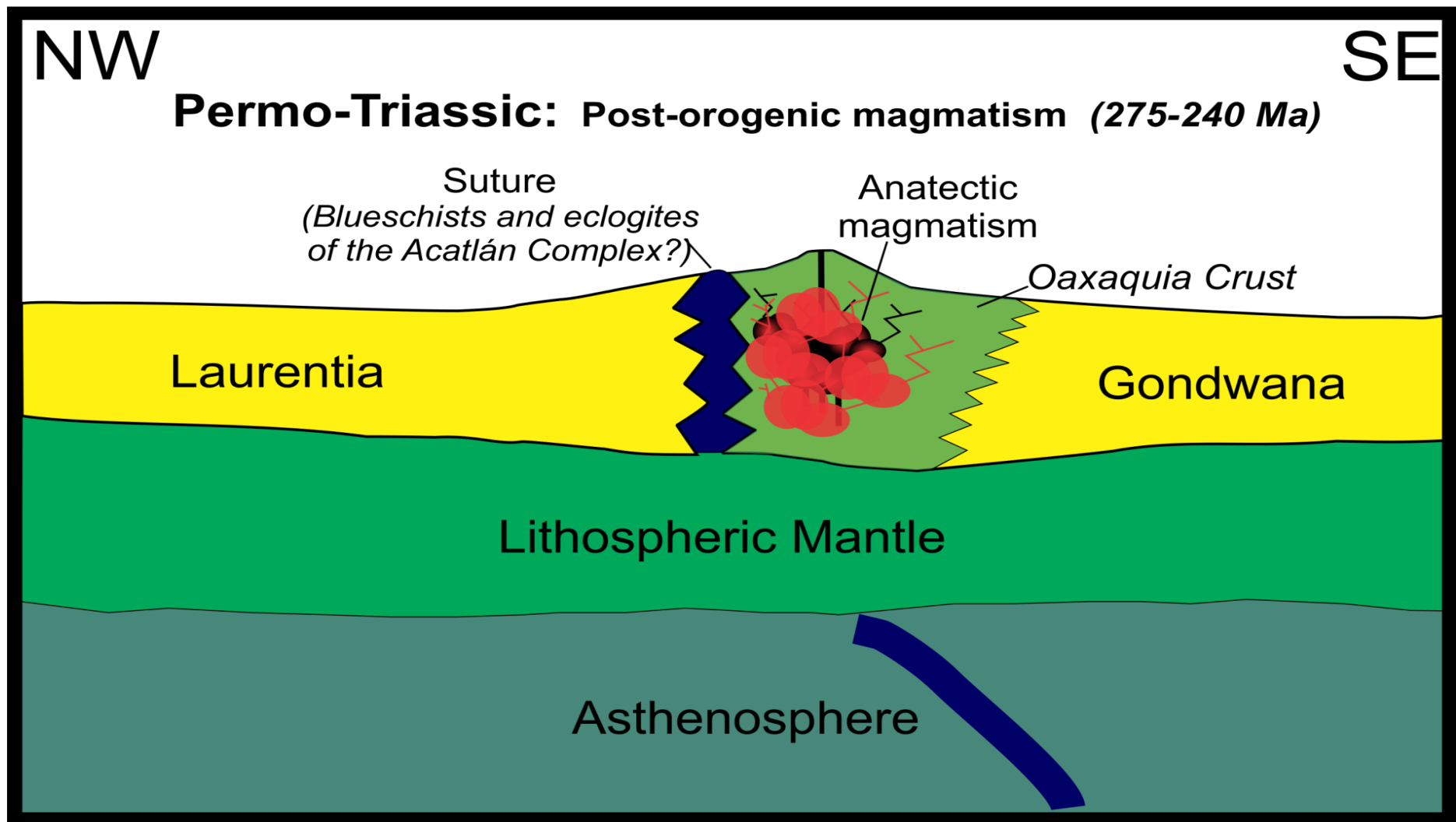


Figure 5.5. Schematic evolutionary model for the basement of the Western Gulf of Mexico after the amalgamation of Pangaea.

5.3 Summary

- The Late Carboniferous-Early Permian granitoids (ca. 326-286 Ma) of the Western Gulf of Mexico and the Oaxaca area of Southern Mexico are related to subduction of the Rheic Ocean beneath Gondwana, prior to the formation of Pangaea.
- The Late Carboniferous-Early Permian arc system was choked and stopped as Laurentia collided with Gondwana, during the formation of Pangaea.
- After the final amalgamation of Pangaea had occurred, a post-collisional anatectic phase followed, inheriting trace element signatures from Oaxaquia continental crust and the Late Carboniferous-Early Permian arc rocks from which they formed.
- These represent the Permo-Triassic granitoids (ca. 274-248 Ma) of the Western Gulf of Mexico, Oaxaca area and Chiapas Massif.
- Permo-Triassic granitoids from Sonora and Colombia appear unrelated to the anatectic event, instead likely forming from the eastward subduction of the Paleo-Pacific beneath Pangaea.
- The initial phase of Pangaea break-up displaced the Oaxaca and Mixteca terranes to the South in the Early Jurassic.
- The Permo-Triassic anatectic province was fragmented further during the opening of the Gulf of Mexico in the Late Jurassic. The transform fault that rotated the Maya block to the south pulled portions of the anatectic province with it (basement of the Western Gulf of Mexico) and displacing the Chiapas Massif to the south, causing the lineated trend that we see today (Figure 2.2).

6 Geological Overview of the Cuicateco Terrane

6.1 Introduction

Terrestrial Mexico is comprised of accreted allochthonous and autochthonous blocks (Sedlock et al., 1993), known as terranes (defined as “a fault bounded package of rocks of regional extent characterised by a geological history which differs from that of neighbouring terranes”; Howell, 1985). The Cuicateco terrane covers an area of approximately 20,000 km² in Southern Mexico and is bounded by the Zapoteco terrane to the west and Maya terrane to the east (Figure 6.1). Previous studies in the north (Angeles-Moreno, 2006; Mendoza-Rosales et al., 2010) and south (Perez-Guiterrez et al., 2009) of the Cuicateco terrane indicate that they do not share the same tectonic history. For this reason the north and south regions will be treated as separate entities in this study. This chapter will present a geological overview of the Cuicateco terrane, as well as other Cretaceous terranes found in Mexico. Observations and interpretations from fieldwork carried out during this study will be discussed in Chapter 7.

6.2 Northern Cuicateco Terrane

The north of the Cuicateco terrane can be separated into 4 principal units: i) the Mazateco Metamorphic Complex (subdivided into the Mazatlán de las Flores schist and the La Nopalera Schist), ii) Pochotepec Formation, iii) Teotitlán Migmatitic Complex and iv) Chivillas Formation (Figure 6.2). Volcano-sedimentary successions of possible Cretaceous age have also been reported in the Xonamanca Formation of the Sierra de Zongolica (Figure 6.2; Carrasco et al., 1975).

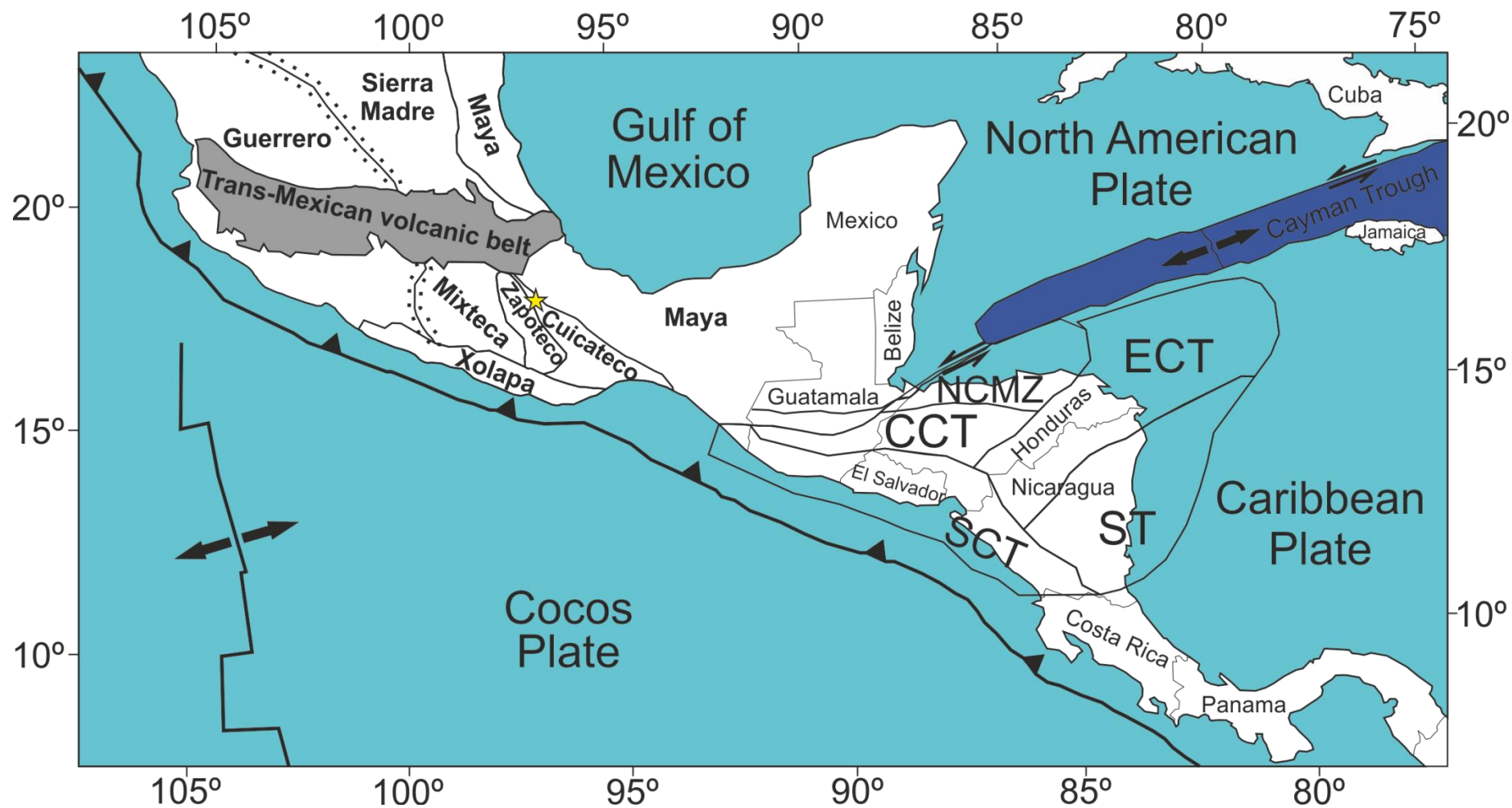


Figure 6.1. Map showing the terranes of Southern Mexico and Central America, adapted from Rogers et al. (2007). CCT= Central Chortis terrane, NCMZ= Northern Chortis Metamorphic Zone, ECT= Eastern Chortis terrane, SCT= Southern Chortis terrane, ST= Siuna terrane. The dashed line represents the Arperos basin suture between the Guerrero terrane and continental Mexico. The yellow star highlights the study area of this project in the northern Cuicateco terrane.

6.2.1 Chivillas Formation

6.2.1.1 Geology

The Chivillas Formation (Figure 6.2) is the youngest stratigraphic unit of the northern Cuicateco terrane, with an estimated thickness of ~4900m (Mendoza-Rosales et al., 2010). It is in faulted contact with the Teotitlán Migmatitic Complex, Mazateco Metamorphic Complex and Pochotepec Formation, as well as the Zapoteco terrane along the Oaxaca Normal Fault (Figure 6.2). The formation is comprised of volcanic and sedimentary successions that formed in a submarine basin.

The igneous component of the Chivillas Formation consists of pillow basalts, massive lava flows and gabbros (Carrasco, 1978; Alzaga Ruiz & Pano Arciniega, 1989). The presence of vesicles and amygdales within the pillow basalts suggests that these were deposited in a shallow marine environment where CO₂ was able to degas from the lavas (Mendoza-Rosales et al., 2010).

The igneous rocks are interbedded with sedimentary units, suggesting contemporaneous formation/deposition. These sedimentary units are composed of siliciclastic turbidite deposits which include fine grained sandstones, calcareous shales, black limestones, siltstones, coarse grained sandstones, clast supported breccias, calcareous debris flows, clast supported conglomerates and matrix supported conglomerates (Mendoza-Rosales et al., 2010).

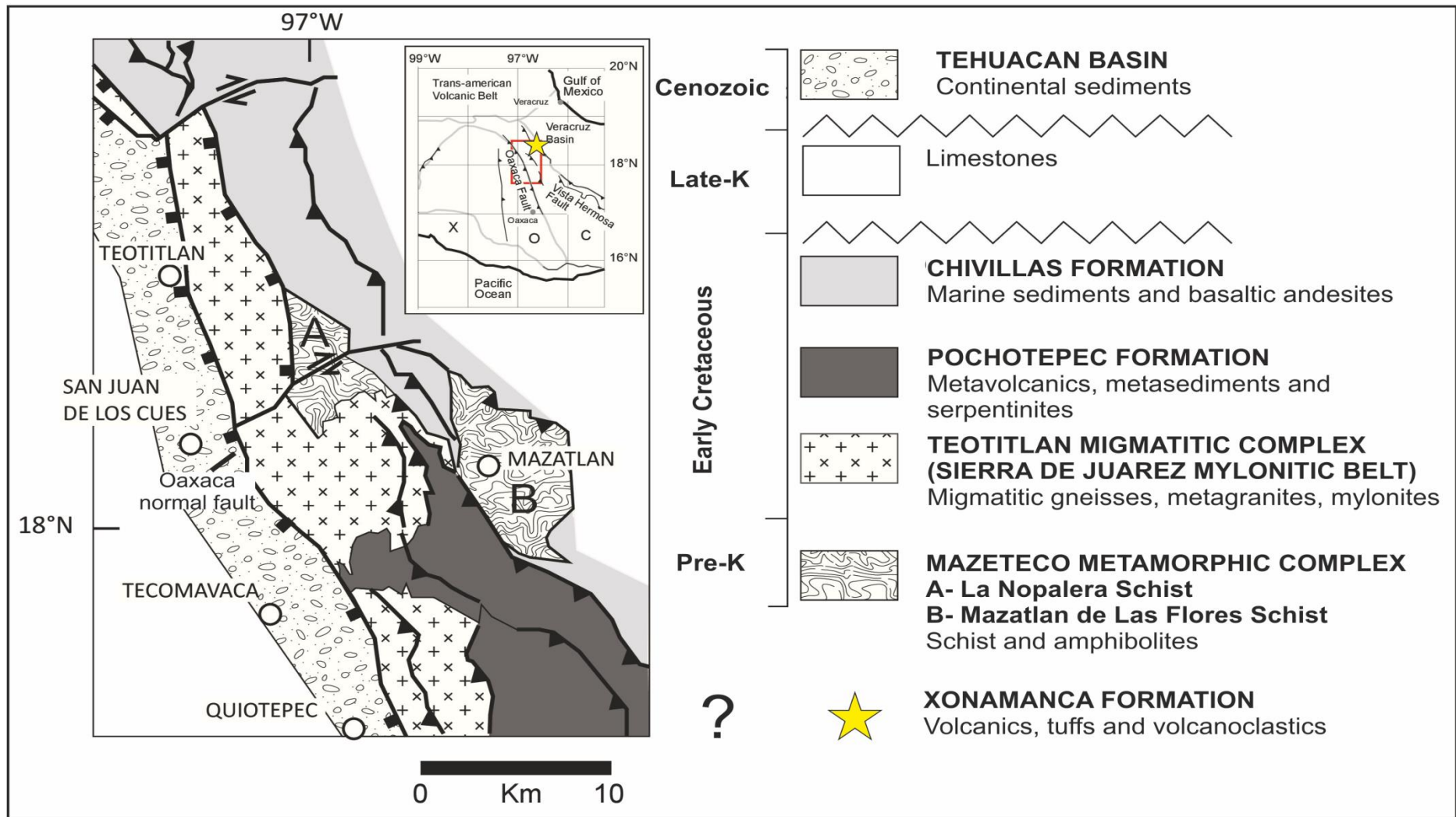


Figure 6.2. Simplified geological map of the northern Cuicateco terrane, modified from Angeles-Moreno et al. (2012).

6.2.1.2 Age

Ammonite fossils (*Cassicolaria sp.*, *Tintinnopsella sp.*, *Lorenziella sp.*, *Olcostephanus sp.* and *Spitidiscus sp.*) found in the sedimentary successions indicate a Tithonian–Valanginian (151–136 Ma) depositional age (Alzaga Ruiz & Pano Arciniega, 1989). Additional age constraints have been reported by Mendoza et al., (2010) through U/Pb analysis on detrital zircons found in Chivillas Formation sandstones. These yield a maximum depositional age (youngest population of zircons) of 126 Ma. This study will provide additional ages for the sediments of the Chivillas Formation in Chapter 8.

6.2.2 Teotitlán Migmatitic Complex

6.2.2.1 Geology

The Teotitlán Migmatitic Complex (Angeles-Moreno, 2006), also known as the Sierra de Juarez Mylonitic Belt (Alaniz-Alvarez et al., 1994; Mendoza-Rosales et al., 2010) stretches for 160 km between Tehuacan and Oaxaca, along the western boundary of the Cuicateco terrane (Figure 6.2). It is composed of migmatitic diorite-tonalite gneiss, quartz diorite with garnet, diopside-garnet gneiss, granitic dykes, pegmatites, aplites, volcano-sedimentary rocks and serpentinites (Delgado-Argote, 1989; Mendoza-Rosales et al., 2010; Angeles-Moreno, 2006). The complex has subsequently been affected by several brittle-ductile faulting events producing mylonitic structures (Angeles-Moreno, 2006).

6.2.2.2 Age

The complex yields ages that are older in its southern extent where syntectonic granites have been dated at 169.3 ± 1.7 Ma via $^{40}\text{Ar}/^{39}\text{Ar}$ on metamorphic

Chapter 6: Geological overview of the Cuicateco terrane

muscovite (Alaniz-Alvarez et al., 1996). In contrast, the north of the complex yields ages of 145 Ma to 132 Ma (U-Pb zircon) from granitic gneisses (Angeles-Moreno, 2006). It is worth noting that the difference in ages observed in the north and south of the complex may in fact be a product of the different dating techniques used rather than true age variance. Ages from the north of the complex have been obtained using the more modern and robust U/Pb dating technique on zircon whereas to the south of the complex ages are limited to $^{40}\text{Ar}/^{39}\text{Ar}$ on metamorphic muscovite which can be affected by weathering and metamorphism.

6.2.3 Pochotepec Formation

6.2.3.1 Geology

The Pochotepec Formation is in faulted contact with the Teotitlán Migmatitic Complex and Chivillas Formation (Figure 6.2). The formation is composed of igneous rocks such as meta-gabbros, meta-basalts, meta-rhyolites and meta-pyroclastics as well as meta-sedimentary successions such as greenschists and pelitic schists (Angeles-Moreno, 2006; Angeles-Moreno et al., 2012). There are also minor exposures of lenticular marble and serpentinite bodies which suggest the unit formed in association with an oceanic basin.

It has been proposed that the Pochotepec Formation may be related to the Chivillas Formation due to the compositional similarities between the two units (Angeles-Moreno, 2006). In this scenario the Pochotepec Formation would represent deeper structural levels of the Chivillas Formation, where it was exposed to higher degrees of metamorphism. However, no ages have been obtained for the rocks of the Pochotepec Formation so this hypothesis is speculative (new ages presented in

Chapter 8). The unit may instead be associated with an igneous event that predates the Cretaceous magmatism seen in the Teotitlán Migmatitic Complex and Chivillas Formation.

6.2.4 Mazateco Metamorphic Complex

6.2.4.1 Geology

The Mazateco Metamorphic Complex can be split into two separate metamorphic units: the La Nopalera Schist (~20 km²) and the Mazatlán de Las Flores Schist (~30 km²) as shown in Figure 6.2. The La Nopalera Schist is in faulted contact with the Teotitlán Migmatitic Complex and the Chivillas Formation. The Mazatlán de Las Flores Schist is in faulted contact solely with the Chivillas Formation.

The La Nopalera Schist consists of a biotite-muscovite-garnet schist, closely interbedded with quartzite and amphibolites (Angeles-Moreno, 2006; Angeles-Moreno et al., 2012). The Mazatlán de Las Flores Schist is compositionally similar to the La Nopalera Schist, containing chlorite-muscovite and actinolite schists. However, the amphibolites found in the La Nopalera Schist are not present in the Mazatlán de Las Flores Schist.

6.2.4.2 Age

The La Nopalera Schist yields an Ar-Ar plateau age (muscovite) of 132 Ma (Angeles-Moreno, 2006). This age most likely represents the cooling age of the migmatization event recorded in the Teotitlán Migmatitic Complex, rather than the depositional age of the meta-sediments.

Chapter 6: Geological overview of the Cuicateco terrane

The rocks of the Mazateco Metamorphic Complex are compositionally similar to other meta-sedimentary units that outcrop to the east of the Cuicateco terrane, in the Vista Hermosa area (Angeles-Moreno et al., 2012). These meta-sediments have been dated to the Paleozoic (K-Ar on muscovite and whole rock samples; Carfantan, 1986; Vasquez-Meneses et al., 1989). Elsewhere, in the Sierra de Juarez, Albarradas area, 60 km east of Oaxaca City, low grade meta-sediments (similar to the Mazateco Metamorphic Complex) are unconformably overlain by pre-Cretaceous redbeds (Angeles-Moreno et al., 2012). This suggests the Mazateco Metamorphic Complex is older and probably unrelated to the Cretaceous rocks in the northern Cuicateco.

6.2.5 Xonamanca Formation

6.2.5.1 Geology

The Xonamanca Formation of the Sierra de Zongolica (Figure 6.2) was first reported by Carrasco et al. (1975). It was described as a composite unit containing lithic greywackes, feldspathic greywackes, pyroclastic rocks and micritic limestones. Since this initial study very little has been carried out on the Xonamanca Formation, however Angeles-Moreno (2006) has reported the occurrence of green volcanoclastic rocks. More detailed information on the Xonamanca Formation based on work of this study will be reported in Chapter 7.

6.2.5.2 Age

Existing age estimates for the Xonamanca Formation are restricted to echinoid fossils found in the limestones. These constrain the limestones to the Berriasian-Valanginian (146-136 Ma; Carrasco et al., 1975). This study will present U/Pb ages on zircons found in tuffs of the Xonamanca Formation in Chapter 8.

6.2.6 Existing models for the origin of the northern Cuicateco terrane

It is widely agreed that the volcanic and sedimentary protoliths in the area formed in an extensional basin during the Jurassic-Early Cretaceous (Sedlock, 1993; Delgado-Argote, 1989; Angeles-Moreno, 2006; Mendoza et al., 2010), the nature and orientation of this basin however is still contentious.

6.2.6.1 Back-Arc Basin

One possibility for the formation of the northern Cuicateco terrane is that it is linked to a back-arc basin associated with subduction of the Farallon plate beneath the North American plate, along the west coast of present-day Mexico (Figure 6.3). In this scenario the serpentinites of the Teotitlán Migmatitic Complex are proposed to represent the roots of an eroded volcanic arc (Delgado-Argote, 1989).

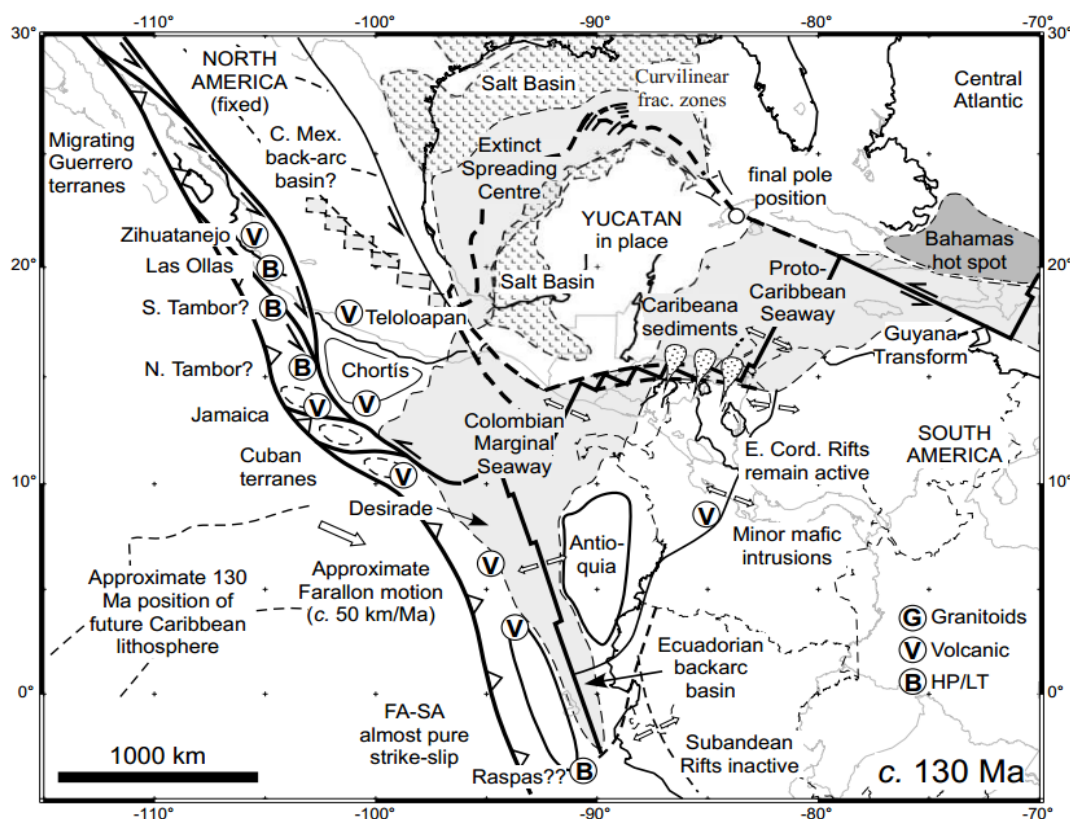


Figure 6.3. Early Cretaceous plate reconstruction of the Americas, showing a possible back-arc basin running through Mexico (Pindell & Kennan, 2009)

Chapter 6: Geological overview of the Cuicateco terrane

This proposed back arc setting for the northern Cuicateco terrane may be related to the Arperos back-arc basin (Elias-Herrera & Ortega-Gutierrez, 1998; Freydier et al., 2000; Dickinson & Lawton, 2001; Martini et al., 2011). Outcrops of back arc basin rocks have been identified in several areas along western Mexico (Figure 6.1) which are thought to be related to the separation of the Guerrero terrane from continental Mexico during the Early Cretaceous due to slab rollback of the eastward subducting Farallon plate (Elias-Herrera et al., 2000; Centeno-Garcia et al., 2008; Martini et al., 2011). Additional details of the Arperos basin are discussed further in Section 6.4.1.4.

After the initial proposal of a back-arc basin origin for the northern Cuicateco by Delgado-Argote (1989) the model has fallen out of favour and has not been considered in recent studies. The main issue with this model is the lack of any substantial arc rocks in the region, with the possible exception of the serpentinites that are purportedly the roots of an eroded arc (Delgado-Argote, 1989). Another issue is the large distance the Cuicateco terrane would have been from the subducting Farallon plate (using current models on plate boundaries during the Late Jurassic-Early Cretaceous; Figure 6.3).

6.2.6.2 Pull-Apart Basin

This model proposed by Angeles-Moreno (2006) interprets the units of the northern Cuicateco as having formed in a pull-apart basin (Figure 6.4). In this scenario large-scale right-lateral faulting caused trans-tensional activity to occur in the Cuicateco region and subsequently initiated rifting. As this rifting progressed sedimentation and simultaneous volcanism began, activity that is now recorded in

Chapter 6: Geological overview of the Cuicateco terrane

the Chivillas Formation. The rocks of the Pochotepec Formation are interpreted to represent deeper portions of these volcano-sedimentary successions that have undergone metamorphism to amphibolites and schists. The gneisses and migmatites of the Teotitlán Migmatitic Complex represent the deepest portions of this rift basin that have been subsequently exposed via normal faulting (Angeles-Moreno, 2006).

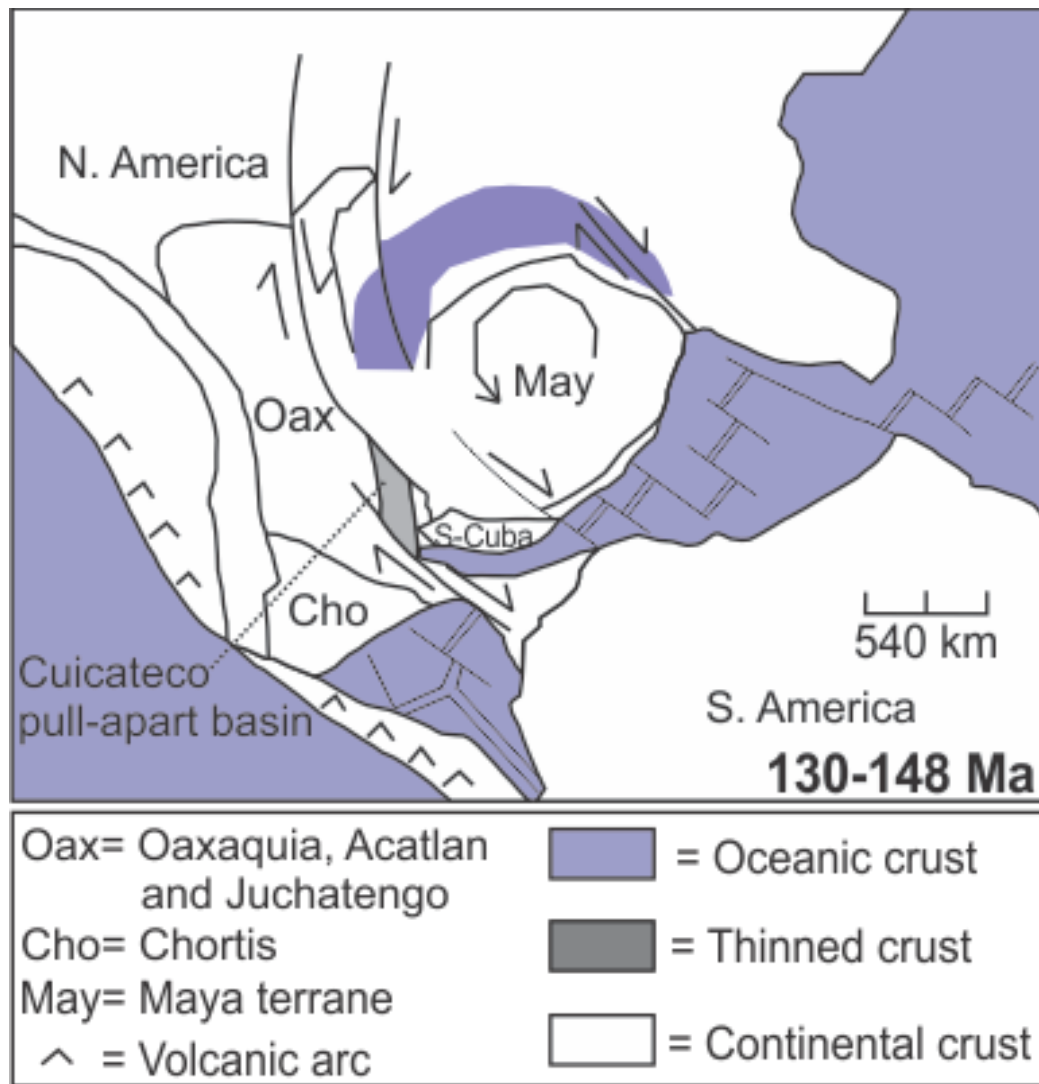


Figure 6.4. Pull-apart basin model for the formation of the Cuicateco terrane, from Angeles-Moreno (2006).

Granitic Gneisses from the Teotitlán Migmatitic Complex have been dated at 145Ma to 132 Ma (U/Pb zircon; Angeles-Moreno, 2006). This has led to the interpretation that the proposed pull-apart basin was linked to right lateral faulting

Chapter 6: Geological overview of the Cuicateco terrane

associated with the separation of North and South America rather than the opening of the Gulf of Mexico as it is believed ocean floor spreading in the Gulf of Mexico ceased in the Valanginian (Marton and Buffer, 1999).

This model, however, proposes that the basin opened with an east-west orientation rather than the north-south orientation advocated by other authors (Sedlock et al., 1993; Mendoza-Rosales et al., 2010). The model also lacks input from any kind of geochemical analysis on the igneous rocks which could significantly contribute to an assessment of the tectonic environment of basin formation.

6.2.6.3 Ridge-Transform Intersection

This model, proposed by Mendoza-Rosales et al. (2010) suggests that the extensional basin, in which the Chivillas Formation of the Cuicateco terrane is found, was formed at a ridge-transform intersection in association with the final stages of the north-south opening of the Gulf of Mexico (Figure 6.5). U/Pb ages on zircon obtained by Mendoza-Rosales et al. (2010) from sediments in the Chivillas area suggest a maximum age of deposition of 126 Ma. Field observations suggest that sedimentation and volcanism were contemporaneous; indicating that the age of basin formation cannot be any older than 126 Ma.

It is proposed that the right lateral transform of the Tamaulipas-Golden Line-Chiapas fault (Pindell, 1985; Figure 6.5) which accommodated the southward migration of the Yucatán block during the opening of the Gulf of Mexico was displaced to the west at its southernmost point and continued along a strike-slip fault in association with the Teotitlán Migmatitic Complex. This right lateral motion is

proposed to be the driving force for extension in the basin observed in the Chivillas Formation.

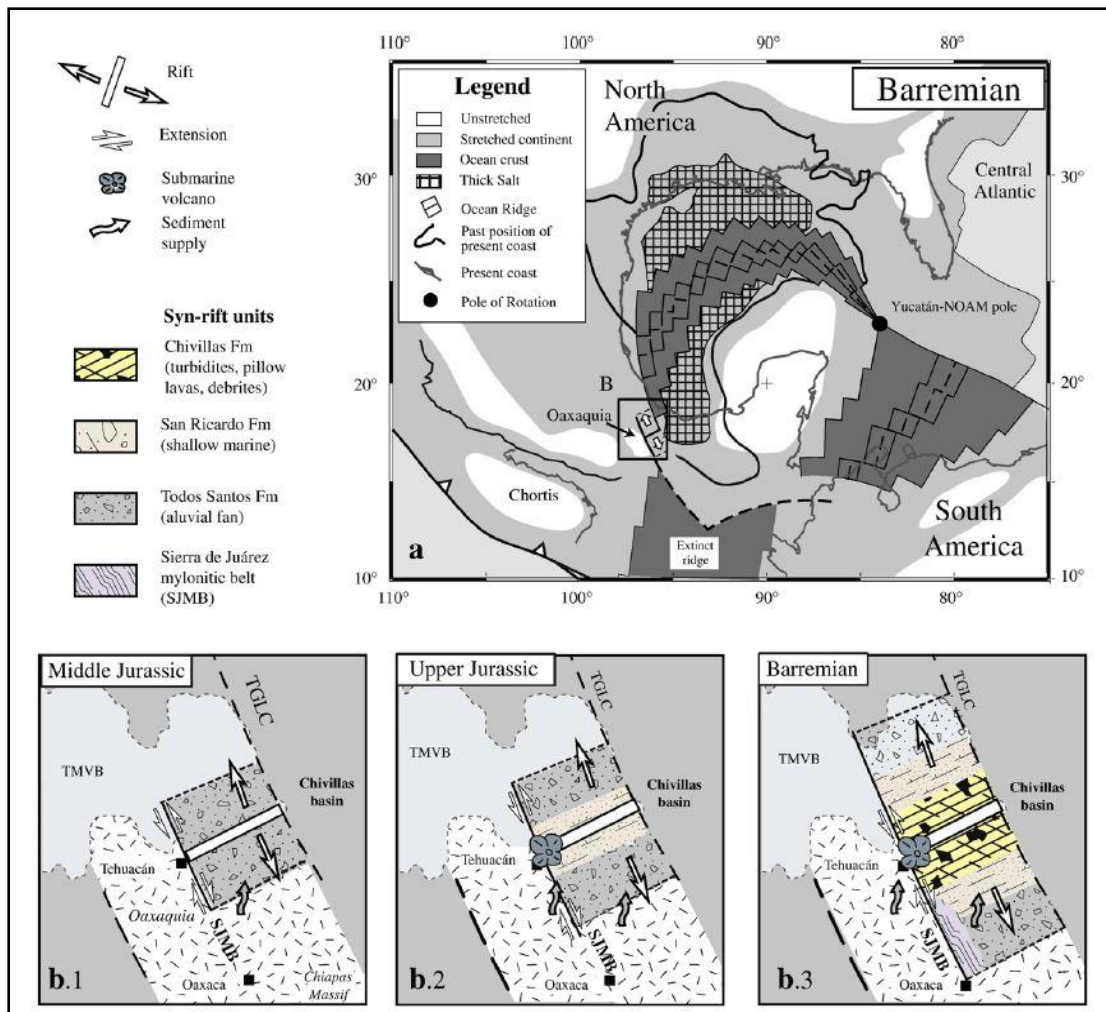


Figure 6.5. Ridge-transform intersection origin for the Cuicateco basin from Mendoza et al. (2010). Adapted from Pindell & Kennan, (2001). TGLC= Tamaulipas-Golden Line-Chiapas fault.

In this scenario initial rifting would form fluvial and shallow marine sedimentary deposits and then as rifting advanced this sedimentation would evolve into deposits more associated with deep marine settings. This is what is observed in the area, with the Todos Santos and San Ricardo Formations (of the Maya terrane, extending into the Chiapas Massif; Figure 6.12) representing fluvial and shallow

Chapter 6: Geological overview of the Cuicateco terrane

marine deposits and the sediments of the Chivillas Formation being consistent with the deposition of turbidites at greater depths.

This is the most recent model on the formation of the Cuicateco terrane and it is consistent with the reported geochemical, geochronological and field data. However, only a limited number of samples were analysed from a confined area of the Chivillas Formation when making this interpretation. A wider study is required in order to assess the validity of this model.

6.2.7 Deformation and Metamorphism

The first deformation phase within the Cuicateco terrane is defined by foliations and sheath folds observed in the schists of the Mazateco Metamorphic Complex. The deformation orientation and direction are unclear from field observations due to over-printing of subsequent deformation events but it likely occurred during the Palaeozoic (Angeles-Moreno, 2006). The first metamorphic event coincides with this deformation event and is most obvious in the meta-sediments and meta-volcanics of the Mazateco Metamorphic Complex (Angeles-Moreno, 2006).

The second deformation and metamorphic events of the Cuicateco terrane have been interpreted to have occurred in right lateral trans-tensional deformation associated with basin formation during the Cretaceous (Angeles-Moreno, 2006). At deep structural levels the second deformation event is characterised by amphibolite facies metamorphism, migmatization, magmatism and metasomatism of the Teotitlán Migmatitic Complex (Angeles-Moreno, 2006). The age of migmatization and cooling associated with deformation has been dated by $^{40}\text{Ar}/^{39}\text{Ar}$ and U/Pb at

Chapter 6: Geological overview of the Cuicateco terrane

140-131 Ma (Angeles-Moreno, 2006). At shallower structural levels this deformation caused lower grade greenschist facies metamorphism and metasomatism of the Pochotepec Formation and Mazateco Metamorphic Complex (Angeles-Moreno, 2006).

The third deformation event recorded in the units of the Cuicateco terrane can be attributed to compression experienced during the Laramide Orogeny (orogenic event initiating ca. 80 Ma in relation to flat-slab subduction of the Farallon Plate beneath North America). Significant shortening occurred in this area around 82 Ma, developing folds and thrusts with a northeast vergence (Angeles-Moreno, 2006). These features are associated with the dramatic Zongolica fold and thrust belt which is the southern extension to the Sierra Madre Oriental fold and thrust belt that extends along the length of eastern Mexico. This extensive compressional event inverted the northern Cuicateco basin, causing juxtaposition between the units of the Teotitlán Migmatitic Complex, Chivillas Formation, Pochotepec Formation and Mazateco Metamorphic Complex.

During the Eocene and the earliest part of the Miocene the area was affected by normal and oblique lateral faulting under brittle conditions, resulting in the development of cleavage planes (Angeles-Moreno, 2006). Age constraints for the upper limit of deformation come from pyroclastic rocks interbedded with syn-tectonic sediments in Tehuacan which yield an age of 50.2 ± 1.4 Ma (K-Ar biotite) (Angeles-Moreno, 2006). The youngest age constraints available for this deformation event are indicated by a 20 Ma ignimbrite cut by lateral faults associated with the fourth deformation event (Angeles-Moreno, 2006).

Chapter 6: Geological overview of the Cuicateco terrane

The final deformation event in the Cuicateco terrane is an extensional event defined by high angle brittle normal faulting (60-70°) of probable Miocene-Pleistocene age (Angeles-Moreno, 2006). This event is observed throughout the northern Cuicateco units but is most obvious in the Teotitlán Migmatitic Complex due to its proximity to the main area of displacement, along the Oaxaca normal fault (Angeles-Moreno, 2006).

6.2.8 Basement

The composition of the basement in the Cuicateco terrane is unclear as there are no known exposures. With its proximity to the Oaxacan Complex (Figure 6.10) in the Zapoteco terrane, it is possible that it forms part of the Oaxaquia micro-continent. This would give the basement of the northern Cuicateco a Grenvillian age (1200-900 Ma). Alternatively, the basement of the Cuicateco terrane could be composed of the Permo-Triassic igneous rocks that make up the Western Gulf of Mexico (see Chapters 2-5).

6.3 Southern Cuicateco Terrane

6.3.1 Geology

The southern Cuicateco (Figure 6.1) is very similar to that of the northern Cuicateco. Previous studies (Perez-Gutiérrez et al., 2009) report amphibolites and serpentinites that have volcanic protoliths in contact with phyllites and schists. These lithologies are consistent with deposits forming in a submarine (potentially oceanic) basin. Younger igneous bodies that intrude the metavolcanic-sedimentary units of the southern Cuicateco have been dated to 16 Ma (Williams and McBirney, 1969;).

Chapter 6: Geological overview of the Cuicateco terrane

This could relate to Neogene arc activity or alternatively interactions with the Chortis block as it migrated eastwards across Southern Mexico (see section 6.4.3). The southern Cuicateco shares the same tectonic boundaries as the northern Cuicateco (Vista-Hermosa reverse fault to the east and Oaxaca normal fault to the west).

6.3.2 Age

Amphibolites from the southern Cuicateco have been dated by U/Pb geochronology on zircons by Perez-Gutiérrez et al. (2009). They obtained an age of 65 ± 1.2 Ma which has been interpreted as the age of crystallisation in the igneous protolith. Detrital zircon analysis on volcanoclastic phyllites in the same study yielded a population at 78 Ma (constraining the maximum age of deposition for the sediment). These geochronological results show that there is a large age gap between the Early Cretaceous northern Cuicateco and Late Cretaceous southern Cuicateco. This strongly suggests that the two basins formed independently from each other. Perez-Gutiérrez et al. (2009) interpret the southern Cuicateco to have formed as an oceanic basin in relation to Maastrichtian arc magmatism in Southern Mexico.

6.4 Other Cretaceous terranes of Mexico

6.4.1 Guerrero Terrane

6.4.1.1 Geology

The Guerrero terrane (Campa & Coney, 1983), also known as the Guerrero composite terrane (Centeno-García et al., 2008; Keppie, 2004), or the Guerrero super terrane (Dickinson & Lawton, 2001) makes up a large proportion of Mexico's

Chapter 6: Geological overview of the Cuicateco terrane

Western continental margin. The terrane is composed of volcanic and volcanoclastic successions that were mainly deposited in submarine environments (Centeno-García et al., 2011; Martini et al., 2011). The terrane can be further divided into subterranes based on subtle differences in stratigraphy, structures, geochronology and geochemistry. These are known as the Tahue, Zihuatanejo, Arcelia, Teloloapan and Guanajuato terranes (Centeno-García, 2005; Centeno-García et al., 2008; Figure 6.6).

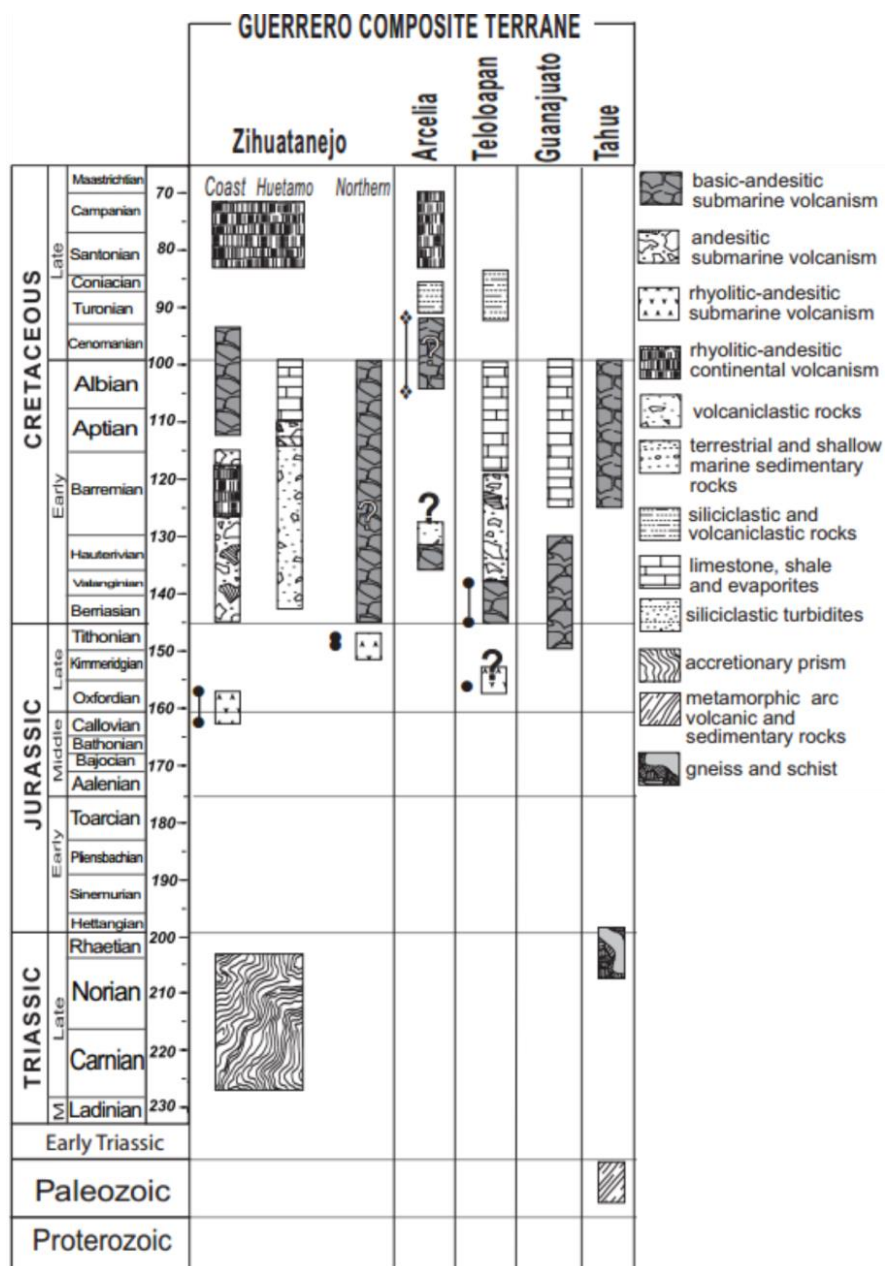


Figure 6.6. Stratigraphic column of the Guerrero subterranes, adapted from Centeno-García et al. (2008).

Chapter 6: Geological overview of the Cuicateco terrane

The basement of the Guerrero terrane is preserved in the Arteaga Complex of the Zihuatanejo subterrane (Figure 6.6; Centeno-García et al., 1993, 2003), and consists of Triassic turbidite deposits. These deposits display strong correlation to the turbidites of the Potosí fan, which cover large portions of Central Mexico. The Potosí Fan was deposited as a large drainage area of western equatorial Pangea during the Late Triassic (Silva-Romo et al., 2000; Barboza-Gudino et al.; 2010; Martini et al 2011).

6.4.1.2 Age

A number of U/Pb geochronological studies on zircons have been carried out on the igneous suites of the Guerrero terrane, yielding Late Jurassic-Early Cretaceous ages. The oldest of the igneous rocks (lava flows, tuffs and high level intrusions) can be found in the Zihuatanejo subterrane and have been dated to 163-152 Ma (Centeno-García et al., 2003; Bissig et al., 2008). These have been interpreted to represent crystallization ages during arc magmatism. Martini et al. (2011) obtained a slightly younger age of 144 ± 1.4 Ma for tonalites of the El Paxtle Assemblage (Teloloapan subterrane), which again has been interpreted as the age of crystallisation during arc magmatism.

6.4.1.3 Tectonic Setting

It is universally accepted that the volcano-sedimentary successions that make up the Guerrero terrane formed in an arc environment throughout the Late Jurassic-Early Cretaceous. However, the nature of this arc and where it formed has been controversial over the last 30 years. Some propose the terrane to be allochthonous, forming as an exotic island arc system (Lapierre et al., 1992; Tardy et al., 1994;

Chapter 6: Geological overview of the Cuicateco terrane

Dickinson & Lawton, 2001; Talavera-Mendoza et al., 2007). This arc was separated from terrestrial Mexico by the Arperos basin, which formed part of the Mezcalera oceanic plate. In this model the Mezcalera plate was subducted towards the west, beneath the Farallon oceanic plate (Figure 6.7; Tardy et al., 1994). Dickinson & Lawton, (2001) proposed a similar model for the Guerrero terrane but suggested the Mezcalera plate was subducting beneath both the Farallon plate to the west and continental Mexico to the east. Accretion of the Guerrero terrane to continental Mexico in these models occurred as the Mezcalera plate was consumed by subduction. Other allochthonous models propose multiple intra-oceanic arc systems separated by small oceanic basins (Figure 6.7; Talavera-Mendoza et al., 2007). These arcs accreted to continental Mexico in several stages throughout the Cretaceous, collectively forming the Guerrero terrane.

Alternatively, other authors suggest the Guerrero terrane formed as a para-autochthonous continental arc that was separated from continental Mexico through back arc extension via the Arperos basin (Figure 6.7, Lang et al., 1996; Cabral-Cano et al., 2000; Elías-Herrera et al., 2000; Centeno-García et al., 2008; Martini et al., 2009; Martini et al., 2011; Martini et al., 2014; Betania Palacios-Garcia & Martini, 2014). The terrane was later re-accreted back on to continental Mexico as the Arperos basin underwent subduction.

6.4.1.4 Arperos Basin

The Arperos basin separated the Guerrero terrane from mainland Mexico during the Late Jurassic-Early Cretaceous and has been subsequently closed. Exposures of the rocks that formed in the Arperos basin mark the suture zone

Chapter 6: Geological overview of the Cuicateco terrane

between the Guerrero terrane and continental Mexico (Figure 6.1). These rocks are composed of rhyolites, pillow basalts, basaltic lava flows and sedimentary successions that were mainly erupted and deposited in a submarine environment. Research on the sandstones deposited in the basin suggest an asymmetrical provenance, with rocks to the southwest recording Guerrero terrane signatures, progressing to continental Mexico signatures to the east (Martini et al., 2011).

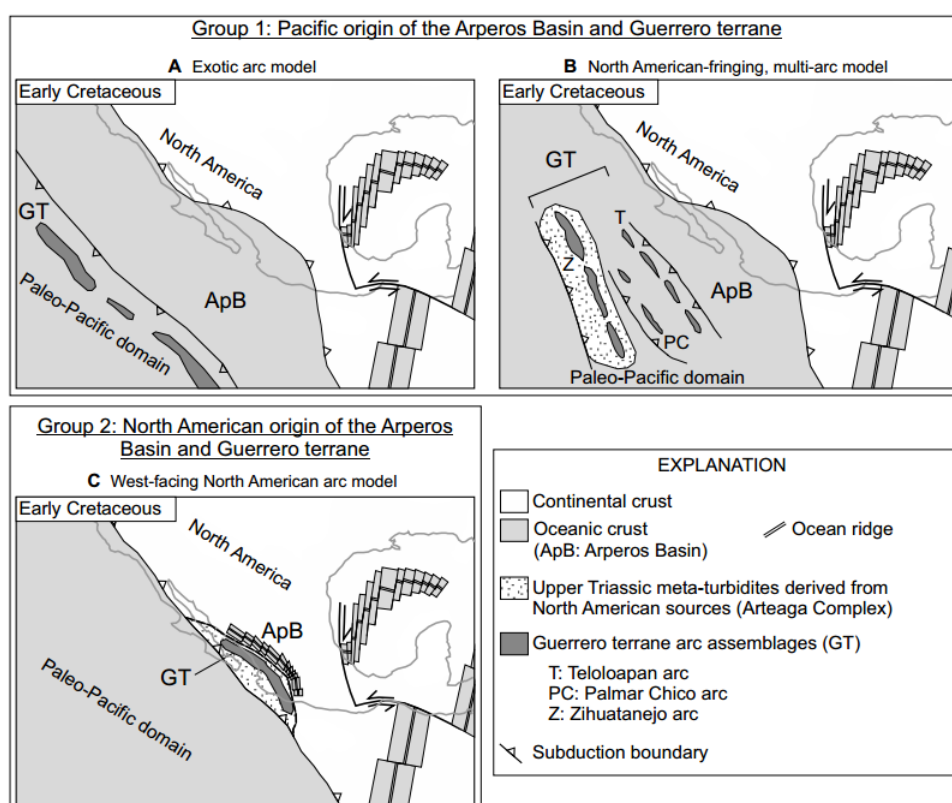


Figure 6.7. Existing models on the origins of the Arperos basin from Martini et al. (2014). Group 1 models predict a large Arperos basin (Tardy et al., 1994; Dickinson and Lawton, 2001; Talavera-Mendoza et al., 2007). The group 2 model predicts a smaller back-arc basin origin for the Arperos basin (Cabral-Cano et al., 2000; Elías-Herrera et al., 2000; Centeno-García et al., 2008; Martini et al., 2011; Martini et al., 2014).

Authors who propose an allochthonous model for the Guerrero terrane (Tardy et al., 1994; Dickinson & Lawton, 2001; Talavera-Mendoza et al., 2007) believe the Arperos basin was extensive, making up a part of the paleo-Pacific

Chapter 6: Geological overview of the Cuicateco terrane

oceanic plate (Figure 6.7). Other authors think the basin was smaller in size, forming as a back arc to the Guerrero arc system (Figure 6.7; Cabral Cano et al., 2000; Elías-Herrera et al., 2000; Centeno-García et al., 2008; Martini et al., 2011 & 2014). The marginal back-arc basin has been favoured in recent years because of similarities in the basement of the Guerrero terrane and continental Mexico (discussed in Section 6.4.1.1; Figure 6.8).

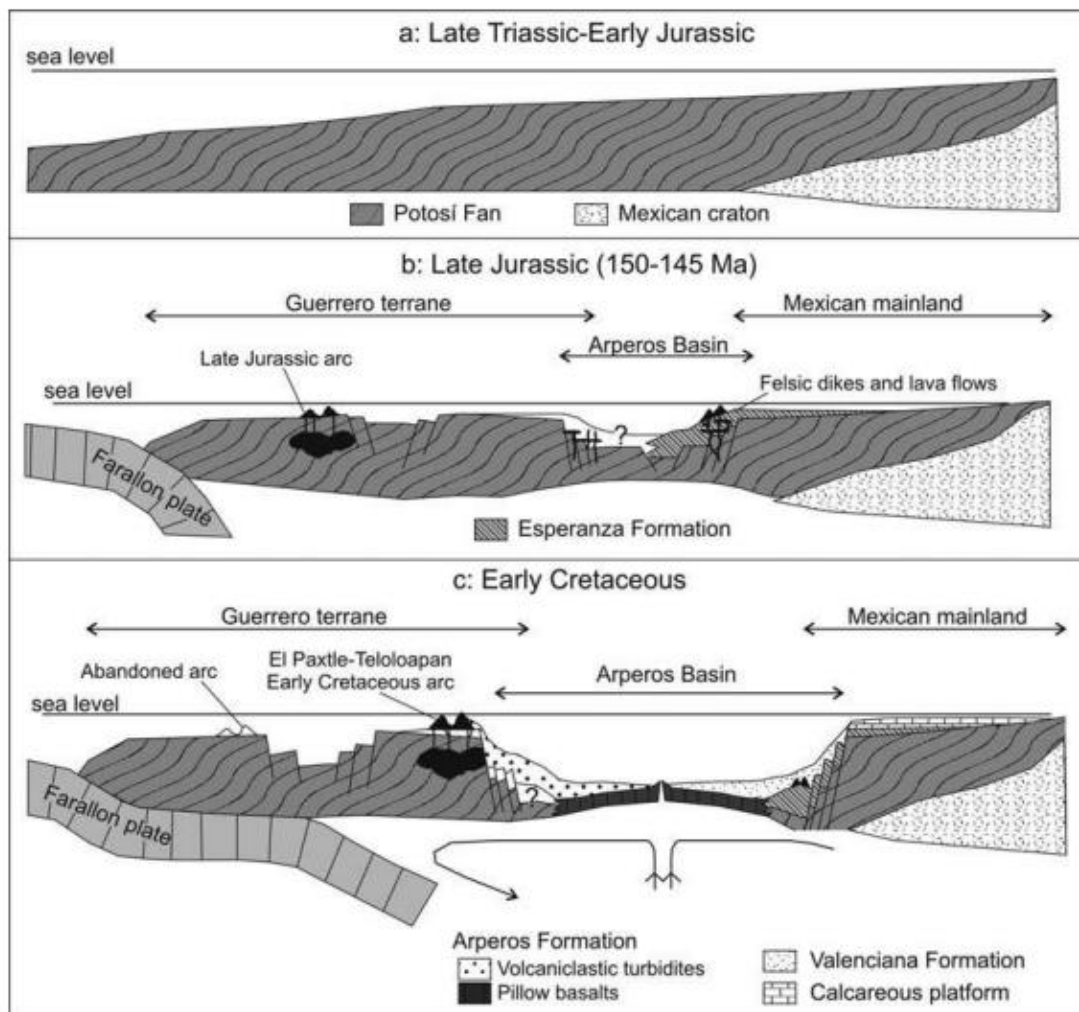


Figure 6.8. Back-arc model for the opening of the Arperos basin from Martini et al. (2011).

The initiation of rifting in the Arperos basin is recorded in rhyolites of the Esperanza Formation (Figure 6.8) which yield an age of 150 Ma (U/Pb on zircons;

Chapter 6: Geological overview of the Cuicateco terrane

Martini et al., 2011). The youngest ages obtained from igneous rocks in the Arperos basin are in meta-volcanics of the Palmar Chico Assemblage which yield an age of 130 Ma (U/Pb on zircon; Martini et al., 2014). Detrital zircon studies on sandstones from the Arperos basin produce main peaks of 133 and 131 Ma (Martini et al., 2011). Younger peaks of 118 and 119 Ma have been obtained from sandstones of the Ojo de Agua Assemblage (Martini et al., 2014). These are interpreted to have formed when the Guerrero terrane and terrestrial Mexico were in close proximity to each another. This indicates that the Arperos basin was closed by the Early Aptian, although Martini et al. (2014) interpret metamorphically reset basalts that yield a ^{40}Ar - ^{39}Ar age of 101 Ma to represent the time of Arperos basin closure.

6.4.2 Xolapa Terrane

The Xolapa terrane defines the southernmost extent of continental Mexico along its Pacific margin, covering an area approximately 40,000 km². It is in tectonic contact with the Cuicateco, Zapoteco, Mixteco and Guerrero terranes (Figure 6.1). The terrane is composed mostly of migmatitic orthogneisses and paragneisses that have been intruded by intermittent magmatism since the Jurassic (Solari et al., 2007; Torres-de Leon et al., 2012). The origins and relationships of this area to the rest of continental Mexico are still unclear. Some authors propose an allochthonous arc system origin that accreted to Mexico during the Mesozoic (Campa & Coney, 1983; Sedlock et al., 1993), whereas others suggest that the area is in fact autochthonous and is a result of thinning and re-heating of existing continental crust during the Tertiary (Ducea et al., 2004; Ratschbacher et al., 2009).

Chapter 6: Geological overview of the Cuicateco terrane

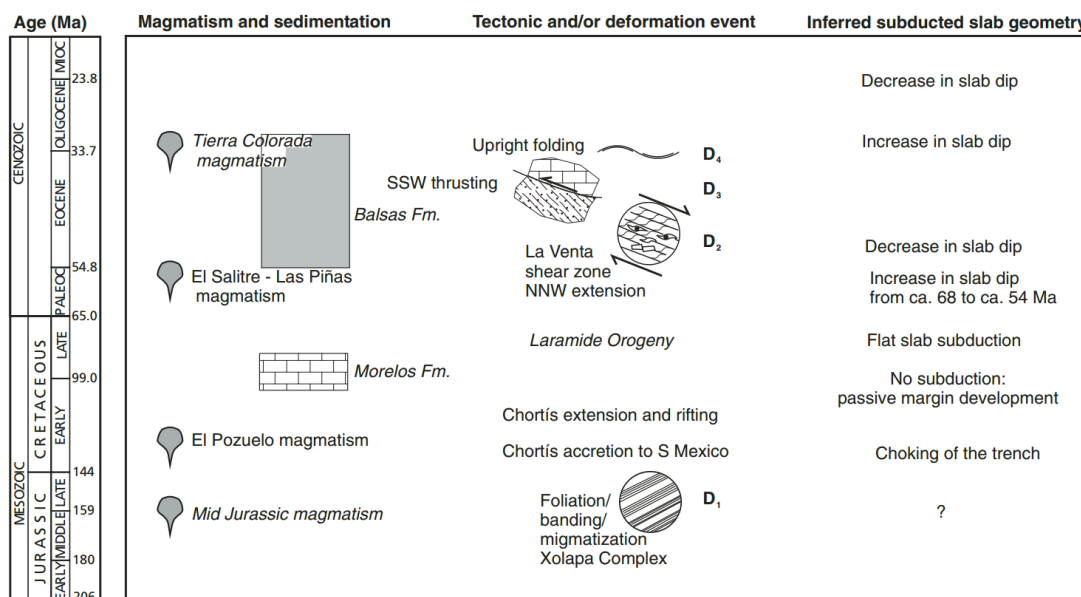


Figure 6.9. Timeline of magmatism in the Xolapa terrane since the Jurassic, from Solari et al. (2007).

It is believed that the magmatic rocks belonging to the Xolapa terrane formed in association with arc volcanism or collisions between the Chortis block and Southern Mexico (Figure 6.9; Solari et al., 2007). Previous geochronological studies in the area (U/Pb zircon) place the first magmatic event at ca. 165-158 Ma (Ducea et al., 2004), followed by one at 129 Ma, ca. 55 Ma (Solari et al., 2007) and ca. 34-28 Ma (Herrmann et al., 1994; Ducea et al., 2004). A migmatization event is thought to have occurred between this sporadic magmatism at ca. 134 due to crustal thickening in association with interactions with the Chortis Block (Solari et al., 2007).

6.4.3 Chortis Block

The Chortis block lies to the south of the Maya terrane of Southern Mexico (Figure 6.1) and makes up the only continental portion of the Caribbean Plate (Rogers et al., 2007). It is widely accepted that the area is not autochthonous but instead originated to the south of Mexico (Figure 6.3), migrating east at least 1100 km during the Tertiary along the Motagua-Polochic transform fault (Malfait &

Chapter 6: Geological overview of the Cuicateco terrane

Dinkelman, 1972; Pindell & Dewey, 1982; Pindell et al., 1988; Sedlock et al., 1993; Dickinson & Lawton, 2001; Rogers et al., 2007; Pindell & Kennan, 2009; Ratschbacher et al., 2009; Torres-de Leon et al., 2012; Talavera-Mendoza et al., 2013). An alternative theory is that the block migrated north-eastwards from the Pacific Ocean during the Eocene, along a pole of rotation found near Santiago de Chile (Keppie & Moran-Zenteno, 2005). Within the Chortis Block five separate terranes have been identified known as the Northern Chortis magmatic zone, the Central Chortis terrane, Southern Chortis terrane, Eastern Chortis terrane and the Siuna terrane (Figure 6.1).

The Central Chortis terrane covers an area 110,000 km² in size and is made up of Grenvillian to Palaeozoic continental metamorphic rocks that include phylites, schists, para and orthogneisses (Rogers et al., 2007) dated between 1Ga (U/Pb zircon; Manton, 1996) to 220 Ma (K/Ar biotite; MMAJ, 1980). Towards the north of the terrane, dacite plutons dated from 124 Ma (U/Pb on zircon; Drobe & Cann, 2000) to ca. 60 Ma (K/Ar on biotite & hornblende; Horne et al., 1976; Emmet, 1983) intrude Palaeozoic to Triassic metamorphic rocks (Rogers et al., 2007). This terrane shows similarities to the Zapoteco, Mixteco and Teloloapan terranes of Southern Mexico, in terms of both the age and composition of its basement, as well as the age of magmatic events found within it (Rogers et al., 2007).

The Eastern Chortis terrane covers an area of 185,500 km² and consists of a Jurassic metasedimentary basin that may relate to the southern rifted margin of the North American plate during its separation from the South American Plate in the Jurassic (Rogers et al., 2007). This basin has been intruded intermittently by

Chapter 6: Geological overview of the Cuicateco terrane

magmatism from 140 Ma (Rb/Sr whole rock granite; Donnelly et al., 1990) to 70 Ma (K/Ar on plagioclase found in a basaltic andesite; Weiland et al., 1992).

The Northern Chortis metamorphic zone is a subterrane of the Central Chortis terrane and is defined by Early Cretaceous to Early Tertiary magmatism (124-30 Ma; U/Pb zircon; Manton & Manton 1984) that formed in association with a basement of sheared, high grade gneiss (Manton, 1996; Rogers et al., 2007). The sporadic magmatism of the Northern Chortis metamorphic zone can be related to the arc magmatism observed in the Xolapa terrane of Southern Mexico which suggests proximity between the two areas in the past.

The Southern Chortis terrane covers an area of 120,000 km² (Rogers et al., 2007) and is characterized by Miocene pyroclastic strata thought to be associated with the late Cenozoic Central America volcanic arc (Rogers et al., 2007). Basement exposures in the terrane are limited to one outcrop of meta-igneous rock (Markey, 1995) that has not been dated but are proposed to be related to the Jurassic-Cretaceous arc of the Guerrero terrane, Southern Mexico (Rogers et al., 2007).

The Siuna terrane lies to the south of the Chortis block, in Northern Nicaragua and is composed of serpentinites and ultramafic cumulates (Rogers et al., 2007). It is thought that the terrane formed as an Early Cretaceous island arc built on oceanic basement, accreted to the southern margins of the Chortis in the Late Cretaceous (Venable, 1994). Rogers et al. (2007) suggest that the area could represent the westernmost accreted terrane formed from the collision of the Caribbean arc into the continental margins of Chortis.

6.5 Adjacent Terranes

6.5.1 Zapoteco Terrane

The Zapoteco terrane (Sedlock et al., 1993) also referred to as the Oaxaca terrane (Campa & Coney, 1983; Centeno-Garcia & Keppie, 1999) consists of Proterozoic basement unconformably overlain by a Palaeozoic sedimentary cover (Figure 6.1; Sedlock et al., 1993; Angeles-Moreno, 2006).

The basement of the Zapoteco terrane (Oaxacan Complex; Figure 6.10), outcrops of which cover an area of 10,000 km² (Keppie et al., 2003) is composed of banded gneiss, charnockite, garnet-rich paragneiss, marble, syenitic intrusions, orthogneiss, meta-anorthosite, anorthositic gabbro and granitic pegmatite (Ortega-Gutierrez, 1984; Sedlock et al., 1993; Angeles-Moreno, 2006). It is widely accepted that the complex is part of the Precambrian-Palaeozoic micro-continent of Oaxaquia that forms the backbone of Mexico, and proposed to extend southwards from the Ouachita suture in Coahuila to the Isthmus of Tehuantepec in southern Mexico (Figure 6.10; Ortega-Gutiérrez et al., 1995; Keppie et al., 2003; Angeles-Moreno, 2006). It is thought that the Oaxaquia micro-continent formed in sporadic episodes of arc/backarc magmatism and migmatization events off the Northern Boundary of the Amazonia Craton (Solari et al., 2003; Keppie & Ortega-Gutiérrez, 2010). Ages of ca 1300-1200 Ma (U/Pb zircon from para and orthogneisses; Keppie & Dostal, 2007), ca. 1140 Ma (U/Pb zircon from anorthosites; Keppie et al., 2003), 1105 Ma (U/Pb zircon from migmatites; Solari et al., 2003), ca. 1010 Ma (U/Pb zircon from AMCG suite; Keppie et al., 2003) and 917 Ma (U/Pb zircon from calc-alkaline granitoid pluton; Ortega-Obregón et al., 2003) have been obtained by various authors from

Chapter 6: Geological overview of the Cuicateco terrane

the Oaxacan Complex. Other Precambrian outcrops that have comparable ages (Figure 6.10) and thought to be related to Oaxaquia are the Huiznopala Gneiss in Huiznopala, Hidalgo state (Lawlor et al., 1999), Novillo Gneiss in the Novillo canyon, Ciudad Victoria, Tamaulipas (Stewart et al., 1999) and the Guichicovi Complex, near the Tehuantepec isthmus (Weber & Kohler, 1999).

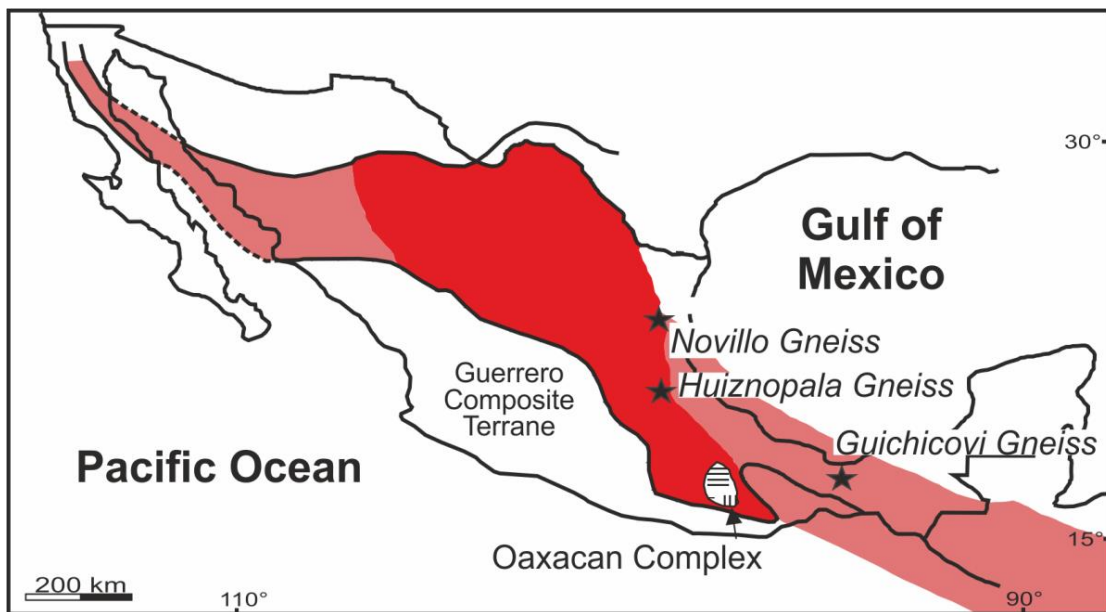


Figure 6.10. Map showing the location of the Grenvillian aged Oaxaquia basement. The dark red marks the boundaries set by Ortega-Gutierrez et al. (1995) and the light red marks possible extensions proposed by Keppie et al. (2003).

The Precambrian basement rocks that make up the Zapoteco terrane are covered by marine and continental Palaeozoic, Mesozoic and Cenozoic sedimentary rocks (Angeles-Moreno, 2006). The earliest unit dating back to the Early Ordovician, known as the Tiñu Formation (Navarro-Santillan et al., 2002), is made up of siltstones and limestones that unconformably overlie the Oaxacan Complex (Figure 6.11). Above these Ordovician units lie Carboniferous-Permian rocks known as the Ixtaltepec, Santiago and Matzitz Formation (Centeno-Garcia & Keppie, 1999) which are primarily made up of sandstones and conglomerates (Figure 6.11)

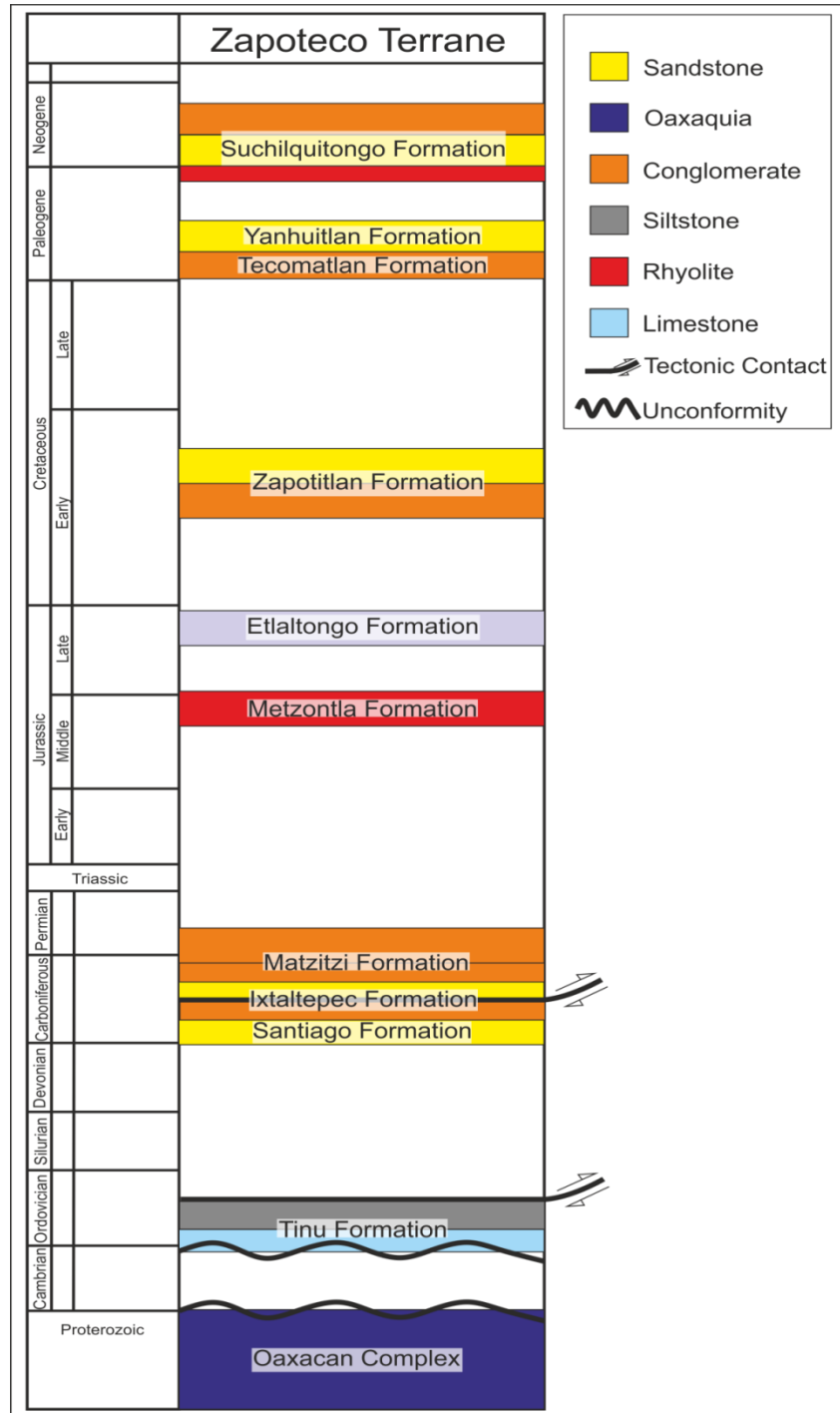


Figure 6.11. Stratigraphic column for the Zapoteco terrane, adapted from Angeles-Moreno (2006).

Mesozoic strata of the Zapoteco terrane are Callovian to Campanian in age. The oldest rocks belong to the Metzontla Formation which consists of tonolite dykes (Torres-Vargas et al., 1986), and are successively overlain by the late Jurassic red beds and limestones of the Etlaltongo Formation (Alzaga-Ruiz, 1991), Middle

Chapter 6: Geological overview of the Cuicateco terrane

Cretaceous sandstones and conglomerates of the Zapotitlan Formation (Angeles-Moreno, 2006). These were followed by marine deposits in the late Cretaceous (Figure 6.11)

Cenozoic units range in age from the Palaeocene until the end of the Miocene; these include the Tecomatlan, Yanhuitlan and Suchilquitongo Formations (Angeles-Moreno, 2006; Ferrusquía-Villafranca, 1990). They consist of interbedded conglomerates, volcanoclastics and volcanic rocks, suggesting contemporaneous sedimentation and magmatism (Figure 6.11; Angeles-Moreno, 2006).

6.5.2 Maya Terrane

The Maya terrane lies to the east of the Cuicateco, and is separated from it by the Vista Hermosa thrust fault (Figure 6.1). Some authors prefer to split this extensive terrane and instead name it the Yucatán-Chiapas block (Dickinson & Lawton, 2001).

Basement rocks of the Maya terrane have been constrained to be Grenvillian in age from studies of the Guichicovi Complex (Figure 6.10). Felsic orthogneisses have been dated at 1.23 Ga with intruded charnockites at 991 Ma (U/Pb zircon; Weber & Kohler, 1999). These ages correspond to other high grade units from around Mexico e.g., Oaxacan Complex, suggesting that parts of the Maya terrane basement are derived from the microplate Oaxaquia (Ortega-Gutierrez et al., 1995). Basement rocks from the Palaeozoic, consisting of metasedimentary and intrusive rocks have also been well documented in the Chiapas Massif (Weber et al., 2008; Weber et al., 2009), the Mayan Mountains in Belize (Martens et al., 2010), Altos Cuchumatanes (Solari et al., 2009) and also in Guatemala (Ratschbacher et al., 2009).

Chapter 6: Geological overview of the Cuicateco terrane

These rocks are thought to be related to a magmatic event occurring in the Maya Block in the Devonian (Martens et al., 2010). The basement rocks are covered by Late Palaeozoic sedimentary strata belonging to the Santa Rosa Formation (Weber et al., 2006).

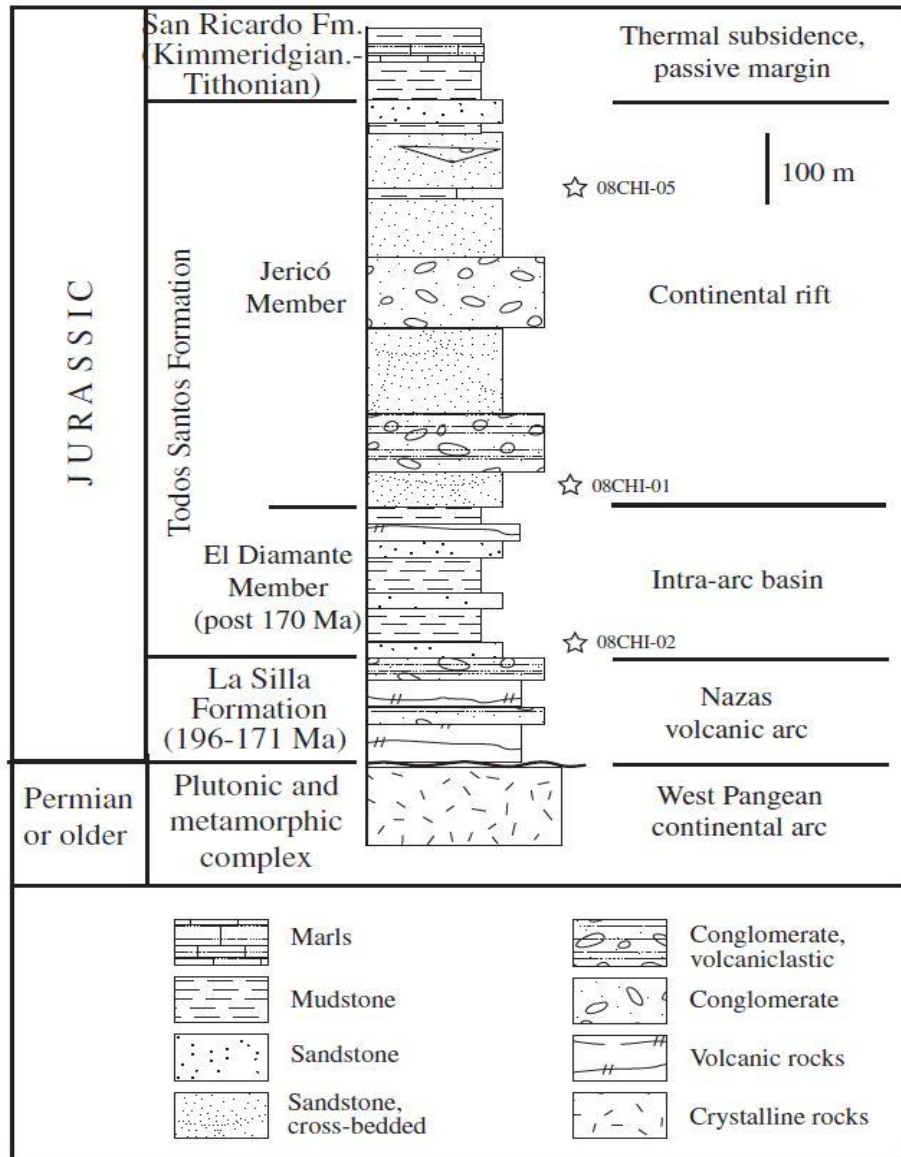


Figure 6.12. Stratigraphic column of the southwestern area of the Maya terrane (Godínez-Urban et al., 2011).

The sedimentary cover of the Maya terrane consists of the Jurassic Todos Santos Formation (Figure 6.12), lying along its western boundary (in contact with the Cuicateco terrane). This unit is composed of red fluvial sandstones, mudstones and

Chapter 6: Geological overview of the Cuicateco terrane

conglomerates containing volcanic-lithic detritus (Godinez-Urban et al., 2011). Detrital zircons from sandstones found in the formation are very uniform and suggest an age of Callovian or younger (Godinez-Urban et al., 2011). It has therefore been proposed that the formation was deposited in a rift basin in association with the early stages of the opening of the Gulf of Mexico (Figure 6.12; Godinez-Urban et al., 2011). Salt deposits that outcrop between the Todos Santos Formation and the San Ricardo Formation are also believed to be related to the continental rifting stage of the Gulf of Mexico opening (see Section 6.6). The latest sequences of the Maya terrane consist of deformed and undeformed Cretaceous and Tertiary marine sediments (Perez-Gutierrez et al., 2009).

6.6 Gulf of Mexico

The Gulf of Mexico is an asymmetric oceanic basin that separates the southern states of the USA from the south of Mexico. The basin formed in association with the opening of the Atlantic Ocean in the Jurassic. The initiation of continental rifting in the Gulf of Mexico is poorly defined (Salvador, 1987; Marton and Buffler, 1994), but some authors place it in the Bathonian (Pindell and Kennan, 2001). Salt was deposited in the basin until the beginning of sea-floor spreading during the Oxfordian, ca. 158 Ma (Figure 6.13; Pindell and Kennan, 2009). It is well documented that the Yucatán block prior to the initiation of rifting in the Gulf of Mexico lay between Texas and Venezuela (Pindell and Dewey, 1982; Pindell, 1985; Schouten and Klitgord, 1994; Dickinson and Lawton, 2001; Jacques et al., 2004; Bird et al., 2005; Imbert, 2005; Imbert and Phillippe, 2005; Pindell et al, 2005). For it to fit into this area a clockwise rotation of 45°-60° needed to occur relative to its current

Chapter 6: Geological overview of the Cuicateco terrane

position (Figure 6.13; Pindell & Dewey, 1982; Pindell, 1985; Marton and Buffler, 1994). The pole of rotation was situated between Florida and Yucatán (Marton and Buffler, 1994). The migration of Yucatán to its current position was accommodated by the Tamaulipas-Golden Lane-Chiapas transform fault zone (Figure 6.13; Pindell, 1985). Seismic line interpretations along the Florida Straits (Marton and Buffer, 1999) indicate that extension in the Gulf of Mexico stopped in the Valanginian (139-134 Ma).

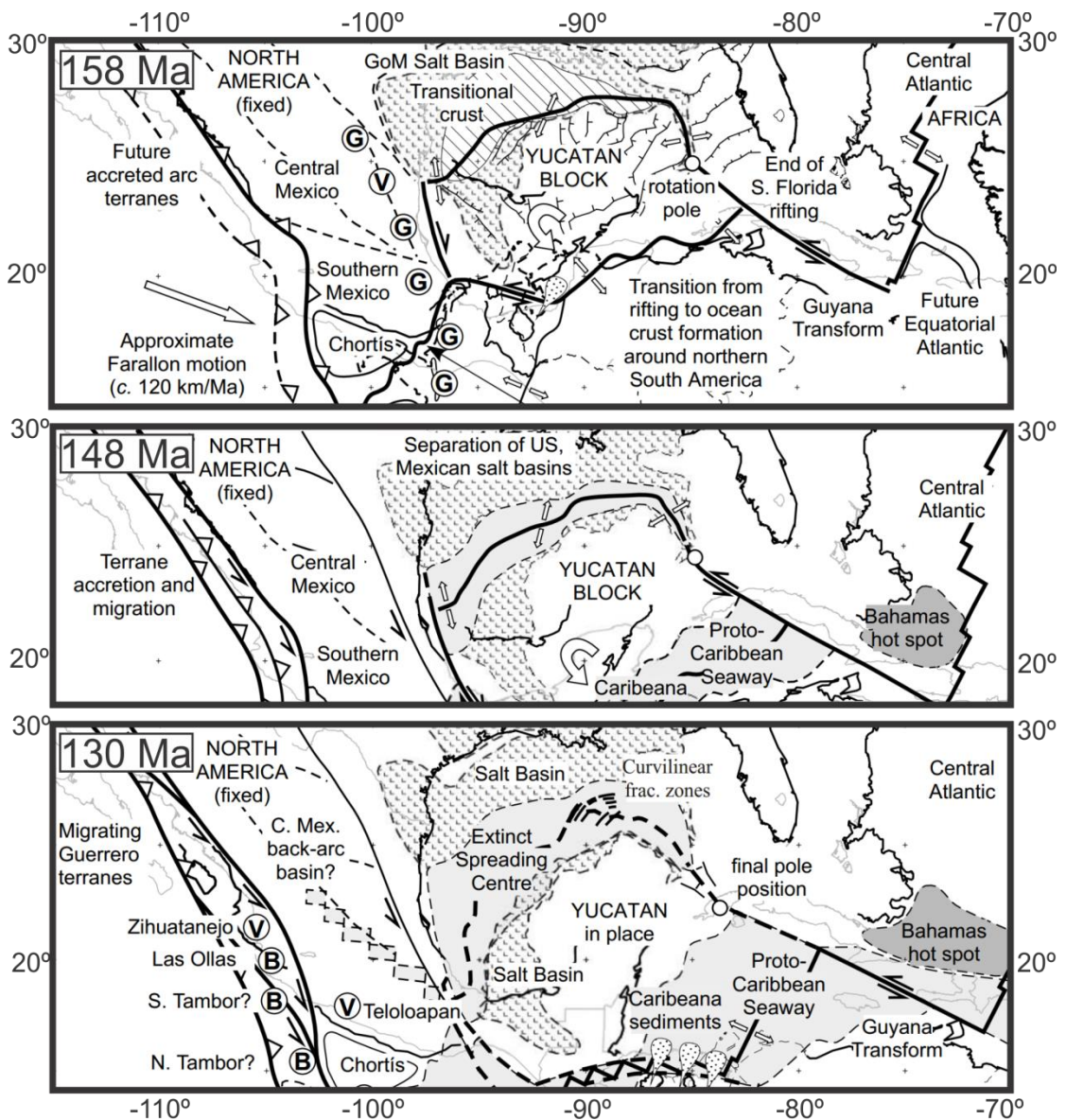


Figure 6.13. Model for the opening of the Gulf of Mexico, adapted from Pindell & Kennan (2009).

6.7 Summary

- The Cuicateco terrane lies in Southern Mexico and is in faulted contact with the Zapoteco terrane to the west along the Oaxaca normal fault and with the Maya terrane to the east along the Vista-Hermosa reverse fault.
- The northern Cuicateco appears to have formed in an extensional event during the Early Cretaceous, predating similar lithologies of the southern Cuicateco by ~60-70 Ma.
- The Early Cretaceous extensional event may relate to rifting associated with the breakup of Pangaea, either through the opening of the Gulf of Mexico (Mendoza et al., 2010) or through the separation of North and South America (Angeles-Moreno, 2006).
- Alternatively, the Early Cretaceous northern Cuicateco may be associated with subduction related extension, as is seen in the Arperos basin in Mexico throughout the Early Cretaceous (Cabral Cano et al., 2000; Elías-Herrera et al., 2000; Centeno-García et al., 2008; Martini et al., 2011 & 2014).
- The south of the Cuicateco terrane, although similar in lithology, is substantially younger (Late Cretaceous) than the northern Cuicateco and therefore they are not likely to be related.

7 Fieldwork and Petrography

7.1 Introduction

Samples from the Cuicateco terrane were collected over two field seasons during 2011 and 2014. Due to the size of the study area and inaccessibility of the regions by foot, samples were mostly collected from outcrops along road sides. This chapter will present field and petrographic observations made from the study area and the collected samples.

The northern Cuicateco, as previously described in Chapter 6, can be split into four principle units of the Mazateco Metamorphic Complex, Chivillas Formation, Pochotepec Formation and the Teotitlán Migmatitic Complex. The Mazateco Metamorphic Complex is comprised of rocks of probable Paleozoic age, with a genesis unrelated to the other units in the northern Cuicateco. For this reason it was decided to focus the sampling on the Chivillas Formation, Pochotepec Formation and Teotitlán Migmatitic Complex. This study also conducted a short field trip in May 2014 to the Xonamanca Formation, which outcrops ~50 km to the north of the Cuicateco terrane (Figure 7.1). There have been very few studies on the Xonamanca Formation but it is reported to be composed of Early Cretaceous volcano-sedimentary successions (Carrasco et al., 1975; Servicio Geológico Mexicano map, 2001; Angeles-Moreno, 2006) which may be similar to the Early Cretaceous successions of the northern Cuicateco terrane. In total 48 samples were collected from the northern Cuicateco and Xonamanca Formation for petrographic, geochemical and geochronological analysis (Figure 7.1; Appendix B).

Chapter 7: Fieldwork and Petrography

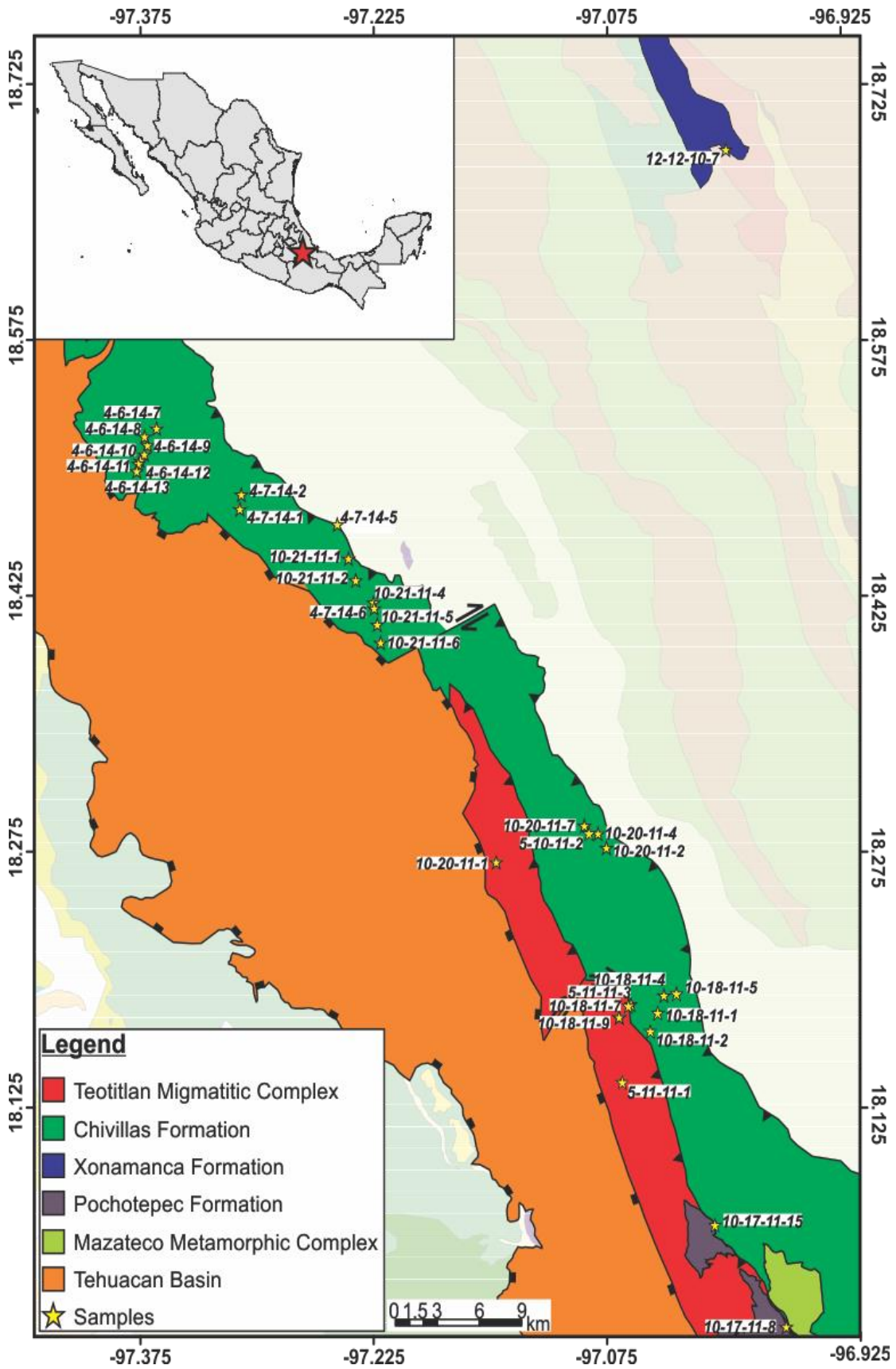


Figure 7.1. Map showing the location of all samples analysed for geochemical and geochronological studies from the Cuicateco terrane. Geological projection from Mexicano, S.G. (2001) map.

7.2 The Chivillas Formation

7.2.1 Fieldwork

In total 27 samples were collected from the Chivillas Formation for geochemical and geochronological analysis (Figure 7.1). The igneous suite of the Chivillas Formation is characterised by plutonic, hypabyssal and extrusive mafic rocks. The extrusive rocks appear to have been erupted in a submarine basin and are preserved as well defined pillow basalts and inter-pillow breccias (Figure 7.3 A-D). Vesicles and amygdales found in the pillow basalts suggest they were extruded at fairly low pressures and therefore in a shallow water column (<1km), where volatiles were able to degas from the magmas (assuming CO₂ is the main volatile degassing).

Stratigraphically lower portions of the igneous suite in the Chivillas Formation are characterised by homogeneous diorite and micro-diorite intrusions that display massive textures (Figure 7.3 F). These plutonic rocks may represent the magma chambers from which the extrusive rocks erupted. Younger generations of basaltic magmatism are observed to intrude these plutonic rocks (Figure 7.3 G&H). The igneous rocks range from being reasonably fresh to showing signs of significant hydrothermal alteration. A slight green colouration to the rocks suggests they are likely to have been exposed to low grades of metamorphism.

Chapter 7: Fieldwork and Petrography



Chapter 7: Fieldwork and Petrography

Figure 7.2. Photographs of Chivillas Formation. A&B) Examples of pillow basalts. C&D) Inter-pillow breccias. E) Vesicles found in the pillow basalts. F) Massive homogeneous diorite G&H) Basaltic dykes intruding into plutonic diorites.

The sedimentary successions observed within the Chivillas Formation are composed of sandstones, conglomerates and lithofacies that are consistent with typical bouma sequences, associated with turbidite deposits (Figure 7.3 A-C). The conglomerates contain clasts of banded quartzofeldspathic rock, quartz white-mica schist and granites (Figure 7.3 D&E), indicating a continental provenance.

The turbidite deposits consist of basal sandstones with normal grading overlain by laminated sandstones and in some instances by slate. In a few areas the lithofacies included basal conglomerates, indicating that an almost complete bouma sequence is present within the Chivillas Formation. Some of the finer slates include carbonaceous material, along with a few carbonate beds (cm's). From the field outcrops it is unclear where the carbonates belong in the lithofacies.

The proximity of the igneous rocks and sedimentary successions throughout the Chivillas Formation suggest that they likely formed contemporaneously. This is confirmed by peperite deposits that are found in the area, where basalts have intruded through wet sediment (Figure 7.3 G&H).

Chapter 7: Fieldwork and Petrography



Chapter 7: Fieldwork and Petrography

Figure 7.3. A-C) Turbidite deposits. Bouma sequence include A,B,C,E. Found in close association with the pillow basalts. D) Folding and deformation of the turbidite deposits. Possibly related to soft sediment slumping. E&F) Interclasts and clasts (tens of cms) of sandstones, granite, schists and quartz in a conglomerate. G&H) Peperite deposits where magmas have intruded wet sediments.

7.2.2 Petrography

7.2.2.1 Igneous suite

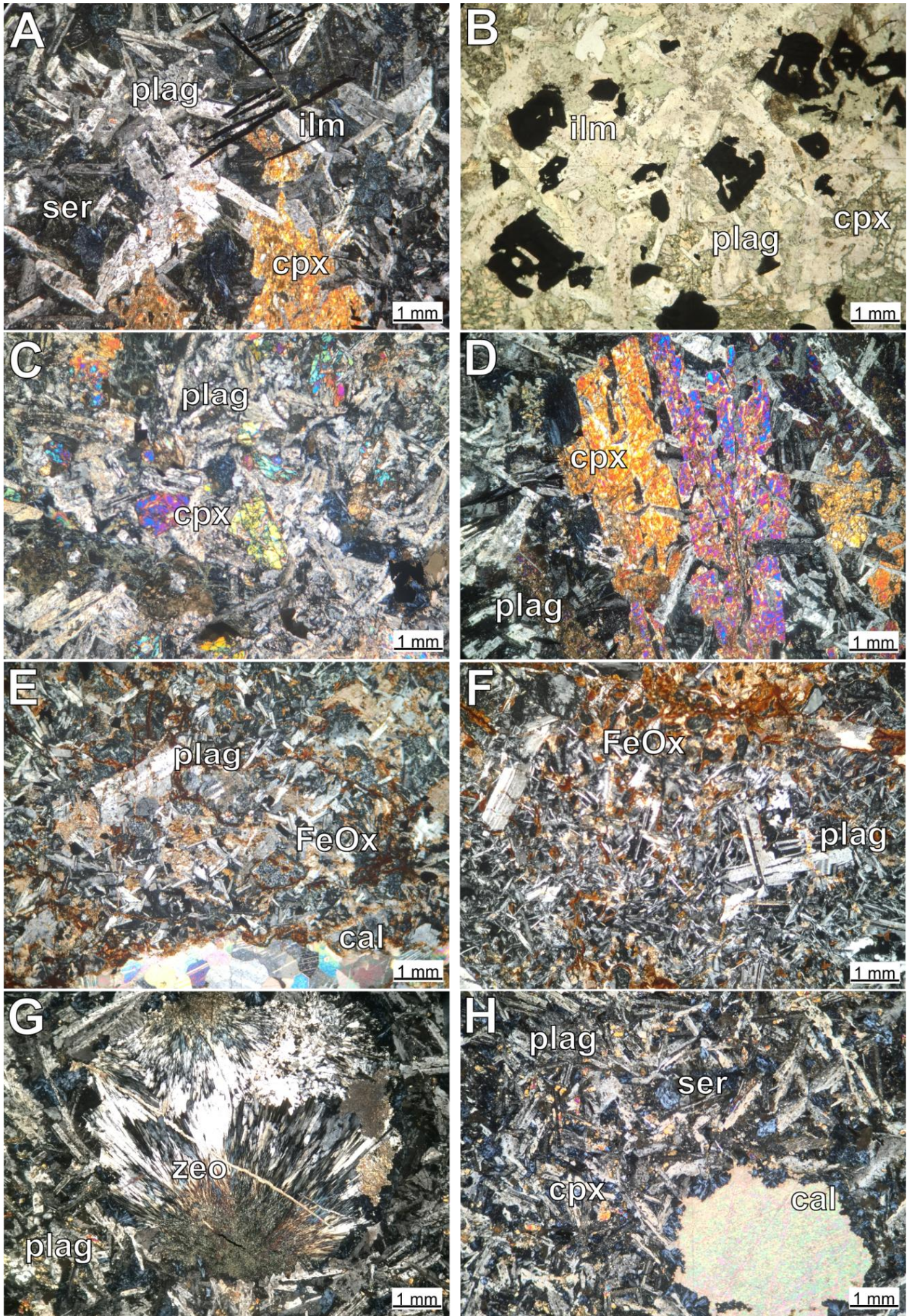
The plutonic rocks of the Chivillas Formation are phaneritic in texture and contain crystals that are 1-7 mm in size. They are predominantly composed of plagioclase (60-80 %¹) that has been partially sericitised (Figure 7.4 A-D). The dominant mafic mineral is clinopyroxene, which contributes 15-30 % of the rock (Figure 7.4 A-D). Skeletal and tabular ilmenite is also relatively abundant (10-20 %), and has been partially broken down into leucoxene (Figure 7.4 A&B).

The extrusive igneous rocks of the Chivillas Formation are aphanitic in texture and contain crystals of fairly uniform size (300-1000 µm), with amygdales that are 1000-5000 µm. They are primarily composed of plagioclase feldspar (70-90 %) that has undergone moderate sericitic alteration (Figure 7.4 E&F). Opaque minerals, which appear to be mainly ilmenite, contribute 5-10 % of the rocks. The mafic phases of the extrusive rocks are again dominated by clinopyroxene (10-20 %; Figure 7.4 H).

Hydrothermal alteration is a common feature of the igneous rocks in the Chivillas Formation. Serpentine can be found throughout the samples in the form of lizardite and antigorite (Figure 7.4 A-F). Calcite is also found in veins and filling amygdales, along with iron oxides (more common in the extrusive rocks; Figure 7.4 E-H). Zeolites are another mineral found to be filling the amygdales (Figure 7.4 G).

¹ All mineralogical percentages are vol.%

Chapter 7: Fieldwork and Petrography



Chapter 7: Fieldwork and Petrography

Figure 7.4. Photomicrographs of the igneous rocks found in the Chivillas Formation. A-D) PPL and XPL view of diorites containing plagioclase laths, clinopyroxene and ilmenite. Serpentine has formed as a result of hydrothermal alteration. E) XPL of a hydrothermally altered basalt with calcite veining. F) XPL view of a hydrothermally altered basalt showing somewhat of a porphyritic texture. Mainly composed of plagioclase. Also contains serpentine and abundant iron oxide G&H) XPL view of a hydrothermally altered basalt. Amygdules are filled with calcite, serpentine and zeolites. Acronyms: ser= serpentine, plag= plagioclase, cal= calcite, FeOx= Iron oxide, cpx= clinopyroxene, ilm= ilmenite, zeo= zeolite.

7.2.2.2 *Sedimentary suite*

The sandstones of the Chivillas Formation contain detrital grains that are angular to sub-angular in habit and 0.5 to 5 mm in size. They are dominated by quartz (50-60 %) and are arkosic in composition (25-35 % feldspars; Figure 7.5 A-F), indicating that they likely derived from a granitic source (continental provenance; Folk, 1974). The feldspars have been partially altered to sericite (Figure 7.5 A-F) and lithic fragments make up around 10-15 % of the sandstones that are mostly composed of chert. Minor phases (2-5 %) include zircon (Figure 7.5 A-F) and titanite (Figure 7.5 E).

The sandstones range from arenites (matrix ~ 5 %; Figure 7.5 A-C) to borderline greywackes (matrix ~ 15 %; Figure 7.5 D; Dott, 1964). There is also a varying amount of calcite cement found in the sandstones which fill any initial porosity. This is most prominent in Figure 7.5 F where calcite cement appears to make up ~20 % of the rock.

Chapter 7: Fieldwork and Petrography

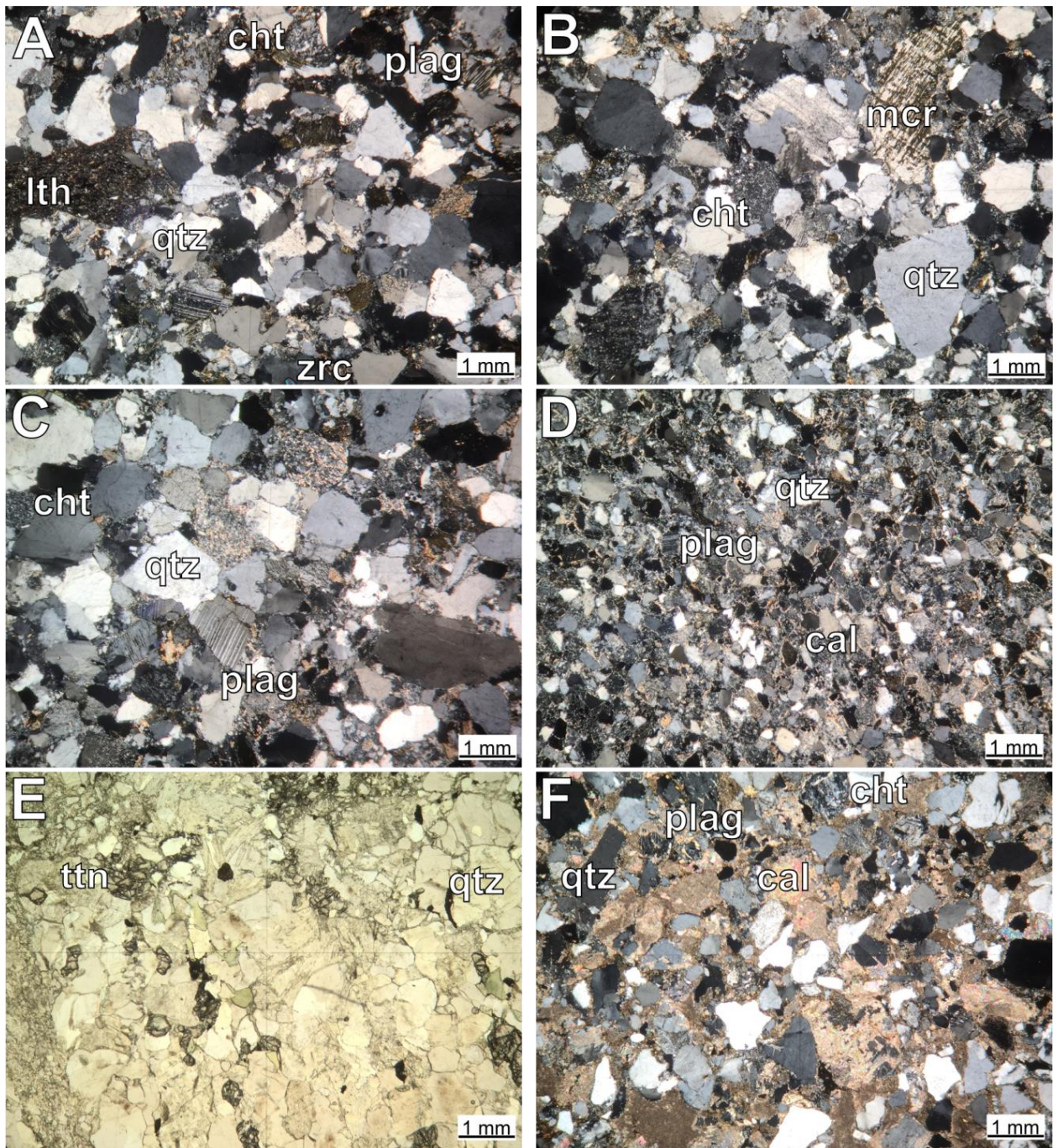


Figure 7.5. Photomicrograph of the sediments from the Chivillas Formation. A-C) XPL view of crystal supported (90 %) arkosic sandstones, containing quartz, plagioclase and microcline (partly seriticised), zircon and lithic fragments (including chert).D) XPL view of clast supported (85 %) arkosic sandstone, predominantly composed of quartz and plagioclase. The cement is composed of clays and calcite E) PPL view of an arkosic sandstone that contains titanite F). XPL view of a crystal supported (85 %) arkosic sandstone, containing quartz, plagioclase and chert fragments. Calcite acts as a cement. Acronyms: qtz= quartz, plag= plagioclase, mcr= microcline; cal= calcite, cht= chert, ttn= titanite, lth= lithic fragment.

7.3 Teotitlán Migmatitic Complex

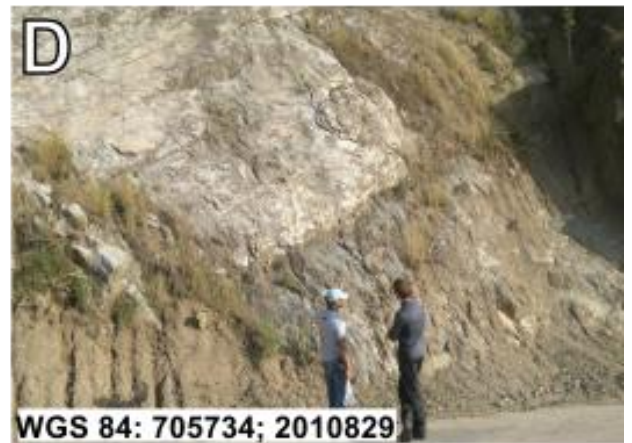
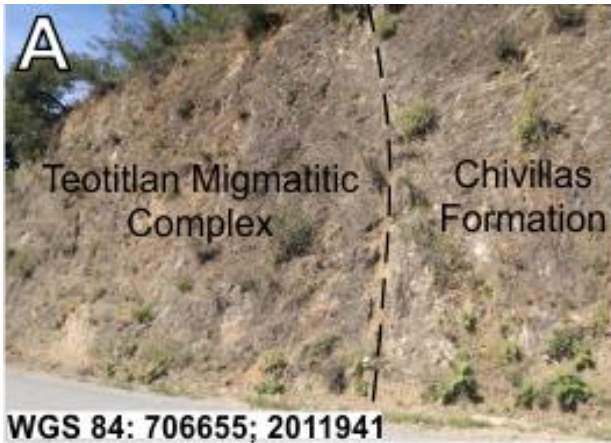
7.3.1 *Fieldwork*

In total 11 samples were collected from the Teotitlán Migmatitic Complex for geochemical and geochronological analysis (Figure 7.1). The area comprises several generations of granitoids that intrude into amphibolite, orthogneiss and paragneiss host rock (Figure 7.6 A-H). It is evident that there has been partial melting of the host rocks, causing migmatitic textures in the amphibolites and gneiss (Figure 7.6 F). This unit of the Cuicateco terrane can be interpreted as a volcano-sedimentary succession that has undergone amphibolite facies metamorphism and has been later intruded by generations of granitoids, causing migmatization of the amphibolites and gneiss.

A small sliver of ultramafic cumulate rock is observed in faulted contact with the Teotitlán Migmatitic Complex (Figure 7.6 B&C). It is difficult to determine the relationship of this cumulate to the rest of the Cuicateco terrane. It may be related to the granitoid intrusions observed in the Teotitlán Migmatitic Complex. Alternatively, it may relate to the oceanic crust of the Chivillas Formation to which it is also in faulted contact with.

The contact between sediments of the Chivillas Formation and granitoids of the Teotitlán Migmatitic Complex is observed along a sub vertical reverse fault (95/82°; Figure 7.6 A) which likely relates to compression during the Laramide Orogeny.

Chapter 7: Fieldwork and Petrography



Chapter 7: Fieldwork and Petrography

Figure 7.6. Photographs of the Teotitlán Migmatitic Complex. A) Faulted contact between sediments of the Chivillas Formation and the granitoids of the Teotitlán Migmatitic Complex. B&C) Ultramafic cumulitic rock found in faulted contact with the rest of the Complex. D-F) Generations of granitoids intruding into amphibolites and paragneiss. G&H) Garnet bearing paragneiss and orthogneiss that the granites of D-F are also found to intrude.

7.3.2 Petrography

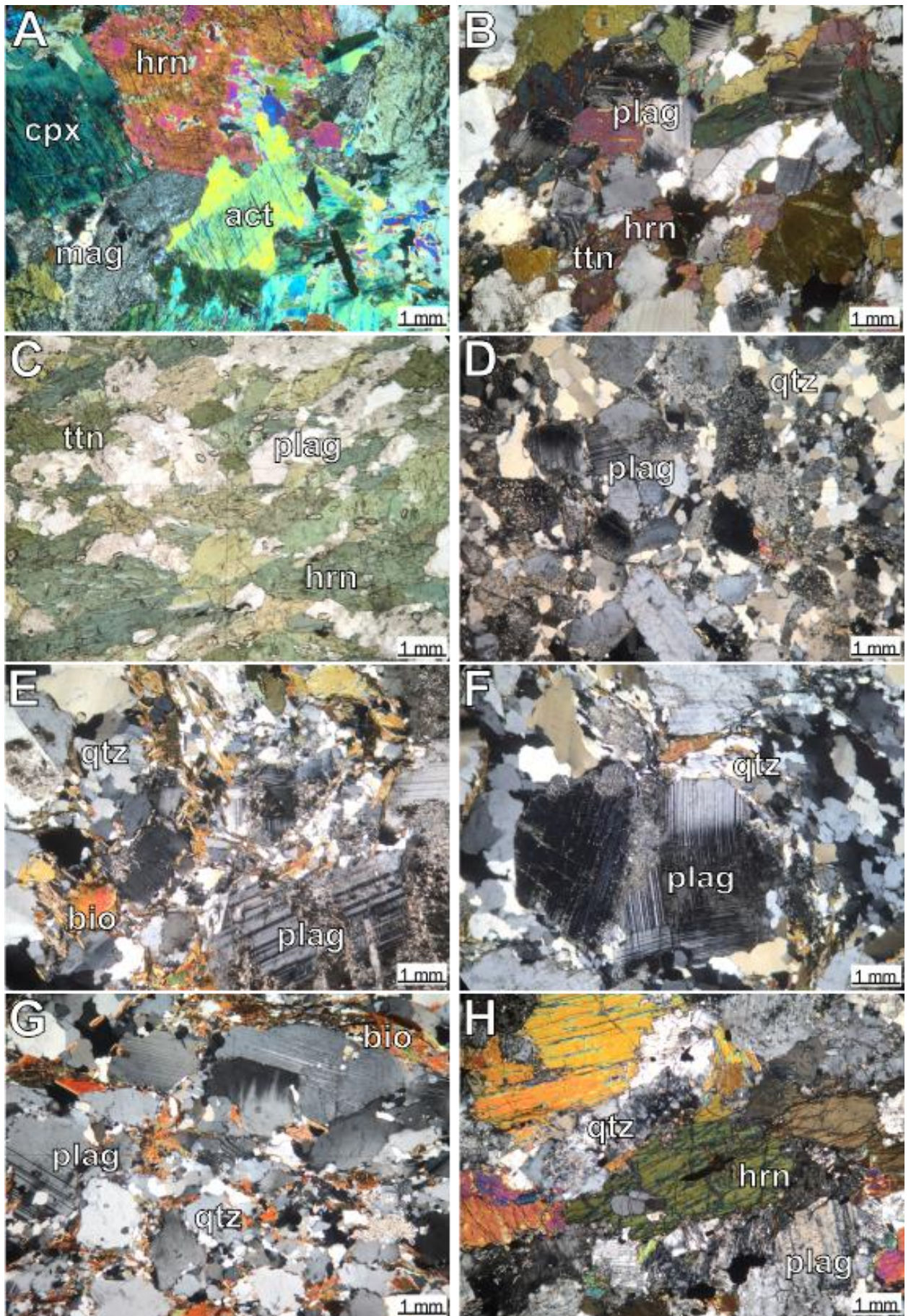
7.3.2.1 *Ultramafic cumulate*

The ultramafic cumulate found in the Teotitlán Migmatitic Complex contains large crystals that are 10-40 mm in size. They appear to have initially formed through the crystallisation of orthopyroxene and clinopyroxene, with subsequent interstitial plagioclase crystallisation (Figure 7.7 A). It has subsequently undergone amphibolite facies metamorphism, forming brown and green amphiboles (Figure 7.7 A). There is also evidence for retrogressive metamorphism with actinolite and titanite forming from the breakdown of the green and brown amphiboles (Figure 7.7 A).

7.3.2.2 *Amphibolites*

The amphibolites of the Teotitlán Migmatitic Complex contain crystals that are 1-10 mm in size, principally composed of hornblende (50-70 %) and plagioclase (20-40 %; partially altered to saussurite and sericite) that display weak compositional banding (Figure 7.7 B&C). Accessory minerals include titanite (5 %) and interestingly a relative abundance of zircon (Figure 7.7 C). In some examples metamorphic clinopyroxene is present (5-10 %), suggesting a high grade amphibolite facies of metamorphism.

Chapter 7: Fieldwork and Petrography



Chapter 7: Fieldwork and Petrography

Figure 7.7. Photomicrographs of the Teotitlán Migmatitic Complex. A) XPL view of an ultramafic cumulitic rock containing amphiboles and pyroxenes. B&C) PPL and XPL view of a poorly foliated amphibolite. Accessory minerals include titanite, apatite and zircon D) XPL view of an aplitic dyke, containing quartz and plagioclase. Quartz recrystallised into fine aggregates. E) XPL view of a tonalite that contains large partly sericitised plagioclase crystals, biotite, dynamically recrystallised quartz and minor zircon. F) XPL view of a tonalite containing fresh plagioclase and quartz. Quartz has been dynamically recrystallised G).XPL view of a biotite gneiss containing quartz, plagioclase, biotite. Accessory minerals include zircon. H) XPL view of amphibolitic gneiss, containing hornblende and plagioclase. Accessory minerals include apatite and opaques. Fabric defined by hornblende. Acronyms: plag= plagioclase, bio= biotite, qtz= quartz, hrn= hornblende, ttn= titanite, cpx= clinopyroxene, act= actinolite, mag= magnetite.

7.3.2.3 *Granitoids*

Petrographic interpretations on the granitoids of the Teotitlán Migmatitic Complex reveal crystals that are 0.5 to 15 mm in size. The granitoids are composed of 40-50 % feldspars, which are dominated by the plagioclase member (95%), indicating a tonalitic composition (Figure 7.7 D-F). The feldspars have subsequently moderately been altered to sericite and saussurite. Quartz in the tonalites (25-40 %) has been widely recrystallised, forming quartz-rich veins that tend to wrap around the more resilient plagioclase crystals (Figure 7.7 D-F), and indicating deformation has occurred. This deformation appears to be fairly low grade as the plagioclase only shows evidence for brittle deformation (deformed twins and fractures). Biotite is also present in varying amounts in the tonalites (5-25 %) and is often altered to chlorite.

7.3.2.4 *Gneiss*

The gneisses of the Teotitlán Migmatitic Complex contain crystals that are 0.3 to 15 mm in size. They are variable in composition, with some examples containing quartz (30 %), plagioclase (45 %) and biotite (15 %; Figure 7.7 G). A weak foliation is defined by the biotite, although some grow with a random orientation suggesting

Chapter 7: Fieldwork and Petrography

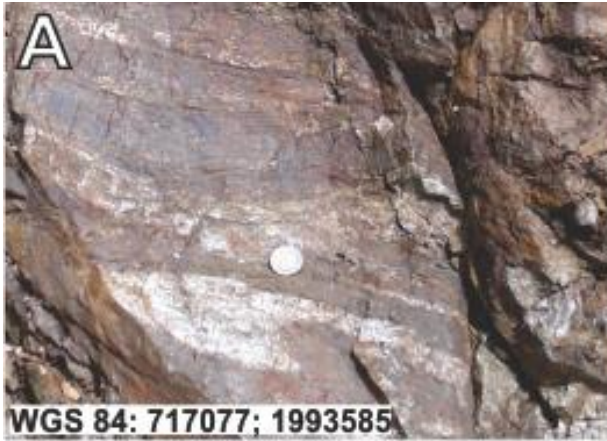
that biotite may have grown syn- to post-kinematically (Figure 7.7 G). The quartz is commonly recrystallised into quartz ribbon (Figure 7.7 G). Other examples lack quartz and biotite and are instead composed of hornblende (15 %) and partially seriticised plagioclase (70 %), with minor apatite and opaque minerals (Figure 7.7 H).

7.4 Pochotepec Formation

7.4.1 Fieldwork

In total two samples were collected from the Pochotepec Formation for geochronological analysis from a dirt road linking the towns of Pochotepec and La Toma (Figure 7.1). The formation is characterised by moderately-severely weathered metasediments (schists and calc-silicates), mafic magmatism and granitoid intrusions that have all undergone greenschist-amphibolite facies metamorphism (Figure 7.8 A-H). The granitoids intrude into the metasediments (Figure 7.8 A&B). Pegmatites associated with the granitoids display an unusual texture (possibly graphic) involving blue quartz and plagioclase (Figure 7.8 C). Amphibolites are found close to the town of La Toma, interbedded with the schists (Figure 7.8 G&H). The Pochotepec Formation appears to have been affected by widespread deformation with folding observed in the granitoids and metasediments (Figure 7.8 A&E). Crenulations observed in the schists suggest that more than one deformation event has occurred (Figure 7.8 F). No contact was observed between the Pochotepec Formation and the other units of the Cuicateco terrane.

Chapter 7: Fieldwork and Petrography



Chapter 7: Fieldwork and Petrography

Figure 7.8. Photographs of the Pochotepec Formation. A&B) folded granites intruding into schists. C) Banding of blue quartz found in a pegmatite. D) Quartz-mica schist. E) Isoclinal folding in a quartz-white mica schist. F) Crenulated feldspar-white mica-chlorite banded schist. G&H) Intrusions of granitoids and amphibolites into schists.

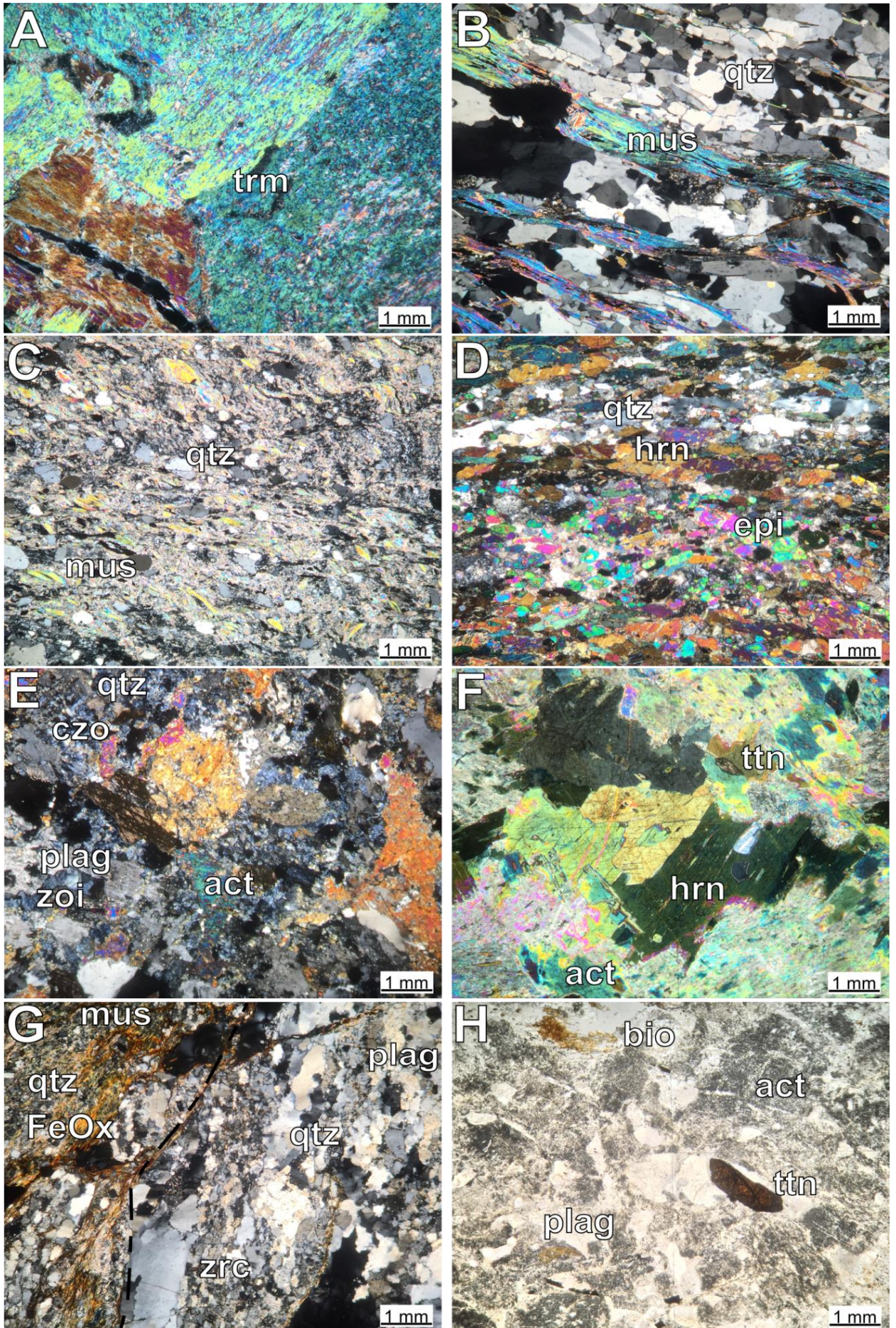
7.4.2 Petrography

7.4.2.1 Metasediments

Metasediments of the Pochotepec Formation are dominated by schists, with minor examples of para-amphibolites. The para-amphibolites contain large crystals that range in size between 2 and 12 mm that are primarily composed of tremolite (80 %), and quartz (20 %; Figure 7.9 A). The petrographic interpretations indicate that the protolith might have been a dolomitic limestone.

Petrographic interpretations on the schists reveal metamorphic minerals that range in size between 0.1 and 20 mm, primarily composed of micas (20-60 %; Figure 7.9 B&C) that include both muscovite and biotite (chloritized in some examples). Recrystallised quartz and plagioclase are also common in the schists (30-70 %) and often define a foliation (Figure 7.9 B&C). Accessory minerals found in the schists include zircon and apatite (<1%).

Chapter 7: Fieldwork and Petrography



Chapter 7: Fieldwork and Petrography

Figure 7.9. Photomicrographs of the Pochotepec Formation. A) XPL view of tremolite in a calc-silicate rock. B) XPL view of quartz-muscovite schist. Foliation defined by muscovite C) XPL view of greenschist facies arkosic arenite. Foliation defined by quartz ribbons. D) XPL view of a nematoblastic epidote amphibolite E) XPL view of titanite, clinozoisite, zoisite bearing amphibolite F) XPL view of a coarse amphibolite. Protolith is likely a plutonic rock. G) XPL view of quartz-chlorite schist being intruded by a lineated granite H) PPL of a granite containing titanite. Plag= plagioclase, bio= biotite, qtz= quartz, hrn= hornblende, ttn= titanite, trm= tremolite, act= actinolite, epi= epidote, zoi= zoisite, czo= clinozoisite, FeOx= Iron oxide, mus= muscovite, zrc= zircon.

7.4.2.2 *Amphibolites*

The amphibolites from the Pochotepec Formation range from being compositionally banded, where the crystals are 0.1 to 1 mm in size (Figure 7.9 D), to having more of a phaneritic igneous like texture, where the crystals are 5 to 20 mm in size (probably relating to a meta-plutonic rock; Figure 7.9 F). The main amphibole present is hornblende (30-60 % of the rock) but actinolite can also be found and this may have formed from the regressive breakdown of hornblende (Figure 7.9 E-F). Other common metamorphic minerals include epidote, clinozoisite, zoisite and titanite (Figure 7.9 E). Quartz is also a common mineral in the compositionally banded amphibolites (10-20%; Figure 7.9 D).

7.4.2.3 *Granites*

The granites of the Pochotepec Formation contain crystals that are 0.5 to 10 mm in size and predominately composed of quartz (35-50 %) and seriticised alkali feldspars (25-40 %; Figure 7.9 G&H). The quartz has commonly been recrystallised, forming aggregates and ribbons (Figure 7.9 G&H). Minor phases in the granites include biotite (5-10 %), titanite (5 %) and zircon (Figure 7.9 G&H). The presence of actinolite, clinozoisite and epidote in some samples indicates that the rocks have undergone greenschist facies metamorphism.

7.5 Xonamanca Formation

7.5.1 *Fieldwork*

In total five samples were collected for geochemical and geochronological analysis from the Xonamanca Formation (Figure 7.1). Little has been reported on the Xonamanca Formation in the past, likely due to the thick vegetation that covers the area and makes finding outcrops difficult (Figure 7.10 A&B). The formation is composed of a volcano-sedimentary succession of red tuffs that are interbedded with extrusive volcanic rocks and volcanoclastic material (Figure 7.10 C-E). The volcano-sedimentary unit of the Xonamanca Formation is overlain by dark micritic limestones that contain echinoid fossils dating to the Valanginian (140-136 Ma; Carrasco et al., 1975; Figure 7.10 F-H).

Chapter 7: Fieldwork and Petrography



Chapter 7: Fieldwork and Petrography

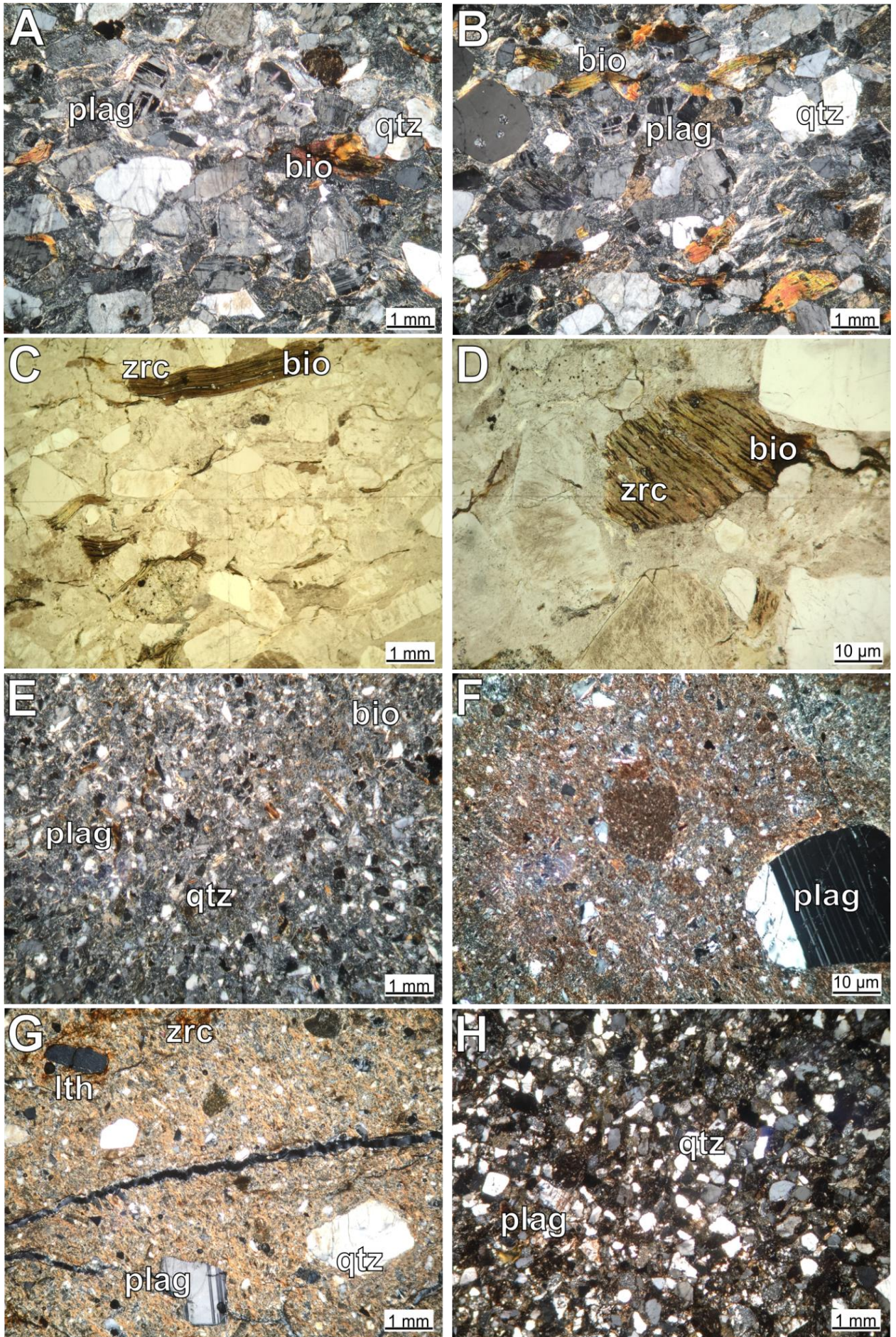
Figure 7.10. Photographs of the Xonamanca Formation. A&B) Photos showing dense vegetation in the area C-E) Cliff face exposing successions of red tuffs, lavas and volcanoclastics F-H) Limestone outcrops that cover the volcanic successions of the Xonamanca Formation.

7.5.2 Petrography

The tuffs of the Xonamanca Formation are predominantly composed of fresh plagioclase, quartz and biotite (Figure 7.11 A-H) sitting in a matrix of devitrified and altered glass. Small amounts of lithic fragments are also present and are associated with iron oxides in some instances (Figure 7.11 G). Evidence of compaction can be seen in the welded tuffs (Figure 7.11 A-D) whereby devitrified and altered glass (possible fiammes) and biotite define a weak fabric. Alternatively this foliation may have formed in response to a pyroclastic surge. The unwelded tuffs range from being poorly sorted (70 % devitrified glass and ash matrix and 30 % larger crystals and lithic fragments; Figure 7.11 F&G) to well sorted (30 % ash matrix and 70 % larger crystals; Figure 7.11 E&H).

Zircons found in the tuffs of the Xonamanca Formation are seen to be associated with biotite (Figure 7.11 C&D). This biotite is likely to have crystallised in the same eruption that formed the tuffs. We can therefore be fairly confident that any geochronological work on the tuffs would record the timing of eruption rather than any contamination from lithic fragments.

Chapter 7: Fieldwork and Petrography



Chapter 7: Fieldwork and Petrography

Figure 7.11. Photomicrographs of the Xonamanca Formation. A-D) PPL and XPL view of a moderately well sorted, fresh welded tuff containing quartz, plagioclase, biotite and zircons (associated with the biotite). The biotite defines a foliation probably related to compaction E) XPL view of a moderately well sorted tuff, containing small crystals of plagioclase, quartz and biotite. Appears matrix supported F&G) XPL view of a poorly sorted tuff with large crystals of plagioclase in a fine groundmass of ash, lithics, plagioclase and quartz. H) XPL view of a crystal supported tuff containing plagioclase and quartz. Acronyms: plag=plagioclase, Qtz= quartz, lth= lithic fragments, bio= biotite, zrc= zircon.

7.6 Summary

- The igneous rocks of the Chivillas Formation are composed of submarine pillow basalts and plutonic diorites that were contemporaneously formed alongside turbidite deposits that display continental signatures. The contact between the Chivillas Formation and the Teotitlán Migmatitic Complex was observed along a sub vertical thrust fault, likely relating to the compressive deformation associated with the Laramide Orogeny.
- The Teotitlán Migmatitic Complex is composed of several generations of tonalites that intrude into migmatized amphibolites and gneisses that have subsequently been deformed. A small sliver of ultramafic cumulate rock may be related to the tonalite intrusions or alternatively to the marine basin of the Chivillas Formation.
- The Pochotepec Formation is composed of sediments, mafic magmatism and granitoids that have undergone greenschist to amphibolite facies metamorphism. No contact was observed during this study between the Pochotepec Formation and the rest of the units in the Cuicateco terrane.
- The Xonamanca Formation is composed of a volcano-sedimentary unit that is dominated by tuffs and pyroclastic deposits. The tuffs yield zircons that appear to be associated with the age of magmatism and so have been used for geochronology in Chapter 8.

8 Zircon U/Pb Geochronology results for the Cuicateco terrane.

8.1 Introduction

This chapter presents U/Pb geochronological results on zircons separated from 14 samples collected from various units of the northern Cuicateco terrane and the Xonamanca Formation (Figure 8.1). Separation as well as analysis (via LA-ICP-MS) was carried out at the facilities at National Autonomous University of Mexico (UNAM) in Juriquilla, Mexico. Further information concerning the method for extracting the zircons, analysis procedure and corrections of initial results are given in Appendix A and F.

Ages have been determined using the radiometric method of uranium-lead (U-Pb) dating on zircons. Results of the analysis have been graphically presented in either a Tera-Wasserburg in association with a $^{206}\text{Pb}/^{238}\text{U}$ weighted-mean age calculation or Wetherill Concordia diagram in association with a $^{207}\text{Pb}/^{206}\text{Pb}$ weighted-mean age calculation, depending on the age of the zircons present. The Tera-Wasserburg and $^{206}\text{Pb}/^{238}\text{U}$ weighted-mean age calculation are more reliable with Phanerozoic zircons whereas the Wetherill Concordia and $^{207}\text{Pb}/^{206}\text{Pb}$ weighted-mean age calculations are more reliable with Precambrian zircons (Jackson et al., 2004; Ludwig, 2012). Most of the age calculations have been made using weighted mean plots but in samples where there is a large range in the population age then the TuffZirc plot has been used which calculates the median age of a population. All figures presented in this section have been constructed using the excel macro

Chapter 8: U/Pb Geochronology for the Cuicateco terrane

“isoplot 4.15” created by Dr. Ken Ludwig at the Berkeley Geochronology Center (Ludwig, 2012).

The data presented will constrain crystallization and depositional ages of the rocks found within the Cuicateco terrane. CL images used in conjunction with Th/U ratios as well as REE patterns have been used to distinguish between metamorphic and igneous zircon growth. Zircons forming in metamorphic environments usually, but not exclusively, yield Th/U ratios of <0.1 whereas igneous zircons generally have ratios >0.2 . Magmatic REE patterns typically have pronounced Eu negative anomalies and steep/enriched HREE patterns whereas the Eu anomaly is usually less pronounced/absent and HREE patterns are suppressed in metamorphic zircons (Rubatto and Hermann, 2007). The U concentration of the zircons will be used to identify any grains that are likely to have undergone metamictization (Nasdala et al., 2001). On samples that have a sedimentary protolith the detrital zircons will be used to identify the provenance of the grains as well as constrain the maximum age of deposition, using the youngest population of zircons.

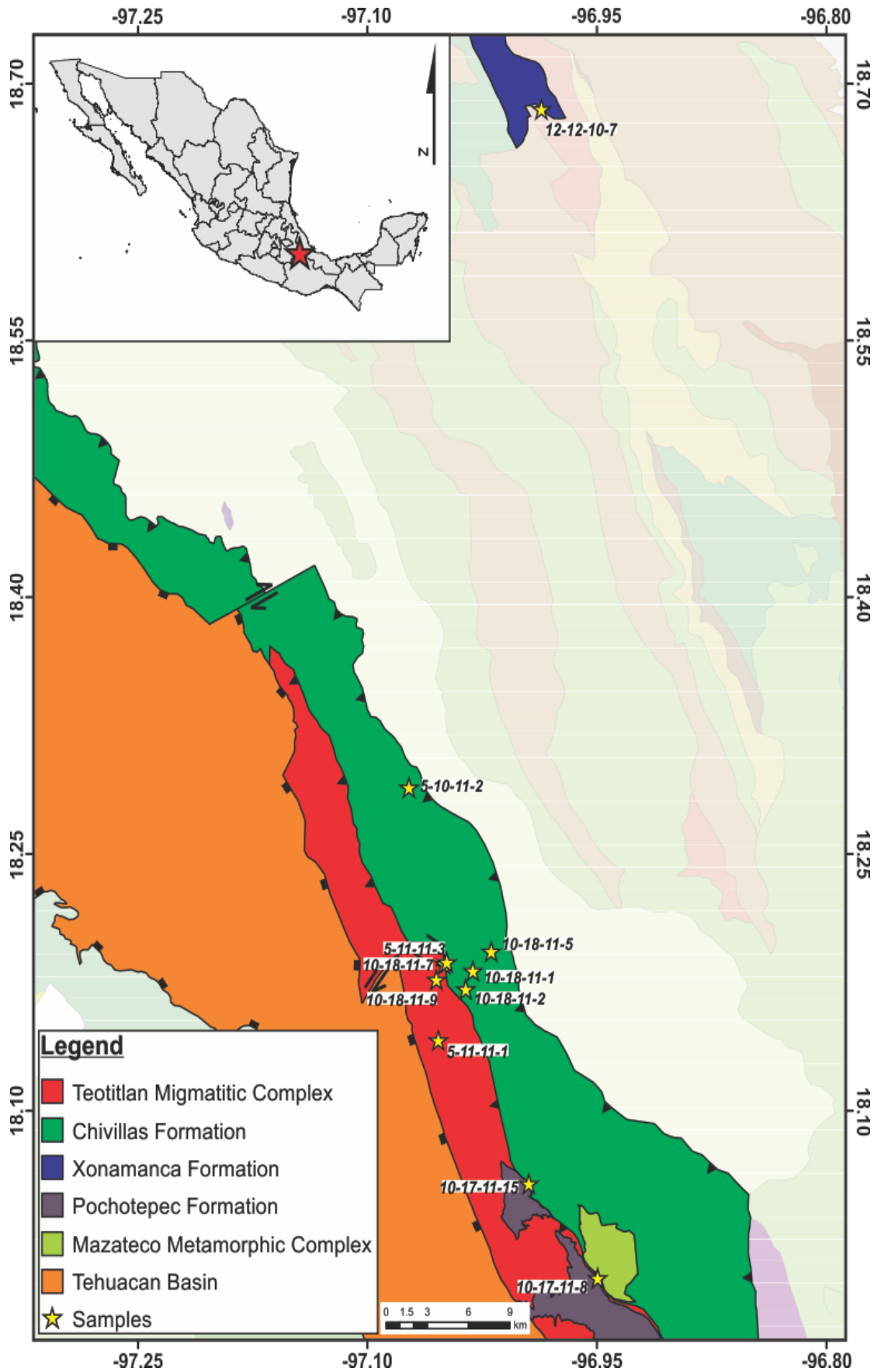


Figure 8.1. Map showing localities of the samples used in the geochronological study. Geological projection from Mexicano, S.G. (2001) map.

8.2 Pochotepec Formation

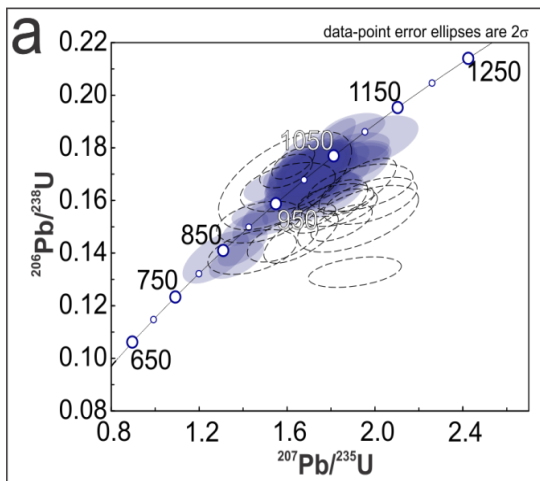
8.2.1 Sample 10-17-11-15c

Sample 10-17-11-15c is composed of a quartz, two-mica schist containing garnet that has subsequently been altered. Zircons are subhedral-subrounded and 100-400 μm along their longest axis, with aspect ratios of 1:1-4:1. The CL textures are characterised by faint oscillatory zoning throughout the grains (Figure 8.2 h). There is one example of a potential inherited core that is dark in colour, suggesting high U.

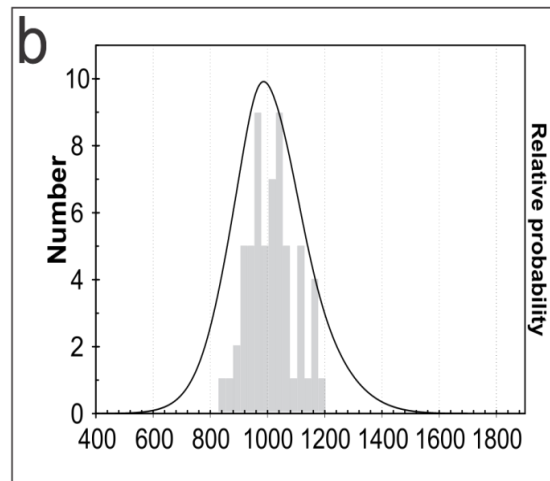
Th/U ratios and U concentrations are uniform throughout the grains (0.2-0.6 and 60-300 ppm respectively; Figure 8.2 d & e). The potential core highlighted in the CL observations is anomalous and displays Th/U ratios of 0.15 and U concentrations of 900 ppm. From the Wetherill plot a single Proterozoic population can be identified (Figure 8.2 a). Interestingly, the high-U core yielded an age comparable to the other zircons (966 ± 39 Ma), which may be explained by metamictization causing an artificially young age.

Of the 79 analysed zircons 61 were deemed reliable enough to be used in age calculations (<10% discordant and <10% inversely discordant). Weighted mean plots yield an age of 996 ± 25 Ma, with an MSWD = 0.5 (Figure 8.2 c). This age, along with the uniform REE patterns and Th/U ratios, suggests that the sedimentary protolith had a very homogeneous source of 1100-850 Ma (Figure 8.2 b), likely relating to the Mexican aspect of the Grenville orogeny (Oaxaquia), with the calculated age representing the maximum age of deposition for the sediment.

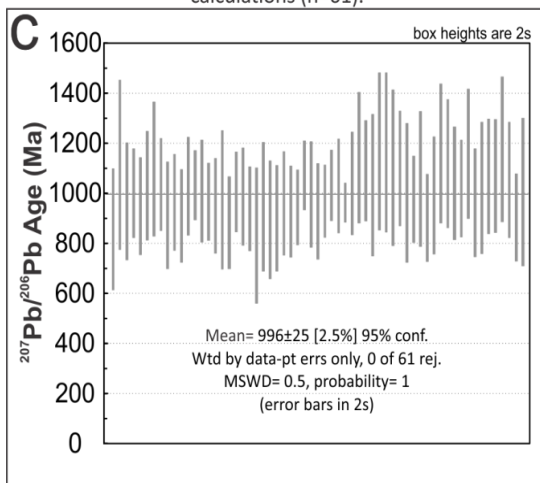
10-17-11-15c



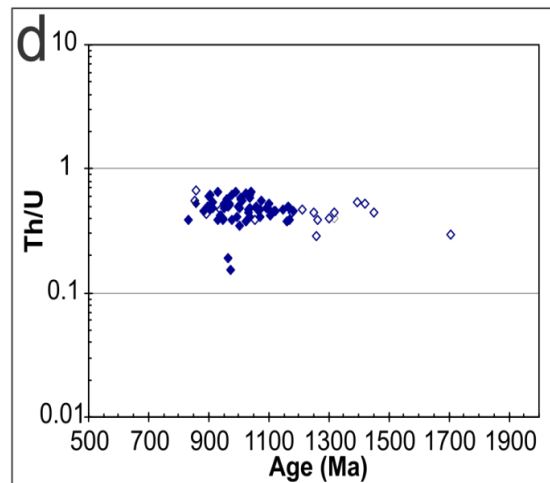
Wetherill diagram for all of the analysis (n=79). The dotted ellipses represent zircons that were disregarded (>10% discordant and >10% inversely discordant), the shaded ellipses represent zircons that were considered for age calculations (n=61).



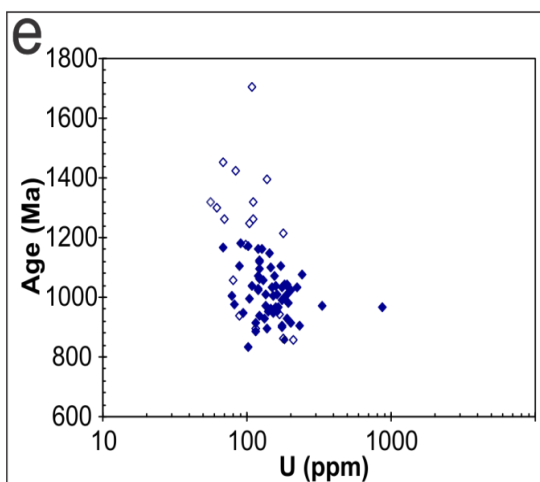
Probability density plot for the zircons that were considered in age calculations.



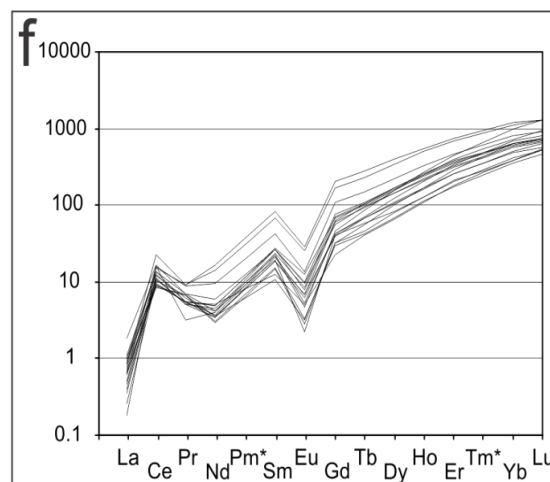
Weighted mean plots for the zircons considered for age calculations.



Th/U vs Age (Ma) diagram for all of the analysed grains. The blue points represent those that were considered for age calculations and the clear points those that were disregarded.



Age (Ma) vs. U (ppm) diagram for all of the analysed zircons. The blue points represent those that were used in age calculations and the clear points those that were disregarded.



Condrile normalised REE diagram for the disregarded zircons.

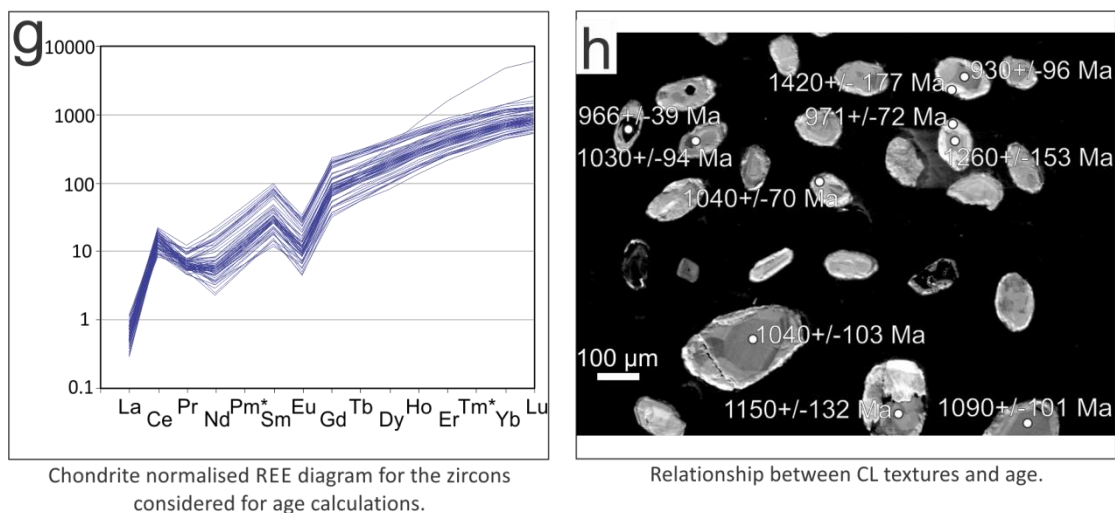


Figure 8.2. Geochronology results for sample 10-17-11-15c of the Pochotepec Formation.

8.2.2 Sample 10-17-11-8a

This sample was collected from a folded and lineated granite and contains subhedral zircons that are 100-250 μm along their longest axis, with aspect ratios of 2:1-5:1. The CL textures clearly define a core and rim relationship in the grains (Figure 8.3 I). The cores are characterised by dark CL response (possibly due to high U) and oscillatory zoning, whereas the rims are more homogeneous and light coloured (possibly due to lower U).

Th/U ratios and U concentrations are quite varied (0.01-1.1 and 10-3000 ppm respectively; Figure 8.3 i & j). The higher U concentrations are linked to the cores as suggested by the CL images. Correlations between the youngest core ages and high-U concentrations are evident, suggesting metamictization. To account for this, zircons with $U > 1000$ ppm have not been used in age calculations. The Wetherill diagram shows that both cores and rims yield Precambrian, mostly Mesoproterozoic ages (Figure 8.3 a & b). The similarity in age between the igneous crystallization and

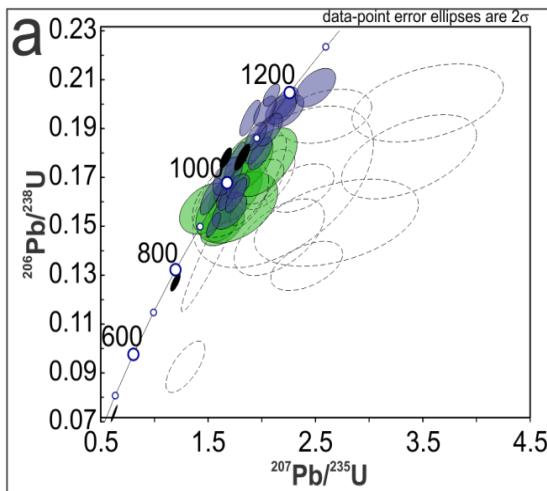
Chapter 8: U/Pb Geochronology for the Cuicateco terrane

metamorphic overgrowths in the zircons makes it difficult to distinguish between the two events as there is a lot of overlap.

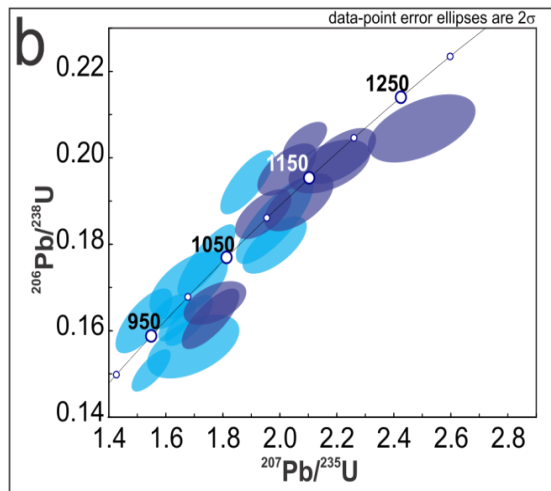
Of the 49 analysed zircons 28 were deemed reliable enough to be used in age calculations (<10% discordant, <4% error and <8% inversely discordant). Averages of cores and rims yielded ca. 1051 ± 42 Ma and ca. 1173 ± 120 Ma, which are equivalent within error (Figure 8.3 c & d). The large degree of error in the metamorphic rim ages probably relates to their low U concentrations.

The core ages show wide spread of isotopic ratios, perhaps due to partial resetting by metamorphism. Interestingly, there is some correlation between the concentrations of REE and age. The cores with REE patterns similar to the metamorphic rims yield ages younger than the cores with higher REE concentrations, which are generally more typical of igneous systems (Figure 8.3 g & h). A plausible interpretation is that cores richer in REE represent the igneous age and those with low REE represent partial reset by metamorphism. The average age of cores with high REE is 1119 ± 62 Ma, with a MSWD of 1.3 (Figure 8.3 e) and the average of cores with low REE is 1019 ± 56 Ma, with a MSWD of 2.0 (Figure 8.3 f). These ages are interpreted as the best constraints for the igneous and metamorphic ages respectively.

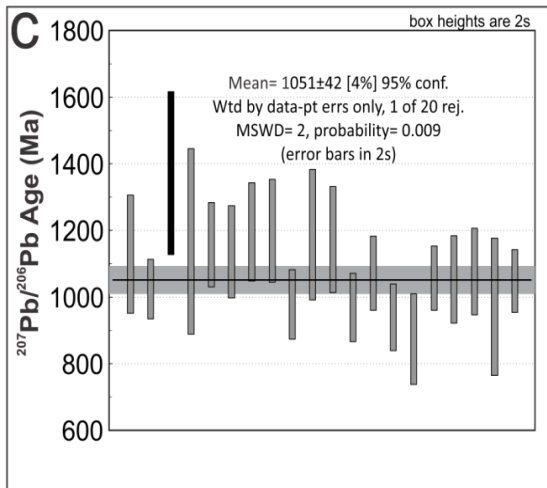
10-17-11-8A



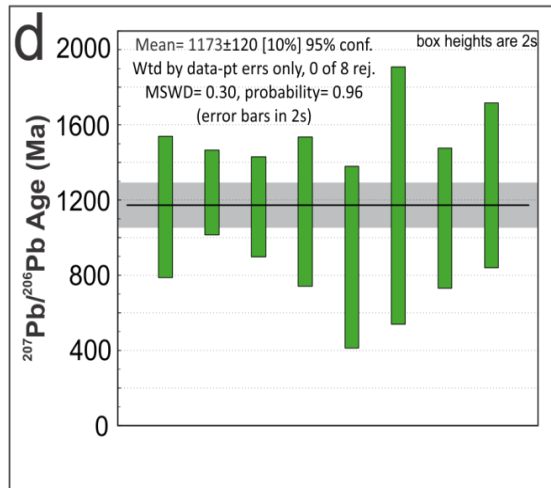
Wetherill diagram of all analyses. Green ellipses represent zircon rims with <4% error and <10% discordance (n=8). Blue analyses are cores with <2.5% error, <8% discordant, and <6% reverse discordant (n=20). Dashed ellipses are discarded analysis.



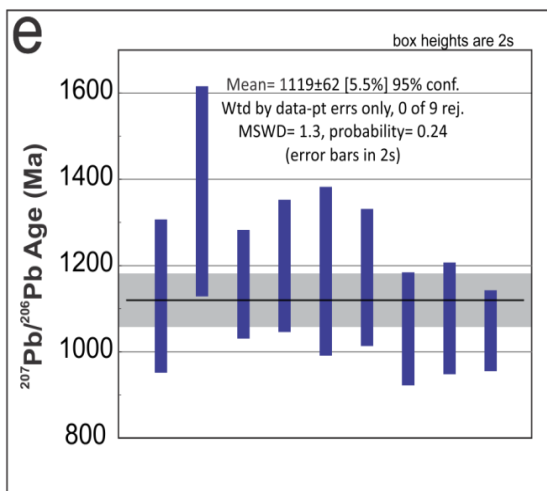
Wetherill diagram for the zircon cores in the sample. Dark blue ellipses are cores with high REE concentrations and light blue are cores with low REE concentrations.



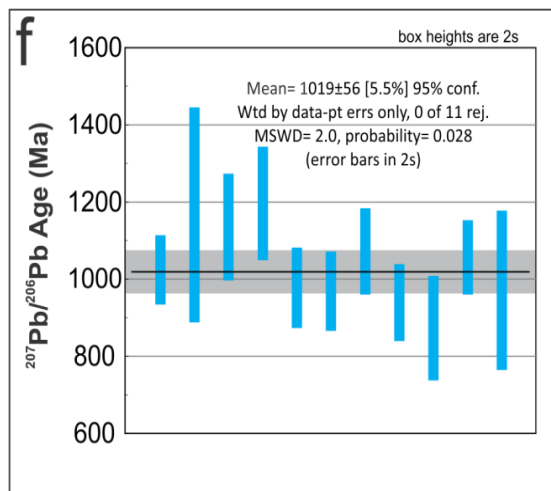
Weighted-mean plot of zircon cores (n=20), using the $^{207}\text{Pb}/^{206}\text{Pb}$ isotopic system.



Weighted-mean plot of zircon rims (n=8), using the $^{207}\text{Pb}/^{206}\text{Pb}$ isotopic system.



Weighted mean plot for the cores considered for age calculations with high REE values (n=9).



Weighted mean plot for the cores considered for age calculations with low REE values (n=11).

Chapter 8: U/Pb Geochronology for the Cuicateco terrane

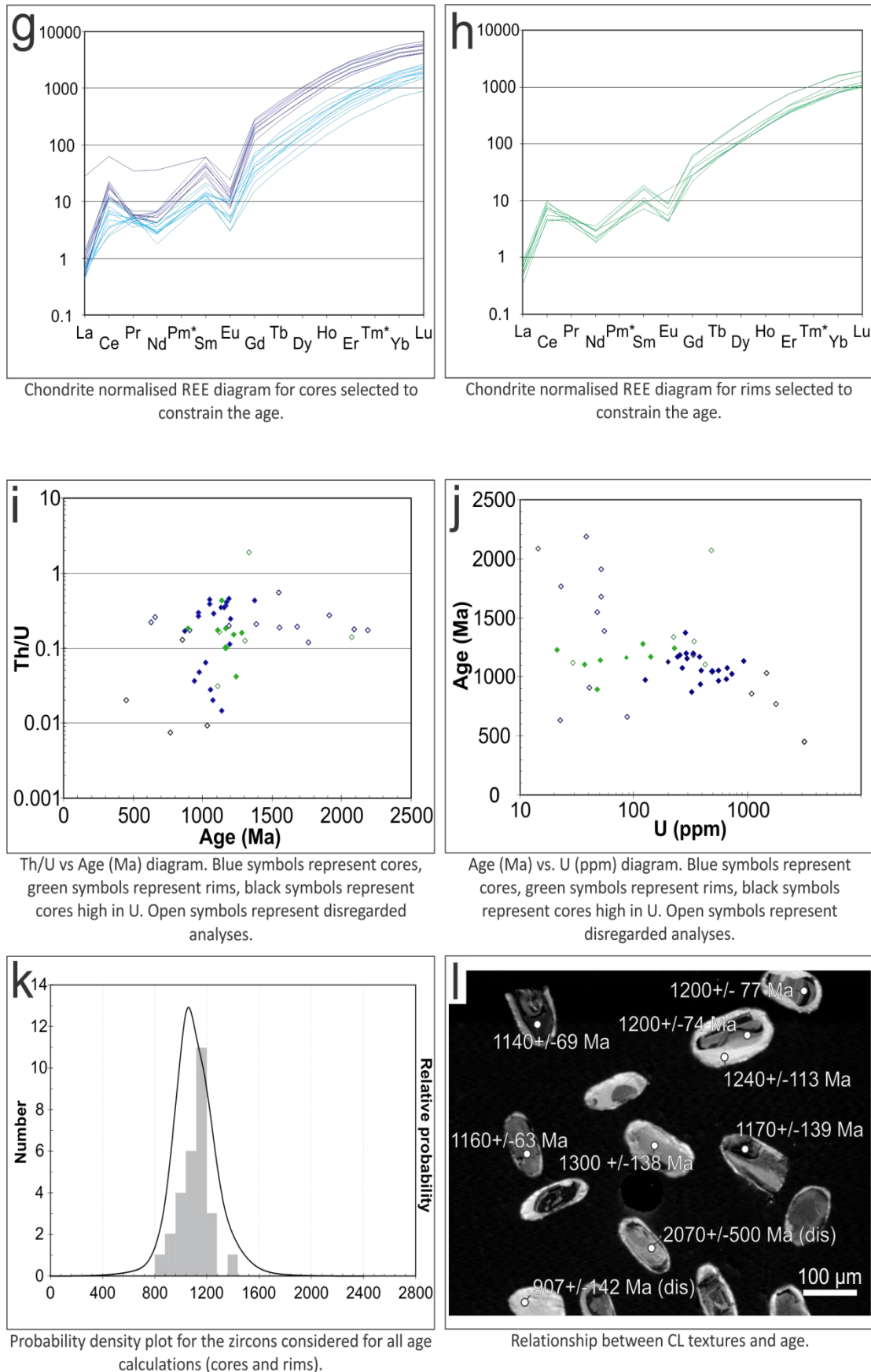


Figure 8.3. Geochronology results for sample 10-17-11-8a of the Pochotepec Formation.

8.3 Xonamanca Formation

8.3.1 *Sample 12-12-10 7B*

This sample is a lapilli-tuff containing clasts of quartz, plagioclase and minor biotite. The zircons are euhedral to subhedral in shape and 100-200 μm along their longest axis, with aspect ratios of 2:1-7:1. The CL textures are characterised by sector and oscillatory zoning, typical of igneous zircons (Figure 8.4 j).

The Tera-Wasserburg and Wetherill plots (Figure 8.4 a & b) reveal a range of zircon populations in the sample. Of the 30 grains that were analysed, 24 were deemed reliable to use for age calculations (<4% error and <20% discordance). The oldest concordant population relates to Grenvillian age inherited grains (1006 \pm 95 Ma, 1030 \pm 51 Ma, 1038 \pm 85 Ma and 1109 \pm 122 Ma). The second inherited population is Palaeozoic in age (251 \pm 6 Ma, 315 \pm 10 Ma and 421 \pm 6 Ma). The most abundant concordant population relates to zircons that are Cretaceous in age.

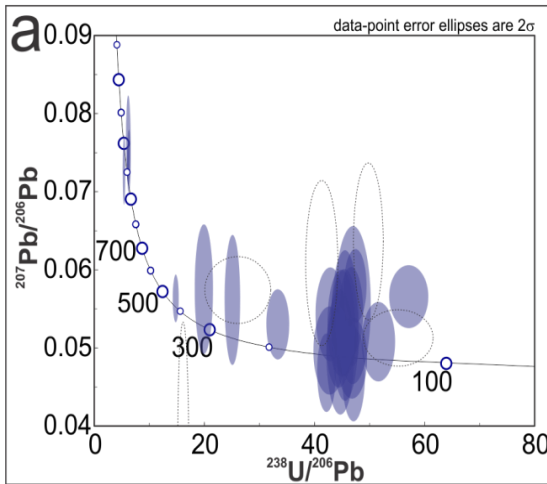
The Th/U ratio and U concentrations for the oldest population of zircons span a narrow range (0.34-0.58 and 57-339 ppm respectively; Figure 8.4 d & e). The Palaeozoic population yield comparable Th/U ratios and U concentrations to the Grenvillian zircons (0.24-1.1 & 72-276 ppm respectively; Figure 8.4 d & e). In the Cretaceous population the Th/U ratio is again comparable to the inherited populations (0.23-0.59; Figure 8.4 d) but the U concentrations are higher (193-1098 ppm; Figure 8.4 e).

The 17 concordant grains of the youngest population have been further filtered in terms of their REE concentrations (grains with LREE enrichment have been

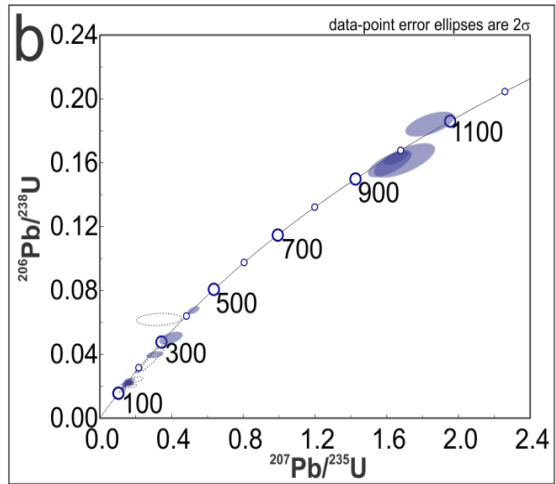
Chapter 8: U/Pb Geochronology for the Cuicateco terrane

disregarded; Figure 8.4 f), leaving 11 suitable for age calculations. Weighted mean plots for the youngest population yield an age of 140.0 ± 4.3 Ma, with an MSWD of 5.1 (one age was rejected by the algorithm; Figure 8.4 c). This can be interpreted as the igneous crystallization age of the Xonamanca volcanism. Inherited populations may be derived from crustal recycling during melting or from lithic fragments that are commonly found in these tuffs. The oldest inherited population are likely to be igneous and metamorphic zircons related to Oaxaquia continental crust. The younger Palaeozoic zircons may be derived from the igneous and metamorphic events of the Acatlán Complex (Nance et al., 2006).

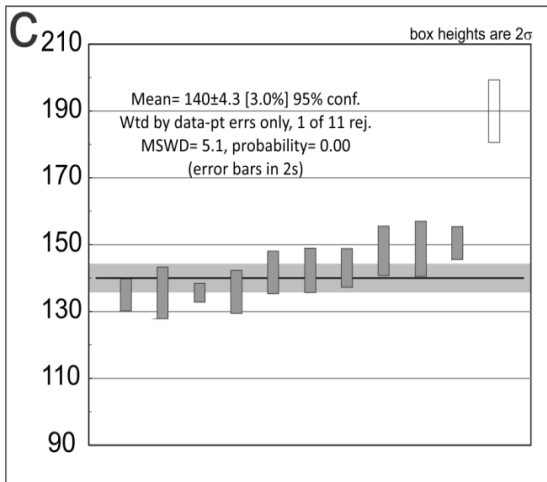
12-12-10 7B



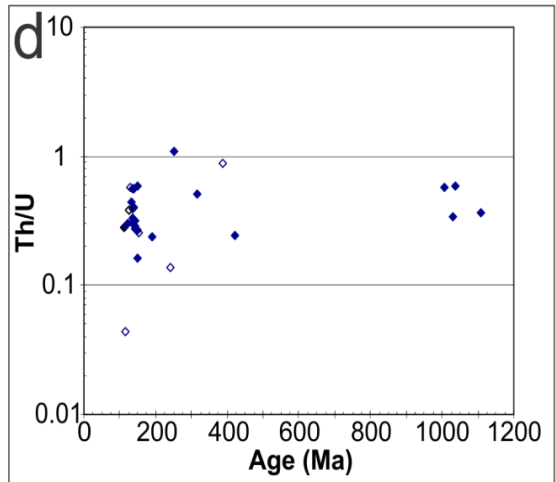
Tera Wasserburg diagram for all of the analysed zircons (n=30). The coloured ellipses represent grains that were used in age calculations (n=25) and the dashed ellipses those that were disregarded (>20% discordant, >4% error).



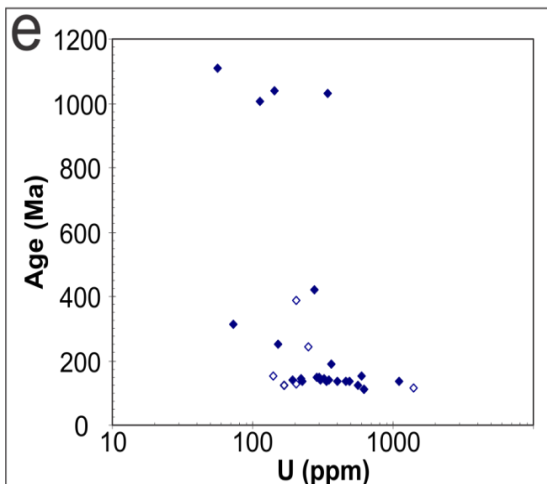
Wetherill diagram for all of the analysed zircons (n=30). The coloured ellipses represent grains that were used in age calculations (n=25) and the dashed ellipses those that were disregarded (>20% discordant, >4% error).



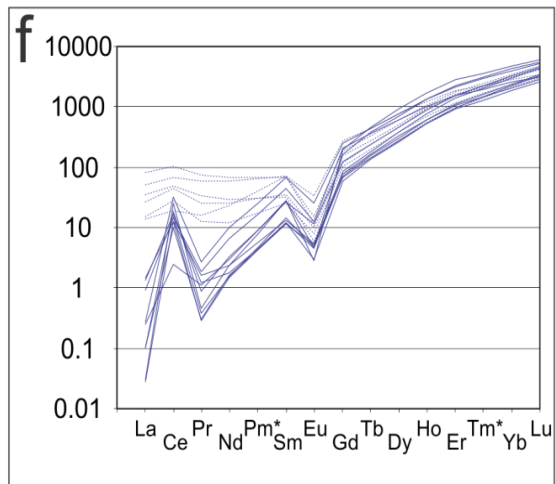
Weighted mean plot for the youngest population of zircons (n=11)



Th/U vs. age (Ma) diagram for all of the analysed grains. The blue points represent zircons used in age calculations and clear points those that were disregarded.



Age (Ma) vs. U (ppm) diagram for all of the analysed grains. Blue points represent zircons used for age calculations and clear points those that were disregarded.



Zircon chondrite-normalized REE patterns of Cretaceous analyses. Dotted patterns indicate analyses with high and relatively flat LREE, indicative of inclusions in zircon.

Chapter 8: U/Pb Geochronology for the Cuicateco terrane

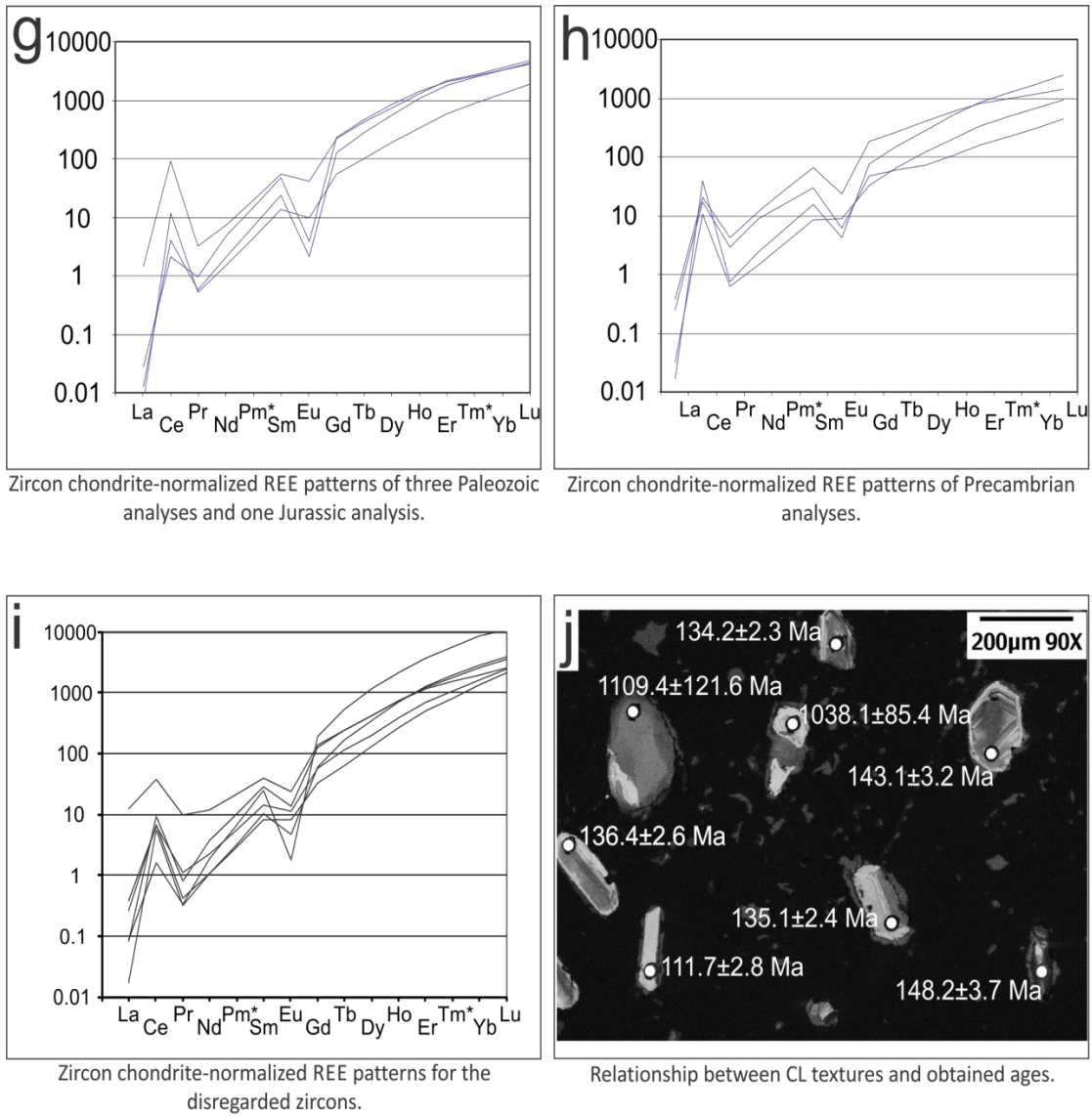


Figure 8.4. Geochronology results for sample 12-12-10-7b of the Xonamanca Formation.

8.3.2 Sample 12-12-10 7C

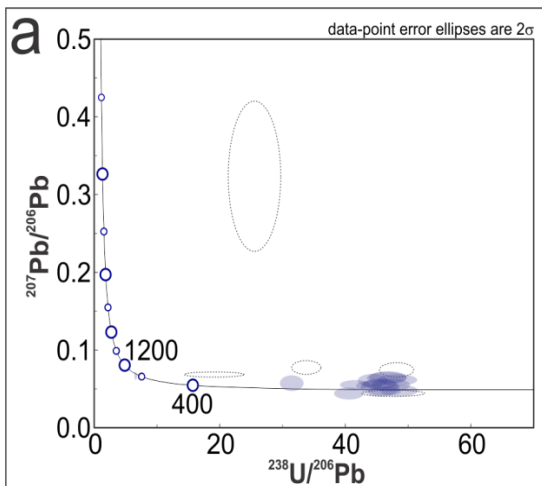
This sample is a red andesitic tuff containing clasts of predominantly plagioclase and quartz. The zircons are euhedral to subhedral in shape and 100-300 μm along their longest axis, with aspect ratios of 2:1-5:1. The CL textures are characterised by sector and oscillatory zoning, typical of igneous zircons (Figure 8.5 h).

Of the 20 analysed grains, 15 were deemed reliable enough for age calculations ($< 35\%$ discordance, $< 4\%$ error). The Tera-Wasserburg plots reveals a Cretaceous population of zircons, with minor inheritance from Jurassic (201 ± 5 Ma) and Grenvillian (861 ± 102 Ma) zircons (Figure 8.5 a & b).

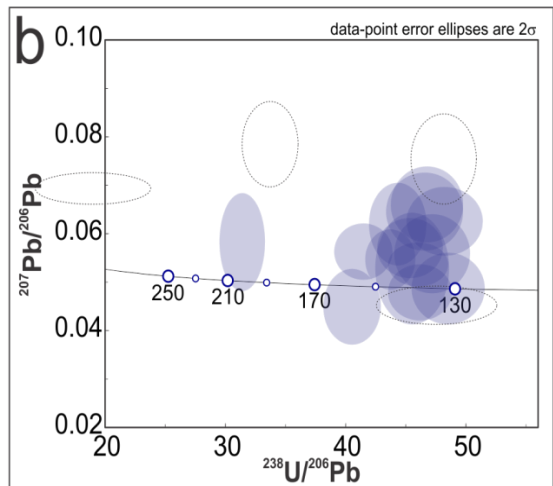
The Th/U ratios and U concentrations for the Cretaceous population yield results that span a fairly narrow range (0.27-0.71 & 132-440 ppm respectively; Figure 8.5 d & e) that are consistent with zircons that formed during an igneous event. The two inherited grains reveal comparable Th/U and U concentration results to the Cretaceous population.

The weighted mean plot for the Cretaceous population of zircons ($n=13$) yield an age of 139 ± 3.8 Ma, with an MSWD of 3.2 (one age was rejected by the algorithm; Figure 8.5 c). This can be interpreted as the crystallization age for the extrusive igneous rocks of the Xonamanca Formation.

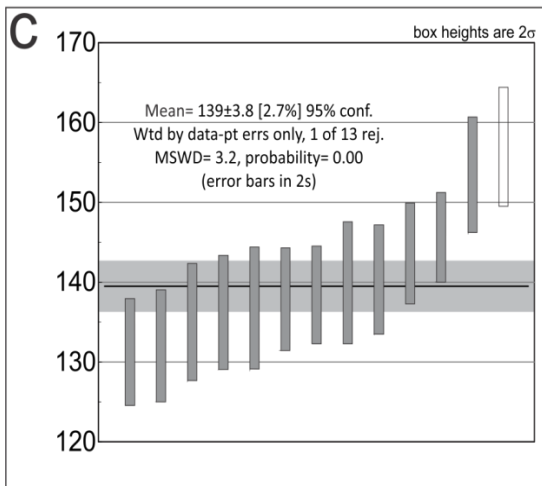
12-12-10 7C



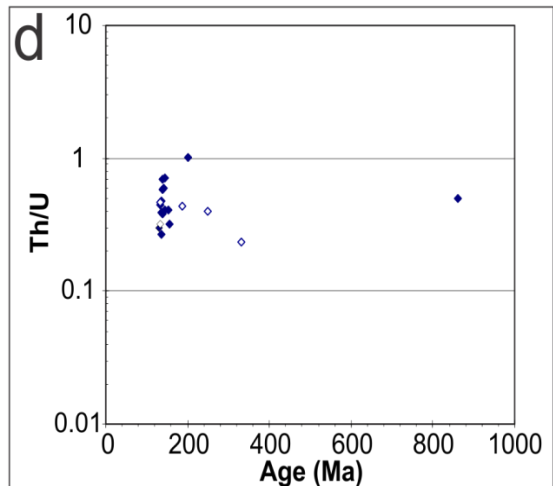
Tera Wasserburg diagram for all of the analysed zircons (n=20). The coloured ellipses represent grains that were used in age calculations (n=15) and the dashed ellipses those that were disregarded (>35% discordant, 4% error).



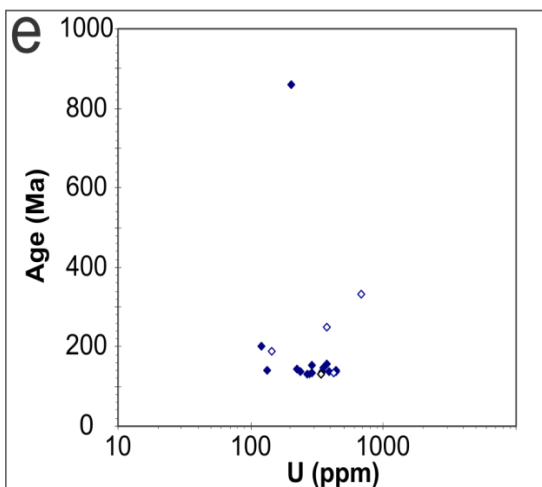
Tera Wasserburg diagram for the Mesozoic zircons.



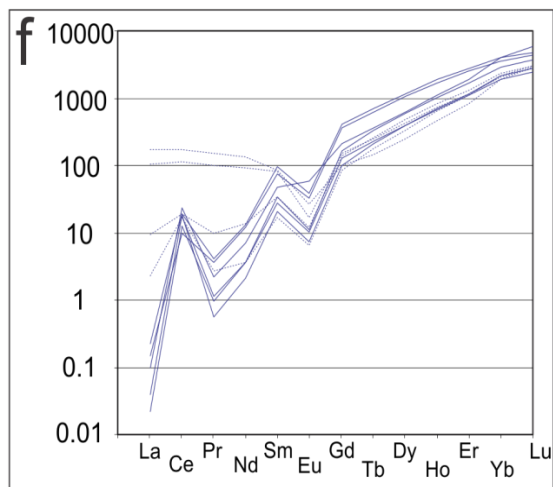
Weighted mean plot for the youngest population of zircons. (n=13).



Th/U vs. age (Ma) diagram for all of the analysed grains. The blue points represent zircons used in age calculations and clear points those that were disregarded.



Age (Ma) vs. U (ppm) diagram for all of the analysed grains. Blue points represent zircons used for age calculations and clear points those that were disregarded.



Zircon chondrite-normalized REE patterns of Cretaceous analyses. Dotted patterns indicate analyses with slight to strong enrichment in LREE.

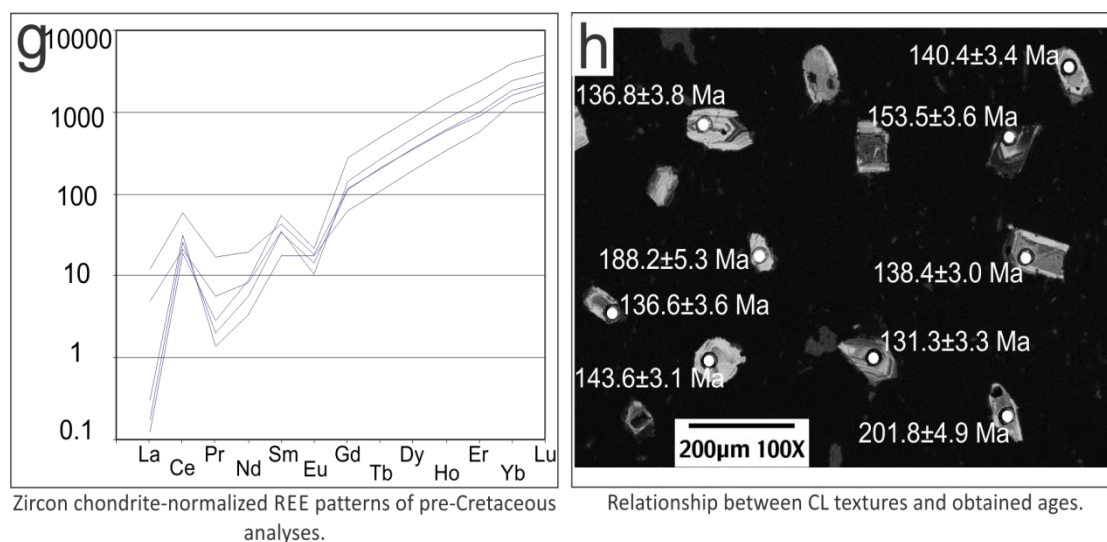


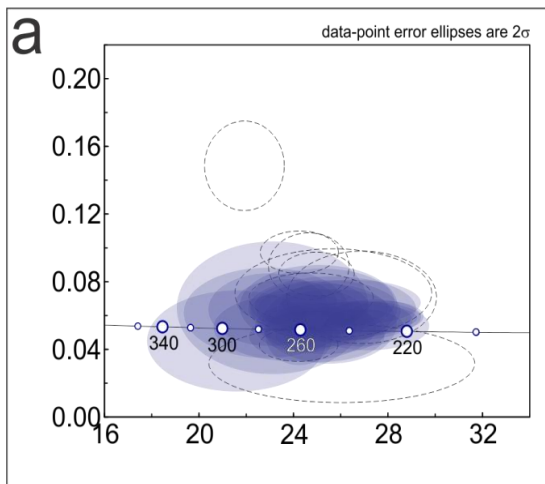
Figure 8.5. Geochronology results for sample 12-12-10-7c of the Xonamanca Formation.

8.4 Teotitlán Migmatitic Complex

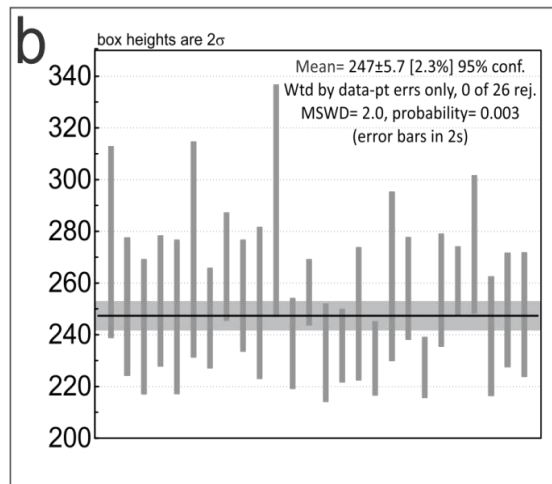
8.4.1 Sample 5-11-11-01

This sample is an amphibolitic gneiss primarily composed of hornblende and plagioclase. It contains euhedral zircons that are 100-300 μm along their longest axis, with aspect ratios of 2:1-4:1. CL textures are characterised by oscillatory zoning, typical of igneous zircons (Figure 8.6 g). This indicates that the zircons are likely to record the age of magmatism rather than the subsequent amphibolite grade metamorphism. The Th/U ratios and U concentrations support the CL observations, with uniform results that are typical of igneous zircons (0.6-1.6 & 20-300 ppm respectively; Figure 8.6 c & d). Of the 35 analysed grains 26 were considered suitable to be used in age calculations (< 15% reverse discordance, < 30 % discordance). The weighted mean plot for the sample yields an age of 247 ± 5.7 Ma with an MSWD of 2 (Figure 8.6 b). This can be interpreted as the igneous crystallization age of the protolith.

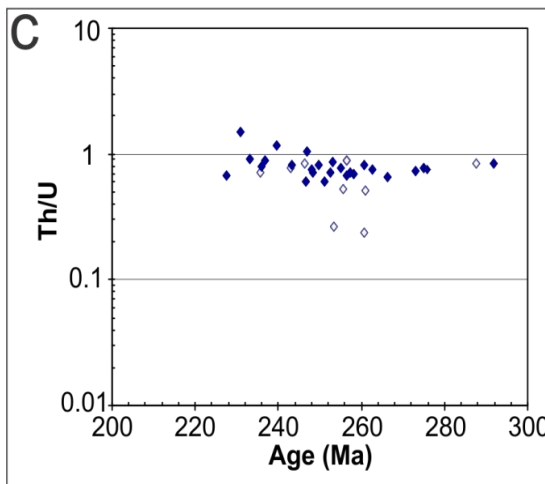
5-11-11-1



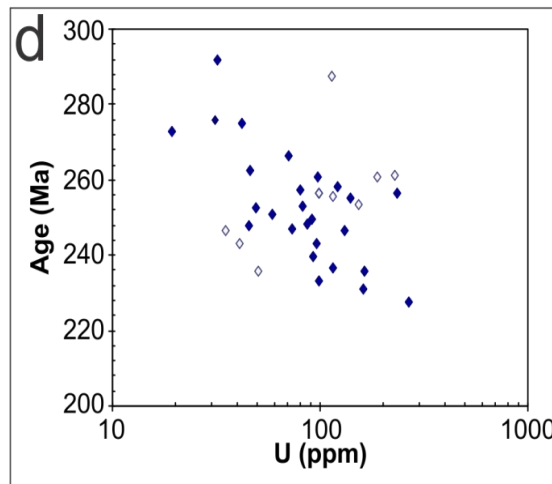
Tera-Wasserburg of all analyses (n=35). Dashed ellipses are analyses disregarded from average calculations due to >15% reverse discordance or >30% discordance.



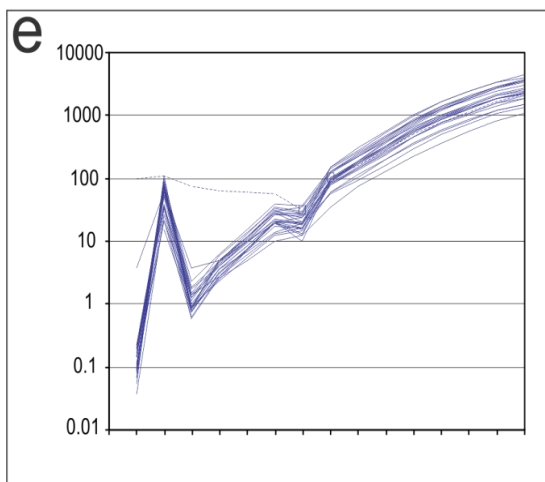
Weighted-mean calculation of age based on the 26 most suitable analyses.



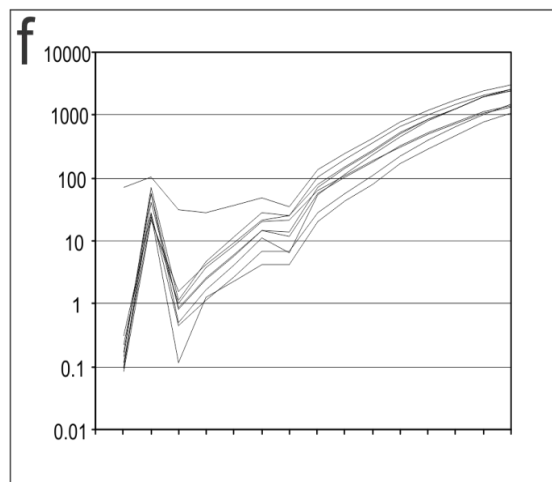
Age (Ma) vs Th/U plot for all of the analysed grains. Blue dots represent analysis that were used in age calculations (n=26) and the clear dots are the disregarded analysis (> 30% discordance, >15% reverse discordance).



U (ppm vs Age (Ma) plot for all of the analysed grains. Blue dots represent analysis that were used in age calculations (n=26) and the clear dots are the disregarded analysis (> 30% discordance, >15% reverse discordance).



Chondrite-normalized REE patterns of Permo-Triassic analyses (n=26). One analyses (dashed) may have contained inclusions that enriched the LREE.



Chondrite-normalized REE patterns of disregarded analyses (>30% discordance or >15% reverse discordance).

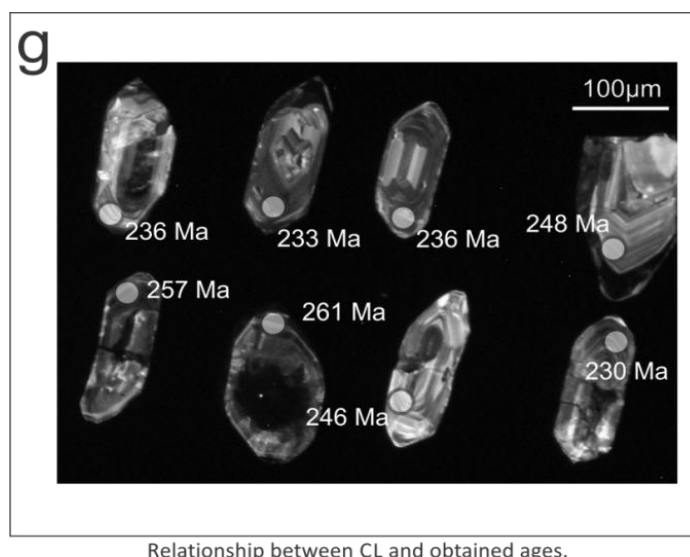
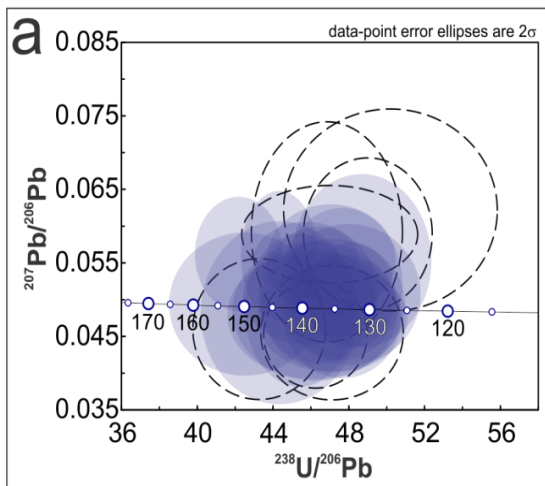


Figure 8.6. Geochronology results for sample 5-11-11-1 of the Teotitlán Migmatitic Complex.

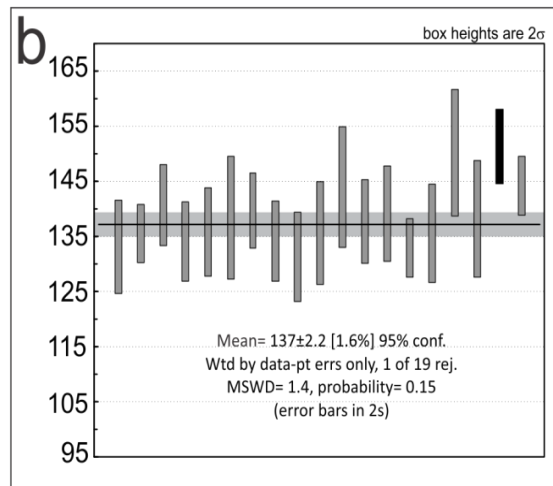
8.4.2 Sample 5-11-11-03

This sample is an orthogneiss with a proto-mylonitic texture. Potassium feldspar is present as porphyroblasts, in addition to partially chloritized biotite and hornblende. It contains euhedral zircons which are 100-300 μm along their longest axis, with aspect ratios of 2:1-5:1. The CL textures are characterised by oscillatory zoning, typical of igneous zircons (Figure 8.7 g). The Th/U ratios and U concentrations span a narrow range that also support an igneous origin for the zircons (0.3-0.6 & 150-450 ppm respectively; Figure 8.7 c & d). Therefore the zircons present in the sample represent the igneous crystallization age rather than subsequent metamorphism. The Tera-Wasserburg plot (Figure 8.7 a) reveals one uniform Cretaceous population of zircons. Of the 26 analysed grains, 19 were considered suitable for age calculations (<15% discordant, <3% reverse discordant). The weighted mean plot yields an age of 137 ± 2.2 Ma, with an MSWD of 1.4 (one age was rejected by the algorithm; Figure 8.7 b) and this can be interpreted as the age of igneous crystallization.

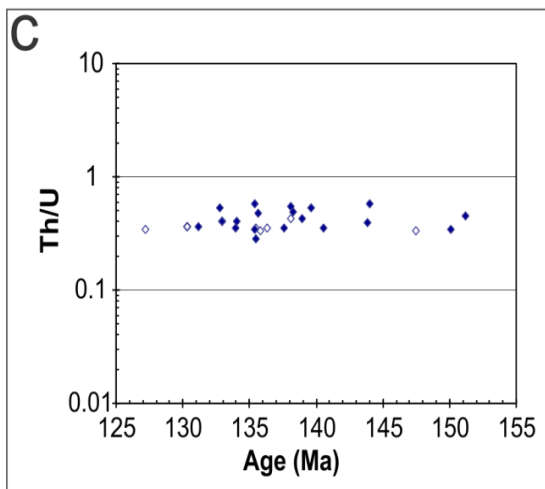
5-11-11-3



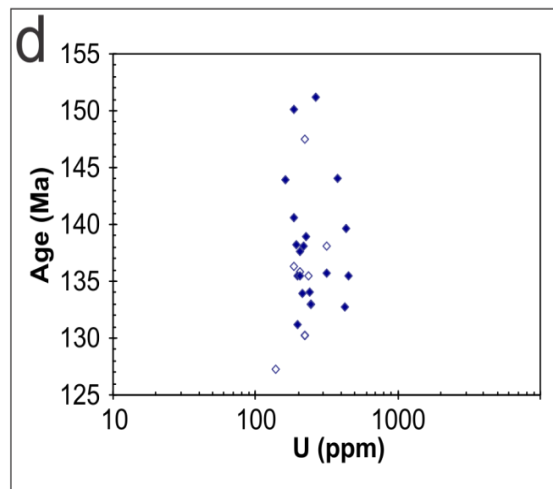
Tera Wasserburg diagram of all analyses (n=26). Dashed ellipses represent disregarded analyses (>15% discordance or >3% reverse discordance).



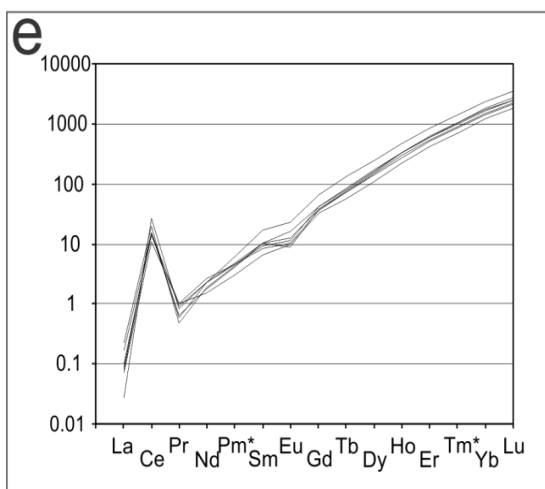
Weighted mean plot for the concordant zircons.



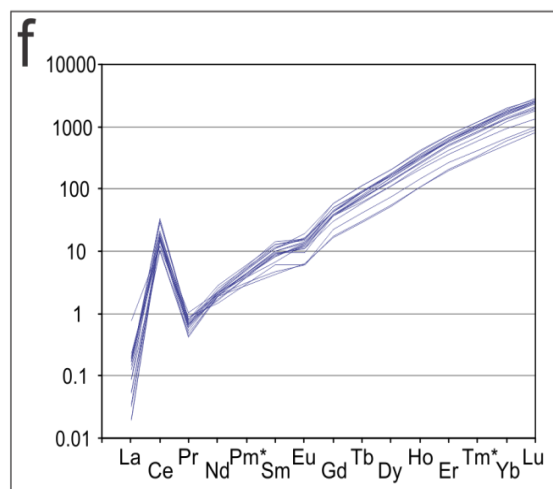
Th/U Vs Age (Ma), all analyses (n=26). Open symbols represent disregarded analyses.



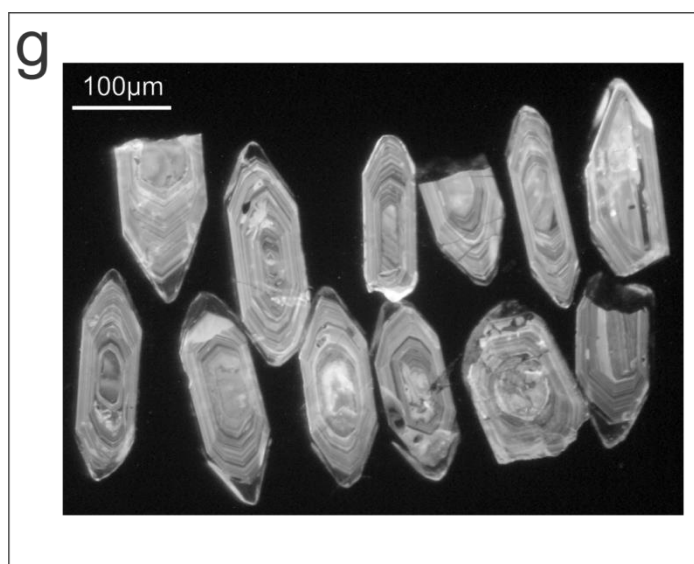
Age (Ma) vs U (ppm), all analyses (n=26). Open symbols represent disregarded analyses.



Chondrite-normalized REE concentrations of disregarded analyses.



Chondrite-normalized REE concentrations of analyses used to constrain the age.



CL examples of the analysed zircons.

Figure 8.7. Geochronology results for sample 5-11-11-3 of the Teotitlán Migmatitic Complex.

8.4.3 Sample 10-18-11-7A

This sample is a tonalite that has undergone low grade deformation as well as retrogressive recrystallization. Zircons in the sample are euhedral to subhedral and 100-200 μm along their longest axis, with aspect ratios of 2:1-4:1. The CL textures are characterised by oscillatory and sector zoning, typical of igneous zircons, with evidence of inherited cores in some of the grains (Figure 8.8 g).

The sample spans a relatively narrow range in Th/U ratios and U concentrations (0.2-0.75 & 130-650 ppm respectively; Figure 8.8 d & e) which are consistent with values associated with igneous zircons, supporting observations made in the CL interpretation. Two grains have been disregarded due to high U concentrations which may have caused by metamictization.

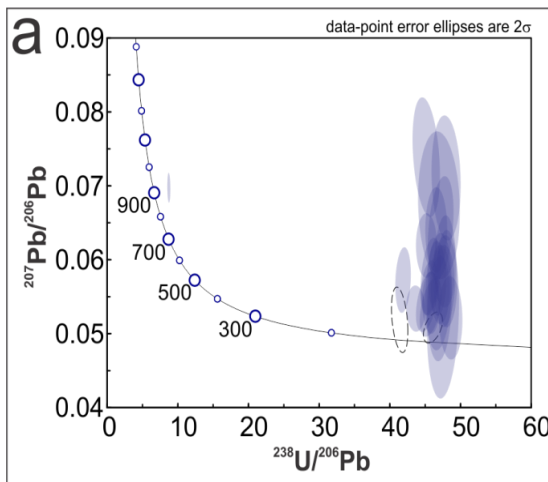
The Tera-Wasserburg plot (Figure 8.8 a) reveals one dominant Cretaceous population of zircons, with a single inherited Mesoproterozoic core. The analyses

Chapter 8: U/Pb Geochronology for the Cuicateco terrane

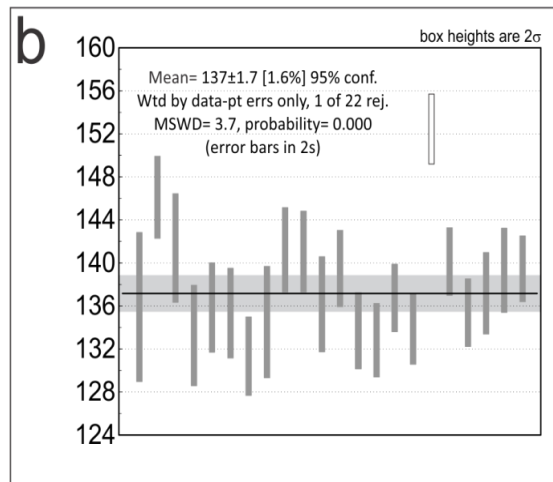
appear somewhat affected by discordance, possibly caused by common Pb contamination. However this is unlikely to have major consequence on the population average age.

Of the 25 analysed zircons, 23 were considered suitable to be used for age calculations (low U concentrations). The weighted mean plot yields an age of 137.2 ± 1.7 Ma, with an MSWD of 3.7 (one age was rejected by the algorithm; Figure 8.8 b). This can be interpreted as the igneous crystallization age of the tonalite.

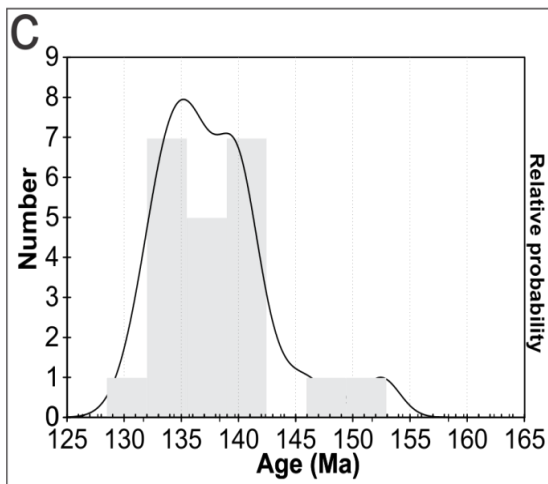
10-18-11-7A



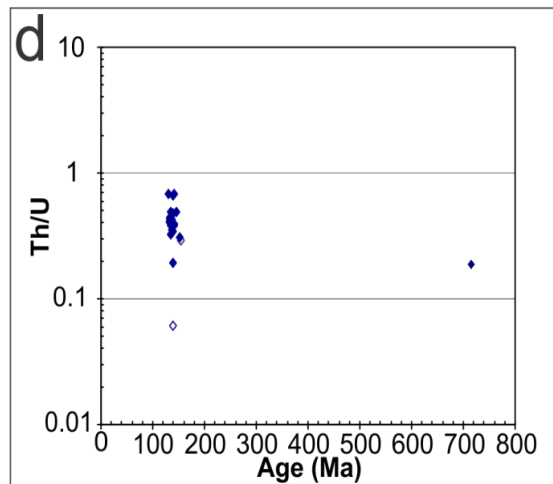
Tera Wasserburg diagram for all of the analysed grains (n=25). The coloured ellipses represent zircons used in age calculations (n=23) and the dashed ones those that were discarded (high U concentrations).



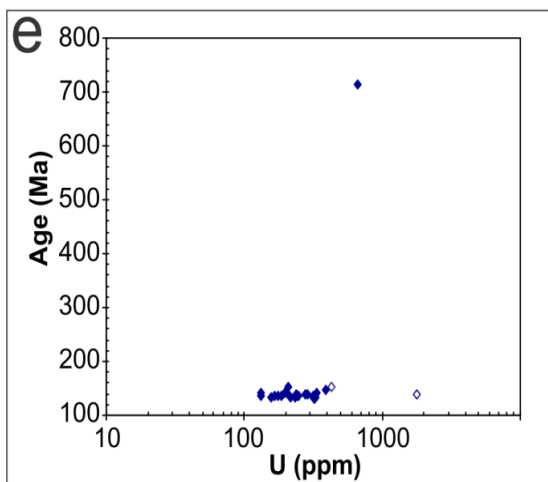
Weighted mean plot for the Jurassic-Cretaceous analysis.



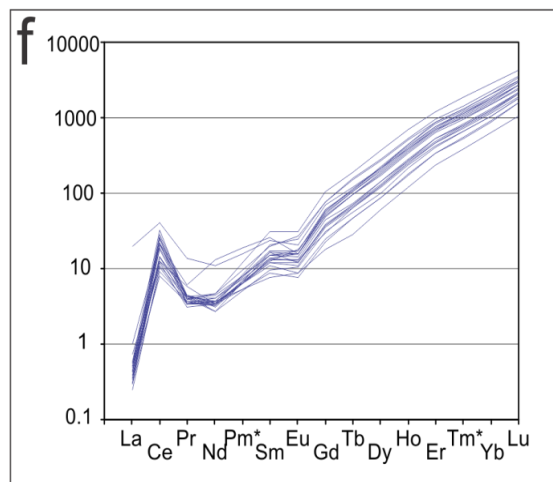
Relative probability plot for the Jurassic-Cretaceous analysis.



Th/U vs. Age (Ma) diagram for all of the analysed grains. Blue points are those used for age calculations and clear points those that were disregarded.



Age (Ma) vs. U (ppm) diagram for all of the analysed grains. The blue points represent zircons used in age calculations and the clear ones those that were disregarded.



Chondrite normalised REE plot for the zircons used in age calculations (Jurassic-Cretaceous)

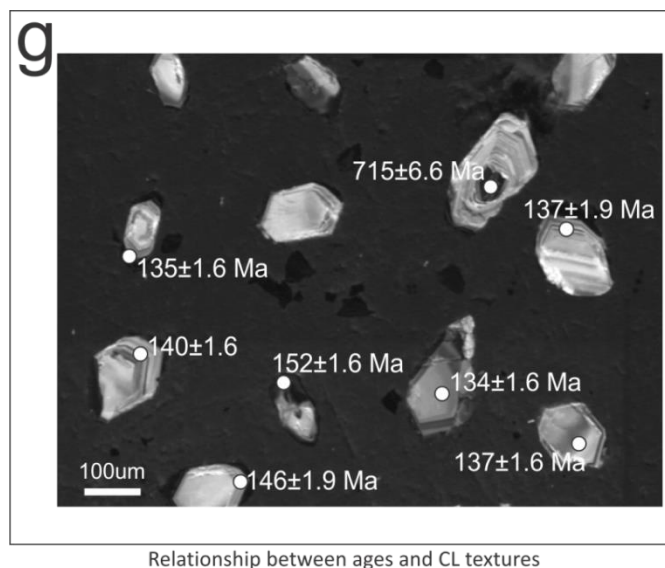
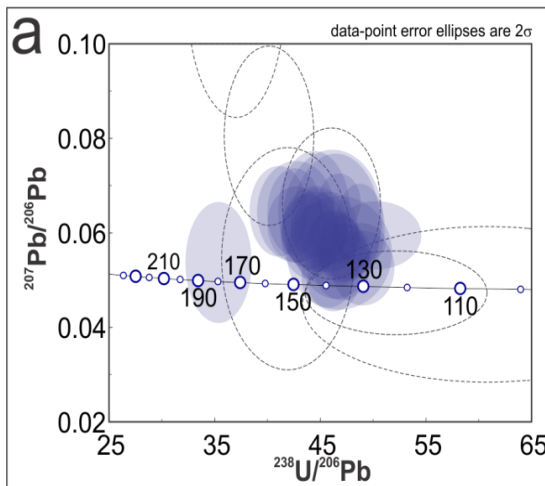


Figure 8.8. Geochronology results for sample 10-18-11-7a of the Teotitlán Migmatitic Complex.

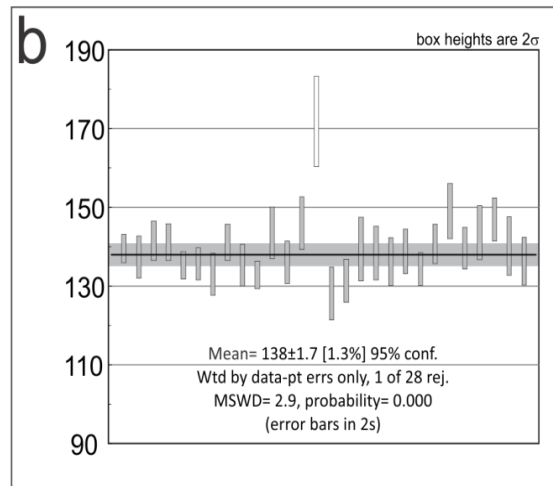
8.4.4 Sample 10-18-11-9d

This sample is a biotite tonalite that has been strongly overprinted by hydrothermal alteration, producing chlorite, epidote and sericitised plagioclase. There is an incipient foliation defined by biotite/chlorite and recrystallized quartz aggregates. The sample contains euhedral zircons 100-400 μm along their longest axis with aspect ratios of 2:1-7:1. The CL images show oscillatory and sector zoning typical of igneous zircons (Figure 8.9 g). There is no indication of any inherited cores in the sample. Th/U ratios and U concentrations range between 0.05-0.9 & 100-600 ppm respectively (Figure 8.9 c & d). The Tera-Wasserburg diagram shows one Jurassic-Cretaceous population of zircons (Figure 8.9 a). Of the 35 analysed grains, 26 were deemed reliable enough to be used in age calculations (<30% discordant). A weighted mean plot yields an age of 138 ± 1.7 Ma, with an MSWD of 2.9 (one age was rejected by the algorithm; Figure 8.9 b). This can be interpreted as the igneous crystallization age of the tonalite.

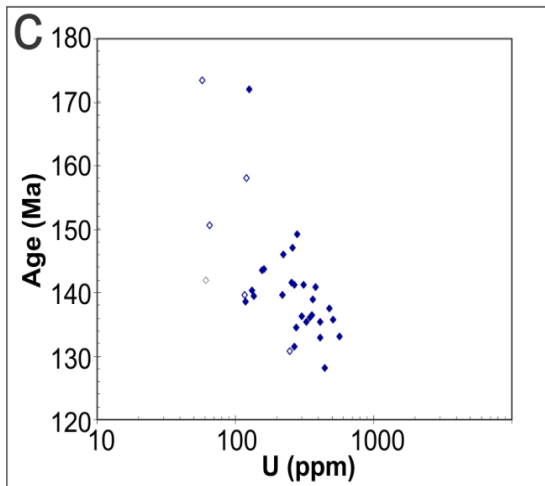
10-18-11-9D



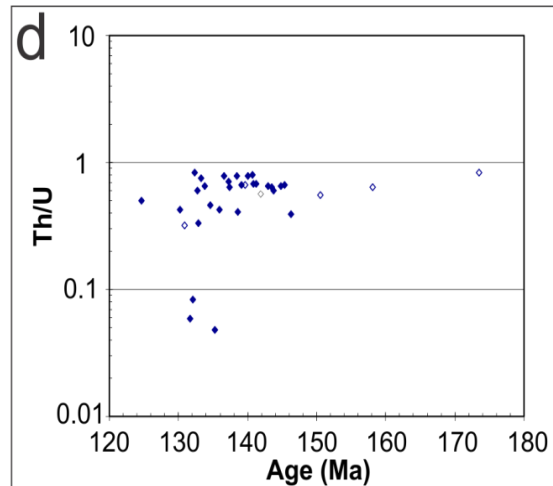
Tera Wasserburg diagram for all of the analysed grains (n=35). The coloured ellipses represent zircons used in age calculations (n=26) and the dashed ones those that were discarded (>30% discordance).



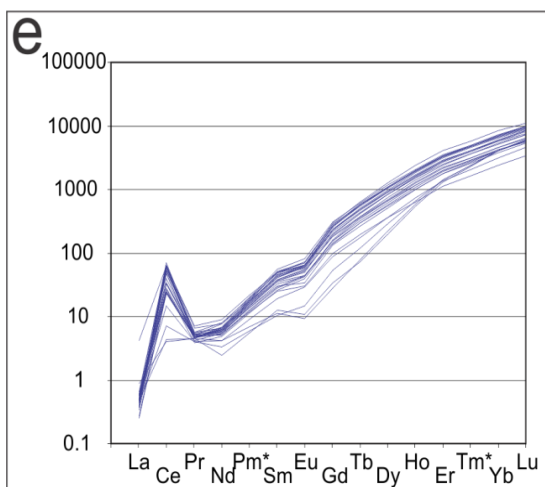
Weighted mean plot for the Jurassic-Cretaceous analysis



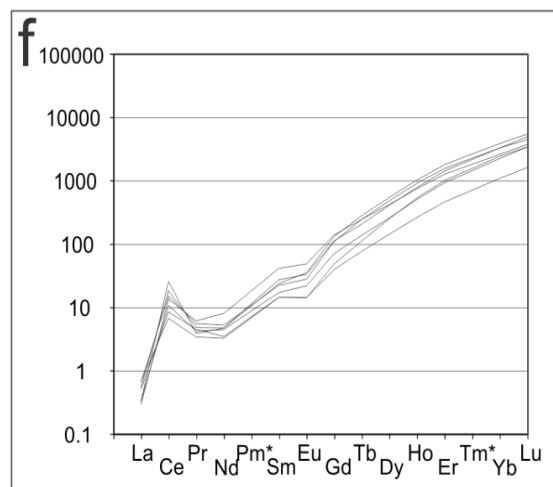
Age (Ma) vs. U (ppm) diagram for all of the analysed grains. The blue points represent zircons used in age calculations and the clear ones those that were disregarded.



Th/U vs. Age (Ma) diagram for all of the analysed grains. Blue points are those used for age calculations and clear points those that were disregarded.



Chondrite normalised REE plot for the zircons used in age calculations.



Chondrite normalised REE plot for the discarded zircons.

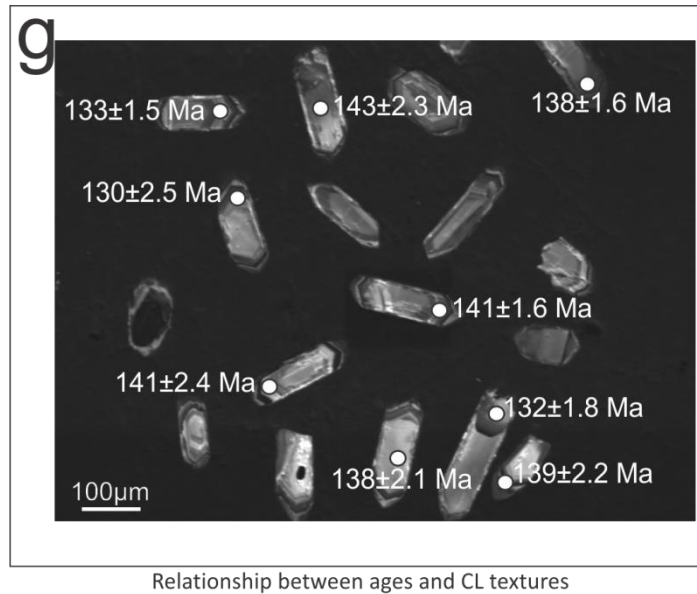


Figure 8.9. Geochronology results for sample 10-18-11-9d of the Teotitlán Migmatitic Complex.

8.4.5 Sample 10-18-11-9E

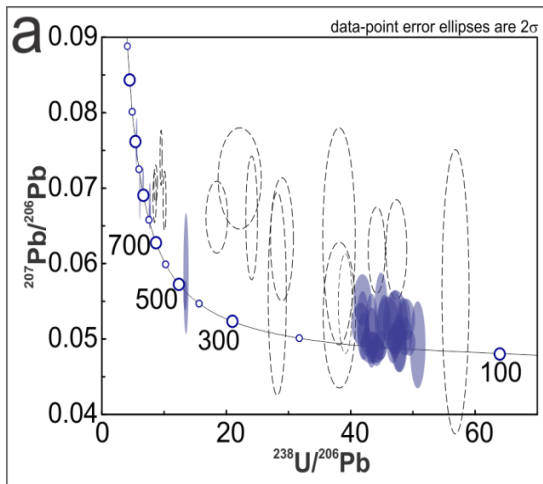
Sample 10-18-11-9E is a foliated tonalite, found in the Teotitlán migmatitic complex. It contains euhedral-subhedral zircons that are 100-300 μm along their longest axis, with aspect ratios of 1:1-5:1. The CL textures are characterised by dark grains (high U) that have oscillatory zoning, typical of igneous zircons (Figure 8.10 j). Inherited cores are also a common feature and typically appear brighter (lower U) on CL images.

Th/U ratios and U concentrations of the cores are variable (0.04-0.4 and 150-1100 ppm respectively; Figure 8.10 e & f). The same is true for the rims which have Th/U ratios of 0.01-0.6 (Figure 8.10 e) and U concentrations of 450-2300 (Figure 8.10 f). The Tera-Wasserburg plot (Figure 8.10 a) shows a spread of Jurassic-Cretaceous ages as well as inherited cores from the Precambrian & Ordovician.

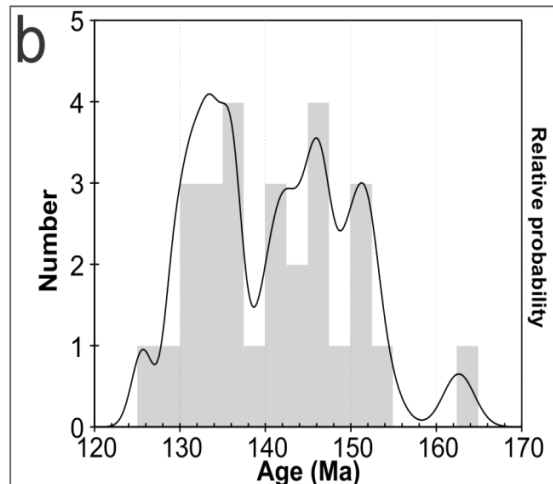
Chapter 8: U/Pb Geochronology for the Cuicateco terrane

It does not appear that metamictization has occurred in the zircons as the high-U grains yield comparable ages to those with low-U. The high U zircons have therefore been used in the age calculations. Of the 50 analysed zircons 26 were considered suitable to be used in age calculations for the Jurassic-Cretaceous population (< 20% Phanerozoic discordance, < 5% Precambrian discordance, < 5% error). Relative probability plots for the sample show a large spread in ages for the youngest population of zircons (Figure 8.10 b). This is probably due to core-rim mixing during analysis; therefore the youngest zircons present can be interpreted as the age of the latest igneous crystallization event. Weighted mean and TuffZirc median plots yield comparable results (133 ± 1.7 Ma and $133+2.5-2.8$ Ma respectively; Figure 8.10 c and Figure 8.10 d). This can be interpreted as the age of crystallisation in an igneous event.

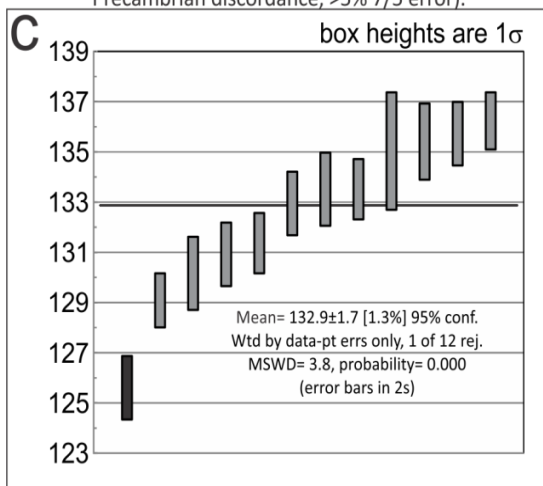
10-18-11-9E



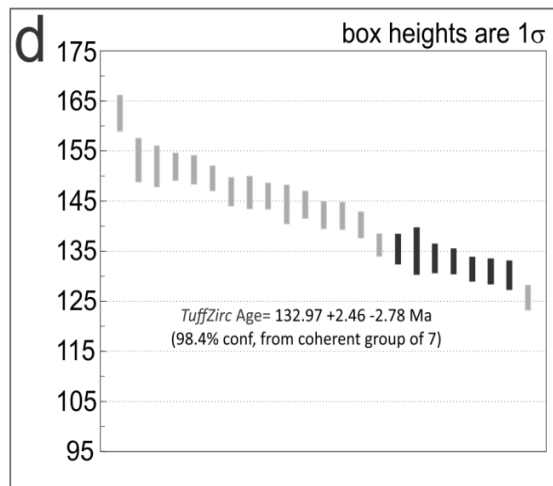
Tera Wasserburg diagram for all of the analysed grains (n=50). The coloured ellipses represent analysis that were used in age calculations (n=34) and the dashed ellipses those that were discarded (>20% Phanerozoic discordance, >5% Precambrian discordance, >5% 7/5 error).



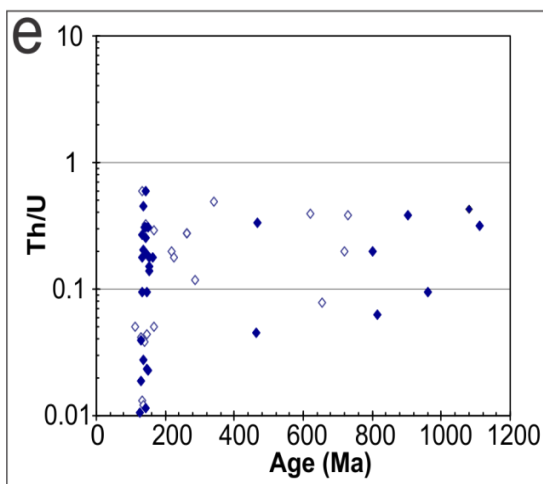
Relative probability plot for the Cretaceous zircons used in age calculations.



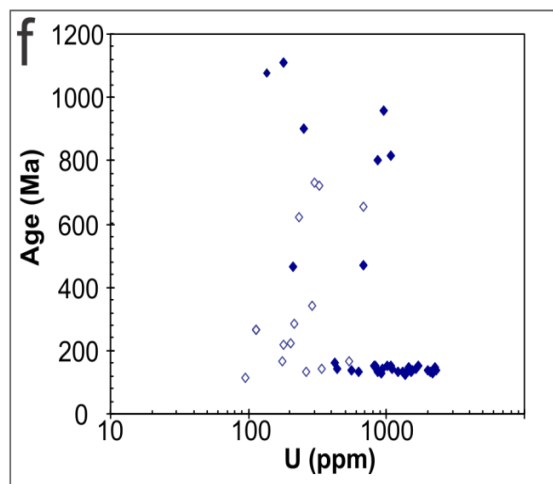
Weighted mean plots for the younger peak of Cretaceous zircons used in the age calculations.



Tuffzirc age for the youngest population of zircons.



Th/U vs. Age (Ma) diagram for all of the analysed grains. Blue points are those used for age calculations and clear points those that were disregarded.



Age (Ma) vs. U (ppm) diagram for all of the analysed grains. The blue points represent zircons used in age calculations and the clear ones those that were disregarded.

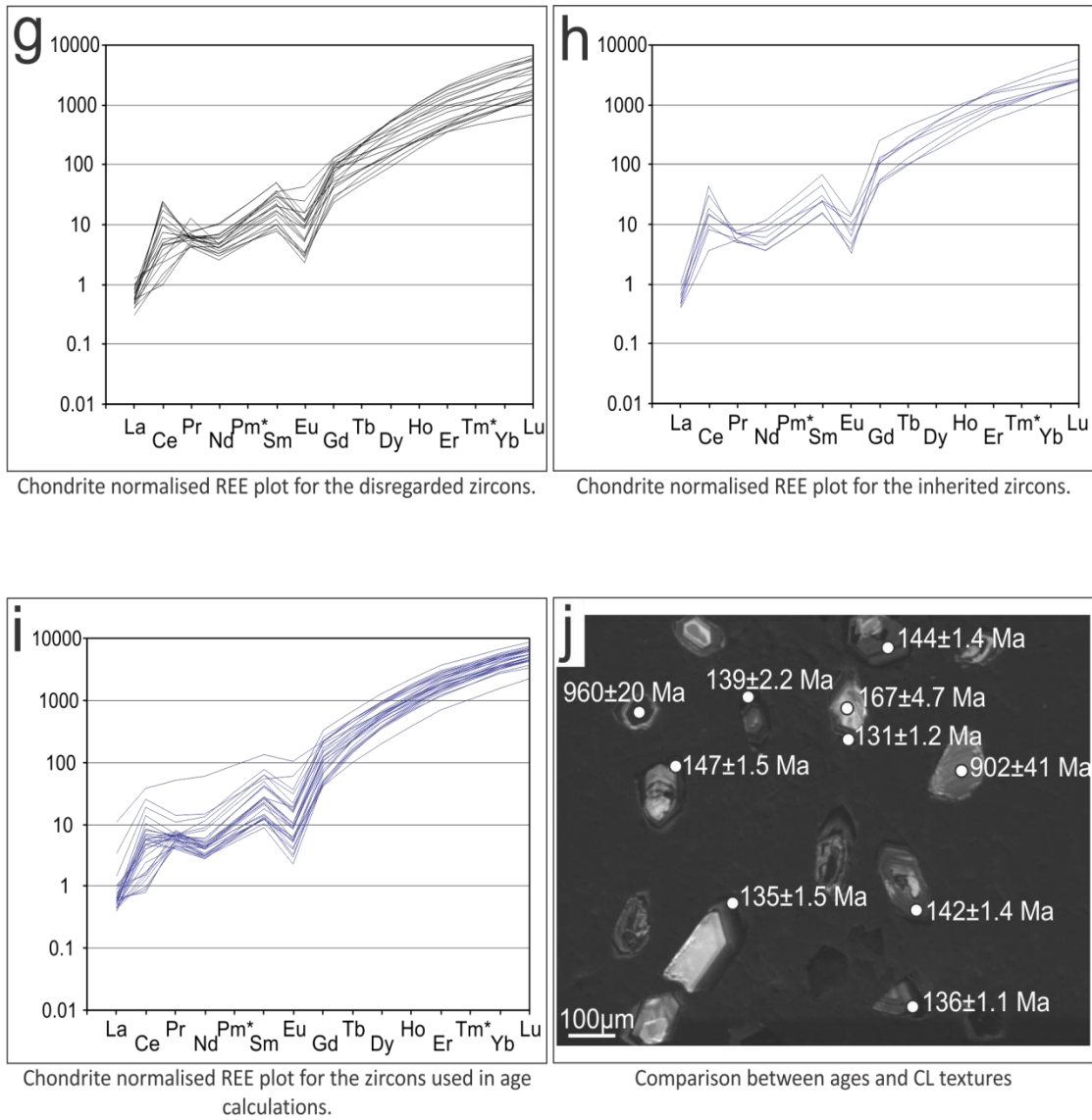


Figure 8.10. Geochronology results for sample 10-18-11-9e of the Teotitlán Migmatitic Complex.

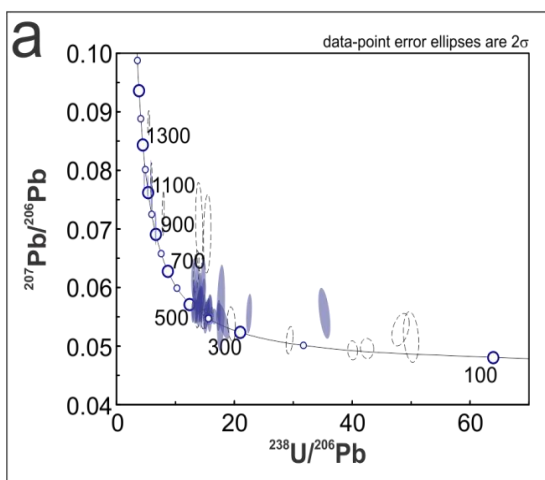
8.4.6 Sample 10-18-11-9F

This sample is a biotite gneiss with minor garnet and staurolite. The sample contains subhedral-subrounded zircons 100-400 μm along their longest axis, with aspect ratios of 1:1-6:1. The CL textures are characterised by oscillatory zoning in most of the grains (some more homogenous) and core and rim relationships (Figure 8.11 k).

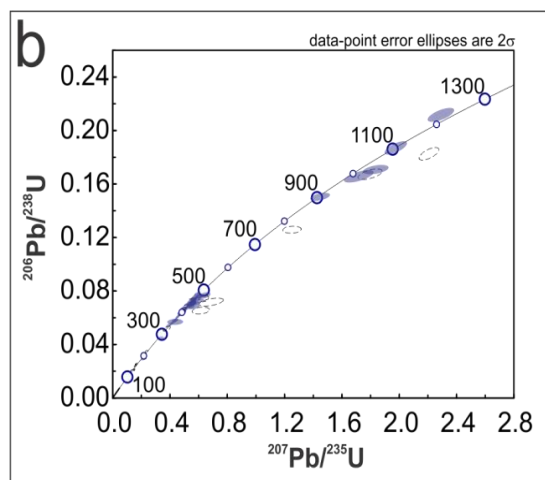
The Th/U and U concentrations of the zircons are highly variable (0.003-0.9 & 90-1400ppm respectively; Figure 8.11 e & f), suggesting they did not all form in the same event. Of the 60 analysed grains 45 were deemed reliable enough to be used in age calculations (<20% Phanerozoic discordance, <5% Precambrian discordance, <1900 ppm U).

The Tera-Wasserburg & Wetherill plots (Figure 8.11 a & b) show that the analysed cores formed in a Precambrian event (900-1200 Ma), and were most probably derived from Oaxaquia continental crust. The rest of the zircon grains crystallized during the Cambrian-Devonian (Figure 8.11 c) and so may be derived from the Acatlán Complex (Nance et al., 2006). Tuffzirc ages for the youngest population of zircons yield an age of $354 \pm 7.8 - 7.6$ Ma (Figure 8.11 d). This can be interpreted as the maximum age of deposition for a sedimentary protolith that contains zircons dominantly from the Cambrian-Devonian.

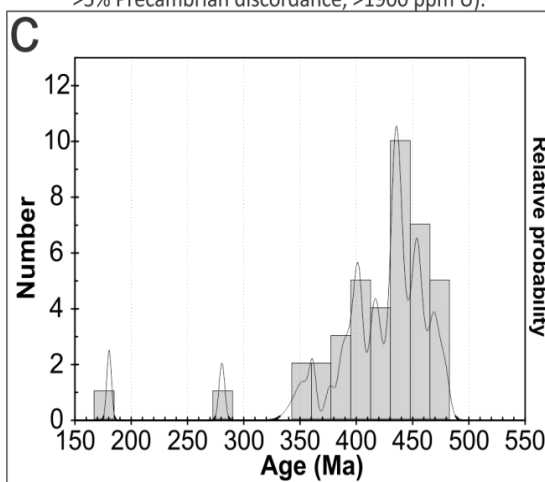
10-18-11-9F



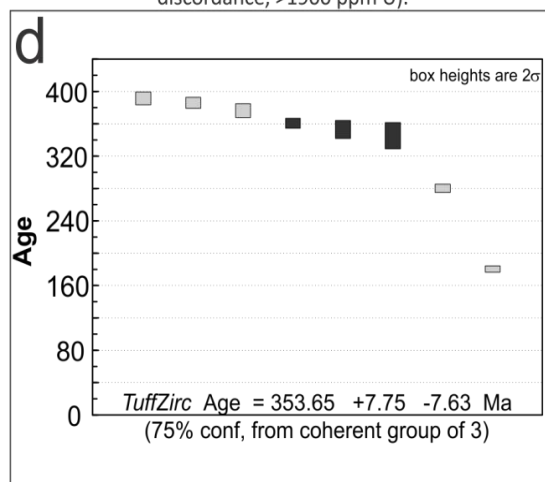
Tera Wasserburg diagram for all of the analysed grains (n=60). The coloured ellipses represent analysis that were used in age calculations (n=45) and the dashed ellipses those that were discarded (>20% Phanerozoic discordance, >5% Precambrian discordance, >1900 ppm U).



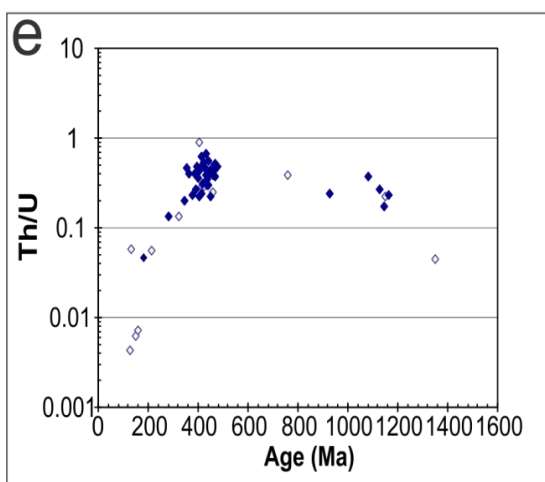
Wetherill diagram for all of the analysed grains (n=60). The coloured ellipses represent analysis that were used in age calculations (n=45) and the dashed ellipses those that were discarded (>20% Phanerozoic discordance, >5% Precambrian discordance, >1900 ppm U).



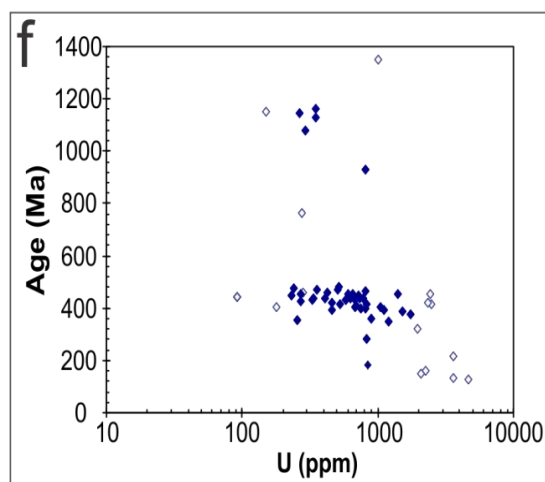
Relative probability plot for the zircons used in age calculations (<800 Ma).



TuffZirc age for the youngest group of zircons used in the age calculations.



Th/U vs. Age (Ma) diagram for all of the analysed grains. Blue points are those used for age calculation and clear points those that were disregarded.



Age (Ma) vs. U (ppm) diagram for all of the analysed grains. The blue points represent zircons used in age calculations and the clear ones those that were disregarded.

Chapter 8: U/Pb Geochronology for the Cuicateco terrane

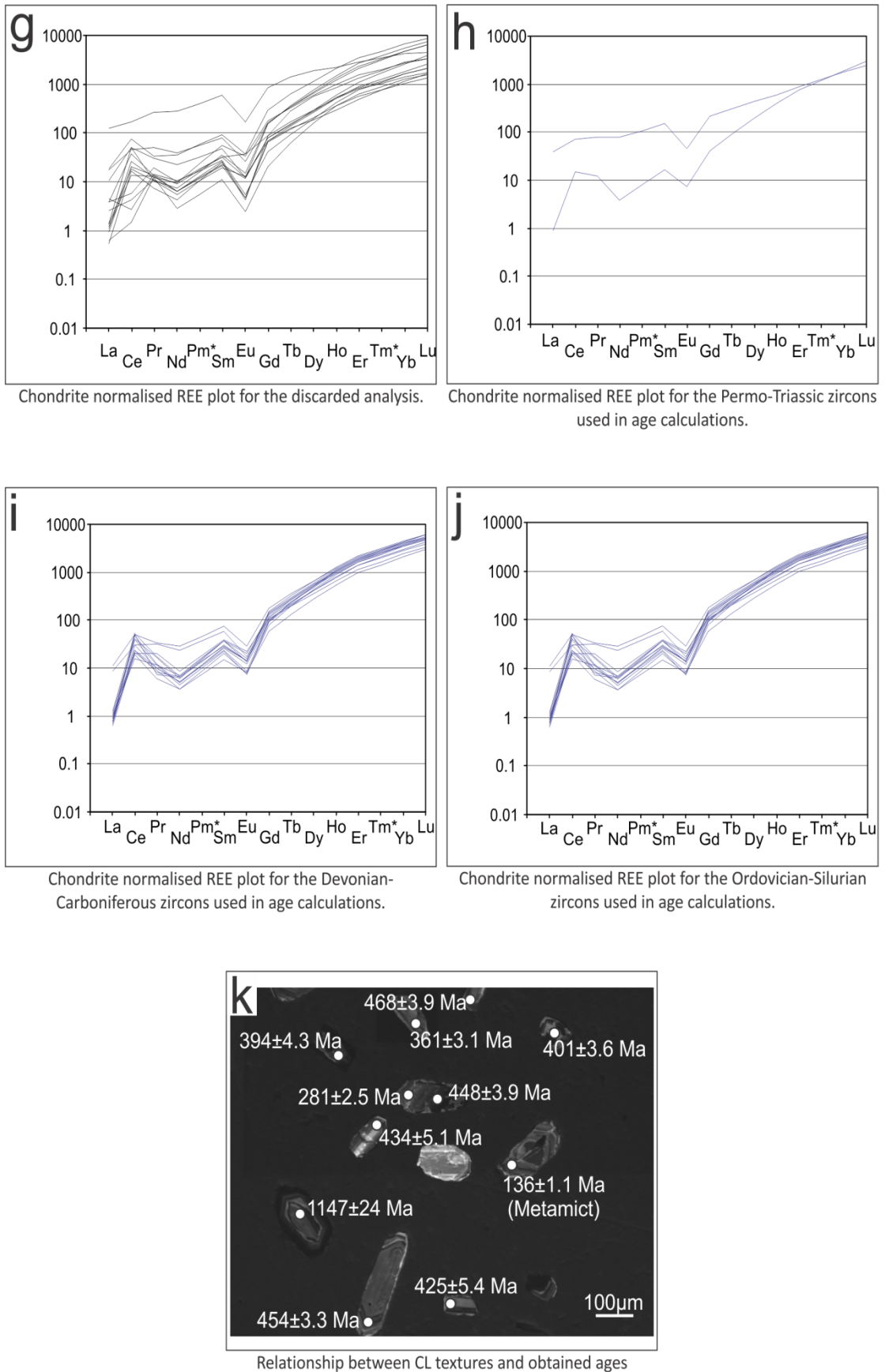


Figure 8.11. Geochronology results for sample 10-18-11-9f of the Teotitlán Migmatitic Complex.

8.5 Chivillas Formation

8.5.1 Sample 10-18-11-1B

This sample is a coarse arkosic sandstone that contains euhedral-subhedral zircons 100-300 μm along their longest axis, with aspect ratios of 2:1-6:1. The CL textures are characterised by oscillatory zoning typical of igneous zircons, some however are dark in colour and others are light, suggesting variable U concentrations in the grains (Figure 8.12 l). In some of the dark zircons core and (potentially metamorphic) rim relationships are evident.

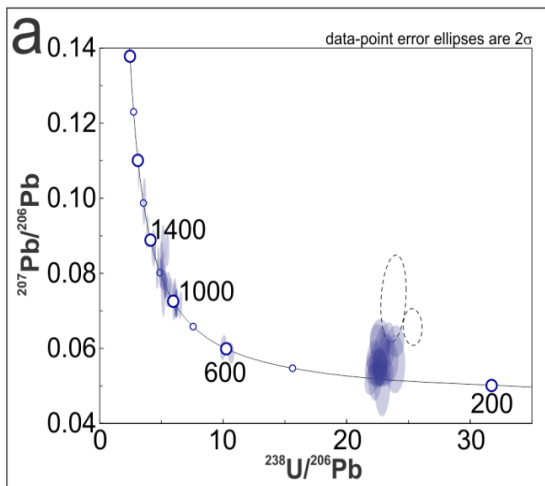
The Th/U and U concentrations of the zircons are highly variable (0.02-1 & 30-1050ppm respectively; Figure 8.12 f & g), suggesting they did not all form in the same event. Of the 60 analysed grains 57 were deemed reliable enough to be used in age calculations (<24% discordant). The Tera-Wasserburg & Wetherill plots show that there are Precambrian populations of zircons as well as a Permian population (Figure 8.12 a & b).

The majority of the Precambrian zircons are Grenvillian in age (1250-900 Ma) and can be related to the Oaxaquia micro-continent (Figure 8.12 c). There are six grains however that pre-date the Grenville orogeny (1.3-1.8 Ga), which may relate to the initial stages of the Oaxaquia microcontinent formation, where it existed as an island arc (Weber and Schulze, 2014). Weighted mean plots for the Permian population (n=23) of zircons yield an age of 278.1 ± 2.2 Ma (MSWD= 2.5; 2 ages were rejected by the algorithm; Figure 8.12 e).

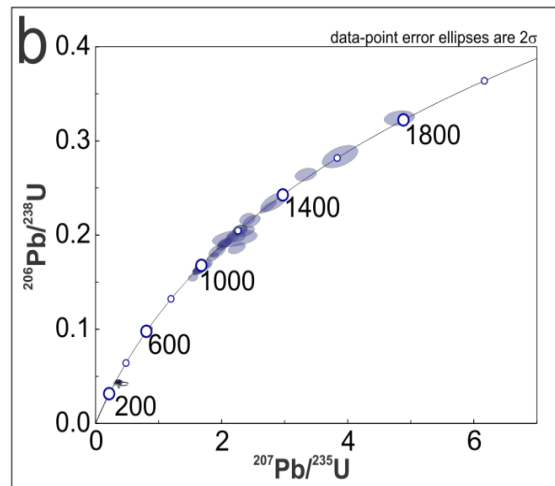
Chapter 8: U/Pb Geochronology for the Cuicateco terrane

This sample therefore contains zircons from pre-Oaxaquia Precambrian igneous/metamorphic events (1.8-1.3 Ga), the Oaxaquia igneous and metamorphic suite (1250-900 Ma) and an igneous event at 278 ± 2.2 Ma, likely relating to the magmatism discussed in Chapters 2-5, which constrains the maximum age of deposition.

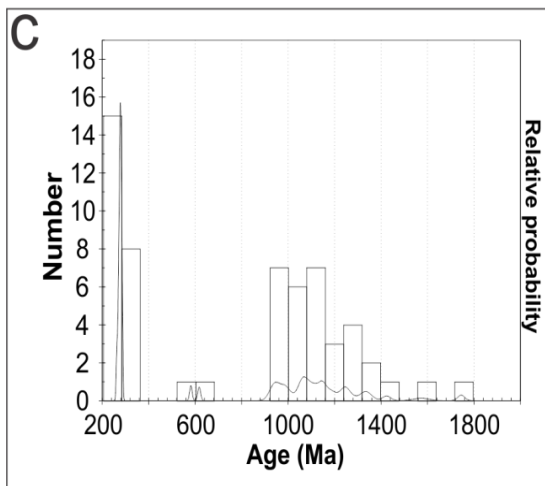
10-18-11-1B



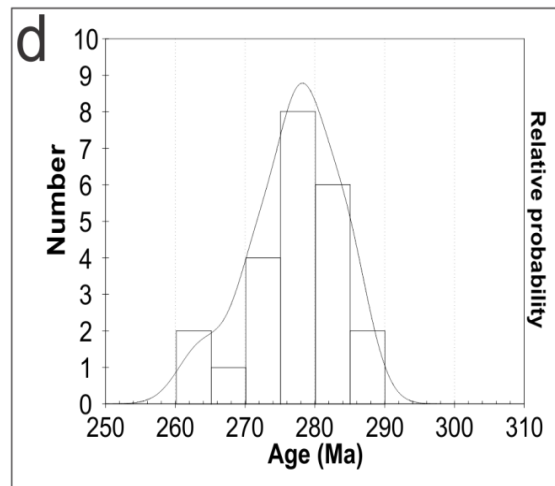
Tera Wasserburg diagram for all of the analysed grains (n=60). The coloured ellipses represent zircons that were used in age calculations (n=57) and dashed ellipses those that were disregarded (>24% discordance).



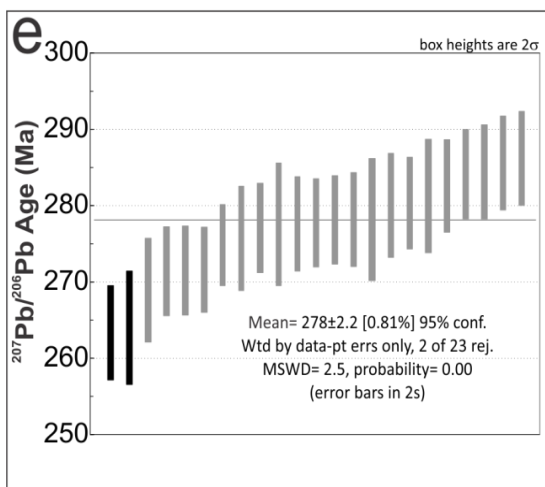
Wetherill diagram for all of the analysed grains (n=60). The coloured ellipses represent zircons that were used in age calculations (n=57) and dashed ellipses those that were disregarded (>24% discordance).



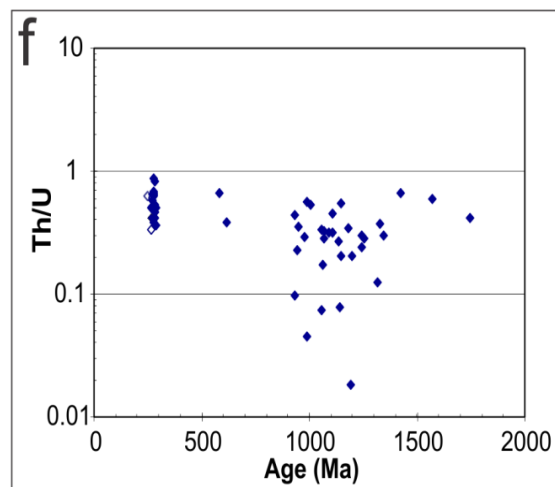
Probability density plot for all of the analysed zircons used in age calculations.



Probability density plot for the youngest group of concordant zircons.

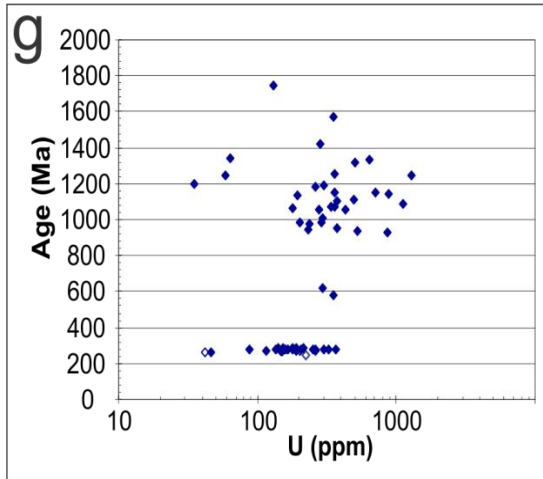


Weighted mean plot for the youngest population of concordant zircons.

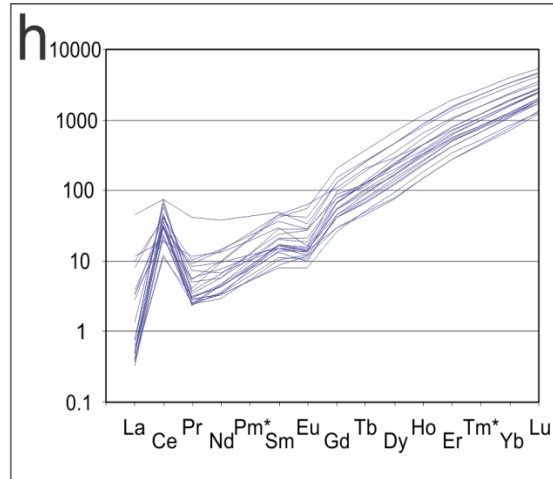


Th/U vs. age (Ma) diagram for all of the analysed grains. The blue points represent zircons used in age calculations and clear points those that were disregarded.

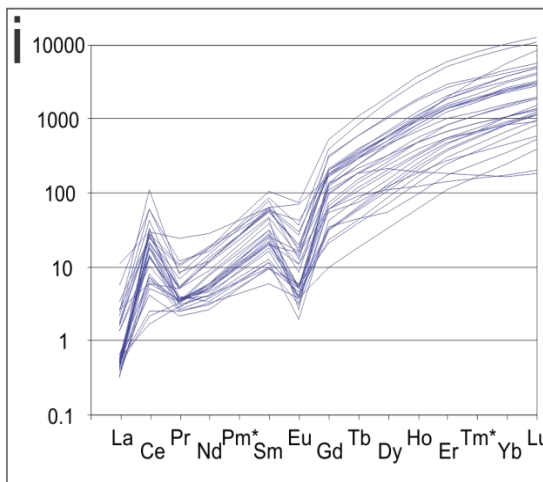
Chapter 8: U/Pb Geochronology for the Cuicateco terrane



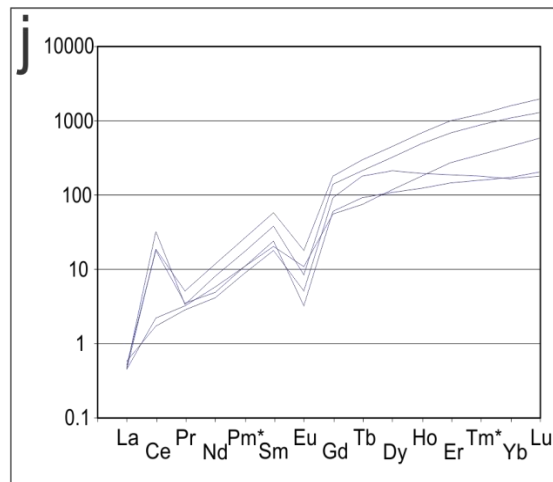
Age (Ma) vs. U (ppm) diagram for all of the analysed grains. Blue points represent zircons used for age calculations and clear points those that were disregarded.



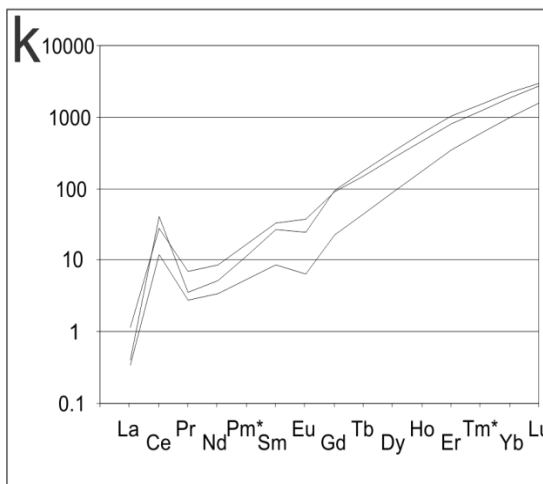
Chondrite-normalized REE of the Permian zircons.



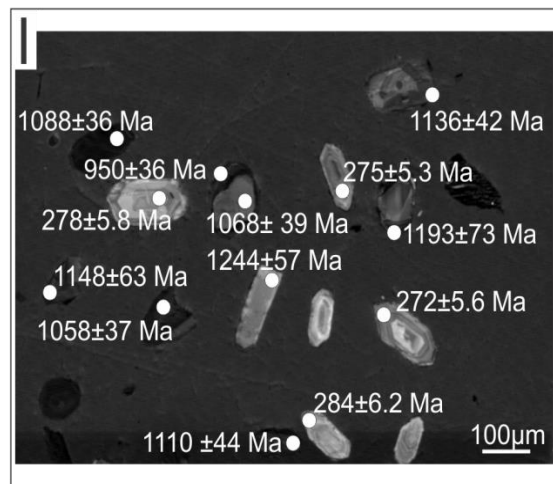
Chondrite-normalized REE of the Proterozoic zircons with Yb/Gd ratios of >10.



Chondrite-normalized REE of Proterozoic analyses where Yb/Gd <10



Chondrite-normalized REE of the disregarded zircons.



Comparison between CL textures and age.

Figure 8.12. Geochronology results for sample 10-18-11-1b of the Chivillas Formation.

8.5.2 Sample 10-18-11-2A

This sample is a medium-coarse greywacke that contains subhedral-subrounded zircons 100-400 μm along their longest axis, with aspect ratios of 1:1-6:1. The CL textures are characterised by oscillatory and sector zoning typical of igneous zircons, however some grains are more homogeneous (Figure 8.13 k.). The colour of the grains under CL ranges from dark (high U) to light (low U). The observations from the CL images suggest that the zircons are of heterogeneous provenance.

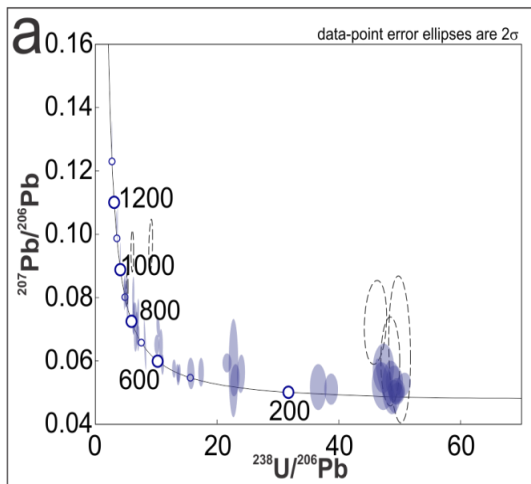
The Th/U and U concentrations of the zircons are variable (0.07-1.1 & 50-1100ppm respectively; Figure 8.13 f & g), suggesting they did not all form in the same event. Of the 48 analysed grains 42 were deemed reliable enough to be used in age calculations (<20% discordant). The Tera-Wasserburg & Wetherill plots (Figure 8.13 a & b) show that there are populations of zircons ranging in age from the Precambrian-Cretaceous.

Grenvillian-age zircons related to the Oaxaquia microcontinent (1250-900) are a common component in the Precambrian zircons (Figure 8.13 d). Other Precambrian populations pre- and post-date Oaxaquia (2.1-1.5 Ga and 850-750 Ma respectively). There are also small populations of Cambrian-Permian zircons most likely from the Acatlán Complex. The most numerous, as well as the youngest population is Cretaceous in age (Figure 8.13 e). Weighted mean plots for the Cretaceous population (n=9) of zircons yield an age of 130 ± 2.2 Ma, with an MSWD of

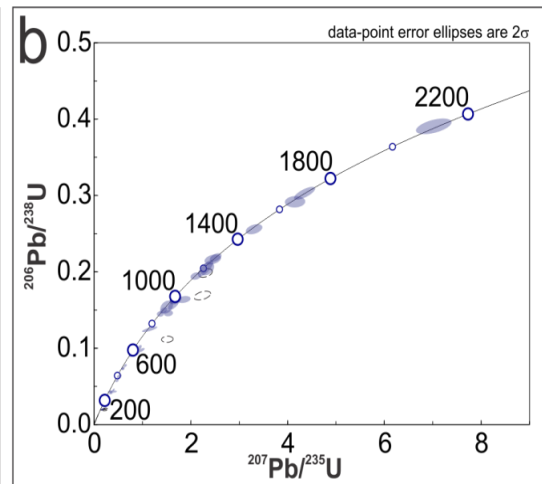
Chapter 8: U/Pb Geochronology for the Cuicateco terrane

3.4 (two ages were rejected by the algorithm; Figure 8.13 c). This Early Cretaceous population of detrital zircons likely derives from the plutonic and extrusive igneous rocks of the Teotitlán Migmatitic Complex and Xonamanca Formation respectively. This sample can therefore be interpreted as a greywacke that contains zircons from a wide variety of source regions, with the Early Cretaceous population constraining the maximum depositional age to 130 ± 2.2 Ma.

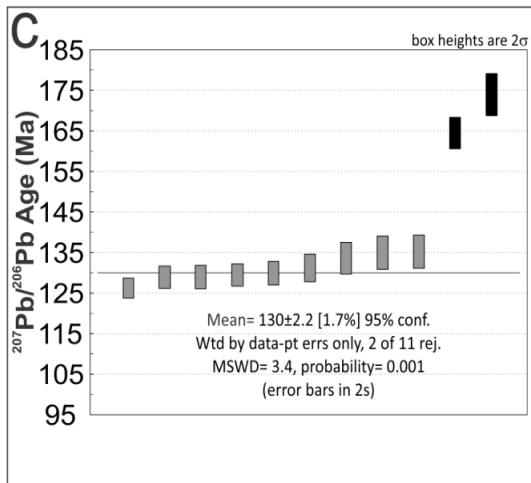
10-18-11 2A



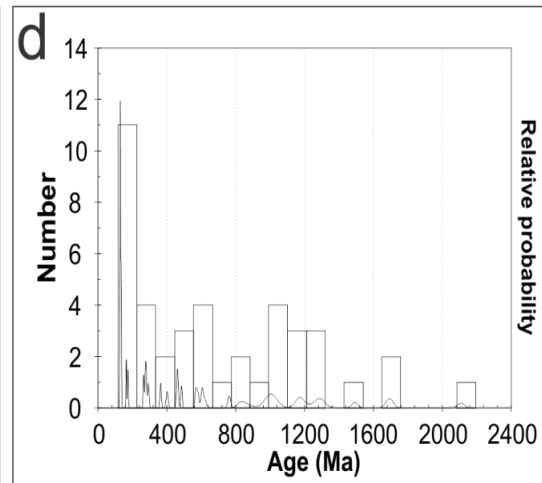
Tera Wasserburg diagram for all of the analysed zircons (n=48). The coloured ellipses represent grains that were used in age calculations (n=42) and the dashed ellipses those that were disregarded (>20% discordant).



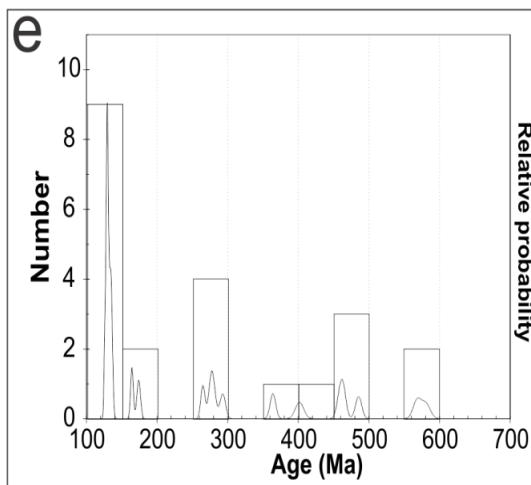
Wetherill diagram for all of the analysed zircons (n=48). The coloured ellipses represent grains that were used in age calculations (n=42) and the dashed ellipses those that were disregarded (>20% discordant).



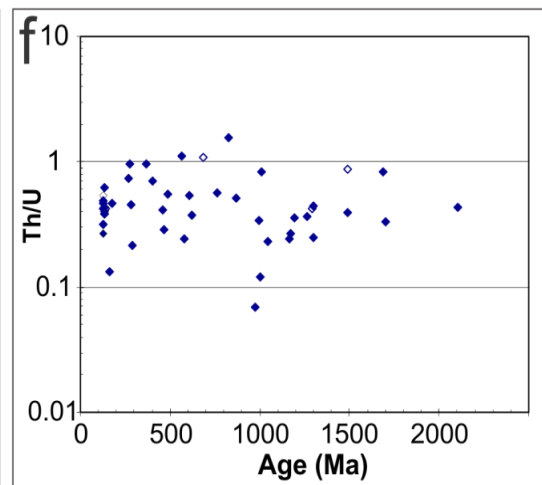
Weighted mean plot for the Jurassic-Cretaceous zircons.



Probability density plot for all of the analysed zircons.

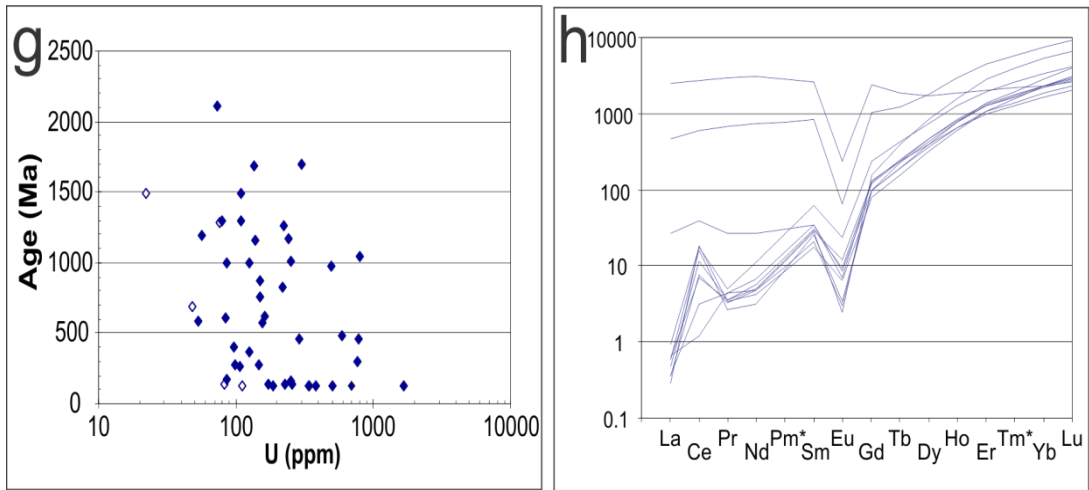


Probability density plot for the Phanerozoic zircons.



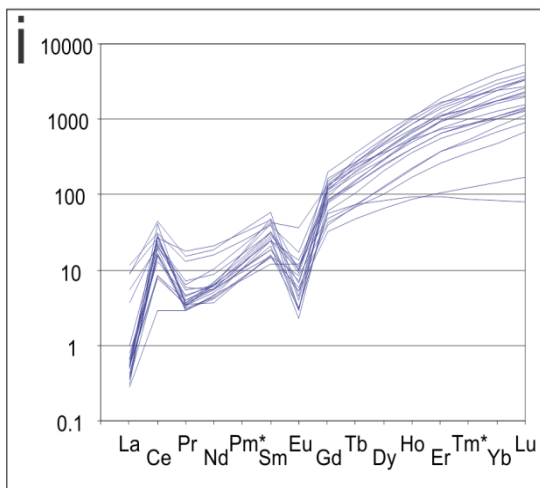
Th/U vs. age (Ma) diagram for all of the analysed zircons. Blue points represent grains that were used in age calculations and clear points those that were disregarded.

Chapter 8: U/Pb Geochronology for the Cuicateco terrane

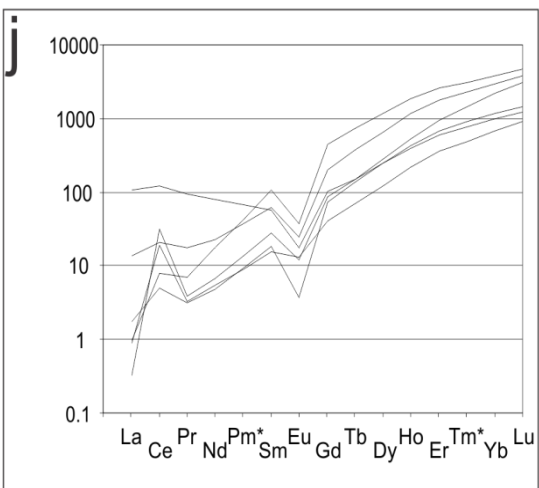


Age (Ma) vs. U (ppm) diagram for all of the analysed zircons. Blue points represent grains that were used in age calculations and clear points those that were disregarded.

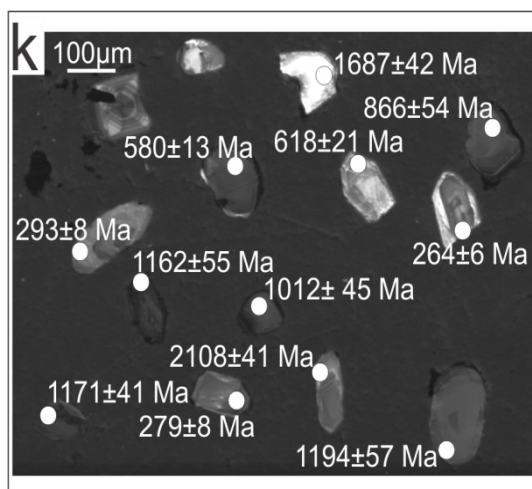
Chondrite normalised REE plot for the Jurassic-Cretaceous zircons.



Chondrite normalised REE plot for the Proterozoic zircons.



Chondrite normalised REE plot for the disregarded zircons.



Relationship between CL textures and age.

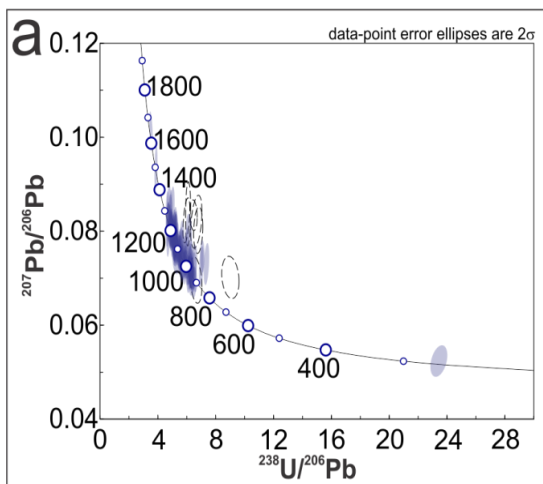
Figure 8.13. Geochronology results for sample 10-18-11-2a of the Chivillas Formation.

8.5.3 Sample 10-18-11-5B

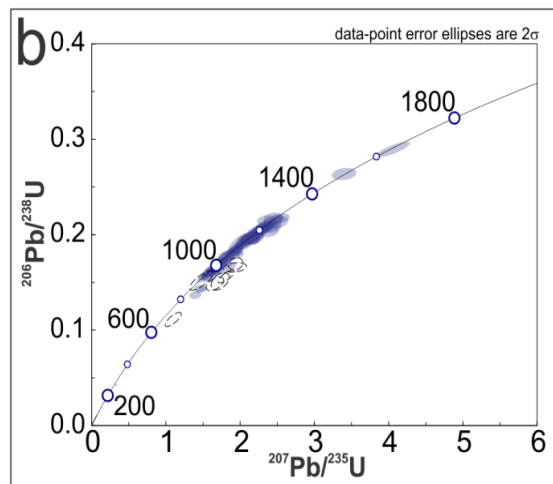
This sample is a red sandstone that contains subhedral-subrounded zircons 100-400 μm along their longest axis, with aspect ratios of 1:1-6:1. There is a variety of CL textures; some grains are characteristically igneous with oscillatory and sector zoning, whilst others are more homogeneous indicating metamorphic origins (Figure 8.14 j). There are core and rim relationships in some of the zircons where zoned igneous cores are surrounded by homogeneous metamorphic overgrowths, suggesting igneous events pre-date metamorphic events.

The Th/U and U concentrations of the zircons are variable (0.03-0.8 & 50-1000ppm respectively; Figure 8.14 e & f), suggesting they did not all form in the same event. Of the 109 analysed grains 102 were deemed reliable enough to be used in age calculations (<5% error and <7% discordant). The Tera-Wasserburg & Wetherill plots (Figure 8.14 a & b) show that the zircons are Precambrian in age. There is one anomalous grain that is Permian in age. However, this is the only zircon out of 109 analyses that appears to be younger than Precambrian so it is likely that the grain has suffered Pb loss. Grenvillian-age zircons related to the Oaxaquia microcontinent are the dominant zircon populations present in the sample (Figure 8.14 c). TuffZirc median ages (Figure 8.14 d) for the youngest population of zircons yield an age of 1000 ± 23 -13 Ma which can be interpreted as the maximum age of deposition for the sandstone. There are 7 zircons in the sample that pre-date (1.6-1.3 Ga) the Grenvillian population. As before, these older zircons, may relate to the initial stages of Oaxaquia formation.

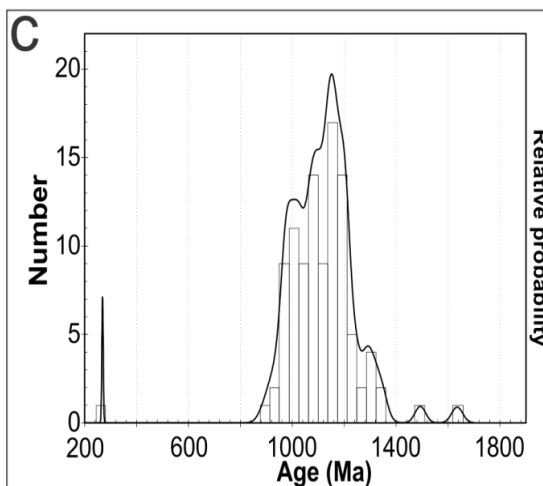
10-18-11 5B



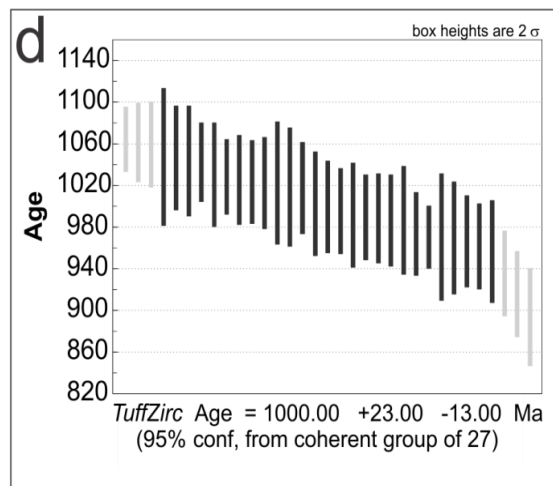
Tera Wasserburg diagram for all of the analysed grains (n=109). The coloured ellipses represent zircons that were used in age calculations (n=102) and the dashed ellipses those that were discarded (>5% error and 7% discordance).



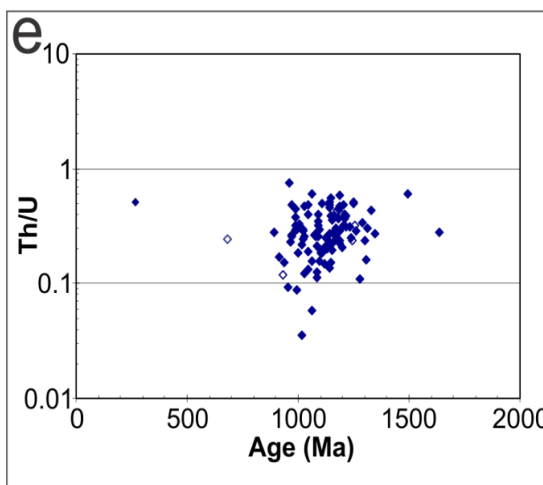
Wetherill diagram for all of the analysed grains (n=109). The coloured ellipses represent zircons that were used in age calculations (n=102) and the dashed ellipses those that were discarded (>5% error and 7% discordance).



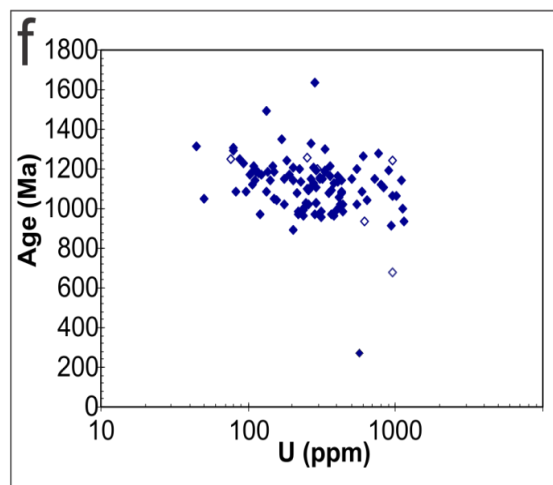
Probability density plot for the zircons used in age calculations.



TuffZirc age for the youngest population of concordant zircons.



Th/U vs. age (Ma) diagram for all of the analysed grains. Blue points represent those used in age calculations and clear points those that were discarded.



Age (Ma) vs. U (ppm) diagram for all of the analysed grains. Blue points represent those used in age calculations and clear points those that were discarded.

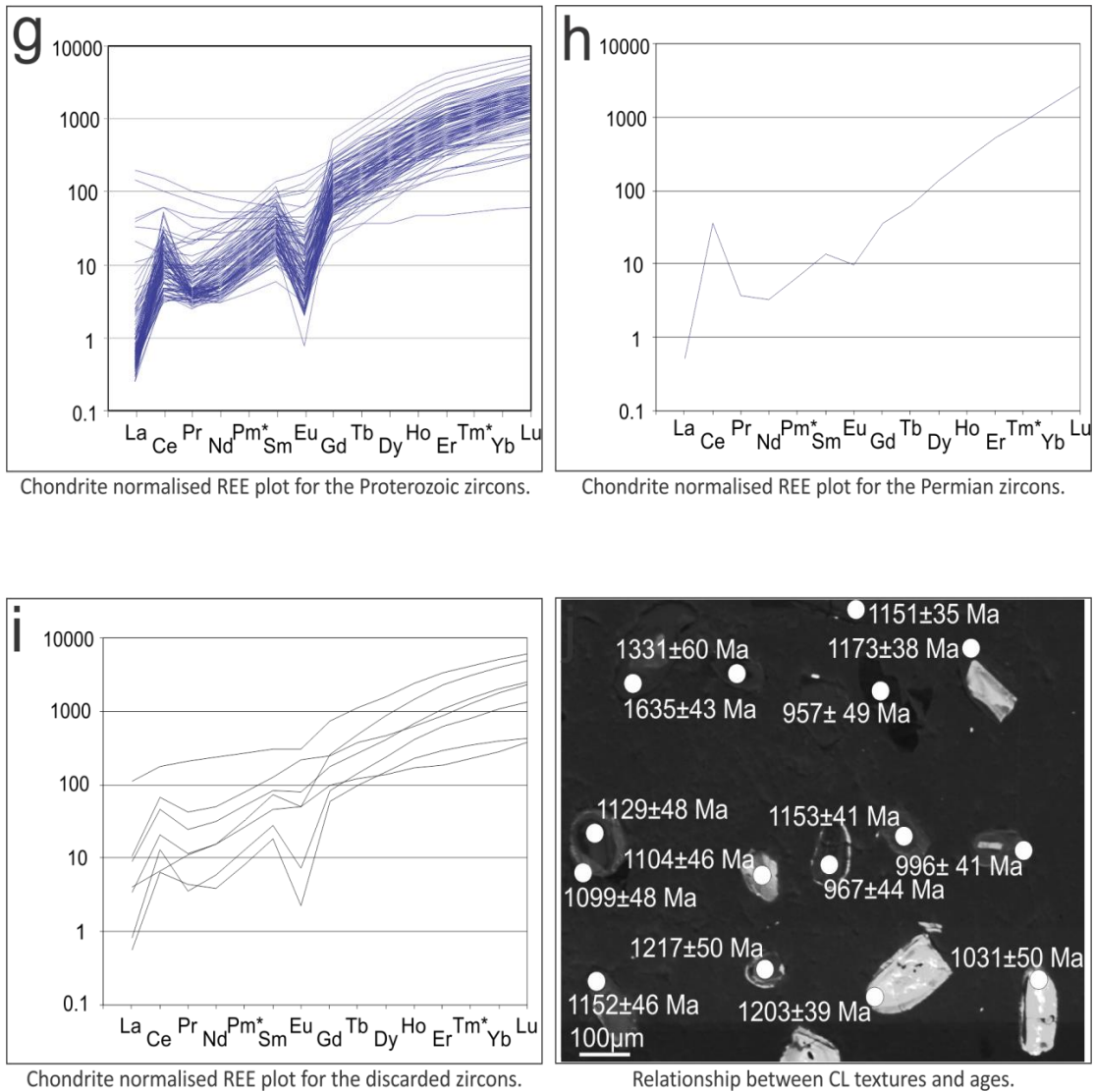


Figure 8.14. Geochronology results for sample 10-18-11-5b of the Chivillas Formation.

8.5.4 Sample 5-10-11-02

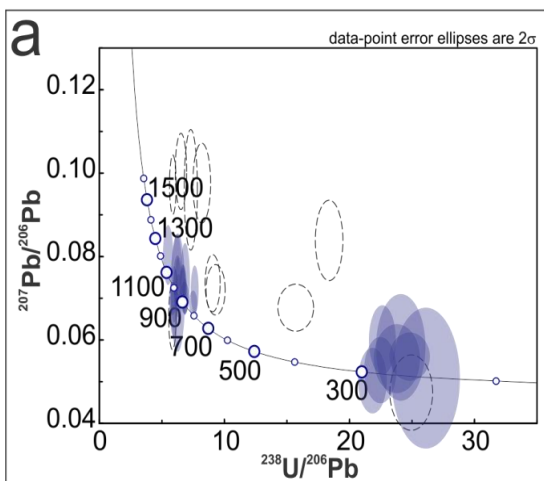
This sample is a fine grained sandstone that contains subhedral-subrounded zircons that are 150-350 μm along their longest axis, with aspect ratios of 2:1-4:1. The CL textures are characterised by oscillatory and sector zoning, typical of igneous zircons. Core and rim relationships are observed in some of the grains. There are also fractures along the c-axis in some of the zircons which may have allowed for contamination from common lead.

The Th/U ratios for the zircons (0.1-0.8) also suggest an igneous origin, although there are 2 grains with values <0.1 which may indicate metamorphic growth (Figure 8.15 d). The U concentrations (Figure 8.15 e) in the zircons range from 40-350 ppm and so there is no indication that they have undergone metamictization.

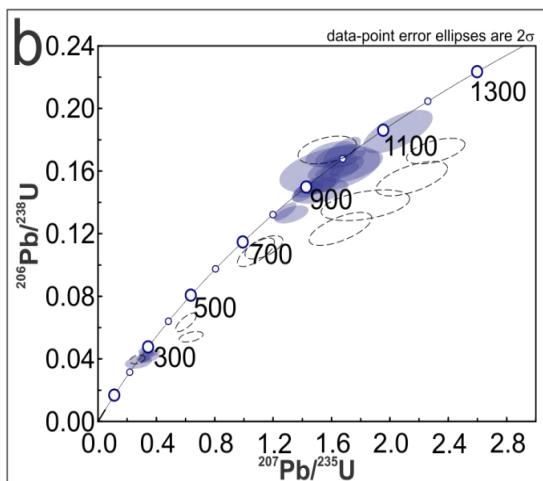
Of the 39 analysed grains, 27 were considered suitable for age calculations ($<5\%$ inverse discordance, $<20\%$ Phanerozoic discordance, $<10\%$ Precambrian discordance). The Tera-Wasserburg and Wetherill diagrams (Figure 8.15 a & b) show that there are two distinct zircon populations present in the sample. The first relates to Grenvillian zircons which are likely derived from the Oaxaquia continental crust, with the second population yielding a Permian age. At least some of the discordant grains appear to form a mixing line between the 2 concordant populations of zircons, likely caused by combined core and rim ablation during analysis.

The weighted mean plot for the youngest population of zircons yields an age of 272 ± 14 Ma, with an MSWD of 4.7 (Figure 8.15 c). This can be interpreted as the maximum age of deposition for the sandstone.

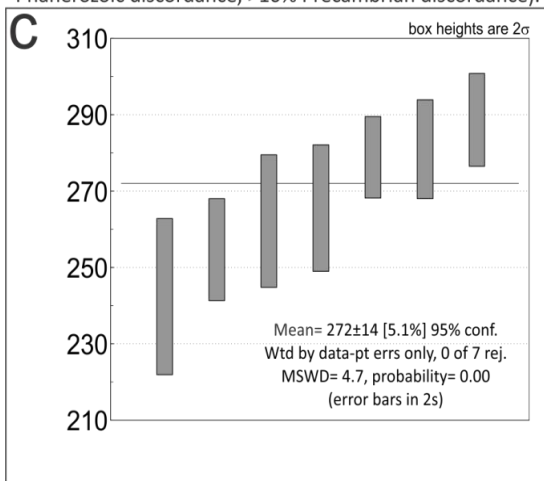
5-10-11-2



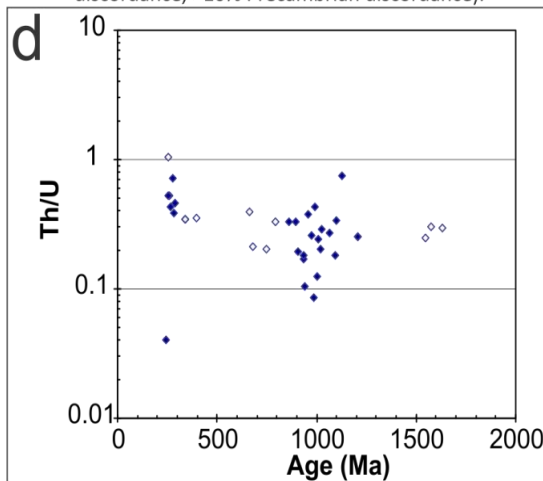
Tera Wasserburg diagram for all of the analysed grains (n=39). The coloured ellipses represent zircons that were used in age calculations (n=27) and the dashed ellipses those that were discarded (>5% inverse discordance, >20% Phanerozoic discordance, >10% Precambrian discordance).



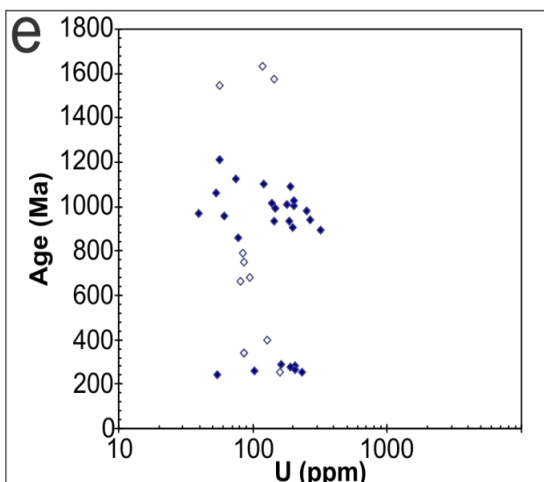
Wetherill diagram for all of the analysed grains (n=36). The coloured ellipses represent zircons that were used in age calculations (n=27) and the dashed ellipses those that were discarded (>5% inverse discordance, >20% Phanerozoic discordance, >10% Precambrian discordance).



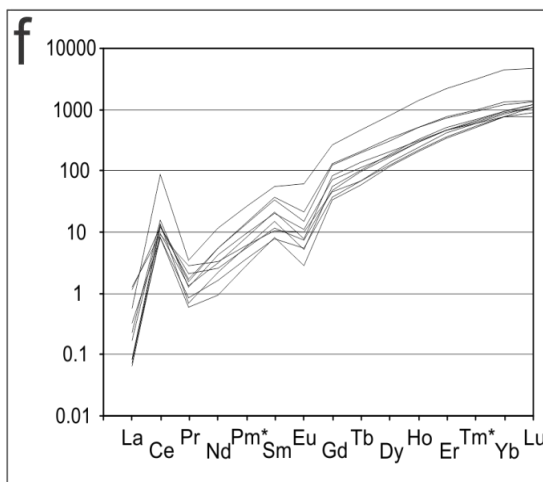
Weighted mean plot for the youngest population of concordant zircons.



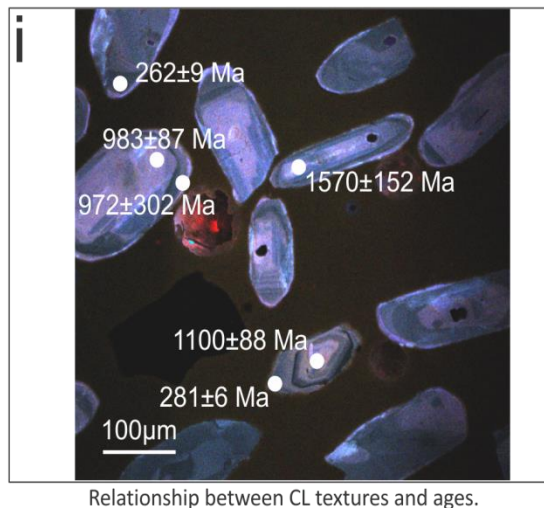
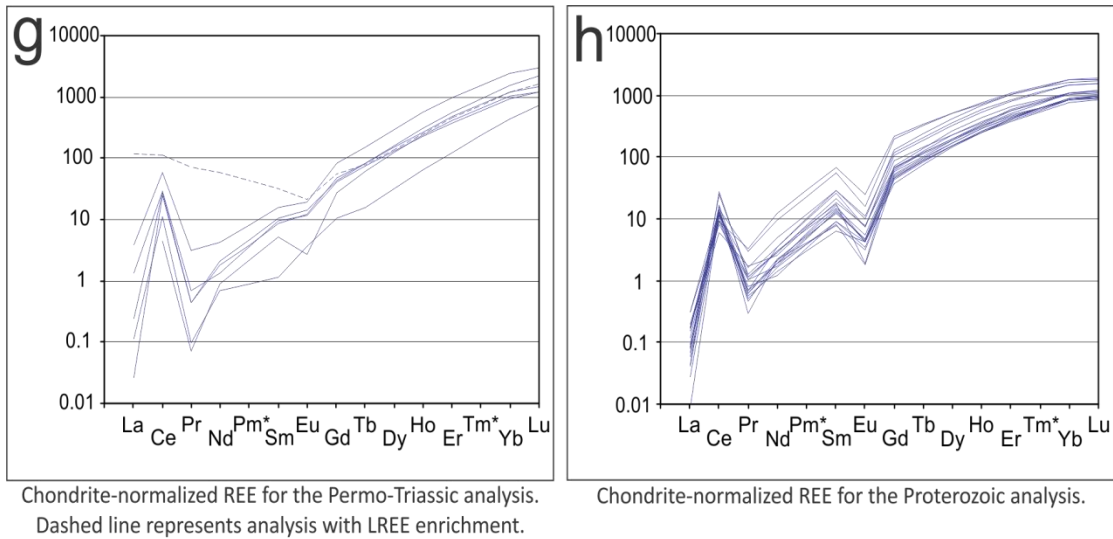
Th/U vs. age (Ma) diagram for all of the analysed grains. The blue points represent zircons used in age calculations and clear points those that were disregarded.



Age (Ma) vs. U (ppm) diagram for all of the analysed grains. Blue points represent zircons used for age calculations and clear points those that were disregarded.



Chondrite-normalized REE for the disregarded analysis.



Relationship between CL textures and ages.

Figure 8.15. Geochronology results for sample 5-10-11-2 of the Chivillas Formation.

8.6 Summary

- The Pochotepec Formation appears to be comprised of old sediments and granitoids that pre-date Cretaceous magmatism, containing zircons that are Grenville in age. Therefore the Pochotepec Formation likely represents a sliver of Oaxaquia type continental crust, and not deeper portions of the Chivillas Formation as suggested by Angeles-Moreno, (2006).

Chapter 8: U/Pb Geochronology for the Cuicateco terrane

- The extrusive rocks of the Xonamanca Formation and granitoids of the Teotitlán Migmatitic Complex record ages that overlap (within error) with each other (140 Ma and 138-133 Ma respectively), indicating they may be related to the same igneous event.
- The amphibolites of the Teotitlán Migmatitic Complex appear unrelated to the other igneous rocks in the area, yielding Permo-Triassic igneous zircons (247 Ma). Instead these amphibolites may have formed in the igneous event discussed in Chapters 2-5.
- Meta-sediments of the Teotitlán area predate the Cretaceous magmatism, and yield a maximum depositional age of Carboniferous-Devonian (354 Ma).
- The Chivillas Formation sediments display a range of provenances, with influence from the initial stages of Oaxaquia formation (1.8-1.3 Ga), the main zircon crystallization phase of Oaxaquia (1.2-0.9 Ga), Permo-Triassic magmatism and Cretaceous magmatism. The Cretaceous population (130±2.2 Ma) constrains the maximum depositional age of the sediments, and therefore the magmatism in the basin (as seen in field relationships discussed in Chapter 7). This replicates the Barremian maximum depositional age obtained by detrital zircons in Mendoza et al. (2010) and paleontological ages in Alzaga and Pano (1989).

9 Major, trace element and Hf-Nd geochemistry of the Northern Cuicateco terrane.

9.1 Introduction

This chapter presents major, trace and isotopic geochemical results in order to determine the tectonomagmatic setting of the northern Cuicateco terrane. In turn these interpretations will be applied to the Cretaceous tectonic reconstructions of Mexico, after the breakup of Pangaea.

As discussed in Chapter 6, the northern Cuicateco terrane can be divided into 5 units: 1) Chivillas Formation, 2) Teotitlán Migmatitic Complex, 3) Mazateco Metamorphic Complex (further subdivided into the Mazatlán de Las Flores Schist and la Nopalera Schist), 4) Pochotepec Formation and 5) Xonamanca Formation. Geochronological work (Chapter 8) has revealed that magmatism in the Cuicateco terrane is related to distinct events, with Precambrian and Permian activity predating the more widespread Cretaceous magmatism. This chapter will concentrate on the Cretaceous igneous rocks of the Cuicateco, which are found in the Xonamanca Formation, Teotitlán Migmatitic Complex and Chivillas Formation.

9.2 Analytical techniques

As noted in Chapter 7, 48 samples were collected from the northern Cuicateco during two field expeditions in October 2011 and April 2014. 30 of the freshest samples (Figure 9.1) were selected for geochemical analysis of major and trace elements by ICP-OES and ICP-MS at Cardiff University, UK. In addition, a

Chapter 9: Geochemistry and Hf-Nd isotope results

representative batch of six samples was selected for whole rock Hf and Nd radiogenic isotopic analysis under the supervision of Dr. Bodo Weber at Centro de Investigación Científica y de Educación Superior de Ensenada (CICESE) research institute (Ensenada, Mexico). Detailed descriptions of analytical techniques are presented in Appendix A.

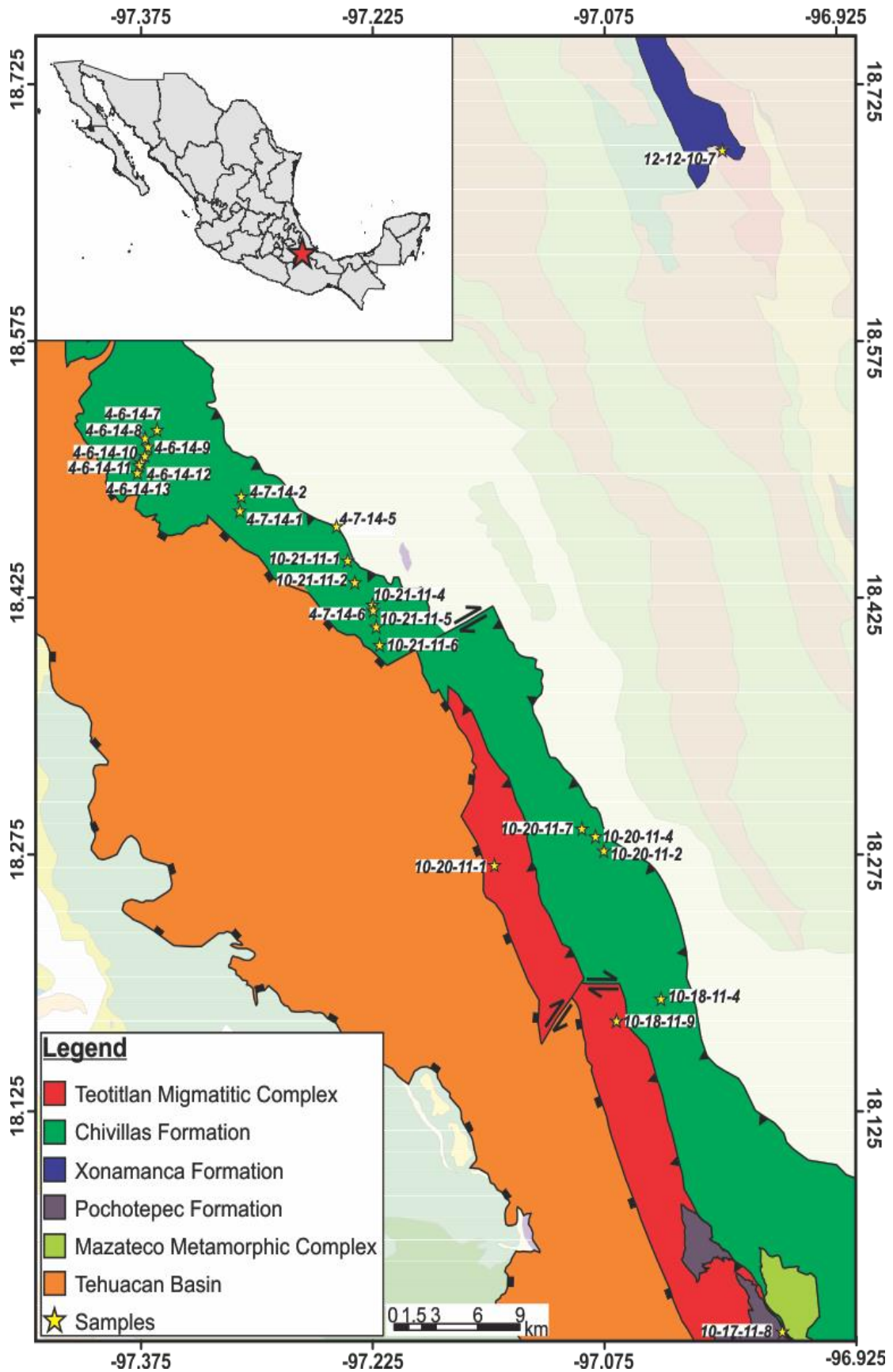


Figure 9.1. Map showing the location of the samples used for geochemical analysis from the northern Cuicateco terrane. Geological projection Mexicano, S.G. (2001) map.

9.3 Alteration and element mobility

When interpreting geochemical data care must first be taken to consider subsequent alteration events that may affect a rock, causing element mobility and masking the original magmatic signatures. Factors that can cause such element mobility include surface weathering, interactions with hydrothermal fluids, and metamorphism. As previously highlighted in Chapters 6 and 7 the Cuicateco terrane has undergone lower greenschist facies metamorphism so it is important to assess how this has affected the composition of my analysed igneous rocks before interpreting petrological processes associated with their formation.

The degree of element mobility is qualitatively determined using loss of ignition values (%LOI) and element mobility diagrams. The %LOI is measured based on the weight % of a sample that is lost after ignition for 2 hours at 900°C in a furnace. The volatiles that are lost from a sample during this ignition process give an indication into how much sub-solidus alteration has occurred. Low %LOI values in this study are considered to be <5 wt.%, moderate between 5-10 wt.%, and high being >10 wt.%.

Another method of determining the degree of element mobility in the samples analysed is to plot each element against Zr (Cann, 1970). Zr has been selected for this purpose as it is widely accepted to be one of the most immobile elements even during medium to high grade metamorphism (Pearce, 1996). Assuming all the rocks lie on a single fractionation trend and there is no source variation then dispersion away from this trend can be used as an indication of alteration associated with element mobilisation. Scatter or multiple trend lines

Chapter 9: Geochemistry and Hf-Nd isotope results

observed in elements that are known to be immobile up to greenschist facies metamorphism (e.g. light rare earth elements [LREE] and high field strength elements [HFSE]) are more likely to reflect source variability. Where more than five analyses were available to define a representative sample population, the degree of compositional dispersion was quantified here using an R^2 value. For the purposes of this study a good correlation is defined by an $R^2 > 0.75$, a moderate correlation between 0.75 and 0.5, and poor correlations < 0.5 . Elements that are generally immobile under greenschist facies metamorphism include the rare earth elements (REE), Hf, Zr, Nb, Ta, Y, Ti, Cr, Th (Hastie et al., 2007). In suites where the degree of metamorphism is greenschist or lower and the number of analysed samples is < 5 it was assumed that these elements have remained immobile.

9.4 Xonamanca Formation

9.4.1 Element Mobility & Alteration

Three samples from the Xonamanca Formation were collected from extrusive volcanics and tuffs that are poorly exposed due to dense tropical vegetation and weathering. Moderate alteration of the samples is demonstrated by %LOI values of 2.9-5.0% (Appendix G). Samples 12-12 7B and 12-12-7C have suffered higher degrees of alteration (LOI= 5.0 and 4.8 wt.% respectively) when compared to 12-12 7A (LOI= 2.9 wt.%). However, petrographic observations reveal that metamorphic and alteration effects are low in these samples, with notably good preservation of alteration sensitive minerals (e.g. feldspars). This therefore suggests that the tuffs have not been significantly affected by alteration, with the elevated %LOI values instead potentially occurring as a result of biotite dehydration.

Due to the small set of analysed samples from the Xonamanca Formation the Zr mobility plots and R^2 calculations are not appropriate to use in assessing how much element mobility there has been. For this reason they have not been included but can be found in Appendix G.

9.4.2 Classification

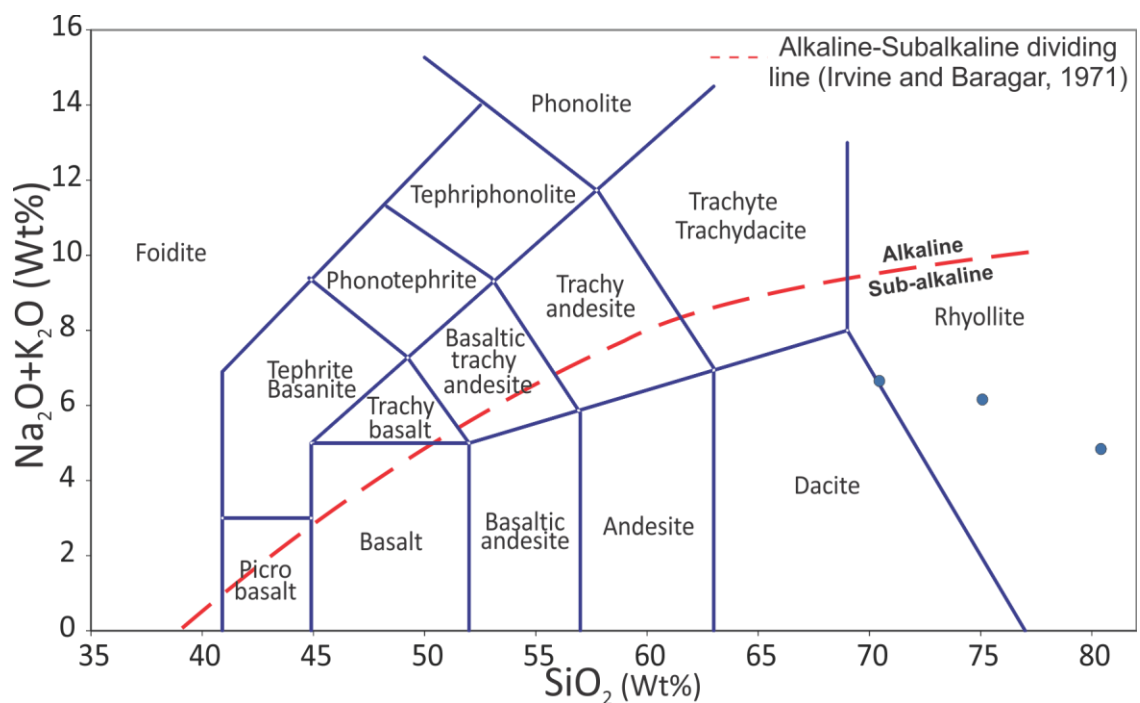


Figure 9.2. Total alkali-silica (TAS) classification (Le Maitre et al., 1989) plot for volcanics collected from the Xonamanca Formation. Major elements are expressed as anhydrous values.

When classifying the rocks within the northern Cuicateco it is important to take into account the degree of element mobility that has occurred. Traditionally the TAS plot (Le Maitre et al., 1989) is used as a means of classifying extrusive rocks, where silica is plotted along the x-axis and the alkalis of Na₂O and K₂O are plotted along the y-axis. Samples from the Xonamanca Formation plot in the subalkaline (Irvine & Baragar, 1971) region of the diagram (Figure 9.2) and appear to be rhyolitic in composition. However, SiO₂ and the alkali major element are easily mobilised

(section 4.4.1), so the TAS classification plot is sensitive to alteration and metamorphism which may cause erroneous results.

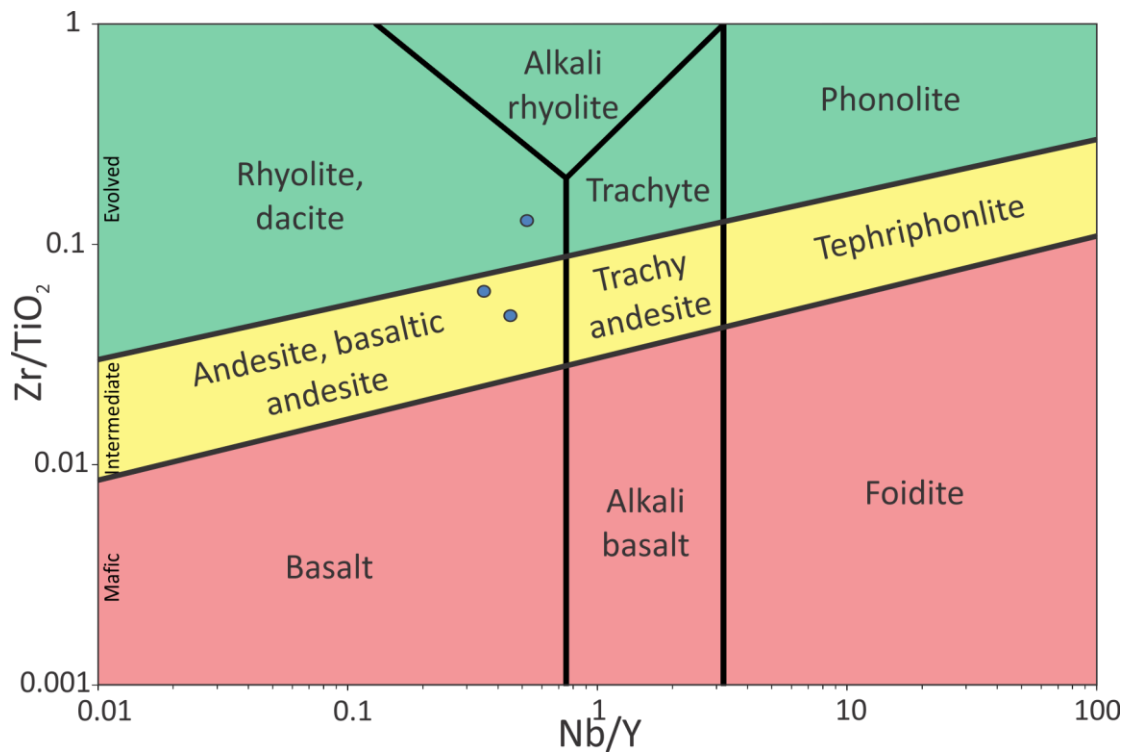


Figure 9.3. Zr/TiO₂ vs Nb/Y (Pearce, 1996b after Winchester & Floyd, 1977) classification plot for volcanics collected from the Xonamanca Formation.

The Zr/TiO₂-Nb/Y plot (Figure 9.3) of Pearce (1996b) after Winchester & Floyd (1977) is perhaps a more robust means of classifying the Xonamanca Formation samples as it uses elements that are regarded to be less-mobile during weathering and metamorphism. The samples plot between the “rhyolite/dacite” and “andesite/basaltic andesite” field boundaries, indicating that they have an intermediate-felsic composition in general agreement with the TAS classification.

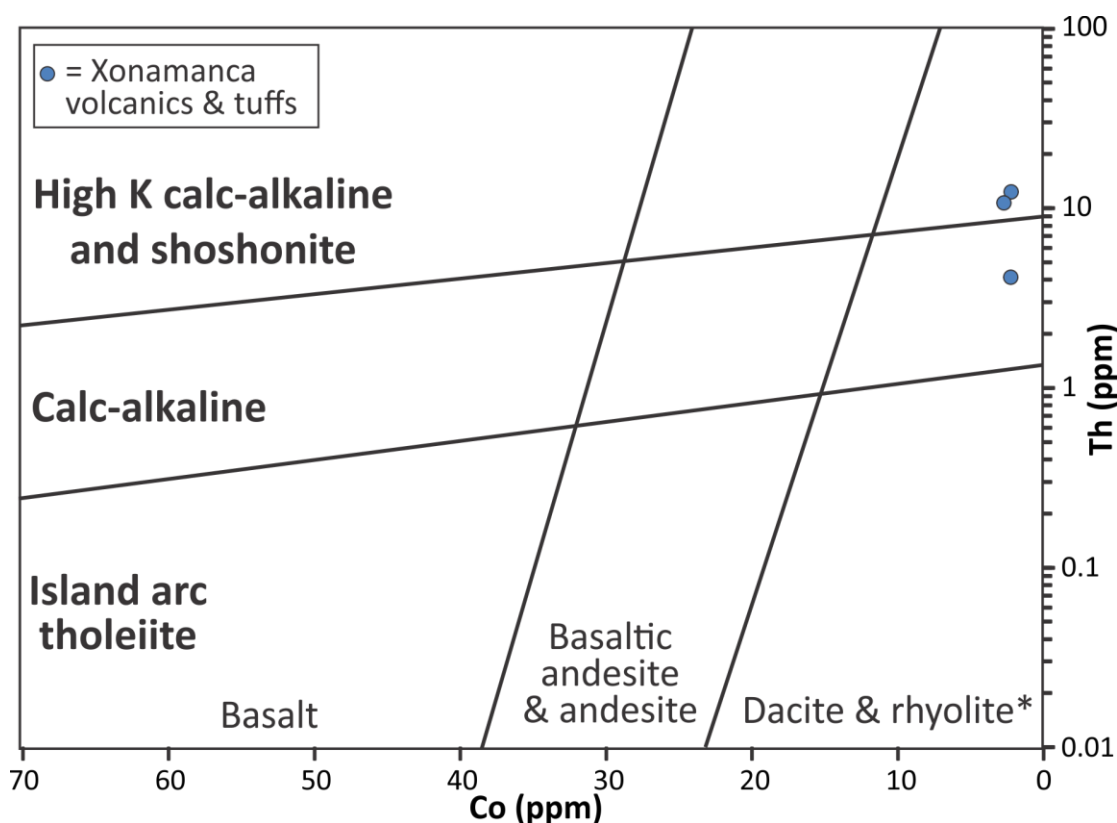


Figure 9.4. Th-Co classification diagram (Hastie et al., 2007) for volcanics collected from the Xonamanca Formation.

The Th-Co diagram (Figure 9.4) of Hastie et al. (2007) uses more immobile elements than the traditional K_2O-SiO_2 diagram (Peccerillo & Taylor, 1976) in classifying subalkaline volcanic rocks. The samples from the Xonamanca Formation plot in the dacite & rhyolite fields, with two samples in the high K calc-alkaline and shoshonite series and one in the calc-alkaline series. The two tuffs that plot in the high K calc-alkaline and shoshonite series are known to contain lithic fragments from the petrography (Chapter 7) which may cause elevated Th concentrations.

9.4.3 Trace element variation

Chondrite normalised REE plots (Figure 9.5) for the Xonamanca Formation display consistent enriched patterns relative to chondrite, as well as enriched LREE when compared to the HREE [$(La/Sm)_N = 1.8-6.0$]. The HREE display flat to slightly

inclined patterns $[(Gd/Yb)_N = 1.4-2.3]$ for each of the samples. The samples also display negative Eu anomalies ($Eu/Eu^{*1}=0.4-0.8$), most prominent in samples 12-12-7B and 12-12-7C, indicating plagioclase fractionation from the magma.

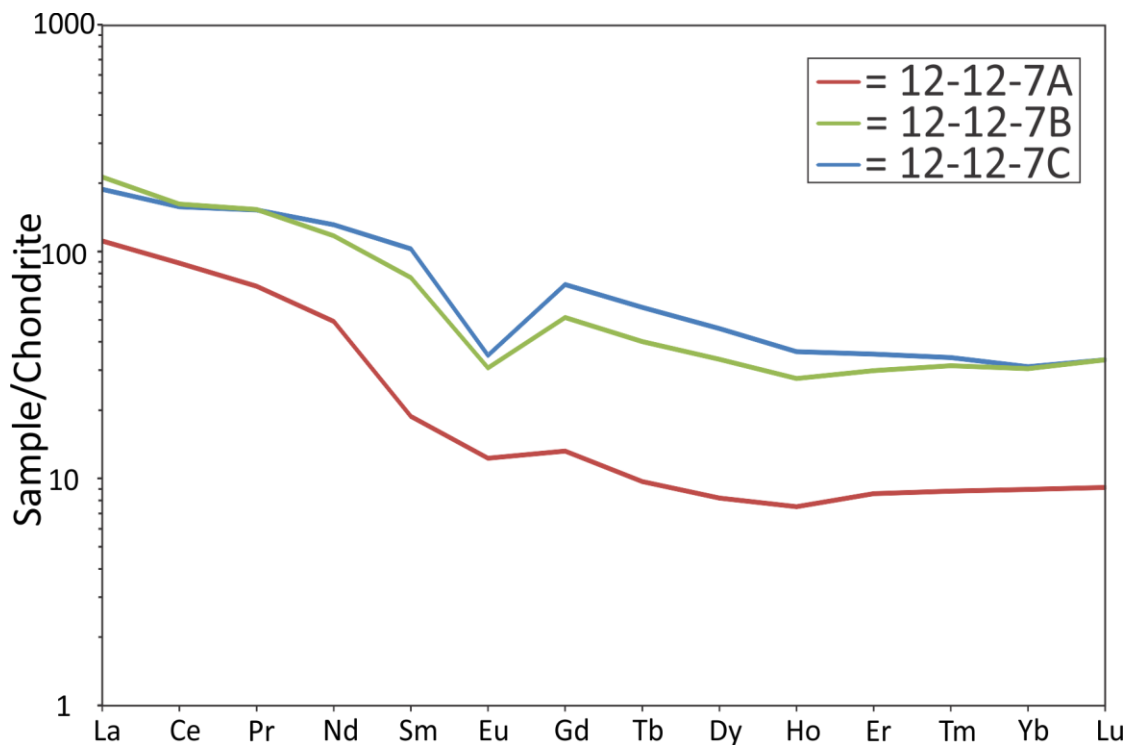


Figure 9.5. Chondrite normalised rare earth element plots for volcanic samples taken from the Xonamanca Formation.

The N-MORB-normalised multi-element diagram for the tuffaceous samples collected from the Xonamanca Formation (Figure 9.6) display pronounced negative Nb ($Nb/Nb^{*1}= 0.15-0.2$), Ta ($Ta/Ta^{*1}= 0.19-0.28$) and Ti ($Ti/Ti^{*1}= 0.06-0.31$) anomalies. There is also a negative Sr anomaly ($Sr/Sr^{*1}=0.1-0.25$) which along with the Eu anomaly of the REE plot is likely to represent fractionation of plagioclase from the magma. Other features that are common to the multi-element and REE plots is the

¹ Eu/Eu* and Ti/Ti* calculated using equation:

$$\frac{Eu}{Eu^*} = \frac{Eu}{0.5 \times (Gd + Sm)}$$

(Eu/Eu* used here for an example). Nb/Nb* & Ta/Ta* use the elements Th & La. Sr/Sr* is calculated using Ce & Nd.

enrichment in the most incompatible elements (Th and the LREEs) relative to N-MORB and overall greater enrichment in samples 12-12-7B and 12-12-7C when compared to 12-12-7A.

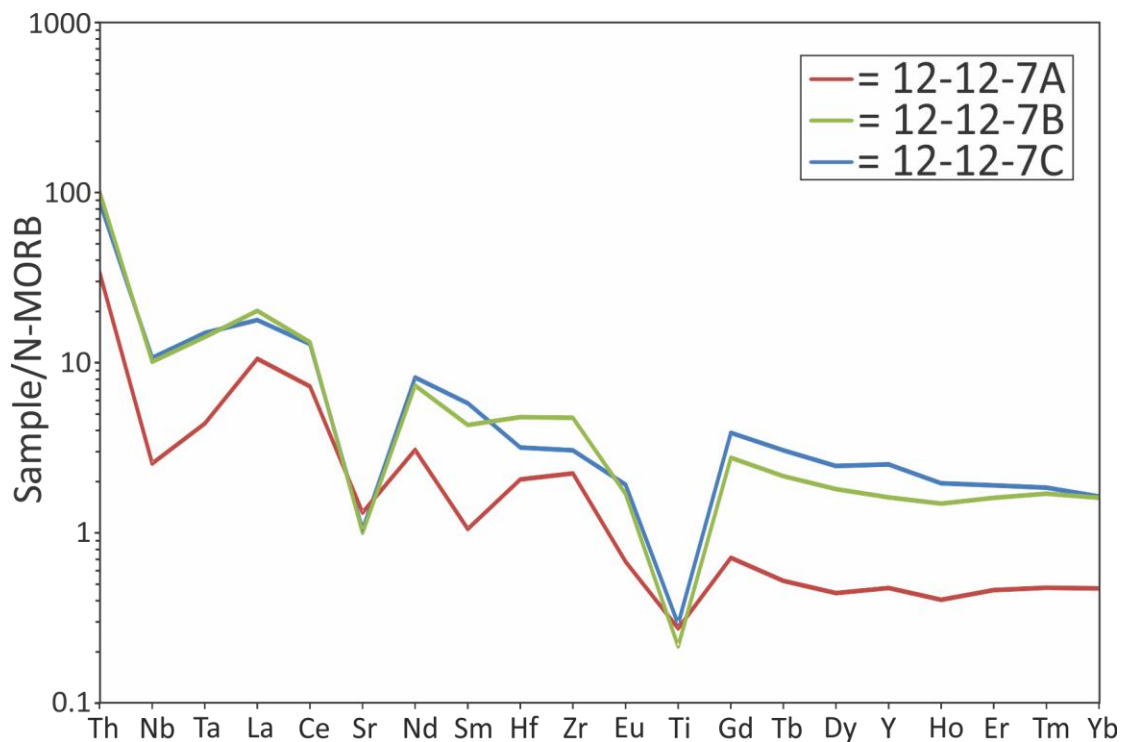


Figure 9.6. N-MORB normalised multi-element plots for volcanic samples taken from the Xonamanca Formation.

9.5 Granites from the Teotitlán Migmatitic Complex

9.5.1 Element Mobility & Alteration

The majority of the four granitoid samples collected from the Teotitlán Migmatitic Complex appear to be relatively unaltered from their LOI (0.6-1.8 wt.%). One sample (10-18-11 4B) collected from a clast within a conglomerate displays slightly higher LOI (3.2 wt.%) compared to the rest of the samples. Despite their relatively low LOI values, alteration of these granites is suggested by petrographic observations. Quartz recrystallisation is observed in sample 10-18-11 9D, as well as

evidence for hydrothermal fluid interaction, with plagioclase altered to saussurite and argillite, widespread chloritization of biotite and secondary crystallisation of epidote (possibly pistachite). Sample 10-18-11 9E displays evidence of deformation, associated with the recrystallisation of quartz, sericitization of plagioclase and chloritization of biotite.

Interpretation of element mobility based on Zr mobility plots (Appendix G) was not carried out due to limited number of granitoid samples. Petrographic observations suggest however that the granites have undergone alteration.

9.5.2 Classification

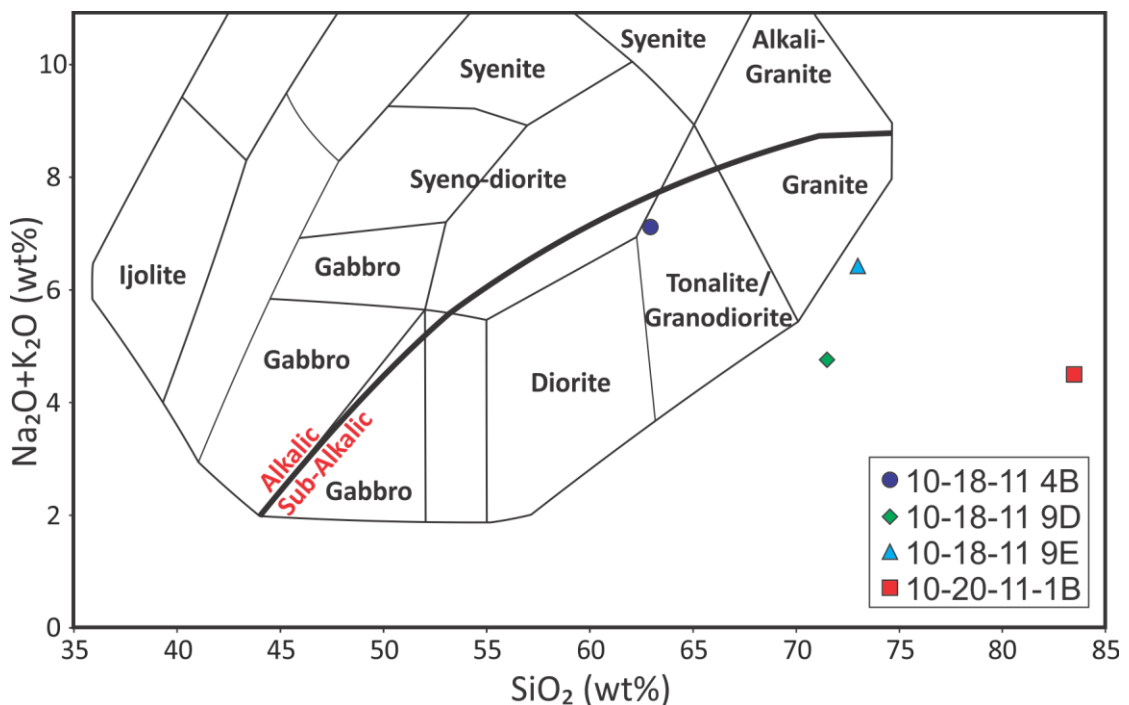


Figure 9.7. Total alkali-silica (TAS) of Le Maitre et al., (1989) showing the composition of the basement samples. Field boundaries taken from Wilson (1989). Major elements are expressed as anhydrous values.

Samples from the Teotitlán Migmatitic Complex present problems when plotted in the TAS classification diagram (Figure 9.7). Three out of the four samples

plot outside of the field boundaries defined in (Wilson, 1989). Sample 10-18-11 4B plots in the tonalite/granodiorite field, with samples 10-18-11 9D, 10-18-11 9E and 10-20-11-1B all plotting outside of the field boundaries but close to the granite or tonalite/granodiorite fields. All of the samples plot below the alkaline-subalkaline dividing line. The alteration of these samples mentioned in Section 9.5.1 has likely influenced where they plot on the TAS diagram.

In the Th-Co diagram (Figure 9.8) all of the samples plot in the dacite/rhyolite field. Samples 10-18-11-9D and 10-20-11-1B plot in the calc-alkaline magma series field whereas 10-18-11-4B and 10-18-11-9E fall in the island arc tholeiite series field.

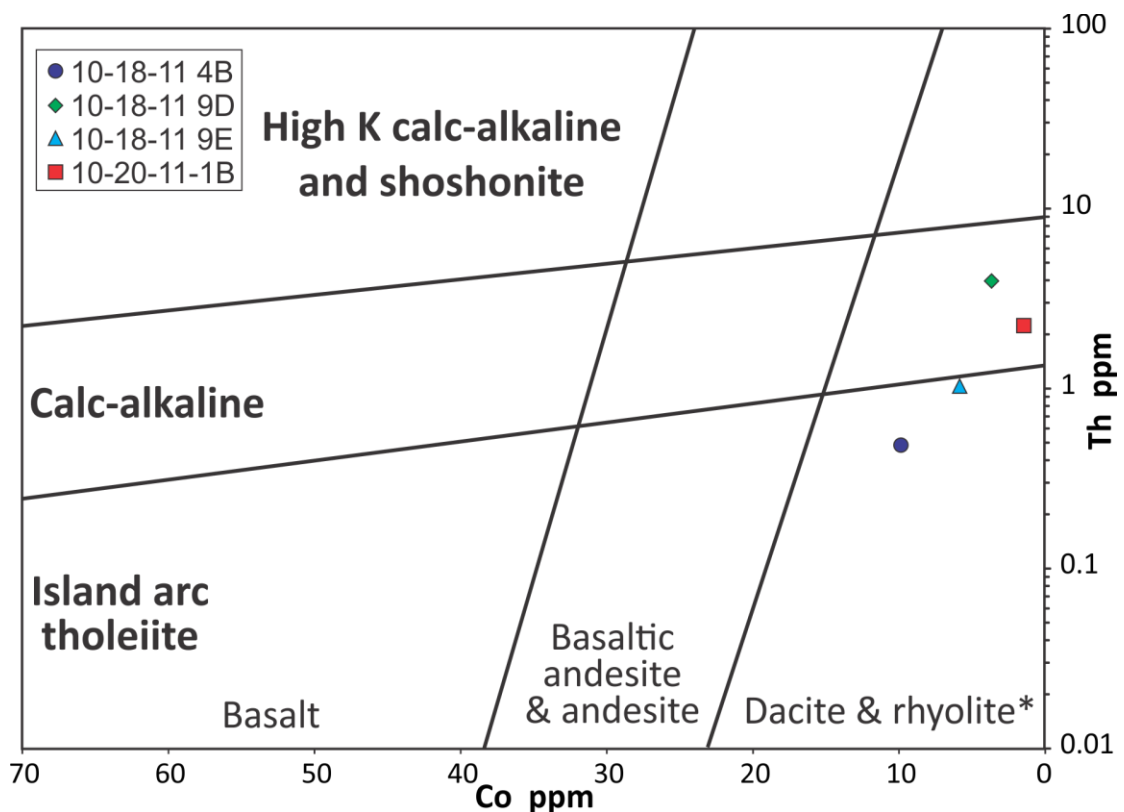


Figure 9.8. Th-Co classification diagram (Hastie et al., 2007) classification plot for the granitoids of the Teotitlán Migmatitic Complex.

Classifying the granitoids of the Teotitlán Migmatitic Complex has been somewhat unsuccessful using geochemical plots due to the mobility of the major

elements and the use of inappropriate trace element field boundaries. The Th-Co classification plot of Hastie et al. (2007) appears to be the more reliable but it is important to use petrographic interpretations to help classify the rocks. The petrographic interpretations of Chapter 7 reveal that the feldspars in samples 10-18-11 9D, 10-18-11 9E and 10-18-11 1B are predominately plagioclase, indicating a tonalite composition, whereas sample 10-18-11 4B contains roughly equal quantities of plagioclase and alkali feldspars, indicating a granite composition.

9.5.3 Trace element variation

Chondrite-normalised REE plots (Figure 9.9) for granitoids from the Teotitlán Migmatitic Complex display enriched trends relative to chondrite values (mean = x12), and enrichment in LREE relative to the MREE $[(La/Sm)_N = 1.7-5]$. In two of the samples the HREEs display a flat pattern $[(Gd/Yb)_N = 0.7-1.2]$, however in samples 10-18-11 9D and 10-20-11 1B they are slightly more depleted in the HREE $[(Gd/Yb)_N = 2.5-2.8]$. A pronounced positive Eu anomaly ($Eu/Eu^{*1} = 4.1$), associated with low REE concentrations is observed in sample 10-18-11 9E, which may reflect residual plagioclase accumulation. A positive anomaly is seen to a lesser extent in samples 10-18-11 9D and 10-20-11 1B ($Eu/Eu^{*1} = 1.18$ and 1.35 , respectively). Sample 10-18-11 9E displays a U-shape REE pattern which is indicative of residual amphibole in the source or extensive amphibole fractional crystallisation from the melt.

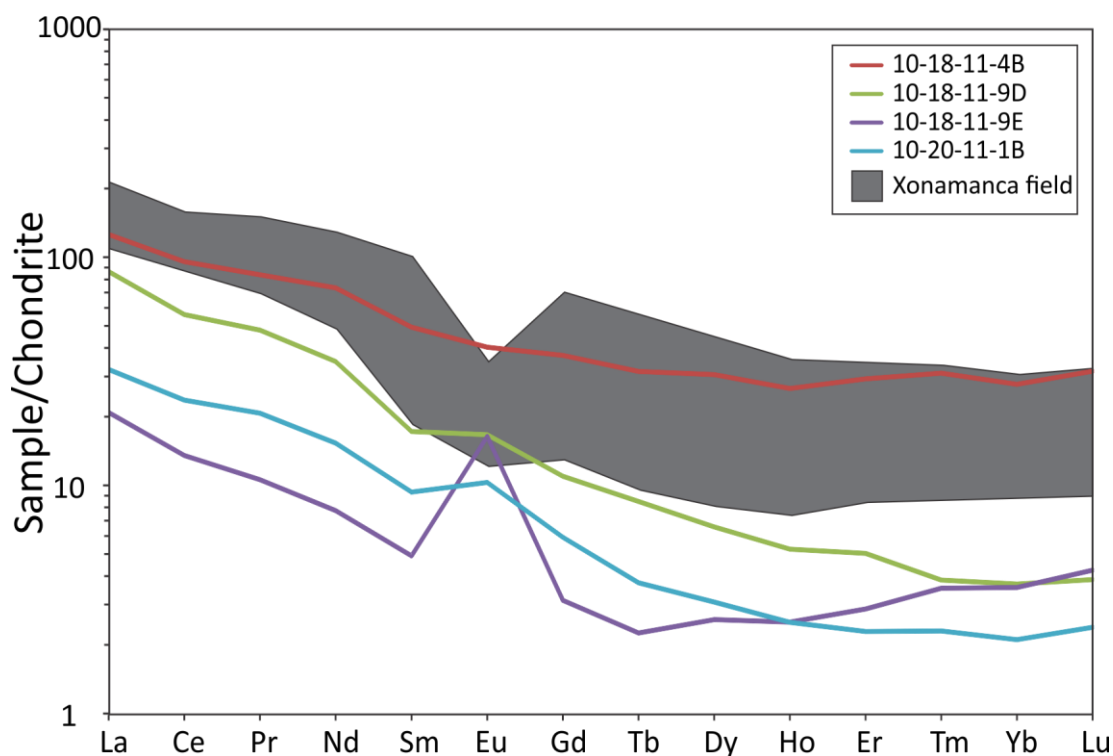


Figure 9.9. Chondrite normalised rare earth element for granite samples taken from the Teotitlán Migmatitic Complex. The grey field represents the analysed samples from the Xonamanca Formation.

The REE patterns of the Teotitlán Migmatitic Complex granitoids are broadly similar to those of the Xonamanca Formation tuffs (grey shaded field in Figure 9.9), with however lower general concentrations. The main difference between the two suites is the positive Eu anomaly observed in several of the Teotitlán Migmatitic Complex granitoids coupled with a negative Eu anomaly in the extrusive rocks of the Xonamanca Formation.

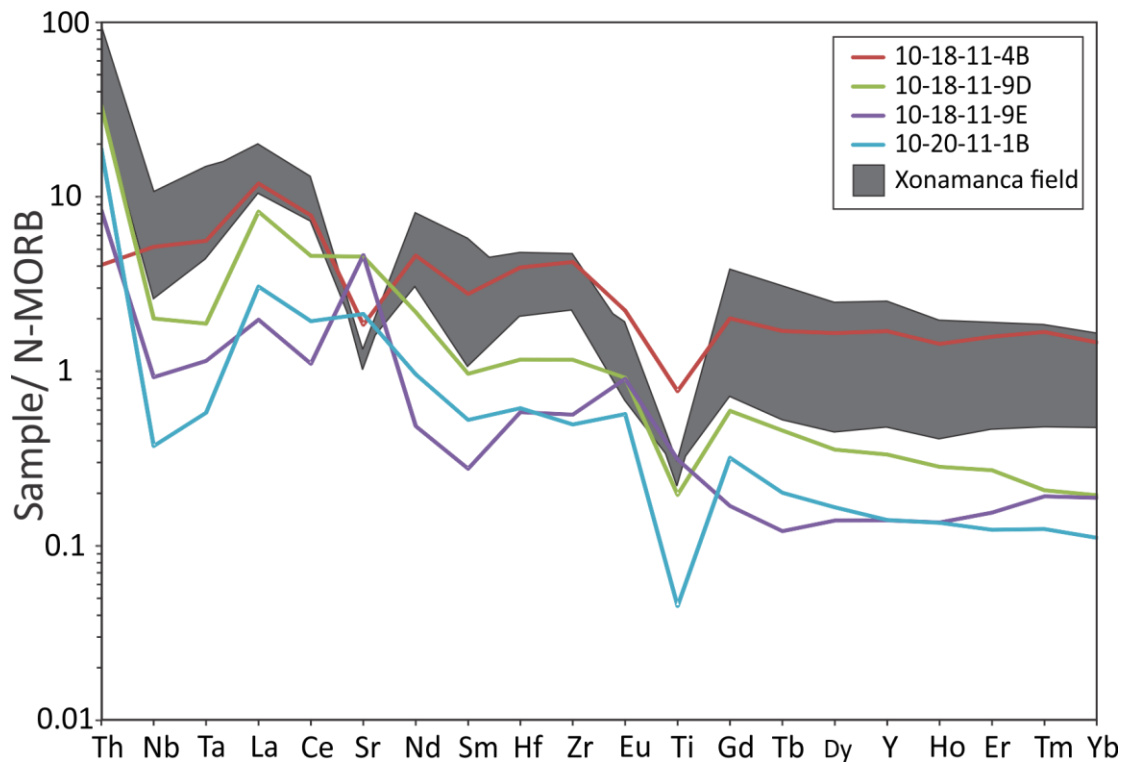


Figure 9.10. N-MORB normalised multi-element plots for granite samples taken from the Teotitlán Migmatitic Complex. The grey field represents the analysed samples from the Xonamanca Formation.

The N-MORB-normalised multi-element plot for the in-situ granitoids of the Teotitlán Migmatitic Complex (Figure 9.10) display enrichment when compared with N-MORB values (mean= x2). The element that yields the greatest amount of enrichment is Th (mean= x16 N-MORB values). Negative anomalies are observed for Nb ($Nb/Nb^* = 0.03-0.3$), Ta ($Ta/Ta^* = 0.05-0.3$) and Ti ($Ti/Ti^* = 0.1-0.8$). Sample 10-18-11-9E is anomalous in that it does not show any Ti anomaly ($Ti/Ti^* = 1.4$). Samples 10-18-11-9D, 10-18-11-9E AND 10-20-11-1B all display positive Sr anomalies, whereas 10-19-11-4B has a negative.

When compared to the samples taken from the Xonamanca Formation (grey field of Figure 9.10) the same trends of Th enrichment and Nb, Ta and Ti negative anomalies are observed. The Xonamanca Formation tuffs are again more enriched

Chapter 9: Geochemistry and Hf-Nd isotope results

than the Teotitlán Migmatitic Complex granitoids and there is a contrast between the negative Sr anomalies of the Xonamanca extrusive rocks and the positive Sr anomalies of the Teotitlán Migmatitic Complex granitoids (excluding 10-18-11-4B).

In the incompatible element ratio diagrams of La/Sm-Gd/Yb, Zr/Y-Nb/Th, Nb/Y-Zr/Y and Zr/Ti-Nb/Y (Figure 9.11 A-D) similarities are again observed between the Teotitlán Migmatitic Complex granitoids and Xonamanca Formation tuffs, with a high degree of overlap recorded between them in each of the plots. One tuff from the Xonamanca Formation appears to be anomalous, displaying slightly different trace element ratios. This may relate to contamination from lithic fragments found in the tuffs (Petrography of Chapter 7).

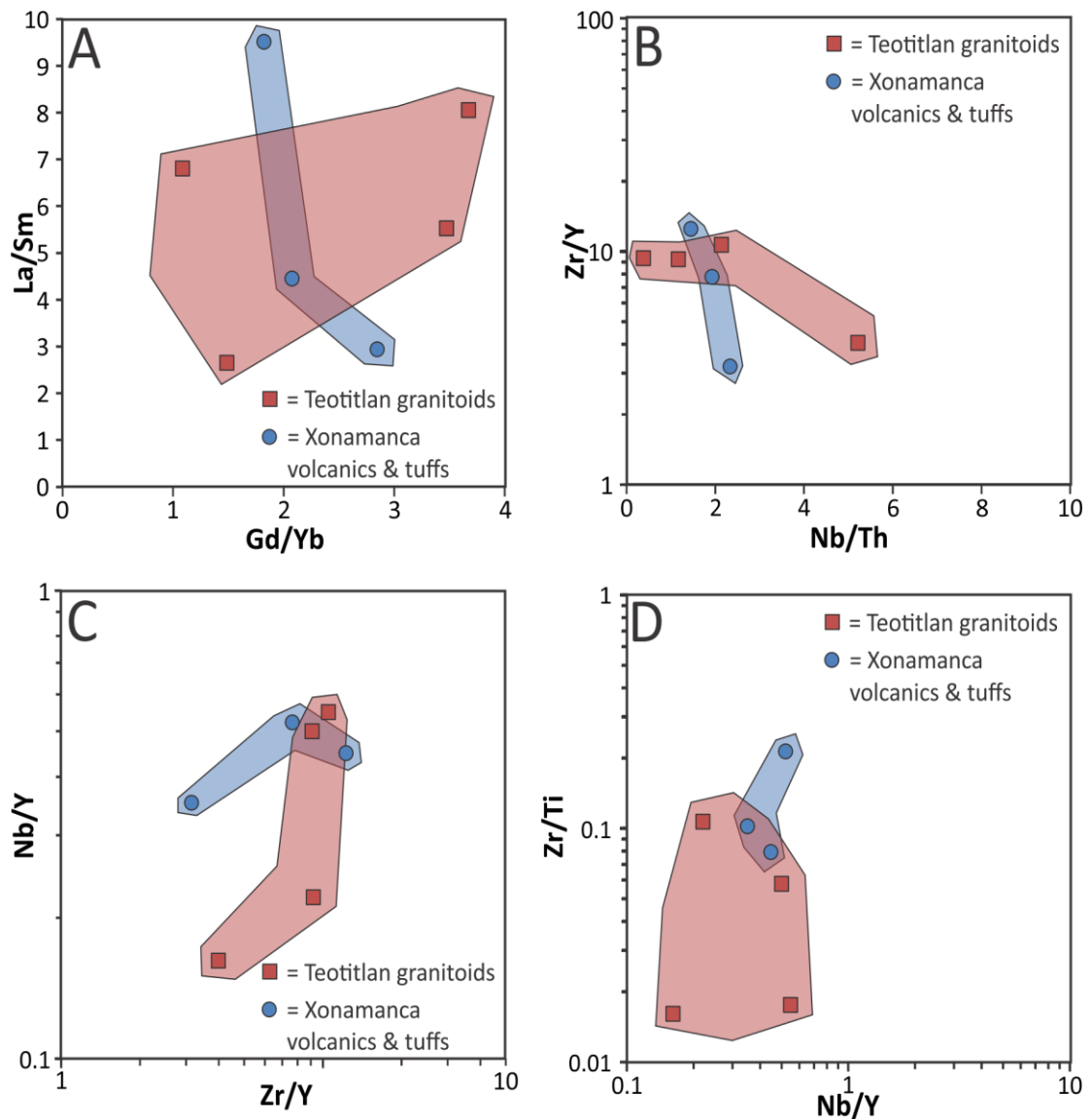


Figure 9.11. La/Sm-Gd/Yb (A), Zr/Y-Nb/Th (B), Nb/Y-Zr/Y (C) and Zr/Y-Nb/Th (D) diagrams for the igneous rocks of the Teotitlán Migmatitic Complex and Xonamanca Formation.

9.6 Chivillas Formation

9.6.1 Element Mobility & Alteration

Twenty three igneous samples, including pillow basalts, lava flows and dykes were collected and analysed from the Chivillas Formations. The LOI for the basalts taken from the Chivillas Formation range from 2.4-5.7wt.% which indicates that there has been a degree of alteration in the samples caused by subsequent

Chapter 9: Geochemistry and Hf-Nd isotope results

weathering, hydrothermal events or metamorphism. Petrographic studies reveal that the rocks have undergone zeolite-lower greenschist facies metamorphism. To assess how subsequent weathering in the area and the metamorphism has affected the mobility of the elements they have been plotted against the immobile element Zr (Figures 9.12 & 9.13).

The igneous samples collected from the Chivillas Formation have been split into 3 groups: 1) enriched, 2) depleted and 3) transitional in accordance to their concentrations of the HFSEs Nb and Ta. Correlations observed in the mobility plots between the groups suggest they formed in the same (or very similar) source region. Elements that display good correlations with Zr (R^2 value >0.75) include La, Ce, Pr, Nd, Sm, Eu and Hf. Moderate correlations ($R^2 < 0.75 > 0.5$) are observed in P_2O_5 , Tb, Dy, Ho, Er, Tm, Yb, Lu, Th and Y. Poor correlations are observed in the remainder of the major elements, large ion lithophile elements (LILEs), Nb, Ta, Sr and Pb. These results indicate that the major elements in the Chivillas Formation igneous rocks may have been mobilised to some degree. However, it should be noted that other factors such as the major elements being compatible and the small degree of compositional variation between samples may also be responsible for the low R^2 values. The most immobile elements based on the R^2 values appear to be LREEs.

The poor correlation observed for Nb and Ta is surprising as the HFSEs are usually considered some of the most immobile elements. Upon closer inspection the poor R^2 values for these elements are mainly due to specific geochemical differences between the groups and are more likely to be a reflection of a heterogeneous source as opposed to sub-solidus element mobility.

Chapter 9: Geochemistry and Hf-Nd isotope results

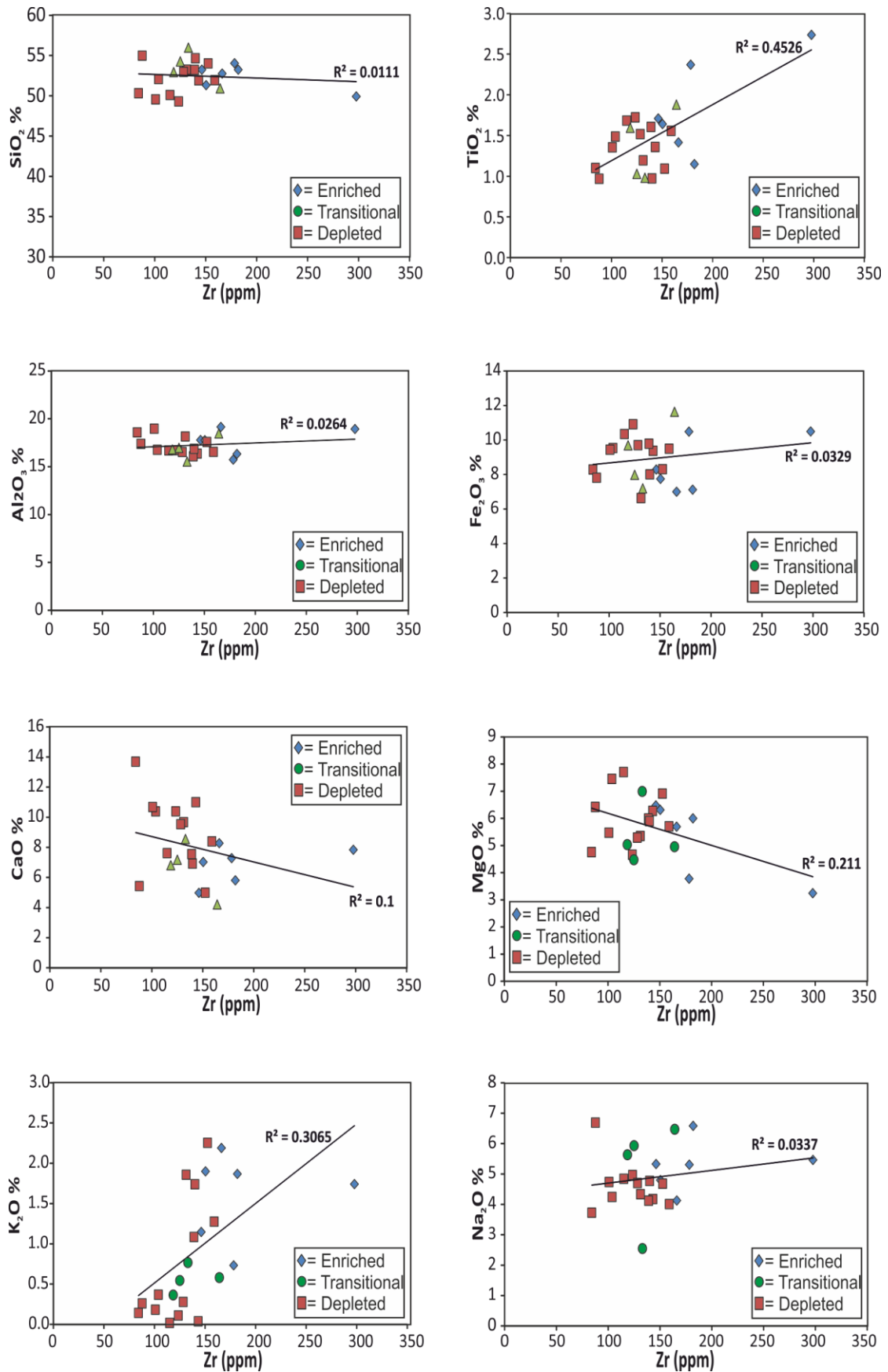


Figure 9.12. Plot showing major elements (anhydrous) vs. Zirconium for samples from the Chivillas Formation.

Chapter 9: Geochemistry and Hf-Nd isotope results

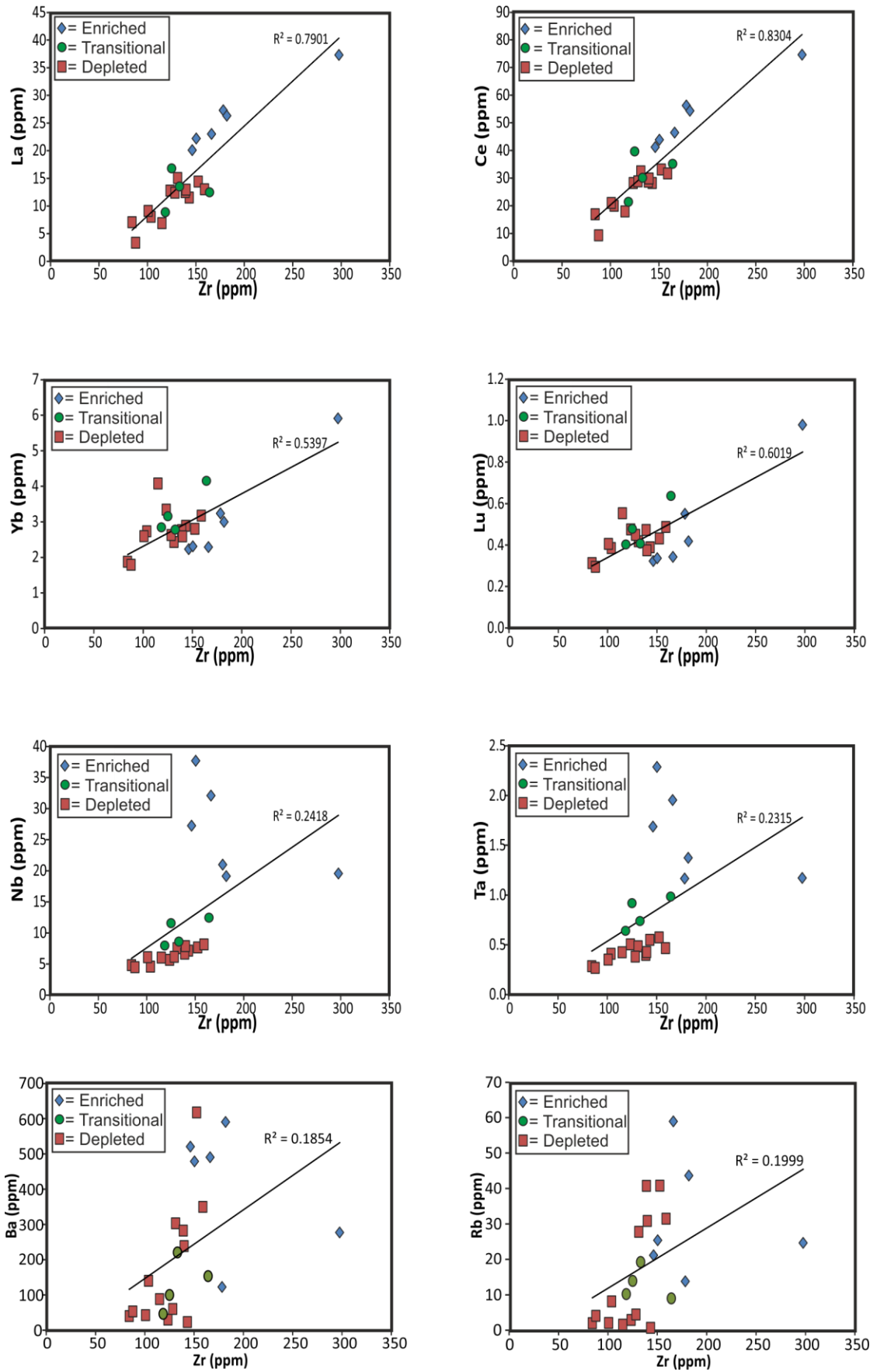


Figure 9.13. Plot showing a representative group of trace elements vs. Zirconium for basaltic samples taken from the Chivillas Formation.

9.6.2 Classification

Samples from the Chivillas Formation in the TAS diagram (Figure 9.14) fall either side of the alkaline-sub alkaline dividing line (Irvine & Baragar, 1971) in the basaltic, basaltic andesite, trachy-basalt and basaltic trachy-andesite fields. The enriched group appears to have a more alkali nature than the depleted group. However, as previously noted the alkalis and silica may have been mobilised by secondary alteration and so the samples have also been plotted on the more robust Zr/TiO₂-Nb/Y plot. This diagram is likely to give a better indication of the original composition of the extrusive rocks.

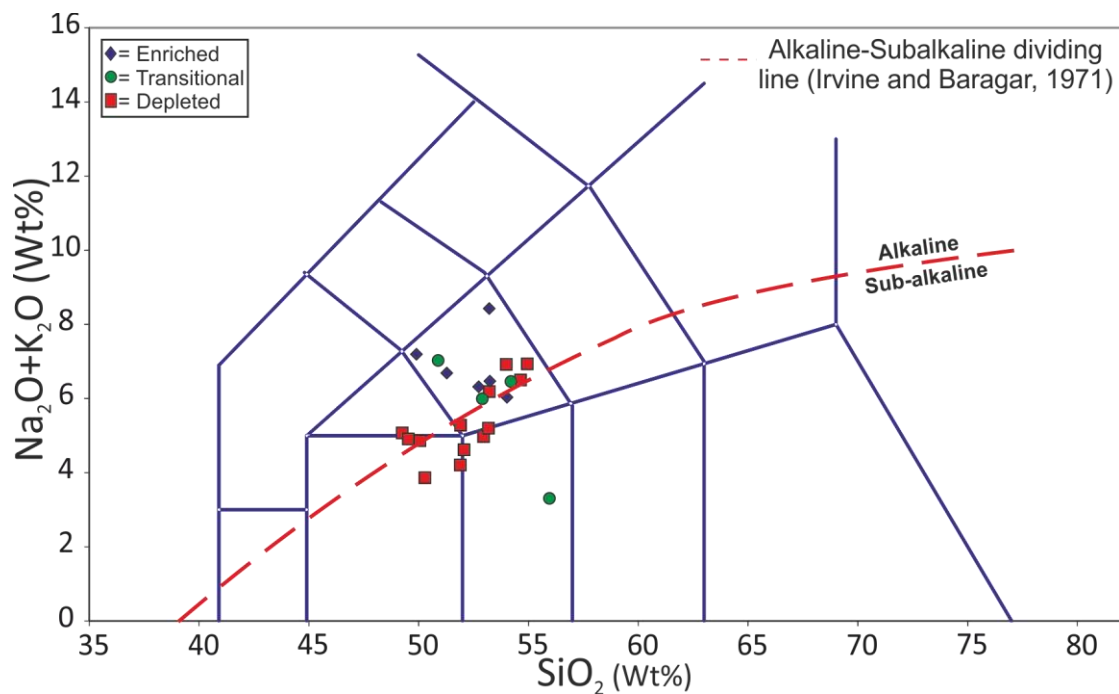


Figure 9.14. Total alkali-silica (TAS) classification plot (Le Maitre et al., 1989) for igneous rocks collected from the Chivillas Formation. Fields are the same as in Figure 9.2.

On the Zr/TiO₂-Nb/Y diagram (Figure 9.15) the depleted group plot well inside the basaltic field and form an oblique trend towards the andesitic field boundary. The enriched group are more variable, with three samples plotting in the

alkali basalt field and three in the basaltic field. This suggests that the alkali nature of the rocks suggested by the TAS diagram is mostly, but not entirely, an artefact of major element mobility.

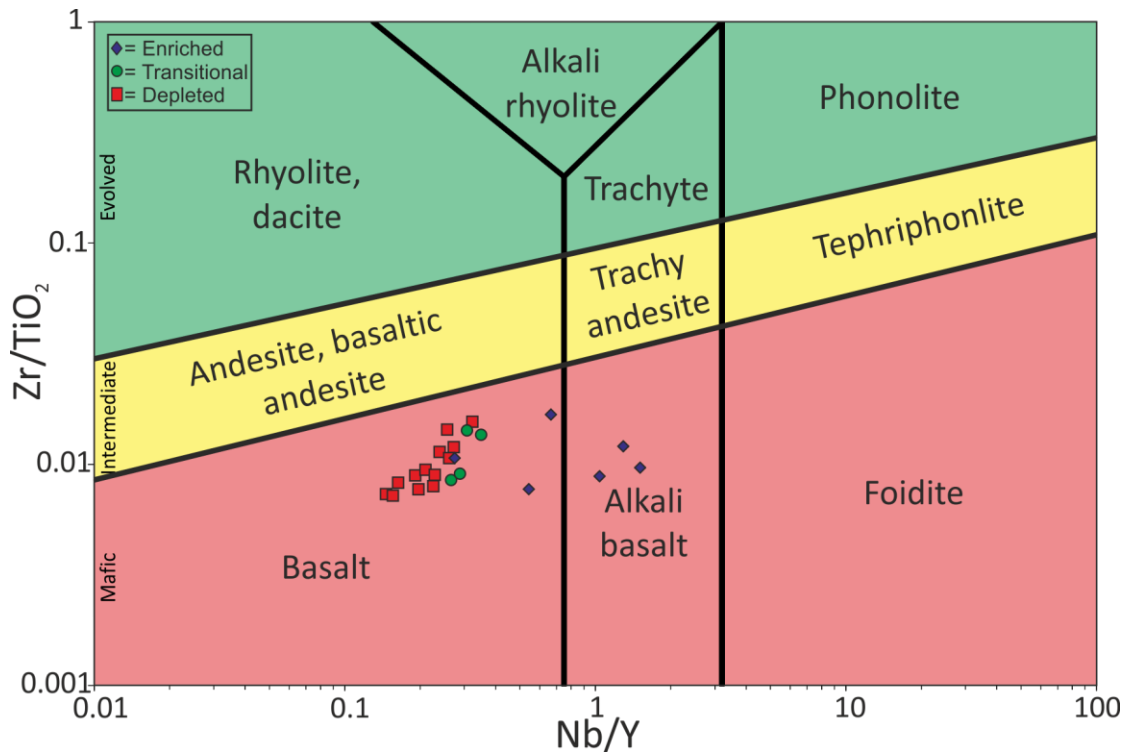


Figure 9.15. Zr/TiO₂ vs Nb/Y (Pearce, 1996 after Winchester & Floyd, 1977) classification plot for igneous rocks from the Chivillas Formation.

In the Th-Co diagram (Figure 9.16) the Chivillas Formation samples mostly plot in the basaltic andesite and andesite field, associated with the calc-alkaline magma series. There is little to distinguish between the groups but there does appear to be a slight trend in the depleted group between the calc-alkaline basaltic andesite and andesite and island arc tholeiite basalt fields. Two samples of the transitional group also plot outside of the calc-alkaline basaltic andesite field, with one in the calc-alkaline basalt field and the other in the island arc tholeiite basaltic andesite & andesite field.

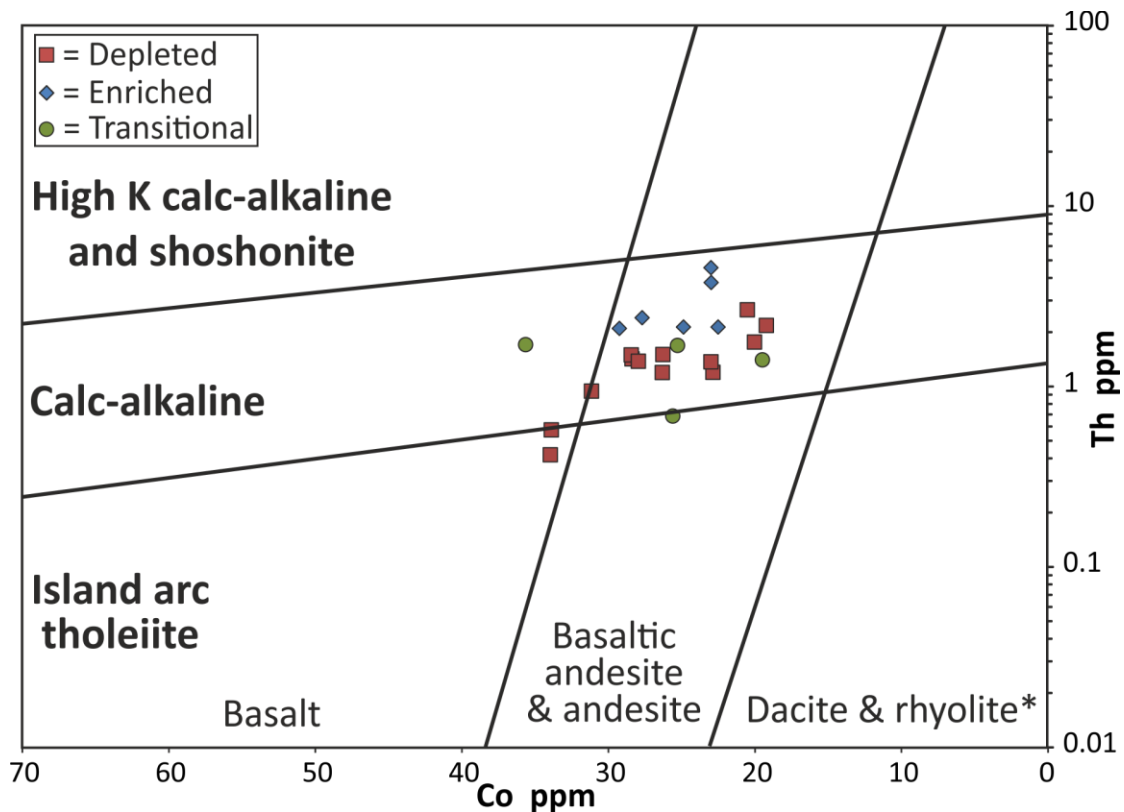


Figure 9.16. Th-Co classification diagram (Hastie et al., 2007) classification plot for igneous rocks from the Chivillas Formation.

9.6.3 Major element variation

The SiO_2 concentrations for the enriched group of the Chivillas Formation range from 48.5-52.4 wt.%. TiO_2 , Fe_2O_3 and MgO ranges from 1.1 to 2.65, 7.4 to 10.2 and 3.2 to 6.2 wt.% respectively which relate to a Mg# of 26 to 48. The total alkalis range from 5.9 to 7.9 wt.% (Na_2O = 4 to 6.2 wt.%; K_2O = 0.7 to 2.1 wt.%). In the transitional group SiO_2 ranges from 47.1 to 53.8 wt.%. TiO_2 , Fe_2O_3 and MgO range from 0.9 to 1.8, 6.9 to 11.2 and 4.0 to 6.7 wt.% respectively which relate to an Mg# of 32 to 52. The total alkalis of the transitional group range from 3.2 to 6.8 wt.% (Na_2O = 2.4 to 6.2 wt.%; K_2O = 0.3 to 0.7 wt.%). SiO_2 in the depleted group ranges from 44.1 to 53.7 wt.%. TiO_2 , Fe_2O_3 and MgO range between 0.9 to 1.6, 6.3 to 9.8 and 4.2 to 7.3 respectively which relate to a Mg# of 38-48. The total alkalis of the

Chapter 9: Geochemistry and Hf-Nd isotope results

depleted group range from 3.7-6.8 wt.% (Na_2O = 3.5-6.5 wt.%; K_2O = 0.0-2.2 wt.%). R^2 values in bivariate plots (Figure 9.17) for the major elements display poor correlations between the groups of the Chivillas Formation which likely relates to major element mobility, low major element variation or major element compatibility as mentioned in Section 9.6.1. Weak negative correlations are observed in the TiO_2 and P_2O_5 plots, with little to no correlation present in Al_2O_3 , Fe_2O_3 , CaO , Na_2O and K_2O . Interestingly a weak positive correlation is observed between SiO_2 and MgO , however, the validity of this correlation is questionable due to the low R^2 value (0.13) and apparent element mobility.

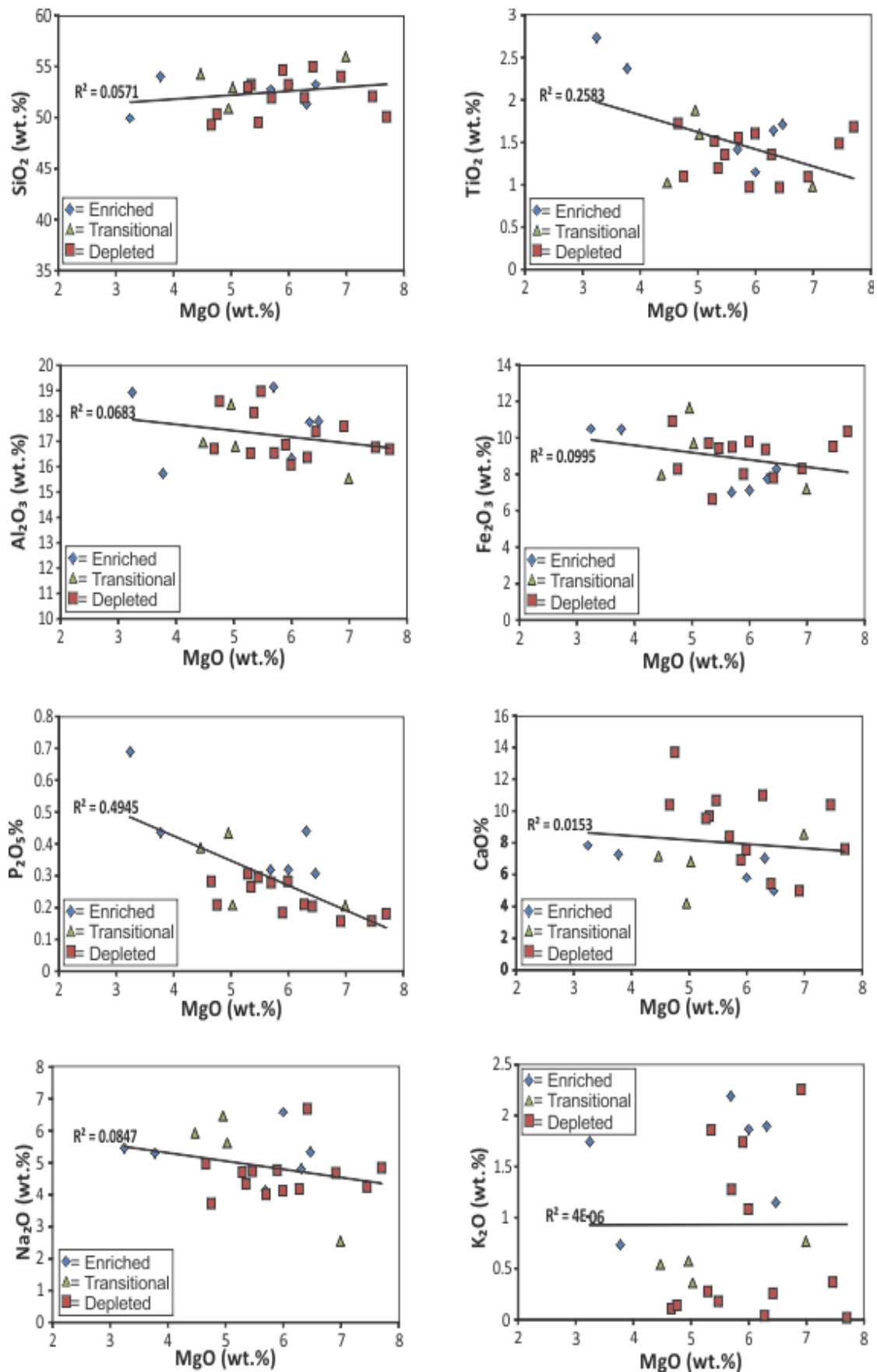


Figure 9.17. Bivariate diagrams of major elements (anhydrous) vs. MgO for basaltic samples taken from the Chivillas Formation.

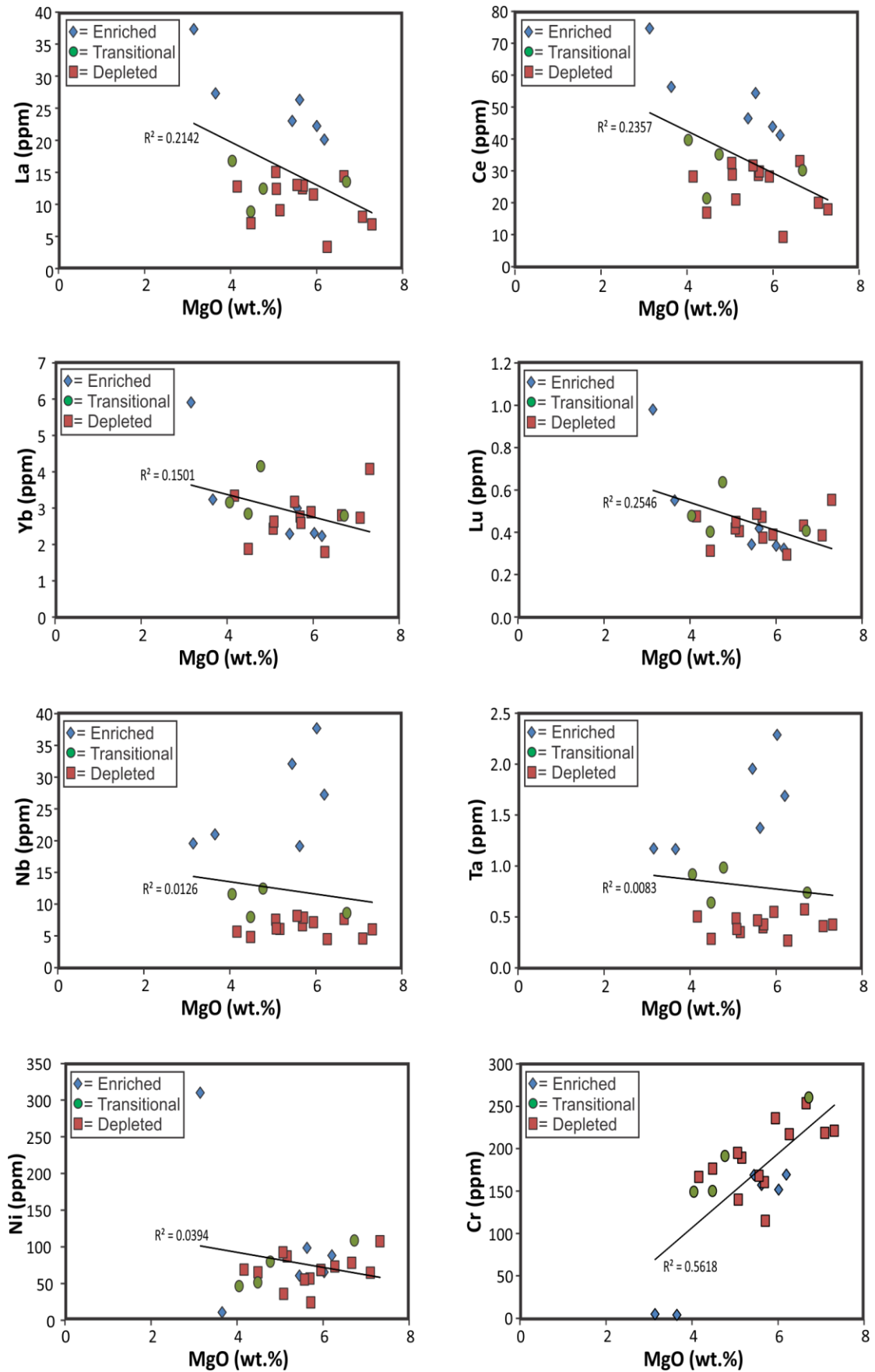


Figure 9.18. Bivariate diagrams of trace elements vs. MgO for basaltic samples taken from the Chivillas Formation.

9.6.4 Trace element variation

The incompatible trace elements display a weak negative correlation with MgO ($R^2 = 0.15-0.25$; Figure 9.18). The greatest amount of variation between the groups is observed in Nb and Ta however it does not appear to have any relation to MgO concentrations ($R^2 = 0.01$ for both plots; Figure 9.18). A moderate positive correlation is observed between MgO and the compatible element Cr which likely relates to a fractional crystallisation trend of mafic minerals.

Chondrite normalised rare earth element plots for the igneous rocks collected from the Chivillas Formation are shown in Figure 9.19. The depleted group have REE patterns (Figure 9.19 A) that are enriched when compared to chondritic values (mean $\times 26$ chondrite). The samples also show a slight enrichment in the LREEs relative to the MREEs ($La/Sm_{CN} = 1.2-2.2$; mean = 1.6). There is one anomalous sample (10-21-11-4A) which does not display this LREE enrichment ($La/Sm_{CN} = 0.77$) indicating that it may have undergone a slightly different evolutionary history than the other depleted samples. The HREE patterns are all relatively flat ($Gd/Yb_{CN} = 1-1.5$; mean = 1.3).

The transitional group of samples (Figure 9.19 B) from the Chivillas basin also show REE patterns that are enriched when compared to chondritic values (mean across values = $\times 31$ chondrite). This enrichment is slightly higher than that observed in the depleted igneous group. Again the LREEs show slight enrichment relative to the MREEs ($La/Sm_{CN} = 1.2-2.1$; mean = 1.7) and the HREE patterns are flat ($Gd/Yb_{CN} = 1.2-1.4$; mean = 1.3). This suggests that the transitional and depleted HFSE samples

Chapter 9: Geochemistry and Hf-Nd isotope results

share a similar evolutionary history but that the transitional samples are slightly more enriched.

The group that is most enriched in the HFSEs (Figure 9.19 C) also displays the greatest amount of REE enrichment relative to chondritic values (mean across samples = $\times 42$ chondrite). Samples of the enriched group also yield the greatest amount of fractionation in the LREE with La/Sm_{CN} ranging between 2.4-3.2 and a mean of 2.8. The enriched group also has a slightly more pronounced HREE slope ($\text{Gd/Yb}_{\text{CN}} = 1.4-1.6$; mean = 1.5) than the depleted and transitional groups.

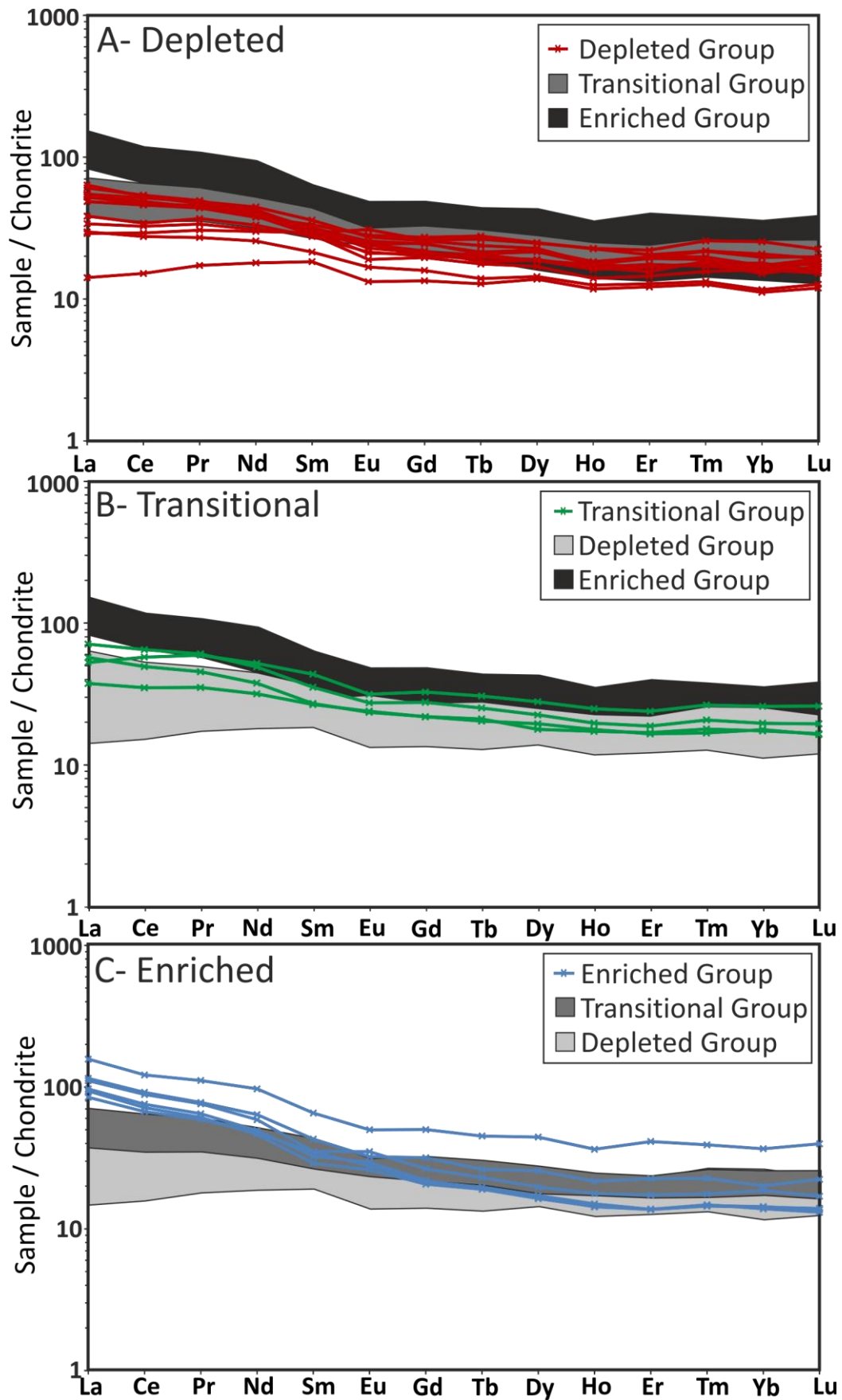


Figure 9.19. Chondrite normalised rare earth element plots for the analysed igneous rocks from the Chivillas Formation.

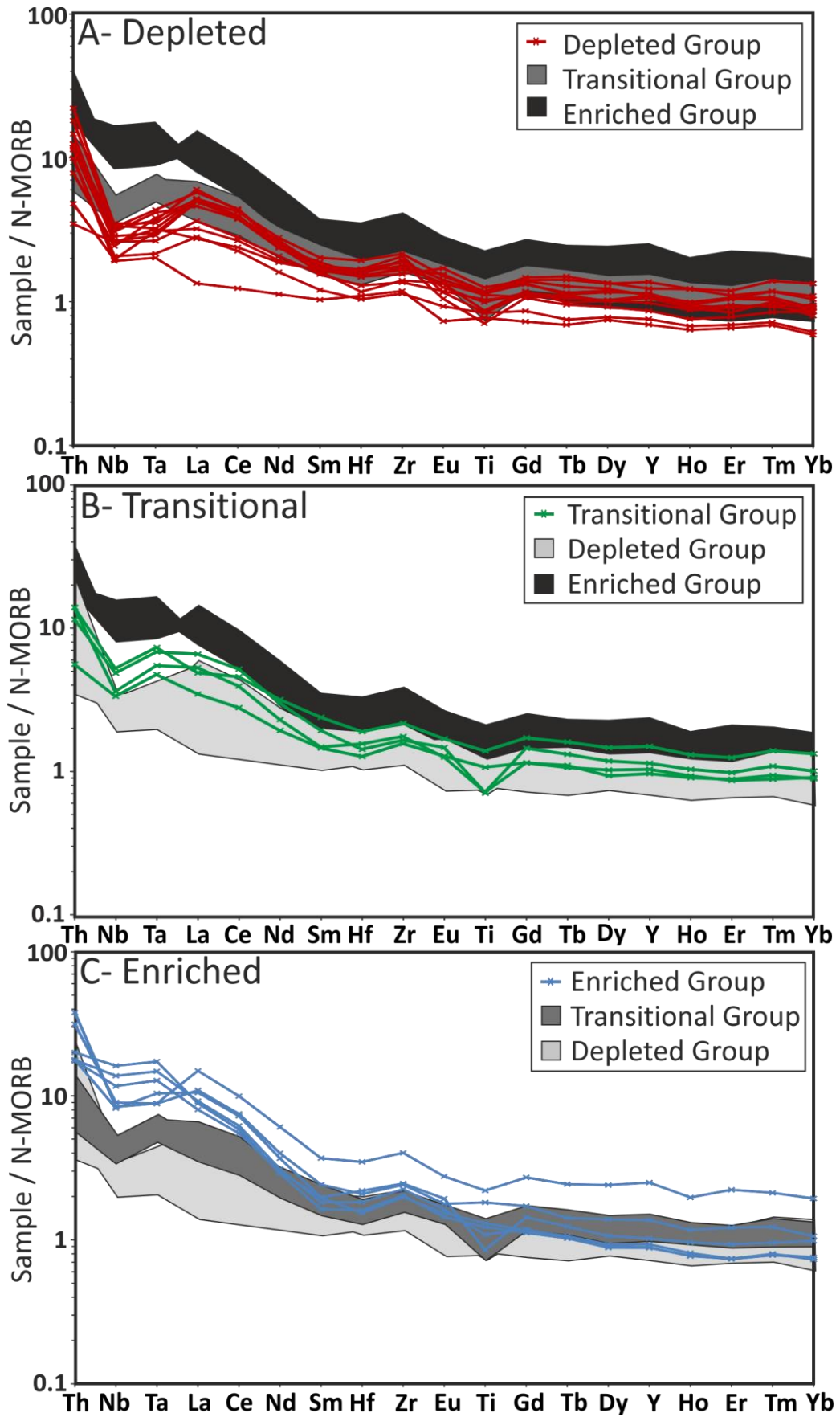


Figure 9.20. N-MORB normalised multi-element plots for the analysed igneous rocks collected from the Chivillas basin.

Chapter 9: Geochemistry and Hf-Nd isotope results

Like the chondrite normalised plots the N-MORB normalised multi element plots (Figure 9.20) for the igneous rocks from the Chivillas Formation display a range of patterns. The depleted group (Figure 9.20 A) display multi-element patterns that are slightly more enriched than N-MORB values (mean= x 2). The samples are variably enriched in the more incompatible elements, most notably Th. Pronounced negative anomalies are observed for Nb ($Nb/Nb^* = 0.25-0.49$, mean= 0.35), Ta ($Ta/Ta^* = 0.24-0.59$, mean= 0.42) and Ti ($Ti/Ti^* = 0.53-0.88$, mean= 0.72). There is one anomalous sample (7-APR-14-2) with a slightly positive Ta anomaly ($Ta/Ta^* = 1.03$) and a noticeably less pronounced Nb anomaly ($Nb/Nb^* = 0.83$). The negative Ti anomaly for this sample is not very distinct but comparable to the rest of the samples ($Ti/Ti^* = 0.82$).

The transitional group (Figure 9.20 B) has slightly more enriched N-MORB-normalised values than the depleted samples (mean= x 3 N-MORB). Again the most incompatible elements are more enriched than the least incompatible ones, as would be expected. The Nb and Ta negative anomalies, although still prevalent, are less pronounced ($Nb/Nb^* = 0.38-0.74$; mean= 0.55; $Ta/Ta^* = 0.57-1.05$, mean= 0.79). The magnitude of the Ti negative anomaly is comparable to the depleted group ($Ti/Ti^* = 0.42-0.82$, mean= 0.62).

The enriched group (Figure 9.20 C) displays the greatest degree of enrichment in the multi-element plots (mean= x 5 N-MORB), most notably in the more incompatible elements. Although the concentrations of Nb and Ta are significantly higher in these samples they still yield a, albeit less pronounced, negative anomaly ($Nb/Nb^* = 0.32-1.1$, mean= 0.73; $Ta/Ta^* = 0.34-1.2$, mean= 0.75).

Chapter 9: Geochemistry and Hf-Nd isotope results

Values for Ti are comparable to the transitional and depleted groups, with slightly negative anomalies ($Ti/Ti^* = 0.5-0.89$, mean = 0.75).

Overall, the main differences observed in the multi-element plots between the igneous groups of the Chivillas Formation are the low concentrations and pronounced negative anomalies of Nb and Ta in the depleted group compared to high concentrations and variable anomalies of Nb and Ta in the enriched group

In the La/Sm-Gd/Yb diagram (Figure 9.21 A) the depleted and transitional groups display comparable results (La/Sm = 1.2-3.5 & 1.9-3.4 respectively; Gd/Yb = 1.3-1.9 & 1.5-1.7 respectively). The enriched group are distinguished from the depleted and transitional groups by having higher La/Sm ratios (3.8-5.2). The Gd/Yb ratios of the enriched group (1.7-2.0) are at the upper limit but comparable to the transitional and depleted groups.

The depleted group in the Zr/Y-Nb/Th diagram (Figure 9.21 B) have Zr/Y ratios of 3-5.8 and Nb/Th ratios that are consistent for the majority of the samples (3-8). One anomalous sample (7-APR-14-2) of the depleted group has a Nb/Th ratio of 14.4. This anomaly (also highlighted in the multi-element plots) may be caused by the mobility of Th during subsequent alteration. The enriched group for the most part have higher Nb/Th ratios (9-15.7) than the depleted group (ignoring the anomalous sample); there are two examples however that display comparable results to the depleted group (4.3 & 5.6). The Zr/Y ratio of the enriched group displays comparable results to the depleted group (4.2-6.7). The transitional group yields intermediate results with Zr/Y ratios of 3.8-4.8 and Nb/Th ratios of 7.3-11.6.

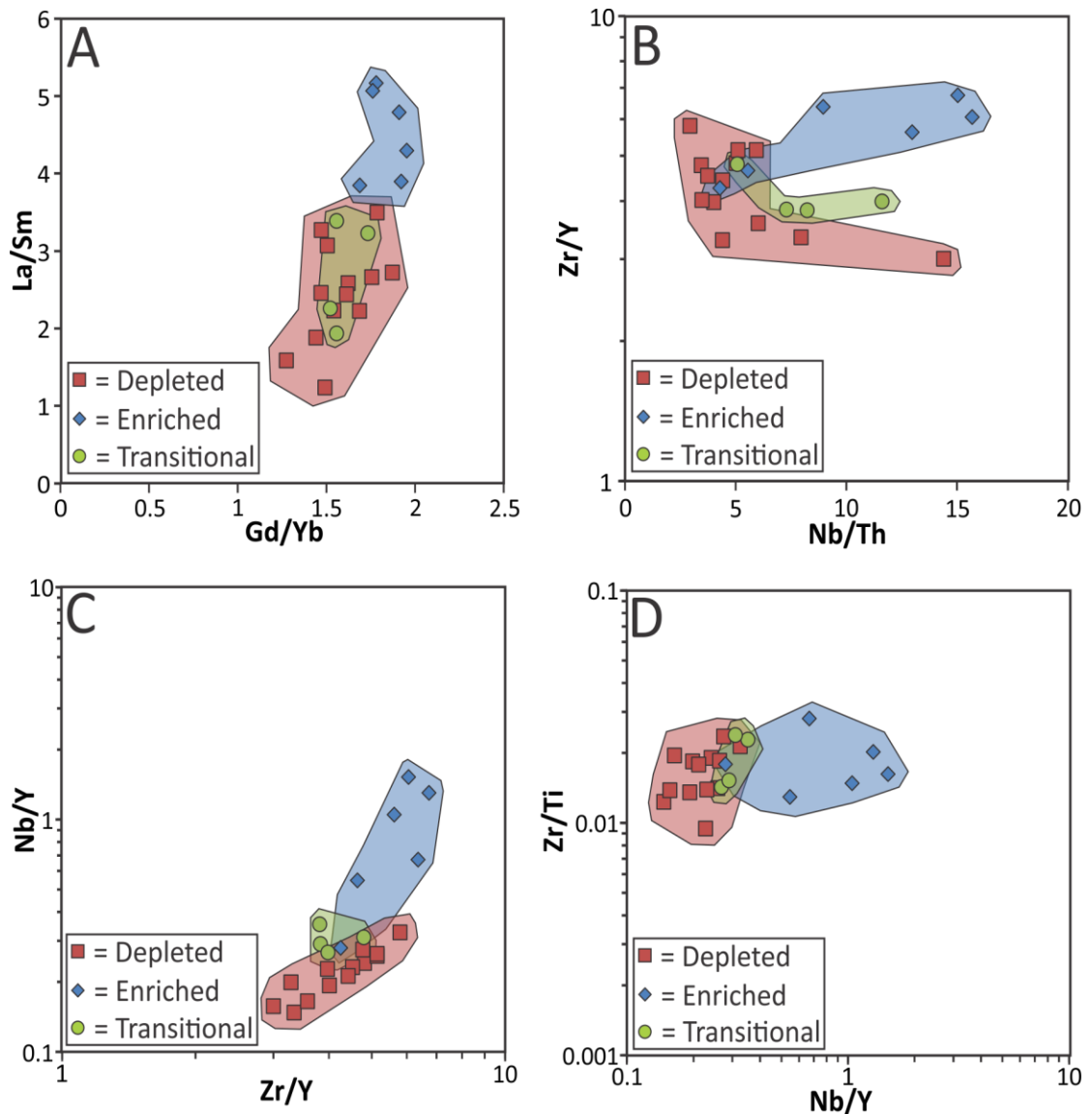


Figure 9.21. La/Sm-Gd/Yb (A), Zr/Y-Nb/Th (B), Nb/Y-Zr/Y (C) and Zr/Y-Nb/Th (D) diagrams for the igneous rocks of the Chivillas Formation.

In the Nb/Y-Zr/Y diagram (Figure 9.21 C) the enriched group are clearly identified by their elevated Nb/Y ratios (0.28-1.52). There is some minor overlap between the enriched and depleted groups but for the most part the depleted group has lower Nb/Y ratios (0.15-0.33). The enriched group also has slightly higher Zr/Y ratios (4.3-6.7) than the depleted group (3-5.8). The field for the transitional group lies between the depleted and enriched groups, with Nb/Y ratios of 0.27-0.35 and Zr/Y ratios of 3.8-4.8.

The enriched group in the Zr/Ti-Nb/Y diagram (Figure 9.21 D) again can be distinguished from the depleted group by their elevated Nb/Y ratios. The Zr/Ti ratio between the groups is actually quite consistent (depleted group= 0.009-0.021; transitional group= 0.14-0.024; enriched group= 0.013-0.028).

9.6.5 Nd & Hf isotopes

Six samples from both the enriched and depleted groups of the Chivillas Formation were selected for Lu-Hf and Sm-Nd isotopic analysis. Sample preparation was carried out at the Centro de Investigacion Cientifica y de Educacion Superior de Ensenada (CICESE) in Baja California, Mexico, and analysed by MC-ICP-MS at Universidad Nacional Autónoma de México (UNAM) in Mexico City, Mexico. Detailed analytical descriptions can be found in Appendix A.

The use of isotopic ratios in igneous geochemistry provides a tracer for the composition of the mantle source during magma genesis, as well as an indication of lithospheric contamination. The Hf and Nd isotopic systems have been selected for this study due to their relative insensitivity to alteration through weathering and metamorphism. Other systems such as the Sr and Pb are more susceptible to element mobility. The Hf and Nd isotope ratios for the igneous rocks of the Chivillas Formation have been age corrected to 130 Ma, inferred from the maximum age of deposition (detrital zircons) of the contemporaneous turbidite deposits in the basin (Chapter 8 of this study), to obtain their initial isotopic ratios². To help identify differences in ratios where the variance is low e.g. in $^{143}\text{Nd}/^{144}\text{Nd}$ (due to the long

²Calculating initial ratios using Nd isotopic system as an example:

$$\frac{^{143}\text{Nd}}{^{144}\text{Nd}}(i) = \frac{^{143}\text{Nd}}{^{144}\text{Nd}}(m) - \frac{^{147}\text{Sm}}{^{144}\text{Nd}}(m) \times (e^{\lambda t} - 1)$$

Where i= initial concentration, m= measured concentration, λ = decay constant and t= time

Chapter 9: Geochemistry and Hf-Nd isotope results

half-life of ^{147}Sm ; 1.06×10^{11} years) epsilon (ϵ) values³ have been calculated (Depaolo & Wasserburg, 1976).

As shown on Figure 9.22 A the depleted group from the Chivillas formation have $^{143}\text{Nd}/^{144}\text{Nd}$ (i) values of 0.51257-0.51265 ($\epsilon\text{Nd}= 1.94\text{-}3.43$) and $^{176}\text{Hf}/^{177}\text{Hf}$ (i) values of 0.28278-0.28280 ($\epsilon\text{Hf}= 2.7\text{-}3.7$), whereas the enriched group have $^{143}\text{Nd}/^{144}\text{Nd}$ (i) values of 0.51267-0.51271 ($\epsilon\text{Nd}= 3.90\text{-}4.79$) and $^{176}\text{Hf}/^{177}\text{Hf}$ (i) values of 0.28279-0.28288 ($\epsilon\text{Hf}= 3.28\text{-}6.33$).

Trace element ratios have also been plotted against the isotope ratios to help identify trends between the enriched and depleted groups of the Chivillas Formation (Figure 9.22 B-G). La/Sm when plotted against the isotopic ratios (Figure 9.22 B-C) yields a weak positive correlation between the two groups, with the depleted group having lower La/Sm values (2.2-3.5) than the enriched group (3.8-4.3). Slight negative correlations are observed between the Hf and Nd isotope ratios and La/Nb (Figure 9.22 D-E) and Lu/Hf (Figure 9.22 F-G). Possible end members for the correlations observed in the isotope results will be investigated further in the discussion section of 9.8.6.

³ Calculating epsilon values for Nd example:

$$\epsilon_{Nd}^t = \left(\frac{^{143}\text{Nd}/^{144}\text{Nd} (\text{rock}, t)}{^{143}\text{Nd}/^{144}\text{Nd} (\text{CHUR}, t)} - 1 \right) \times 10^4$$

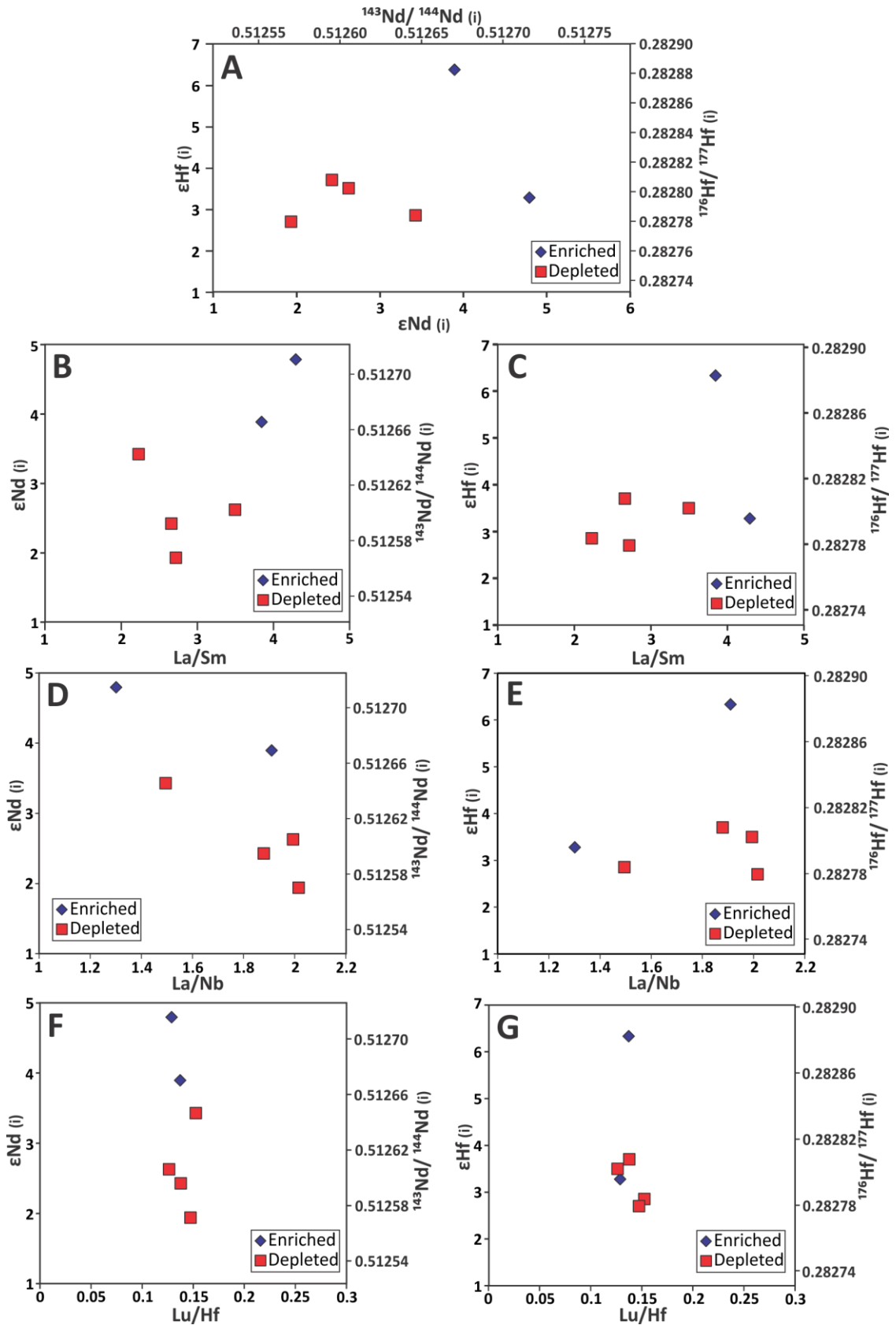


Figure 9.22. Nd and Hf isotope data vs. trace element ratios for the igneous rocks of the Chivillas Formation. All isotopic values have been age corrected to obtain initial values (130 Ma).

9.7 Tectonomagmatic Setting of the Xonamanca Formation & Teotitlán Migmatitic Complex.

Trace element signatures observed in the Xonamanca Formation and Teotitlán Migmatitic Complex (LREE enrichment, negative Nb, Ta and Ti anomalies) are typically, but not exclusively, associated with the magmatism in volcanic arc settings. Similar signatures are seen however in magmas that have been contaminated by continental crust. To help distinguish between subduction and continental crust signatures tectonic discrimination diagrams can be employed. No discrimination plots have been designed specifically for tuffaceous rocks but the diagrams for granitoids (Pearce et al., 1984) can be used for igneous rocks with SiO₂ concentrations of between 56-80 % (Ryan & Williams, 2007). It is therefore appropriate to apply these discrimination diagrams to the tuffs of the Xonamanca Formation where SiO₂ ranges between 67-78%. However, it is important to note that lithic fragments found in the tuffs may affect the results. Four plots from Pearce et al. (1984) have been constructed, which include Nb vs. Y, Ta vs. Yb, Rb vs. Y+Nb and Rb vs. Yb+Ta diagrams (Figures 9.23 & 9.24).

The Xonamanca Formation and Teotitlán Migmatitic Complex samples have been plotted on the same diagrams to enable comparison between the two units. The tuffaceous samples from the Xonamanca Formation display similar results on all of the tectonic discrimination diagrams, with an oblique trend observed between the volcanic arc and within plate granite fields (Figures 9.23 and 9.24). All of the samples from the Teotitlán Migmatitic Complex plot firmly in the volcanic arc field throughout the discrimination diagrams (Figures 9.23 and 9.24).

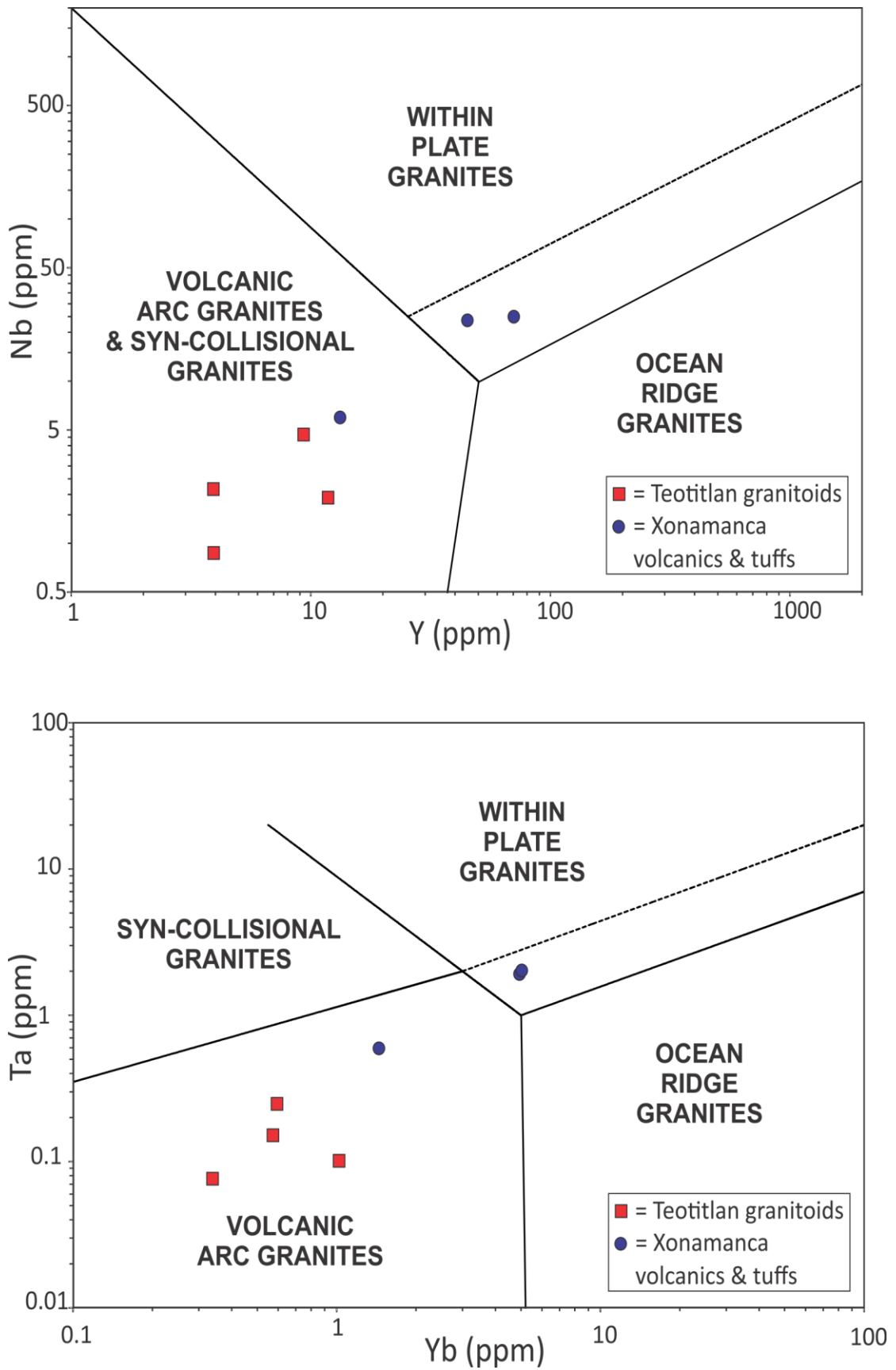


Figure 9.23. Nb vs. Y & Ta vs. Yb discrimination diagrams (Pearce et al., 1984) for samples from the Xonamanca Formation and Teotitlán Migmatitic Complex. Dashed line represents the field boundary for ocean ridge granites at anomalous ridges.

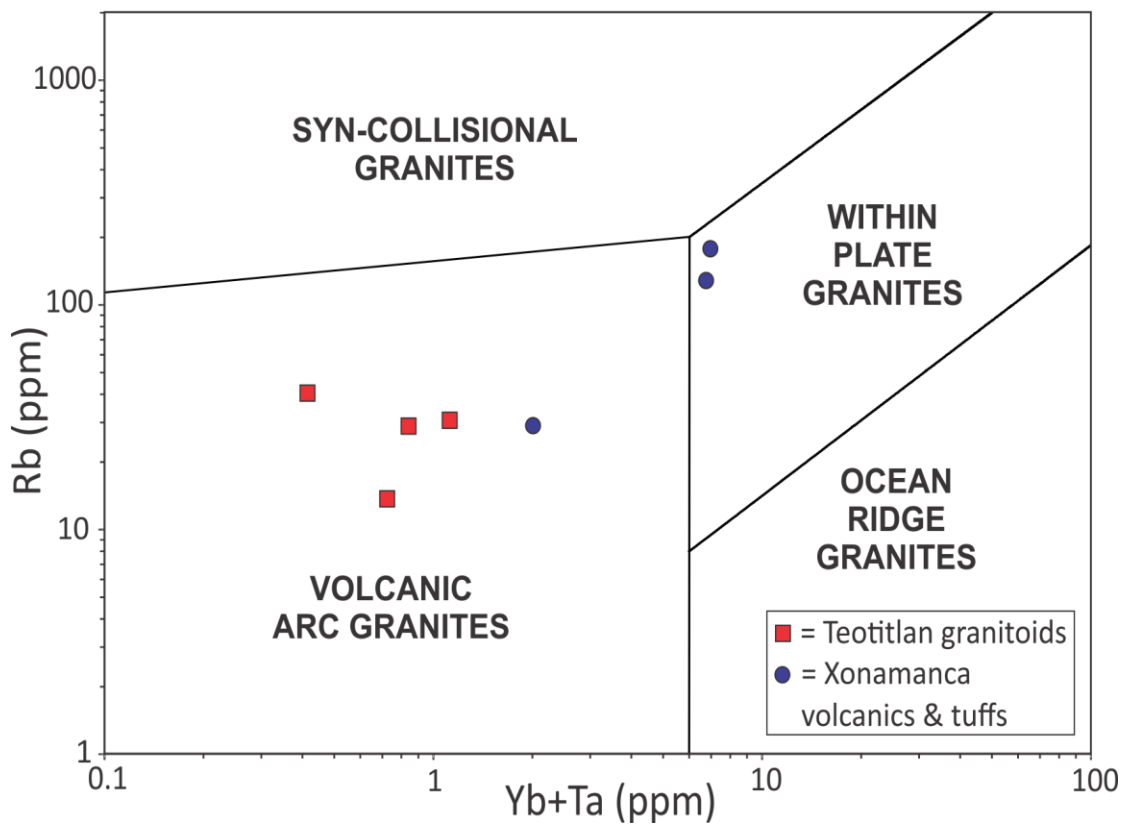
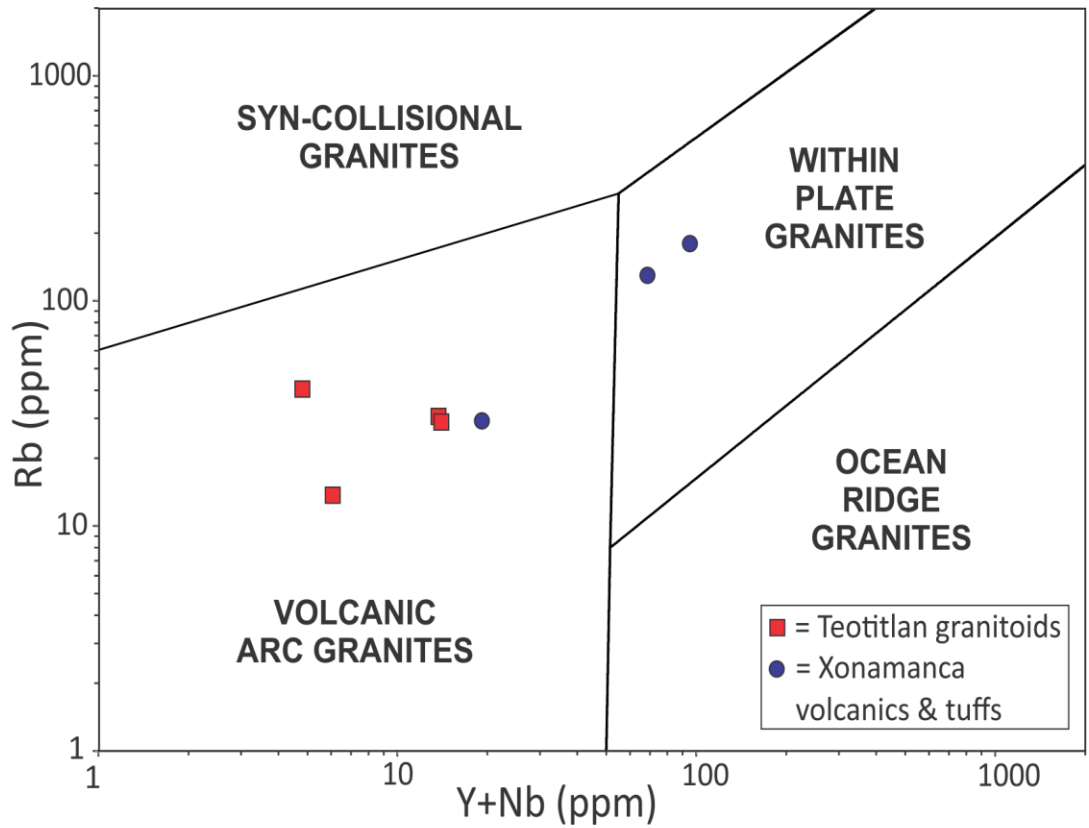


Figure 9.24. Rb vs. Y+Nb & Rb vs. Yb+Ta discrimination diagrams (Pearce et al., 1984) for samples from the Xonamanca Formation and Teotitlán Migmatitic Complex.

These results are consistent with rocks forming in a volcanic arc environment.

The spatial proximity and comparable ages (Chapter 8) between the Xonamanca Formation and Teotitlán Migmatitic Complex suggests that they are likely related to the same volcanic arc. The anomalous samples (12-12-7B and 12-12-7C) of the Xonamanca Formation can be explained by contamination by lithic fragments found in the tuffs which have enriched Rb, Nb, Ta, Y and Yb.

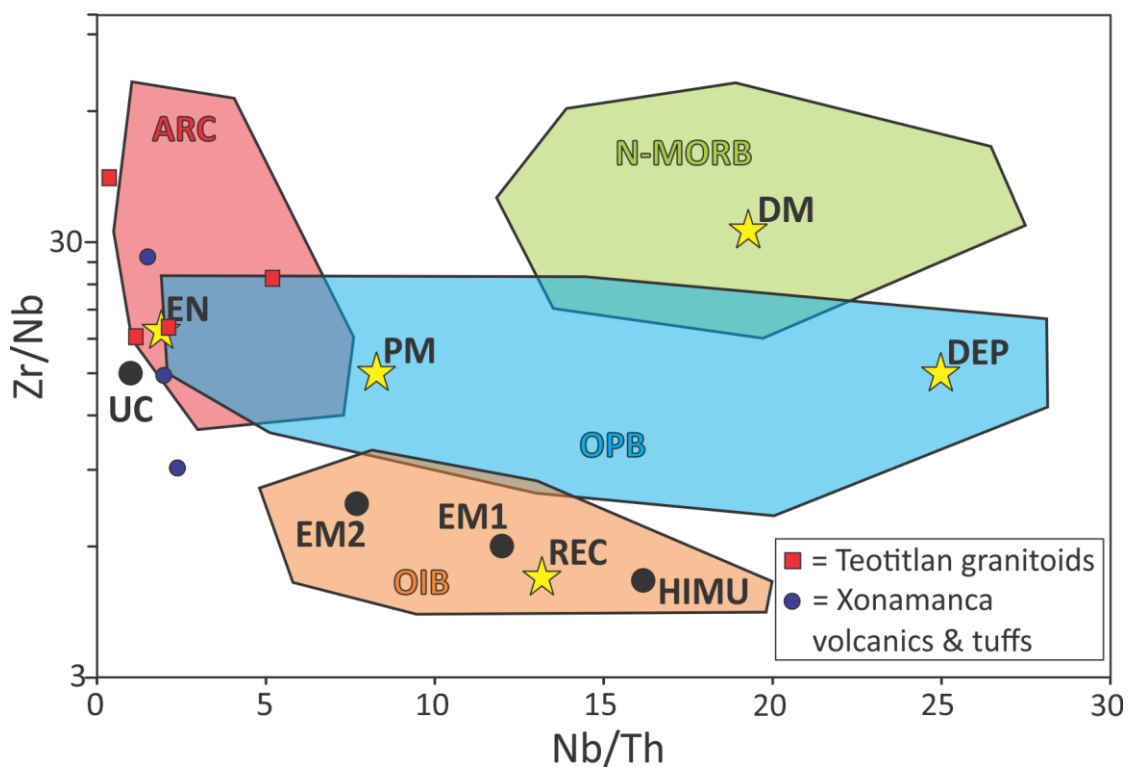


Figure 9.25. Zr/Nb-Nb/Th diagram for the Teotitlán granitoids and Xonamanca volcanics. Field boundaries and end members from Weaver, 1991 and Condie, 2003 & 2005. UC= upper continental crust, PM= primitive mantle, DM= shallow depleted mantle, HIMU= high mu (U/Pb) source, EM1 & EM2= enriched mantle sources, ARC= arc related basalts, N-MORB= normal mid ocean ridge basalts, OPB=ocean plateau basalt, OIB= oceanic island basalt, DEP= deep depleted mantle, EN= enriched component, REC= recycled component.

In the Zr/Nb-Nb/Th (Figure 9.25) plot of Fitton et al., (1997) overlap is observed between the Xonamanca Formation group and Teotitlán Migmatitic Complex group. Both display affinities with an enriched component associated with arc systems (field boundaries from Condie, 2005). The Nb/Y- Zr/Y plot (Figure 9.26)

of Fitton et al., (1997) yields similar comparable results between the two groups, with them both firmly plotting in the non-plume source side of the dividing line, in the arc field boundary (Condie, 2005). There is one anomalous sample from the Xonamanca group of samples which plots within the plume source area, in the oceanic plateau basalt field boundary.

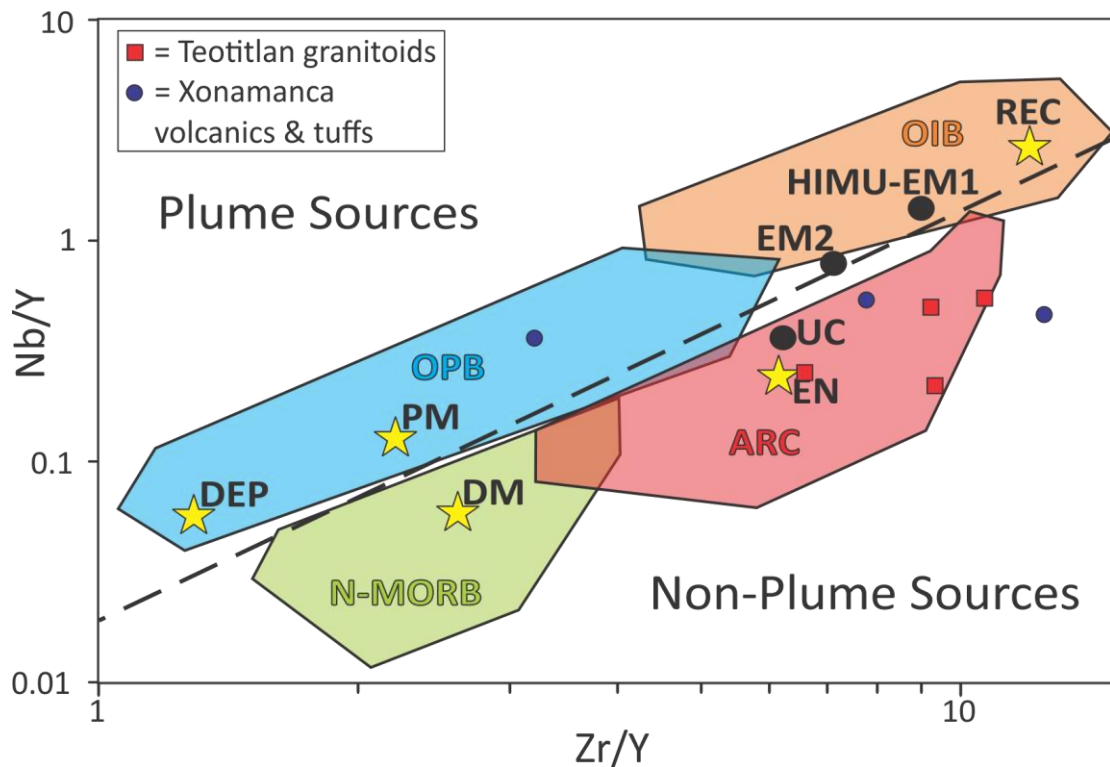


Figure 9.26. Nb/Y-Zr/Y diagram for the Teotitlán granitoids and Xonamanca volcanics. Field boundaries and end members from Condie, 2005. Abbreviations are the same as in Figure 9.25.

All of the in-situ granites from the Teotitlán Migmatitic Complex fall firmly in the volcanic-arc granite field in all the diagrams, showing comparable results to one of the tuffs of the Xonamanca formation. The results from the discrimination diagrams as well as the trace element signatures highlighted earlier (enrichment in the LREEs and negative Nb, Ta & Ti anomalies) indicate that the two units formed as the volcanic and plutonic exposures of an Early Cretaceous continental arc system.

Fractionating plagioclase accumulated in the plutonics of the Teotitlán area (positive Eu and Sr anomalies) and was separated from the Xonamanca tuffs and volcanics (Negative Eu and Sr anomalies) in a magma chamber or as it rose through the continental crust.

9.8 Tectonomagmatic setting of the Chivillas Formation.

The results of the geochemistry from the Chivillas Formation highlight three geochemically distinct groups that formed in an extensional basin (Chapters 6 and 7). Possible causes of the observed geochemical differences between the groups will now be assessed to gain insight into the petrogenesis of the Chivillas Formation.

9.8.1 Degree of partial melting

One possible explanation for the trace element trends observed in the igneous rocks of the Chivillas Formation is the degree of partial melting that occurred in their formation. Different degrees of partial melting may have resulted in the compositional difference between the groups of igneous rocks of the Chivillas basin. Figure 9.27 shows the REE values for the groups of the Chivillas Formation with modelled results for spinel lherzolite from a depleted mantle (DM) source at 1, 5 and 10% partial melting overlain. It can be seen that the enriched group of the Chivillas Formation relates well with the modelled spinel lherzolite (DM) that has undergone 1% partial melting. The transitional group fits more with the 5% partial melt model and the depleted group patterns can be replicated with 5-10% partial melting.

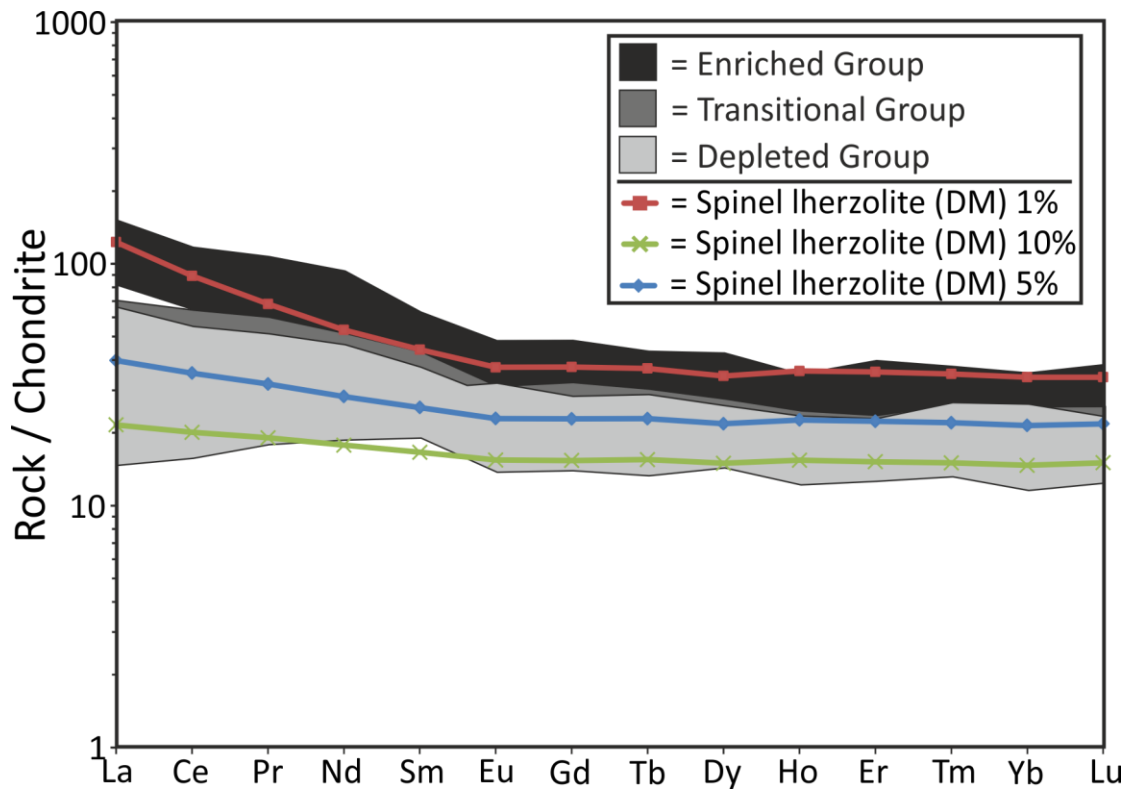


Figure 9.27. Chondrite normalised rare earth element plots for the analysed igneous rocks from the Chivillas Formation with partial melt models overlain.

However, if the degree of partial melting was the only factor influencing the compositional differences between the groups then we would not expect to see the isotopic variance between the depleted and enriched group, as highlighted in Section 9.6.5 (Figure 9.22), because these are not affected by partial melting or fractional crystallisation processes. It also seems unlikely that such a small degree of partial melt, as is needed to produce the enriched group in the model (1%) would get extracted from the mantle. This tells us although the degree of partial melting may contribute to the compositional differences observed in the igneous rocks of the Chivillas Formation, it is unlikely to be the only factor affecting the geochemistry of the rocks.

9.8.2 Fractional Crystallisation trends

Another possible mechanism for the compositional differences in the Chivillas Formation igneous suite is the degree of fractional crystallisation that has occurred in the groups.

The Zr/TiO₂-Nb/Y plot (Figure 9.15) suggests that there may well be some compositional variation caused by fractional crystallisation within the depleted group; evidenced by a compositional trend between the basaltic and andesitic fields on variation diagrams (Figures 9.17 & 9.1). However, there is little evidence for variation caused by fractional crystallisation between the igneous groups, with the majority of the samples having a relatively narrow compositional range in MgO and SiO₂ (~5-7 wt% & 44-53 wt% respectively). There are also no obvious correlations observed in the MgO variation diagrams (Figure 9.17 & 9.18) between the groups, which would indicate fractionation trends. This is especially true for Nb and Ta, which define some of the most important compositional differences between the groups (Figure 9.28).

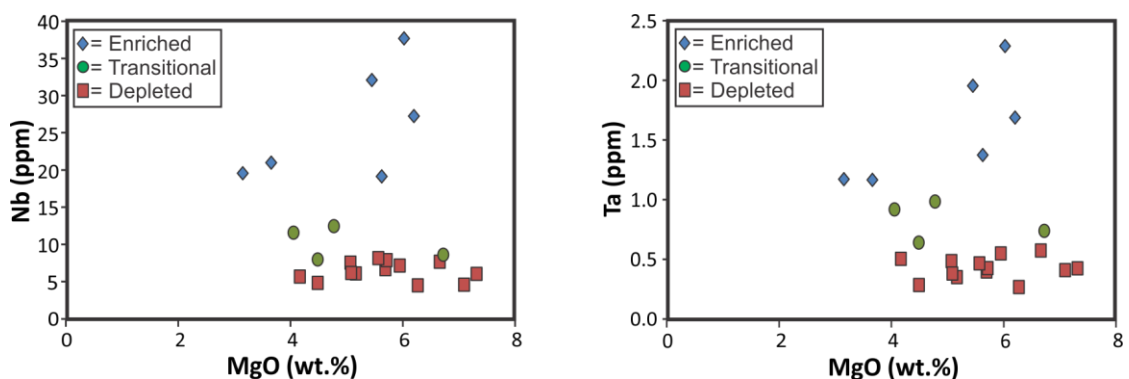


Figure 9.28. Nb & Ta vs. MgO for the igneous rocks of the Chivillas Formation.

We are therefore left to conclude that the composition of the source is likely to be the main driver for the geochemical variance between the enriched and

depleted groups in the Chivillas basin as neither the degree of partial melting or fractional crystallisation can satisfactorily explain the compositional differences.

9.8.3 Composition of source: Subduction fluid vs. continental contamination

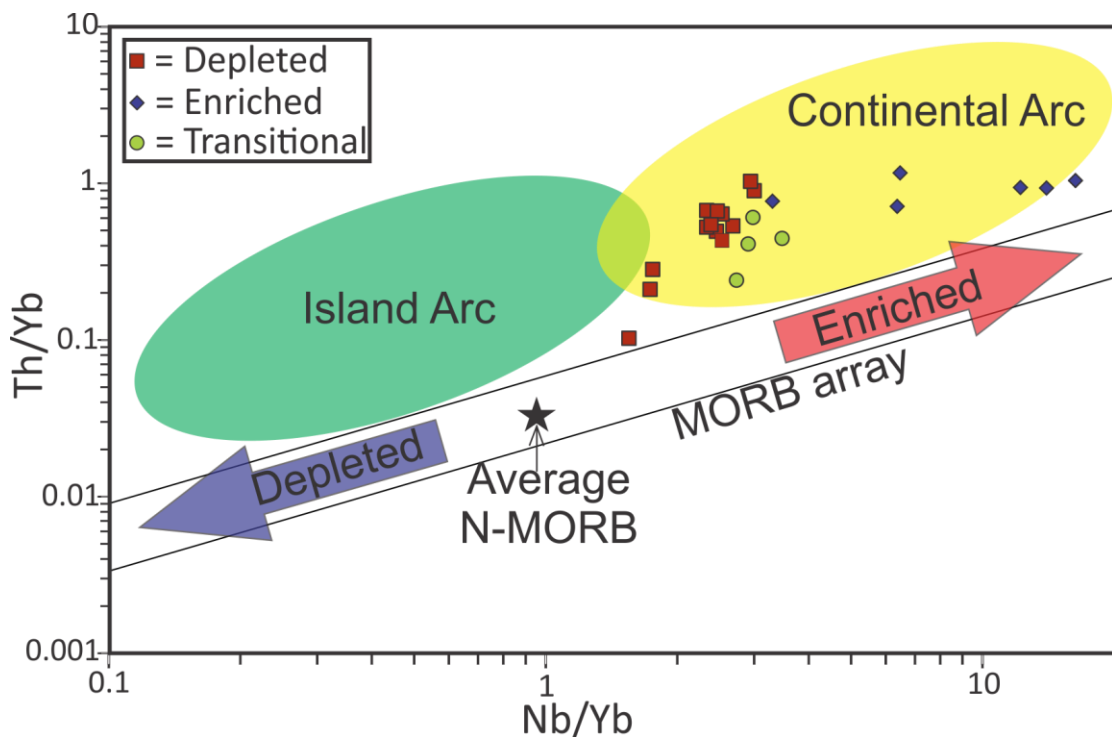


Figure 9.29. Plot of Th/Yb vs. Nb/Yb (Pearce & Peate 1995) for the basaltic samples taken from the Chivillas Formation.

The igneous rocks from the Chivillas basin do not display a N-MORB type signature but are instead enriched in the LREEs relative to the HREEs. The Th/Yb-Nb/Yb diagram from Pearce & Peate (1995) can be used to discriminate arc lavas from MORB and OIB, as well as distinguishing between continental and island arc signatures (Figure 9.29). All of the samples from the Chivillas Formation are displaced above the MORB array suggesting they were formed in a continental arc. However, basalts contaminated by continental crust in environments such as

continental rifts could also yield a similar displacement from the MORB array, giving the appearance of a continental arc signature.

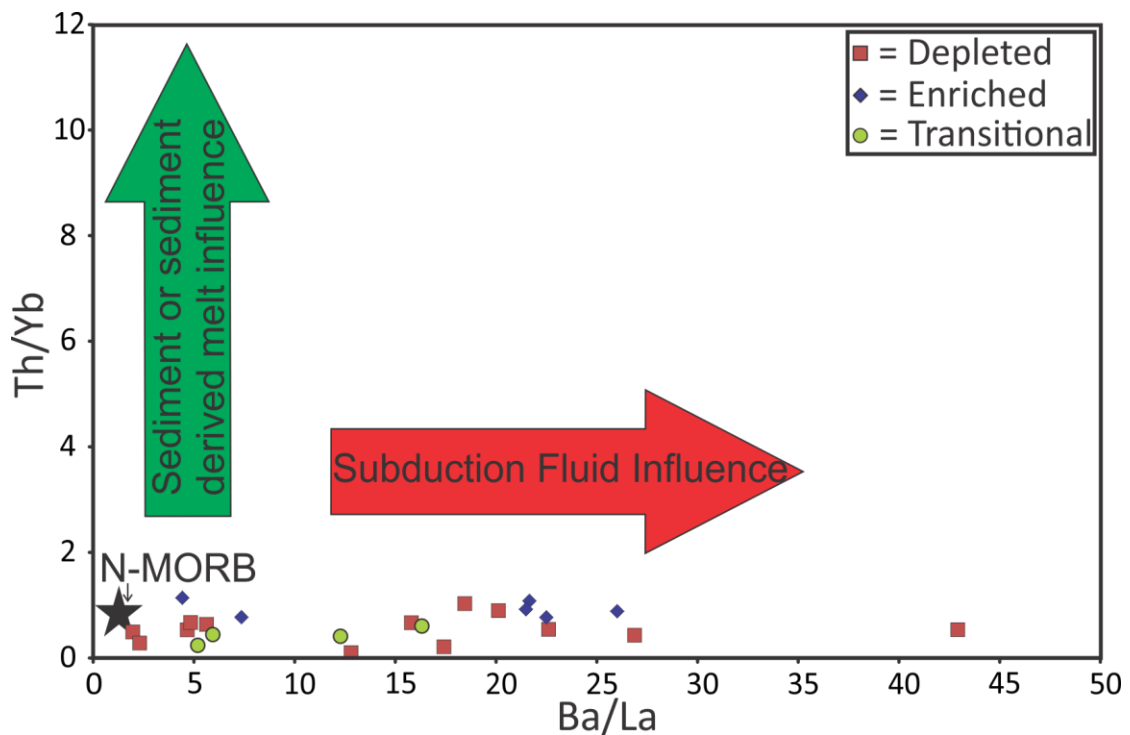


Figure 9.30. Plot of Th/Yb vs. Ba/La (Woodhead et al., 2001) for the volcanic and plutonic samples taken from the Chivillas Formation.

The Th/Yb-Ba/La plot (Woodhead et al., 2001; Figure 9.30) helps distinguish between subduction fluids (Ba/La as a proxy) and input from terrigenous sediments or sediment derived melts (Th/Yb as a proxy). The diagram clearly shows that Th/Yb ratios are low (0.1-1.1) for the Chivillas samples with Ba/La ranging from low to high (2-43). This trend would suggest that the geochemical signatures observed (enrichment in Th and negative Nb, Ta and Ti anomalies) in the igneous rocks of the Chivillas Basin are due to variable influences from subduction derived fluids rather than contamination from continental crust. It has been demonstrated however that Ba has been mobilised (Figure 9.13) therefore the reliability of the Ba/La ratio is questionable. However, the proxy for terrigenous sediment (Th/Yb) is more robust

and less susceptible to element mobility; therefore the low Th/Yb ratios observed has more significance. It indicates that the addition of terrigenous sediments or crustal contamination does not strongly influence the composition of the igneous rocks and an input from subduction fluids appears to be a more likely mechanism.

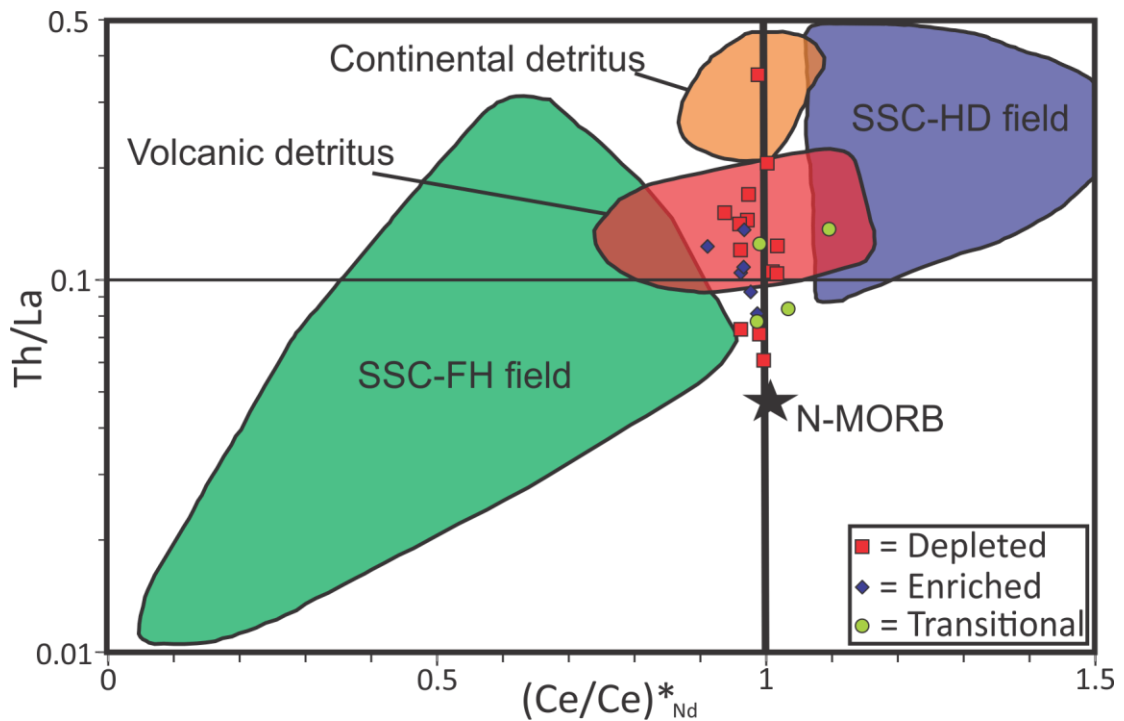


Figure 9.31. Th/La vs. (Ce/Ce)*Nd diagram from Hastie et al., 2013 for the samples from the Chivillas Formation. SSC-FH= slow sediment clay-fish debris/hydrothermal, SSC-HD= slow sediment clay-hydrogenous. The Ce anomaly is calculated from:

$$\frac{Ce_{CN}}{(La_{CN}^{2/3} \times Nd_{CN}^{1/3})}$$

The Th/La-(Ce/Ce)*Nd diagram (Hastie et al., 2013) is another plot that distinguishes between potential inputs to the source region of magmas. In this instance Th/La is used as a proxy for terrigenous sediment and the Ce anomaly as a proxy for pelagic sediment. The diagram (Figure 9.31) suggests that the dominant contaminants are volcanic detritus and the slow sediment clay-fish debris/hydrothermal (SSC-FH) pelagic sediment. Minor contributions also appear to come from the continental detritus and slow sediment clay-hydrogenous (SSC-HD).

As the inputs to the Chivillas basin basalts appear mostly to be a mix of volcanic detritus and pelagic sediment it seems reasonable to interpret them as being derived from sediments that were subducted in a continental arc environment (a mix of arc derived detritus and marine sediment) rather than from continental contamination of the lower crust.

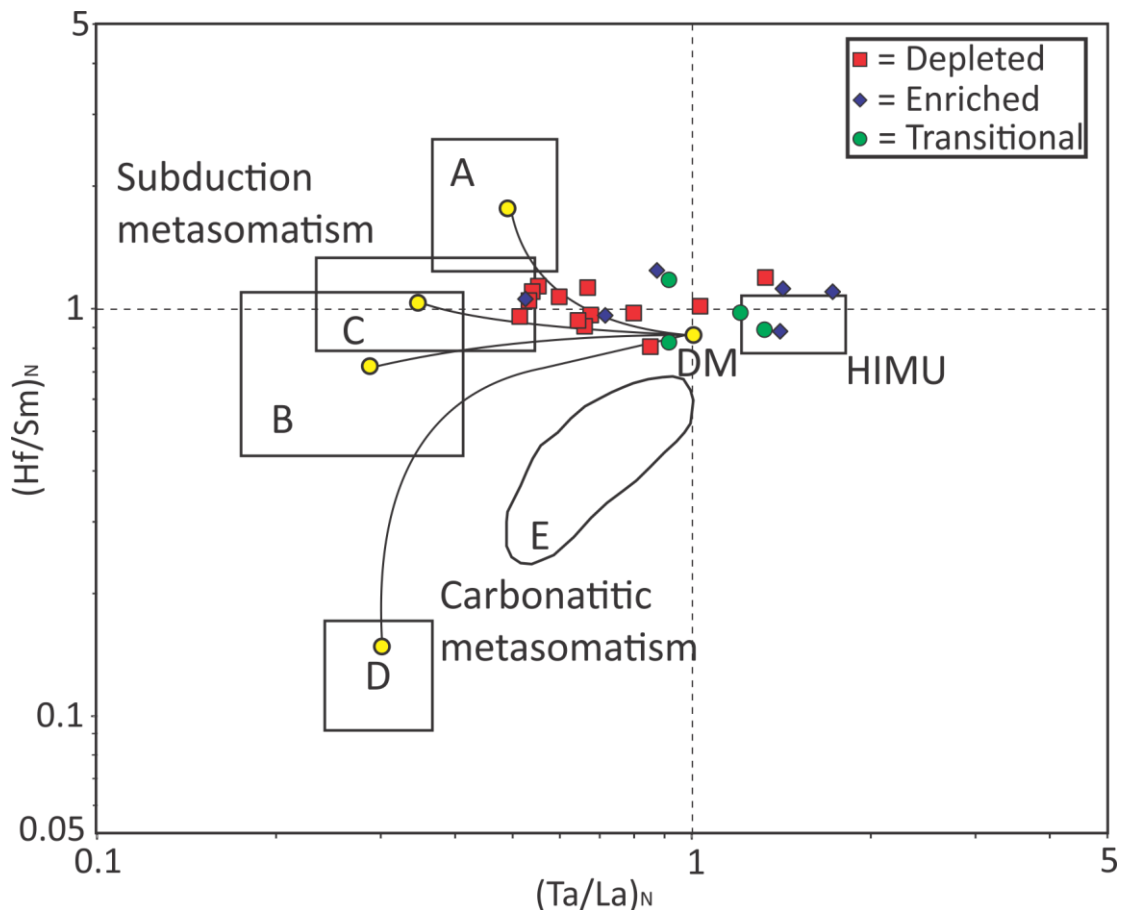


Figure 9.32. $(\text{Hf}/\text{Sm})_N$ - $(\text{Ta}/\text{La})_N$ diagram (Fleche et al., 1998) for the basalts from the Chivillas Formation. Ratios are normalised to primitive mantle. Field A) volcanic arc basalts extracted from a mantle source metasomatized by silicated fluids (Aleutian adakitic rocks; Yogodzinski et al., 1995). Field B) volcanic arc basalts extracted from a hydrated mantle source (Aeolian arc basalts; Francalanci et al., 1993). Field C) late Devonian calc-alkalic mafic igneous rocks from Nova-Scotia; Tate & Clarke, 1995). Field D) carbonatitic lavas from the United Arab Emirates (Woolley et al., 1991). Field E) alkalic basalts from Tanzania, interpreted to have been produced by a lithospheric mantle source metasomatized by carbonatites (Dupuy et al., 1992; Furman, 1995). HIMU field of Tupuai basalts (Chauvel et al., 1992). Mixing line between a depleted mantle source (DM) and the average composition of basaltic or carbonatitic rocks forming in the listed fields.

Chapter 9: Geochemistry and Hf-Nd isotope results

On the Hf/Sm_N-Ta/La_N diagram (Figure 9.32) of Flèche et al. (1998) the depleted group show a trend towards mantle that has been affected by subduction related metasomatism. On this diagram it is difficult to isolate one source influencing the depleted group. The dominant inputs affecting the depleted igneous group of the Chivillas Formation appears to be A (silicate fluid metasomatism) and C (calc-alkaline mafic igneous rocks), with minor contribution from B (volcanic arc basalts extracted from a hydrated mantle source). There does not appear to be any contribution from carbonatitic metasomatism. The enriched and transitional groups plot in and towards the HIMU mantle source field although three samples have similar signatures to the depleted group, and plot in the subduction metasomatism area of Figure 9.32.

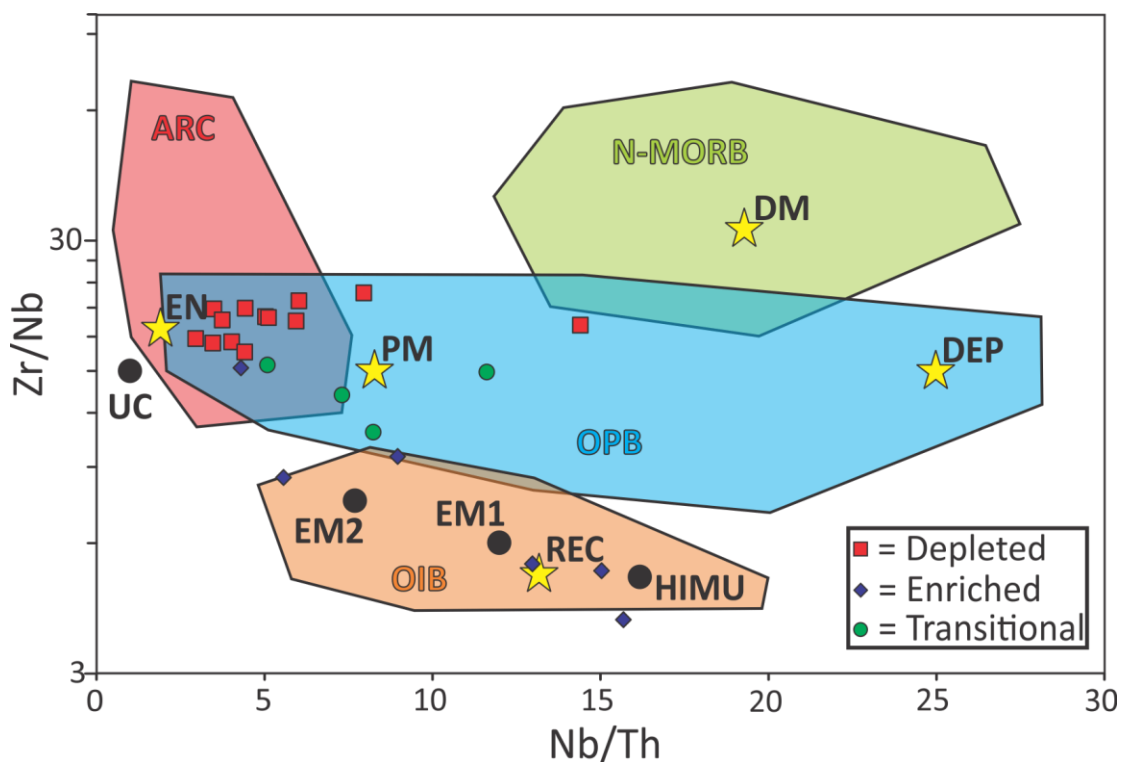


Figure 9.33. Zr/Nb-Nb/Th diagram for the igneous rocks of the Chivillas Formation. Field boundaries and end members from Condie, 2005. Abbreviations are the same as in Figure 9.25.

Chapter 9: Geochemistry and Hf-Nd isotope results

In the Zr/Nb-Nb/Th plot (Figure 9.33) the enriched group from the Chivillas basin plot mostly in the ocean island basalt field boundary, with one overlapping between the arc and oceanic plateau basalt fields. The depleted group plot in the arc field boundary, overlapping with the oceanic plateau basalt field (two examples plot wholly in this field). The transitional group plot between the other two groups in the ocean plateau basalt/arc fields. A trend linking the enriched, depleted and transitional groups is apparent with the high μ (U/Pb) source (HIMU)/recycled component as one end member and an enriched, arc like component as the other. A separate incipient trend may also exist in some of the samples of the depleted group. In this instance an enriched component forms one end member and depleted mantle and/or deep depleted mantle makes up the other.

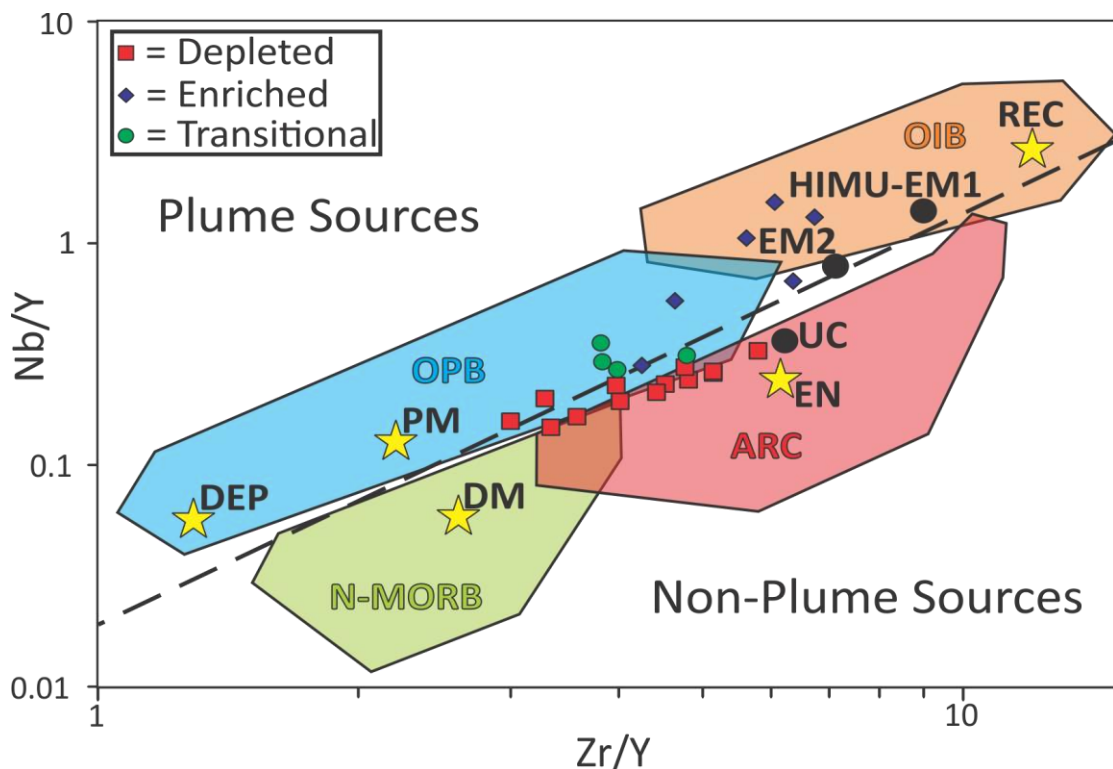


Figure 9.34. Nb/Y-Zr/Y diagram for the igneous rocks of the Chivillas Formation. Field boundaries and end members from Condie, 2005. Abbreviations are the same as in Figure 9.25.

Chapter 9: Geochemistry and Hf-Nd isotope results

In the Nb/Y-Zr/Y plot (Figure 9.34) similar trends are observed as in the Zr/Nb-Nb/Th plot. The enriched group plot in the plume source division of the figure, in the ocean island basalt and oceanic plateau basalt field areas, whereas the depleted group plot mainly in the non-plume source area (MORB), in the arc field boundary. Again, although not so apparent as in the Zr/Nb-Nb/Th plot, there appears to be two mixing lines. One links the enriched, transitional and depleted groups together along a line with EM1/EM2/HIMU as one end member and the arc field boundary as the other. The depleted group again appear to form their own separate mixing line between the arc field and N-MORB field.

From the above discrimination diagrams it is apparent that the trace element trends of the depleted igneous group of the Chivillas Formation are most consistent with magmas that have been influenced by subduction fluid metasomatism, rather than ones that have been contaminated by continental crust. This would suggest that the extension that formed the Chivillas basin was related to a subduction event e.g. in a back arc basin environment. However, metasomatism from subduction fluids does not provide a satisfactory explanation for the trace element trends of the enriched igneous group of the Chivillas Formation, which appear to have formed from a separate mantle source.

9.8.4 Composition of source: OIB

An enriched ocean island basalt (OIB)- like source could potentially explain the enriched group of the Chivillas basin. It is generally accepted that OIB (HIMU, EM1 & EM2 mantle reservoirs) are derived from a deep mantle plume source comprising recycled oceanic crust and associated sediments that have previously

been subducted (e.g. Weaver, 1991; Hofmann, 1997). During subduction, Nb and Ta are retained in the slab by rutile which is a stable phase in the oceanic crust (Foley et al., 2000). This results in the characteristic negative Nb and Ta anomalies in arc rocks. Consequently, recycled oceanic crust that upwells and melts to form OIB is enriched in Nb and Ta (Weaver, 1991).

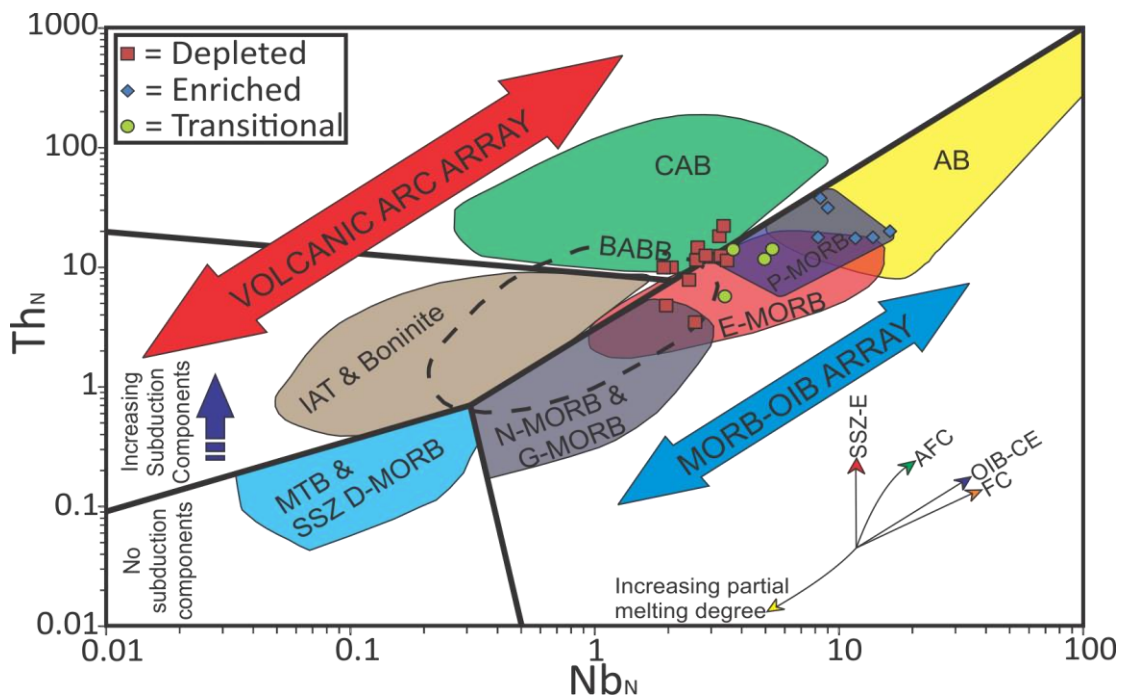


Figure 9.35. Plot of Th_N vs. Nb_N (N-MORB normalised) from Saccani (2015) for the igneous rocks taken from the Chivillas Formation. SSZ-E= supra-subduction zone enrichment, AFC= assimilation-fractional crystallisation, OIB-CE= ocean island-type (plume type) component enrichment; FC= fractional crystallisation, G-MORB= garnet-influenced MORB, E-MORB= enriched-type MORB, P-MORB= plume-type MORB, AB= alkaline ocean-island basalt, IAT= low-Ti, island arc tholeiite, CAB= calc-alkaline basalt, MTB= medium-Ti basalt, D-MORB= depleted-type MORB, BABB= back arc basin basalt.

The Th_N - Nb_N diagram (Saccani, 2015) is an alternative to the Pearce & Peate, (1995) Th/Yb - Nb/Yb plot where Th and Nb are normalised to N-MORB values instead of Yb. It has been suggested that this method can help eliminate mathematical errors introduced through element ratios (Chayes, 1949; Saccani, 2015), subsequently allowing greater precision in distinguishing tectonic environments. In

Figure 9.35 there is a clear distinction between the igneous groups found in the Chivillas Formation. The enriched group display overlap with P-MORB, alkaline ocean-island basalt and E-MORB signatures, the transitional group ranges from P-MORB to E-MORB and the depleted group samples plot in the E-MORB, calc-alkaline basalt and N-MORB fields (Figure 9.35). In terms of tectonic setting it appears they form a trend between an enriched ocean island basalt (OIB) setting which progresses to a more depleted, subduction related, back arc basin setting (Figure 9.36).

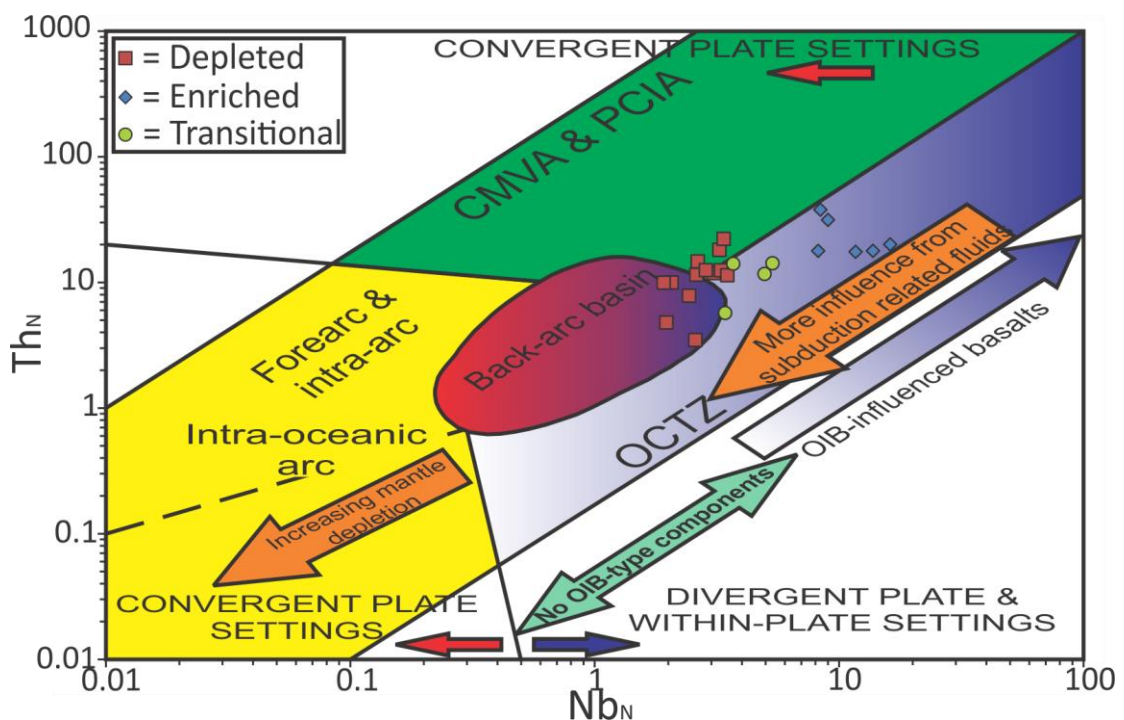


Figure 9.36. Plot of Th_N vs. Nb_N (N-MORB normalised) from Sacconi (2015) for the igneous rocks taken from the Chivillas Formation. CMVA= Continental margin volcanic arc & polygenetic crust island arc, OCTZ= Oceanic subduction-unrelated setting & rifted margin.

The results of the Th_N - Nb_N plot appear to suggest that the enriched group found in the Chivillas Formation formed due to an upwelling of a deep seated mantle plume like source region. In such an environment garnet would be a dominant fractionating phase in the source due to the depth of magma generation associated.

However, the enriched group of the Chivillas Formation have relatively flat HREE patterns (Figure 9.19; Gd/Yb_{CN} ratios 1.37-1.58), suggesting that garnet was not a significant residual phase in the petrogenesis of these magmas. This is displayed in the Dy/Dy* vs. Dy/Yb plot (Figure 9.37) of Davidson et al. (2013) which shows no indication of any influence from garnet in the samples of the Chivillas Formation.

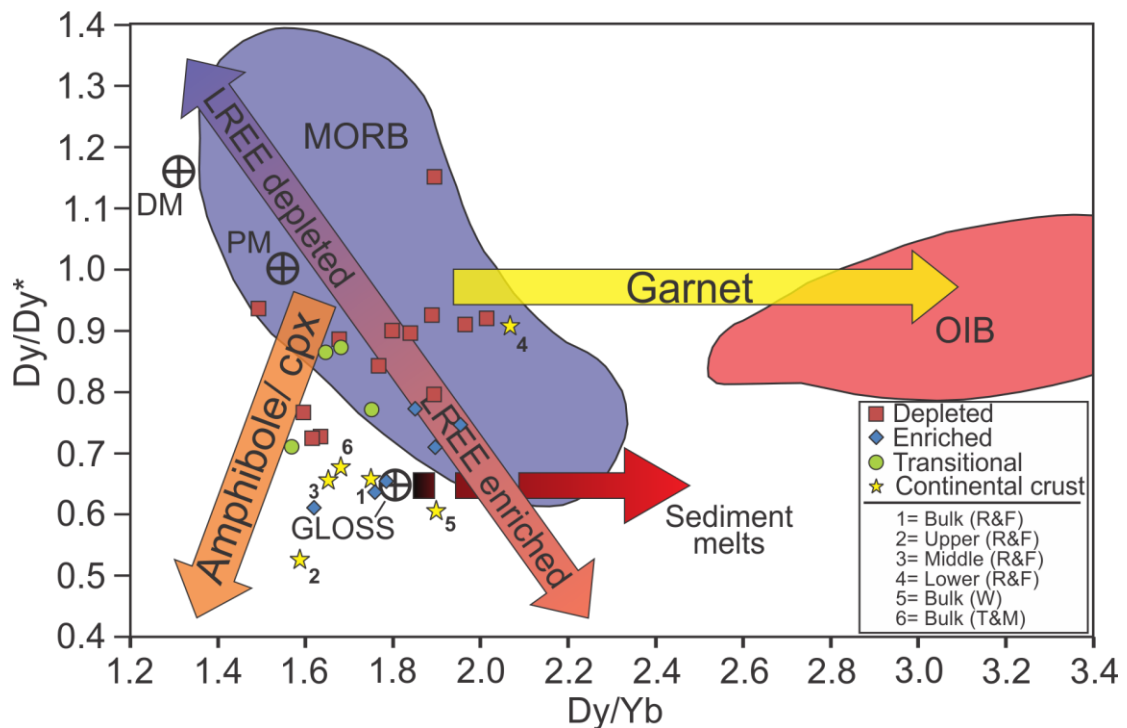


Figure 9.37. Dy/Dy* vs. Dy/Yb diagram of Davidson et al. (2013) for the Western Gulf of Mexico basement samples. The MORB field has been compiled from N-MORB and E-MORB data from the East Pacific Rise (Nui et al., 1999; Regelous et al., 1999; Turner et al., 2011). The OIB field includes data from Hawaii (Sims et al., 1995, 1999) and the Azores (Beier et al., 2010). Continental crustal estimates are from Rudnick & Fountain (1995); Wedepohl (1995); Taylor & McLennan (1985). PM= primitive mantle (Sun & McDonough, 1989); DM= depleted mantle (Salters & Stracke, 2004); GLOSS= average subducting sediment (Plank & Langmuir, 1998). Vectors for mineral control are from Davidson et al. (2013).

The Lu/Hf ratio acts as another proxy for the existence of residual garnet in the source. The enriched group of the Chivillas Formation yield low results (0.09-0.14) when compared to samples where residual garnet is known to be present e.g. lower crustal granulite xenoliths from Kilbourne Hole, New Mexico (Lu/Hf= 0.93-

1.30; Scherer et al., 1997). However interpretation on the Lu/Hf ratio should be done cautiously as amphibole fractionation can also influence the ratio. Figure 9.37 indicates that amphibole fractionation may well influence at least some of the Chivillas Formation samples. Nevertheless, a lack of evidence for residual garnet in the source region of the enriched group of the Chivillas Formation means a mantle plume is unlikely to contribute to the HIMU, EM1 & EM2 like enrichment.

9.8.5 Composition of source: Lower crust ultramafic source

As mentioned previously in Chapter 7 ultramafic rocks with cumulitic textures are present in the Teotitlán area of the northern Cuicateco. These rocks may represent lower crustal cumulates of the Cretaceous arc system that make up the Xonamanca Formation and Teotitlán Migmatitic Complex and could be a source for the enriched igneous group of the Chivillas Formation.

Partial melts from olivine-clinopyroxene-amphibole cumulates been experimentally determined by (Medard et al., 2006) and have been found in island arc volcanics of Sumatra, Bali and Vanuatu (DellaPasqua & Varne, 1997). The experimental results yield nepheline-normative, ultra-calcic igneous melts, with CaO of up to 18.9 wt%, CaO/Al₂O₃ ratios of up to 1.25, low SiO₂ (down to 44 wt %). These results are compositionally distinct from the enriched group of the Chivillas Formation, which have CaO of 5-10 wt % (some samples contain calcite filled amygdules which will raise the CaO further) and CaO/Al₂O₃ ratios of 0.23-0.74. It is therefore unlikely that the igneous rocks of the Chivillas Formation formed by the partial melting of an ultramafic lower crustal source.

9.8.6 Composition of source: slab & sediment melt metasomatism

There are instances in Mexico (Castillo, 2008; Cai et al., 2014) and around the world (Defant et al., 1992; Kepezhinskas et al., 1995; Kepezhinskas et al., 1996; Hastie et al., 2011) of high niobium basalts (HNBs) where metasomatism of the lithospheric mantle from sediment and oceanic slab melts associated with arc systems result in alkali magmas that are enriched in HFSEs such as Nb and Ta. This could help explain the enriched signatures that are observed in some of the igneous rocks of the Chivillas Formation. This explanation correlates with interpretations made on the depleted group of the Chivillas Formation, which indicate an influence from subduction.

To test this hypothesis the Hf and Nd isotopic data from the Chivillas Formation have been compared with various potential end-member components (Figure 9.38). Isotopic ratios for the continental crust of Mexico are represented by three lower crustal xenoliths (Roberts & Ruiz, 1989; Vervoort et al., 2000) which have been age corrected to 130 Ma. Isotopic ratios for the composition of potential marine sediment influencing the Chivillas Formation have been inferred from samples collected from the Middle America Trench by DSDP 487 (DSDP report; Figure 9.39). A stratigraphic study (LaGatta, 2003) revealed the sediments in the trench are composed of terrigenous and pelagic hydrothermal sediments in a ratio of 4:6. The isotopic bulk composition is calculated taking this ratio into consideration (Cai et al., 2014). The DSDP 487 marine sediments range from the Palaeocene-Late Miocene and therefore have not been age corrected as the difference to the initial ϵ_{Hf} & ϵ_{Nd} values is negligible. Other modern day marine sediments have been

collated from (Vervoort et al., 2011). Comparisons have also been made with high Nb basalts taken from the Sierra Chichinautzin Volcanic Field (SCVF) in the Trans-Mexican Volcanic Belt (Figure 9.38; Cai et al., 2014). Fields for N-MORB (Nowell et al., 1998; Kempton et al., 2002; Thompson et al., 2003) and the back arc basin of the East Scotia Ridge (Barry et al., 2006) have also been plotted for comparison.

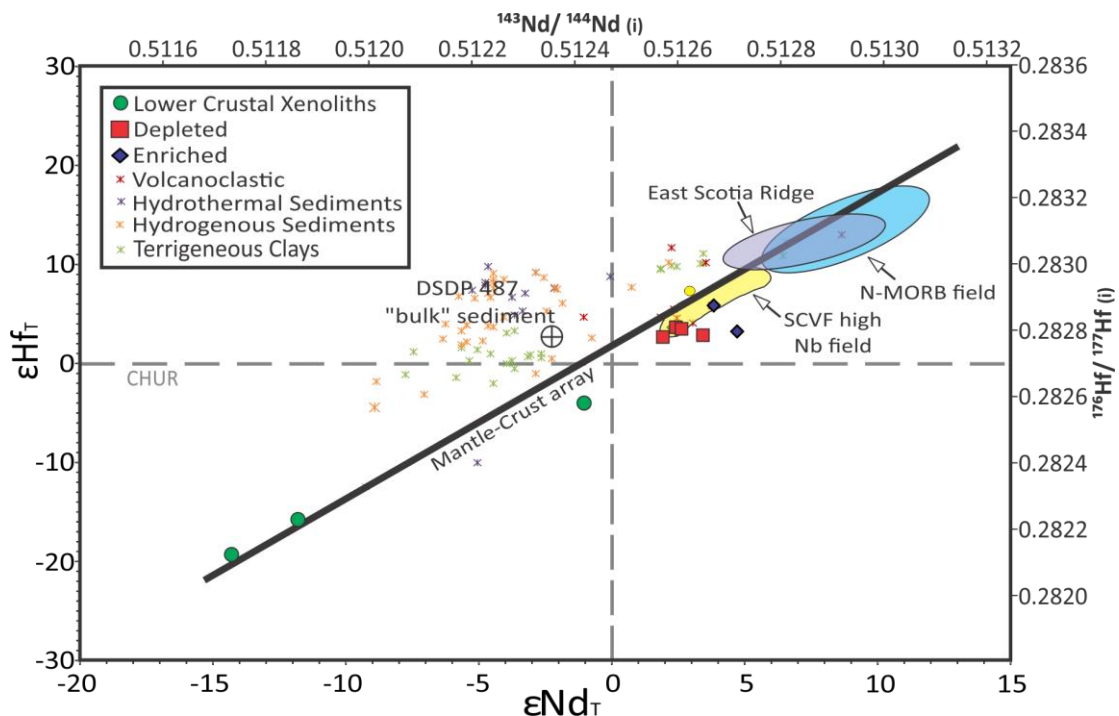


Figure 9.38. Plot of ϵHf_T vs. ϵNd_T (age corrected to 130 Ma) for the igneous samples taken from the Chivillas Formation. MORB field constructed from PetDB (Nowell et al., 1998; Kempton et al., 2002); East Scotia Ridge field from Barry et al (2006); Mantle-Crust array from Vervoort et al (2011); Mexican lower crustal xenoliths from Roberts & Ruiz, (1989) and Vervoort et al., (2000); volcanoclastic, hydrothermal, hydrogenous and terrigenous sediments from Vervoort et al., (2011); DSDP 487 sediment bulk composition calculated from stratigraphy (LaGatta, 2003); SCVF high-Nb field from Cai et al., (2014).

The enriched and depleted samples of the Chivillas Formation have similar isotopic compositions to the SCVF high Nb basalts and form a trend oblique to the mantle-crust array (Figure 9.38). The source of the SCVF high Nb basalts has been attributed to lithospheric mantle that has been metasomatised by subducted slab and sediment melts (Cai et al., 2014 & references therein). Alternatively it is possible

that the trend relates to a mix between Grenvillian continental crust and N-MORB. Potential end members for mixing lines will be explored further in trace element ratio plots.

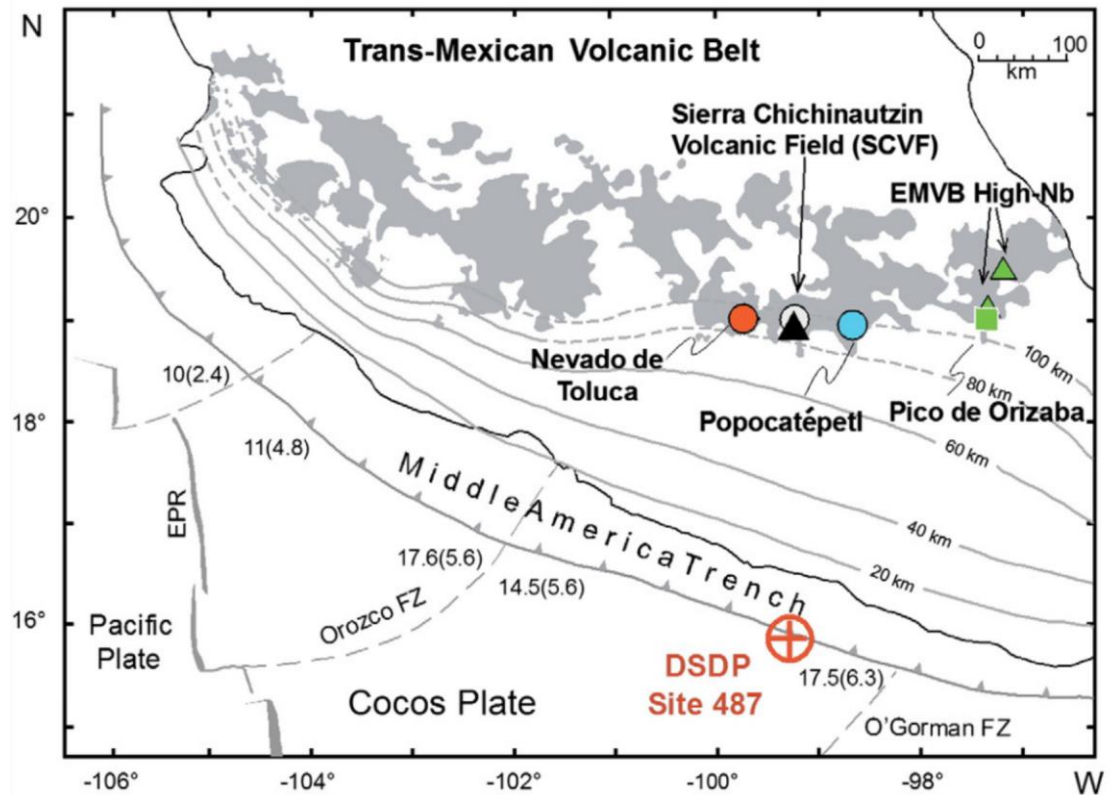


Figure 9.39. Map showing the localities of DSDP site 487 and the Sierra Chichinautzin Volcanic Field (SCVF) taken from Cai et al., (2014).

Although both the depleted and enriched groups of the Chivillas Formation are comparable to the SCVF high Nb rocks (Figure 9.38), the depleted group displays a trend towards lower Nd values. The DSDP 487 “bulk” sediment has similar Hf isotopic ratios to the depleted and enriched groups of the Chivillas Formation but lower Nd isotopic ratios. Therefore the lower Nd isotopic values of the depleted group may indicate derivation from a mantle source that is more influenced by fluids expelled by subducted sediment than the enriched group. There does not appear to be any direct correlation between the East Scotia Ridge or N-MORB fields and the

Chapter 9: Geochemistry and Hf-Nd isotope results

Chivillas samples, although it could be argued that the East Scotia Ridge samples share a similar oceanic sediment end member as the Chivillas samples.

Plots of isotope data vs. incompatible trace element ratios can also be used to help highlight potential end member compositions and mixing trends. Where possible, (dependent on available data) fields have been plotted for the potential high Nb “metasomatised mantle” end member and Mexican continental crust. The N-MORB end member represents an average of samples from the East Pacific Rise (EPR; Class & Lehnert, 2012).

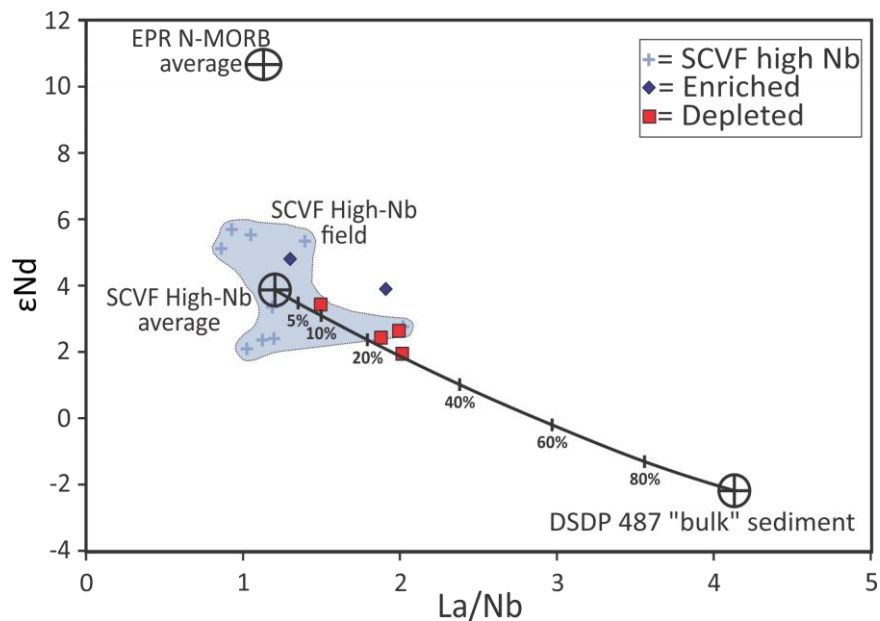


Figure 9.40. ϵNd_T (age corrected to 130 Ma) vs. La/Nb diagram for the igneous samples taken from the Chivillas Formation. SCVF high-Nb field & DSDP 487 "bulk" sediment marker constructed from data in Cai et al., 2014; EPR N-MORB average marker from PetDB (Class & Lehnert, 2011).

In the ϵHf & ϵNd vs. La/Nb diagrams (Figures 9.40 & 9.41) a negative correlation is observed in the samples analysed from the Chivillas Formation (more obvious in the ϵNd than ϵHf plot). The enriched group display La/Nb ratios that are comparable to the SCVF high Nb field. The depleted group show a trend towards the

DSDP 487 bulk sediment composition as in the ϵ_{Hf} vs ϵ_{Nd} diagrams. A mixing line using the SCVF high Nb samples and DSDP 487 bulk sediment as end members (Figures 9.40 & 9.41) suggests that the higher La/Nb ratios and lower isotopic ratios in the depleted group are related to an increased influence from marine sediments (10-30% marine sediment). No comparison with Mexican continental crust can be made in Figures 9.40 and 9.41 due to limited trace element data availability in Roberts & Ruiz, (1989) and Vervoort et al. (2000).

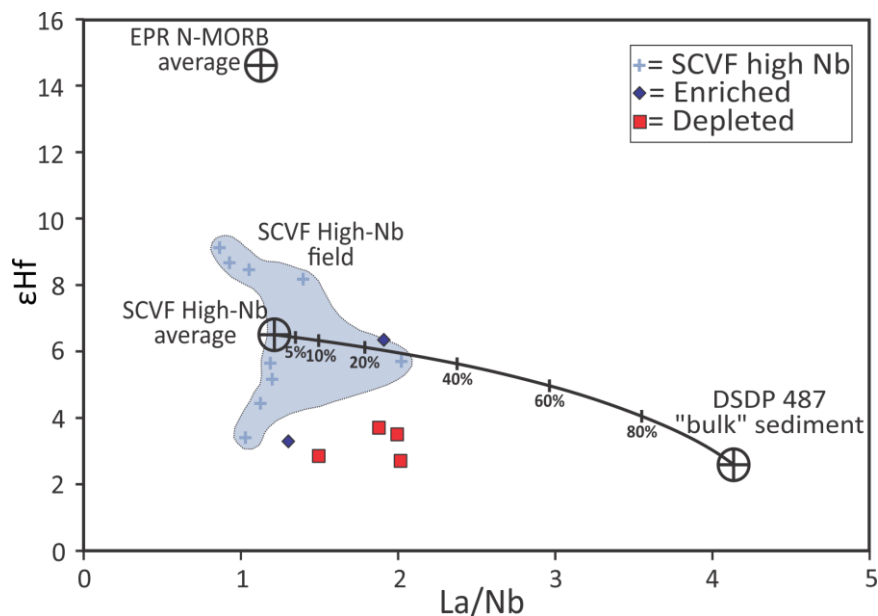


Figure 9.41. ϵ_{Hf_T} (age corrected to 130 Ma) vs. La/Nb diagram for the igneous samples taken from the Chivillas Formation.

Plots of Lu/Hf vs. ϵ_{Nd} and ϵ_{Hf} are shown on Figures 9.42 and 9.43. Again a mixing line between the SCVF high Nb source and DSDP 487 marine sediment reveal that the enriched group plot closer to the SCVF high Nb field than the depleted group which as previously noted appear to contain a greater input from marine sediment (~20-40%). Values for the Mexican lower crustal xenoliths appear to be completely unrelated to the trends observed in the Chivillas Formation samples.

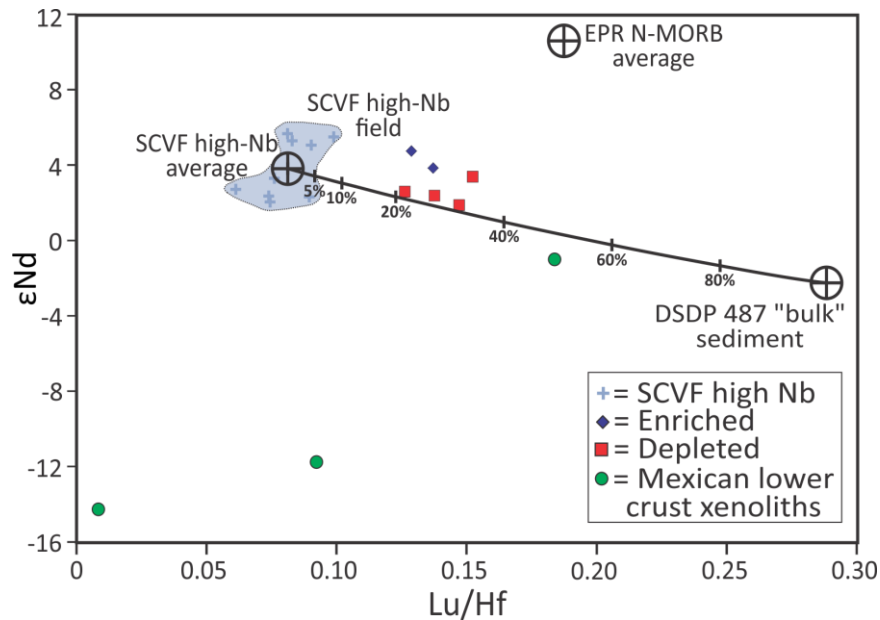


Figure 9.42. ϵNd_T (age corrected to 130 Ma) vs. Lu/Hf diagram for the igneous samples taken from the Chivillas Formation. SCVF high-Nb field & DSDP 487 "bulk" sediment marker constructed from data in Cai et al., 2014; EPR N-MORB average marker from PetDB (Class & Lehnert, 2011); Mexican lower crustal xenoliths from Vervoort et al., 2000 and Roberts & Ruiz, 1989.

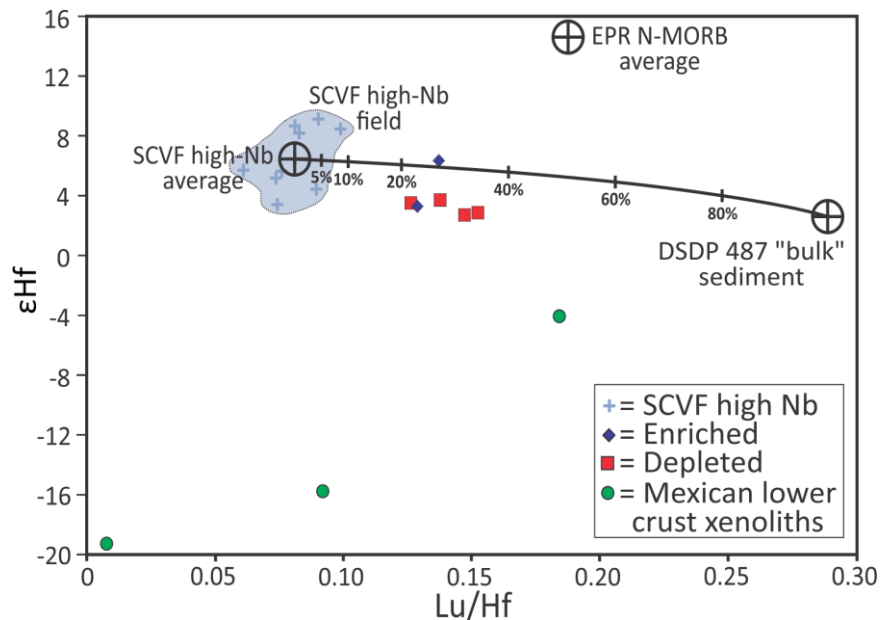


Figure 9.43. ϵHf_T (age corrected to 130 Ma) vs. Lu/Hf diagram for the igneous samples taken from the Chivillas Formation.

In the ϵHf & ϵNd vs. La/Sm plots (Figures 9.44 & 9.45) the enriched group display higher La/Sm than the depleted group and have similar compositions to the SCVF high Nb samples. The depleted group in this instance do not lie on a mixing line

between the SCVF high Nb source and DSDP 487 marine sediment but instead show a progression towards the EPR N-MORB end-member.

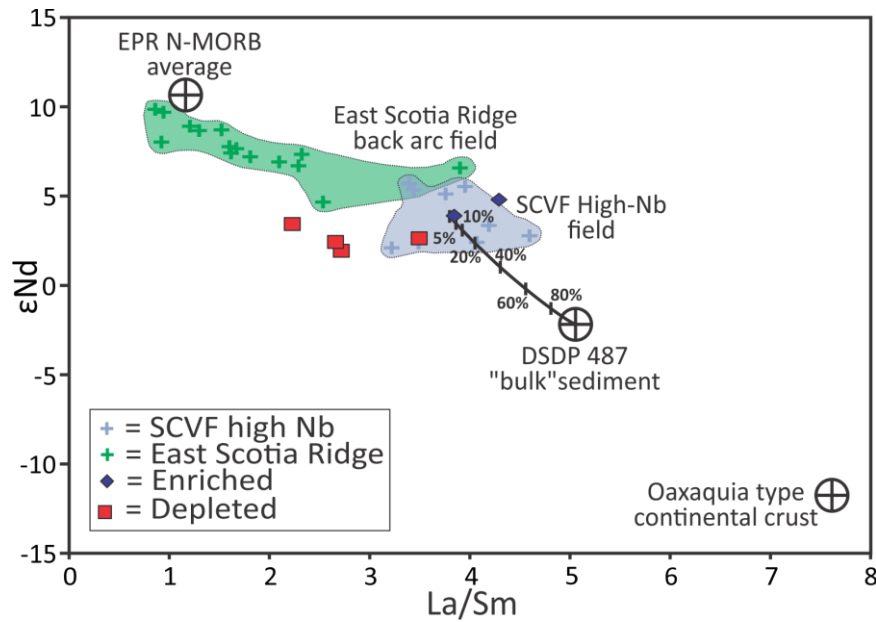


Figure 9.44. ϵNd_{τ} (age corrected to 130 Ma) vs. La/Sm diagram for the igneous samples taken from the Chivillas Formation. SCVF high-Nb field & DSDP 487 "bulk" sediment marker constructed from data in Cai et al., 2014; East Scotia Ridge field from Barry et al., 2006; EPR N-MORB average marker from PetDB (Class & Lehnert, 2011); Mexican lower crustal xenoliths from Vervoort et al., 2000 and Roberts & Ruiz, 1989.

The La/Sm ratio may record the evolution of the magmatism towards the N-MORB end member, as is observed in the back arc samples of the East Scotia Ridge (Figures 9.44 & 9.45). Again the lower continental crust does not appear to have had a significant input to either the enriched or depleted groups of the Chivillas Formation.

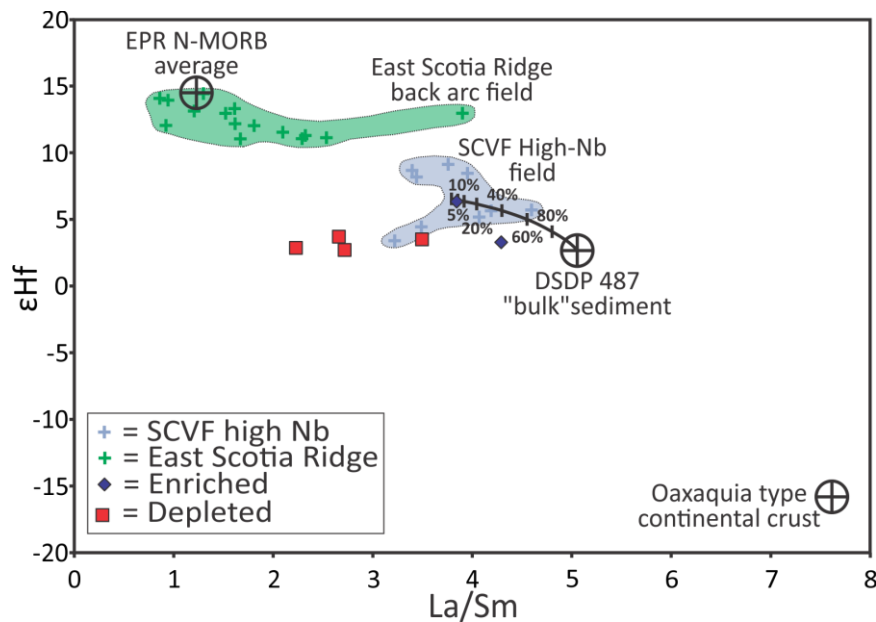


Figure 9.45. ϵHf_T (age corrected to 130 Ma) vs. La/Sm diagram for the igneous samples taken from the Chivillas Formation.

The trends in each of the ratio plots suggest that the enriched group of the Chivillas Formation have a source compositionally similar to the SCVF high Nb lavas found in the Trans Mexican Volcanic Belt (TMVB). Such magmatism has been associated with metasomatism of the overlying lithospheric mantle caused by melts of the subducting oceanic plate and its sediment that is pulled down with it (Cai et al., 2014). The depleted group appears to contain more of an input from a marine sediment end member (e.g. DSDP 487 bulk sediment). The signature of the depleted group is more associated with “typical” asthenospheric mantle metasomatism in subduction environments, as the slab dehydrates it causes fluids to percolate through the overlying mantle wedge that carry mobilised elements from subducting sediments with them. Whether the subducting slab produces melts or just undergoes dehydration is likely to be controlled by its temperature which in turn is dictated by the age of the plate (Defant et al., 1992). This issue will be discussed further in Chapter 10.

Chapter 9: Geochemistry and Hf-Nd isotope results

Studies have shown that slab melt metasomatism of a depleted mantle source breaks down mineral phases such as olivine, orthopyroxene, clinopyroxene and spinel in the mantle peridotite and replaces them with garnet, phlogopite, Na-rich clinopyroxene, Fe enriched orthopyroxene and pargasitic amphibole (e.g. Kepezhinskis et al., 1995; Rapp et al., 1999; Prouteau et al., 2001; Hastie et al., 2011). It is thought that the pargasitic amphibole formed in this reaction scavenges Nb and Ta from the slab derived melts (Sorenson & Grossman, 1989; Hastie et al., 2011). If this metasomatised mantle source subsequently undergoes partial melting (e.g., through decompression as rifting in a back arc progresses and/or the addition of hydrous liquids from the subducting slab) the pargasitic amphibole is among the first phases to break down (Hastie et al., 2011), producing enriched magmas similar to those of the Chivillas Formation.

The elevated Nb and Ta compositions of the enriched group of the Chivillas Formation can therefore be interpreted as the initial melts of a depleted mantle source containing pargasitic amphibole. As magma generation continued below the Chivillas basin the pargasitic amphibole would have become scarcer. Consequently, the contribution of Nb, Ta and alkalis from the metasomatised mantle to the melt would be considerably reduced, forming the more depleted Chivillas group. The magmas of the depleted group represent a depleted mantle source that has been enriched by subducted sediment and slab-derived fluids. This interpretation of enriched magmatism followed by depleted magmatism is consistent with the field relationships (Chapter 7) whereby the depleted basalts are seen to intrude enriched diorites.

9.8.7 Basin Maturity

There are no examples in the basin of true N-MORB like magmas in the Chivillas Formation which suggests spreading stopped before it evolved into a mature oceanic basin. There is however evidence in the Th/Yb-Nb/Yb plot (Figure 9.29) of a progression towards N-MORB which may represent the latest part of the basins evolution where influence from the subducting slab was becoming more distal and less pronounced. Most of the samples from the Chivillas basin plot in the continental arc field which suggests that they formed at quite an immature phase of basin evolution. However, there are three samples from the depleted group that plot close to the MORB array, suggesting that they may have formed at a later stage of basin evolution. This can also be seen in the La/Sm ratio (depleted group values range from 3.1-1.2) and in the Zr/Nb-Nb/Th plot (Figure 9.33) where the initial trend moves from the OIB field (interpreted here to represent lithospheric mantle altered by slab and sediment melts) to the arc field and then towards the N-MORB field.

9.9 Summary

- Plutonic and volcanic rocks of the Teotitlán Migmatitic Complex and Xonamanca Formation appear to have formed in a continental arc tectonic setting ca. 140-133 Ma (Chapter 8).
- Compositional differences in the rocks of the Chivillas submarine basin do not appear to be controlled by fractional crystallisation processes.
- Degree of partial melting may contribute to the compositional differences, with the enriched groups forming from lower degree of partial melting than

Chapter 9: Geochemistry and Hf-Nd isotope results

the depleted group. However source heterogeneities appear to be a more dominant factor.

- The enriched group relates to unusual subduction associated metasomatism whereby melts from the slab and associated sediments metasomatise the overlying asthenospheric mantle.
- The depleted group displays more typical subduction signatures whereby fluids derived from the dehydrating slab and associated sediments metasomatise the overlying mantle wedge.
- The high niobium basalts of the enriched group likely represent the initial stages of magmatism under low degrees of partial melting where pargasitic amphibole was broken down to form magmas rich in Nb, Ta and alkalis.

10 Petrogenesis and paleogeography of the Cuicateco Terrane

10.1 Introduction

The geochemical results presented in Chapter 9 clearly indicate an influence from subduction in the Early Cretaceous magmatism of the northern Cuicateco terrane. These findings suggest that the Cuicateco basin opened in association with back arc extension, rather than continental rifting in response to the opening of the Gulf of Mexico as suggested Mendoza et al. (2010), or the separation of North and South America as suggested by Angeles-Moreno, (2006). Ages for the extensional igneous rocks of the northern Cuicateco could not be obtained but detrital zircon studies on coeval sediments constrain the maximum age of deposition to the Barremian (131-126 Ma), with population peaks at 130 Ma (this study) and 126 Ma (Mendoza et al., 2010). This chapter will investigate possible relationships between the subduction related northern Cuicateco terrane and other Early Cretaceous subduction systems that existed in Mexico, in order to define a tectonomagmatic model for the origin of the terrane.

10.2 Early Cretaceous subduction in Mexico

As discussed in the geological overview of Chapter 6, subduction in Mexico during the Early Cretaceous is characterised by the Guerrero island arc system and associated back arc of the Arperos basin (Martini et al., 2014 and references therein). The initiation of continental extension in the Arperos basin is recorded in the Esperanza Formation (Figure 10.1), which has been dated by U/Pb on zircon to

Chapter 10: Petrogenesis of the Cuicateco terrane

ca. 150-145 Ma (Martini et al., 2011). The Esperanza Formation is overlain by the Early Cretaceous Valenciana Formation (Figure 10.1) which has been interpreted to have formed from the erosion of the carbonate platform that existed in Mexico during the Early Cretaceous. Thermal resetting of the basalts that formed during oceanic extension in the basin has resulted in imprecise $^{40}\text{Ar}/^{39}\text{Ar}$ plagioclase crystallisation ages (Martini et al., 2014). However, detrital zircons studies on the sediments of the basin indicate it was still being filled until the Barremian (Martini et al., 2011). Sediments of the Ojo de Agua Assemblage in the Guerrero terrane yield a maximum age of deposition of 118 Ma (Martini et al., 2014). These sediments are interpreted to represent syn-collisional deposits during the accretion of the Guerrero terrane to Mexico (Martini et al., 2014).

Prior to the opening of the Arperos basin, arc rocks formed as a result of the subduction of the Farallon plate. These are preserved in the Xolapa terrane of Southern Mexico (Figure 10.1) and have been dated to ca. 165-158 Ma (Guerrero-García et al., 1978; Ducea et al., 2004). Other granitic dykes (El Pozuelo granite) interpreted to be arc related in the Xolapa terrane yield igneous crystallisation ages of ~133-129 Ma (Solari et al., 2007). This magmatism is coeval with the closure of the Arperos basin, so was presumably related to the subduction of this oceanic crust beneath Mexico. However, the proximity of these dykes to the Arperos basin suture zone (tens of kilometres) and the likely shallow angle of subduction of the young (and so hot and buoyant) Arperos oceanic crust, mean that it may be better interpreted as localised near-trench magmatism rather than the arc front itself.

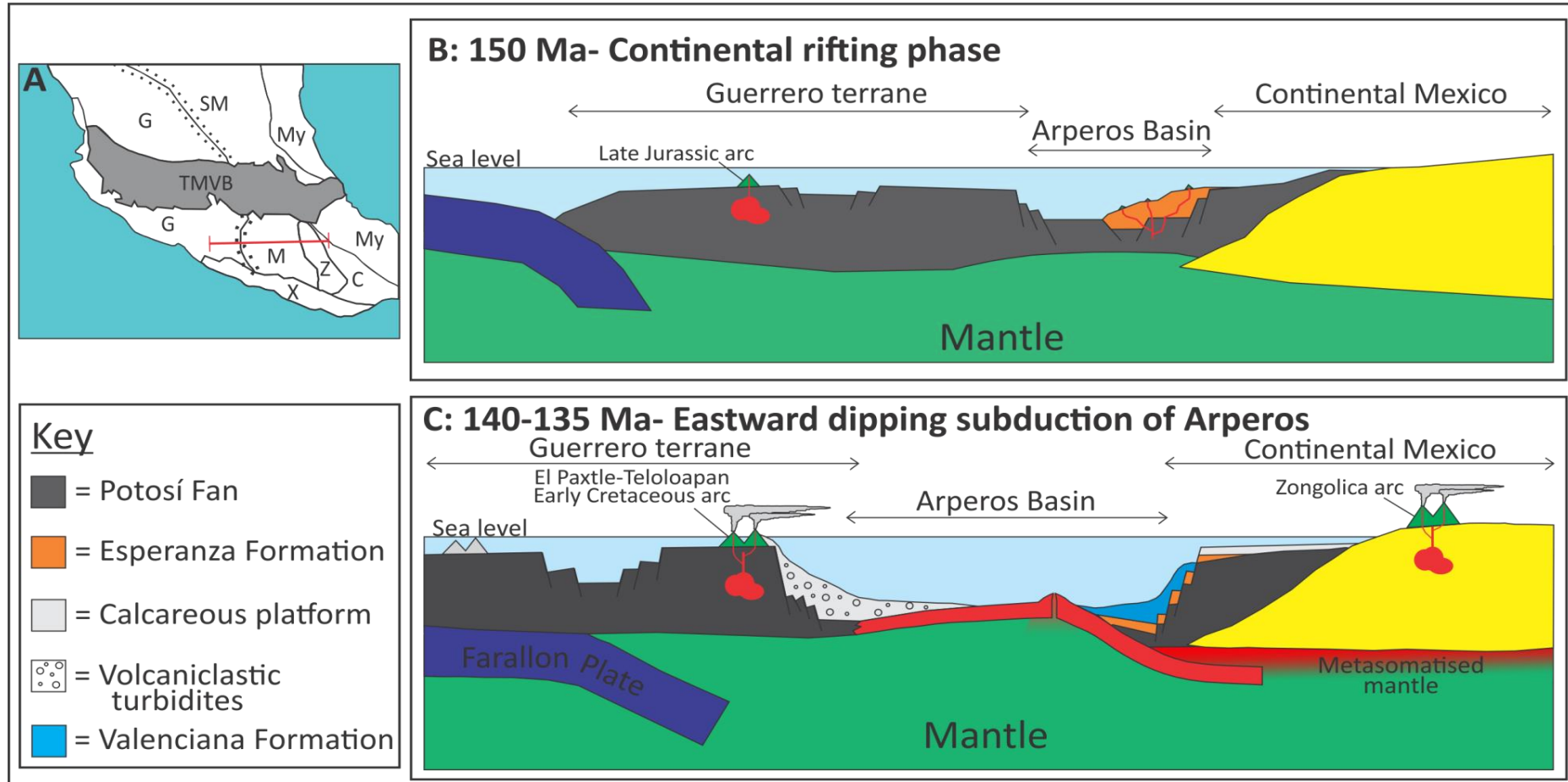


Figure 10.1. A) Present day map of Mexico with terranes (G= Guerrero terrane; M= Mixteca terrane; X= Xolapa terrane; Z= Zapoteco terrane; C=Cuicateco terrane; My= Maya terrane; TMVB= Trans Mexican Volcanic Belt; SM= Sierra Madre terrane.) The dashed lines mark the suture zone of the Arperos basin and the red line marks the approximate transect of B & C. B & C show regional tectonic reconstructions of Southern Mexico during the late Jurassic-Early Cretaceous adapted from Martini et al., (2011).

10.3 Petrogenesis of the Cuicateco terrane

The extrusive and intrusive magmatic rocks of the Xonamanca Formation and Teotitlán Migmatitic Complex, as well as the basalts that formed in the extensional basin of the Chivillas Formation, clearly have signatures that are influenced by subduction (see Chapter 9). The Xonamanca Formation and Teotitlán Migmatitic Complex can be interpreted as having formed in a continental arc environment between 140-133 Ma and so it is proposed here that these units together form part of an Early Cretaceous “Zongolica arc” (named from its location in the Sierra de Zongolica mountains; Figure 10.1 C).

The subduction related geochemical signature of basalts from the extensional basin of the Chivillas Formation suggests that these rocks are likely to have been formed in a back arc environment (Chapter 9). Several examples of unusual basalts (enriched group) that are enriched in Nb and Ta can also be found in the Chivillas Formation, which have been interpreted to have formed from a mantle source that has been metasomatised by slab and sediment-derived melts (Chapter 9). The trace element signatures suggest the Chivillas Formation never evolved into a mature oceanic basin. However, there is evidence for the basin to have been ‘oceanised’ as indicated by an incipient trend towards N-MORB in the Zr/Nb-Nb-Th and Nb/Y-Zr/Y plots (Figures 9.33 and 9.34).

An obvious interpretation for the northern Cuicateco terrane would be to associate the Early Cretaceous extensional basin with the contemporaneous Arperos back arc basin. The suture of the Arperos basin above the Trans Mexican Volcanic Belt (TMVB) lies on strike with the location of the northern Cuicateco terrane (Figure

Chapter 10: Petrogenesis of the Cuicateco terrane

10.1). It is therefore possible that the Cuicateco represents the southern extent of the Early Cretaceous Arperos back arc basin, with the central portions buried beneath the Cenozoic TMVB. However, when tracing the suture of the Arperos basin below the TMVB, outcrops are found running along the western boundary of the Mixteca terrane (Elías-Herrera et al., 1998; Freydier et al., 2000; Martini et al., 2011; Figure 10.1). This indicates that the northern Cuicateco is unlikely to represent the southern extent of the Arperos Basin.

An alternative model linking the Arperos basin and the Cuicateco basin is that the Cuicateco represents a failed rifted limb of the Arperos back arc basin. In this model rifting in the Cuicateco basin would be expected to initiate approximately at the same time (ca. 150 Ma) as in the Arperos Basin (Esperanza Formation). However, extension did not begin in the Cuicateco until the end of the spreading in the Arperos basin, with detrital zircon studies indicating a maximum age of deposition of 126 Ma. It is therefore apparent that the Cuicateco extensional basin is not directly linked to the Arperos back arc basin.

It is generally accepted that the Arperos basin was closing through the Early Cretaceous, eventually leading to the accretion of the Guerrero terrane to continental Mexico by the Aptian (Dickinson and Lawton, 2001; Martini et al., 2011). There are $^{40}\text{Ar}/^{39}\text{Ar}$ ages for Arperos basin basalts that suggest that the accretion did not occur until the Cenomanian (Elías-Herrera et al., 2000; Martini et al., 2014). However, dykes that intrude these basalts have been dated to 129 Ma (U/Pb zircon) which suggests they have been thermally reset.

Chapter 10: Petrogenesis of the Cuicateco terrane

Very little is understood about the mechanism of the Guerrero terrane accretion to continental Mexico and what happened to the oceanic crust that formed in the Arperos basin. It is thought that sea floor spreading in the Arperos basin initiated at ca. 145 Ma, after around 5 Ma of continental extension (Martini et al., 2011). Additionally, syn-tectonic sediments of the Ojo de Agua Assemblage indicate that Guerrero accretion to continental Mexico had initiated by ca. 118 Ma (Martini et al., 2014). This gives an approximate period of 25 Ma where oceanic crust was being formed in the Arperos back arc basin. Given that extension rates of current back arc basins range between 10 mm/year (Mariana Trough) to 150 mm/yr (Lau Basin), the total amount of oceanic crust formed in the Arperos basin could be anywhere between 250-3750 km (assuming extension continued until the basin was closed). These values for basin width may be somewhat of an overestimation as the assumption that the spreading rates remained continuous whilst the basin was being closed seems unlikely. However, we can still infer that a substantial amount of oceanic crust would need to be consumed by subduction, either beneath the Guerrero terrane or continental Mexico.

The existence of the Early Cretaceous Zongolica arc indicates that the closure of the Arperos basin was accommodated (at least in part) through the eastward subduction of the oceanic crust beneath continental Mexico (Figure 10.1 C). This arc system would have formed ~250-300 km from the trench (using its current location from the Arperos suture). Given that this oceanic crust was <10 Ma old, and so was hot and buoyant, it was likely subducted at a shallow angle, which is consistent with the presence of an arc ~250-300 km from the trench. The 133-129 Ma Pozuelo

Chapter 10: Petrogenesis of the Cuicateco terrane

granite (Solari et al., 2007) as discussed in Section 10.2 was probably too close (tens of kilometres) to the trench of the subducting Arperos basin to represent the arc front. It instead may have formed by localised near trench crustal melting. This melting could have occurred as a result of the high heat flux from the young subducting crust, or perhaps more likely, from a slab-window being formed when the spreading ridge of the Arperos basin was subducted. A similar model has been proposed for Pliocene magmatism of Southern Chile (Forsythe et al., 1986).

It seems likely that the magmatism preserved in the Chivillas extensional basin, which has strong subduction signatures, is linked to the proximal Zongolica arc, and is therefore in turn associated with the subduction of the Arperos basin. Whether the Zongolica arc and Chivillas basin magmatism were coeval, or if the extension marks the end of the arc magmatism is difficult to determine. The fact that there is a ~7 Ma gap between the youngest dated granites of the Zongolica arc (133 Ma; Chapter 8) and the maximum age of deposition for the Chivillas basin (126 Ma population of zircons from Mendoza et al., 2010) indicates that the initiation of extension may have stopped arc magmatism. On the other hand the zircons from the sediments of the Chivillas basin are igneous in origin and do not appear to be far travelled. An alternative proximal igneous source of this age is difficult to determine so it may be that the youngest expressions of the Zongolica arc were eroded away into the Chivillas basin.

10.3.1 Mechanism for back arc extension

An issue with the back arc hypothesis for the Early Cretaceous Chivillas basin of the northern Cuicateco terrane is determining the mechanism of extension in a

Chapter 10: Petrogenesis of the Cuicateco terrane

system that was undergoing compression as the Arperos basin was being closed. Extension in back arc environments is classically attributed to older, denser slabs causing roll-back. However, Heuret and Lallemand, (2005) demonstrate that the age of the slab has little control on this roll-back effect, demonstrating that in the right conditions young slabs can roll-back easily also.

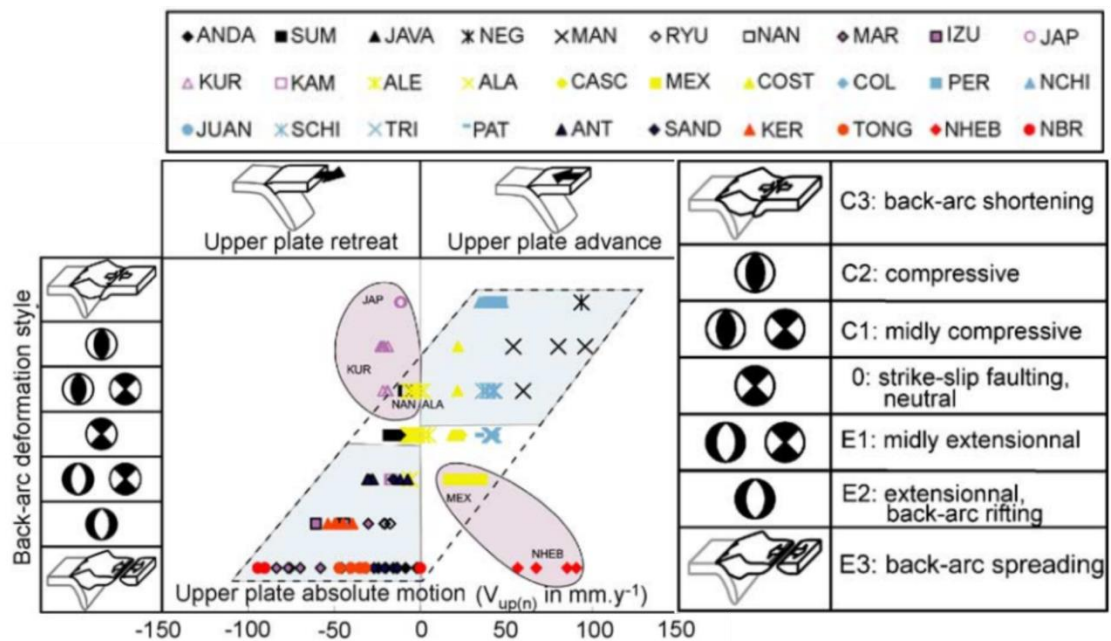


Figure 10.2 Cross-plot of back-arc deformation style versus trench-normal component of upper plate absolute motion ($V_{up(n)}$), adapted from Heuret and Lallemand, (2005). The blue area represents subduction zones that have back-arc deformation style consistent with upper plate motion (correspondence between back-arc extension and upper plate retreat and between back-arc compression and upper plate advance). The red area represents back-arc deformation style inconsistent with upper plate absolute motion: The dashed line delimits the global trend, that is increasing extension with increasing upper plate retreat and conversely for compression. Back arc abbreviations: ANDA=Andaman, SUM= Sumatra, JAVA= Java, NEG=Negros, MAN=Manila, RYU=Ryukyu, NAN=Nankai, MAR=Mariana, IZU=Izu-Bonin, JAP=Japan, KUR=Kuril, KAM=Kamchatka, ALE=Aleutian, ALA= Alaska, CASC=Cascadia, MEX=Mexico, COST=Costa-Rica, COL=Colombia, PER=Peru, NCHI=North Chile, JUAN=Juan Fernandez, SCHI= South Chile, TRI= Chile triple junction, PAT= Patagonia, ANT= Antilles, SAND= Sandwich, KER= Kermadec, TONG= Tonga, NHEB= New Hebrides, NBRIT= New Britain

Extension in a back arc environment is instead thought to be mainly controlled by upper plate absolute motion (Heuret and Lallemand, 2005). Figure 10.2 shows that in the vast majority of cases around the world if the upper plate of a subduction zone is in retreat, then extension will occur in the back arc and, if the

Chapter 10: Petrogenesis of the Cuicateco terrane

upper plate is advancing, then compression in the back arc region will be observed (assuming the subducting plate is at least partially anchored). However, there are some exceptions to this e.g., New Hebrides, where an advancing upper plate is undergoing extension in the back arc region (Figure 10.2). In these scenarios it appears that localised and/or regional asthenospheric flow controls back arc extension (Schellart et al., 2002; Heuret and Lallemand, 2005).

Asthenospheric flow may have been an important control on the extension observed in the Chivillas Formation of the Cuicateco terrane. The initiation of extension in the Chivillas Formation appears to coincide with the magmatism of the Pozuelo granite (Solari et al., 2007) in the Xolapa terrane (interpreted here to represent near trench magmatism in response to ridge subduction of the Arperos oceanic crust). The continual subduction of the spreading centre would have resulted in a tear, or slab-window, to form in the subducting crust. Studies show that localised mantle flow through slab-windows or tears, can cause slab roll-back to occur (Schellart et al., 2002). This therefore represents a potential mechanism for extension in the back arc region of the Zongolica arc, regardless of the absolute motion of the upper crust. The formation of a slab-window during the subduction of the Arperos crust also explains the basalts of the Chivillas Formation that appear to have been enriched by slab and sediment derived melts. Studies have shown (Hastie et al., 2011 and references therein) that phases such as pargasitic amphibole scavenge Nb and Ta during such slab melt-mantle interactions (discussed in Chapter 9).

Another factor that may have facilitated extension in the Chivillas Formation is the delamination of the lithospheric mantle beneath the Zongolica arc causing subsidence of the continental crust. Delamination could have occurred in response to a shallow angle of subduction in the Arperos oceanic crust. Such extensional forces are observed in the forearc region of the TMVB arc system in Mexico today (Gérault et al., 2015).

10.3.2 Back-arc Model: 150-140 Ma

- Extension in the Arperos back arc basin initiated ca. 150 Ma, separating the Guerrero terrane from continental Mexico.
- The continental rifting stage lasted ~5 Ma, and resulted in the felsic magmatism of the Esperanza Formation (Martini et al., 2010).
- Ca. 145 Ma oceanisation of the basin initiated and extension continued for ~5 Ma with passive margins. At ca. 140 Ma the Arperos basin would have been at peak width. Modern analogues of slow spreading ridges (Mariana ridge) and fast spreading ridges (Lau basin) indicate that the Arperos basin could have been 50-750 km wide at this time.
- The eastward dipping subduction of the Arperos oceanic crust beneath continental Mexico initiated ca. 141 Ma.
- Subduction of the Arperos oceanic crust led to the formation of the Zongolica arc system (Figure 10.3 A) ~300 km from the trench, suggesting flat slab subduction. The early arc rocks are found in the volcanics and tuffs of the Xonamanca formation and preserved as tonalites in the Teotitlán Migmatitic Complex, dated to 140-138 Ma (U/Pb zircon).

- Arc magmatism resulted in metasomatism of the overlying mantle by fluids released from the dehydrating slab and sediments (normal subduction related metasomatism).

10.3.3 Back-arc Model: 133 Ma (Figure 10.3 B)

- The rate of subduction of the Arperos oceanic crust exceeded the rate of ocean spreading, leading to the closure of the basin throughout the Valanginian (139-134). By ca. 133 Ma the spreading centre had been subducted.
- As the spreading centre was subducted a slab-window formed, causing near trench magmatism to occur (El Pozuelo granite of the Xolapa terrane).
- The subduction of the ridge initiated localised mantle flow that escaped through the slab-window, causing slab roll-back.
- The slab roll-back caused extension in the back arc region of the Zongolica arc, initiating the Chivillas basin.
- Lithospheric mantle delamination caused by the shallow angle of the subducting slab may also have contributed to the extension.
- The extension appears to have split the Zongolica arc front, causing a southwestern migration of the arc (Teotitlán Migmatitic Complex).
- Ridge subduction led to unusual metasomatism of the overlying mantle caused by slab derived melts.
- Under normal subduction conditions the Nb and Ta are locked in rutile which is a stable phase in the slab. However if partial melts of the slab occur these elements can be released into the mantle.

10.3.4 Back-arc Model 130 Ma (Figure 10.3 C)

- Continuing extension in the Chivillas basin led to decompression melting of the asthenosphere.
- The first phases to break down during this melting are those that formed from the slab melt metasomatism caused by the subduction of the Arperos Ridge. These melts represent the Nb-enriched alkali basalts and diorites that are found in the Chivillas Formation.
- Erosion of the Zongolica arc resulted in the deposition of sediments in the Chivillas basin contemporaneous with magmatism. Sediments in the Arperos basin may also be derived from the Zongolica arc but the magmatism of the Pozuelo granites represents a more proximal source.
- The near trench magmatism of the El Pozuelo granite continued until 129 Ma. This suggests either the subducting ridge had passed deeper into the mantle at this point or upwelling of the asthenosphere through the slab-window had stopped.

10.3.5 Back-arc Model 126 Ma (Figure 10.3 D)

- Magmatism in the Chivillas basin eventually exhausted the alkali and HFSE enriched component in the underlying mantle, caused by slab-window metasomatism.
- Subsequent melts produced magmas more typical of immature back arc basins, with prominent signatures from slab derived fluids (Enriched LREEs and Th; Negative Nb, Ta and Ti anomalies).

Chapter 10: Petrogenesis of the Cuicateco terrane

- These magmas are represented by the depleted basalt groups found in the Chivillas Formation of the Cuicateco terrane.
- The depleted group display trends towards N-MORB in the trace element ratio diagrams (Figures 9.33 and 9.34), indicating that extension in the Chivillas basin eventually led to the oceanisation of the crust. However, Spreading in the Chivillas basin never reached a mature oceanic basin (N-MORB) stage, with an apparent influence from subduction in all of the igneous rocks.
- It is difficult to determine whether at this point the Zongolica arc magmatism and extension in the Chivillas basin were coeval.
- The maximum depositional age of 126 Ma for the sediments and contemporaneous magmatism of the Chivillas basin tells us that basin extension likely stopped by the Aptian.
- The Aptian age for the end of spreading in the Chivillas basin broadly coincides with syn-tectonic sediments of the Ojo de Agua Assemblage (maximum depositional age of 118 Ma), which have been interpreted to have formed during the collision of the Guerrero island arc system to continental Mexico (Martini et al., 2014).
- The maximum age of deposition for the Chivillas basin therefore provides a new constraint on the timing of the collision of the Guerrero terrane with continental Mexico.

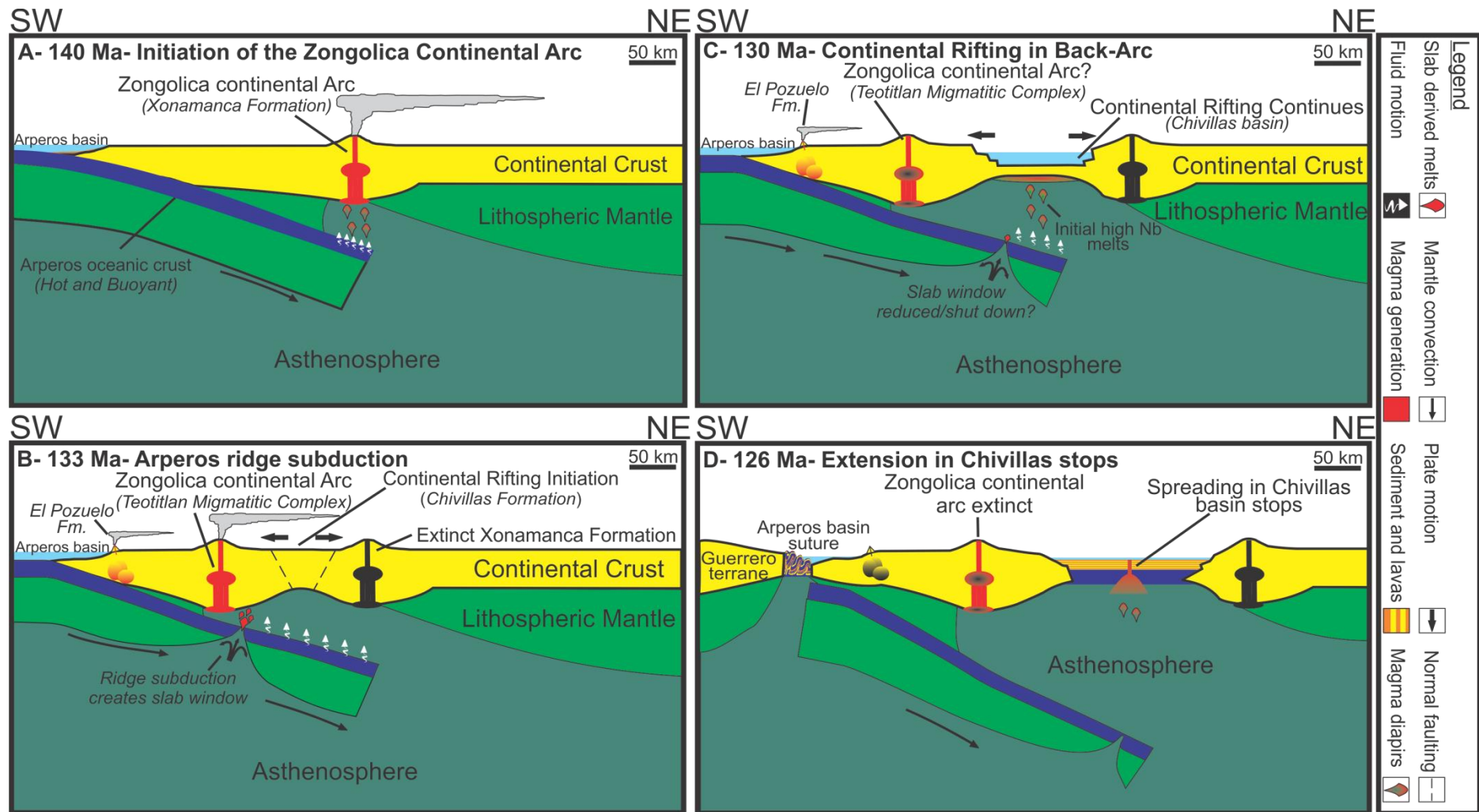


Figure 10.3. Schematic evolutionary model for the northern Cuicateco terrane throughout the Early Cretaceous. A) 140 Ma; B) 133 Ma; C) 130 Ma; D) 126 Ma. The thickness of the crust has been exaggerated for the purpose of the figure.

10.4 Summary

- The Zongolica arc of the Cuicateco terrane (Xonamanca Formation and Teotitlán Migmatitic Complex) formed in response to the subduction of the Arperos oceanic basin ca. 140 Ma.
- The spreading centre of the Arperos basin reached the trench of the Zongolica arc ca. 133 Ma (El Pozuelo Formation). Ridge subduction caused localised asthenospheric convection, which initiated extension in the back arc region of the Zongolica arc. Ridge subduction also triggered enriched slab and sediment derived melts that were released into the overlying mantle.
- Continued extension in the back arc region led to the oceanisation of the basin, as is recorded in the Chivillas Formation of the Cuicateco terrane.
- Spreading in the Chivillas Formation stopped around 126Ma in response to the collision of the Guerrero terrane with continental Mexico.

11 Conclusions

The crystalline basement of the Western Gulf of Mexico provides a rare insight into pre- and post-collisional magmatism associated with the formation of Pangaea in Mexico.

Geochronological results reveal three phases of magmatism in the crystalline basement of the Western Gulf of Mexico, the first relating to the Early Permian, the second to the Late Permian-Earliest Triassic and third to the Early Jurassic.

1. Two granitoids yield a homogeneous **Early Permian** age of 294 Ma, which correlates with Late Carboniferous-Early Permian granitoids of Southern Mexico (Ortega-Obregon et al., 2014).
2. The dominant pulse of magmatism found in the Western Gulf of Mexico occurred in the **Late Permian-Early Triassic**, with 14 samples yielding igneous crystalline ages of 274-243 Ma. Inherited zircon cores are a common feature of this phase of magmatism, with inheritance from Grenville-age zircons (Oaxaquia) and Late Carboniferous-Early Permian zircons. The Late Permian-Early Triassic granitoids of the Western Gulf of Mexico are comparable in age to granitoids found in Northern Mexico (Arvizu & Iriondo, 2011), Southern Mexico (Weber et al., 2005; Ortega-Obregon et al., 2014) and Colombia (Cochrane et al., 2014).
3. The final minor phase of magmatism recorded in the basement of the Western Gulf of Mexico is **Early Jurassic** in age, with two samples yielding ages of 189 Ma and 164 Ma. This igneous event probably relates to the Nazas arc that existed in Mexico during the Early Jurassic (Dickinson & Lawton, 2001).

The major and trace element geochemistry of both the Early Permian and Late Permian-Early Triassic granitoids of the Western Gulf of Mexico display trends that are typical of continental arcs. Granitoids of the same age from Northern Mexico (Arvizu & Iriondo, 2011), Southern Mexico (Weber et al., 2005; Ortega-Obregon et al., 2014) and Colombia (Cochrane et al., 2014) also display major and trace element signatures indicative of a continental arc tectonic setting. However, Hf model ages indicate that whilst the Late Carboniferous-Early Permian granitoids of the Western Gulf of Mexico and Southern Mexico and the Late Permian-Early Triassic granitoids of Northern Mexico and Colombia display evidence for a continental arc setting (mantle source assimilating continental crust), the Late Permian-Early Triassic granitoids of the Western Gulf of Mexico and Southern Mexico do not. It is instead apparent that these granitoids formed from crustal anatexis, with no mantle source contributing to the magmatism. It can therefore be concluded that the arc like major and trace element signatures for the Late Permian-Early Triassic granitoids of the Western Gulf of Mexico and Southern Mexico were inherited from the continental crust from which they formed (Oaxaquia continental crust and Late Carboniferous-Early Permian granitoids). This geochemical inheritance is common in magmatism of a post-collisional tectonic environment (e.g. Pearce et al., 1984; Grimes et al., 2015).

The geochemical data indicate that the Late Carboniferous-Early Permian granitoids of the Western Gulf of Mexico and Southern Mexico (Ortega-Obregon et al., 2014) are related to the same continental arc system on Oaxaquia (Gondwanan) continental crust. This is likely to be associated with the final stages of the closure of the Rheic Ocean, which occurred ca. 290-280, during the amalgamation of Pangaea

(Pindell and Dewey, 1982; Pindell, 1985; Ross, 1986; Sedlock et al., 1993; Dickinson and Lawton, 2001; Talavera-Mendoza et al., 2005; Vega-Granillo et al., 2007 and 2009).

The Late Permian-Early Triassic anatectic magmatism of the Western Gulf of Mexico and Southern Mexico likely relates to a post-collisional igneous event, after the final amalgamation of Pangaea. Late Permian-Early Triassic granitoids of Northern Mexico (Irvizu & Iriondo, 2011) and Colombia (Cochrane et al., 2014) on the other hand appear to be associated with an arc, and are probably formed by subduction of the Paleo-Pacific beneath the Pangaea supercontinent. Subsequent rifting during the breakup of Pangaea and opening of the Gulf of Mexico has resulted in some portions of the Late Permian-Early Triassic anatectic magmatism to move to the south (Oaxaca and Chiapas Massif), and given the basement of the Western Gulf of Mexico a linear trend.

Extension in the northern Cuicateco terrane appears unrelated to the post-Pangaea rifting associated with the opening of the Gulf of Mexico and is instead linked to back arc extension during the subduction of the Arperos Oceanic crust during the Early Cretaceous.

Geochronological results for the units of the Cuicateco terrane reveal the Pochotepc Formation to be composed of Grenville aged meta-sediments and granitoids, most likely related to Oaxaquia continental crust and not deeper portions of the Chivillas Formation as previously suggested by Angeles-Moreno (2006).

Age overlap (within error) is observed between the extrusive volcanic rocks of the Xonamanca Formation (**140-139 Ma**) and the tonalites of the Teotitlán Migmatitic Complex (**138-133 Ma**) indicating that they may have formed in the same igneous event. The host rocks that the tonalites of the Teotitlán Migmatitic Complex intrude into yield igneous crystallization ages of **247 Ma** (amphibolite; probably part of the same igneous event that formed the Permo-Triassic basement of the Western Gulf of Mexico) and detrital zircon maximum depositional ages of **354 Ma** (paragneiss).

Chivillas Formation sediments from this study have been found to have a maximum depositional age of **130 Ma**, which replicates the Barremian maximum depositional age obtained by Mendoza et al. (2010) and Alzaga and Pano (1989). Field relations suggest that sedimentation and magmatism in the Chivillas Formation were contemporaneous. Therefore the maximum depositional age of the sediments can also be used as a best estimate for the age of magmatism.

Major and trace element geochemical results for the extrusive igneous rocks of the Xonamanca Formation and Teotitlán Migmatitic Complex indicate that both suites formed in a continental arc environment. The mafic igneous rocks of the Chivillas Formation can be split into groups that are enriched or depleted in the HFSEs and alkali elements. The depleted group displays trace element signatures that are typical of subduction fluid related magmas, whereas the enriched group appear to be more influenced by slab and sediment derived melts. It is therefore likely that the extensional basin represented by the Chivillas Formation, and the plutonic and extrusive igneous rocks found in the Teotitlán Migmatitic Complex and

Xonamanca Formation respectively are all related to Early Cretaceous subduction, rather than the opening of the Gulf of Mexico as proposed by Mendoza et al. (2010), or the separation of North and South America as proposed by Angeles-Moreno (2006).

The subduction of the Arperos basin beneath continental Mexico is likely to have initiated the Early Cretaceous arc related magmatism observed in the northern Cuicateco terrane. The arc itself, known here as the Zongolica arc, is represented by the 140-133 Ma magmatism found in the Xonamanca Formation and Teotitlán Migmatitic Complex. The eventual subduction of the Arperos ridge led to a slab window forming, causing localised asthenospheric upwelling which initiated extension in the back arc region of the Zongolica arc (Chivillas Formation).

The slab window also caused slab and sediment derived melts to be released into the overlying mantle, carrying with them HFSEs and alkali elements. As extension in the back arc region of the Zongolica arc progressed decompression melting ensued. The first mineral phases to break down during melting were those that had been enriched in the HFSEs and the alkali elements (enriched group of the Chivillas Formation). As the magmatism progressed the enriched mineral phases became more scarce, and typical immature back arc magmas were formed (the depleted group of the Chivillas Formation). Extension in the Chivillas Formation stopped before it evolved into a mature oceanic basin, and was probably due to the consumption of the Arperos basin and the collision of the Guerrero terrane with continental Mexico in the Early Aptian.

The aim of this project was to gain a better understanding of the petrogenesis and tectonic history of the crystalline basement of the Western Gulf of Mexico and the enigmatic Cuicateco terrane of Southern Mexico. From geochemical, isotopic and geochronological interpretations it has succeeded in doing so, and has resulted in tectonomagmatic models that can be applied to, and help refine, existing tectonic models for Mexico over the last ~300 Ma.

In terms of future work the models presented in this study would benefit from more isotopic work, in order to test and strengthen the validity of them e.g. Hf zircon data from the Permo-Triassic granitoids of the Chiapas Massif, Southern Mexico and Early Permian granitoids of the Western Gulf of Mexico. Additionally, further investigation into the centre of the Cuicateco terrane could help determine the extent of the Early Cretaceous units of the northern Cuicateco and identify the boundary with the Late Cretaceous units of the southern Cuicateco.

REFERENCES

- (MMAJ), M. M. A. O. J. 1980. Report on geology survey of the western area (consolidated report). *Japan International Cooperation Agency, Government of Japan*, 6, 177.
- ALANIZ-ALVAREZ, S. A., NIETO-SAMANIEGO, A. F. & ORTEGA-GUTIERREZ, F. 1994. Structural evolution of the Sierra de Juárez Mylonitic Complex, state of Oaxaca, Mexico. *Revista Mexicana de Ciencias Geológicas*, 11, 147–156.
- ALANIZ-ALVAREZ, S. A., VANDER HEYDEN, P., NIETO-SAMANIEGO, A. F. & ORTEGA-GUTIERREZ, F. 1996. Radiometric and kinematic evidence for Middle Jurassic strike-slip faulting in southern Mexico related to the opening of the Gulf of Mexico. *Geology*, 24, 443-446.
- ALVA-VALDIVIA, L. M., GOGUITCHAICHVILI, A., GRAJALES, M., DE DIOS, A. F., URRUTIA-FUCUGAUCHI, J., ROSALES, C. & MORALES, J. 2002. Further constraints for Permo-Carboniferous magnetostratigraphy: case study of the sedimentary sequence from San Salvador–Patlanoaya (Mexico). *Comptes Rendus Geoscience*, 334, 811-817.
- ALZAGA-RUIZ, H. 1991. Estratigrafía y consideraciones paleogeográficas de las rocas del Jurásico Tardío–Cretácico Temprano, en el área de Tomellín–Santiago Nacaltepec, Oaxaca, México. *Revista del Instituto Mexicano del Petróleo*, 23, 17-27.
- ALZAGA RUIZ, H. & PANO ARCINIEGA, A. 1989. Origen de la formación chivillas y presencia del Jurásico tardío en la región de Tehuacan. Puebla, Mexico. *Revista del Instituto Mexicano del Petróleo*, 21, 5-15.
- ANDERSON, T. H. & SCHMIDT, V. A. 1983. THE EVOLUTION OF MIDDLE AMERICA AND THE GULF OF MEXICO CARIBBEAN SEA REGION DURING MESOZOIC TIME. *Geological Society of America Bulletin*, 94, 941-966.
- ANGELES-MORENO, E. 2006. *Petrografía, geología estructural y geocronología del borde noroccidental del terreno Cuicateco, Sierra Mazateca, Estado de Oaxaca, Mexico*. M.S. thesis, Universidad Nacional Autónoma de México.
- ANGELES-MORENO, E., ELIAS-HERRERA, M., MACIAS-ROMO, C., SANCHEZ-ZAVALA, J. L. & ORTEGA-GUTIERREZ, F. 2012. Geological Map of the Western Border of the Cuicateco Terrane, Southern Mexico. *Geological Society of America*
- ARVIZU, H. E. & IRIONDO, A. 2011. Hf isotopic study of zircons from Permian granitoids of NW Mexico: Evidence for mixing of magmas derived from multiple crustal sources. *Revista Mexicana De Ciencias Geológicas*, 28, 493-518.
- BARBOZA-GUDINO, J. R., OROZCO-ESQUIVEL, M. T., GOMEZ-ANGUIANO, M. & ZAVALA-MONSIVAIS, A. 2008. The early mesozoic volcanic arc of western North America in northeastern Mexico. *Journal of South American Earth Sciences*, 25, 49-63.
- BARBOZA-GUDINO, J. R., ZAVALA-MONSIVÀIS, A., VENEGAS-RODRÌGUEZ, G. & BARAJAS-NIGOCHÉ, L. D. 2010. Late Triassic stratigraphy and facies from northeastern Mexico: tectonic setting and provenance. *Geosphere*, 6, 621-640.
- BARRY, T. L., PEARCE, J. A., LEAT, P. T., MILLAR, I. L. & LE ROEX, A. P. 2006. Hf isotope evidence for selective mobility of high-field-strength elements in a subduction setting: South Sandwich Islands. *Earth and Planetary Science Letters*, 252, 223-244.
- BEIER, C., TURNER, S., PLANK, T. & WHITE, W. 2010. A preliminary assessment of the symmetry of source composition and melting dynamics across the Azores plume. *Geochemistry Geophysics Geosystems*, 11.
- BELL, R. T. & JEFFERSON, C. W. 1987. An hypothesis for an Australia–Canadian connection in the Late Proterozoic and the birth of the Pacific Ocean. *Proc. Pacific Rim Congress*, 87, 39-50.
- BETANIA PALACIOS-GARCIA, N. & MARTINI, M. 2014. From back-arc rifting to arc accretion: the Late Jurassic–Early Cretaceous evolution of the Guerrero terrane recorded by a

- major provenance change in sandstones from the Sierra de los Cuarzos area, central Mexico. *International Geology Review*, 56, 1377-1394.
- BETTENCOURT, J. S., LEITE, W. B., JR., RUIZ, A. S., MATOS, R., PAYOLLA, B. L. & TOSDAL, R. M. 2010. The Rondonian-San Ignacio Province in the SW Amazonian Craton: An overview. *Journal of South American Earth Sciences*, 29, 28-46.
- BIRD, D. E., BURKE, K., HALL, S. A. & CASEY, J. F. 2005. Gulf of Mexico tectonic history: Hotspot tracks, crustal boundaries, and early salt distribution. *Aapg Bulletin*, 89, 311-328.
- BISSIG, T., MORTENSEN, J. K., TOSDAL, R. M. & HALL, B. V. 2008. The rhyolite-hosted volcanogenic massive sulfide district of Cuale, Guerrero terrane, west-central Mexico: Silver-rich, base metal mineralization emplaced in a shallow marine continental margin setting. *Economic Geology*, 103, 141-159.
- BOGDANOVA, S. V., BINGEN, B., GORBATSHEV, R., KHERASKOVA, T. N., KOZLOV, V. I., PUCHKOV, V. N. & VOLOZH, Y. A. 2008. The East European Craton (Baltica) before and during the assembly of Rodinia. *Precambrian Research*, 160, 23-45.
- BOHNEL, H. 1999. Paleomagnetic study of Jurassic and Cretaceous rocks from the Mixteca terrane (Mexico). *Journal of South American Earth Sciences*, 12, 545-556.
- BOUVIER, A., VERVOORT, J. D. & PATCHETT, P. J. 2008. The Lu–Hf and Sm–Nd isotopic composition of CHUR: Constraints from unequilibrated chondrites and implications for the bulk composition of terrestrial planets. *Earth and Planetary Science Letters*, 273, 48-57.
- BROOKFIELD, M. E. 1993. NEOPROTEROZOIC LAURENTIA-AUSTRALIA FIT. *Geology*, 21, 683-686.
- BURG, J. P., VAN DEN DRIESSCHE, J. & BRUN, J. P. 1994. Syn- to post-thickening extension in the Variscan Belt of western Europe: Modes and structural consequences. *Géologie de la France*, 3, 33-51.
- CABRAL-CANO, E., LANG, H. R. & HARRISON, C. G. A. 2000. Stratigraphic assessment of the Arcelia-Teloloapan area, southern Mexico: implications for southern Mexico's post-Neocomian tectonic evolution. *Journal of South American Earth Sciences*, 13, 443-457.
- CAI, Y., LAGATTA, A., GOLDSTEIN, S. L., LANGMUIR, C. H., GOMEZ-TUENA, A., MARTIN-DEL POZZO, A. L. & CARRASCO-NUNEZ, G. 2014. Hafnium isotope evidence for slab melt contributions in the Central Mexican Volcanic Belt and implications for slab melting in hot and cold slab arcs. *Chemical Geology*, 377, 45-55.
- CAMPA, M. F. & CONEY, P. J. 1983. Tectono-stratigraphic terranes and mineral-resource distributions in Mexico *Canadian Journal of Earth Sciences*, 20, 1040-1051.
- CANN, J. R. 1970. Rb, Sr, Y, Zr and Nb in some ocean floor basaltic rocks. *Earth and Planetary Science Letters*, 10, 7-11.
- CARDONA, A., VALENCIA, V., GARZON, A., MONTES, C., OJEDA, G., RUIZ, J. & WEBER, M. 2010. Permian to Triassic I to S-type magmatic switch in the northeast Sierra Nevada de Santa Marta and adjacent regions, Colombian Caribbean: Tectonic setting and implications within Pangea paleogeography. *Journal of South American Earth Sciences*, 29, 772-783.
- CARRASCO, V. B. 1978. Estratigrafía de unas lavas almohadilladas y rocas sedimentarias del Cretácico inferior en Tehuacan, Puebla. *Revista del Instituto Mexicano del Petróleo*, 10, 78-82.
- CARRASCO, V. B., FLORES, V. & GODOY, D. 1975. Tobas del Cretácico Inferior del área de Fortín Zongolica, Estado de Veracruz. *Revista Instituto Mexicano del Petróleo*, Vol. VII, 7-27.

- CASTILLO, P. R. 2008. Origin of the adakite-high-Nb basalt association and its implications for postsubduction magmatism in Baja California, Mexico. *Geological Society of America Bulletin*, 120, 451-462.
- CAWOOD, P. A. & BUCHAN, C. 2007. Linking accretionary orogenesis with supercontinent assembly (vol 82, pg 217, 2007). *Earth-Science Reviews*, 85, 82-82.
- CAWOOD, P. A. & PISAREVSKY, S. A. 2006. Was Baltica right-way-up or upside-down in the Neoproterozoic? *Journal of the Geological Society*, 163, 753-759.
- CENTENO-GARCIA, E. 2005. Review of upper Paleozoic and lower Mesozoic stratigraphy and depositional environments of central and west Mexico: Constraints on terrane analysis and paleogeography. In: IN ANDERSON, T. H., NOURSE, J.A., MCKEE, J.W., AND STEINER, M.B., EDS (ed.) *The Mojave-Sonora Megashear Hypothesis: Development, Assessment, and Alternatives: Geological Society of America Special Paper*.
- CENTENO-GARCIA, E., BUSBY, C., BUSBY, M. & GEHRELS, G. 2011. Evolution of the Guerrero composite terrane along the Mexican margin, from extensional fringing arc to contractional continental arc. *Geological Society of America Bulletin*, 123, 1776-1797.
- CENTENO-GARCIA, E., CORONA-CHAVEZ, P., TALAVERA-MENDOZA, O. & IRIONDO, A. 2003. Geologic and tectonic evolution of the western Guerrero terrane—A transect from Puerto Vallarta to Zihuatanejo, Mexico. *Geologic Transects across Cordilleran Mexico: Puerto Vallarta, Jalisco, Mexico, Guidebook for the Field Trips of the 99th Geological Society of America Cordilleran Section Annual Meeting. Universidad Nacional Autónoma de México, Instituto de Geología, Special Paper*, 201-228.
- CENTENO-GARCIA, E., GUERRERO-SUASTEGUI, M. & TALAVERA-MENDOZA, O. 2008. The Guerrero Composite Terrane of western Mexico: Collision and subsequent rifting in a supra-subduction zone. *Formation and Applications of the Sedimentary Record in Arc Collision Zones*, 436, 279-308.
- CENTENO-GARCIA, E. & KEPPIE, J. D. 1999. Latest Paleozoic early Mesozoic structures in the central Oaxaca Terrane of southern Mexico: deformation near a triple junction. *Tectonophysics*, 301, 231-242.
- CENTENO-GARCIA, E., RUIZ, J., CONEY, P. J., PATCHETT, P. J. & ORTEGA-GUTIÉRREZ, F. 1993. Guerrero terrane of Mexico: its role in the Southern Cordillera from new geochemical data. *Geology*, 21, 419-422.
- CHAPPELL, B. W. & WHITE, A. J. R. 1974. two contrasting granite types. *Pacific Geology*, 8, 173-174.
- CHAUVEL, C., HOFMANN, A. W. & VIDAL, P. 1992. HIMU EM - THE FRENCH-POLYNESIAN CONNECTION. *Earth and Planetary Science Letters*, 110, 99-119.
- CHAYES, F. 1949. ON RATIO CORRELATION IN PETROGRAPHY. *Journal of Geology*, 57, 239-254.
- CLASS, C. L., K. 2012. *Expert MORB (Mid-Ocean Ridge Basalt) Compilation*. [Online]. PetDB EarthChem Library. <http://dx.doi.org/10.1594/IEDA/100060>.
- COCHRANE, R., SPIKINGS, R., GERDES, A., ULIANOV, A., MORA, A., VILLAGOMEZ, D., PUTLITZ, B. & CHIARADIA, M. 2014. Permo-Triassic anatexis, continental rifting and the disassembly of western Pangaea. *Lithos*, 190, 383-402.
- COCKS, L. R. M. & TORSVIK, T. H. 2011. The Palaeozoic geography of Laurentia and western Laurussia: A stable craton with mobile margins. *Earth-Science Reviews*, 106, 1-51.
- CONDIE, K. C. 2003. Incompatible element ratios in oceanic basalts and komatiites: Tracking deep mantle sources and continental growth rates with time. *Geochemistry Geophysics Geosystems*, 4.
- CONDIE, K. C. 2005. High field strength element ratios in Archean basalts: a window to evolving sources of mantle plumes? *Lithos*, 79, 491-504.

- D'AGRELLA-FILHO, M. S., PACCA, I. I. G., TRINDADE, R. I. F., TEIXEIRA, W., RAPOSO, M. I. B. & ONSTOTT, T. C. 2004. Paleomagnetism and Ar-40/Ar-39 ages of mafic dikes from Salvador (Brazil): new constraints on the Sao Francisco craton APW path between 1080 and 1010 Ma. *Precambrian Research*, 132, 55-77.
- D'AGRELLA-FILHO, M. S., TRINDADE, R. I. F., ELMING, S.-A., TEIXEIRA, W., YOKOYAMA, E., TOHVER, E., GERALDES, M. C., PACCA, I. I. G., BARROS, M. A. S. & RUIZ, A. S. 2012. The 1420 Ma Indivai Mafic Intrusion (SW Amazonian Craton): Paleomagnetic results and implications for the Columbia supercontinent. *Gondwana Research*, 22, 956-973.
- DALZIEL, I. W. D. 1991. PACIFIC MARGINS OF LAURENTIA AND EAST ANTARCTICA AUSTRALIA AS A CONJUGATE RIFT PAIR - EVIDENCE AND IMPLICATIONS FOR AN EOCAMBRIAN SUPERCONTINENT. *Geology*, 19, 598-601.
- DALZIEL, I. W. D. & SOPER, N. J. 2001. Neoproterozoic extension on the Scottish Promontory of Laurentia: Paleogeographic and tectonic implications. *Journal of Geology*, 109, 299-317.
- DAVIDSON, J., TURNER, S. & PLANK, T. 2013. Dy/Dy*: Variations Arising from Mantle Sources and Petrogenetic Processes. *Journal of Petrology*, 54, 525-537.
- DE LAMOTTE, D. F., FOURDAN, B., LELEU, S., LEPARMENTIER, F. & DE CLARENS, P. 2015. Style of rifting and the stages of Pangea breakup. *Tectonics*, 34, 1009-1029.
- DEFANT, M. J., JACKSON, T. E., DRUMMOND, M. S., DEBOER, J. Z., BELLON, H., FEIGENSON, M. D., MAURY, R. C. & STEWART, R. H. 1992. THE GEOCHEMISTRY OF YOUNG VOLCANISM THROUGHOUT WESTERN PANAMA AND SOUTHEASTERN COSTA-RICA - AN OVERVIEW. *Journal of the Geological Society*, 149, 569-579.
- DELGADO-ARGOTE, L. A. 1989. Regional implications of the Jurassic-Cretaceous volcanosedimentary Cuicateco terrane, Oaxaca, Mexico. *Geofísica Internacional*, 28-5.
- DELLAPASQUA, F. N. & VARNE, R. 1997. Primitive ankaramitic magmas in volcanic arcs: A melt-inclusion approach. *Canadian Mineralogist*, 35, 291-312.
- DEPAOLO, D. J. & WASSERBURG, G. J. 1976. ND ISOTOPIC VARIATIONS AND PETROGENETIC MODELS. *Geophysical Research Letters*, 3, 249-252.
- DEWEY, J. F., DALZIEL, I. W. D., REAVY, R. J. & STRACHAN, R. A. 2015. The Neoproterozoic to Mid-Devonian evolution of Scotland: a review and unresolved issues. *Scottish Journal of Geology*, 51, 5-30.
- DICKINSON, W. R. & LAWTON, T. F. 2001. Carboniferous to Cretaceous assembly and fragmentation of Mexico. *Geological Society of America Bulletin*, 113, 1142-1160.
- DILEK, Y. & ALTUNKAYNAK, S. 2007. Cenozoic crustal evolution and mantle dynamics of post-collisional magmatism in western Anatolia. *International Geology Review*, 49, 431-453.
- DONNELLY, T., HORNE, G., FINCH, R. & LÓPEZ-RAMOS, E. 1990. Northern Central America: The Maya and Chortis blocks. *The Caribbean Region: Boulder, Colorado, The Geological Society of America, The Geology of North America*, H, 37-76.
- DROBE, J. & CANN, R. M. 2000. Cu-Au Skarn Mineralization, Minas de Oro District, Honduras, Central America. *Exploration and Mining Geology*, 9, 51-63.
- DUCEA, M. N., GEHRELS, G. E., SHOEMAKER, S., RUIZ, J. & VALENCIA, V. A. 2004. Geologic evolution of the Xolapa Complex, southern Mexico: Evidence from U-Pb zircon geochronology. *Geological Society of America Bulletin*, 116, 1016-1025.
- DUNCAN KEPPIE, J., NANCE, R. D., MURPHY, J. B., MILLER, B. V., DOSTAL, J. & ORTEGA-RIVERA, A. 2009. Pressure-temperature-time evolution of high-pressure rocks of the Acatlan Complex (southern Mexico): Implications for the evolution of the Iapetus and Rheic Oceans: Comment. *Geological Society of America Bulletin*, 121, 1456-1459.

- DUPUY, C., LIOTARD, J. M. & DOSTAL, J. 1992. ZR/HF FRACTIONATION IN INTRAPLATE BASALTIC ROCKS - CARBONATE METASOMATISM IN THE MANTLE SOURCE. *Geochimica Et Cosmochimica Acta*, 56, 2417-2423.
- EISBACHER, G. H. 1985. LATE PROTEROZOIC RIFTING, GLACIAL SEDIMENTATION, AND SEDIMENTARY CYCLES IN THE LIGHT OF WINDERMERE DEPOSITION, WESTERN CANADA. *Palaeogeography Palaeoclimatology Palaeoecology*, 51, 231-254.
- ELIAS-HERRERA, M. & ORTEGA-GUTIERREZ, F. 1998. The Early Cretaceous Arperos oceanic basin (western Mexico). Geochemical evidence for an aseismic ridge formed near a spreading center - Comment. *Tectonophysics*, 292, 321-326.
- ELIAS-HERRERA, M., SANCHEZ-ZAVALA, J. L. & MACIAS-ROMO, C. 2000. Geologic and geochronologic data from the Guerrero terrane in the Tejupilco area, southern Mexico: new constraints on its tectonic interpretation. *Journal of South American Earth Sciences*, 13, 355-375.
- EMMET, P. 1983. *Geology of the Agalteca Quadrangle, Honduras, Central America*. M.S. thesis, University of Texas at Austin.
- ERSOY, Y. & HELVACI, C. 2010. FC-AFC-FCA and mixing modeler: A Microsoft Excel spreadsheet program for modeling geochemical differentiation of magma by crystal fractionation, crustal assimilation and mixing. *Computers & Geoscience*, 36, 383-390.
- ESTRADA-CARMONA, J., WEBER, B., MARTENS, U. & LOPEZ-MARTINEZ, M. 2012. Petrogenesis of Ordovician magmatic rocks in the southern Chiapas Massif Complex: relations with the early Palaeozoic magmatic belts of northwestern Gondwana. *International Geology Review*, 54, 1918-1943.
- FALEIDE, J. I., TSIKALAS, F., BREIVIK, A. J., MJELDE, R., RITZMANN, O., ENGEN, O., WILSON, J. & ELDHOLM, O. 2008. Structure and evolution of the continental margin off Norway and Barents Sea. *Episodes*, 31, 82-91.
- FANG, W., VAN DER VOO, R., MOLINA-GARZA, R., MORAN-ZENTENO, D. & URRUTIA-FUCUGAUCHI, J. 1989. Paleomagnetism of the Acatlan terrane, southern Mexico: evidence for terrane rotation. *Earth and Planetary Science Letters*, 94, 131-142.
- FERRUSQUÍA-VILLAFRANCA, I. 1990. Biostratigraphy of the Mexican Continental Miocene: Part II, The southeastern (Oaxacan) Faunas. *Paleontologia Mexicana*, 56, 57-109.
- FITTON, J. G., SAUNDERS, A. D., NORRY, M. J., HARDARSON, B. S. & TAYLOR, R. N. 1997. Thermal and chemical structure of the Iceland plume. *Earth and Planetary Science Letters*, 153, 197-208.
- FLÈCHE, M. R., CAMIRÉ, G. & JENNER, G. A. 1998. Geochemistry of post-Acadian, Carboniferous continental intraplate basalts from the Maritimes Basin, Magdalen Islands, Québec, Canada. *Chemical Geology*, 148, 115-136.
- FOLEY, S. F., BARTH, M. G. & JENNER, G. A. 2000. Rutile/melt partition coefficients for trace elements and an assessment of the influence of rutile on the trace element characteristics of subduction zone magmas. *Geochimica Et Cosmochimica Acta*, 64, 933-938.
- FORSYTHE, R. D., NELSON, E. P., CARR, M. J., KAEDING, M. E., HERVE, M., MPODOZIS, C., SOFFIA, J. M. & HARAMBOUR, S. 1986. PLIOCENE NEAR-TRENCH MAGMATISM IN SOUTHERN CHILE - A POSSIBLE MANIFESTATION OF RIDGE COLLISION. *Geology*, 14, 23-27.
- FRANCALANCI, L., TAYLOR, S. R., MCCULLOCH, M. T. & WOODHEAD, J. D. 1993. GEOCHEMICAL AND ISOTOPIC VARIATIONS IN THE CALC-ALKALINE ROCKS OF AEOLIAN ARC, SOUTHERN TYRRHENIAN SEA, ITALY - CONSTRAINTS ON MAGMA GENESIS. *Contributions to Mineralogy and Petrology*, 113, 300-313.
- FREYDIER, C., LAPIERRE, H., RUIZ, J., TARDY, M., MARTINEZ, J. & COULON, C. 2000. The Early Cretaceous Arperos basin: an oceanic domain dividing the Guerrero arc from nuclear

- Mexico evidenced by the geochemistry of the lavas and sediments. *Journal of South American Earth Sciences*, 13, 325-336.
- FRIMMEL, H. E., ZARTMAN, R. E. & SPATH, A. 2001. The Richtersveld Igneous Complex, South Africa: U-Pb zircon and geochemical evidence for the beginning of Neoproterozoic continental breakup. *Journal of Geology*, 109, 493-508.
- FURMAN, T. 1995. MELTING OF METASOMATIZED SUBCONTINENTAL LITHOSPHERE - UNDERSATURATED MAFIC LAVAS FROM RUNGWE, TANZANIA. *Contributions to Mineralogy and Petrology*, 122, 97-115.
- GALAZ E, G., KEPPIE, J. D., LEE, J. K. W. & ORTEGA-RIVERA, A. 2013. A high-pressure folded klippe at Tehuitzingo on the western margin of an extrusion zone, Acatlan Complex, southern Mexico. *Gondwana Research*, 23, 641-660.
- GERAULT, M., HUSSON, L., MILLER, M. S. & HUMPHREYS, E. D. 2015. Flat-slab subduction, topography, and mantle dynamics in southwestern Mexico. *Tectonics*, 34, 1892-1909.
- GODINEZ-URBAN, A., LAWTON, T. F., MOLINA GARZA, R. S., IRIONDO, A., WEBER, B. & LOPEZ-MARTINEZ, M. 2011. Jurassic volcanic and sedimentary rocks of the La Silla and Todos Santos Formations, Chiapas: Record of Nazas arc magmatism and rift-basin formation prior to opening of the Gulf of Mexico. *Geosphere*, 7, 121-144.
- GRIFFIN, W. L., WANG, X., JACKSON, S. E., PEARSON, N. J., O'REILLY, S. Y., XU, X. & ZHOU, X. 2002. Zircon chemistry and magma mixing, SE China: In-situ analysis of Hf isotopes, Tonglu and Pingtan igneous complexes. *Lithos*, 61, 237-269.
- GRIMES, C. B., WOODEN, J. L., CHEADLE, M. J. & JOHN, B. E. 2015. "Fingerprinting" tectono-magmatic provenance using trace elements in igneous zircon. *Contributions to Mineralogy and Petrology*, 170.
- GUERRERO-GARCÍA, J., SILVER, L. T. & ANDERSON, T. H. 1978. Estudios geocronológicos en el Complejo Xolapa. *Sociedad Geológica Mexicana: Dominican Republic, Boletín del Instituto de Estudios de Población y Desarrollo*, 39, 22-23.
- HANDSCHY, J. W., KELLER, G. R. & SMITH, K. J. 1987. THE OUACHITA SYSTEM IN NORTHERN MEXICO. *Tectonics*, 6, 323-330.
- HANS WEDEPOHL, K. 1995. The composition of the continental crust. *Geochimica et Cosmochimica Acta*, 59, 1217-1232.
- HASTIE, A. R., KERR, A. C., PEARCE, J. A. & MITCHELL, S. F. 2007. Classification of altered volcanic island arc rocks using immobile trace elements: Development of the Th-Co discrimination diagram. *Journal of Petrology*, 48, 2341-2357.
- HASTIE, A. R., MITCHELL, S. F., KERR, A. C., MINIFIE, M. J. & MILLAR, I. L. 2011. Geochemistry of rare high-Nb basalt lavas: Are they derived from a mantle wedge metasomatised by slab melts? *Geochimica Et Cosmochimica Acta*, 75, 5049-5072.
- HASTIE, A. R., MITCHELL, S. F., TRELOAR, P. J., KERR, A. C., NEILL, I. & BARFOD, D. N. 2013. Geochemical components in a Cretaceous island arc: The Th/La-(Ce/Ce*)(Nd) diagram and implications for subduction initiation in the inter-American region. *Lithos*, 162, 57-69.
- HATCHER, R. D. 2002. *Alleghanian (Appalachian) orogeny, a product of zipper tectonics: Rotational transpressive continent-continent collision and closing of ancient oceans along irregular margins.*
- HERRMANN, U., NELSON, B. K. & RATSCHBACHER, L. 1994. The origin of a terrane: U/Pb zircon geochronology and tectonic evolution of the Xolapa Complex (Southern Mexico). *Tectonics*, 13, 455-474.
- HEURET, A. & LALLEMAND, S. 2005. Plate motions, slab dynamics and back-arc deformation. *Physics of the Earth and Planetary Interiors*, 149, 31-51.
- HEYDOLPH, K., HOERNLE, K., HAUFF, F., VAN DEN BOGAARD, P., PORTNYAGIN, M., BINDEMAN, I. & GARBE-SCHOENBERG, D. 2012. Along and across arc geochemical

- variations in NW Central America: Evidence for involvement of lithospheric pyroxenite. *Geochimica Et Cosmochimica Acta*, 84, 459-491.
- HOFFMAN, P. F. 1991. DID THE BREAKOUT OF LAURENTIA TURN GONDWANALAND INSIDE-OUT. *Science*, 252, 1409-1412.
- HORNE, G., PUSHKAR, P. & SHAFIQUZZAH, M. 1976. Laramide plutons on the landward continuation of the Bonacca ridge, northern Honduras. *Guatemala, Publicaciones Geológicas del ICAITI*, 5, 84-90.
- IMBERT, P. 2005. The Mesozoic opening of the Gulf of Mexico: Part 1, Evidence for oceanic accretion during and after salt deposition. *Transactions of the 25th Annual GCSSEPM Research Conference: Petroleum systems of divergent continental margins*, 1119-1150.
- IMBERT, P. & PHILLIPPE, Y. 2005. The Mesozoic opening of the Gulf of Mexico: Part 2, Integrating seismic and magnetic data into a general opening model. *Transactions of the 25th Annual GCSSEPM Research Conference: Petroleum systems of divergent continental margins*, 1151-1189.
- IRVINE, T. N. & BARAGAR, W. R. A. 1971. GUIDE TO CHEMICAL CLASSIFICATION OF COMMON VOLCANIC ROCKS. *Canadian Journal of Earth Sciences*, 8, 523-+.
- JACKSON, S. E., PEARSON, N. J., GRIFFIN, W. L. & BELOUSOVA, E. A. 2004. The application of laser ablation-inductively coupled plasma-mass spectrometry to in situ U-Pb zircon geochronology. *Chemical Geology*, 211, 47-69.
- JACQUES, J. M., PRICE, A. D. & BAIN, J. E. 2004. Digital integration of potential fields and geologic data sets for Plate tectonic and basin dynamic modeling -the first step toward identifying new play concepts in the Gulf of Mexico Basin. *The Leading Edge*, 23, 384-389.
- JAVADI, H. R., FOROUTAN, M., ASHTIANI, M. E., ANGEL URBINA, J., SAIDI, A. & FARIDI, M. 2011. Tectonics changes in NW South American Plate and their effect on the movement pattern of the Bocono Fault System during the Merida Andes evolution. *Journal of South American Earth Sciences*, 32, 14-29.
- JOHNSON, S. P., RIVERS, T. & DE WAELE, B. 2005. A review of the Mesoproterozoic to early Palaeozoic magmatic and tectonothermal history of south-central Africa: implications for Rodinia and Gondwana. *Journal of the Geological Society*, 162, 433-450.
- KEMPTON, P. D., PEARCE, J. A., BARRY, T. L., FITTON, J. G., LANGMUIR, C. & CHRISTIE, D. M. 2002. Sr-Nd-Pb-Hf isotope results from ODP Leg 187: Evidence for mantle dynamics of the Australian-Antarctic Discordance and origin of the Indian MORB source. *Geochemistry Geophysics Geosystems*, 3.
- KEPEZHINSKAS, P., DEFANT, M. J. & DRUMMOND, M. S. 1996. Progressive enrichment of island arc mantle by melt-peridotite interaction inferred from Kamchatka xenoliths. *Geochimica Et Cosmochimica Acta*, 60, 1217-1229.
- KEPEZHINSKAS, P. K., DEFANT, M. J. & DRUMMOND, M. S. 1995. Na metasomatism in the island-arc mantle by slab melt-peridotite interaction: Evidence from mantle xenoliths in the north Kamchatka arc. *Journal of Petrology*, 36, 1505-1527.
- KEPPIE, D. J., DOSTAL, J., MURPHY, B. J. & NANCE, D. 2008. Synthesis and tectonic interpretation of the westernmost Paleozoic Variscan orogen in southern Mexico: From rifted Rheic margin to active Pacific margin. *Tectonophysics*, 461, 277-290.
- KEPPIE, J. D. 2004. Terranes of Mexico revisited: A 1.3 billion year odyssey. *International Geology Review*, 46, 765-794.
- KEPPIE, J. D. & DOSTAL, J. 2007. Rift-related basalts in the 1.2-1.3 Ga granulites of the northern Oaxacan Complex, southern Mexico: evidence for a rifted arc on the northwestern margin of Amazonia. *Proceedings of the Geologists Association*, 118, 63-74.

- KEPPIE, J. D., DOSTAL, J., CAMERON, K. L., SOLARI, L. A., ORTEGA-GUTIERREZ, F. & LOPEZ, R. 2003. Geochronology and geochemistry of Grenvillian igneous suites in the northern Oaxacan Complex, southern Mexico: tectonic implications. *Precambrian Research*, 120, 365-389.
- KEPPIE, J. D., DOSTAL, J., ORTEGA-GUTIERREZ, F. & LOPEZ, R. 2001. A Grenvillian arc on the margin of Amazonia: evidence from the southern Oaxacan Complex, southern Mexico. *Precambrian Research*, 112, 165-181.
- KEPPIE, J. D. & MORAN-ZENTENO, D. J. 2005. Tectonic implications of alternative Cenozoic reconstructions for southern Mexico and the Chortis block. *International Geology Review*, 47, 473-491.
- KEPPIE, J. D. & ORTEGA-GUTIERREZ, F. 2010. 1.3-0.9 Ga Oaxaquia (Mexico): Remnant of an arc/backarc on the northern margin of Amazonia. *Journal of South American Earth Sciences*, 29, 21-27.
- KEPPIE, J. D. & RAMOS, V. A. 1999. Odyssey of terranes in the Iapetus and Rheic Oceans during the Paleozoic. In: RAMOS, V. A. (ed.) *Laurentia-Gondwana Connections Before Pangea*, Geological Society of America.
- KIRSCH, M., KEPPIE, J. D., MURPHY, J. B. & LEE, J. K. W. 2013. Arc plutonism in a transtensional regime: the late Palaeozoic Totoltepec pluton, Acatlan Complex, southern Mexico. *International Geology Review*, 55, 263-286.
- KNELLER, E. A., JOHNSON, C. A., KARNER, G. D., EINHORN, J. & QUEFFELE, T. A. 2012. Inverse methods for modeling non-rigid plate kinematics: Application to mesozoic plate reconstructions of the Central Atlantic. *Computers & Geosciences*, 49, 217-230.
- LABAILS, C., OLIVET, J.-L., ASLANIAN, D. & ROEST, W. R. 2010. An alternative early opening scenario for the Central Atlantic Ocean. *Earth and Planetary Science Letters*, 297, 355-368.
- LAGATTA, A. B. 2003. *Arc magma genesis in the Eastern Mexican Volcanic Belt*. Masters Thesis, Columbia University.
- LANG, H. R., BARROS, J. A., CABRAL-CANO, E., DRAPER, G., HARRISON, C. G. A., JANSMA, P. E. & JOHNSON, C. A. 1996. Terrane deletion in northern Guerrero state. *Geofísica Internacional*, 35, 349-359.
- LAPIERRE, H., TARDY, M., COULON, C., HERNANDEZ, E. O., BOURDIER, J. L., REYES, J. M. & FREYDIER, C. 1992. CHARACTERIZATION, GENESIS AND GEODYNAMIC EVOLUTION OF GUERRERO TERRANE (WESTERN MEXICO). *Canadian Journal of Earth Sciences*, 29, 2478-2489.
- LAWLOR, P. J., ORTEGA-GUTIERREZ, F., CAMERON, K. L., OCHOA-CAMARILLO, H., LOPEZ, R. & SAMPSON, D. E. 1999. U-Pb geochronology, geochemistry, and provenance of the Grenvillian Huiznopala Gneiss of Eastern Mexico. *Precambrian Research*, 94, 73-99.
- LAWTON, T. F. & MOLINA GARZA, R. S. 2014. U-Pb geochronology of the type Nazas Formation and superjacent strata, northeastern Durango, Mexico: Implications of a Jurassic age for continental-arc magmatism in north-central Mexico. *Geological Society of America Bulletin*, 126, 1181-1199.
- LE MAITRE, R. W., BATEMAN, P., DUDEK, A., KELLER, J., LAMEYRE LE BAS, M. J., SABINE, P. A., SCHMID, R., SORENSEN, H., STRECKEISEN, A., WOOLLEY, A. R. & ZANETTIN, B. 1989. A classification of igneous rocks and glossary of terms *Blackwell, Oxford*.
- LI, X. H., LI, Z. X., GE, W. C., ZHOU, H. W., LI, W. X., LIU, Y. & WINGATE, M. T. D. 2003a. Neoproterozoic granitoids in South China: crustal melting above a mantle plume at ca 825 Ma? *Precambrian Research*, 122, 45-83.
- LI, X. H., LI, Z. X., ZHOU, H. W., LIU, Y., LIANG, X. R. & LI, W. X. 2003b. SHRIMP U-Pb zircon age, geochemistry and Nd isotope of the Guandaoshan pluton in SW Sichuan: Petrogenesis and tectonic significance. *Science in China Series D-Earth Sciences*, 46, 73-83.

- LI, Z. X., BOGDANOVA, S. V., COLLINS, A. S., DAVIDSON, A., DE WAELE, B., ERNST, R. E., FITZSIMONS, I. C. W., FUCK, R. A., GLADKOCHUB, D. P., JACOBS, J., KARLSTROM, K. E., LU, S., NATAPOV, L. M., PEASE, V., PISAREVSKY, S. A., THRANE, K. & VERNIKOVSKY, V. 2008. Assembly, configuration, and break-up history of Rodinia: A synthesis. *Precambrian Research*, 160, 179-210.
- LI, Z. X., LI, X. H., KINNY, P. D., WANG, J., ZHANG, S. & ZHOU, H. W. 2003c. Geochronology of Neoproterozoic syn-rift magmatism in the Yangtze Craton South China and correlations with other continents: evidence for a mantle superplume that broke up Rodinia. *Precambrian Research*, 122, 85-109.
- LI, Z. X., ZHANG, L. & POWELL, C. M. 1995. South China in Rodinia: part of the missing link between Australia–East Antarctica and Laurentia? *Geology*, 23, 407-410.
- LIMARINO, C. O. & SPALLETTI, L. A. 2006. Paleogeography of the upper Paleozoic basins of southern South America: An overview. *Journal of South American Earth Sciences*, 22, 134-155.
- LOPEZ-RAMOS, E. 1979. *Geología de México*, Edición privada.
- LUDWIG, K. R. 2012. User's manual for Isoplot 3.75; A geochronological toolkit for Microsoft Excel. *Berkeley Geochronology Center Special Publication* 5, 1-75.
- MAC NIOCAILL, C., VAN DER PLUIJM, B. A. & VAN DER VOO, R. 1997. Ordovician paleogeography and evolution of the Iapetus Ocean. *Geology*, 25, 159–162.
- MALFAIT, B. T. & DINKELMAN, M. G. 1972. CIRCUM-CARIBBEAN TECTONIC AND IGNEOUS ACTIVITY AND EVOLUTION OF CARIBBEAN PLATE. *Geological Society of America Bulletin*, 83, 251-272.
- MALOD, J. A., MOUGENOT, D., RAILLARD, S. & MAILLARD, A. 1991. NEW CONSTRAINTS ON THE KINEMATICS OF MADAGASCAR - TECTONIC STRUCTURES OF THE DAVIE RIDGE. *Comptes Rendus De L Academie Des Sciences Serie Ii*, 312, 1639-1646.
- MANTON, W. 1996. The Grenville of Honduras. *The Geological Society of America Abstracts with Programs*, 28, 493.
- MANTON, W. & MANTON, R. 1984. Geochronology and Late Cretaceous–Tertiary tectonism of Honduras. *Tegucigalpa, Honduras, Direccion General de Minas e Hidrocarburos*, 55.
- MARKEY, R. 1995. Mapa Geológica de Honduras, Hoja de Moroceli (Geologic Map of Honduras, Morocelli sheet). *Tegucigalpa, Honduras, Instituto Geográfico Nacional, escala 1:50,000*.
- MARTENS, U., WEBER, B. & VALENCIA, V. A. 2010. U/Pb geochronology of Devonian and older Paleozoic beds in the southeastern Maya block, Central America: Its affinity with peri-Gondwanan terranes. *Geological Society of America Bulletin*, 122, 815-829.
- MARTINI, M., FERRARI, L., LOPEZ-MARTINEZ, M., CERCA-MARTINEZ, M., VALENCIA, V. A. & SERRANO-DURAN, L. 2009. Cretaceous-Eocene magmatism and Laramide deformation in southwestern Mexico: No role for terrane accretion. In: KAY, S. M., RAMOS, V. A. & DICKINSON, W. R. (eds.) *Backbone of the Americas: Shallow Subduction, Plateau Uplift, and Ridge and Terrane Collision*.
- MARTINI, M., MORI, L., SOLARI, L. & CENTENO-GARCIA, E. 2011. Sandstone Provenance of the Arperos Basin (Sierra de Guanajuato, Central Mexico): Late Jurassic-Early Cretaceous Back-Arc Spreading as the Foundation of the Guerrero Terrane. *Journal of Geology*, 119, 597-617.
- MARTINI, M., SOLARI, L. & LOPEZ-MARTINEZ, M. 2014. Correlating the Arperos Basin from Guanajuato, central Mexico, to Santo Tomas, southern Mexico: Implications for the paleogeography and origin of the Guerrero terrane. *Geosphere*, 10, 1385-1401.
- MARTON, G. & BUFFLER, R. T. 1994. Jurassic reconstruction of the Gulf of Mexico basin. *International Geology Review*, 36, 545-586.

- MARTON, G. L. & BUFFLER, R. T. 1999. *Jurassic-Early Cretaceous tectono-paleogeographic evolution of the southeastern Gulf of Mexico Basin. Sedimentary Basins of the World*, Amsterdam, Elsevier Science.
- MARZOLI, A., RENNE, P. R., PICCIRILLO, E. M., ERNESTO, M., BELLINI, G. & DE MIN, A. 1999. Extensive 200-million-year-old continental flood basalts of the Central Atlantic Magmatic Province. *Science*, 284, 616-618.
- MATTE, P. 2001. The Variscan collage and orogeny (480-290 Ma) and the tectonic definition of the Armorica microplate: a review. *Terra Nova*, 13, 122-128.
- MATTEINI, M., JUNGES, S. L., DANTAS, E. L., PIMENTEL, M. M. & BUEHN, B. 2010. In situ zircon U-Pb and Lu-Hf isotope systematic on magmatic rocks: Insights on the crustal evolution of the Neoproterozoic Goias Magmatic Arc, Brasilia belt, Central Brazil. *Gondwana Research*, 17, 1-12.
- MCKERROW, W. S., MAC NIOCAILL, C. & DEWEY, J. F. 2000. The Caledonian Orogeny redefined. *Journal of the Geological Society*, 157, 1149-1154.
- MCMENAMIN, M. A. S. & MCMENAMIN, D. L. S. 1990. The Emergence of Animals: The Cambrian Breakthrough. 217.
- MEDARD, E., SCHMIDT, M. W., SCHIANO, P. & OTTOLINI, L. 2006. Melting of amphibole-bearing wehrlites: An experimental study on the origin of ultra-calcic nepheline-normative melts. *Journal of Petrology*, 47, 481-504.
- MEERT, J. G. & VANDERVOO, R. 1996. Paleomagnetic and Ar-40/Ar-39 study of the Sinyai dolerite, Kenya: Implications for Gondwana assembly. *Journal of Geology*, 104, 131-142.
- MENDOZA-ROSALES, C. C., CENTENO-GARCIA, E., SILVA-ROMO, G., CAMPOS-MADRIGAL, E. & PABLO BERNAL, J. 2010. Barremian rift-related turbidites and alkaline volcanism in southern Mexico and their role in the opening of the Gulf of Mexico. *Earth and Planetary Science Letters*, 295, 419-434.
- MEXICANO, S. G. 2001. *Carta Geològico-Minera Orizaba E14-6, Veracruz, Puebla y Oaxaca*, 1:250000.
- MOLINA-GARZA, R. S., VAN DER VOO, R. & URRUTIA-FUCUGUACHI, J. 1992. Paleomagnetism of the Chiapas massif, southern Mexico: Evidence for rotation of the Maya block and implications for the opening of the Gulf of Mexico. *Geological Society of America Bulletin*, 104, 1156-1168.
- MOLINA GARZA, R. S. & GEISSMAN, J. W. 1999. Paleomagnetic data from the Caborca terrane, Mexico: Implications for Cordilleran tectonics and the Mojave-Sonora megashear hypothesis. *Tectonics*, 18, 293-325.
- MOORES, E. M. 1991. Southwest U.S.–East Antarctic (SWEAT) connection: a hypothesis. *Geology*, 19, 425-428.
- NANCE, R. D., GUTIERREZ-ALONSO, G., DUNCAN KEPPIE, J., LINNEMANN, U., MURPHY, J. B., QUESADA, C., STRACHAN, R. A. & WOODCOCK, N. H. 2010. Evolution of the Rheic Ocean. *Gondwana Research*, 17, 194-222.
- NANCE, R. D., MILLER, B. V., KEPPIE, J. D., MURPHY, J. B. & DOSTA, J. 2006. Acatlan complex, Southern Mexico: Record spanning the assembly and breakup of Pangea. *Geology*, 34, 857-860.
- NASDALA, L., WENZEL, M., VAVRA, G., IRMER, G., WENZEL, T. & KOBER, B. 2001. Metamictisation of natural zircon: accumulation versus thermal annealing of radioactivity-induced damage. *Contributions to Mineralogy and Petrology*, 141, 125-144.
- NAVARRO-SANTILLAN, D., SOUR-TOVAR, F. & CENTENO-GARCIA, E. 2002. Lower Mississippian (Osagean) brachiopods from the Santiago Formation, Oaxaca, Mexico: stratigraphic and tectonic implications. *Journal of South American Earth Sciences*, 15, 327-336.

- NIU, Y. L., COLLERSON, K. D., BATIZA, R., WENDT, J. I. & REGELOUS, M. 1999. Origin of enriched-type mid-ocean ridge basalt at ridges far from mantle plumes: The East Pacific Rise at 11 degrees 20 ' N. *Journal of Geophysical Research-Solid Earth*, 104, 7067-7087.
- NOWELL, G. M., KEMPTON, P. D., NOBLE, S. R., FITTON, J. G., SAUNDERS, A. D., MAHONEY, J. J. & TAYLOR, R. N. 1998. High precision Hf isotope measurements of MORB and OIB by thermal ionisation mass spectrometry: insights into the depleted mantle. *Chemical Geology*, 149, 211-233.
- OFTEDAL, B. T., ANDRESEN, A. & MULLER, R. 2005. *Early Triassic syn-rift sedimentation at hold with hope, Northeast Greenland*.
- ORTEGA-GUTIERREZ, F. 1984. Evidence of Precambrian evaporites in the Oaxacan granulite complex of southern Mexico. *Precambrian Research*, 23, 377-393.
- ORTEGA-GUTIERREZ, F., ELIAS-HERRERA, M., MORAN-ZENTENO, D. J., SOLARI, L., LUNA-GONZALEZ, L. & SCHAAF, P. 2014. A review of batholiths and other plutonic intrusions of Mexico. *Gondwana Research*, 26, 834-868.
- ORTEGA-GUTIERREZ, F., RUIZ, J. & CENTENO-GARCIA, E. 1995. Oaxaquia, a Proterozoic microcontinent accreted to North America during the late Paleozoic. *Geology*, 23, 1127-1130.
- ORTEGA-OBREGON, C., DUNCAN KEPPIE, J., MURPHY, J. B., LEE, J. K. W. & ORTEGA-RIVERA, A. 2009. Geology and geochronology of Paleozoic rocks in western Acatlan Complex, southern Mexico: Evidence for contiguity across an extruded high-pressure belt and constraints on Paleozoic reconstructions. *Geological Society of America Bulletin*, 121, 1678-1694.
- ORTEGA-OBREGÓN, C., KEPPIE, J. D., SOLARI, L. A., ORTEGA-GUTIÉRREZ, F., DOSTAL, J., LOPEZ, R., ORTEGA-RIVERA, A. & LEE, J. W. K. 2003. Geochronology and geochemistry of the 917 Ma, calc-alkaline Etlá granitoid pluton (Oaxaca, southern Mexico): evidence of post-Grenvillian subduction along the northern margin of Amazonia. *International Geology Review* 45, 596–610.
- ORTEGA-OBREGON, C., SOLARI, L., GOMEZ-TUENA, A., ELIAS-HERRERA, M., ORTEGA-GUTIERREZ, F. & MACIAS-ROMO, C. 2014. Permian-Carboniferous arc magmatism in southern Mexico: U-Pb dating, trace element and Hf isotopic evidence on zircons of earliest subduction beneath the western margin of Gondwana. *International Journal of Earth Sciences*, 103, 1287-1300.
- PAULSSON, O. & ANDREASSON, P. G. 2002. Attempted break-up of Rodinia at 850 Ma: geochronological evidence from the Seve-Kalak Superterrane, Scandinavian Caledonides. *Journal of the Geological Society*, 159, 751-761.
- PEARCE, J. 1996a. Sources and settings of granitic rocks. *Episodes*, 19, 120-125.
- PEARCE, J. A. 1996b. A user's guide to basalt discrimination diagrams. in Wyman, D.A., ed., *Trace element geochemistry of volcanic rocks: applications for massive sulphide exploration: Geological Association of Canada, short course notes*, 12, 34.
- PEARCE, J. A., HARRIS, N. B. W. & TINDLE, A. G. 1984. TRACE-ELEMENT DISCRIMINATION DIAGRAMS FOR THE TECTONIC INTERPRETATION OF GRANITIC-ROCKS. *Journal of Petrology*, 25, 956-983.
- PEARCE, J. A. & PEATE, D. W. 1995. TECTONIC IMPLICATIONS OF THE COMPOSITION OF VOLCANIC ARC MAGMAS. *Annual Review of Earth and Planetary Sciences*, 23, 251-285.
- PEASE, V., DALY, J. S., ELMING, S. A., KUMPULAINEN, R., MOCZYDLOWSKA, A., PUCHKOV, V., ROBERTS, D., SAINTOT, A. & STEPHENSON, R. 2008. Baltica in the Cryogenian, 850-630 Ma. *Precambrian Research*, 160, 46-65.

- PECCERILLO, A. & TAYLOR, S. R. 1976. GEOCHEMISTRY OF EOCENE CALC-ALKALINE VOLCANIC-ROCKS FROM KASTAMONU AREA, NORTHERN TURKEY. *Contributions to Mineralogy and Petrology*, 58, 63-81.
- PEREZ-GUTIERREZ, R., SOLARI, L. A., GOMEZ-TUENA, A. & VALENCIA, V. A. 2009. The Cuicateco terrane: Upper Cretaceous oceanic basin with subduction influence in southern Mexico? New structural, geochemical and geochronological data. *Revista Mexicana De Ciencias Geologicas*, 26, 222-242.
- PINDELL, J. & DEWEY, J. F. 1982. PERMO-TRIASSIC RECONSTRUCTION OF WESTERN PANGEA AND THE EVOLUTION OF THE GULF OF MEXICO CARIBBEAN REGION. *Tectonics*, 1, 179-211.
- PINDELL, J. & KENNAN, L. 2001. Kinematic Evolution of the Gulf of Mexico and Caribbean. *GCSSEPM Foundation 21st Annual Research Conference Transactions. Petroleum Systems of Deep-Water Basins*, 193-220.
- PINDELL, J., KENNAN, L., MARESCH, W. V., STANEK, K. P., DRAPER, G. & HIGGS, R. 2005. Plate-kinematics and crustal dynamics of circumCaribbean arc-continent interactions, and tectonic controls on basin development in Proto-Caribbean margins. *Caribbean-South American Plateinteractions, Venezuela. Geological Society of America, Special Paper*, 394, 7-52.
- PINDELL, J. L. 1985. ALLEGHENIAN RECONSTRUCTION AND SUBSEQUENT EVOLUTION OF THE GULF OF MEXICO, BAHAMAS, AND PROTO-CARIBBEAN. *Tectonics*, 4, 1-39.
- PINDELL, J. L., CANDE, S. C., PITMAN, W. C., ROWLEY, D. B., DEWEY, J. F., LABRECQUE, J. & HAXBY, W. 1988. A PLATE-KINEMATIC FRAMEWORK FOR MODELS OF CARIBBEAN EVOLUTION. *Tectonophysics*, 155, 121-138.
- PINDELL, J. L. & KENNAN, L. 2009. Tectonic evolution of the Gulf of Mexico, Caribbean and northern South America in the mantle reference frame: an update. *Origin and Evolution of the Caribbean Plate*, 328, 1-55.
- PIQUE, A. & SKEHAN, J. W. 1992. LATE PALEOZOIC OROGENIES IN WESTERN AFRICA AND EASTERN NORTH-AMERICA - THE DIACHRONOUS CLOSURE OF THEIR OCEAN. *Tectonics*, 11, 392-404.
- PISAREVSKY, S. A., NATAPOV, L. M., DONSKAYA, T. V., GLADKOCHUB, D. P. & VERNIKOVSKY, V. A. 2008. Proterozoic Siberia: A promontory of Rodinia. *Precambrian Research*, 160, 66-76.
- PLANK, T. & LANGMUIR, C. H. 1998. The chemical composition of subducting sediment and its consequences for the crust and mantle. *Chemical Geology*, 145, 325-394.
- POOLE, F. G., BOUCOT, A. J., AMAYA-MARTINEZ, R., SANDBERG, C. A., HARRIS, A. G. & PAGE, W. R. 2003. Early Devonian brachiopods in west-central Sonora indicate depositional continuity along southern margin of Laurentia. *Geological Society of America Abstracts with Programs*, 35, 13-14.
- POOLE, F. G., PERRY, W. J., MADRID, R. J. & AMAYA-MARTINEZ, R. 2005. Tectonic synthesis of the Ouachita-Marathon-Sonora orogenic margin of southern Laurentia: Stratigraphic and structural implications for timing of deformational events and plate-tectonics model *Geological Society of America Special Paper*, 293, 543-596.
- PRAVE, A. R. 1996. Tale of three cratons: Tectonostratigraphic anatomy of the Damara orogen in northwestern Namibia and the assembly of Gondwana. *Geology*, 24, 1115-1118.
- PROUTEAU, G., SCAILLET, B., PICHAVANT, M. & MAURY, R. 2001. Evidence for mantle metasomatism by hydrous silicic melts derived from subducted oceanic crust. *Nature*, 410, 197-200.
- RADHAKRISHNA, T. & MATHEW, J. 1996. Late Precambrian (850-800 Ma) palaeomagnetic pole for the south Indian shield from the Harohalli alkaline dykes: Geotectonic implications for Gondwana reconstructions. *Precambrian Research*, 80, 77-87.

- RAPP, R. P., SHIMIZU, N., NORMAN, M. D. & APPLGATE, G. S. 1999. Reaction between slab-derived melts and peridotite in the mantle wedge: experimental constraints at 3.8 GPa. *Chemical Geology*, 160, 335-356.
- RATSCHBACHER, L., FRANZ, L., MIN, M., BACHMANN, R., MARTENS, U., STANEK, K., STUEBNER, K., NELSON, B. K., HERRMANN, U., WEBER, B., LOPEZ-MARTINEZ, M., JONCKHEERE, R., SPERNER, B., TICHOMIROVA, M., MCWILLIAMS, M. O., GORDON, M., MESCHEDÉ, M. & BOCK, P. 2009. The North American-Caribbean Plate boundary in Mexico-Guatemala-Honduras. *Origin and Evolution of the Caribbean Plate*, 328, 219-293.
- REGÉLOUS, M., NIU, Y. L., WENDT, J. I., BATIZA, R., GREIG, A. & COLLERSON, K. D. 1999. Variations in the geochemistry of magmatism on the East Pacific Rise at 10 degrees 30' N since 800 ka. *Earth and Planetary Science Letters*, 168, 45-63.
- RILEY, T. R., MILLAR, I. L., WATKEYS, M. K., CURTIS, M. L., LEAT, P. T., KLAUSEN, M. B. & FANNING, C. M. 2004. U-Pb zircon (SHRIMP) ages for the Lebombo rhyolites, South Africa: refining the duration of Karoo volcanism. *Journal of the Geological Society*, 161, 547-550.
- ROBERTS, S. J. & RUIZ, J. 1989. GEOCHEMISTRY OF EXPOSED GRANULITE FACIES TERRAINS AND LOWER CRUSTAL XENOLITHS IN MEXICO. *Journal of Geophysical Research-Solid Earth and Planets*, 94, 7961-7974.
- ROGERS, R. D., MANN, P. & EMMET, P. A. 2007. Tectonic terranes of the Chortis block based on integration of regional aeromagnetic and geologic data. *The Geological Society of America Special Paper*, 428, 65-88.
- ROSS, C. A. 1986. Paleozoic evolution of southern margin of Permian basin. *Geological Society of America Bulletin*, 97, 536-554.
- RUBATTO, D. & HERMANN, J. 2007. Zircon behaviour in deeply subducted rocks. *Elements*, 3, 31-35.
- RUDNICK, R. L. & FOUNTAIN, D. M. 1995. Nature and composition of the continental crust: A lower crustal perspective. *Reviews of Geophysics*, 33, 267-309.
- RYAN, K. A. & WILLIAMS, D. M. 2007. Testing the reliability of discrimination diagrams for determining the tectonic depositional environment of ancient sedimentary basins. *Chemical Geology*, 242, 103-125.
- SACCANI, E. 2015. A new method of discriminating different types of post-Archean ophiolitic basalts and their tectonic significance using Th-Nb and Ce-Dy-Yb systematics. *Geoscience Frontiers*, 6, 481-501.
- SAHABI, M., ASLANIAN, D. & OLIVET, J. L. 2004. A new starting point for the history of the central Atlantic. *Comptes Rendus Geoscience*, 336, 1041-1052.
- SALTERS, V. J. M. & STRACKE, A. 2004. Composition of the depleted mantle. *Geochemistry Geophysics Geosystems*, 5.
- SALVADOR, A. 1987. LATE TRIASSIC-JURASSIC PALEOGEOGRAPHY AND ORIGIN OF GULF OF MEXICO BASIN. *Aapg Bulletin-American Association of Petroleum Geologists*, 71, 419-451.
- SAMSON, S. D. 2001. Timing of Alleghanian magmatism revisited. *Geological Society of America Abstracts with Programs*, 33, 7.
- SCHELLART, W. P., LISTER, G. S. & JESSELL, M. W. 2002. Analogue modeling of arc and backarc deformation in the New Hebrides arc and North Fiji Basin. *Geology*, 30, 311-314.
- SCHERER, E. E., CAMERON, K. L., JOHNSON, C. M., BEARD, B. L., BAROVICH, K. M. & COLLERSON, K. D. 1997. Lu-Hf geochronology applied to dating Cenozoic events affecting lower crustal xenoliths from Kilbourne Hole, New Mexico. *Chemical Geology*, 142, 63-78.

- SCHOUTEN, H. & KLITGORD, K. D. 1994. Mechanistic solutions to the opening of the Gulf of Mexico. *Geology*, 22, 507-510.
- SCHULZE, C. 2011. Petrología y geoquímica de las rocas del área de Pluma Hidalgo, Oaxaca e implicaciones tectónicas para el Proterozoico de Oaxaca: . *Universidad Autónoma Nacional de México, México, PhD thesis*, 311 pp.
- SEDLOCK, R. L., ORTEGA-GUTIÉRREZ, F. & SPEED, R. C. 1993. *Tectonostratigraphic terranes and tectonic evolution of Mexico*, Boulder, Colo.
- SEMPERE, T., CARLIER, G., SOLER, P., FORNARI, M., CARLOTTO, V., JACAY, J., ARISPE, O., NERAUDEAU, D., CARDENAS, J., ROSAS, S. & JIMENEZ, N. 2002. Late Permian-Middle Jurassic lithospheric thinning in Peru and Bolivia, and its bearing on Andean-age tectonics. *Tectonophysics*, 345, 153-181.
- SILVA-ROMO, G., ARELLANO-GIL, J., MENDOZA-ROSALES, C. & NIETO-OBREGON, J. 2000. A submarine fan in the Mesa Central, Mexico. *Journal of South American Earth Sciences*, 13, 429-442.
- SIMS, K. W. W., DEPAOLO, D. J., MURRELL, M. T., BALDRIDGE, W. S., GOLDSTEIN, S., CLAGUE, D. & JULL, M. 1999. Porosity of the melting zone and variations in the solid mantle upwelling rate beneath Hawaii: Inferences from U-238-Th-230-Ra-226 and U-235-Pa-231 disequilibria. *Geochimica Et Cosmochimica Acta*, 63, 4119-4138.
- SIMS, K. W. W., DEPAOLO, D. J., MURRELL, M. T., BALDRIDGE, W. S., GOLDSTEIN, S. J. & CLAGUE, D. A. 1995. MECHANISMS OF MAGMA GENERATION BENEATH HAWAII AND MID-OCEAN RIDGES - URANIUM/THORIUM AND SAMARIUM/NEODYMIUM ISOTOPIC EVIDENCE. *Science*, 267, 508-512.
- SOLARI, L., DOSTAL, J., ORTEGA-GUTIÉRREZ, F. & KEPPIE, J. D. 2001. The 275 Ma arc-related La Carbonera stock in the northern Oaxacan Complex of southern Mexico: U-Pb geochronology and geochemistry. *Revista Mexicana de Ciencias Geológicas*, 18, 149-161.
- SOLARI, L. A., DE LEON, R. T., PINEDA, G. H., SOLE, J., SOLIS-PICHARDO, G. & HERNANDEZ-TREVINO, T. 2007. Tectonic significance of Cretaceous-Tertiary magmatic and structural evolution of the northern margin of the Xolapa Complex, Tierra Colorada area, southern Mexico. *Geological Society of America Bulletin*, 119, 1265-1279.
- SOLARI, L. A., GOMEZ-TUENA, A., ORTEGA-GUTIERREZ, F. & ORTEGA-OBREGON, C. 2011. The Chuacus Metamorphic Complex, central Guatemala: geochronological and geochemical constraints on its Paleozoic - Mesozoic evolution. *Geologica Acta*, 9, 329-+.
- SOLARI, L. A., KEPPIE, J. D., ORTEGA-GUTIÉRREZ, F., CAMERON, K. L., LOPEZ, R. & HAMES, W. E. 2003. 990 and 1100 Ma Grenvillian tectonothermal events in the northern Oaxacan Complex, southern Mexico: roots of an orogen. *Tectonophysics*, 365, 257-282.
- SOLARI, L. A., ORTEGA-GUTIERREZ, F., ELIAS-HERRERA, M., ORTEGA-OBREGON, C., MACIAS-ROMO, C. & REYES-SALAS, M. 2014. Detrital provenance of the Grenvillian Oaxacan Complex, southern Mexico: a zircon perspective. *International Journal of Earth Sciences*, 103, 1301-1315.
- SOLARI, L. A., ORTEGA-GUTIERREZ, F., ELIAS-HERRERA, M., SCHAAF, P., NORMAN, M., TORRES DE LEON, R., ORTEGA-OBREGON, C., CHIQUIN, M. & MORAN ICAL, S. 2009. U-Pb zircon geochronology of Palaeozoic units in Western and Central Guatemala: insights into the tectonic evolution of Middle America. *Origin and Evolution of the Caribbean Plate*, 328, 295-313.
- SORENSEN, S. S. & GROSSMAN, J. N. 1989. ENRICHMENT OF TRACE-ELEMENTS IN GARNET AMPHIBOLITES FROM A PALEO-SUBDUCTION ZONE - CATALINA SCHIST, SOUTHERN-CALIFORNIA. *Geochimica Et Cosmochimica Acta*, 53, 3155-3177.

- SPIKINGS, R., COCHRANE, R., VILLAGOMEZ, D., VAN DER LELIJ, R., VALLEJO, C., WINKLER, W. & BEATE, B. 2015. The geological history of northwestern South America: from Pangaea to the early collision of the Caribbean Large Igneous Province (290-75 Ma). *Gondwana Research*, 27, 95-139.
- STEIN, M. & GOLDSTEIN, S. L. 1996. From plume head to continental lithosphere in the Arabian-Nubian shield. *Nature*, 382, 773-778.
- STEWART, J. H., BLODGETT, R. B., BOUCOT, A. J., CARTER, J. L. & LOPEZ, R. 1999. Exotic Paleozoic strata of Gondwanan provenance near Ciudad Victoria, Tamaulipas, Mexico. *Geological Society of America Special Paper*, 336, 227-245.
- STOLFOVA, K. & SHANNON, P. M. 2009. Permo-Triassic development from Ireland to Norway: basin architecture and regional controls. *Geological Journal*, 44, 652-676.
- SUN, S.-S. & MCDONOUGH, W. F. 1989. Chemical and isotopic systematics of oceanic basalts: implications for mantle composition and processes. *Geological Society, London, Special Publications*, 42, 313-345.
- TALAVERA-MENDOZA, O., RUIZ, J., CORONA-CHAVEZ, P., GEHRELS, G. E., SARMIENTO-VILLAGRANA, A., LUIS GARCIA-DIAZ, J. & SALGADO-SOUTO, S. A. 2013. Origin and provenance of basement metasedimentary rocks from the Xolapa Complex: New constraints on the Chortis-southern Mexico connection. *Earth and Planetary Science Letters*, 369, 188-199.
- TALAVERA-MENDOZA, O., RUIZ, J., GEHRELS, G. E., MEZA-FIGUEROA, D. M., VEGA-GRANILLO, R. & CAMPA-URANGA, M. F. 2005. U-Pb geochronology of the Acatlan Complex and implications for the Paleozoic paleogeography and tectonic evolution of southern Mexico. *Earth and Planetary Science Letters*, 235, 682-699.
- TALAVERA-MENDOZA, O., RUIZ, J., GEHRELS, G. E., VALENCIA, V. A. & CENTENO-GARCIA, E. 2007. Detrital zircon U/Pb geochronology of southern Guerrero and western Mixteca arc successions (southern Mexico): New insights for the tectonic evolution of southwestern North America during the late Mesozoic. *Geological Society of America Bulletin*, 119, 1052-1065.
- TARDY, M., LAPIERRE, H., FREYDIER, C., COULON, C., GILL, J. B., DELEPINAY, B. M., BECK, C., MARTINEZ, J., TALAVERA, O., ORTIZ, E., STEIN, G., BOURDIER, J. L. & YTA, M. 1994. THE GUERRERO SUSPECT TERRANE (WESTERN MEXICO) AND COEVAL ARC TERRANES (THE GREATER-ANTILLES AND THE WESTERN-CORDILLERA-OF-COLOMBIA) - A LATE MESOZOIC INTRAOCEANIC ARC ACCRETED TO CRATONAL AMERICA DURING THE CRETACEOUS. *Tectonophysics*, 230, 49-73.
- TATE, M. C. & CLARKE, D. B. 1995. Petrogenesis and regional tectonic significance of Late Devonian mafic intrusions in the Meguma Zone, Nova Scotia. *Canadian Journal of Earth Sciences*, 32, 1883-1898.
- TAYLOR, S. R. & MCLENNAN, S. M. 1985. *The continental crust: Its composition and evolution*.
- TEKLAY, M., KRONER, A. & MEZGER, K. 2002. Enrichment from plume interaction in the generation of Neoproterozoic arc rocks in northern Eritrea: implications for crustal accretion in the southern Arabian-Nubian Shield. *Chemical Geology*, 184, 167-184.
- TORRES-DE LEON, R., SOLARI, L. A., ORTEGA-GUTIERREZ, F. & MARTENS, U. 2012. THE CHORTIS BLOCK-SOUTHWESTERN MEXICO CONNECTIONS: U-Pb ZIRCON GEOCHRONOLOGY CONSTRAINTS. *American Journal of Science*, 312, 288-313.
- TORRES-VARGAS, G., MURILLO-MUNETON, G. & GRAJALES-NISHIMURA, M. 1986. Estudio petrográfico y radiométrico de la porción límite entre los complejos Acatlán y Oaxaqueño. *en VII Convención Geológica Nacional, México*, 148-149.
- TORSVIK, T. H., SMETHURST, M. A., MEERT, J. G., VANDERVOO, R., MCKERROW, W. S., BRASIER, M. D., STURT, B. A. & WALDERHAUG, H. J. 1996. Continental break-up and

- collision in the Neoproterozoic and Palaeozoic - A tale of Baltica and Laurentia. *Earth-Science Reviews*, 40, 229-258.
- TROMPETTE, R. 1997. Neoproterozoic (similar to 600 Ma) aggregation of western Gondwana: A tentative scenario. *Precambrian Research*, 82, 101-112.
- TURNER, S., BEIER, C., NIU, Y. & COOK, C. 2011. U-Th-Ra disequilibria and the extent of off-axis volcanism across the East Pacific Rise at 9 degrees 30 ' N, 10 degrees 30 ' N, and 11 degrees 20 ' N. *Geochemistry Geophysics Geosystems*, 12.
- VALENTINE, J. W. & MOORES, E. M. 1970. PLATE-TECTONIC REGULATION OF FAUNAL DIVERSITY AND SEA LEVEL - A MODEL. *Nature*, 228, 657-&.
- VEGA-GRANILLO, R., CALMUS, T., MEZA-FIGUEROA, D., RUIZ, J., TALAVERA-MENDOZA, O. & LOPEZ-MARTINEZ, M. 2009. Structural and tectonic evolution of the Acatlan Complex, southern Mexico: Its role in the collisional history of Laurentia and Gondwana. *Tectonics*, 28.
- VEGA-GRANILLO, R., TALAVERA-MENDOZA, O., MEZA-FIGUEROA, D., RUIZ, J., GEHRELS, G. E., LOPEZ-MARTINEZ, M. & DE LA CRUZ-VARGAS, J. C. 2007. Pressure-temperature-time evolution of Paleozoic high-pressure rocks of the Acatlan Complex (southern Mexico): Implications for the evolution of the Iapetus and Rheic Oceans. *Geological Society of America Bulletin*, 119, 1249-1264.
- VENABLE, M. 1994. *A geological, tectonic, and metallongenetic evaluation of the Siuana terrane (Nicaragua)*. Ph.D. dissertation, University of Arizona.
- VERVOORT, J. D., PATCHETT, P. J., ALBAREDE, F., BLICHERT-TOFT, J., RUDNICK, R. & DOWNES, H. 2000. Hf-Nd isotopic evolution of the lower crust. *Earth and Planetary Science Letters*, 181, 115-129.
- VERVOORT, J. D., PLANK, T. & PRYTULAK, J. 2011. The Hf-Nd isotopic composition of marine sediments. *Geochimica Et Cosmochimica Acta*, 75, 5903-5926.
- VIELE, G. W. & THOMAS, W. A. 1989. Tectonic synthesis of the Ouachita orogenic belt. In: HATCHER, R. D., JR., ET AL., EDS (ed.) *The Appalachian-Ouachita orogenic belt in the United States: Boulder, Colorado, Geological Society of America, Geology of North America*.
- VILLAGOMEZ, D., SPIKINGS, R., MAGNA, T., KAMMER, A., WINKLER, W. & BELTRAN, A. 2011. Geochronology, geochemistry and tectonic evolution of the Western and Central cordilleras of Colombia. *Lithos*, 125, 875-896.
- VINASCO, C. J., CORDANI, U. G., GONZALEZ, H., WEBER, M. & PELAEZ, C. 2006. Geochronological, isotopic, and geochemical data from Permo-Triassic granitic gneisses and granitoids of the Colombian Central Andes. *Journal of South American Earth Sciences*, 21, 355-371.
- WATSON, E. B. & HARRISON, T. M. 1983. ZIRCON SATURATION REVISITED - TEMPERATURE AND COMPOSITION EFFECTS IN A VARIETY OF CRUSTAL MAGMA TYPES. *Earth and Planetary Science Letters*, 64, 295-304.
- WEAVER, B. L. 1991. THE ORIGIN OF OCEAN ISLAND BASALT END-MEMBER COMPOSITIONS - TRACE-ELEMENT AND ISOTOPIC CONSTRAINTS. *Earth and Planetary Science Letters*, 104, 381-397.
- WEBER, B., CAMERON, K. L., OSORIO, M. & SCHAAP, P. 2005. A late permian tectonothermal event in Grenville crust of the southern Maya terrane: U-Pb zircon ages from the Chiapas massif, southeastern Mexico. *International Geology Review*, 47, 509-529.
- WEBER, B. & KOHLER, H. 1999. Sm-Nd, Rb-Sr and U-Pb geochronology of a Grenville terrane in southern Mexico: origin and geologic history of the Guichicovi complex. *Precambrian Research*, 96, 245-262.
- WEBER, B., SCHAAP, P., VALENCIA, V. A., IRIONDO, A. & ORTEGA-GUTIERREZ, F. 2006. Provenance ages of late Paleozoic sandstones (Santa Rosa Formation) from the

- Maya block, SE Mexico. Implications on the tectonic evolution of western Pangea. *Revista Mexicana De Ciencias Geologicas*, 23, 262-276.
- WEBER, B., SCHERER, E. E., SCHULZE, C., VALENCIA, V. A., MONTECINOS, P., MEZGER, K. & RUIZ, J. 2010. U-Pb and Lu-Hf isotope systematics of lower crust from central-southern Mexico - Geodynamic significance of Oaxaquia in a Rodinia Realm. *Precambrian Research*, 182, 149-162.
- WEBER, B. & SCHULZE, C. H. 2014. Early Mesoproterozoic (> 1.4 Ga) ages from granulite basement inliers of SE Mexico and their implications on the Oaxaquia concept - Evidence from U-Pb and Lu-Hf isotopes on zircon. *Revista Mexicana De Ciencias Geologicas*, 31, 377-394.
- WEBER, B., VALENCIA, V. A., SCHAAF, P. & ORTEGA-GUTIERREZ, F. 2009. Detrital zircon ages from the Lower Santa Rosa Formation, Chiapas: implications on regional Paleozoic stratigraphy. *Revista Mexicana De Ciencias Geologicas*, 26, 260-272.
- WEBER, B., VALENCIA, V. A., SCHAAF, P., POMPA-MERA, V. & RUIZ, J. 2008. Significance of Provenance Ages from the Chiapas Massif Complex (Southeastern Mexico): Redefining the Paleozoic Basement of the Maya Block and Its Evolution in a Peri-Gondwanan Realm. *Journal of Geology*, 116, 619-639.
- WEIL, A. B., VAN DER VOO, R., MAC NIOCAILL, C. & MEERT, J. G. 1998. The Proterozoic supercontinent Rodinia: paleomagnetically derived reconstructions for 1100 to 800 Ma. *Earth and Planetary Science Letters*, 154, 13-24.
- WEILAND, T. J., SUAYAH, I. B. & FINCH, R. C. 1992. PETROLOGIC, STRATIGRAPHIC AND TECTONIC SIGNIFICANCE OF MESOZOIC VOLCANIC-ROCKS IN THE RIO-WAMPU AREA, EASTERN HONDURAS. *Journal of South American Earth Sciences*, 6, 309-325.
- WILLIAMS, I. S. & MCBIRNEY, A. R. 1969. Volcanic history of Honduras. *Berkeley, University of California Press, University of California Publications in Geological Sciences*, 85, 1-99.
- WILSON, M. 1989. *Igneous Petrogenesis*, Springer Netherlands.
- WINCHESTER, J. & FLOYD, P. 1977. Geochemical discrimination of different magma series and their differentiation products using immobile elements. *Chemical geology*, 20, 325-343.
- WINGATE, M. T. D., CAMPBELL, I. H., COMPSTON, W. & GIBSON, G. M. 1998. Ion microprobe U-Pb ages for Neoproterozoic basaltic magmatism in southcentral Australia and implications for the breakup of Rodinia. *Precambrian Research*, 87, 135-159.
- WINGATE, M. T. D., PISAREVSKY, S. A. & EVANS, D. A. D. 2002. Rodinia connections between Australia and Laurentia: NoSWEAT, no AUSWUS? *Terra Nova*, 14, 121-128.
- WOODHEAD, J. D., HERGT, J. M., DAVIDSON, J. P. & EGGINS, S. M. 2001. Hafnium isotope evidence for 'conservative' element mobility during subduction zone processes. *Earth and Planetary Science Letters*, 192, 331-346.
- WOOLLEY, A. R., BARR, M. W. C., DIN, V. K., JONES, G. C., WALL, F. & WILLIAMS, C. T. 1991. EXTRUSIVE CARBONATITES FROM THE UYAYNAH AREA, UNITED-ARAB-EMIRATES. *Journal of Petrology*, 32, 1143-1167.
- YOGODZINSKI, G. M., BROWN, S. T., KELEMEN, P. B., VERVOORT, J. D., PORTNYAGIN, M., SIMS, K. W. W., HOERNLE, K., JICHA, B. R. & WERNER, R. 2015. The Role of Subducted Basalt in the Source of Island Arc Magmas: Evidence from Seafloor Lavas of the Western Aleutians. *Journal of Petrology*, 56, 441-492.
- YOGODZINSKI, G. M., KAY, R. W., VOLYNETS, O. N., KOLOSKOV, A. V. & KAY, S. M. 1995. MAGNESIAN ANDESITE IN THE WESTERN ALEUTIAN KOMANDORSKY REGION - IMPLICATIONS FOR SLAB MELTING AND PROCESSES IN THE MANTLE WEDGE. *Geological Society of America Bulletin*, 107, 505-519.
- ZHANG, C. L., LI, Z. X., LI, X. H., YE, H. M., WANG, A. G. & GUO, K. Y. 2006. Neoproterozoic bimodal intrusive complex in the southwestern Tarim Block, Northwest China: Age,

geochemistry, and implications for the rifting of Rodinia. *International Geology Review*, 48, 112-128.

ZHOU, J. X., MALCOLM, M. T. & KORSCH, R. J. 1994. Characterisation of a plume-related ~800 Ma magmatic event and its implications for basin formation in central-southern Australia. *Earth and Planetary Science Letters*, 121, 349-367.